Study of the coupling between turbulent convection and solar-like oscillations

Jordan Philidet

PSL UNIVERSITÉ PARIS

THÈSE DE DOCTORAT
DE L'UNIVERSITÉ PSL

Préparée à Observatoire de Paris

Study of the coupling between turbulent convection and solar-like oscillations

Soutenue par
Jordan Philidet
Le 08 Septembre 2021

École doctorale n°127
Astronomie et Astrophysique en Ile-de-France

Spécialité
Astrophysique

Composition du jury :

Marie-Christine Angonin Professeure, Observatoire de Paris (SYRTE)	*Présidente*
Jørgen Christensen-Dalsgaard Professor, Aarhus University	*Rapporteur*
Hiromoto Shibahashi Professor, University of Tokyo	*Rapporteur*
Laurent Gizon Professor, Max-Planck Institute for Solar System Research	*Examinateur*
Marc-Antoine Dupret Professor, Université de Liège	*Examinateur*
Friedrich Kupka Professor, Unversity of Applied Sciences Technikum Wien	*Examinateur*
Marie-Jo Goupil Astronome, Observatoire de Paris (LESIA)	*Co-directrice de thèse*
Kevin Belkacem Chargé de recherche, Observatoire de Paris (LESIA)	*Co-directeur de thèse*

l'Observatoire de Paris | PSL

Oui, si le souvenir, grâce à l'oubli, n'a pu contracter aucun lien, jeter aucun chaînon entre lui et la minute présente, s'il est resté à sa place, à sa date, s'il a gardé ses distances, son isolement dans le creux d'une vallée, ou à la pointe d'un sommet, il nous fait tout à coup respirer un air nouveau, précisément parce que c'est un air qu'on a respiré autrefois, cet air plus pur que les poètes ont vainement essayé de faire régner dans le Paradis et qui ne pourrait donner cette sensation profonde de renouvellement que s'il avait été respiré déjà, car les vrais paradis sont les paradis qu'on a perdus.

Marcel Proust

Acknowledgements

My thanks go first to the members of my defense committee, for having accepted to take part in my jury. Special thanks go to the two referees, Joergen Christensen-Dalsgaard and Hiromoto Shibahashi, for having had the patience to go through this manuscript in great detail, and for the constructive criticism that it has received in the process. The other members of the jury are also to be thanked of course, including Marc-Antoine Dupret and Friedrich Kupka for a very interesting discussion during the defense; Laurent Gizon, not only for an equally constructive discussion, but also for having given me the opportunity to pursue my academic career with him in Göttingen; and naturally Marie-Christine Angonin, for having accepted to preside over the jury. I would also like to take this opportunity to thank Hans Ludwig, with whom I have the pleasure of collaborating, and for his kind invitation to Heidelberg, which I thoroughly enjoyed. To all of you, my warmest thanks.

Ce travail de thèse a beau être présenté en anglais, il serait néanmoins impensable que ceux et celles qui doivent en être crédité le soit dans cette langue; les Anglais n'ont pas plus le monopole du coeur que Mitterrand, après tout. Ma plus chaleureuse gratitude va d'abord à mes deux directeurs de thèse, qui ont accepté d'ouvrir la porte du monde académique au pauvre petit étudiant éperdu que j'étais il y a trois ans, et sans qui ce voyage n'aurait pas été possible. Kévin, tout d'abord, qui a eu la patience de subir les assauts répétés de mes incessantes questions, dont l'insatiable curiosité a largement contribué à alimenter la mienne, et avec qui, au delà du point de vue scientifique, j'ai eu un immense plaisir à travailler quotidiennement. Marie-Jo, ensuite, pour sa capacité à toujours mettre le doigt sur 'la' question essentielle, pour sa rigueur scientifique absolument exemplaire et dont j'ai eu beaucoup à apprendre, et enfin pour sa contagieuse bonne humeur et sa gentillesse extraordinaire. Ces trois ans n'auraient pas eu la même saveur et ne m'auraient pas appris autant sans vous deux; c'est d'autant plus vrai de la seconde moitié, pendant laquelle l'encadrement que vous avez dispensé a confiné à la perfection. Pour ça, et pour, je l'espère, de nombreuses autres années à venir, merci.

Je tiens à étendre ces remerciements aux collègues du Pôle Etoile du LESIA plus généralement. La peine qui est celle de tous les doctorants est moins rude à supporter lorsqu'elle est partagée, alors un grand merci à Kévin BB, Guillaume, Pierre, Keegan, Victor, Steven, Charlotte et Maëlle. Merci également à Réza, Caroline, Benoît, Rhita, Claude, Coralie, Daniel, Eric, Yveline et Richard, que j'ai eu beaucoup de plaisir à côtoyer pendant trois ans, sans qui les repas et pauses café auraient été beaucoup moins intéressants, et grâce à qui j'ai pu, par moments et au fil de nos discussions, jeter un oeil furtif au plus profond des insondables arcanes du fonctionnement de la recherche française. Grâce à vous tous, je garde un souvenir aussi cher qu'inoubliable de mon passage au LESIA. J'en profite aussi pour remercier Frank, avec qui j'ai passé de très bons moments, que ce soit à Meudon, à Midgar ou à Arkham.

Un immense merci également à tous ceux et celles qui m'ont supporté/soutenu tout au long de ces trois années, que ce soit en présentiel ou par Zoom. Merci aux colocs de la première heure, François et Val (et évidemment Andréane et Constance, félicitations à vous tous encore une fois !), sans qui ma première année de thèse aurait été bien plus morne, et que j'ai été désolé de devoir quitter pour des cieux plus meudonnais. Merci à Tim et Giulia (je ne sais pas comment on dit bon courage en russe, mais bon courage !), et à Quentin (viel Glück, ça je sais dire). Merci aux camarades du seul et vrai An Zéro : Julie, Pierre et Anise (grâce à qui je sais un peu plus ce qu'il se passe dans le vrai monde réel), Mylène, Florian et Aymeric (force et courage pour votre dernière année !), et Erwan bien sûr (notre papa à tous, enfin presque tous !). Merci à Raph, Nat, Julien et Gaylor, pluie de coeurs violets sur vous, et à l'année prochaine ! From Kald'hun and me, a huge thank you to Keegan (what a storyteller !) and Guillaume again, as well as Julianna, Sara, Giorgos and Christina : see you all in Aendrim !

Enfin, je ne saurais clore ces remerciements sans une mention spéciale à ma famille, que ce soit la branche rhodanienne ou la branche ligérienne, pour tout le soutien et l'amour qu'elle m'a prodigué. En particulier – et peu importe que ce soit le plus gros cliché de l'histoire des remerciements de thèse –, je ne saurais jamais vraiment assez remercier mes parents, qui m'ont toujours encouragé à suivre la voie qui me plaisait, quelle qu'elle fût, et à qui revient, en un sens, une partie du mérite de ce travail. Et finalement, merci aussi aux deux versions 2.0 de moi-même : Quentin (gamsahamnida comme on dit, et pense à moi quand tu seras millionaire !) et Nathan

(t'inquiète pas, je suis sûr que la LDC c'est pour bientôt).

Thesis abstract

Asteroseismology has revolutionised our understanding of stellar interiors, through the observations of oscillations on the surface of stars. In solar-like oscillators, which exhibit a convective envelope, the turbulent motions caused by convection have a substantial impact on the properties of the acoustic modes, whether on their frequencies or their amplitude. This impact results from a turbulence/oscillation coupling, which must therefore be understood and realistically modelled in order to allow for accurate seismic diagnosis. In turn, this coupling offers a way to constrain the little-understood properties of convection using the observed acoustic mode properties. This last point forms the overarching motivation behind the work presented in this thesis.

The first part of this thesis focuses on the asymmetry displayed by the line profiles of solar-like oscillations, which carries the signature of the localisation of the driving source close to the surface of the star. In this context, I developed a formalism designed to give quantitative predictions for solar-like mode asymmetry, and to directly relate the observed asymmetries to the underlying properties of turbulence in this region. Applying this formalism to the solar case allowed me to successfully reproduce the observations throughout the entire p-mode spectrum for spectroscopic measurements, as well as in the low-frequency part of the spectrum for photometric measurements. In particular, it led me to the determination of the sign of the asymmetry depending on the stochastic excitation occurring above or beneath the photosphere. It also allowed be to shed a new light upon the issue of asymmetry reversal between the velocity and intensity measurements.

In a second part, I interested myself with the modelling of the turbulence/oscillation modelling more generally. I investigated Lagrangian stochastic models of turbulence as an alternative way, compared to more traditional approaches, to model the coupling between turbulent convection and solar-like oscillations. First, a linear perturbative treatment of this class of models led me to establish a wave equation which, by construction, contains a stochastic part representing the impact of turbulence on the modes. This stochastic wave equation includes the effect of turbulence, and therefore the effect of the coupling with oscillations, in a consistent way, while allowing for the introduction of a realistic model of turbulence, taking into account the large range of time and spatial scales characterising stellar turbulent convection. This formalism then allowed me to simultaneously build physically-grounded prescriptions for the driving and damping of the modes, as well as for the modal part of the surface effects. In parallel, I developed a more direct numerical implementation of Lagrangian stochastic models, which allows, in conjunction with my analytical formalism, to explore the impact of the physical parameters of turbulent convection on the observed properties of the solar-like modes. I propose a test case where exact analytical results can be derived, and the close agreement reached between those and numerical results validates this implementation.

Résumé de la thèse

L'astérosismologie a révolutionné notre compréhension des intérieurs stellaires, grâce à l'observation des oscillations à la surface des étoiles. En ce qui concerne les oscillateurs de type solaire, qui possèdent une enveloppe convective, les mouvements turbulents dus à la convection ont un impact important sur les propriétés des modes acoustiques, tant du point de vue de leur fréquence que de leur amplitude. Cet impact résulte d'un couplage entre convection et oscillations, qui doit donc être compris et correctement modélisé pour permettre des diagnostics sismiques fiables dans ces étoiles. En retour, ce couplage offre l'opportunité d'utiliser les propriétés observées des modes pour contraindre la convection stellaire – dont les propriétés restent encore relativement mal comprises à ce jour. C'est ce dernier point qui constitue la motivation sous-tendant le travail présenté dans cette thèse.

La première partie de cette thèse se concentre sur l'asymétrie exhibée par les profils des modes dans le spectre des oscillateurs de type solaire, qui porte la signature de la localisation de leur source d'excitation proche de la surface de l'étoile. Dans ce contexte, j'ai développé un formalisme conçu pour fournir des prédictions quantitatives concernant ces asymétries, mais également pour relier directement les asymétries observées aux propriétés sous-jacentes de la convection turbulente dans cette région. L'application de ce formalisme au cas du Soleil m'a permis de reproduire les observations à travers tout le spectre des modes acoustiques pour les mesures spectroscopiques, ainsi que pour les modes acoustiques de basse fréquence pour les mesures photométriques. En particulier, elle m'a permis de déterminer la dépendance du signe de l'asymétrie en fonction de la position de la source relativement à la photosphère, ainsi que d'apporter un éclairage nouveau sur la question de l'inversion d'asymétrie entre les observations effectuées en vitesse et en intensité.

Dans une seconde partie, je me suis penché sur la question de la modélisation du couplage turbulence/oscillation de manière plus générale. J'y examine les modèles de turbulence Lagrangiens stochastiques en tant qu'alternative aux approches traditionnelles pour le traitement du couplage entre convection turbulente et oscillations de type solaire. Premièrement, un traitement perturbatif linéaire de ce type de modèle m'a permis d'exhiber une équation d'onde possédant, par construction, un caractère stochastique représentant l'impact de la turbulence sur les modes. Cette équation d'onde stochastique présente l'avantage d'inclure dès le début l'effet de la turbulence, et par suite celui du couplage, de manière cohérente, tout en permettant l'introduction d'un modèle de turbulence réaliste, et prenant en compte le large éventail d'échelles temporelles et spatiales caractérisant la convection turbulente stellaire. Ce formalisme m'a ensuite permis de construire une prescription simultanée, sur la base de relations de fermeture physique, pour le taux d'excitation et d'amortissement des modes acoustiques, mais également pour la partie modale des effets de surface. En parallèle, j'ai développé une implémentation numérique plus directe des modèles Lagrangiens stochastiques, qui permet, en conjonction avec mon formalisme analytique, d'explorer l'impact des paramètres physiques contrôlant la convection turbulente sur les propriétés observées des modes de type solaire. Le très bon accord obtenu en comparant les résultats numériques à un cas test dans le cadre duquel des résultats analytiques exacts peuvent être établis m'a permis de valider cette implémentation.

Contents

List of Figures

Acronyms

BFGS Broyden-Fletcher-Goldfarb-Shanno. 238, 239

BiSON Bi-State Optical Network. xiii, 49, 90

CDF Cumulative Density Function. 228

CFL Courant-Friedrichs-Lewy. 226

CoRoT COnvection, ROtations et Transits planétaires. xvii, 54, 58, 71

CPBL Convective Planetary Boundary Layer. 158, 250

CSPM Corrective Smoothed Particle Method. 233

DNS Direct Numerical Simulation. 9–11, 14, 172

ED-QNA Eddy-Damped Quasi-Normal Approximation. 28

GGM Gas-Γ_1 Model. xiii, 63–67, 157, 242–244, 249

GLM Generalised Langevin Model. 173–175, 178, 273

GOLF Global Oscillation at Low Frequencies. xiii, 45

GONG Global Oscillation Network Group. xiii, 60, 61, 63, 78, 140

HR Hertzsprung–Russell. xviii, 57, 63, 84

IPM Isotropisation of Production Model. 176

JWKB Jeffreys-Wentzel–Kramers–Brillouin. 287

LES Large-Eddy Simulation. 10–13, 59, 60, 73, 152, 157, 183, 225, 251

MCMC Markov Chain Monte-Carlo. 237–239

MDI Michelson Doppler Imager. xiii, 79, 81, 82

MHD MagnetoHydroDynamics. xviii, 10

MLE Maximum Likelihood Estimator. 237–239

MLT Mixing-Length Theory. xiii, 4, 16, 18–21, 23–25, 28, 29, 50, 54, 56–60, 62, 63, 65–67, 72, 73, 157, 158, 183, 251

PCM Plume Closure Model. 103

PDF Probability Density Function. xiv, xviii, 28, 72, 73, 158–171, 173, 174, 176, 178–183, 185, 192, 194, 195, 227–229, 237, 239, 248, 250, 252, 263–265, 274, 275, 277, 278, 283

PLATO PLAnetary Transits and Oscillations. xvii

PT-MCMC Parallel-Tempered Markov Chain Monte-Carlo. 239

QNA Quasi-Normal Approximation. 27, 103, 202

RANS Reynolds-Averaged Navier-Stokes. 157, 158

RGM Reduced-Γ_1 Model. xiii, 63–67, 157, 242–244, 249

RLM Refined Langevin Model. 178, 273, 274, 276, 278

SDE Stochastic Differential Equation. xiv, 72, 73, 158, 166, 168, 170, 175, 177, 178, 182, 185, 187, 188, 191, 226, 229, 230, 244, 246, 248, 251, 252, 273, 274, 276, 278

SGS Sub-Grid Scales. 11, 12

SLM Simplified Langevin Model. 173, 175, 176

SoHO SOlar and Heliospheric Observatory. 81, 84, 90

SPH Smoothed Particle Hydrodynamics. xiv, xviii, 182, 189, 191, 226, 227, 229–232, 234, 236, 244, 246, 248, 251, 288

SPM Sun PhotoMeters. 84, 90

TESS Transiting Exoplanet Survey Satellite. xvii

Foreword

Asteroseismology has enabled us to make a significant leap forward in our understanding of the physics of stellar interiors. Stars play the role of a resonant cavity for the waves that they feature, so that these waves take the form of resonant global modes. The frequencies of these modes carry the signature of the mechanical and thermal structure of the star in which they develop, thus allowing us to probe the stellar interior without having direct observational access to it. But the Fourier power spectrum of these oscillations gives us access to more than just their frequencies, it also provides us with the shape of their line profile in the Fourier domain. In the case of solar-like oscillations – that is, oscillations featuring the same behaviour and properties as the oscillations of the Sun –, these line profiles bear the mark of the energetic processes pertaining to the oscillations – how they are driven, and how they are damped. These energetic aspects are tightly related to the physics of the convective envelope in these stars, and more specifically of their highly turbulent superficial layers. The same way mode frequencies tell us a lot about stellar structure, mode line profiles tell us as much about the behaviour of the turbulent convection just beneath the surface of solar-like stars.

Since the early days (only 60 years ago!), when solar "5-minute oscillations" had just been discovered, we have come far. Observations of solar-like oscillations have become increasingly accurate, and have spanned across increasingly long periods of time. As a result, observed power spectra are now considerably more resolved, and contain substantially more information, than before. Not only have thousands of modes now been resolved for the Sun, but modes are also being observed in the spectrum of an ever-increasing number of other solar-like stars. The advent of the space-borne mission CoRoT, shortly followed by *Kepler*, as well as the more recent mission TESS, has made this number quite literally explode, going from one (the Sun) to several thousands in a matter of years. And the road does not stop here, since the mantle is about to be picked up by the PLATO mission in a few years, bringing with it the promise of yet another blow in the amount of seismic data at our disposal. The fact that one has to plot the evolution of the number of known oscillators available for study on a logarithmic plot is perhaps the clearest sign of the vigour currently characterising the field of asteroseismology. And of course, the larger the amount of data, and the more accurate the data is, the more information can be extracted on the physics underlying the oscillations, and the stars at the surface of which they are observed.

But in order for this incredible wealth of data to be exploited, our theoretical understanding of solar-like oscillations, and of how their properties relate to those of the medium in which they develop, has to be continuously improved. This is particularly the case when it comes to the question of how the properties of the modes relate to the properties of turbulent convection in solar-like stars. Our ability to use the observed characteristics of solar-like mode line profiles to learn more about the behaviour of the convective envelope in these stars is contingent on our theoretical understanding of the coupling between the two: one cannot evolve much faster than the other. This, in one sentence, summarises the overarching motivation behind the projects that I undertook during my PhD, and that I present in this thesis: *to build a theoretical framework in which the properties of turbulent convection can be constrained using the observed line profile of solar-like modes of oscillation.*

The first project I undertook in this context has to do with an aspect of observed solar-like mode line profiles that has not recently received as much attention as others – like their amplitude or their linewidth for instance –, namely the asymmetry they feature in the Fourier domain. Since observations have uncovered this asymmetry, first in the Sun, and very recently in other solar-like oscillators observed with the *Kepler* telescope, it was discovered that this asymmetry mainly stems from a combination of two different aspects of the physics of the mode: the fact that the source of excitation of the modes is localised in a thin layer just beneath the surface of the star; and the correlation that exists between the motions entailed by the resonant modes and those due to the convective background noise, also close to the surface of the star. A puzzling aspect of mode asymmetry is the observation that they are not the same depending on how the modes are observed, through spectroscopy (i.e in terms of surface velocity), or through photometry (i.e in terms of emergent intensity). Not only are the asymmetries not the same between the two observables, they are even reversed in sign. Upon discovery, this was dubbed the "asymmetry reversal puzzle", and several conflicting explanations have been proposed to explain it. Solving this puzzle is

essential in order to understand how – and why – asymmetries vary across the Hertzsprung–Russell (HR) diagram: at the present time, asymmetries in solar-like oscillators other than the Sun can only be observed in intensity.

Observed asymmetries can be used to constrain both the properties of the source of excitation, and of the correlated background. But so far, the models that were developed to that end are extremely simplified; in particular, the source of excitation is almost systematically prescribed empirically, both in its radial dependence and its frequency dependence. By contrast, physical models have been developed for mode excitation for a long time, but mainly to account for the observed amplitudes of the modes. This first project, therefore, consisted in adapting these excitation models to yield not only theoretical predictions for the amplitude of the modes, but more generally a synthetic oscillation power spectrum from which the exact shape of the mode line profiles can be extracted, including their asymmetry. My goal, in taking on this first project, was to then compare the predictions made with this theoretical model to observations, in order to constrain the physical properties of the source of excitation. Conversely, the model I developed also contains the effect of the correlated background, so that it allowed me to determine the dominant process at hand in solar-like mode asymmetry. For the moment, I focused exclusively on the Sun, as a first validating step. First, I considered the solar oscillation power spectrum as observed spectroscopically, i.e in terms of surface velocity, because, for the Sun, it is the easiest to model. In a second part of the project, I also considered the solar oscillation spectrum as observed photometrically, i.e in terms of emergent intensity. This required to adapt my model to intensity measurements instead of simply velocity, and allowed me to tackle the asymmetry reversal puzzle.

The second project I undertook concerns turbulence–oscillation coupling as a whole, instead of focusing on one specific observational aspect of this coupling. Traditional approaches designed to model stellar convection and its interaction with pulsations in solar-like oscillators are either based on mixing-length theories, or else on 3D hydrodynamic or magnetohydrodynamic (MHD) simulations. These approaches show unavoidable limitations, among which the impossibility to include the full effect of the turbulent cascade in a realistic way. The starting idea behind this second project, therefore, was to exploit mesh-free, Lagrangian Probability Density Function (PDF) models – the kind of which has been used in the fluid dynamics community to model turbulence for a long time – in the context of stellar turbulent convection, to circumvent the limitations of classical approaches. In these models, the turbulent medium is no longer described by grid-based quantities pertaining to a flow, but by a set of fluid particles whose position and properties are tracked over time. Because of the turbulent nature of stellar convection, the particle properties evolve according to a system of stochastic differential equations. This method is coupled with a Smoothed Particle Hydrodynamics (SPH) procedure to extract the relevant mean flow quantities directly from the set of fluid particles. The stochastic evolution of the set of fluid particles is perfectly equivalent, from a statistical point of view, to the temporal evolution of the PDF of all Eulerian quantities pertaining to the turbulent convection. By construction, this PDF contains the information on both the turbulence and the oscillations. That means this method is perfectly suited for the study of the coupling between the two.

The first step of this second project was to derive the stochastic equations for the temporal evolution of the fluid particles that are relevant in the stellar context. Once this was done, I pursued two different avenues of research. First, I developed a code to numerically implement these methods. As a first step, I focused on a "1.5D" model in the sense that both vertical and horizontal velocities are modelled, but only their vertical position is accounted for. The simulated box features modes of oscillation that can be directly extracted from the simulation, including not only their frequency, but also the shape of their line profile. The second path I followed is more analytical: I used this Lagrangian stochastic formalism to derive an intrinsically stochastic, linear wave equation, governing the behaviour of the oscillating modes, while at the same time encompassing the impact of turbulent convection on the waves. This stochastic wave equation naturally contains the information on every aspect of turbulence–oscillation coupling: not only the effect on mode frequency (commonly referred to as "surface effects"), but also every energetic aspect of solar-like oscillations, namely the driving and damping of the modes by the turbulent convection.

The structure of this manuscript follows the summary given above. It is split into three parts. In Part I, I propose a short discussion designed to introduce the two subjects of this thesis: first the turbulent convection occurring in stellar interiors (Chapter 1); and secondly the stellar oscillations, with a particular focus on the core subject of the work presented in the main body of this thesis, namely the various ways in which turbulent convection and solar-like oscillations are entangled and coupled (Chapter 2). Emphasis will be put on the work already produced on the subject, the questions that have been answered, and those that have not. My motivations and goals, which I summarised above, will perhaps appear more clearly in the end of this first introductory part, and particularly

in Chapter 3. Part II is devoted to my work in the scope of the first project mentioned above, on solar-like mode asymmetry. I introduce the subject and the literature thereon in Chapter 4, while Chapter 5 is devoted to the theoretical development of the synthetic velocity power spectrum model on which I worked, as well as its application to the solar case, and Chapter 6 is devoted to the adaptation of this model to intensity measurements. In Part III, I present the work I produced in the scope of the second project mentioned above. I introduce the basics of the theory of stochastic processes in Chapter 7, which are central in the subsequent chapters. I then set out to describe how Lagrangian stochastic models can be applied to the case of solar-like oscillations. I present the analytical developments briefly described above in Chapter 8, while the numerical implementation of the aforementioned Lagrangian stochastic model is the subject of Chapter 9. Finally, I end each of the last two parts by summarising not only my findings, but also the perspectives opened by these findings, as well as the multiple open paths which I have yet to walk.

Part I

Introduction

1 Turbulent convection in the stellar context

Contents

> Etre toujours paisible, cela ne dépend pas plus du progrès que du fleuve ; n'y élevez point de barrage ; n'y jetez pas de rocher ; l'obstacle fait écumer l'eau et bouillonner l'humanité. De là des troubles ; mais, après ces troubles, on reconnaît qu'il y a du chemin de fait.
>
> Victor Hugo

Convection happens whenever a large temperature difference exists between two layers in a fluid, in the direction of gravity. From there, indeed, troubles; or to be more exact – albeit less literal –, any small displacement of a parcel of fluid, caused by a seemingly random local fluctuation, gives birth to an instability, and leads to motions of the fluid over distances similar to the largest scale of the system. This happens, for instance, in a pan full of water when the bottom is heated up; or in the lower Earth atmosphere, when the ocean or the ground is hot enough (in this context, it is referred to as a *Convective Boundary Layer*); or else, in certain regions of stellar interiors. Stellar convection is no different than convection in any other context[1], and is characterised by a very efficient mixing of all quantities pertaining to the fluid – in particular momentum, energy and chemical composition. For that reason, convection is key to understanding stellar structure and evolution.

But stellar convection is also incredibly hard to understand, and the reason is that it is characterised by very turbulent motions, hence my consistent association of the word "convection" with the word "turbulent" in this entire manuscript. As always when studying turbulence, the properties of the flow must be studied from a statistical point of view: the question is not "what is the velocity of the flow?", but "what is the average velocity of the flow, and how much, on average, does the actual velocity deviate from the mean?". The uncertainty regarding turbulence modelling is directly at the heart of the uncertainty regarding convection modelling in the stellar context.

The work presented in this thesis pertains to the interplay between these convective motions and stellar oscillations. Following the advice of the King to Alice, I start from the beginning, and devote this first chapter to an introductory discussion of stellar convection. This is in no way, naturally, an exhaustive account of our current understanding of every aspect of stellar convection. Rather, this chapter is structured in two parts. In a first part, I present how the phenomenon of convection naturally arises from first principles, and I outline some of its most general properties. In a second part, I focus on the various ways stellar physicists have found to describe and study

[1] I do not dare take the leap and state that the star itself is no different than the pan, because at least pans are not partially ionised, and do not host nuclear fusion reactions, however bad the cook is.

convective transport in the stellar context: 3D hydrodynamic simulations, as well as analytical models based on the Mixing Length Theory (MLT), or the more refined Reynolds-stress models.

1.1 Energy transport in stellar interiors

Stars, in the broadest definition of the term, are self-gravitating bodies comprised of a more or less ionised gas. In particular, stellar matter is sufficiently dense that it can be described as a continuous medium, and its motion modelled through the equations of hydrodynamics. Those are the fundamental equations governing the behaviour of the plasma constituting the stars, directly derived from first principles, and all phenomena described in this manuscript are, at some point or another, contained within these equations – although some digging may be necessary to unveil them. I give a detailed derivation of the equations of hydrodynamics in Appendix A. In particular, Equation A.36 governs the evolution of the internal energy of the fluid, with the divergence term representing all modes of non-local transport of energy, while the right-hand side contains all the source terms, which happen to be entirely due to the conversion of macroscopic kinetic energy into microscopic internal energy. In the stellar context, the transport terms are of particular interest, as they describe how the energy "created"[2] in the center of the star travels outwards to be finally radiated by its surface, allowing it to shine. Provided conduction is neglected – as I did in deriving Equation A.36 –, the transport of internal energy can be due to viscous transport, represented by the flux $\mathbf{F}^{\text{visc}}$ (Equation A.34), radiative transport, represented by the flux $\mathbf{F}^{\text{rad}}$, and convective transport, represented by the flux $\mathbf{F}^{\text{conv}}$ (Equation A.32). The question of which process dominates energy transport in a given region of the star is important to predict its evolution, and is the subject of the following section.

1.1.1 Prevalence of convective transport: the Schwarzschild criterion

Viscous transport can already be ruled out as a dominant contribution. Indeed, the prevalence of viscous effects can be measured by the Reynolds number associated to the flow, and which corresponds to the ratio between the advection and viscous terms in the Navier-Stokes equation (Equation A.24). The Reynolds number is defined by (e.g. Lesieur 2008)

$$\text{Re} \equiv \frac{UL}{\nu} , \tag{1.1}$$

where U is the characteristic velocity of the flow, L its characteristic length scale, and ν is the kinematic viscosity of the fluid. For a fully ionised hydrogen plasma, the kinematic viscosity may be estimated by $\nu \sim 1.2 \times 10^{-20} \times T^{5/2}\rho^{-1}$ m^2.s^{-1} (Miesch 2005). For instance, close to the surface of the Sun, this yields $\nu \sim 0.01$ m^2.s^{-1}. With typical velocities $U \sim 3$ km.s^{-1} and typical length scales $L \sim 3$ Mm, one would find Re $\sim 10^{12}$. For a rotating star, typical values of the Reynolds number would be $\sim 10^{16}$ (Kippenhahn and Weigert 1994). At any rate, in the stellar context, the Reynolds number characterising the flow is always much larger than unity, meaning that the effect of viscosity – and in particular viscous transport of energy – is negligible compared to the radiative or convective flux.

The question that remains now is this: on which condition is convective transport more efficient than radiative transport – or indeed, efficient at all? Equation A.32 shows that convective transport stems from the fact that parcels of fluid carry the enthalpy of the medium where they initially lie and transport it to other regions of the flow during their movement. More specifically, parcels that are travelling upwards take enthalpy from a hot region to a cold region. Once it is there, it gives away its enthalpy by cooling down. On the other hand, parcels that are travelling downwards take less enthalpy with them, precisely because they come from a cooler medium, therefore characterised by a lesser specific enthalpy. As a result, the enthalpy transported by the upwards travelling parcels is greater than the enthalpy transported by the downwards travelling ones, resulting in a net flux of enthalpy directed upwards. It is apparent, therefore, that in order for convective transport to be efficient, the medium has to allow for fluid parcels to travel as far as possible before giving away their enthalpy. This only happens if the medium is subjected to a *convective instability*, which I now describe.

[2] Naturally, energy cannot be created out of nowhere, although that would probably solve a lot of problems. This energy is actually stored in the form of potential energy in the bonds maintaining the integrity of the nuclei present in the center of the star, and is released when these nuclei undergo fusion reactions.

The question of whether a medium is unstable to convective motions can be formulated thus: when will a fluid parcel accidentally displaced upwards continue to travel upwards instead of falling back down? While being displaced, the parcel undergoes a change in density, due to the fact that it is travelling to a region characterised by a different thermodynamic state. Therefore, the answer is: the parcel will continue travelling upwards if it ends up with a lower density – or in other words, a higher temperature[3] – than that of its surroundings, because of the same buoyancy force that keeps balloons in the air. But when does that happen? If we consider that the parcel does not have time to exchange any heat with its surroundings during its upwards travel, then the thermodynamic transformation it undergoes is adiabatic. Therefore, if the parcel goes from a region characterised by a pressure p to a region characterised by a pressure $p + \delta p$, its temperature will change by

$$\delta T_{\text{parcel}} = \left(\frac{\mathrm{d}T}{\mathrm{d}p}\right)_{\text{ad}} \delta p \equiv \frac{T}{p}\nabla_{\text{ad}}\delta p \,, \tag{1.2}$$

where $\nabla_{\text{ad}} \equiv (\mathrm{d}\ln T/\mathrm{d}\ln p)_{\text{ad}}$ is called the *adiabatic gradient*, and only depends on the thermodynamic equation of state associated to the fluid. On the other hand, the background temperature 'felt' by the parcel will have changed by an amount

$$\delta T_{\text{medium}} = \left(\frac{\mathrm{d}T}{\mathrm{d}p}\right)_{\text{medium}} \times \delta p \equiv \frac{T}{p}\nabla_{\text{rad}}\delta p \,, \tag{1.3}$$

where δp is identical because mechanical equilibrium is reached at all times, and the background gradient $(\mathrm{d}\ln T/\mathrm{d}\ln p)_{\text{medium}}$ is equal to the radiative gradient because the background is in radiative equilibrium. Resulting from this is the following proposition: that a medium is subjected to a convective instability *if and only if* we have (Böhm-Vitense 1992)

$$\nabla_{\text{ad}} < \nabla_{\text{rad}} \,. \tag{1.4}$$

This criterion is known as the *Schwarzschild criterion* for convective instability. In regions where this criterion is verified, the convective instability can develop, and the energy is efficiently transported by convection. Although radiative transfer is still responsible for a non-negligible portion of the total energy flux, these regions are still called *convective zones*. On the other hand, regions where the Schwarzschild criterion is not verified exhibit a very inefficient convective transport of energy, and the energy flux is exclusively due to radiative transfer: they are called *radiative zones*.

1.1.2 Convective zones in stellar interiors

The question remains: when is the Schwarzschild criterion verified? For which type of stars, and where in the star? The plasma in stellar interiors behaves like an ideal gas to a satisfactory degree, so that its pressure p, density ρ, temperature T and molecular weight μ (assumed constant for the sake of this discussion) are related through

$$p = \frac{\rho R T}{\mu} \,, \tag{1.5}$$

where R is the ideal gas constant. Then, introducing the first adiabatic exponent $\Gamma_1 \equiv c_p/c_V$, where c_P and c_V are the specific heat per unit mass at constant pressure and volume respectively, and using the fact that $c_P - c_V = R$, one finds that the adiabatic gradient is simply (Böhm-Vitense 1992)

$$\nabla_{\text{ad}} = \frac{\Gamma_1 - 1}{\Gamma_1} \,. \tag{1.6}$$

For instance, for a monoatomic ideal gas, $\Gamma_1 = 5/3$, so that $\nabla_{\text{ad}} = 0.4$. However, this value drops substantially in ionisation regions (i.e. regions where the temperature is high enough to strip electrons away from atoms of a given element, but not so high that the element in question is completely ionised). Indeed, part of the energy

[3] The reason a lower density means a higher temperature relates to the fact that mechanical equilibrium can be considered to be reached instantaneously, and therefore the pressure associated to the parcel is identical to the pressure of its surroundings. At equal pressure, a hotter element is lighter. If the chemical composition of the fluid is also susceptible to vary, then the thermodynamic variance of the system is 3, and not 2, so that even at equal pressure, the temperature – which now depends on composition in addition to density –, does not necessarily decrease with density. Then the criterion derived here must be modified to account for adiabatic composition gradient.

provided to the gas will be used to ionise the gas, instead of heating it. As a result, the energy needed to increase the temperature of one kilogram of gas by one degree – which is the definition of c_V – is considerably higher in an ionisation region. Then $\Gamma_1 = R/c_V + 1$ becomes much closer to unity, and ∇_{ad} becomes much smaller. According to Equation 1.4, it results in the following statement: that *ionisation regions are more susceptible to convective instability* (Böhm-Vitense 1992).

I now turn to the radiative gradient. Under the assumption that the star behaves like a black body in radiative and mechanical equilibrium[4], then it is given by (Böhm-Vitense 1992)

$$\nabla_{\text{rad}} = \frac{3\pi\kappa_R p}{16\sigma g T^4} F^{\text{rad}} \,. \tag{1.12}$$

According to Equation 1.4, convective instability happens when the radiative gradient is sufficiently high, which we now see happens, for a given temperature T, if either the product $\kappa_R p$ or the radiative flux F^{rad} is high enough.

When is the product $\kappa_R p$ high? Roughly speaking, for a given optical depth[5], the opacity is inversely proportional to pressure. In the atmosphere, the opacity and pressure are both low. In deeper layers of the star, pressure increases, but if opacity remains sensibly the same, the pressure increase is not sufficient to put the radiative gradient above the instability threshold. If opacity increases steeply with depth, however, pressure is still high (because opacity in the atmosphere remains low, and $p \propto \kappa_R^{-1}$), and opacity is much higher as well. If the increase in opacity is steep enough, this can be sufficient to give rise to a convective instability. Therefore, *convective instability arises in regions where the opacity increases steeply with depth* (Böhm-Vitense 1992), rather than where the absolute opacity is high. It so happens that those precisely correspond to ionisation regions, which I already argued have a small adiabatic gradient, and are therefore even more likely to be unstable to convection.

When is the radiative flux high? This flux describes the amount of radiative energy which flows through a given layer *per unit surface*. As such, it is not the raw amount of radiative energy generated by nuclear fusion that is important, so much as the concentration in space of the region in which these reactions take place. In main-sequence stars, there are mainly two types of fusion reaction chains that can be responsible for the radiative flux coming out of the core, both of which ultimately lead to the fusion of hydrogen into helium. The pp-chain involves the direct fusion of two hydrogen nuclei into deuterium, and the generation rate of energy ϵ scales as T^4; the CNO-chain involves the fusion of hydrogen nuclei with heavier nuclei of carbon, oxygen and nitrogen, and its generation rate of energy is much more sensible to temperature, with $\epsilon \propto T^{16}$. As such, the pp-chain is the dominant process for stars with a cooler core – with temperature $T < 1.7 \times 10^7$ K –, while the CNO-chain prevails

[4] I recall that, in that case, the radiative flux F^{rad} is given by

$$F^{\text{rad}} = -\frac{4}{3\kappa_R \rho} \frac{\mathrm{d}B}{\mathrm{d}r} \,, \tag{1.7}$$

where κ_R is the Rosseland mean opacity per unit mass, defined by

$$\frac{1}{\kappa_R} \int_0^{+\infty} \frac{\mathrm{d}B_\lambda}{\mathrm{d}T} \,\mathrm{d}\lambda \equiv \int_0^{+\infty} \frac{1}{\kappa_\lambda} \frac{\mathrm{d}B_\lambda}{\mathrm{d}T} \,\mathrm{d}\lambda \,, \tag{1.8}$$

and κ_λ is the monochromatic opacity per unit mass at wavelength λ; and

$$B(T) = \int_0^{+\infty} B_\lambda(T) \,\mathrm{d}\lambda \,, \tag{1.9}$$

where $B_\lambda(T)$ is the Planck function associated to the wavelength λ, which represents the energy radiated per unit surface, solid angle, wavelength and time by a body at thermodynamic equilibrium, also referred to as *black body radiation*. It only depends on the temperature T of the body, and is given by

$$B_\lambda(T) = \frac{2hc^2}{\lambda^5} \frac{1}{\exp^{hc/\lambda kT} - 1} \,, \tag{1.10}$$

where h is the Planck constant, c the speed of light in vacuum, and k the Boltzmann constant. The total specific intensity associated to a black body is obtained by integrating the monochromatic specific intensity B_λ over all wavelengths, and yields

$$B(T) = \frac{\sigma}{\pi} T^4 \,, \tag{1.11}$$

where $\sigma = 2\pi^5 k^4/(15c^2h^3)$ is the Stefan-Boltzmann constant.

[5] The optical depth is a non-dimensional variable defined through its differential form by $\mathrm{d}\tau = -\kappa_R \rho \,\mathrm{d}r$, where r is the radial coordinate, and the minus sign ensures that τ decreases towards the surface. The optical depth can be thought of as the radial coordinate counted in units of the local photon mean free path.

for stars with a hotter core. In the latter case, because energy generation is so strongly dependent on temperature, it only occurs in a very concentrated region in the very center of the star, in which case the radiative flux is very high. On the other hand, in stars where energy is generated through pp-chains predominantly, energy generation occurs in a larger central region, and the radiative flux is much weaker. In light of Equation 1.4, it results that *the center of the star is subjected to convective instability if the core is hot enough for CNO-chains to be dominant over pp-chain in energy generation* (Böhm-Vitense 1992).

The above discussion allows me to draw the following qualitative picture

- hot stars where $T_{\rm eff} \gtrsim 9000$ K feature a convective core, because CNO-chain reactions prevail in the core of stars with such effective temperatures. On the other hand, the star is so hot that all the hydrogen and helium is already ionised, even close to the surface, so that there cannot be any convective instability in the envelope;

- cooler stars with $T_{\rm eff} \lesssim 9000$ K have a radiative core, because pp-chains prevail over CNO-chains. However, these stars are cold enough to feature ionisation regions in their envelope, meaning they have a convective envelope. More precisely, in the effective temperature range [7000 – 9000] K, there is only a hydrogen ionisation region, which means the convective zone is very thin. Below 7000 K, the hydrogen ionisation region is adjacent to the first helium ionisation region (i.e. the region where He is partially ionised in He^{+}), which is in turn adjacent to the more deeply located second helium ionisation region (i.e. the region where He is partially ionised in He^{++}), so that the convective envelope is much thicker;

- in the intermediate range, stars are too hot to have ionisation-driven convective instabilities, and too cold to feature core convection: these stars are mainly radiative;

- in very cool stars, like M stars for instance, the hydrogen and helium convective regions extend so far down the center that they actually take up the entire volume of the star. These stars are entirely convective – with the exception of a very thin radiative surface layer, where the density is too low to allow for an efficient convective transport;

- in evolved stars, there may be ionisation regions for elements other than hydrogen and helium, in which case the corresponding convective zones are the regions where the temperature lies within the range where the element in question is partially ionised. This is also the case for main-sequence stars of spectral type O or B for instance, which feature iron ionisation zone in regions where $T \sim 2 \times 10^6$ K.

In the rest of this manuscript, I will interest myself with solar-like stars, with masses and effective temperatures similar to the Sun. These stars – and the Sun in particular – fall in the second category, and possess a convective envelope (with an outer part due to hydrogen ionisation, and an inner part due to helium ionisation), and a radiative core.

1.2 Modelling convection: a complicated task

As it transpired from Section 1.1, in regions that are prime for a convective instability, the convective flux plays a crucial role in transporting energy outwards. This has a number of implications as regards stellar structure and evolution. For instance, the extra energy loss due to convection 'forces' the star to increase its internal energy generation rate in order to stay at thermodynamic equilibrium. This requires increasing the core temperature, which the star does by contracting: convection makes stars shrink. In turn, because of the increase in the core temperature, the luminosity of the star is also increased. The presence of a convective flux also decreases the part played by the radiative flux in the total energy flux. This means that the actual temperature gradient is less steep than what it would be without convection. Therefore, the density profile in the interior of the star is also impacted by convection.

In addition, while the previous discussion focused on the energetic aspects of convection, it must be understood that such large-scale convective motions also transport momentum, as represented by the term $\partial_i(\rho u_i u_j)$ in Equation A.24, and therefore also angular momentum. In parallel, convection also transports chemical elements, in such a way that convective zones can be considered fully mixed – meaning that their chemical composition is uniform. Convective motions are also known to penetrate, by inertia, into neighbouring radiative zones over a certain distance, so that the convective transport also has a non-negligible impact just outside the convective

zones – a phenomenon known as *convective overshooting* if the convective elements quickly loose their thermal integrity, or *convective penetration* if they travel further away and transfer their enthalpy much less efficiently to the convectively stable background (Zahn 1991). This convective mixing is susceptible to drastically alter the later evolutionary stages of the star, by changing the spatial distribution of fuel in its interior.

These quick considerations are enough to make it clear that the modelling of the convective flux – both in terms of energy and momentum – is a crucial task for improving the accuracy of our stellar evolutionary and structural models. Sure enough, the modelling of convection has been the subject of considerable efforts, which I outline in the following.

1.2.1 Exact equations and Large-Eddy Simulations

The exact equations

The equations of hydrodynamics, governing the motions of the fluid, are expressed in their exact form by the continuity equation (Equation A.15), the Navier-Stokes equation (Equation A.24) and the energy equation (Equation A.36), which stem from the conservation of mass, momentum and energy respectively. I reproduce them for more clarity here

$$\frac{\partial \rho}{\partial t} + \frac{\partial \rho u_i}{\partial x_i} = 0 \,, \tag{1.13}$$

$$\frac{\partial \rho u_i}{\partial t} + \frac{\partial (p\delta_{ij} + \rho u_i u_j - \sigma_{ij})}{\partial x_j} = \rho g_i \,, \tag{1.14}$$

$$\frac{\partial \rho e}{\partial t} + \frac{\partial}{\partial x_i}\left(\rho h u_i + F_i^{\mathrm{rad}} + \sigma_{ij} u_j\right) = u_i \frac{\partial p}{\partial x_i} - u_i \frac{\partial \sigma_{ij}}{\partial x_j} \,, \tag{1.15}$$

where I recall that ρ is the fluid density, u_i its velocity, p the gas pressure, σ_{ij} the viscous tensor, g_i the gravitational acceleration, e the internal energy per unit mass, h the enthalpy per unit mass and F_i^{rad} the radiative flux. I also recall that the decomposition of the stress force is such that $-p\,\delta_{ij}$ constitutes its isotropic part, and σ_{ij} its deviatoric part. As such, the viscous tensor is constrained to be traceless; however, up to now, I have given no further information on σ_{ij}, which I have left in an undetermined form. As it happens, it can be expressed solely in terms of the velocity field, in the form (e.g. Lesieur 2008)

$$\sigma_{ij} = \nu\rho\left(\frac{\partial u_i}{\partial x_j} + \frac{\partial u_j}{\partial x_i}\right) - \frac{2}{3}\nu\rho\delta_{ij}\frac{\partial u_k}{\partial x_k} \,, \tag{1.16}$$

where ν is the kinematic viscosity of the fluid, and $\mu \equiv \nu\rho$ the dynamic viscosity coefficient. It is immediately seen that the viscous stress tensor is traceless, as indicated above. If the dynamic viscosity μ is known, σ_{ij} is in closed form.

This set of equations must be supplemented with a model for the pressure p. As density ρ and internal energy e are both modelled, all one needs to do is to add an equation of state of the form $p = p(\rho, e)$ to the system. For instance, the ideal gas law (Equation 1.5) can be used[6], where $T = e/c_V$. Concerning the radiative flux F^{rad}, one would also need to add a treatment for radiative transfer. We already saw that if the gas can be considered at local thermodynamic equilibrium, the radiative flux is given by Equation 1.12, as a function of Rosseland mean opacity per unit mass κ_R, density ρ and temperature T. As for pressure p, the opacity κ_R can be obtained through a suitable equation of state[7] in the form $\kappa_R = \kappa_R(\rho, e)$, in which case F^{rad} is now known as a function of modelled variables

[6]The ideal gas law also requires the molecular weight, or equivalently the chemical composition, to be known. This would be true of any equation of state: the indetermination of the chemical composition increases the variance of the system, thus requiring an additional constraint. Either the composition can be considered known in advance, or a transport equation for chemical composition must be derived. I will follow the former course in this discussion, and consider the chemical composition known.

[7]In fact, except for very approximate relations valid only in certain regions of the star, there exists no such simple analytical relation for opacity. Physically, the opacity κ_R represents the fractional change per unit length in specific intensity of a photon flux, and is due to the absorption of the photons by the medium, and especially by the electrons – the energy of the destroyed photon then being made available to the matter for ionisation, dissociation or heating. The total opacity is therefore the result of all possible state transitions for the electrons present in the medium – with the numerous bound-bound transitions allowed by the quantisation of bound energy states around atoms resulting in a multitude of frequency-selective *absorption lines*, while bound-free transitions (i.e. ionisation processes) and free-free transitions (if the gas is already fully ionised) are responsible for *continuous absorption* (in terms of frequency). Because of the complexity of this picture, κ_R is usually provided as a function of two independent thermodynamic variables – for instance density and temperature, but this choice is not unique – in the form of opacity tables. Fundamentally, however, this is no different than giving an analytical expression, and still constitutes an equation of state.

only. Of course, the assumption that the gas is at local thermodynamic equilibrium is a strong one, and while it is valid in the bulk of the star, it must be supplemented with a more realistic treatment of radiative transfer in the superficial layers of the star, close to its atmosphere. For the sake of the following discussion, I leave this matter aside, and consider that the radiative flux is in closed form.

On the applicability of Direct Numerical Simulations, or lack thereof

The entire system of equations described above is in closed form, and with the exception of rotation or magnetic fields – which can be incorporated into these equations if need be –, the gas-related behaviour in the stellar interior, including convection, is contained exactly and in its entirety within these equations. One could therefore naively ask oneself: why are we even discussing this? Modelling convective transport seems to be a matter for Direct Numerical Simulations (DNS thereafter), where the integration of the above differential equations forward in time should tell us anything we might want to know about convection. Then, the only remaining complications would concern the initial state from which one should start, the boundary conditions which one should enforce, and the numerical scheme one should adopt for the integration in time.

As the reader is no doubt aware, the answer to this naive question is this: that the computational cost of such an operation would be so tremendously enormous that it cannot even remotely begin to be applicable in the stellar context. The reason for this, as we will now see, is the highly turbulent nature of the flow. I briefly touched upon the subject of the Reynolds number characterising the gas flow in stellar interiors in Section 1.1.1, only to point out its high typical value. By construction of the Reynolds number, this means that the advection term in the Navier-Stokes equation (Equation 1.14) largely dominates the linear contribution from the viscous stress force, and therefore the equation of motion is strongly non-linear. As a consequence, the different scales of motion are coupled together, and can exchange energy[8]. As such, even if the flow is initially characterised by a very coherent velocity field with only one typical scale, the kinetic energy will eventually be distributed over a wide range of scales, and the flow will feature a much more complicated structure. Resulting from these considerations is the familiar observation that *flows with a high Reynolds number are very turbulent*.

More specifically, the flow of kinetic energy from scale to scale is described by the idea of *turbulent cascade*, first introduced by Richardson (1922). The idea is that kinetic energy from the mean flow is injected in the turbulence at the largest scale of motion – corresponding to the mean-flow scale –, and is then transferred to smaller and smaller scales, until the scale of motion becomes so small that viscous effects can no longer be neglected, and the kinetic energy is dissipated into heat. This cascade of energy from large to small scales reaches an equilibrium when the rate at which energy is injected at large scales equals the rate at which it is dissipated at small scales. Can the smallest scale of turbulence be quantified? The answer is given by the historical work by Kolmogorov (1941), and happens to be 'yes'. One of the fundamental hypotheses underlying this work is the assumption that all the information about the specific geometry of the large-scale eddies – imposed by the geometry of the flow – is lost along the way as energy is transferred through the turbulent cascade. As such, the statistics of the small-scale flow take a somewhat universal form, in the sense that they should exhibit some degree of similarity. The important quantities characterising the turbulent cascade are the rate ϵ at which energy is injected at large scales, and the viscosity ν controlling the small scales at which it is dissipated. This led the author to his *first similarity hypothesis*, which can loosely be expressed in the following terms: for flows with a high Reynolds number, there exists a scale $l_{\max}$ such that for any scale $l < l_{\max}$, the statistics of the flow take the form of a universal function of

[8]This statement may need a clearer definition of the notion of 'scales of motion'. An intuitive picture is to regard the flow as a superposition of vaguely defined regions – usually called *eddies* – over which the velocity field is somewhat coherent. These eddies are of very different sizes l, and large eddies are susceptible to contain smaller ones. These eddy-sizes are referred to as the *scales of motion* of the flow. However, a more rigorous definition can be constructed from the Fourier decomposition of the velocity field at a given time

$$\widehat{\mathbf{u}}(\mathbf{k},t) \equiv \frac{1}{\sqrt{2\pi}} \int \mathrm{d}^3\mathbf{x}\, \mathbf{u}(\mathbf{x},t) \exp^{-j\mathbf{k}\cdot\mathbf{x}} \,, \tag{1.17}$$

where $\mathbf{k}$ denotes a 3-dimensional wavevector. Instead of being described in real space, the velocity field is now described in wavevector space: for a given $\mathbf{k}$, the quantity $l \equiv 2\pi/|\mathbf{k}|$ is the scale of motion represented by this wavevector component, and $E(\mathbf{k},t) \equiv \left|\widehat{\mathbf{u}}(\mathbf{k},t)\right|^2$ is the specific kinetic energy per unit wavevector characterising this region of wavevector space, which gives a much firmer definition for the otherwise somewhat vaguely defined *energy of the eddies of size l*. An equation of transport *in wavevector space* for $E(\mathbf{k},t)$ can be derived from the Navier-Stokes equation (Equation 1.14), and the non-linear advection term gives rise to a non-local energy flux, meaning that kinetic energy can flow from scale to scale. This is really what is meant by the statement that, in high Reynolds number flows, *the different scales of motion are coupled together, and can exchange energy* – a statement that would not be true if the equation of motion were linear.

ϵ and ν only. The range $l < l_{\max}$ defines the *universal equilibrium range* of turbulence[9].

From these two parameters, a unique, universal typical length and velocity can be constructed (e.g. Pope 2000)

$$\eta \equiv (\nu^3/\epsilon)^{1/4} , \tag{1.18}$$

$$u_\eta \equiv (\epsilon\nu)^{1/4} , \tag{1.19}$$

which are the Kolmogorov scale and velocity respectively. It can be seen that the Reynolds number associated with the scale η is unity, meaning that the Kolmogorov scale actually represents the smallest, dissipative scale of turbulence. In order to quantify η, one still need to quantify ϵ. If l_0 is the size of the largest eddies, u_0 their typical velocity and τ_0 their typical timescale, then the rate at which energy is injected in the turbulent cascade is given, through dimensional arguments, by $\epsilon \sim u_0^2/\tau_0 \sim u_0^3/l_0$. Making the large-scale Reynolds number appear, one can write

$$\epsilon \sim \frac{\mathrm{Re}^3\nu^3}{l_0^4} . \tag{1.20}$$

Plugging Equation 1.20 into Equation 1.18, one finally obtains the ratio of the smallest to largest scales of turbulence as (Pope 2000)

$$\frac{\eta}{l_0} \sim \mathrm{Re}^{-3/4} . \tag{1.21}$$

In other words, *the higher the Reynolds number, the larger the range of length scales that need to be resolved in order to describe the entire turbulent cascade*.

Let me quickly compute an estimate of how ridiculously expensive this can become in the stellar context. For the above-mentioned value of the Reynolds number $\mathrm{Re} \sim 10^{12}$, we have $\eta/l_0 \sim 10^{-9}$. Roughly speaking, this means the number of grid points for a 3D DNS of turbulence, if one wished to resolve all of these scales, would be of the order of 10^{27}. The current record for the number of operations performed by a computer per second is held by the Fugaku supercomputer in Kobe, at 442 petaflops (`https://www.top500.org/`). It would take about 3×10^9 seconds, or 100 years, for this computer to advance the simulation *by one time step, and provided the size of the box is l_0 – i.e. provided the simulation is very local*. This is the reason why *there is no such thing as a Direct Numerical Simulation of stellar turbulent convection*: all such simulations are incapable of resolving all relevant length scales, and must be regarded as what they really are, *Large-Eddy Simulations*.

Large-Eddy Simulations (LES)

LES have been used to model convection in the stellar context ever since computers became fast and powerful enough to run the simulations in a reasonable amount of time, whether it be global simulations of an entire convection zone, or more local simulations focused on the transition region between a convection zone and a radiative zone – in particular the surface layers of a star with a convective envelope. Since the early 2D simulations of convection using only limited microphysical ingredients (see for instance the early works of Graham (1975) or Latour et al. (1976)), LES have been considerably refined, with simulations now ranging from 1D to 3D, more realistic treatments of radiative transfer (with the non-local, and sometimes non-grey equation of radiative transfer having long since replaced, for surface convection, the more simplistic diffusion approximation), and the inclusion of magnetic fields in the scope of the magneto-hydrodynamics (MHD) equations, as well as rotation. LES have been used to study, for instance, surface granulation (e.g. Stein and Nordlund 1998), the effect of convection on the surface abundances and the formation of spectral lines in stellar atmospheres (e.g. Allende Prieto et al. 2001, 2002; Asplund et al. 2000a,b; Asplund 2000; Asplund et al. 2004, 2005b,a), its interplay with rotation or magnetic fields in dynamo processes (e.g. Glatzmaier and Roberts 1995), or the overshooting into neighbouring radiative regions (e.g. Freytag et al. 1996; Tremblay et al. 2015; Kupka et al. 2018). The range of applications of LES for stellar convection is so vast that being exhaustive in that regard would require a volume of its own. I refer the interested

[9]This must not be confused with the *inertial subrange* of turbulence, for which the Kolmogorov second similarity hypothesis is needed. This second hypothesis states that there exists a lower limit scale $l_{\min}$ – in addition to the upper limit $l_{\max}$ – such that for any scale $l_{\min} < l < l_{\max}$, the statistics of the flow take the form of a universal function of ϵ only. This second hypothesis is stronger than the first one, because now the statistics are independent of ν, but on the other hand it is only valid in the inertial subrange $l_{\min} < l < l_{\max}$, instead of the larger universal range.

reader to the many reviews dedicated to that very question, among which Nordlund et al. (2009) or Kupka and Muthsam (2017) for instance.

However, let me discuss briefly the ways in which the resolution issue raised above is tackled in such simulations. In a DNS, nearly all of the computational efforts are focused on the small, dissipative scales, deep within the universal range of turbulence. But these scales only contain a negligible fraction of the total energy of the flow, while almost all of the energy is contained in the largest eddies (also called, as a result, the *energy-bearing* eddies). This observation naturally leads to the conclusion that only the largest scales need to be described by the exact equations of hydrodynamics, while the smaller scales – also referred to as the *subgrid scales*, SGS thereafter –, having more universal statistical properties, can be described by a much simpler model that does not require them to be resolved. It is useful to make a distinction between two different approaches, namely 1) the LES where the numerical viscosity inherent to the numerical scheme is *implicitly* expected to contain all phenomena occurring at scales smaller than the grid resolution, and 2) those where the SGS are *explicitly* modelled.

When it comes to modelling stellar convection, most LES fall into the first category. With a typical grid step of $\sim$ 10 km in local "box-in-a-star" simulations, and a typical Kolmogorov scale of $\sim$ 1 cm, the effective viscosity is some 6 orders of magnitude higher than the actual viscosity in the real system (see Table 1 of Freytag et al. 2012, for more details). Naturally, the picture is more dire still in global "star-in-a-box" simulations of an entire stellar convection zone. This effective viscosity – which I recall is not explicitly enforced in the integrated equations, but rather stems from the numerical scheme – is used to mimic the effect of all the unresolved scales. However, in order to lower the relative effect of these scales on the large-scale flow, and thus reduce the influence of this artificial dissipation, it is common practice to include *hyperdiffusion* – or *hyperviscosity* – in the scheme. For the sake of this short discussion, let me remark that the viscous term in the Navier-Stokes equation, which is given by the divergence of the viscous tensor (Equation 1.16), reduces in the incompressible limit (where $\boldsymbol{\nabla} \cdot \mathbf{u} = 0$) to

$$\frac{\partial \mathbf{u}}{\partial t} = ... + \nu \, \nabla^2 \mathbf{u} \, . \tag{1.22}$$

The hyperdiffusion approach (Borue and Orszag 1995, 1996) consists in replacing the Laplacian-based viscous force by an expression using a higher derivative of the velocity

$$\frac{\partial \mathbf{u}}{\partial t} = ... + \nu_H (-1)^{m+1} \nabla^{2m} \mathbf{u} \, , \tag{1.23}$$

where ν_H is referred to as the hyperviscosity, and m is an integer, usually equal to 2 or 4. The effect of this modification is best viewed in Fourier space, where the original $\nu \mathbf{k}^2 \widehat{\mathbf{u}(\mathbf{k})}$ is replaced by $\nu_H \mathbf{k}^{2m} \widehat{\mathbf{u}(\mathbf{k})}$. For large scales (i.e small values of $|\mathbf{k}|$), the dissipative effects are therefore reduced, while they are enhanced for small scales. Effectively, this causes the dissipative range to be narrower in wavevector space, thus reducing the amount of energy-containing $\mathbf{k}$-components (or modes) of the velocity. As a result, the effect of not resolving all the modes is drastically reduced, at the expense of the model equation not being the Navier-Stokes equation anymore. Hydrodynamic codes for stellar convection using hyperviscosity include, for instance, the `MURaM` code (Vögler et al. 2005), the `Stagger` code (Stein and Nordlund 1998; Magic et al. 2013), or the `MUSIC` code (Viallet et al. 2011, 2016).

An alternative to letting the numerical viscosity represent unresolved scales is to derive a model for the effect of the small scales on the large scales. In this approach, a spatial filtering operation is applied to the flow, in order to separate the total flow into a *filtered* component (corresponding to the large scales) and a *residual* component (corresponding to the small scales). The idea of spatial filtering makes this approach conceptually different than the one described above, which instead relies on a completely uncontrolled separation between the *resolved* and *unresolved* components. Now, the spatial filtering is explicit, and is independent from the resolution of the grid. This perhaps makes the term *Large Eddy Simulation* more befitting of this approach alone, while the one described above is more of a 'poorly-resolved DNS' approach. However, as we will now see, this approach also ultimately takes the form of an effective viscosity, so that this is more of a debate on semantics.

For the sake of this discussion, let me consider the velocity $\mathbf{u}(\mathbf{x}, t)$ as the only flow variable that needs to be modelled, and let me consider an incompressible flow. In an 'explicit' LES, a new variable $\overline{\mathbf{u}}(\mathbf{x}, t)$ is created beforehand, which is defined by

$$\overline{\mathbf{u}}(\mathbf{x}, t) \equiv \int \mathrm{d}^3\mathbf{x}' \; \mathbf{u}(\mathbf{x}', t) G(\mathbf{x} - \mathbf{x}', \mathbf{x}) \, , \tag{1.24}$$

where G is a filtering operator, whose properties can depend on the slow variable $\mathbf{x}$ in addition to the fast variable $\mathbf{x}-\mathbf{x}'$. This new quantity is the filtered component of the velocity, while $\mathbf{u}' \equiv \mathbf{u}-\overline{\mathbf{u}}$ refers to its residual component. Instead of the Navier-Stokes equation, it is the filtered Navier-Stokes equation that needs to be integrated. It is obtained by applying the filtering operation to Equation 1.14, which yields (for an incompressible flow)

$$\frac{\partial \overline{u_i}}{\partial t} + \frac{\partial(\overline{p}\delta_{ij}/\overline{\rho} + \overline{u_i}\,\overline{u_j} - \eta\partial_j\overline{u_i} - \sigma^R_{ij})}{\partial x_j} = g_i \,. \tag{1.25}$$

Formally, the filtered Navier-Stokes equation is almost identical to the full, exact Navier-Stokes equation, with the key difference that a new stress tensor appears, called the *residual stress tensor*, in the form of[10]

$$\sigma^R_{ij} \equiv \overline{u_i u_j} - \overline{u_i}\,\overline{u_j} \,. \tag{1.26}$$

I insist on the fact that in this approach, Equation 1.25 is still an exact equation, stemming directly and without assumptions from the Navier-Stokes equation itself. However, the quantity σ^R_{ij} is not known, and needs to be expressed as a function of $\overline{\mathbf{u}}$ itself and the filtering operator G: this is where the modelling part begins.

The most common model for σ^R_{ij} is the Smagorinsky model, which is essentially a down-gradient approximation for the transport of momentum by residual motions. It yields (Smagorinsky 1963)

$$\sigma^R_{ij} = -2\nu_S \overline{S}_{ij} \,, \tag{1.27}$$

where $\overline{S}_{ij}$ is the *filtered* rate of strain

$$\overline{S}_{ij} \equiv \frac{1}{2}\left(\frac{\partial \overline{u_i}}{\partial x_j} + \frac{\partial \overline{u_j}}{\partial x_i}\right) , \tag{1.28}$$

the *eddy viscosity* is given by

$$\nu_S = l_S^2 \overline{S} \equiv l_S^2 \sqrt{2\overline{S}_{ij}\overline{S}_{ij}} \,, \tag{1.29}$$

and l_S is the *Smagorinsky lengthscale*. The fundamental assumption is that this lengthscale is comparable to the width Δ of the spatial filter G, so that $l_S = C_S\Delta$, and C_S is a somewhat universal constant of order unity.

A useful limit in order to understand the implications of this model is the case where the characteristic filtered rate of strain $\overline{S}$ can be approximated by its standard-deviation (in the sense of ensemble average). In that case, ν_S becomes uniform (Pope 2000), and *the filtered Navier-Stokes equation becomes identical to the exact Navier-Stokes equation, where ν is replaced with $\nu_{\mathit{eff}} = \nu + \nu_S$*. In flows with very high Reynolds number, $\nu \ll \nu_S$ and the *effective* Kolmogorov scale is equal to l_S, which is itself of the order of the filtering width Δ: ultimately, from the point of view of the large-scale flow, adopting the Smagorinsky model amounts to artificially enhancing viscosity. Hydrodynamic codes for stellar convection that use a Smagorinsky SGS model include, for instance, the work of Robinson et al. (2003), the CO^{5}BOLD code (Freytag et al. 2012), the `StellarBox` code (Wray et al. 2015) or the `ANTARES` code (Muthsam et al. 2010).

Albeit not exhaustive, this introductory discussion shows that all LES strategies – the implicit use of numerical viscosity to mimic the effect of the unresolved scales, the additional inclusion of hyperdiffusion, or explicit SGS modelling, through the Smagorinsky model or otherwise – ultimately rely on the same fundamental assumption: that the resulting effective viscosity accurately represents the effect of the entire turbulent cascade (which is impossible to resolve) on the volume-averaged flow (which is the part that can be resolved). As such, a natural question is this: to what degree is this assumption verified? How sensitive are LES to the treatment of small scales? The answer to this kind of question always depends on what one wishes to achieve with the simulation. For instance, Stein and Nordlund (1998), Robinson et al. (2003), Kupka (2009) or Kitiashvili et al. (2013) showed that in a star with a convective envelope, such as the Sun, the properties of convection close to the surface – and more specifically in the super-adiabatic region – tend to depend on the grid resolution and the treatment of the SGS. On the other hand, the bulk of the convection zone is rather insensitive to such considerations (Kupka 2009; Beeck et al.

[10]The reader already familiar with Reynolds-stress models will undoubtedly have noticed the similarity between the filtered Navier-Stokes equation and the Reynolds-averaged Navier-Stokes equation, or equivalently between the residual stress tensor and the Reynolds stress tensor. It must be understood, however, that these are fundamentally different quantities and approaches, as one is the result of spatial filtering while the other is the result of ensemble averaging. In particular, we have in general $\overline{\overline{\mathbf{u}}} \neq \overline{\mathbf{u}}$, so that $\overline{\mathbf{u}'} \neq \mathbf{0}$.

2012). As far as oscillation excitation goes, it was shown by Jacoutot et al. (2008) that excitation rates are very sensitive to these matters as well (see also Prentice and Dyt 2003). All in all, the takeaway message is this: unlike the bulk of the convective region, surface convection is rather sensitive to the specific treatment of small scales in the simulation. Fundamentally, this is because the structure of convection becomes more complex as one gets closer to the surface, where the fluid parcels travelling upwards are suddenly forced to go back down; in particular, mode excitation is particularly sensitive to the detailed properties of the turbulent convection (as we will see in much more details in Section 2.2), which explains the sensitivity of the numerically computed excitation rates with the small-scale treatment in the LES.

1.2.2 Mixing-length formalisms

Mean equations and the closure problem in the Boussinesq approximation

As we saw in Section 1.2.1, the core problem in considering the exact equations of hydrodynamics directly is that the ensuing spatial structure of the turbulent flow is too complicated and involves too wide a range of scales to be exactly simulated. On the other hand, the *mean* flow, defined as an average over a large number of realisations of the same flow (or *ensemble average*), does not exhibit such a complex behaviour, while containing most of the information in which one may be interested anyway. It is only natural, therefore, that one may wish to consider the mean equations of hydrodynamics, rather than the exact ones. To do this, one first needs to separate each flow variable into an average and a residual (or fluctuating) part. There are several ways of performing this separation. The natural decomposition is

$$Q = \overline{Q} + Q' \,, \tag{1.30}$$

where $\overline{Q}$ corresponds to the actual ensemble average[11] (or Reynolds average) of Q, and Q' refers to the fluctuations of Q around its ensemble average. But another possibility is to write

$$Q = \widetilde{Q} + Q'' \,, \tag{1.31}$$

where $\widetilde{Q} \equiv \overline{\rho Q}/\overline{\rho}$ is called the *mass average* (or *Favre average*) of Q (Favre 1969), and Q'' refers to the fluctuations of Q around its Favre average. In particular, while it stems immediately from Equations 1.30 and 1.31 that $\overline{Q'} = \widetilde{Q''} = 0$, we have $\overline{Q''} \neq 0$ and $\widetilde{Q'} \neq 0$. It can already be seen from Equations 1.13 to 1.15 that the Favre average is a more natural choice of decomposition: indeed, the exact equations naturally take the form of transport equations not for ρ, $\mathbf{u}$ and e, but for ρ, $\rho\mathbf{u}$ and ρe (or, in other words, for the momentum and energy per unit volume rather than per unit mass). Therefore, we will consider the following decomposition

$$\begin{aligned} &\rho \equiv \overline{\rho} + \rho' \,, && p \equiv \overline{p} + p' \,, && \sigma_{ij} \equiv \overline{\sigma_{ij}} + \sigma'_{ij} \,, && \mathbf{u} \equiv \widetilde{\mathbf{u}} + \mathbf{u}'' \,, \\ &\mathbf{g} \equiv \widetilde{\mathbf{g}} + \mathbf{g}'' \,, && e = \widetilde{e} + e'' \,, && h = \widetilde{h} + h'' \,. \end{aligned} \tag{1.32}$$

The choice of which variable should be decomposed according to its Reynolds average, and which according to its Favre average is completely arbitrary. However, this choice happens to simplify the subsequent equations, as we will see below. Plugging this decomposition into Equations 1.13 to 1.15 and taking the ensemble average, one finds

$$\frac{\partial \overline{\rho}}{\partial t} + \frac{\partial \overline{\rho}\widetilde{u_i}}{\partial x_i} = 0 \,, \tag{1.33}$$

$$\frac{\partial \overline{\rho}\widetilde{u_i}}{\partial t} + \frac{\partial \left(\overline{p}\delta_{ij} + \overline{\rho}\widetilde{u_i}\,\widetilde{u_j} + \overline{\rho}\widetilde{u_i''u_j''} - \overline{\sigma_{ij}} \right)}{\partial x_j} = \overline{\rho}\widetilde{g_i} \,, \tag{1.34}$$

$$\frac{\partial \overline{\rho e}}{\partial t} + \frac{\partial \left(\overline{\rho}\widetilde{h}\,\widetilde{u_i} + \overline{\rho}\widetilde{h''u_i''} + \overline{F_i^{\mathrm{rad}}} + \overline{\sigma_{ij}}\widetilde{u_j} + \overline{\sigma'_{ij}u''_j} \right)}{\partial x_i} = \widetilde{u_i}\frac{\partial \overline{p}}{\partial x_i} - \overline{u_i''\frac{\partial p'}{\partial x_i}} - \widetilde{u_i}\frac{\partial \overline{\sigma_{ij}}}{\partial x_j} - \overline{u_i''\frac{\partial \sigma'_{ij}}{\partial x_j}} \,. \tag{1.35}$$

Those are still exact equations, but the key difference is that they do not model the evolution of the total flow variables ρ, $\mathbf{u}$ and e, but the mean flow variables $\overline{\rho}$, $\widetilde{\mathbf{u}}$ and $\widetilde{e}$ instead. These equations can be integrated exactly

[11] This notation must not be confused with the filtering operator introduced in LES (see Section 1.2.1). I will not come back to this filtering process in the future, and this notation will always be meant as a Reynolds average from now on.

without having the scale resolution problem that DNS have. The price to pay, however, is heavy: the non-linear, quadratic advection terms in both the Navier-Stokes equation and the energy equation give rise, once they are averaged, to second-order terms in the fluctuating quantities, which are not directly expressed in terms of the mean flow variables themselves. In other words, the system of equations is no longer closed, and must be supplemented with some model for the unclosed terms.

In semi-analytical models of convection based on these mean equations, it is very common to adopt the *Boussinesq approximation*, which renders the task of closing the equations slightly less daunting (Houdek and Dupret 2015). The Boussinesq approximation consists in *i) neglecting the fluctuations of the fluid density ρ' everywhere, except in the gravitational force, and ii) neglecting the fluctuations of the gas pressure p' everywhere.* In essence, this amounts to considering that 1) when a fluid parcel is displaced to a neighbouring region, the difference in density is too small to have an effect on the inertia of the parcel, but 2) that gravity is sufficiently strong to make even this small change in density appreciable in the gravitational force; and finally, that 3) the dynamical time is much smaller than any other time scale in the system, so that the fluid always has time to adapt to the new condition for mechanical equilibrium. Of course, the second remark is not anecdotal, since the difference in gravitational force is precisely what is usuqlly referred to as the Archimedes force (or buoyancy force), and is responsible for the convective instability in the first place. The Boussinesq approximation is similar to considering the incompressible limit, but not perfectly equivalent to it. Indeed, in the incompressible limit, there is no buoyancy force, and the pressure is mechanically constrained by the Poisson equation instead of evolving as a thermodynamic variable. The Boussinesq approximation is justified if two conditions are verified (Spiegel and Veronis 1960): any given parcel of fluid must remain confined within a layer whose thickness is much smaller than the local density scale height $H_\rho \equiv |\,\mathrm{d}\ln\rho_0/\,\mathrm{d}z|^{-1}$, where ρ_0 is the equilibrium density and z is the vertical coordinate (i.e. the coordinate along the direction of the gravitational acceleration); and the typical density fluctuations must remain much smaller than the average density value. The full impact of the Boussinesq approximation will be seen later, upon writing the equations on the fluctuating part of the flow. But it already allows us to simplify the mean equations. Indeed, the fact that we neglect p' makes the velocity-pressure-gradient correlation (i.e. the second term on the right-hand side of Equation 1.35) vanish from the energy equation.

Furthermore, another common approximation is to consider that the *mean* viscous stress tensor is negligible – otherwise stated, that the viscous force has no effect on the large-scale mean flow. This is justified by the very high Reynolds number characterising stellar convection. This means that the term $\overline{\sigma_{ij}}$ is discarded in both Equations 1.34 and 1.35. However, the viscous-stress-velocity correlation (which appears both on the left-hand side and the right-hand side of Equation 1.35) cannot *a priori* be neglected, because it is where turbulent dissipation originates from. By definition, the *turbulent dissipation tensor* is defined by (e.g. Pope 2000)

$$\epsilon_{ij} \equiv \overline{\sigma'_{ik}\frac{\partial u''_j}{\partial x_k} + \sigma'_{jk}\frac{\partial u''_i}{\partial x_k}}\,. \tag{1.36}$$

Under the assumption that the dissipation tensor is isotropic, one can define a *scalar turbulent dissipation* ϵ in such a way that

$$\epsilon_{ij} = \frac{2}{3}\overline{\rho}\epsilon\delta_{ij}\,. \tag{1.37}$$

The isotropy of the dissipation tensor is also a consequence of the high Reynolds number of the flow, and stems directly from the Kolmogorov hypotheses (Kolmogorov 1941). Essentially, the idea is that by the time the turbulent kinetic energy has trickled down the entire turbulent cascade, and is ready to be dissipated into heat at the viscous scales of motion, all directional information has already been lost.

Putting everything together – the Boussinesq approximation, the neglect of the mean viscous stress force, the isotropy of dissipation –, Equations 1.33 to 1.35 become

$$\frac{\partial\overline{\rho}}{\partial t} + \frac{\partial\overline{\rho}\widetilde{u_i}}{\partial x_i} = 0\,, \tag{1.38}$$

$$\frac{\partial\overline{\rho}\widetilde{u_i}}{\partial t} + \frac{\partial\left(\overline{p}\delta_{ij} + \overline{\rho}\widetilde{u_i}\,\widetilde{u}_j + \overline{\rho}\widetilde{u''_i u''_j}\right)}{\partial x_j} = \overline{\rho}\widetilde{g_i}\,, \tag{1.39}$$

$$\frac{\partial\overline{\rho}\widetilde{e}}{\partial t} + \frac{\partial\left(\overline{\rho}\widetilde{h}\,\widetilde{u_i} + \overline{\rho}\widetilde{h''u''_i} + \overline{F_i^{\mathrm{rad}}}\right)}{\partial x_i} = \widetilde{u_i}\frac{\partial\overline{p}}{\partial x_i} + \overline{\rho}\epsilon\,. \tag{1.40}$$

Furthermore, taking the average of the ideal gas equation of state (Equation 1.5), and recalling that for an ideal gas $e = c_V T$, one obtains

$$\overline{p} = \frac{R\overline{\rho}\,\widetilde{e}}{\mu c_V} \,, \tag{1.41}$$

meaning that the mean gas pressure is already in closed form (provided the molecular weight μ is known). Let me also assume that the radiative flux is taken care of through the appropriate treatment of radiative transfer – not that this task is trivial, of course, but this is not the core subject of the discussion here, so that I will leave this question aside in the following –, so that the *mean* radiative flux $\overline{\mathbf{F}^{\mathrm{rad}}}$ is known as a function of the mean flow quantities $\overline{\rho}$, $\widetilde{\mathbf{u}}$ and $\widetilde{e}$.

Then there are two quantities left to close: the *Reynolds stress tensor* and the *mean convective flux*, defined respectively by

$$\sigma^t_{ij} \equiv \overline{\rho}\widetilde{u''_i u''_j} \,, \tag{1.42}$$

$$\overline{F_i}^{\mathrm{conv}} \equiv \overline{\rho}\widetilde{h'' u''_i} \,. \tag{1.43}$$

These two quantities are fundamental to the modelling of convection, because they describe the transport of *mean* momentum and enthalpy by the *residual* fluctuating flow. *In the Boussinesq approximation, all modelling efforts are therefore focused on these two quantities.*

A general picture of convective transport in a static background

In general, we are particularly interested in the vertical components of these two second-order moments, because these are the only components that need to be modelled in order to include convection in 1D stellar models. We will denote the vertical component of the convective flux as F_c, and the vertical-vertical component of the Reynolds-stress tensor as p_t, also commonly referred to as the *turbulent pressure*. In the following, I will discuss these two scalar quantities, which pertain only to the vertical motions of the gas.

A common picture of the convective motions of the gas consists in describing the flow as a set of convective cells. Locally, the flow can be viewed as being comprised of vertical columns of gas, some of them flowing upwards, other downwards. Let me denote the relative cross-section, density, vertical velocity and temperature of the upwards-travelling columns as σ_u, ρ_u, v_u and T_u respectively, and those of the downwards-travelling columns as σ_d, ρ_d, v_d and T_d respectively, all of these quantities being defined at a given depth in the star. Then during a time $\mathrm{d}t$, the upwards-travelling (resp. downwards-travelling) gas carry a mass $\sigma_u\rho_u\mathrm{v}_u\,\mathrm{d}t\,\mathrm{d}S$, a momentum $\sigma_u\rho_u\mathrm{v}_u^2\,\mathrm{d}t\,\mathrm{d}S$ and an enthalpy $\sigma_u\rho_u c_P T_u\mathrm{v}_u\,\mathrm{d}t\,\mathrm{d}S$ (resp. idem with d indices) through a horizontal surface $\mathrm{d}S$[12] at this depth, from bottom to top (resp. from top to bottom). Then the net mass, momentum and enthalpy flux (i.e. the net quantity flowing through the layer per unit time and per unit surface) is given by the difference between the quantity carried upwards and the quantity carried back down, so that

$$F_m = \sigma_u\rho_u\mathrm{v}_u - \sigma_d\rho_d\mathrm{v}_d \,, \tag{1.44}$$

$$p_t = \sigma_u\rho_u\mathrm{v}_u^2 - \sigma_d\rho_d\mathrm{v}_d^2 \,, \tag{1.45}$$

$$F_c = \sigma_u\rho_u c_P T_u\mathrm{v}_u - \sigma_d\rho_d c_P T_d\mathrm{v}_d \,, \tag{1.46}$$

where F_m is the vertical mass flux. Of course, there can actually be no net mass flux in any direction, as this would quickly either deplete the star of all its matter (although that would considerably simplify the treatment of the convective flux, we would still like the star to exist), or on the contrary end up concentrating all the matter in an arbitrarily small central region (which would violate the condition of hydrostatic equilibrium). As such, we have $F_m = 0$, which yields the following constrain

$$\sigma_u\rho_u\mathrm{v}_u = \sigma_d\rho_d\mathrm{v}_d \,. \tag{1.47}$$

In turn, this condition allows us to rewrite the convective flux and turbulent pressure thus

$$p_t = \sigma_u\rho_u\mathrm{v}_u\left(\mathrm{v}_u - \mathrm{v}_d\right) \,, \tag{1.48}$$

$$F_c = \sigma_u\rho_u c_P\mathrm{v}_u\left(T_u - T_d\right) \,. \tag{1.49}$$

[12] The *relative* cross-sections σ_u and σ_d are defined in such a way that the upflows (resp. downdrafts) take up a portion σ_u (resp. σ_d) of the surface $\mathrm{d}S$. As such, they have no dimension, and $\sigma_u + \sigma_d = 1$.

Then, because the velocity difference $\mathrm{v}_u - \mathrm{v}_d$ and the temperature difference $T_u - T_d$ are already first-order differences compared to $\mathrm{v} \equiv (\mathrm{v}_u + \mathrm{v}_d)/2$ and $T_0 \equiv (T_u + T_d)/2$ respectively, one can remark that replacing σ_u, ρ_u and v_u by 0.5, ρ_0 and v respectively would only result in second-order corrections to the above expressions. Following that remark, one finally obtains

$$p_t = \rho_0 \mathrm{v} \Delta \mathrm{v} \tag{1.50}$$

$$F_c = \rho_0 c_P \mathrm{v} \Delta T \ , \tag{1.51}$$

where $\Delta \mathrm{v} \equiv (\mathrm{v}_u - \mathrm{v}_d)/2$ is the difference between v_u (or v_d) and the mean velocity v, and $\Delta T \equiv (T_u - T_d)/2$ is the difference between T_u (or T_d) and the mean temperature T_0.

The hard question still remains however: how to quantify the velocity difference $\Delta \mathrm{v}$ and the temperature difference ΔT, as well as the *mean norm* of the velocity v? This is where the mixing-length theory (thereafter shortened to MLT) kicks in.

Standard MLT

The following discussion is based on Böhm-Vitense (1992), where the focus is on the convective flux only. Therefore, I will only consider F_c in the following, even though p_t can be treated similarly.

Let me take a closer look at the gas. Each column can be thought of as a set of individual small volumes of gas, usually referred to as *gas bubbles*, which all travel up or down over different distances, with their own velocity and temperature. If we consider the set of bubbles which, at a given time, have arrived at a given layer of vertical coordinate z, we find that these bubbles have all come from different layers, either lower if they are travelling up, or higher if they are travelling down. Let us consider one such upwards-travelling bubble, initially coming from a layer of vertical coordinate $z - s$, meaning that its temperature at $z - s$ was equal to the mean temperature $T_0(z - s)$. Upon arriving at the layer z, the bubble has undergone a change of temperature due to energy exchanges with the background, which is proportional to the travel distance s, and which we denote as $(\mathrm{d}T/\mathrm{d}z)_{\mathrm{bubble}} \times s$, where $(\mathrm{d}T/\mathrm{d}z)_{\mathrm{bubble}} < 0$ because the bubble is *giving* energy to its surroundings. But the background seen by the bubble has also changed, due to the temperature stratification, by an amount $(\mathrm{d}T_0/\mathrm{d}z) \times s$. Therefore, the bubble has developed a net temperature difference with the background

$$\Delta T(s) = \left[\left(\frac{\mathrm{d}T}{\mathrm{d}z} \right)_{\mathrm{bubble}} - \frac{\mathrm{d}T_0}{\mathrm{d}z} \right] s \ . \tag{1.52}$$

This can be rewritten by remarking that

$$\left(\frac{\mathrm{d}T}{\mathrm{d}z} \right)_{\mathrm{bubble}} = \left(\frac{\mathrm{d}\ln T}{\mathrm{d}\ln p} \right)_{\mathrm{bubble}} \times \frac{T_0}{p_0} \times \left(\frac{\mathrm{d}p}{\mathrm{d}z} \right)_{\mathrm{bubble}} \ , \tag{1.53}$$

where $(\mathrm{d}\ln T/\mathrm{d}\ln p)_{\mathrm{bubble}}$ only depends on the nature of the thermodynamic transformation undergone by the bubble during its travel, and will be denoted as ∇_{bubble} in the following, and $(\mathrm{d}p/\mathrm{d}z)_{\mathrm{bubble}} = \mathrm{d}p_0/\mathrm{d}z$, where p_0 is the equilibrium gas pressure, because, as we mentioned before, the pressure in the bubble instantaneously adapts to the ceaselessly changing mechanical equilibrium condition, so that it is equal to the pressure of the background at all time. Introducing the *pressure scale height* $H_p \equiv -1/(\mathrm{d}\ln p_0/\mathrm{d}z)$, one obtains $(\mathrm{d}T/\mathrm{d}z)_{\mathrm{bubble}} = -T_0 \nabla_{\mathrm{bubble}}/H_p$. By the same token, one also has $\mathrm{d}T_0/\mathrm{d}z = -T_0 \nabla / H_p$, where $\nabla \equiv \mathrm{d}\ln T_0/\mathrm{d}\ln p_0$ is the background gradient. With these notations, Equation 1.52 can be rewritten

$$\Delta T(s) = \frac{T_0}{H_p} (\nabla - \nabla_{\mathrm{bubble}}) \, s \ . \tag{1.54}$$

From this, one can also derive the velocity with which the bubble arrives at the layer of depth z. Indeed, during its travel time, a buoyancy force is exerted on the bubble, which can be expressed in terms of the difference between the density of the bubble and the density of the background $\Delta\rho$

$$f_b = -\Delta\rho g = \rho_0 \frac{d\mathrm{v}}{dt} \ , \tag{1.55}$$

where f_b is the buoyancy force per unit volume, g is the norm of the gravitational acceleration, and the second equality then stems from Newton's second law. Let me discard, for simplicity, the possibility that the chemical

composition of the gas may also change during its motion, because of changes in the ionisation processes in the different regions through which the bubble is travelling. Let me also remark, as I did before, that the pressure in the bubble is equal to the pressure of the background at all time. Then the ideal gas law simply yields $\Delta\rho/\rho_0 = -\Delta T/T_0$, and we obtain

$$\frac{\mathrm{d}v}{\mathrm{d}t} = \frac{\Delta T}{T_0} g \,. \tag{1.56}$$

Multiplying by $v\,\mathrm{d}t$, this yields

$$v\ \mathrm{d}v = \frac{\Delta T}{T_0} g v\,\mathrm{d}t = \frac{\Delta T}{T_0} g\,\mathrm{d}z' \,, \tag{1.57}$$

which can then be integrated over z' between $z - s$ and z. But here, ΔT refers to the difference in temperature between the bubble and the background after the bubble has risen from the initial layer at $z - s$ to the layer z'. As such, it is equal to $\Delta T(z' - (z - s))$. Performing the change of variables $s' \equiv z' - z + s$, we now have

$$v\ \mathrm{d}v = \frac{g}{T_0} \Delta T(s')\,\mathrm{d}s' \,, \tag{1.58}$$

which should now be integrated between $s' = 0$ and $s' = s$, using Equation 1.54 for $\Delta T(s')$. Assuming the bubble is initially at rest, one finds

$$v(s) = \left[\frac{g\,(\nabla - \nabla_{\mathrm{bubble}})}{H_p}\right]^{1/2} s \,. \tag{1.59}$$

Equations 1.54 and 1.59, valid for one gas bubble with a travel distance s, must now be averaged over all bubbles. If l is the average distance over which gas bubbles travel before they are assimilated to their new environment (meaning the bubble can be considered as having been 'destroyed'), then for any given layer, the distance over which a bubble travels before reaching the layer is $l/2$ – in other words, on average, the bubbles that do go through a given layer spend as much time travelling *to* the layer from birth than *from* the layer to their demise. Then, an average temperature difference (resp. average velocity) can be obtained by setting $s = l/2$ in Equation 1.54 (resp. Equation 1.59), and the total convective flux given by Equation 1.51 becomes

$$F_c = \frac{\rho_0 c_P T_0 \sqrt{g}}{H_p^{3/2}} (\nabla - \nabla_{\mathrm{bubble}})^{3/2} \left(\frac{l}{2}\right)^2 \,. \tag{1.60}$$

The equilibrium quantities ρ_0, c_P, T_0, g and H_p are considered known; then the convective flux only depends on the difference between the bubble gradient and the background gradient (i.e. how fast does the temperature difference between the bubble and its surroundings grow as the bubble rises?), and the average length travelled by the bubble l (i.e. how far away do the bubbles go before they die?).

Let me first discuss the temperature gradient of the bubble ∇_{bubble}. On the one hand, it must be smaller than the background temperature gradient, because only then would the temperature of the bubble fall off more slowly than that of its surroundings, thus allowing for an upwards buoyancy force to drag the bubble further up. On the other hand, it must be steeper than the adiabatic gradient, because otherwise the cooler surroundings would heat up the bubble instead of the other way around, thus violating the second law of thermodynamics. We therefore have $\nabla_{\mathrm{ad}} < \nabla_{\mathrm{bubble}} < \nabla$, and I can already say this about the efficiency of the convective transport of enthalpy: the closer ∇_{bubble} is to ∇_{ad}, the longer it takes for the bubble to be 'destroyed', and the higher the convective efficiency is; on the contrary, the closer it is to ∇, the smaller the buoyancy force driving convection, and the smaller the convective efficiency. This qualitative picture can be rendered more quantitative by introducing the *convective efficiency* Γ. This quantity is constructed on the basis of the following enthalpy budget: if no enthalpy was lost to heat exchange during the bubble's travel over the distance l (i.e. if the thermodynamic transformation undergone by the bubble were adiabatic), then the total enthalpy carried upwards by the bubble per unit volume would be given by $h_{\mathrm{total}} = \rho_0 c_P \Delta T_{\mathrm{ad}}(l)$, with $\Delta T_{\mathrm{ad}}(l)$ being given by Equation 1.54 with $\nabla_{\mathrm{bubble}} = \nabla_{\mathrm{ad}}$, so that

$$h_{\mathrm{total}} = \frac{\rho_0 c_P T_0}{H_p} (\nabla - \nabla_{\mathrm{ad}})\, l \,. \tag{1.61}$$

In reality, the motion is not adiabatic: the enthalpy per unit volume effectively carried upwards is only

$$h_{\text{gain}} = \frac{\rho_0 c_P T_0}{H_p} (\nabla - \nabla_{\text{bubble}}) \, l \, , \tag{1.62}$$

while the difference originates from heat loss by radiation

$$h_{\text{loss}} = h_{\text{total}} - h_{\text{gain}} = \frac{\rho_0 c_P T_0}{H_p} (\nabla_{\text{bubble}} - \nabla_{\text{ad}}) \, l \, . \tag{1.63}$$

Then the efficiency of convection is defined by the ratio of the enthalpy effectively transported upwards to the enthalpy lost along the way, so that (Böhm-Vitense 1992)

$$\Gamma \equiv \frac{h_{\text{gain}}}{h_{\text{loss}}} = \frac{\nabla - \nabla_{\text{bubble}}}{\nabla_{\text{bubble}} - \nabla_{\text{ad}}} \, . \tag{1.64}$$

As such, Γ is an alternative way of describing how close the actual bubble gradient is to the adiabatic gradient. In particular, I reiterate the remark I made earlier: the more adiabatic the transformations of the bubble, the more efficient the convective transport of enthalpy.

But on the other hand, the convective efficiency can be expressed as the ratio of the radiative transfer through the surface of the bubble to the enthalpy change of the bubble during its lifetime, both of which are ultimately proportional to the temperature difference between the bubble and its surroundings, so that $\nabla_{\text{bubble}} - \nabla$ ends up disappearing from the expression. I do not detail the entire derivation, which involves the specific geometry of the bubble, as well as the exact temperature stratification inside the bubble, and can become quite complicated. I simply give the estimate by Böhm-Vitense (1958)

$$\Gamma = \frac{\rho_0^2 c_P T_0 \kappa_R l \mathrm{v}}{24 \sigma T^4} \, . \tag{1.65}$$

This relation does not give, as one may be tempted to suggest, a closed form for the bubble gradient ∇_{bubble}, because the velocity v appearing in Equation 1.65 depends itself on ∇_{bubble}. However, this expression allows for an estimation of Γ in the stellar context. More specifically, in the bulk of the stellar convective zone, because of the high density ρ_0 and mean-Rosseland opacity κ_R, we have $\Gamma \gg 1$. Equation 1.65 then tells us that this is only possible if $\nabla_{\text{bubble}} \sim \nabla_{\text{ad}} = (\Gamma_1 - 1)/\Gamma_1$. This means that throughout most of the convective zone, the radiative transfer between the bubble and its surroundings is so inefficient that the bubble keeps almost all of its enthalpy to be given back to the background only once the bubble is dissolved. In that case, the convective flux is given by Equation 1.60 with ∇_{bubble} now being a known quantity, so that F_c only depends on l. Only close to the surface of the star does the efficiency of convection drop to a value comparable to unity, in which case a non-negligible portion of the enthalpy of the bubbles is now lost to radiation, and the convective transport is not as efficient as in the bulk. This region is referred to as the *superadiabatic region*, because $\nabla_{\text{bubble}} > \nabla_{\text{ad}}$. In this region, determining the convective flux is much more complicated (see Böhm-Vitense (1958) for German-speaking readers, or (Kippenhahn et al. 1967) for the less fortunate).

Apart from the superadiabatic region, the convective flux is given throughout the stellar interior as a function of the average travelling distance l of the bubbles, also referred to as the *mixing length*. The mixing length constitutes a free parameter in MLT, whether it be the standard form presented until now, or the more refined variants that I will present below. It is therefore necessary to give a prescription for l. A simple argument can be used to justify that it cannot exceed H_p by much. Indeed, H_p represents the e-folding length of the background gas pressure. Since the expansion of the gas bubbles during their ascension happens at mechanical equilibrium, it also corresponds to the e-folding length for the expansion of the bubbles, and therefore also for the relative upflow cross-section σ_u. But σ_u cannot exceed unity: in other words, the expansion of the bubbles must stop before they take up more space than is physically available. As a consequence, the mixing length is at most of the order of H_p. In practical applications, l is usually chosen to actually be of the order of the pressure scale height, even though it could *a priori* be much smaller. In that spirit, a *mixing length parameter* α_{MLT} is introduced so that

$$l = \alpha_{\text{MLT}} H_p \, . \tag{1.66}$$

The free parameter of the theory is now α_{MLT}, which is a non-dimensional parameter that takes typical values between ~ 0.1 and ~ 1. There is no way to *physically constrain* the value of this parameter, because it stems from

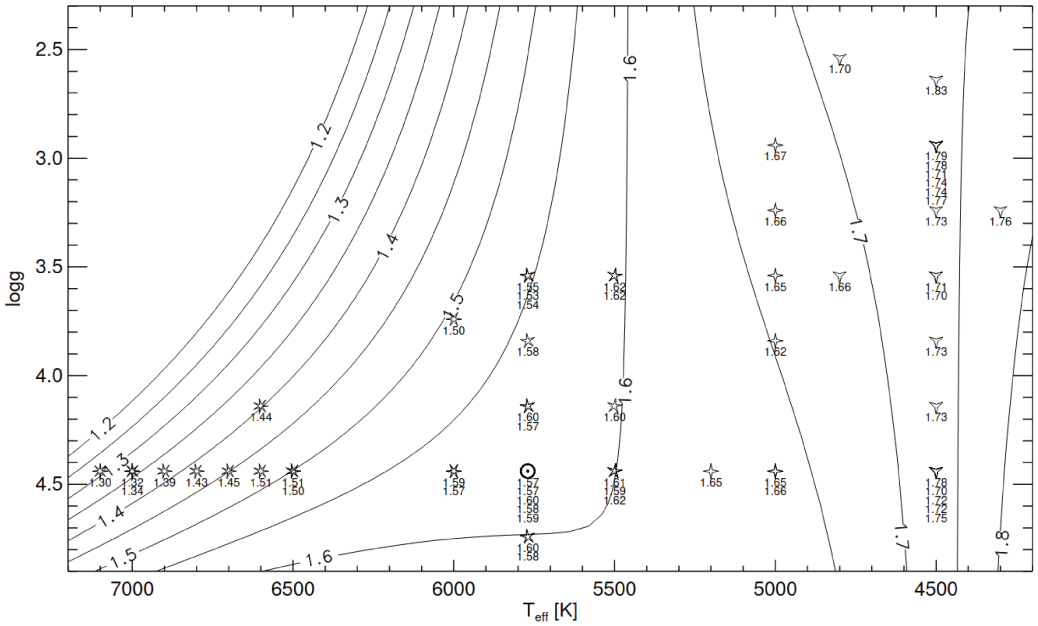

Figure 1.1: Calibrated value of the mixing-length parameter $\alpha_{\rm MLT}$ as a function of effective temperature $T_{\rm eff}$ and surface gravity g, obtained by calibrating 1D solar-type stellar models on 2D radiation hydrodynamical simulations of their atmosphere. Each symbol corresponds to one stellar model. The lines are obtained by interpolation between the discrete symbols, through a fitting procedure. Credits: Ludwig et al. (1999).

a picture of convection which is already a rough approximation of a more complex reality: indeed, 3D simulations show that stellar convection is more complicated than a set of well-behaved gas bubbles gently rising and falling repeatedly, within equally well-behaved up- and downwards gas columns. The standard MLT picture, however, is still valuable, as even this simplified picture provides with a satisfactory expression for the convective flux. This is at the expense of having to *calibrate* the MLT parameter. The usual procedure consists in matching averages of 3D hydrodynamic simulations of convection with 1D stellar envelope models, where the convective flux is given by the standard MLT prescription. This procedure is performed for a grid of models with different stellar parameters, which eventually leads to a map of $\alpha_{\rm MLT}$ as a function of the effective temperature[13] $T_{\rm eff}$ and the surface gravity g (Trampedach et al. 1999, 2014; Ludwig et al. 1999, 2008; Magic et al. 2015), as illustrated, for instance in Figure 5 of Ludwig et al. (1999), which we reproduce here (see Figure 1.1). Another approach consists in calibrating $\alpha_{\rm MLT}$ against a solar model – the Sun being, by far and for obvious reasons, the star for which the global parameters and the specific internal physics are known with the greatest precision –, and then assuming that this value is universal, at least for main-sequence stars. However, there is no physical justification for this assumption, which is in essence impossible to verify. At any rate, the resulting calibrated value of $\alpha_{\rm MLT}$ is, by construction, extremely model-dependent, in the sense that it depends on every other physical ingredient put in the model. As such, the accuracy of $\alpha_{\rm MLT}$ only stands as long as every single other aspect of stellar physics is perfectly known – which is, of course, impossible, or at least currently far from our grasp. This is one of the major concerns with MLT, and one of the main reasons why alternative modelling approaches have been investigated to circumvent it (see the use of 3D simulations, upon which I have already touched in Section 1.2.1, or Reynolds-stress models, which will be the subject of Section 1.2.3).

Time-dependent Mixing-Length Theories

One of the most important assumptions made in standard MLT is that the average flow (in the sense of ensemble average) is independent of time, so that the bubbles travel through a static medium. In reality, this is not the case, primarily because the convective zone, as the rest of the star, is subjected to oscillations (a matter that I will

[13] I have not had the opportunity to define this quantity yet: it corresponds to the temperature of a hypothetical spherical black-body having the same radius $R_\star$ and radiating the same luminosity $L_\star$ as the star, and is therefore defined in such a way that $L_\star = 4\pi R_\star^2 T_{\rm eff}^4$. Since the star does not behave like a black-body (in particular because of the absorption lines in the atmosphere), $T_{\rm eff}$ is not equal to the actual thermodynamic temperature characterising the surface of the star.

introduce in Section 2.1). In order to describe the effect of the oscillations on the behaviour of convection – or the other way around –, it is necessary to account for the time-dependence of the mean flow in the treatment of the convective flux F_c and the turbulent pressure p_t. This yields what is commonly referred to as *time-dependent MLT*, which I briefly discuss here.

Subtracting the average flow equations (Equations 1.33 to 1.35) from the total equations (Equations 1.13 to 1.15), one finds the equations on the convective fluctuations in the following form

$$\frac{\partial \rho'}{\partial t} + \frac{\partial \rho' \widetilde{u_i}}{\partial x_i} + \frac{\partial \overline{\rho} u_i''}{\partial x_i} + \frac{\partial \rho' u_i''}{\partial x_i} = 0 \,, \tag{1.67}$$

$$\frac{\partial \left(\rho' \widetilde{u_i} + \overline{\rho} u_i''\right)}{\partial t} + \frac{\partial \left(\rho' \widetilde{u_i} u_j'' + \rho' u_i'' \widetilde{u_j} + \rho' u_i'' u_j'' + \overline{\rho} \widetilde{u_i} u_j'' + \overline{\rho} u_i'' \widetilde{u_j} - \overline{\rho} \widetilde{u_i'' u_j''} + p' \delta_{ij} - \sigma'_{ij}\right)}{\partial x_j} = \rho' \widetilde{g_i} + \overline{\rho} g_i'' \,, \tag{1.68}$$

$$\frac{\partial \left(\rho' \widetilde{e} + \overline{\rho} e''\right)}{\partial t} + \frac{\partial \left(\rho' \widetilde{u_i} h'' + \rho' u_i'' \widetilde{h} + \rho' u_i'' h'' + \overline{\rho} \widetilde{u_i} h'' + \overline{\rho} u_i'' \widetilde{h} - \overline{\rho} \widetilde{u_i'' h''} + F_i'^{\,\mathrm{rad}}\right)}{\partial x_i}$$
$$= -u_i'' \frac{\partial \overline{p}}{\partial x_i} - \widetilde{u_i} \frac{\partial p'}{\partial x_i} - \overline{u_i'' \frac{\partial p'}{\partial x_i}} + u_i'' \frac{\partial \overline{\sigma_{ij}}}{\partial x_j} + \widetilde{u_i} \frac{\partial \sigma'_{ij}}{\partial x_j} + \widetilde{u_i} \frac{\partial \overline{\sigma_{ij}}}{\partial x_j} \,. \tag{1.69}$$

I already mentioned that the Boussinesq approximation simplifies the mean equations, but it simplifies the convective equations even more drastically, because it allows to neglect all the terms containing ρ', with the exception of $\rho' \widetilde{g_i}$, and all the pressure-work terms on the right-hand side of the energy equation. Furthermore, it is customary in MLT to neglect not only the mean viscous force, but also all viscous effects completely. Finally, in a local framework, the gravitational acceleration is assumed to have a constant value, so that $\widetilde{g_i} = g_i$ and $g_i'' = 0$. Under these approximations, one obtains

$$\frac{\partial u_i''}{\partial x_i} = 0 \,, \tag{1.70}$$

$$\frac{\partial \overline{\rho} u_i''}{\partial t} + \frac{\partial \left(\overline{\rho} \widetilde{u_i} u_j'' + \overline{\rho} u_i'' \overline{u_j} + \overline{\rho} \left(u_i'' u_j'' - \widetilde{u_i'' u_j''}\right) + p' \delta_{ij}\right)}{\partial x_j} = \rho' g_i \,, \tag{1.71}$$

$$\frac{\partial \overline{\rho} e''}{\partial t} + \frac{\partial \left(\overline{\rho} \widetilde{u_i} h'' + \overline{\rho} u_i'' \widetilde{h} + \overline{\rho} \left(u_i'' h'' - \widetilde{u_i'' h''}\right) + F_i'^{\,\mathrm{rad}}\right)}{\partial x_i} = 0 \,. \tag{1.72}$$

The continuity equation is no longer a transport equation for the fluctuating density ρ', but becomes a mechanical constraint on the fluctuating velocity u_i''. As for the other two equations, they can be rearranged with the help of the mean continuity equation (Equation 1.33) and the mean energy equation (Equation 1.35), to yield the following transport equations for u_i'' and the temperature fluctuations around its Reynolds average $T' \equiv T - \overline{T}$ (Gough 1977a)

$$\frac{\partial u_i''}{\partial t} + \left(u_j'' \frac{\partial u_i''}{\partial x_j} - \overline{u_j'' \frac{\partial u_i''}{\partial x_j}}\right) - u_3'' \delta_{i3} \frac{\partial r^2 \overline{\rho}}{\partial t} = -\frac{1}{\overline{\rho}} \frac{\partial p'}{\partial x_i} + \overline{\delta} \frac{T'}{\overline{T}} g_i \,, \tag{1.73}$$

$$\frac{\partial T'}{\partial t} + \left(u_i'' \frac{\partial T'}{\partial x_i} - \overline{u_i'' \frac{\partial T'}{\partial x_i}}\right) + \left(\left(\overline{c_{PT}} - \overline{\delta}\right) \frac{\partial \ln \overline{T}}{\partial t} - \overline{\nabla_{\mathrm{ad}}}\, \overline{\delta_T} \frac{\partial \ln \overline{p}}{\partial t}\right) T' - \beta u_3'' = -\frac{1}{\overline{\rho}\, \overline{c_P}} \frac{\partial F_i'^{\,\mathrm{rad}}}{\partial x_i} \,, \tag{1.74}$$

where r denotes the radial coordinate, u_3'' is the radial component of u_i'', $\delta \equiv -(\partial \ln \rho / \partial \ln T)_p$ is the expansion coefficient at constant pressure, c_{PT} and δ_T are the partial derivatives of c_P and δ with respect to T at constant pressure, and $\beta \equiv \overline{\delta} \partial_r \overline{p} / \overline{c_P} - \partial_r \overline{T} / \overline{\rho}$ is the superadiabatic temperature gradient. In Equation 1.73, the third term on the left-hand side stems from $u_i'' \partial_j \left(\overline{\rho} \widetilde{u_j}\right)$ on the left-hand side of Equation 1.71, where the mean continuity equation makes the time derivative of the mean density appear; the second term on the right-hand side corresponds to the buoyancy force $\rho' g_i$, where the density fluctuations are expressed in terms of temperature fluctuations. In Equation 1.74, the third term on the left-hand side stems from $h'' \partial_i \left(\overline{\rho} \widetilde{u_i}\right)$ on the left-hand side of Equation 1.72, and the fourth term stems from $u_i'' \partial_i \left(\overline{\rho} \widetilde{h}\right)$, where the mean continuity equation, the relation between fluctuating enthalpy and fluctuating temperature, and the mean energy equation have been used.

Equations 1.73 and 1.74 are almost linear, including the divergence of the radiative flux which is usually linear in the temperature fluctuations. In fact, they would be completely linear, were it not for the term $u_i \partial_i'' u_j'' - \overline{u_i'' \partial_i u_j''}$ in

the momentum equation, and the term $u_i'' \partial_i T' - \overline{u_i'' \partial_i T'}$ in the temperature equation. Different versions of the MLT (and *a fortiori* time-dependent MLT) differ only in their treatment of these non-linear terms. There are mainly two such versions of time-dependent MLT currently in use in the context of stellar convection

- The formalism developed by Gough (1969), later generalised to the time-dependent case by Gough (1977b), and later used, for instance, by Balmforth (1992b); Houdek et al. (1995); Rosenthal et al. (1995); Chaplin et al. (2005), whereby the eddies grow linearly in time (the non-linear terms are discarded) until they die. Then Equations 1.73 and 1.74 form a system of linear differential equations[14], into which an Ansatz $\propto \exp(j\mathbf{k} \cdot \mathbf{r} + \sigma_c t)$ can be injected for both u_i'' and T'. This yields a dispersion relation between the linear growth rate σ_c of the eddies and their wavevector k. Together with the introduction of an eddy survival probability, this gives an expression for the flux of u_i'' and T' (i.e. for the convective flux and the turbulent pressure). It is necessary to introduce a mixing length for two reasons: the eddy wavevectors are given by a unique eddy size which acts as a free parameter in the model; and the eddy survival probability is defined in such a way that the eddy has a probability $\mathrm{d}x/l$ of being destroyed over a travelling distance $\mathrm{d}x$, where l is the total distance travelled by the eddy on average, and therefore corresponds to a mixing length. A time-independent version of MLT can be recovered by neglecting the explicit time derivatives in Equations 1.73 and 1.74 and considering that the eddy wavevector is time-independent. Otherwise, the instantaneous properties of the background both at the instant t considered *and* the time of birth t_0 of the eddy must be explicitly taken into account;

- The formalism developed by Unno (1967), later generalised to the time-dependent case by Unno (1977), and later used, for instance, by Grigahcène et al. (2005); Dupret et al. (2005c,b,a, 2009); Belkacem et al. (2008, 2009, 2012), whereby the non-linear advection term acts as a dragging force that exactly balances the buoyancy force. In a static atmosphere (i.e. in the time-independent limit of MLT), all time derivatives are neglected in Equations 1.73 and 1.74, including the acceleration terms $\partial_t u_i''$ and $\partial_t T'$, and the non-linear terms are written in a down-gradient approximation in the form $u_i'' \partial_i u_j'' - \overline{u_i'' \partial_i u_j''} = 2u_3''^2/l$ and $u_i'' \partial_i T' - \overline{u_i'' \partial_i T'} = 2u_3'' T'/l$, where a mixing length is necessary to describe the divergence of the second-order moments. This yields algebraic equations for u_i'' and T', from which the convective flux F_c and turbulent pressure p_t can be directly extracted. In the time-dependent generalisation, the acceleration terms are restored, but all the mean variables are supposed to be time-independent.

Each of these formalisms yields an equilibrium value for F_c and p_t in the limit of a static convection zone, after which a perturbative approach gives a time-dependent correction δF_c and δp_t as a function of the more readily available fluctuations of the mean density, temperature, etc. This gives a prescription for the convective flux and turbulent pressure which accounts for the varying properties of the background from which the eddies are born, through which they travel, and to which they give their energy back when they are dissolved. This is at the expense of having to set not only a value for the static mixing length l, but also now an expression for its time-dependent fluctuations δl.

The non-local Mixing-Length Theory

Another important approximation underlying the standard MLT is the assumption that the mixing length l is much smaller than the stratification length scale, so that the mean variables are considered uniform over one eddy travel distance. However, this is far from the truth: the mixing-length parameter α_{MLT} being of order unity, this means l is of the order of the pressure scale height H_p. Spiegel (1963) proposed to generalise the standard MLT to cases where l is not necessarily small, in a way which I summarise below.

The turbulent eddies are described in phase space, by means of a density of eddies per unit phase-volume $\psi(t, \mathbf{x}, \mathbf{u})$, meaning that at time t, the number of eddies whose position lie within $\mathrm{d}^3\mathbf{x}$ of $\mathbf{x}$ and whose velocity lies within $\mathrm{d}^3\mathbf{u}$ of $\mathbf{u}$ is $\psi(t, \mathbf{x}, \mathbf{u})\, \mathrm{d}^3\mathbf{x}\, \mathrm{d}^3\mathbf{u}$. The evolution equation for the density function ψ takes the form of a Fokker-Planck equation (Gardiner 1994), and can be written as (Spiegel 1963)

$$\frac{\partial \psi}{\partial t} + \frac{\partial u_i \psi}{\partial x_i} + \frac{\partial (\mathrm{d}u_i/\mathrm{d}t)\psi}{\partial u_i} = q_+ - q_- \,, \tag{1.75}$$

[14] The pressure fluctuations p' is eliminated, as usual, by taking the curl of Equation 1.73, or rather, in this case, the curl of its curl.

where the second term on the left-hand side represents the fact that the velocity u_i of the eddies entails a variation of eddy positions, and therefore a flow of ψ in **x**-space, the third term on the left-hand side represents the fact that the acceleration $\mathrm{d}u_i/\,\mathrm{d}t$ of the eddies (due to buoyancy and pressure forces) entails a variation of eddy velocities, and therefore a flow of ψ in **u**-space, the term q_+ represents the rate of creation of convective eddies, and the term q_- represents the rate at which they are annihilated. Immediately, the flux of ψ in **u**-space can be assimilated in the source term q_+, so that one can define

$$Q_+ \equiv l\left(q_+ - \frac{\partial(\mathrm{d}u_i/\,\mathrm{d}t)\psi}{\partial u_i}\right) . \tag{1.76}$$

Furthermore, by definition of the mixing length, eddies travel over a distance l before they are annihilated, meaning that eddies of vertical velocity v are annihilated at a rate v/l. As such

$$q_- \equiv \frac{\mathrm{v}\psi}{l} . \tag{1.77}$$

Equation 1.75 then becomes

$$\frac{\partial\psi}{\partial t} + \frac{\partial u_i\psi}{\partial x_i} = \frac{Q_+}{l} - \frac{\mathrm{v}\psi}{l} . \tag{1.78}$$

For a static convection zone, the time derivative can be dropped, and if, in addition, the convection zone is assumed to have plane-parallel geometry, then $\partial u_i\psi/\partial x_i = \mu\,\mathrm{d}(\mathrm{v}\psi)/\,\mathrm{d}z$, where z is the vertical coordinate, and μ is the cosine of the angle between the direction of u_i (i.e. the eddy trajectory) and the vertical direction. Then one obtains

$$\mu\frac{\mathrm{d}\Psi}{\mathrm{d}z} = \frac{Q_+}{l} - \frac{\Psi}{l} , \tag{1.79}$$

where $\Psi \equiv \mathrm{v}\psi$. Equation 1.79 immediately strikes by its formal similarity with the equation for radiative transfer (Mihalas and Mihalas 1984), and must therefore be thought of as an equation for convective transfer, where Ψ is the specific convective intensity (i.e. the amount of convective energy that passes through a surface whose normal vector is inclined by an angle of cosine μ with respect to the vertical direction, per unit time, surface area and solid angle), and the mixing length l is a mean free path for the convective eddies, and plays the role of opacity for radiative transfer. It is only natural, therefore, to redefine the vertical coordinate in units of the mean free path l, in the form of a 'convective depth' σ, so that $\mathrm{d}\sigma = \mathrm{d}z/l$, in which case the equation of convective transfer becomes

$$\mu\frac{\mathrm{d}\Psi}{\mathrm{d}\sigma} = Q_+ - \Psi , \tag{1.80}$$

whose formal solution is given for $\mu > 0$ by (Mihalas and Mihalas 1984)

$$\Psi(\sigma,\mu) = \int_\sigma^{+\infty} \frac{\mathrm{d}s}{\mu}\,\exp^{(\sigma-s)/\mu} Q_+(s) , \tag{1.81}$$

and for $\mu < 0$

$$\Psi(\sigma,\mu) = \int_\sigma^{0} \frac{\mathrm{d}s}{\mu}\,\exp^{(\sigma-s)/\mu} Q_+(s) . \tag{1.82}$$

Let me now denote the excess enthalpy (with respect to the local surroundings) of the eddies of position **x** and velocity **u** as h_+ for the eddies flowing upwards, and h_- for those flowing downwards (with the understanding that $h_- = -h_+$, and $h_+ > 0$). Then the total *upwards* (resp. *downwards*) enthalpy fluxes are obtained by multiplying $\Psi(\sigma,\mu > 0)$ (resp. $\Psi(\sigma,\mu < 0)$) by μh_+ (resp. μh_-) and integrating over all solid angles covering the top (resp. bottom) hemisphere, so that

$$F_{c,+} = 2\pi\int_0^1 \mathrm{d}\mu \int_\sigma^{+\infty} \mathrm{d}s\ \exp^{(\sigma-s)/\mu} h_+(s)Q_+(s) , \tag{1.83}$$

and

$$F_{c,-} = 2\pi\int_{-1}^0 \mathrm{d}\mu \int_\sigma^{0} \mathrm{d}s\ \exp^{(\sigma-s)/\mu} h_-(s)Q_+(s) . \tag{1.84}$$

The net enthalpy flux is obtained by forming the sum of $F_{c,+}$ and $F_{c,-}$. After permutation of the integrals over s and μ, and after having substituted μ for μ^{-1}, one finally obtains

$$F_c(\sigma) = 2\pi \int_0^{+\infty} h_+(s) Q_+(s) E_2(|\sigma - s|) \, \mathrm{d}s \, , \tag{1.85}$$

where E_2 is the second exponential integral defined by

$$E_2(x) = \int_1^{+\infty} \frac{\mathrm{d}t}{t^2} \exp^{-xt} \, . \tag{1.86}$$

This is perfectly equivalent to the Milne equation obtained from the equation of radiative transfer for the radiative energy flux – or, to a factor 4π, the Eddington flux (Mihalas and Mihalas 1984). Essentially, $h_+ Q_+$ plays the role of a convective source, and the *local* convective flux is a *non-local* combination of all convective sources in the vicinity, with a weighting function given by E_2 and therefore having a typical width of the order of l. If l is much smaller than the stratification length scale, then $F_c \sim 2\pi h_+ Q_+$, meaning the convective flux is equal to the local convective source only: one recovers the local, standard MLT. In general, however, Equation 1.85 is not closed, because the convective source inside the integral is itself a function of the convective flux. As such, one now has an integro-differential equation to solve in order to find F_c, very similar to the integro-differential equation obtained for the radiative flux when the radiative source is a function of the specific intensity (when scattering is taken into account for instance).

The fact that Equation 1.85 is integro-differential makes the numerical treatment of convective transfer substantially more complex. Spiegel (1963) suggested that the source function $h_+ Q_+$ be taken to be equal to the convective heat flux *as computed in the local MLT*. However, this is only valid for high convective depths σ, and also requires the total enthalpy flux to be exclusively convective (without a contribution from radiation). If σ is small, or l high, then the buoyancy force felt by an eddy, instead of depending on the local superadiabatic gradient $\beta \equiv \nabla - \nabla_{\mathrm{ad}}$, becomes an average buoyancy force over the trajectory of the eddy, and therefore depends on a non-local mean value of the superadiabatic gradient. The author therefore suggested that the source function should equal the local convective flux *where the superadiabatic gradient is replaced by a non-local average over a vicinity of height l.* The mean is weighted by a sine squared, peaking at the center of the trajectory, and vanishing at its starting and ending points.

To further extend this formalism to high values of l, and in analogy with radiative transfer, Gough (1977b) suggested to adopt a convective version of the Eddington approximation, whereby Ψ is considered to be a linear function of μ, in which case the ratio of the second- to zero-order moments of Ψ with respect to μ is exactly $1/3$. In radiative transfer, this relation is then used to close the infinite hierarchy of moment equations at second order, thus yielding (Mihalas and Mihalas 1984)

$$\frac{1}{3} \frac{\mathrm{d}^2 J}{\mathrm{d}\tau^2} = J - S \, , \tag{1.87}$$

where J is the specific radiative intensity, τ the optical depth, and S the local radiative source (which, if the medium is in radiative equilibrium, is equal to the Planck function). Similarly, for convective transfer, this approximation yields

$$\frac{1}{b^2} \frac{\mathrm{d}^2 F_c}{\mathrm{d}\sigma^2} = F_c - F_{c,\mathrm{local}} \, , \tag{1.88}$$

$$\frac{1}{c^2} \frac{\mathrm{d}^2 \beta}{\mathrm{d}\sigma^2} = \beta - \beta_{\mathrm{local}} \, , \tag{1.89}$$

where $F_{c,\mathrm{local}}$ is the convective flux computed in the local MLT with the non-local superadiabatic gradient β, for which one therefore needs the second equation, where β_{local} is the local superadiabatic gradient. The turbulent pressure is obtained through a similar equation

$$\frac{1}{a^2} \frac{\mathrm{d}^2 p_t}{\mathrm{d}\sigma^2} = p_t - p_{t,\mathrm{local}} \, . \tag{1.90}$$

Instead of adopting the radiative pressure-to-density ratio of $1/3$, this factor is supplemented by the factors $1/a^2$, $1/b^2$ and $1/c^2$. The local, standard MLT corresponds to the limit $a, b, c \to +\infty$. These three non-dimensional

parameters therefore control the 'non-locality' of the theory, with a controlling how far away a convective source acts upon the turbulent pressure, b controlling how far away it acts upon the convective flux, and c controlling how far away the stratification acts upon the eddy buoyancy force. To reflect the uncertainty in the formalism, they are left as free parameters in the model, and as for the mixing length, they need to be calibrated, for example through the use of 3D simulations (see for instance Dupret et al. 2006).

A final note on Mixing-Length Theories

The above introductory discussion only scratches the surface of the wealth of mixing-length theories that were developed over the years, and the numerous and still ongoing efforts to refine them. I refer the reader who wishes to know more to the review by Houdek and Dupret (2015), from which a large portion of this discussion is inspired. From this limited account, however, one can already spot a common denominator to all these approaches: the physical picture of convection is always somewhat simplified in MLT, in order to allow for tractable derivations; each step in the simplification comes at the price of an increasing uncertainty in the theory, which is illustrated by the presence of a certain number of free parameters (mixing length l, or equivalently mixing-length parameter $\alpha_{\rm MLT}$; perturbation of the mixing length δl for time-dependent MLT; parameters of non-locality a, b and c for non-local MLT). Because the underlying picture of convection is too simple, these parameters cannot be constrained by physical arguments, and it will always be necessary to calibrate them against observations, laboratory experiments, or else numerical models such as 3D simulations. For the same reason, the question of their universality is also a very complex one – why should the mixing length, which is a construction of the mind rather than a creation of Nature, be the same in all stars? As such, it has been argued that MLT, whether in its standard form or its more refined versions, does not deserve the name of 'theory' so much as that of 'empirical prescription'[15]. However, with simplicity comes applicability, so that MLT is still to this day a tool of choice to describe the effect of convection, in evolutionary models for instance.

1.2.3 Reynolds-stress models

As we have seen in Section 1.2.2, averaging the exact equations of hydrodynamics yields equations for the mean flow that feature second-order moments in the fluctuating quantities – namely the Reynolds stress tensor in the mean momentum equation, and the convective flux in the mean energy equation. In MLT, the overarching goal was to provide with algebraic expressions for both these quantities as a function of the mean flow itself, so as to close the system. Alternatively, one can use the exact equations of hydrodynamics again to derive transport equations for these second-order moments. Instead of integrating differential equations for the mean flow where the second-order correlations are injected as algebraic expressions in the system, one ends up integrating differential equations for the mean flow *and* at least the second-order correlations. This is at the heart of *Reynolds-stress models*. Let me immediately remark that this solution does not free us from having to close the system, as it might appear at first glance. Indeed, the transport equations for second-order correlations derived from the equations of hydrodynamics contain third-order correlations, for which one has the same problem all over again. This procedure leads to an infinite hierarchy of transport equations for correlation products of higher and higher order, so that there will always be more unknowns than equations. If, up to this point, the reader has not yet lost the candid and naive hope that a convection model can be derived from first principles only, let me cruelly dispel this illusion: *turbulence needs closure, always has, and always will* (whether it be in the context of a convectively unstable region or not).

Reynolds-stress models have been used for a long time in the hydrodynamics community to model turbulent flows (see seminal papers by Chou (1945); Rotta (1951), or else Chapter 11 of Pope (2000)). However, it was some time before they found applications in the stellar context. Xiong (1989) followed this approach to derive transport equations for the velocity variance, the temperature variance and the velocity-temperature covariance, which correspond to all the second-order moments one can form with the fluctuating velocity and temperature. In order to derive these equations, the author made a number of approximations to simplify the formalism: the fluctuations of the gravitational potential are neglected under the Cowling approximation (the validity of which I will discuss in Section 2.1.1), the radiative flux is described in the diffusion approximation, the turbulence is assumed subsonic (i.e. the relative fluctuations of density and temperature are supposed to be much smaller than unity) and anelastic (i.e. the material derivative of the fluctuating density is taken to be zero), the density fluctuations are assumed to only be due to temperature changes, without contribution from the pressure changes.

[15] In the words of Spiegel (1963): "It should be stressed that the word *theory* in [the] context [of MLT] is perhaps a misnomer."

Those are approximations pertaining directly to the nature of the fluctuating fields, and are not so much closure relations as physically grounded approximations. But, as I mentioned above, one also needs to adopt closure relations. Here the author chose to assume that 1) the Reynolds stress tensor is isotropic, so that only a scalar (the turbulent kinetic energy) is needed to describe the entire tensor, 2) the fluctuating velocity is completely uncorrelated with the fluctuating pressure gradient, and therefore vanishes from the energy equation, and 3) all third-order moments can be written in the down-gradient approximation. These are strong assumptions, especially in the superadiabatic region. The third assumption is important, in particular, because third-order moments are responsible for the non-local behaviour of convection. In the down-gradient approximation (also referred to as diffusion approximation), any third order moment is written as

$$\overline{u_k' xy} = -\nu_{xy} \frac{\partial \overline{xy}}{\partial x_k} \,, \tag{1.91}$$

where u_k' is the fluctuating k-th component of the velocity, x and y are any scalar turbulent quantities, and ν_{xy} is a diffusion coefficient pertaining to the transport of $\overline{xy}$ by the small-scale motions u_k'. Because this mode of transport is due to the turbulent motion of the gas, ν_{xy} is often called *turbulent viscosity*, and in analogy with the actual fluid viscosity, is prescribed by

$$\nu_{xy} = \sqrt{\overline{u_i' u_i'}} l_{xy} \,, \tag{1.92}$$

where l_{xy} is the mean free path of the turbulent eddies transporting the fluctuating quantities. This mean free path is perfectly equivalent to the notion of mixing length already introduced above for MLT, and must likewise be given an arbitrary value (here the author chose all l_{xy} to be equal to the local pressure scale height to within a factor of order unity, which is of course akin to the free parameter $\alpha_{\rm MLT}$ in MLT). It becomes apparent, then, that Reynolds-stress models actually rely on the same mixing length idea underlying the MLT, although the notion of mixing length appears at higher order.

Going beyond Xiong's work, Canuto (1993), and later Canuto (1997), proposed a refined version of this approach, where the velocity-pressure-gradient correlations are not neglected, the turbulent dissipation evolves according to its own transport equation, and most importantly, transport equations are derived for the third-order moments as well, meaning that the equations are closed at fourth order, and the non-local fluxes are modelled exactly. As such, his model is comprised of

- transport equations for the first-order moments: mean density $\overline{\rho}$, mean velocity $\widetilde{u_i}$ and mean temperature $\widetilde{T}$;
- transport equations for the second-order moments: Reynolds stress tensor $\widetilde{u_i'' u_j''}$, convective flux $c_P \widetilde{u_i'' T''}$ and temperature potential $\widetilde{T''^2}/2$;
- transport equations for the third-order moments: $\Pi_{ijk} \equiv \overline{u_i'' u_j'' \partial_k p'}$, $\Pi_{ij}^{\theta} \equiv \overline{u_i'' T'' \partial_j p'}$ and $\Pi_i^{\theta\theta} \equiv \overline{T''^2 \partial_i p'}$;
- transport equation for the turbulent dissipation rate ϵ (which I recall is defined by Equations 1.36 and 1.37);
- algebraic expressions for $\overline{u_i''}$, $\overline{T''}$, $\overline{p' u_i''}$, $\overline{p' \partial_i u_i''}$, $\overline{u_i'' Dp'/Dt}$ and $\overline{T'' Dp'/Dt}$.

Insofar as transport equations are derived up to third order, the small scale advection terms in the first- and second-order moment equations have their own transport equations, and therefore do not need to be closed, which is a considerable improvement compared to Reynolds-stress models stopping at second order. As an illustrative example, let us consider the transport equation on the Reynolds stress tensor. It is obtained by the following procedure: first, one multiplies Equation 1.14 on ρu_i by u_j

$$u_j \frac{\partial \rho u_i}{\partial t} + u_j \frac{\partial \left(p\delta_{ik} + \rho u_i u_k - \sigma_{ik} \right)}{\partial x_k} = \rho u_j g_i \,. \tag{1.93}$$

Then by permuting indices i and j and making use of Equation 1.13 to pull the density out of the derivatives, one obtains

$$\rho u_i \frac{\partial u_j}{\partial t} + \rho u_i u_k \frac{\partial u_j}{\partial x_k} + u_i \frac{\partial \left(p\delta_{jk} - \sigma_{jk} \right)}{\partial x_k} = \rho u_i g_j \,. \tag{1.94}$$

Then, forming the sum of Equations 1.93 and 1.94 yields

$$\frac{\partial \rho u_i u_j}{\partial t} + \frac{\partial \rho u_i u_j u_k}{\partial x_k} = -\left(u_j \frac{\partial p}{\partial x_i} + u_i \frac{\partial p}{\partial x_j}\right) + (u_j g_i \rho + u_i g_j \rho) + \left(u_i \frac{\partial \sigma_{jk}}{\partial x_k} + u_j \frac{\partial \sigma_{ik}}{\partial x_k}\right) . \tag{1.95}$$

Taking the Reynolds average and remarking that

$$\overline{\rho u_i u_j} = \overline{\rho}\widetilde{u_i}\widetilde{u_j} + \overline{\rho}\widetilde{u_i'' u_j''} , \tag{1.96}$$

$$\overline{\rho u_i u_j u_k} = \overline{\rho}\widetilde{u_i}\widetilde{u_j}\widetilde{u_k} + \overline{\rho}\widetilde{u_i}\widetilde{u_j'' u_k''} + \overline{\rho}\widetilde{u_j}\widetilde{u_i'' u_k''} + \overline{\rho}\widetilde{u_k}\widetilde{u_i'' u_j''} + \overline{\rho}\widetilde{u_i'' u_j'' u_k''} , \tag{1.97}$$

one finds

$$\begin{aligned} &\frac{\partial \overline{\rho}\widetilde{u_i}\widetilde{u_j}}{\partial t} + \frac{\partial \overline{\rho}\widetilde{u_i'' u_j''}}{\partial t} + \frac{\partial \overline{\rho}\left(\widetilde{u_i}\widetilde{u_j}\widetilde{u_k} + \widetilde{u_i}\widetilde{u_j'' u_k''} + \widetilde{u_j}\widetilde{u_i'' u_k''} + \widetilde{u_k}\widetilde{u_i'' u_j''} + \widetilde{u_i'' u_j'' u_k''}\right)}{\partial x_k} \\ &\quad = -\left(\widetilde{u_i}\frac{\partial \overline{p}}{\partial x_j} + \widetilde{u_j}\frac{\partial \overline{p}}{\partial x_i} + \overline{u_i''}\frac{\partial \overline{p}}{\partial x_j} + \overline{u_j''}\frac{\partial \overline{p}}{\partial x_i} + \overline{u_i''\frac{\partial p'}{\partial x_j}} + \overline{u_j''\frac{\partial p'}{\partial x_i}}\right) + \overline{\rho}\left(\widetilde{u_i} g_j + \widetilde{u_j} g_i\right) + \left(\overline{u_i''\frac{\partial \sigma_{jk}}{\partial x_k}} + \overline{u_j''\frac{\partial \sigma_{ik}}{\partial x_k}}\right) . \end{aligned} \tag{1.98}$$

Here, I have already neglected the mean viscous stress tensor $\overline{\sigma_{ij}}$, and I have considered $\mathbf{g}$ to be unperturbed by the turbulence. From this one must subtract the equation on $\overline{\rho}\widetilde{u_i}\widetilde{u_j}$. The latter is obtained by performing the exact same operation on Equation 1.34, which yields

$$\frac{\partial \overline{\rho}\widetilde{u_i}\widetilde{u_j}}{\partial t} + \frac{\partial \overline{\rho}\widetilde{u_i}\widetilde{u_j}\widetilde{u_k}}{\partial x_k} + \widetilde{u_i}\frac{\partial \overline{\rho}\widetilde{u_j'' u_k''}}{\partial x_k} + \widetilde{u_j}\frac{\partial \overline{\rho}\widetilde{u_i'' u_k''}}{\partial x_k} = -\left(\widetilde{u_i}\frac{\partial \overline{p}}{\partial x_j} + \widetilde{u_j}\frac{\partial \overline{p}}{\partial x_i}\right) + \overline{\rho}\left(\widetilde{u_i} g_j + \widetilde{u_j} g_i\right) . \tag{1.99}$$

Again, the mean viscous stress tensor has been neglected. Subtracting Equation 1.99 from Equation 1.98, and using Equation 1.33 to pull $\overline{\rho}$ out of the time derivative, one finally obtains

$$\begin{aligned} \frac{\partial \widetilde{u_i'' u_j''}}{\partial t} + \widetilde{u_k}\frac{\partial \widetilde{u_i'' u_j''}}{\partial x_k} + \frac{1}{\overline{\rho}}\frac{\partial \overline{\rho}\widetilde{u_i'' u_j'' u_k''}}{\partial x_k} &= -\left(\widetilde{u_i'' u_k''}\frac{\partial \widetilde{u_j}}{\partial x_k} + \widetilde{u_j'' u_k''}\frac{\partial \widetilde{u_i}}{\partial x_k}\right) \\ &\quad - \frac{1}{\overline{\rho}}\left(\overline{u_i''}\frac{\partial \overline{p}}{\partial x_j} + \overline{u_j''}\frac{\partial \overline{p}}{\partial x_i} + \overline{u_i''\frac{\partial p'}{\partial x_j}} + \overline{u_j''\frac{\partial p'}{\partial x_i}}\right) + \frac{1}{\overline{\rho}}\left(\overline{u_i''\frac{\partial \sigma_{jk}}{\partial x_k}} + \overline{u_j''\frac{\partial \sigma_{ik}}{\partial x_k}}\right) . \end{aligned} \tag{1.100}$$

On the left-hand side, we recognise the mean material derivative (i.e. the material derivative following the mean flow velocity $\widetilde{\mathbf{u}}$ instead of the actual flow velocity $\mathbf{u}$), as well as the non-local flux of turbulent kinetic energy. This quantity, which is closed using the mixing-length hypothesis in Xiong (1989) for instance, does not need to be closed here, because the system of equations contains a transport equation for $\widetilde{u_i'' u_j'' u_k''}$ itself. As for the right-hand side, only the second and third brackets need to be closed. The quantities that are not closed in the second bracket ($\overline{u_i''}$ and the velocity-pressure-gradient correlation – or *acoustic energy flux* – $\overline{u_i''\partial_j p'}$) are expressed by assuming that the density, pressure and temperature fluctuations follow polytropic relations. The last bracket, on the other hand, is rewritten

$$\overline{u_i''\frac{\partial \sigma_{jk}}{\partial x_k}} + \overline{u_j''\frac{\partial \sigma_{ik}}{\partial x_k}} = \frac{\partial\left(\overline{u_i''\sigma_{jk}} + \overline{u_j''\sigma_{ik}}\right)}{\partial x_k} - \left(\overline{\sigma_{jk}\frac{\partial u_i''}{\partial x_k}} + \overline{\sigma_{ik}\frac{\partial u_j''}{\partial x_k}}\right) . \tag{1.101}$$

The first term corresponds to the viscous flux, and can be incorporated in the total non-local transport term, with the kinetic energy flux. It is then argued that the viscous flux is negligible compared to the kinetic energy flux, and can therefore be discarded. The second term, on the other hand, *defines* the turbulent dissipation tensor ϵ_{ij}, in such a way that $\epsilon_{ij} \equiv \overline{u_i''\partial_k\sigma_{jk} + u_j''\partial_k\sigma_{ik}}$ (see Equation 1.36). In turn, for high-Reynolds number flows, the turbulent dissipation tensor is assumed to be isotropic, which *defines* the scalar turbulent dissipation rate ϵ, in such a way that $\epsilon_{ij} \equiv 2\overline{\rho}\epsilon\delta_{ij}/3$ (see Equation 1.37). All in all, the last bracket on the right-hand side of Equation 1.100 only depends on ϵ, and is closed by adding to the system a transport equation for the turbulent dissipation rate.

This brief derivation makes salient the key points in deriving a Reynolds-stress model, namely that 1) the non-local transport terms only need to be closed at the last order of the system of equations, 2) certain additional moments appearing in the equations, essentially involving either the compressibility[16] term $\overline{u_i''}$ and the fluctuation of the pressure gradient $\boldsymbol{\nabla} p'$ require special treatment (in Canuto (1997) this is done by considering a polytropic gas), and 3) special care must be taken to model the turbulent dissipation rate ϵ. This last point, in particular, constitutes one of the major difficulties in deriving a Reynolds-stress model, because while it is possible to derive an exact equation for ϵ from first principle (Pope 2000) – by plugging Equation 1.16 into the definition of the turbulent dissipation –, this exact equation proves very impractical to close. It is important to understand that the impossibility to close the exact equation on ϵ is not just a purely mathematical tantrum thrown by the equation, but instead has a more fundamental, physical origin: this definition of ϵ makes it pertain to the dissipative scales of motion, which, for high-Reynolds number flows such as those considered here, are far removed from the large scales of motion. While closure relations can reasonably be linked to the large scales, it is extremely difficult to link them to what is happening at the other end of the turbulent spectrum. Therefore, in order to 'derive'[17] a model equation for ϵ, it is best viewed in terms of its effect on the large scales, namely as a sink of energy corresponding to the rate of injection of energy into the turbulent cascade. This invariably leads to *a model equation that is purely empirical in nature*, and moreover relies on the mixing-length hypothesis to close the non-local transport of ϵ (Pope 2000) – more specifically, the term corresponding to the advection of ϵ by the small-scale turbulent motions is closed by the down-gradient approximation (Equation 1.91). For instance, Canuto (1997) considered two different forms, one of which is an extension of the standard form to compressible flows

$$\frac{\partial \epsilon}{\partial t} + \widetilde{u_i}\frac{\partial \epsilon}{\partial x_i} - \frac{1}{\overline{\rho}}\frac{\partial}{\partial x_i}\left(\overline{\rho}\nu_{ij}\frac{\partial \epsilon}{\partial x_j}\right) = -C_{\epsilon,1}\frac{\epsilon}{k}\widetilde{u_i''u_j''}\frac{\partial \widetilde{u_i}}{\partial x_j} - C_{\epsilon,2}\frac{\epsilon^2}{k} + C_{\epsilon,3}\frac{\epsilon}{\overline{\rho}k}\overline{p'\frac{\partial u_i''}{\partial x_i}} + C_{\epsilon,4}m\left(1-\gamma^{-1}\right)\frac{\epsilon F_i^{\mathrm{conv}}}{\overline{p}k}\frac{\partial \overline{p}}{\partial x_i} - \epsilon\frac{\partial \widetilde{u_i}}{\partial x_i}\,, \quad (1.102)$$

where $k \equiv \widetilde{u_i''u_i''}/2$ is the turbulent kinetic energy, m is the polytropic index of the gas, γ the polytropic exponent, $\nu_{ij} \equiv C_{\epsilon,5}k\widetilde{u_i''u_j''}/\epsilon$ is an anisotropic viscosity tensor describing the small-scale, turbulent transport of ϵ, and $C_{\epsilon,i}$ ($i = 1$ to 5) are empirical, dimensionless parameters of order unity.

As a final note on Reynolds-stress models, let me remark that closing the system of equations at third order requires a closure relation for fourth-order correlation products. This is often done by adopting the Eddy-Damped Quasi-Normal Approximation, which I briefly discuss now. The idea stems from the mathematical identity that, if X_i ($i = 1$ to N) are N random variables that each follow a normal distribution, regardless of their mutual correlations, then (Millionshchikov 1941) *any correlation product formed using an odd number of X_i is zero, and any correlation product formed using an even number of X_i can be written as a function of the covariance matrix associated to the vector of random variables* $\mathbf{X}$ *only.* The function in question becomes increasingly complex as the order of the correlation product considered becomes higher. However, the special case of fourth-order correlation products yields the simple following relation

$$\overline{X_iX_jX_kX_l} = \overline{X_iX_j}\ \overline{X_kX_l} + \overline{X_iX_k}\ \overline{X_jX_l} + \overline{X_iX_l}\ \overline{X_jX_k}\,. \quad (1.103)$$

When the random vector $\mathbf{X}$ does not follow a multivariate Gaussian distribution, it is customary to define the *fourth-order cumulant* C_{ijkl} of the distribution as the difference between the actual fourth-order moment and the Gaussian fourth-order moments, so that

$$\overline{X_iX_jX_kX_l} = \overline{X_iX_j}\ \overline{X_kX_l} + \overline{X_iX_k}\ \overline{X_jX_l} + \overline{X_iX_l}\ \overline{X_jX_k} + C_{ijkl}\,. \quad (1.104)$$

Then closing the fourth-order moments amounts to closing the fourth-order cumulant. The most drastic approximation one can adopt is the *Quasi-Normal Approximation* (QNA), which consists in setting $C_{ijkl} = 0$. However, this poses a number of problems as regards the predicted evolution of the third-order moments. In particular, since the third-order moments (of velocity for instance) are no longer non-locally transported by the turbulent motions

[16] The reason this moment is referred to as the *compressibility* becomes apparent when it is rewritten thus: $\overline{u_i''} = -\overline{\rho' u_i''}/\overline{\rho}$, where $\rho' \equiv \rho - \overline{\rho}$. As such, if the fluid is incompressible (or even in the slightly less strict Boussinesq approximation), we have $\rho' = 0$, and therefore $\overline{u_i''} = 0$.

[17] Model equations for the turbulent dissipation are not so much derived as they are guessed, and then confronted to laboratory experiments on turbulence, or else – for Reynolds numbers that are not too high – direct numerical simulations.

of the gas, they locally accumulate without any way to escape anywhere. This non-physical accumulation of third-order moment leads to an ever-increasing skewness of the statistical velocity distribution, and as a result eventually violates the condition that the flow must be realisable[18] – more specifically, some wavevectors can end up with a negative energy. In order to circumvent this unwanted behaviour, the next level of approximation consists in modelling the effect of the non-vanishing cumulant by adding an extra viscosity in the third-order equation: this is the *Eddy-Damped Quasi-Normal Approximation* (or ED-QNA, Lesieur 2008). This approximation requires the introduction of a typical damping time τ, which must be prescribed accordingly. This poses two problems. First, there are multiple time scales in the problem (for instance, the acoustic time scale $\tau_a \equiv L/c$, where L is the typical scale of the mean flow, and c the speed of sound, the shear time scale $\tau_s \equiv (\partial_i \widetilde{u}_j \partial_i \widetilde{u}_j)^{1/2}$, as well as the local thermal time scale that can become relevant for third-order moments involving the temperature), which can be very different from one another. There is no physical justification for one to be chosen over the others. The second problem is the unavoidable – and undoubtedly unsurprising by now – consequence that a non-dimensional parameter of order unity must be introduced to account for the uncertainty not only on the exact value of the damping time τ, but more generally on the very notion of the cumulant being modelled by a damping time. The hope in closing the system of equations at such a high order, therefore, is that this uncertainty will have but a small effect on the predicted behaviour of the large-scale flow, compared, for instance, with the large sensitivity of the predictions made by MLT depending on the chosen value of $\alpha_{\rm MLT}$. Nevertheless, even the ED-QNA fails to correctly predict the fourth-order moments observed in 3D Large-Eddy Simulations (Kupka and Montgomery 2002; Montgomery and Kupka 2004; Kupka and Robinson 2007), so that more refined closure relations are necessary (e.g Gryanik and Hartmann 2002; Gryanik et al. 2004).

1.2.4 Concluding remarks

Each method listed in Section 1.2 for the modelling of stellar turbulent convection has its own strengths, but also its own weaknesses. Mixing length formalisms are historically the first models that were used to describe the convective flux in stars, and to include the effect of convection in 1D stellar evolutionary models. Standard MLT yields very simple expressions for the convective flux and the turbulent pressure, and is therefore easy to implement. As a result, it remains, to this day, a widely used tool for convection modelling. More refined versions of MLT, accounting for the time-dependence of the background in which convection arises, as well as the non-local nature of convection, have been developed. Nevertheless, the core assumptions underlying MLT have always remained the same, in particular the Boussinesq or anelastic approximation, and the mixing length hypothesis. Consequently, some aspects of turbulent convection are inherently discarded in all versions of MLT, in particular the spatial and temporal structure of the turbulent cascade, which is reduced to a single spatial scale and timescale. As we will see in Chapter 2, while this may be sufficient to describe the equilibrium state of convection in the bulk of the convectively unstable region, the effect of turbulent convection on the waves that travel in the stellar medium is highly sensitive to these approximations. Furthermore, MLT being more of an empirical prescription than a *bona fide* theory, it depends on a number of free parameters that are very complicated to constrain physically. The more refined Reynolds-stress models suffer from the same fundamental limitations.

On the other hand, 3D hydrodynamic simulations have become the subject of an increasing interest in the context of stellar convection modelling, especially (but not only) in the uppermost layers of stellar convective zones (Kupka and Muthsam 2017). The advantage of these simulations lies in the fact that the flow is computed from first principles, instead of relying on *ad-hoc* prescriptions. However, there are substantial caveats, not the least of which concerns the grid resolution achieved in these simulations. Because of the highly turbulent nature of stellar convection, all relevant length scales cannot be resolved, so that *ad-hoc* prescriptions must be adopted to model the small, unresolved scales, very often through the introduction of an effective viscosity – of through the introduction of nothing, in which case the numerical scheme 'takes care' of the unresolved scales. Because of this resolution problem, the flow no longer evolves according to the exact equations of hydrodynamics, and the equations therefore are not derived directly from first principles. Nevertheless, these large-eddy simulations have found an increasing use to describe surface stellar convection, in particular to build patched stellar models, because

[18] In the vocabulary of statistics, the term *realisability* usually refers to the Probability Density Function (or PDF) associated to the considered random variables. A PDF is said to be realisable if it is everywhere positive (or at least non-negative), and if it is normalised to unity. In the scope of fluid dynamics, and more particularly of Reynolds stress models of turbulence, the term realisability more often than not refers to the flow itself. In that case, the flow is said to be realisable if the determinant of the Reynolds stress tensor is everywhere positive. A corollary of that condition is that the energy spectrum must be positive for every wavevector Pope (2000)

they significantly improve the realism of the superficial layers of 1D stellar models, compared to MLT (Schlattl et al. 1997). However, as for MLT, they show their limitations when it comes to modelling the detailed structure of turbulence in the superadiabatic region, which, as will become apparent in Chapter 2, is of particular importance for the coupling of convection with the waves that travel in its midst. Furthermore, these simulations have a high computational cost, which limits their use for parametric studies, where the physics of convection may be explored through the use of various control parameters.

I conclude on the matter of stellar convection by saying this: that many modelling approaches have been developed, which have considerably deepened our understanding of the structure and dynamics of stellar convective regions; but that there is still much that is not understood, in particular as far as surface convection is concerned, and that no ideal approach seems to stand out as *the* ultimate method. Consequently, the question of how to model convection is not a closed one. This is particularly the case in regard to the interaction of convection with stellar oscillations, as I will show in Chapter 2, and more specifically in Sections 2.2 to 2.4.

2 Impact of turbulent convection on solar-like oscillations

Contents

> La lumière ne peut-elle pénétrer ces masses ? Revenons à ce cri : Lumière ! et obstinons-nous-y ! Lumière ! Lumière ! Qui sait si ces opacités ne deviendront pas transparentes ?
>
> Victor Hugo

To the utter dismay of generations of astronomers, this most passionate cry has fallen into the deaf ears of Nature, who, as usual, could not care less that it does not make our task easy: no, stars are not transparent, and with the exception of their most superficial atmospheric layers, their deep interior eludes our direct gaze. While stellar interiors are opaque to light, however, they are transparent to other kinds of waves, in particular sound waves. Acoustic oscillations can propagate through the stratified gaseous medium constituting the star, and by rebounding on its surface, lead to the development of global modes of oscillation. These modes check two very important boxes: they carry the signature of the physical conditions prevailing in a substantial portion of the interior of the star; and they can be observed through the perturbations they entail at the visible surface of the star, either by means of the *velocity power spectrum* measured via the Doppler effect incurred by spectral absorption lines in the atmosphere, or by means of the *intensity power spectrum* measured via the total emergent intensity. From there, the idea that observing surface oscillations gives us access to the internal structure of the star: this is at the heart of *helioseismology* – when applied to the Sun –, and its younger brother *asteroseismology* – when applied to other stars. In the immortal[1] words of Marie-Antoinette: if they have no electromagnetic waves, let them have acoustic ones! And undoubtedly, the advent of asteroseismology has revolutionised our understanding of stellar interiors. In this chapter, I start by giving a quick and general introduction on stellar oscillations in Section 2.1, particularly from a theoretical point of view. As for Chapter 1, this outline is not meant as an exhaustive account of all the

[1] albeit wrongly attributed

refinements brought to stellar oscillation analysis over the decades of existence of asteroseismology, but is rather meant as a simple theoretical framework in which the rest of the discussion can be articulated. It is largely, if not entirely, inspired by Unno et al. (1989), and more particularly their Chapter III; naturally, this is where I would refer the interested reader, should he or she want to know more.

I will specifically focus on solar-like oscillations, which are modes of acoustic nature that develop partly in the convective envelope of solar-type stars, and are therefore susceptible to be coupled with turbulent convection. In solar-like oscillators, oscillation-convection coupling is at its strongest close to the surface of the star, where the convective transport is not as efficient as in the bulk. This coupling is a burden, as much as it is a blessing. A burden, because convection changes the frequency of the modes. This frequency change is primarily due to a combination of physical processes happening at the surface of the star, and collectively referred to as *surface effects*. If one wishes to use individual mode frequencies to probe the interior of the star, one has to treat or avoid the surface effects in some way. The problem of correcting the surface effects, therefore, is the same as the problem of modelling turbulent convection, which, as we saw in Chapter 1, is not a small one. Additionally, turbulent convection plays a very important role in the energetic aspects of solar-like oscillations. Indeed, the turbulent motions entailed by convection inject energy in the modes, and are therefore directly responsible for their excitation. In parallel, the same turbulent motions can also take energy from the modes (in other words, damp them), therefore affecting their typical life time, or even their linear stability.

A burden, yes, but also a blessing in disguise. Because solar-like oscillations bear the mark of turbulent convection, observations on the former give information on the latter. The difficulties we encounter to model stellar convection, preventing us from deploying the full arsenal of p-mode frequencies to probe stellar interiors, are indeed great. But this winter of despair can also be seen as a spring of hope, as an opportunity to use observed p-mode properties precisely to constrain our stellar convection models. To that end, it is necessary to gain a better theoretical knowledge of the coupling between what we can observe (the p-modes), and what we wish to study (the turbulent convection). This is the overarching motivation behind the work I present in this thesis. In the second part of this chapter, I present the extent to which the turbulence-oscillation coupling, and all of its consequences, have been studied before, more particularly the energetic aspects pertaining to the driving (Section 2.2) and the damping (Section 2.3) of the modes by turbulent convection, as well as the surface effects (Section 2.4). In doing so, I will focus as much on what has been done, as on what still needs to be done; as much on what is fairly well understood, as on what remains unclear; as much on the closed questions, as on the open ones; as much on the basis of the work presented in this thesis, as on the reason why it is necessary. By the end of this Chapter, I will therefore be able to present, in Chapter 3, both the context, and the research problems underlying the work presented in this manuscript.

2.1 Stellar oscillations: a quick introduction

I presented in detail the equations of hydrodynamics in Appendix A, in the form of a transport equation for density (which I later put in the form of Equation 1.13), momentum (which I later put in the form of Equation 1.14), and internal energy (which I later put in the form of the entropy equation A.39). Those are the starting equations, from which all the properties of the oscillations can be derived (with the exception of the impact of magnetic fields, which I neglected above, and will continue to neglect in this entire manuscript). During the course of this introductory discussion, I will be led to adopt a certain number of approximations without which the derivation would become unnecessarily complicated. I can already list those we adopt from the very beginning

- I will neglect all viscous effects, which amounts to setting $\sigma_{ij} = 0$ in the momentum equation and in the entropy equation;
- I will neglect all effects of turbulence – or, in other words, all effects of convection. This amounts to discarding the contribution of turbulence to the velocity $\mathbf{u}$ of the flow, which now only contains a contribution from the equilibrium background and a contribution from the oscillations;
- I will, as I did before, discard the energy generation due to nuclear reactions.

These approximations are important ones – for instance, energy generation is actually not negligible in the core of the star, while the effect of convection is not negligible in convective regions, and in particular in the superadiabatic region, as we will see later on in this Chapter. However, they are sufficient for the sake of this basic discussion. I

will be led to relax the first hypothesis for the energy equation, as well as the second hypothesis, after this Section. However, I will continue to adopt the third hypothesis throughout the rest of this thesis. With these approximations in mind, the continuity, Navier-Stokes[2] and entropy equations become

$$\left(\frac{\partial}{\partial t} + u_i \frac{\partial}{\partial x_i}\right)\rho + \rho \frac{\partial u_i}{\partial x_i} = 0 \,, \tag{2.1}$$

$$\rho\left(\frac{\partial}{\partial t} + u_j \frac{\partial}{\partial x_j}\right)u_i = -\frac{\partial p}{\partial x_i} - \rho \frac{\partial \Phi}{\partial x_i} \,, \tag{2.2}$$

$$\rho T\left(\frac{\partial}{\partial t} + u_i \frac{\partial}{\partial x_i}\right)s = -\frac{\partial F_i^{\rm rad}}{\partial x_i} \,, \tag{2.3}$$

where I have used the continuity equation to rearrange the first term in the momentum equation, and I have introduced the *gravitational potential* Φ, defined in such a way that $\mathbf{g} = \boldsymbol{\nabla}\Phi$. To this system of equations I must add one on the gravitational potential Φ and another one on the radiative flux. The former only depends on the mass distribution inside the star, and is locally given by the Poisson equation

$$\boldsymbol{\nabla}^2\Phi = 4\pi G\rho \,, \tag{2.4}$$

where $\boldsymbol{\nabla}^2$ is the Laplacian operator, and $G = 6.67 \times 10^{-11}$ m^3.kg^{-1}.s^{-2} is the gravitational constant. As for the radiative flux, it is given in the diffusion limit by Equation 1.12, which I recall here for the sake of clarity

$$\mathbf{F}^{\rm rad} = -\frac{16\sigma T^3}{3\pi\kappa_R\rho}\boldsymbol{\nabla}T \,. \tag{2.5}$$

The system comprised of Equations 2.1 to 2.5, in addition to equations of state for pressure $p(\rho, T)$, entropy $s(\rho, T)$ and opacity $\kappa_R(\rho, T)$, form the basis on which oscillations can be described.

2.1.1 Linear perturbation theory for adiabatic oscillations

Linearisation of the equations of hydrodynamics

Setting all time derivatives to zero in this system, and furthermore setting the velocity to zero (in the absence of rotation and convection, there is no background velocity), one obtains the equations of stellar equilibrium. The standard form of these equations is found by further assuming spherical symmetry for the star, which amounts to neglecting all external forces which could break the spherical symmetry by imposing a preferred direction, such as global or differential rotation, magnetic fields, or the presence of a binary companion for instance. If there is spherical symmetry, then the resulting equilibrium quantities only depend on the radial coordinate r. I now set out to linearly perturb the full system of equations around this state, meaning that I will derive the Taylor development of each of these equations and truncate the development at first-order in the fluctuating quantities. In that spirit, one can define the *Eulerian perturbation* of a quantity f as[3]

$$f'(\mathbf{x}, t) \equiv f(\mathbf{x}, t) - f_0(\mathbf{x}) \,, \tag{2.6}$$

with the understanding that $f' \ll f_0$. The reason this perturbation is called Eulerian is because it corresponds to the difference between f *as measured in a Eulerian frame of reference* and its equilibrium counterpart. Naturally, one can do the exact same thing in a Lagrangian frame. For any given Eulerian position $\mathbf{x}$, there is a parcel of fluid which would lie at this position in the absence of oscillations – i.e. in the equilibrium state. In the presence of oscillations, this parcel is displaced, and I denote its actual position at time t as $\mathbf{X}(\mathbf{x}, t)$. This allows me to define the *fluid displacement* at $\mathbf{x}$ as

$$\boldsymbol{\xi}(\mathbf{x}, t) \equiv \mathbf{X}(\mathbf{x}, t) - \mathbf{x} \,. \tag{2.7}$$

[2] which now corresponds to the Euler equation

[3] I warn the reader that the notation f' in this chapter must not be confused with the similar notation adopted in the previous chapter, where it referred to fluctuations around a time-dependent *ensemble average*. Here, it refers to fluctuations around a time-independent *equilibrium value*.

The Lagrangian frame is the frame in which the fluid parcel is immobile – otherwise stated, the frame which follows the movement of the parcel –, so that one can define the *Lagrangian perturbation* of f as

$$\delta f(\mathbf{x}, t) \equiv f(\mathbf{x} + \boldsymbol{\xi}(\mathbf{x}, t), t) - f_0(\mathbf{x}) \,. \tag{2.8}$$

This constitutes an exact definition of the Lagrangian perturbation. However, in a linear perturbation framework, the fluid displacement is assumed to be much smaller than all other length scales in the system, so that Equation 2.8 can be linearised thus

$$\begin{aligned} \delta f(\mathbf{x}, t) &\sim f(\mathbf{x}, t) + \boldsymbol{\xi}(\mathbf{x}, t) \cdot \boldsymbol{\nabla} f - f_0(\mathbf{x}) \\ &\sim f'(\mathbf{x}, t) + \boldsymbol{\xi}(\mathbf{x}, t) \cdot \boldsymbol{\nabla} f_0 \,. \end{aligned} \tag{2.9}$$

In order to obtain the second equality, I used the definition of f' (Equation 2.6), as well as the fact that the additional term $\boldsymbol{\xi} \cdot \boldsymbol{\nabla} f'$ is of second-order in the fluctuating quantities, and can therefore be discarded.

I express the linear, homogeneous system of partial differential equations yielded by the linearisation of the system using the Eulerian decomposition

$$\frac{\partial \rho'}{\partial t} + u_i \frac{\partial \rho_0}{\partial x_i} + \rho_0 \frac{\partial u_i}{\partial x_i} = 0 \,, \tag{2.10}$$

$$\rho_0 \frac{\partial u_i}{\partial t} = -\frac{\partial p'}{\partial x_i} - \rho' \frac{\partial \Phi_0}{\partial x_i} - \rho_0 \frac{\partial \Phi'}{\partial x_i} \,, \tag{2.11}$$

$$\rho_0 T_0 \frac{\partial s'}{\partial t} + \rho_0 T_0 u_i \frac{\partial s_0}{\partial x_i} = -\frac{\partial F_i'^{\mathrm{rad}}}{\partial x_i} \,, \tag{2.12}$$

$$\frac{\partial^2 \Phi'}{\partial x_i \partial x_i} = 4\pi G \rho' \,, \tag{2.13}$$

$$F_i'^{\mathrm{rad}} = -\frac{16\sigma T_0^3}{3\pi \kappa_{R,0} \rho_0} \frac{\partial T_0}{\partial x_i} \left(3\frac{T'}{T_0} - \frac{\kappa_R'}{\kappa_{R,0}} - \frac{\rho'}{\rho} + \frac{\partial_i T'}{\partial_i T_0} \right) \,, \tag{2.14}$$

to which must be added the linearisation of the equations of state

$$\delta p = \left(\frac{\partial p}{\partial \rho} \right)_T \delta \rho + \left(\frac{\partial p}{\partial T} \right)_\rho \delta T \,, \tag{2.15}$$

$$\delta s = \left(\frac{\partial s}{\partial \rho} \right)_T \delta \rho + \left(\frac{\partial s}{\partial T} \right)_\rho \delta T \,, \tag{2.16}$$

$$\delta \kappa_R = \left(\frac{\partial \kappa_R}{\partial \rho} \right)_T \delta \rho + \left(\frac{\partial \kappa_R}{\partial T} \right)_\rho \delta T \,. \tag{2.17}$$

These last three equations must necessarily be written in terms of Lagrangian perturbations: indeed, they pertain to thermodynamic transformations undergone by a given parcel of fluid, so that only in the Lagrangian frame do the coefficients $(\partial X / \partial Y)_Z$ correspond to actual thermodynamic coefficients. Of course, the same kind of relation can be derived for Eulerian quantities instead, by plugging Equation 2.9 into these last three relations. However, the coefficients appearing in front of ρ' and T' would not coincide with the thermodynamic coefficients, and would also contain a contribution from the stratification. In other words, they would not depend only on the thermodynamic state of the gas, but also on the specific structure of the star.

This system of twelve equations has twelve unknowns in the form of ρ', $\mathbf{u}$, Φ', s', $\mathbf{F}'^{\mathrm{rad}}$, p', T' and κ_R' (I recall that the only reason why the velocity perturbation $\mathbf{u}$ is not denoted with a $'$ is that we considered $\mathbf{u}_0 = \mathbf{0}$, so that the velocity perturbation corresponds to the total velocity). All the other quantities depend on the equilibrium structure of the star only, including all the thermodynamic coefficients in the last three equations. However, several changes of variables will help put this system in a more practical form. First, I adopt an Ansatz of the form

$$f'(\mathbf{x}, t) \equiv F'(\mathbf{x}) \exp^{j\omega t} \tag{2.18}$$

for every Eulerian perturbation f', where ω represents the angular frequency associated to the oscillations. For the sake of clarity, I will not change the notations of the wave variables; it must be noted, however, that from this point

onwards, the wave variables actually refer to the time-independent F' rather than the time-dependent f'. Adopting Equation 2.18 transforms the system of equations into differential equations on the space variable only, the entire time-dependence being contained within ω. Secondly, I replace the Eulerian perturbation of velocity $\mathbf{u}$ by the fluid displacement $\boldsymbol{\xi}$. To do this, let me remark that by definition of these two quantities, we have $D\boldsymbol{\xi}/Dt = \mathbf{u}$. But the advection term in the material derivative of $\boldsymbol{\xi}$ then yields $(\mathbf{u}\cdot\boldsymbol{\nabla})\boldsymbol{\xi}$, which is of second-order in the fluctuating quantities, so that it can be discarded, and we simply have $\partial\boldsymbol{\xi}/\partial t = \mathbf{u}$, or using the Ansatz above, $\mathbf{u} = j\omega\boldsymbol{\xi}$.

With these changes in mind, let me derive the new form of the system of equations. Equation 2.10 becomes

$$j\omega\rho' + j\omega\xi_i\frac{\partial\rho_0}{\partial x_i} + \rho_0\frac{\partial\, j\omega\xi_i}{\partial x_i} = 0\,. \tag{2.19}$$

Dividing by $j\omega$, we recognise that the first two terms together equal the Lagrangian perturbation of density, so that the linearised continuity equation reads

$$\delta\rho + \rho_0\frac{\partial\xi_i}{\partial x_i} = 0\,. \tag{2.20}$$

Similarly, the velocity equation reads

$$-\omega^2\xi_i = -\frac{1}{\rho_0}\frac{\partial p'}{\partial x_i} - \frac{\rho'}{\rho_0}\frac{\partial\Phi_0}{\partial x_i} - \frac{\partial\Phi'}{\partial x_i}\,, \tag{2.21}$$

which can be further split into a radial and horizontal parts

$$-\omega^2\xi_r = -\frac{1}{\rho_0}\frac{\partial p'}{\partial r} - \frac{\rho'}{\rho_0}\frac{\mathrm{d}\Phi_0}{\mathrm{d}r} - \frac{\partial\Phi'}{\partial r}\,, \tag{2.22}$$

$$-\omega^2\boldsymbol{\xi}_h = -\boldsymbol{\nabla}_h\left(\frac{p'}{\rho_0} + \Phi'\right)\,, \tag{2.23}$$

where ξ_r is the radial component of $\boldsymbol{\xi}$, $\boldsymbol{\xi}_h$ is the horizontal displacement defined by $\boldsymbol{\xi}_h \equiv \boldsymbol{\xi} - \xi_r\mathbf{e_r}$ ($\mathbf{e_r}$ is the unit radial vector pointing outwards), the operator $\boldsymbol{\nabla}_h$ is the horizontal gradient defined by $\boldsymbol{\nabla}_h \equiv \boldsymbol{\nabla} - \mathbf{e_r}\partial_r$, and we have used the spherical symmetry of the static equilibrium state to justify that the horizontal gradient of both ρ_0 and Φ_0 vanishes.

The horizontal displacement equation can be used to eliminate $\boldsymbol{\xi}_h$ from Equation 2.20. One finds

$$\delta\rho + \frac{\rho_0}{r^2}\frac{\partial r^2\xi_r}{\partial r} + \frac{\rho_0}{\omega^2}\boldsymbol{\nabla}_h^2\left(\frac{p'}{\rho_0} + \Phi'\right) = 0\,, \tag{2.24}$$

where $\boldsymbol{\nabla}_h^2$ is the horizontal Laplacian operator, defined by $\boldsymbol{\nabla}_h^2 \equiv \boldsymbol{\nabla}^2 - \partial_r^2$, and I recall that in spherical coordinates, the divergence operator contains a curvature term, which explains the presence of r^2 inside the radial derivative of ξ_r. Using a similar decomposition, one can rewrite the Poisson equation

$$\frac{1}{r^2}\frac{\partial}{\partial r}\left(r^2\frac{\partial\Phi'}{\partial r}\right) + \boldsymbol{\nabla}_h^2\Phi' = 4\pi G\rho'\,. \tag{2.25}$$

Let me now turn to the entropy equation. Replacing u_i by $j\omega\xi_i$ and using Equation 2.9, it reads

$$j\omega\rho_0 T_0\delta s = -\frac{\partial F_i'^{\mathrm{rad}}}{\partial x_i}\,. \tag{2.26}$$

As for the radiative flux, it can be split into its radial and horizontal components, so that

$$F_r'^{\mathrm{rad}} = -\frac{16\sigma T_0^3}{3\pi\kappa_{R,0}\rho_0}\frac{\mathrm{d}T'}{\mathrm{d}r} - \frac{16\sigma T_0^3}{3\pi\kappa_{R,0}\rho_0}\frac{\partial T_0}{\partial r}\left(3\frac{T'}{T_0} - \frac{\kappa_R'}{\kappa_{R,0}} - \frac{\rho'}{\rho_0}\right)\,, \tag{2.27}$$

$$\mathbf{F}_h'^{\mathrm{rad}} = -\frac{16\sigma T_0^3}{3\pi\kappa_{R,0}\rho_0}\boldsymbol{\nabla}_h T'\,, \tag{2.28}$$

where I have used the spherical symmetry of the star to write $\boldsymbol{\nabla}_h f_0 = \mathbf{0}$ for all equilibrium quantities. Using Equation 2.28 to eliminate $\mathbf{F}_h'^{\mathrm{rad}}$ from Equation 2.26, one finds

$$j\omega\rho_0 T_0 \delta s = -\frac{1}{r^2}\frac{\partial r^2 F_r'^{\mathrm{rad}}}{\partial r} + \boldsymbol{\nabla}_h^2\left(\frac{16\sigma T_0^3}{3\pi\kappa_{R,0}\rho_0}T'\right), \tag{2.29}$$

where I have once again used the spherical symmetry of the star to justify that the equilibrium radiative diffusion coefficient only depends on the radial coordinate, and therefore commutes with the horizontal gradient.

Finally, one can decrease the order of the system by expressing the Eulerian and Lagrangian density perturbations ρ' and $\delta\rho$ as functions of the Eulerian pressure perturbation p' and the Lagrangian entropy perturbation δs. To do this, I start by considering p as a function of the two thermodynamic state variables ρ and s, so that

$$\delta p = \left(\frac{\partial p}{\partial \rho}\right)_s \delta\rho + \left(\frac{\partial p}{\partial s}\right)_\rho \delta s\,. \tag{2.30}$$

Since the quantities p/ρ^2 and ρ, on the one hand, and T and s on the other hand, are conjugated pairs of state variables[4], one can write

$$\left(\frac{\partial T}{\partial \rho}\right)_s = \left(\frac{\partial p/\rho^2}{\partial s}\right)_\rho, \tag{2.31}$$

and pulling $1/\rho^2$ from the constant-density derivative on the right-hand side, this yields

$$\left(\frac{\partial p}{\partial s}\right)_\rho = \rho^2\left(\frac{\partial T}{\partial \rho}\right)_s = \rho^2\left(\frac{\partial T}{\partial p}\right)_s\left(\frac{\partial p}{\partial \rho}\right)_s. \tag{2.32}$$

Plugging this into Equation 2.30, and rearranging to isolate $\delta\rho$ instead, one finds

$$\delta\rho = \left(\frac{\partial \rho}{\partial p}\right)_s \delta p - \rho^2\left(\frac{\partial T}{\partial p}\right)_s \delta s\,. \tag{2.33}$$

We recognise the adiabatic exponent $\Gamma_1 \equiv (\partial \ln p/\partial \ln \rho)_s$ and the adiabatic gradient $\nabla_{\mathrm{ad}} \equiv (\partial \ln T/\partial \ln p)_s$, both of which have already been introduced in Chapter 1, and finally, splitting δp into p' and $\boldsymbol{\xi}\cdot\boldsymbol{\nabla} p_0$, and since the equilibrium pressure p_0 only depends on the radial coordinate

$$\delta\rho = \frac{\rho_0}{p_0\Gamma_1}p' + \frac{\rho_0\xi_r}{p_0\Gamma_1}\frac{\mathrm{d}p_0}{\mathrm{d}r} - \frac{\rho_0^2 T_0\nabla_{\mathrm{ad}}}{p_0}\delta s\,. \tag{2.34}$$

Using Equation 2.9, one can obtain a similar relation for ρ'

$$\rho' = \frac{\rho_0}{p_0\Gamma_1}p' + \frac{\rho_0\xi_r}{p_0\Gamma_1}\frac{\mathrm{d}p_0}{\mathrm{d}r} - \frac{\rho_0^2 T_0\nabla_{\mathrm{ad}}}{p_0}\delta s - \xi_r\frac{\mathrm{d}\rho_0}{\mathrm{d}r}\,. \tag{2.35}$$

Eliminating all occurrences of $\delta\rho$ or ρ' from the other equations using Equations 2.34 and 2.35 respectively,

[4] I recall that the pairs (A, B) and (C, D) of state variables are said to be conjugated if there exists a fifth state variable X such that *for any elementary thermodynamic transformation*, we have $\mathrm{d}X = A\,\mathrm{d}B + C\,\mathrm{d}D$. In our case, X is the internal energy per unit mass, as illustrated by the thermodynamic relation we already used above to write the entropy equation in the first place. Then it is straightforwardly seen that, on the one hand, $(\partial(\partial X/\partial B)_D/\partial D)_B = (\partial A/\partial D)_B$, and on the other hand, $(\partial(\partial X/\partial D)_B/\partial B)_D = (\partial C/\partial B)_D$. But the Schwarz theorem stipulates that these two second derivatives are equal, so long as the function X checks all the necessary regularity boxes, which leads to what is usually referred to as the Maxwell relation $(\partial A/\partial D)_B = (\partial C/\partial B)_D$.

one obtains

$$\frac{\rho_0}{p_0\Gamma_1}p' + \frac{\rho_0\xi_r}{p_0\Gamma_1}\frac{\mathrm{d}p_0}{\mathrm{d}r} - \frac{\rho_0^2 T_0 \nabla_{\mathrm{ad}}}{p_0}\delta s + \frac{\rho_0}{r^2}\frac{\partial r^2\xi_r}{\partial r} + \frac{\rho_0}{\omega^2}\boldsymbol{\nabla}_h^2\left(\frac{p'}{\rho_0} + \Phi'\right) = 0\,, \tag{2.36}$$

$$\omega^2\xi_r - \frac{1}{\rho_0}\frac{\partial p'}{\partial r} - \left(\frac{1}{p_0\Gamma_1}p' + \frac{\xi_r}{p_0\Gamma_1}\frac{\mathrm{d}p_0}{\mathrm{d}r} - \frac{\rho_0 T_0\nabla_{\mathrm{ad}}}{p_0}\delta s - \frac{\xi_r}{\rho_0}\frac{\mathrm{d}\rho_0}{\mathrm{d}r}\right)\frac{\mathrm{d}\Phi_0}{\mathrm{d}r} - \frac{\partial\Phi'}{\partial r} = 0\,, \tag{2.37}$$

$$j\omega\rho_0 T_0\delta s = -\frac{1}{r^2}\frac{\partial r^2 F_r'^{\mathrm{rad}}}{\partial r} + \boldsymbol{\nabla}_h^2\left(\frac{16\sigma T_0^3}{3\pi\kappa_{R,0}\rho_0}T'\right)\,, \tag{2.38}$$

$$\frac{1}{r^2}\frac{\partial}{\partial r}\left(r^2\frac{\partial\Phi'}{\partial r}\right) + \boldsymbol{\nabla}_h^2\Phi' = 4\pi G\left(\frac{\rho_0}{p_0\Gamma_1}p' + \frac{\rho_0\xi_r}{p_0\Gamma_1}\frac{\mathrm{d}p_0}{\mathrm{d}r} - \frac{\rho_0^2 T_0\nabla_{\mathrm{ad}}}{p_0}\delta s - \xi_r\frac{\mathrm{d}\rho_0}{\mathrm{d}r}\right)\,, \tag{2.39}$$

$$\begin{aligned} F_r'^{\mathrm{rad}} = &-\frac{16\sigma T_0^3}{3\pi\kappa_{R,0}\rho_0}\frac{\mathrm{d}T'}{\mathrm{d}r} - \frac{16\sigma T_0^3}{3\pi\kappa_{R,0}\rho_0}\frac{\partial T_0}{\partial r}\left[3\frac{T'}{T_0} - \frac{\kappa_R'}{\kappa_{R,0}}\right. \\ &\left. -\left(\frac{1}{p_0\Gamma_1}p' + \frac{\xi_r}{p_0\Gamma_1}\frac{\mathrm{d}p_0}{\mathrm{d}r} - \frac{\rho_0 T_0\nabla_{\mathrm{ad}}}{p_0}\delta s - \frac{\xi_r}{\rho_0}\frac{\mathrm{d}\rho_0}{\mathrm{d}r}\right)\right]\,, \end{aligned} \tag{2.40}$$

$$\delta s = \left(\frac{\partial s}{\partial p}\right)_T\left(p' + \xi_r\frac{\mathrm{d}p_0}{\mathrm{d}r}\right) + \left(\frac{\partial s}{\partial T}\right)_p\left(T' + \xi_r\frac{\mathrm{d}T_0}{\mathrm{d}r}\right)\,, \tag{2.41}$$

$$\kappa_R' = \left(\frac{\partial\kappa_R}{\partial p}\right)_T\left(p' + \xi_r\frac{\mathrm{d}p_0}{\mathrm{d}r}\right) + \left(\frac{\partial\kappa_R}{\partial T}\right)_p\left(T' + \xi_r\frac{\mathrm{d}T_0}{\mathrm{d}r}\right) - \xi_r\frac{\mathrm{d}\kappa_{R,0}}{\mathrm{d}r}\,. \tag{2.42}$$

Since I have eliminated the density variable as well as the two horizontal components of the fluid displacement and of the radiative flux from the system, there are now only seven equations, with seven unknowns in the form of p', ξ_r, δs, Φ', $F_r'^{\mathrm{rad}}$, T' and κ_R'. However, there actually is an eighth unknown in the system, in the form of the angular frequency ω. Therefore the system cannot be solved without an additional constraint: I will return to this matter later on.

On the adiabaticity of stellar oscillations and validity of the Cowling approximation

It is possible, under certain circumstances, to approximate the Lagrangian perturbation of entropy δs by a much more practical expression, which frees us from having to include it in the set of wave variables. The most drastic of these approximations is to consider that *all thermodynamic transformations undergone by a given parcel of fluid are isentropic*, that is to say both adiabatic (so that there is no transfer of entropy between the parcel and the neighbouring gas), and reversible, or quasi-static (so that there is no creation of entropy inside the parcel). This assumption is commonly referred to as the *adiabatic approximation*, even though it is actually stronger than mere adiabaticity. The adiabatic approximation translates best in the Lagrangian frame of reference: indeed, only in this frame does the variation of a thermodynamic variable correspond to an actual thermodynamic transformation undergone by a physical system. The mathematical translation of that approximation, therefore, is simply $\delta s = 0$ (this is the reason, incidentally, why we chose to write all variables in a Eulerian frame, except for δs). This substantially simplifies the system comprised of Equations 2.36 to 2.42: not only does δs vanish, but that also makes Equations 2.38 and 2.40 to 2.42 useless, as the only reason I needed them in the first place was to describe the non-adiabatic density perturbation.

To what extent can the oscillations be considered adiabatic? To answer this question, one has to compare timescales, more specifically the typical timescale associated to the oscillations, and the typical timescale associated to the thermal processes responsible for heat transfer. The former corresponds to the typical period of the modes: about 5 minutes in the Sun. The latter requires a bit more thought. At first glance, one may be tempted to use the *Kelvin-Helmholtz time scale*, defined as the ratio of the total gravitational potential energy stored in the star to its luminosity: $\tau_{KH} \equiv GM/LR^2$, where M is the mass of the star, L its luminosity, and R its radius. This corresponds to the time it would take for the star to radiate its energy away if there were no supply from nuclear reactions in the core. For the Sun, this is of the order of thirty million years, which is much longer than the oscillation timescale. However, this is only an averaged value of the thermal timescale over the entire star, and does not account for its large variability between the core and the surface. A *local* Kelvin-Helmholtz time scale can be

defined, in the form (e.g. Dziembowski and Koester 1981)

$$\tau_{KH}(m) = \int_m^M \frac{c_P T}{L}\,\mathrm{d}m\,, \tag{2.43}$$

where the virial theorem[5] was used to equate the opposite of the gravitational potential energy of a given layer with twice its internal energy (the factor 2 was then omitted, because I am only after an order of magnitude), c_P, T and L are now local quantities, and $m(r)$ is the mass coordinate, defined as the total mass contained below the layer of radius r. Throughout most of the interior of the star, the local thermal timescale is still much greater than the period of the oscillations. In that case, the gas has no time to exchange heat during a cycle of the modes, so that they can indeed be considered adiabatic to a very good approximation. However, this ceases to be true close to the surface of the star, where the two timescales become comparable. The adiabatic approximation is no longer valid in this region, and the entropy perturbations must then be accounted for. For the sake of this introduction, however, and because I simply aim at presenting some very basic properties of stellar oscillations, I will adopt the adiabatic approximation throughout the entire star.

In the following discussion, and because it further simplifies the formalism while being fairly accurate, especially for modes that have a large number of nodes in the radial direction, I will also adopt the Cowling approximation (Cowling 1941), which consists in neglecting the Eulerian perturbation of the gravitational potential: $\Phi' = 0$. The basis for this approximation is that, if the spherical symmetry of the star is not broken by the oscillations to too large an extent, then the total potential Φ at radius r is given by the total gas mass enclosed by the sphere of radius r centered on the center of the star. The idea, then, is to state that at any given time, the regions of the star where there is an excess of mass due to the oscillations compensate the regions where there is a default, so that in total, the deviation of Φ from its equilibrium value is negligible. As a result of the Cowling approximation, Φ' vanishes from the system of equations, and Equation 2.39 becomes useless.

Under these two approximations – the isentropic character of the oscillations, and the Cowling approximation –, the system of Equations 2.36 to 2.42 reduces to the much simpler form

$$\frac{1}{r^2}\frac{\partial r^2\xi_r}{\partial r} + \frac{p'}{p_0\Gamma_1} + \frac{\xi_r}{p_0\Gamma_1}\frac{\mathrm{d}p_0}{\mathrm{d}r} + \frac{1}{\omega^2}\nabla_h^2\left(\frac{p'}{\rho_0}\right) = 0\,, \tag{2.44}$$

$$\frac{1}{\rho_0}\frac{\partial p'}{\partial r} + \frac{p'}{p_0\Gamma_1}\frac{\mathrm{d}\Phi_0}{\mathrm{d}r} + \left(\frac{1}{p_0\Gamma_1}\frac{\mathrm{d}p_0}{\mathrm{d}r}\frac{\mathrm{d}\Phi_0}{\mathrm{d}r} - \frac{1}{\rho_0}\frac{\mathrm{d}\rho_0}{\mathrm{d}r}\frac{\mathrm{d}\Phi_0}{\mathrm{d}r} - \omega^2\right)\xi_r = 0\,. \tag{2.45}$$

Now, there are only two equations, and three unknowns, in the form of the radial displacement ξ_r and the Eulerian pressure perturbation p' (both of which are functions of the three space coordinates), as well as the angular frequency ω. Of course, the remark I made earlier about needing an additional constraint still holds.

Splitting the radial and horizontal component

For the moment, the wave variables depend both on the radial and horizontal coordinates. However, I have already split all vector variables and operators into a radial and horizontal parts. Therefore, Equations 2.44 and 2.45 is prime for a separation of variables, which can be performed thus. The radial displacement and pressure perturbation can both be written in the form

$$f(r,\theta,\phi) = F(r)Y(\theta,\phi)\,, \tag{2.46}$$

where θ and ϕ are the latitudinal and azimuthal angles, F contains the radial dependence of f, and Y its angular dependence. In the following, I will retain the notation ξ_r and p' for the wave variables, with the understanding that they now refer to the radial function $F(r)$ rather than the 3D function $f(\mathbf{r})$. Plugging this in Equation 2.44, and rearranging to isolate the radial terms from the angular terms, one obtains

$$\frac{r^2\rho_0\omega^2}{p'}\left(\frac{1}{r^2}\frac{\partial r^2\xi_r}{\partial r} + \frac{p'}{p_0\Gamma_1} + \frac{\xi_r}{p_0\Gamma_1}\frac{\mathrm{d}p_0}{\mathrm{d}r}\right) = -\frac{r^2\nabla_h^2 Y}{Y}\,. \tag{2.47}$$

[5]The *virial theorem* states that if the Lagrange function of a system is homologous of degree k – meaning that it goes as the k-th power of the generalised coordinates –, then the *time average* of the kinetic and potential energy (respectively $\langle T\rangle$ and $\langle E_p\rangle$) are related through $2\langle T\rangle = k\langle E_p\rangle$, with the only requirement being that all trajectories of the system in phase space must remain bounded (Landau and Lifshitz 1976). In our particular case, the average kinetic energy is of microscopic origin, and corresponds to the internal energy U of the gas, and the mean potential energy – being of gravitational origin – is homologous of degree -1, so that $\langle U\rangle = -\langle E_{\mathrm{grav}}\rangle/2$.

The left-hand side only depends on r, while the right-hand side[6] only depends on θ and ϕ. Since they are identically equal, neither depends on anything, and they are simply constant. Let me denote this constant as C, then one has

$$\boldsymbol{\nabla}_h^2 Y = -\frac{C}{r^2} Y \,, \tag{2.48}$$

which constitutes a second-order differential equation for Y, with the additional constraint that Y must be 2π-periodic in both θ and ϕ. Solving this equation is equivalent to finding the eigenfunctions of the operator $\boldsymbol{\nabla}_h^2$. Those are given by

$$Y_l^m(\theta, \phi) = P_l^m(\cos\theta) \exp^{jm\phi} \,, \tag{2.49}$$

where P_l^m is the associated Legendre polynomial[7] of degree l and order m, and l is given by $C = l(l+1)$. If we leave it at that, C can take any value, and therefore so can l: this relation just transforms the unknown C into the unknown l. However, the function Y is subjected to certain boundary conditions: the periodicity of Y forces m to take an integer value, and the associated Legendre polynomials can only be regular at the poles if l is also an integer. Therefore, *the entire angular dependency of the wave variables is only parameterised by the two integers l and m* (with the additional constraint that $|m| < l$, otherwise Y_l^m vanishes everywhere).

Now that the angular part of the wave equation is taken care of, one can transform Equations 2.44 and 2.45 into purely radial equations. This is done by replacing the horizontal Laplacian operator by its expression (Equation 2.48), with $C = l(l+1)$. Furthermore, let me remark that $\mathrm{d}\Phi_0/\,\mathrm{d}r = g_0$, where g_0 is the norm of the equilibrium gravitational acceleration[8], and let me use the hydrostatic equilibrium condition to write $\mathrm{d}p_0/\,\mathrm{d}r = -\rho_0 g_0$. One then obtains

$$\frac{1}{r^2}\frac{\mathrm{d}r^2\xi_r}{\mathrm{d}r} + \left(1 - \frac{L_l^2}{\omega^2}\right)\frac{p'}{\rho_0 c^2} - \frac{g_0}{c^2}\xi_r = 0 \,, \tag{2.50}$$

$$\frac{1}{\rho_0}\frac{\mathrm{d}p'}{\mathrm{d}r} + \frac{g_0}{\rho_0 c^2}p' + \left(N^2 - \omega^2\right)\xi_r = 0 \,, \tag{2.51}$$

where $c^2 \equiv p_0\Gamma_1/\rho_0$ is the square of the celerity at which sound waves propagate, and I have introduced the two characteristic squared frequencies

$$N^2 \equiv g_0\left(\frac{1}{p_0\Gamma_1}\frac{\mathrm{d}p_0}{\mathrm{d}r} - \frac{1}{\rho_0}\frac{\mathrm{d}\rho_0}{\mathrm{d}r}\right) \,, \tag{2.52}$$

$$L_l^2 \equiv \frac{l(l+1)c^2}{r^2} \,, \tag{2.53}$$

respectively referred to as the square of the *Brünt-Väisälä frequency* and of the *Lamb frequency*. When the stratification is such that $N^2 > 0$, the buoyancy force acts as a stabilising force, dragging a parcel back down when a local fluctuations displaces it upwards. In this case, the buoyancy force acts as a restoring force, allowing for *buoyancy waves* (or *gravity waves*) to propagate: the Brünt-Väisälä frequency represents the frequency of these waves. On the other hand, if $N^2 < 0$, then $\sqrt{-N^2}$ represents the linear growth rate associated to the convective instability. As for the Lamb frequency, it is better represented in terms of the local horizontal wave vector associated to the angular degree l, $k_h \equiv \sqrt{l(l+1)}/r$. Then we simply have $L_l = k_h c$, and it can be seen that the Lamb frequency corresponds to the angular frequency associated to the horizontal propagation of waves.

2.1.2 Stellar oscillations as resonant modes

The boundary value problem

As I mentioned above, the system comprised of Equations 2.50 and 2.51 has one more unknown than equations, because the angular frequency ω of the waves is also to be determined. Boundary conditions must therefore be

[6] I recall that in spherical coordinates, $\boldsymbol{\nabla}_h^2 = \frac{1}{r^2\sin^2\theta}\left(\sin\theta\frac{\partial}{\partial\theta}\left(\sin\theta\frac{\partial}{\partial\theta}\right) + \frac{\partial^2}{\partial\phi^2}\right)$. As such, while the operator $\boldsymbol{\nabla}_h^2$ does depend on r, this is not the case of $r^2\boldsymbol{\nabla}_h^2$.

[7] The associated Legendre polynomials differ from the actual Legendre polynomials, in the sense that they depend on an additional parameter m – Legendre polynomials do not have an order, only a degree. As it happens, if m is odd, the associated Legendre polynomials are actually not polynomials at all.

[8] In general, we have $\boldsymbol{\nabla}\Phi_0 = -\mathbf{g_0}$; but in the spherically symmetric case, $\mathbf{g_0} = -g_0\mathbf{e_r}$.

added to these two equations, and because the system is of second order in the radial coordinate r, two boundary conditions are needed: one at the center of the star and one at its surface.

The equations can be simplified at the center, because both the gravitational acceleration g_0 and the Brünt-Väisälä frequency vanish, whereas the Lamb frequency diverges. Furthermore, the gradient of ρ_0 vanishes, for regularity reasons. Therefore, the system of equations becomes

$$\frac{\mathrm{d}\left(r^2\xi_r\right)}{\mathrm{d}r} = \frac{l(l+1)}{\omega^2}\frac{p'}{\rho_0}\,, \tag{2.54}$$

$$\frac{\mathrm{d}p'/\rho_0}{\mathrm{d}r} = \omega^2\xi_r\,, \tag{2.55}$$

which amounts to the following second-order differential equation

$$\frac{\mathrm{d}^2\left(r^2\xi_r\right)}{\mathrm{d}r} = l(l+1)\xi_r\,. \tag{2.56}$$

Assuming that the radial displacement goes as a power function of r close to the center, characterised by an exponent α, one finds

$$(\alpha+2)(\alpha+1) = l(l+1)\,, \tag{2.57}$$

with two possible solutions: $\alpha = l-1$ and $\alpha = -l$. Naturally, ξ_r must remain regular at $r = 0$, so that the second solution is not physical. That leaves us with $\xi_r \propto r^{l-1}$, from which one also obtains $p' \propto r^l$. This constitutes the first boundary condition at the center. Concerning the surface, multiple boundary conditions can be adopted. The simplest one consists in assuming that while the surface can be distorted under the influence of the oscillations – meaning that the surface radius changes with time –, the pressure must remain identically null there, lest mechanical work be exerted on the star by a medium that does not contain matter. In other words, the Lagrangian perturbation of the gas pressure must vanish: $\delta p(r = R) = 0$. This constitutes one possible second boundary condition at the surface, although others exist (Unno et al. 1989).

The second-order system of equations, together with these two boundary conditions, form a well-posed boundary value problem, to which a discrete spectrum of eigenfrequencies can be associated. It is common to put this kind of system of equations and boundary conditions in the following canonical form (e.g. Hartman 2002)

$$\frac{\mathrm{d}}{\mathrm{d}r}\left(p(r)\frac{\mathrm{d}f}{\mathrm{d}r}\right) + q(r)f(r) = -\sigma^2 w(r)f(r)\,, \tag{2.58}$$

where the unknowns are the function $f(r)$ and the scalar σ^2, and the functions $p(r)$, $q(r)$ and $w(r)$ are known functions of the radial coordinate r. This canonical form, known as a *Sturm-Liouville type equation*, is very useful, because the solutions $f(r)$ and σ^2 are then given as the eigenvectors and eigenvalues of the linear Hermitian operator

$$\mathcal{L} = -\frac{1}{w(r)}\left[\left(\frac{1}{p(r)}\frac{\mathrm{d}}{\mathrm{d}r}\right) + q(r)\right]\,. \tag{2.59}$$

If, in addition, boundary conditions of the form $\alpha_1 f(r_1) + \beta_1 f'(r_1) = 0$ and $\alpha_2 f(r_2) + \beta_2 f'(r_2) = 0$ are imposed (where r_1 and r_2 are the two radial boundaries, and f' denotes the first derivative of f with respect to r), this becomes a *Sturm-Liouville problem*: the acceptable eigenfunctions are filtered according to whether or not they verify the boundary conditions, and the spectrum of solutions to the problem becomes discrete, with *real eigenfrequencies* σ_n^2 that can be indexed with an integer n (referred to as the *radial order* of the solution), and a unique function $f_n(r)$ associated to each of these real eigenfrequencies having exactly $n-1$ zeros between r_1 and r_2 (Hartman 2002).

Unfortunately, Equations 2.50 and 2.51 do not constitute a Sturm-Liouville type equation. While it might look like a mere mathematical coincidence, this problem actually has a much deeper and physical origin. The fundamental reason is that there are two different restoring forces: the buoyancy force, and the pressure force; and therefore, two different kinds of waves that can propagate in the interior of the star: *gravity waves* and *acoustic waves* (or sound waves)[9]. The coexistence of these two restoring forces is what prevents us from putting the system

[9]With the exception of radial waves, i.e. if $l = 0$: then, gravity waves do not exist, and only acoustic ones can propagate.

in the form of Equation 2.58. However, in the limit of high frequencies ($\sigma^2 \to +\infty$), the buoyancy restoring force becomes negligible, and only acoustic waves remain. On the contrary, in the limit of low frequencies ($\sigma^2 \to 0$), the pressure force becomes negligible, and only gravity waves remain. In these two limits, the problem does reduce to a Sturm-Liouville type, provided simple boundary conditions as those described above are adopted. Whether σ^2 is high or low enough or not, however, the solutions can still be associated each to their own radial order n.

Trapping of stellar oscillations

While the system does not generally constitute a Sturm-Liouville type equation, it can still be put into a more canonical form, by changing variables one last time. Let me introduce the new wave variables (Unno et al. 1989)

$$\widetilde{\xi_r}(r) \equiv r^2 \xi_r(r) \exp\left(-\int_0^r \frac{g_0(r')}{c^2(r')}\,\mathrm{d}r'\right), \tag{2.60}$$

$$\widetilde{\eta}(r) \equiv \frac{p'(r)}{\rho_0(r)} \exp\left(-\int_0^r \frac{N^2(r')}{g_0(r')}\,\mathrm{d}r'\right). \tag{2.61}$$

Then, forming the derivative of these variables with respect to r and using Equations 2.50 and 2.51, one finds

$$\frac{\mathrm{d}\widetilde{\xi_r}}{\mathrm{d}r} = h(r)\frac{r^2}{c^2}\left(\frac{L_l^2}{\omega^2} - 1\right)\widetilde{\eta}(r), \tag{2.62}$$

$$\frac{\mathrm{d}\widetilde{\eta}}{\mathrm{d}r} = \frac{1}{r^2 h(r)}\left(\omega^2 - N^2\right)\widetilde{\xi_r}(r), \tag{2.63}$$

where

$$h(r) \equiv \exp\left(\int_0^r \frac{N^2(r')}{g_0(r')} - \frac{g_0(r')}{c^2(r')}\,\mathrm{d}r'\right). \tag{2.64}$$

Let me perform a local analysis, meaning that I will consider the coefficients in these equations to be independent of r. Then one can inject an Ansatz for the radial dependence of $\widetilde{\xi_r}$ and $\widetilde{\eta}$, in the form

$$f(r) \equiv f \exp^{jk_r r}, \tag{2.65}$$

where the radial function $f(r)$ is replaced with a constant f, and the entire radial dependence is contained within the exponential factor. One can then derive a *dispersion relation* between the time dependence and the radial dependence of the perturbations – in other words, between ω and k_r

$$k_r^2 = \frac{\left(\omega^2 - L_l^2\right)\left(\omega^2 - N^2\right)}{c^2\omega^2}. \tag{2.66}$$

As a first remark, it can be seen that the dispersion relation, like the original wave equation, is independent of the azimuthal order m of the solution. As such, in this simple framework, there is a degeneracy among all modes that share the same radial order n and angular degree l. This degeneracy is lifted whenever the spherical symmetry assumed from the beginning is broken, whether it be by rotation, magnetic fields, etc., in which case modes of different azimuthal order are split from each other. However, in the present discussion, I discard the effect of these symmetry-breaking processes. Equation 2.66 shows that the squared Brünt-Väisälä frequency N^2 and Lamb frequency L_l^2 are key to study the local nature of the oscillations. More precisely, considering a particular solution to the system of equations, characterised by a known angular eigenfrequency ω verifying the boundary conditions described above, and a known angular degree l, then any region in the star falls into either one of these categories

- if the local values of N^2 and L_l^2 are such that $\omega^2 > N^2, L_l^2$ or $\omega^2 < N^2, L_l^2$, then we have $k_r^2 > 0$, and the radial wavevector is real. The Ansatz $\exp^{jk_r r}$ then shows that the perturbations are oscillatory in nature. In other words, they are associated to waves that can propagate in the radial direction. Naturally, they also propagate in the horizontal direction, with a horizontal wave number (already introduced above) $k_h = \sqrt{l(l+1)}/r$. These regions are therefore referred to as *propagative regions*;

- if the local values of N^2 and L_l^2 are such that $N^2 < \omega^2 < L_l^2$ or $L_l^2 < \omega^2 < N^2$, then we have $k_r^2 < 0$, and the radial wavevector is purely imaginary. The Ansatz $\exp^{jk_r r}$ then shows that the perturbations either grow or decay exponentially with r, and cannot propagate. More specifically, the direction of variation must be increasing in the direction of the closest propagative region (increasing with r if the propagative region is located above, decreasing if it is located below). In other words, the perturbations vanish exponentially the further away they are from their propagative regions. These regions are therefore referred to as *evanescent regions*.

From this local analysis stems that fact: that the solutions to the wave equation are only oscillatory in nature in certain regions of the star, depending on their frequency and angular degree. The waves propagate in these regions, and are reflected on the boundary of these regions – also called *turning points* –, only leaving evanescent, non-propagating waves leaking into the neighboring regions. In other words, *the oscillations are trapped*. Because of the multiple reflections of the waves on the turning points, the propagative regions act as *resonant cavities*, and the waves actually take the form of *stationary modes of oscillation*[10]. Unlike what one may have thought at first, it is therefore not the boundary conditions imposed at the center and the surface of the star that trap the oscillations, but the physical conditions reigning inside the star. The eigenfrequencies ω, however, still stem from the global boundary conditions, not to boundary conditions at the turning points of the resonant cavities[11], although the structure of the trapping regions has much more impact than that of the evanescent regions on the eigenfrequencies.

p-modes versus g-modes

The condition of wave trapping depends on the Brünt-Väisälä and Lamb frequency profiles $N^2(r)$ and $L_l^2(r)$, which allows the visualisation of the locations of the resonant cavities in the form of a *propagation diagram*. The propagation diagram largely depends on the type and the mass of the star considered. However, for the sake of this discussion, I do not delve into the entire zoology of stars that can be found in the Universe; rather, I focus on the case of solar-like stars, and more particularly the Sun, as these are the stars in which I will interest myself in this manuscript.

The definition of the Lamb frequency shows that it diverges at the center. In addition, if c decreases with r – which is the case throughout most of the star, with the exception of the chromosphere –, then L_l^2 itself decreases monotonously outwards. This behaviour is quite independent of the type of star considered. The behaviour of $N^2(r)$, however, is much less universal. As we mentioned in Section 2.1.1, it is negative in convective regions, and positive in radiative regions. In the Sun, that means we have $N^2(r) > 0$ up to $r/R \sim 0.7$ (where r/R is the fractional radial coordinate), and $N^2(r) < 0$ from 0.7 to almost 1. Then, because of the fast transition between the convective envelope and the radiative surface, N^2 quickly increases again, and takes positive values in the very superficial layers of the star. We show this behaviour in Figure 2.1. It can be seen, then, that depending on the eigenfrequency, a given mode is either going to be trapped in a central region, where $\omega^2 < N^2 < L_l^2$, or in an envelope region, where $N^2 < L_l^2 < \omega^2$. In the case of the Sun, those two types of trapping regions are quite distinctly separated[12], and are referred to the G-trapping region and P-trapping region respectively. The modes that are trapped in the G region are called *g-modes, or gravity modes*, and the modes that are trapped in the P region are called *p-modes, or acoustic modes*. The reason for the denomination "gravity" and "acoustic" modes will become apparent in a moment.

Let me consider briefly each type of mode, starting with the p-modes. These modes are trapped between a certain point in the interior, referred to as the *inner turning point* r_t, and another point very close to the surface. The inner turning point is reached when the angular frequency of the mode is no longer larger than the local Lamb

[10] As such, the term "propagative region" is perhaps a bit misleading, seeing as stationary modes cannot propagate.

[11] Besides, this would lead to a circular definition, since the turning points themselves – corresponding to the locations where $\omega^2 = N^2$ or $\omega^2 = L_l^2$ – depend on the frequency

[12] For stars where the distinction is not as clear, there can exist modes that have two important trapping regions – one of type G, and one of type P–, separated by a thin evanescent region coupling the two main cavities. Those are referred to as *mixed modes*, and are particularly important in more evolved stars, such as red giants. The reason is that the core contraction increases the Brünt-Väisäiä frequency in the radiative core, while the envelope swelling decreases the Lamb frequency. While mixed modes are a very important subject of study, I choose to focus the discussion on the solar case here, and I only mention them for the sake of completeness.

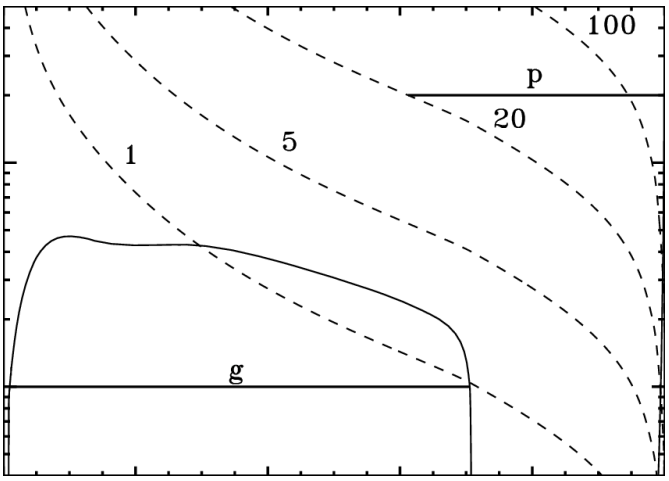

Figure 2.1: Solar propagation diagram, as a function of the fractional radial coordinate $r/R_\odot$ (where $R_\odot$ is the solar radius). The solid line represents the Brünt-Väisälä frequency N, where negative values in the convective envelope are not shown. The dashed lines represent the Lamb frequency L_l for different values of the angular degree l. The horizontal lines show the extent of the propagative regions for two different modes of frequency $\nu = 100\,\mu$Hz and 2000 μHz respectively (we recall that the frequency ν and angular frequency ω are related through $\omega = 2\pi\nu$.), the second one having an angular degree $l = 20$. Credits: Aerts et al. (2010).

frequency. Therefore, it is given by the following implicit relation

$$\omega^2 = \frac{l(l+1)c^2(r_t)}{r_t^2} \,. \tag{2.67}$$

In particular, since L_l^2 increases with l, so does r_t: the higher the angular degree of a p-mode, the narrower the cavity in which it is trapped. When the wave reaches the inner turning point, Equation 2.66 shows that $k_r = 0$: in other words, the wave propagates horizontally. We see now, therefore, that the reason the wave "reflects" at $r = r_t$ has actually nothing to do with an actual reflection, but is due to the *refraction* of the wave that continuously curves its trajectory[13], until it becomes horizontal and goes back up again. This is illustrated in Figure 2.2 for several value of the angular degree l.

As for the outer turning point, it is due to the sudden increase of N^2 at the surface, which in turn provokes a sudden increase of the acoustic cut-off angular frequency ω_{ac}. The outer turning point is therefore independent of angular degree, and only has a very weak dependence on frequency. It is because of this behaviour of N^2 – or equivalently of ω_{ac} – that the p-modes are consistently trapped below the photosphere, and that the atmosphere itself plays the role of an evanescent region. There, of course, the local analysis conducted above is no longer valid, because of the very small scale associated to the stratification. From the point of view of the wave, the change in the physical conditions amounts to a discontinuity, which means that, unlike what happens at the inner turning point, the wave actually undergoes reflection at the surface.

The nature of the p-modes can be unveiled by looking at their dispersion relation. As we have seen in Chapter 1, the bulk of stellar convection zones is characterised by a very efficient convective transport, which means that N^2, which must be negative for the convective instability to arise, is actually barely below zero. As such, we can consider $|N^2| \ll \omega$. Then the dispersion relation (Equation 2.66) takes the simpler form

$$k_r^2 \sim \frac{\omega^2 - L_l^2}{c^2} \,. \tag{2.68}$$

This is further rearranged by remarking that the horizontal wave vector associated to the angular degree l is given by $k_h = \sqrt{l(l+1)}/r$, meaning that $L_l = k_h c$. Therefore, this dispersion relation simply reduces to

$$k^2 = \frac{\omega^2}{c^2} \,, \tag{2.69}$$

[13]The *trajectory* of the wave must be understood as the curve defined in the scope of the ray theory, by analogy with geometrical optics.

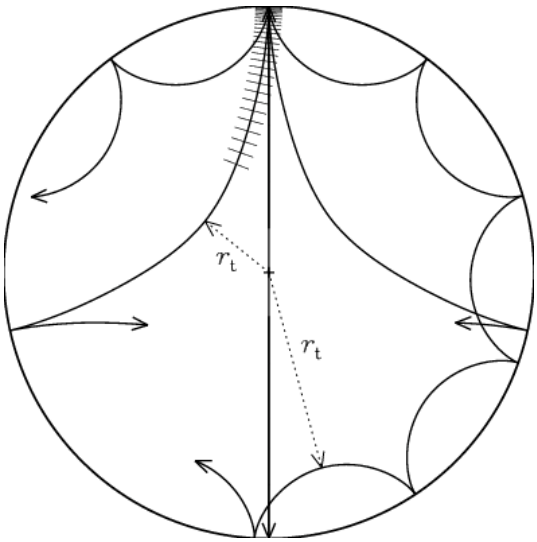

Figure 2.2: Propagation of sound rays in the solar interior for two acoustic modes of different angular degree. The lower turning points r_t of the two modes are represented. The mode with the smaller value of r_t has the lowest angular degree. On the other hand, the upper turning point of the two modes is relatively similar, and located just beneath the surface of the Sun. Credits: Di Mauro (2012).

where $k^2 = k_r^2 + k_h^2$ is the norm of the total wave vector, including its radial and horizontal components. This is identical to the dispersion relation for acoustic waves, which shows that in a p-mode cavity, the waves are acoustic in nature. This is, in fact, not surprising: indeed, I already remarked that there are two restoring forces leading to the propagation of waves in a star. But in a convective zone, the buoyancy force is destabilising, and as such cannot act as a restoring force. This leaves the pressure force as the only possible restoring force, and explains why *the waves propagating in a convective zone are necessarily acoustic waves*. This could have been seen from the start; but it is also instructive to see it arise naturally from the dispersion relation.

As for g-modes, Figure 2.1 shows that they are trapped in a more central region of the star. This is because the condition $\omega^2 < N^2$ can only be fulfilled if $N^2 > 0$, i.e. in a radiative zone. Additionally, the condition $\omega^2 < L_l^2$ cannot be fulfilled for $l = 0$, because $L_{l=0} = 0$. In other words, *all g-modes are non-radial*. This time, both the inner and outer turning points are given by the condition $\omega^2 = N^2$. While the inner turning point is not too dependent on frequency, the outer turning point is deeper in the core for higher frequency modes. Unlike the p-mode turning points, the g-mode turning points are completely independent of l. Similarly to p-modes, the dispersion relation associated to the g-modes tells us about their nature. One can see from Figure 2.1 that in the g-mode frequency range, one pretty much always has $\omega \ll L_l$, so that the dispersion relation (Equation 2.66) reduces to

$$k_r^2 = \frac{L_l^2}{c^2\omega^2}(N^2 - \omega^2) \,, \tag{2.70}$$

which can be rearranged by introducing the horizontal wave vector

$$\frac{k_r^2}{k_h^2} = \frac{N^2}{\omega^2} - 1 \,. \tag{2.71}$$

This reduces exactly to the dispersion relation of internal gravity waves, which is why these modes are called g-modes, or gravity modes, in the first place. In particular, the g-modes dispersion relation is anisotropic, in the sense that it does not only depend on the norm k of the wave vector (like the p-mode dispersion relation), but also on its direction. This is not surprising, of course: while the pressure force, responsible for the propagation of acoustic waves, is isotropic (by definition of the gas pressure), the gravitational force responsible for the propagation of internal gravity waves has a preferred direction – the local direction of the gravitational acceleration.

Solar-like oscillations: what about the effect of convection?

In this introductory discussion, we saw that a star is subjected to a discrete set of resonant oscillating modes. As I hinted in the introduction of this Chapter, these modes can be observed through the oscillating pattern of either

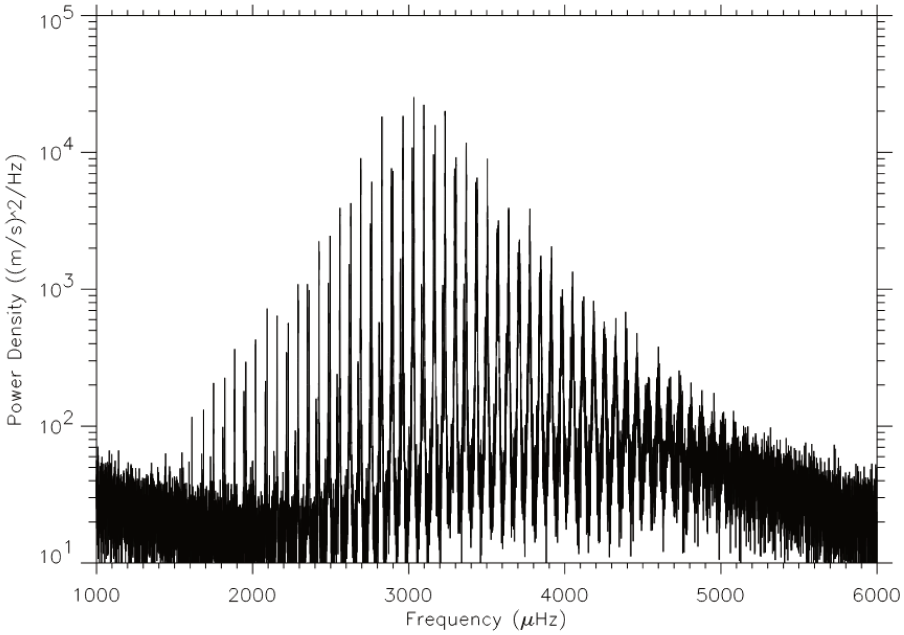

Figure 2.3: Solar velocity power spectrum, as observed by an eight-month run of GOLF measurements. Credits: Lazrek et al. (1997).

the radial velocity of the surface of the star, or its emergent intensity. In practice, a Fourier transform in time of the 'velocity curve' or of the light curve is performed, yielding respectively a *velocity power spectrum* or an *intensity power spectrum* of the star. This is illustrated in Figure 2.3, which shows the velocity power spectrum of the Sun as observed by GOLF: the oscillations take the form of a forest of resonant peaks, whose central frequencies correspond to the eigenfrequencies of the modes. Not only in the remainder of this Chapter, but in the rest of this thesis as well, I will only discuss solar-like oscillations. We saw earlier that, in such stars, g-modes are confined in the core, while the p-mode cavity extends to the surface. As such, only p-modes can be observed on the surface[14]: all the peaks in Figure 2.3 correspond to resonant p-modes. As such, this kind of spectrum is often referred to as a *p-mode spectrum*.

Observations of the p-mode spectrum of a star constitute a gold mine of information on various aspects of the stellar interior. The extraction of the central frequencies of the resonant peaks, in particular, allows for the precise determination of their eigenfrequencies, and give invaluable information on the equilibrium structure of the star – information that cannot be obtained any other way, except through very indirect and more uncertain means. The regularity of the frequency pattern, which is even visible to the naked eye from Figure 2.3 for instance, gives access to seismic indices that can be used to constrain certain stellar parameters, like the radius or the mass of the star. Individual mode frequencies, if they can be identified with the corresponding values of the radial order n, angular degree l and azimuthal order m, can also be used to map the stellar interior, through inversion techniques. The more frequencies are observed, the better the mapping. But in order for this invaluable information to be extracted from the observed spectra, measuring frequencies in a precise and accurate manner is not sufficient: we must also be able to theoretically relate mode frequencies to the structure of the medium in which they develop. In other words, from a given stellar model, we must be able to theoretically – or numerically – predict what the frequencies are going to be: only then does the comparison between predicted and observed frequencies allow us to assess our understanding of stellar interiors. The probing of stars with seismic frequencies can only be as accurate as our stellar models. The problem, then, is that, as we made abundantly clear in Chapter 1, our models for convective motions inside stars are not nearly accurate enough. This is a major obstacle to the use of observed frequencies for internal probing of stars, not only for solar-like oscillators with a convective envelope, but for any star whose observationally available oscillation interact with convection in any way. In particular, the inadequacy

[14]We note, for the sake of completeness, that there are claims that g-modes have been detected in certain solar datasets (García et al. 2007; Fossat et al. 2017; Fossat and Schmider 2018). However, these claims are very controversial, and not only have these detections never been definitely confirmed, they have even been discarded as being 'artifacts of their methodology' (Appourchaux et al. (2018); see also Broomhall et al. (2010)).

of existing models for stellar surface convection in solar-like oscillators causes a discrepancy between the observed and predicted p-mode frequencies, known as "surface effects". This is a part of convection–oscillation coupling that is very important to understand.

The central frequency of the peaks is not the only information that can be extracted from the observed power spectrum: if observations are performed over a sufficiently long period of time, the line profile of the p-modes can also be resolved. In particular, their width in the Fourier domain, as well as their amplitude, can be extracted individually. While the frequencies of the modes are related to the equilibrium structure of the star, their amplitude and linewidth are markers of the energetic aspects of the modes. In solar-type stars, those are also related to surface convection, which is responsible both for the stochastic excitation of the modes, and their linear damping. For all these reasons, therefore, turbulent convection has a significant impact on the p-modes in solar-like oscillators. In this introductory discussion, I have so far elected to neglect convection in the treatment of stellar oscillations: the remainder of this Chapter is dedicated to restoring convection in the linearly perturbed equations governing stellar oscillations, or equivalently, in the wave equation that stems from these linear perturbations. I will split the rest of this discussion three ways: in Sections 2.2 and 2.3, I will focus on the two energetic aspects mentioned above – respectively the stochastic excitation and the linear damping of the modes by convection. I will then discuss 'surface effects' in Section 2.4.

2.2 Mode driving

As I just mentioned, the turbulent convective motions of the gas are responsible for the stochastic driving of the modes. The coexistence of linear damping and inhomogeneous forcing leads to the establishment of a stationary state as regards the energetic behaviour of the modes. This stationary state is responsible for the observed amplitude of the modes, and results from a balance between the damping and driving processes. Understanding the observed mode amplitudes, and, perhaps more importantly, inferring properties of turbulent convection from these observed amplitudes, therefore requires a thorough theoretical understanding of both mode driving and mode damping. Let me, in this section, discuss our current understanding of the former.

2.2.1 An illustrative toy-model for excited harmonic oscillators

Before we dive into the core subject of this section, that is the excitation mechanisms for solar-like p-modes, let us briefly examine the general case of a linear, harmonic oscillator that is both linearly damped and stochastically excited. This illustrative toy model will allow me to introduce a certain number of general properties that will be useful for the rest of the discussion.

Driving-damping balance

Let me denote the oscillating variable as $z(t)$, the linear damping rate as η, the angular eigenfrequency as ω_0, and the forcing term as $f(t)$. Then the equation of evolution governing the behaviour of the oscillator is

$$\frac{\mathrm{d}^2 z}{\mathrm{d}t^2} + 2\eta\frac{\mathrm{d}z}{\mathrm{d}t} + \omega_0^2 z(t) = f(t)\,. \tag{2.72}$$

The general solution of the corresponding homogeneous equation – i.e. the same equation where $f(t)$ has been set to zero – is

$$z_h(t) = A\exp^{-\eta t - j\sqrt{\omega_0^2-\eta^2}t} + B\exp^{-\eta t + j\sqrt{\omega_0^2-\eta^2}t}\,, \tag{2.73}$$

where A and B are two constants that only depend on the initial state. Without loss of generality, we can define the time $t = 0$ in such a way that $B = 0$. The solution of the inhomogeneous equation is then found by varying the constant A. Setting

$$z(t) = A(t)\exp^{-\eta t - j\sqrt{\omega_0^2-\eta^2}t}\,, \tag{2.74}$$

and plugging this into Equation 2.72, one finds

$$\frac{\mathrm{d}^2 A}{\mathrm{d}t^2} - 2j\sqrt{\omega_0^2-\eta^2}\frac{\mathrm{d}A}{\mathrm{d}t} = f(t)\exp^{\eta t + j\sqrt{\omega_0^2-\eta^2}t}\,, \tag{2.75}$$

which can be immediately integrated once with respect to time t to yield

$$\frac{\mathrm{d}A}{\mathrm{d}t} - 2j\sqrt{\omega_0^2 - \eta^2}A = \int_{-\infty}^{t} \mathrm{d}t' \; f(t') \exp^{\eta t' + j\sqrt{\omega_0^2 - \eta^2}t'} \; . \tag{2.76}$$

This first-order differential equation governs the evolution of $A(t)$, which is the instantaneous amplitude of the oscillation. While this is the exact form of the equation, it can be drastically simplified in the case where $\eta \ll \omega_0$, i.e. if the lifetime of the oscillation is much longer than its period. This approximation is relevant to the case of solar-like oscillations, where the typical damping rate does not exceed $\sim$ 10 μHz, while the frequencies are of the order of a few mHz. In this case, not only can the square root $\sqrt{\omega_0^2 - \eta^2}$ be approximated by ω_0, but the first term on the left-hand side becomes negligible compared to the second term on the left-hand side. The reason is that the amplitude of the oscillation varies over time scales comparable to the lifetime of the mode, so that $|\mathrm{d}A/\,\mathrm{d}t| \sim \eta A \ll \omega_0 A$. As such, Equation 2.76 transforms into an algebraic equation. The amplitude becomes

$$A(t) = \frac{j}{2\omega_0} \int_{-\infty}^{t} \mathrm{d}t' \; f(t') \exp^{\eta t' + j\omega_0 t'} \; , \tag{2.77}$$

and the solution of the inhomogeneous equation (Equation 2.72) becomes

$$z(t) = \frac{j}{2\omega_0} \int_{-\infty}^{t} \mathrm{d}t' \; f(t') \exp^{\eta(t'-t) + j\omega_0(t'-t)} \; . \tag{2.78}$$

The instantaneous value of the oscillating variable is therefore the combination of a continuum of kicks $f(t')$ for all times t' in the past, and each kick leads to an oscillating response which dies away after a time $\sim 1/\eta$. Because there are always more kicks to replenish the energy lost to damping, the oscillation always has the same typical amplitude. This is perhaps better seen in terms of the energy of the mode. It is proportional to the modulus square of $z(t)$, and therefore

$$E(t) \propto \frac{\exp^{-2\eta t}}{4\omega_0^2} \int_{-\infty}^{t} \mathrm{d}t_1 \int_{-\infty}^{t} \mathrm{d}t_2 \; f(t_1) f(t_2) \exp^{\eta(t_1+t_2) + j\omega_0(t_2-t_1)} \; . \tag{2.79}$$

Because $f(t)$ is a *stochastic* process, so is $E(t)$. The relevant quantity, in practice, is therefore the *ensemble average* $\langle E(t) \rangle$ of the power spectrum, i.e. its average over a large number of realisations[15]. Using the linearity of the ensemble average to pull it inside the integrals yields an expression of $\langle E(t) \rangle$ as a function of the two-time correlation product of the driving source $f(t)$. Then, changing variables from (t_1, t_2) to (τ, t'), where $t' = (t_1 + t_2)/2$ and $\tau = t_1 - t_2$, and further casting the boundary of the integral over τ to infinity (on the grounds that the correlation product $\langle f(t) f(t+\tau) \rangle$ vanishes quickly when τ is large), one obtains

$$\langle E(t) \rangle \propto \frac{\exp^{-2\eta t}}{4\omega_0^2} \int_{-\infty}^{t} \mathrm{d}t' \int_{-\infty}^{+\infty} \mathrm{d}\tau \langle f(t') f(t'+\tau) \rangle \exp^{2\eta t' + j\omega_0 \tau} \; . \tag{2.80}$$

Forming the time derivative of this expression finally yields

$$\frac{\mathrm{d}\langle E \rangle}{\mathrm{d}t} = -2\eta \langle E \rangle + \underbrace{C \int_{-\infty}^{+\infty} \mathrm{d}\tau \langle f(t') f(t'+\tau) \rangle \exp^{2\eta(t'-t) + j\omega_0 \tau}}_{\equiv \mathcal{P}} \; , \tag{2.81}$$

where C is a constant which, for the purposes of this illustrative toy-model, we do not attempt to quantify, and the last term on the right-hand side correspond to the power injected in the oscillator by the driving source. We denote this power as $\mathcal{P}$.

This last equation governs the evolution of the energy of the mode, which contains two terms: one is a positive contribution from the driving source, and does not depend on the energy itself; the other is a negative contribution

[15] Obviously, if we were to actually observe this oscillator, this would not be true, because we would only have access to one realisation. But if the observations are made over sufficiently long time scales, then the total observation time can be split into shorter periods that are long enough for the definition of the power spectrum to still hold, but short enough that each of these sub-periods are independent of each other. Then the average over the sub-periods is considered to be equivalent to an actual ensemble average: this is the *ergodic principle*. Everything hinges on this principle, which is both indispensable and unverifiable – since there is only one Universe that we can observe.

from the linear damping, and is proportional to the energy itself. In particular, the stationary state of the mode is found by setting the time derivative of the average energy to zero, in which case one finds

$$\langle E \rangle_{\rm stat} = \frac{\mathcal{P}}{2\eta} \, . \tag{2.82}$$

This illustrates perfectly a key property of damped and stochastically excited oscillators: that their observed energy is the result of a balance between the injected power $\mathcal{P}$ and the damping rate η.

Line profile in the power spectrum

In practice, solar-like oscillations are observed not in the time domain, but in the Fourier domain – in other words, the observations provide with the power spectrum of the oscillating quantities. In this toy-model, this is given by

$$P(\omega) = \frac{1}{2T_{\rm obs}^2} \left| \widehat{z}(\omega) \right|^2 \, , \tag{2.83}$$

where $T_{\rm obs}$ is the total observation time, and the Fourier transform of z in time is defined by

$$\widehat{z}(\omega) \equiv \frac{1}{\sqrt{2\pi}} \int_{-\infty}^{+\infty} {\rm d}t \; z(t) \exp^{-j\omega t} \, . \tag{2.84}$$

Plugging Equation 2.84 into Equation 2.83 gives an expression of the power spectrum in terms of $z(t)$

$$P(\omega) = \frac{1}{8\pi T_{\rm obs}^2} \iint {\rm d}t_1 \, {\rm d}t_2 \; z^\star(t_1) z(t_2) \exp^{j\omega(t_1 - t_2)} \, , \tag{2.85}$$

where the notation * refers to a complex conjugate. In turn, plugging Equation 2.78 yields an expression of the power spectrum in terms of the driving source $f(t)$, in the form of a quadruple integral

$$P(\omega) = \frac{1}{32\pi\omega_0^2 T_{\rm obs}^2} \int_{-\infty}^{+\infty} {\rm d}t_1 \int_{-\infty}^{+\infty} {\rm d}t_2 \int_{-\infty}^{t_1} {\rm d}t_3 \int_{-\infty}^{t_2} {\rm d}t_4 f(t_3) f(t_4) \exp^{\eta(t_1 + t_4 - t_3 - t_2) + j\omega_0(t_1 + t_4 - t_3 - t_2)} \exp^{j\omega(t_1 - t_2)} \, . \tag{2.86}$$

Performing the usual integral permutation, it can be shown that the power spectrum is expressed as

$$\langle P(\omega) \rangle = \frac{1}{16\pi T_{\rm obs} \omega_0^2} \frac{F(\omega)}{(\omega - \omega_0)^2 + \eta^2} \, , \tag{2.87}$$

in terms of the *correlation spectrum* of the driving source $f(t)$

$$F(\omega) \equiv \frac{1}{T_{\rm obs}^2 \sqrt{2\pi}} \int_{-\infty}^{+\infty} {\rm d}t' \; \exp^{j\omega(t' - t)} \left\langle f(t) f(t') \right\rangle \, , \tag{2.88}$$

provided *the stochastic process $f(t)$ is stationary* (i.e its multi-time statistics are independent of absolute time, and only depend on time differences). This shows that the Fourier representation of a stochastically excited and linearly damped harmonic oscillator is a Lorentzian profile, centered around the eigenfrequency ω_0 of the mode, and whose linewidth is 2η (this is why the damping rate of a mode can be inferred from observation if the line profile of the mode is resolved, a point on which I will have the opportunity to return in Section 2.3.1). This is only on the condition that $F(\omega)$ does not depend too much on ω over the frequency range $[\omega_0 - 2\eta \, ; \, \omega_0 + 2\eta]$ – i.e. on the condition that the driving source is not too frequency dependent. This is the case if the driving source is incoherent, which is the case in the stellar context. When the observations of the solar power spectrum became precise enough to allow for the spectral resolution of the solar p-mode line profiles, they revealed that the line profiles indeed feature a Lorentzian shape (Gabriel 1995), as illustrated in Figure 2.4, which was a robust giveaway that solar p-modes were indeed stable, and that their observed amplitudes were indeed due to stochastic excitation.

On a final note, let me remark that, while this toy-model may be useful to understand some of the most general properties of stochastically excited oscillators, the picture is very simplified compared to actual solar-like oscillations. This is especially due to the fact that the wave variables, in the stellar context, are not just function of time, but also of space. Therefore, the spatial correlation of the driving source is as important as its temporal correlations, and the spatial structure of the eigenfunctions also have an important role to play.

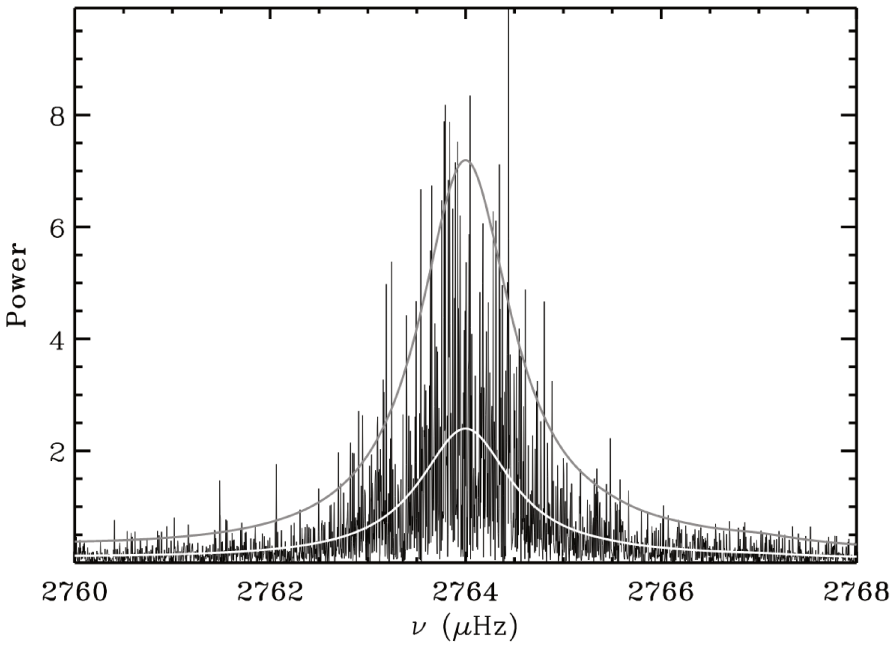

Figure 2.4: Observed line profile of a single radial mode, obtained through spectroscopic measurements made with the Bi-State Optical Network (BiSON). The line profile features the wide stochastic variations expected from a stochastically excited mode, but its overall shape is Lorentzian. The white line correspond to a Lorentzian fit to the data. Credits: Christensen-Dalsgaard (2004).

2.2.2 Turbulent acoustic emission as a source of stochastic driving

When it comes to solar-like oscillations, one of the driving source contributing to $f(t)$ was identified as stemming from *turbulent acoustic emission*. This mechanism has long been recognised as a source of acoustic waves in highly turbulent media (Lighthill 1952). It has two different origins: the turbulent fluctuations of the Reynolds stress force in the momentum equation, and the non-adiabatic pressure fluctuations. Because of the turbulent nature of the flow in the convective region, and especially close to the surface of the star, both these contributions act as a non-coherent, randomly fluctuating force that is able to drive the motions of the gas at all frequencies. Shortly after solar 5-minute oscillations were discovered and ascribed to global modes of oscillation, several authors investigated this mechanism as a possible explanation for their observed amplitude, by applying the work of Lighthill (1952) to a stratified stellar atmosphere (e.g. Unno and Kato 1962; Stein 1967).

In a groundbreaking paper, Goldreich and Keeley (1977b) provided with a theoretical framework to describe the stochastic driving of solar-like p-modes by turbulent acoustic emission, which allowed them to determine the relative strength of different sources of driving, as well as to quantify the rate at which energy is provided to solar-like oscillations. They wrote the perturbed equation of motion as

$$\frac{\partial^2 \mathbf{v}}{\partial t^2} + \mathcal{L}(\mathbf{v}) = \mathbf{N}(t) \,, \tag{2.89}$$

where, under the Cowling approximation

$$\mathcal{L}(\mathbf{v}) \equiv -\frac{1}{\rho_0}\boldsymbol{\nabla}\left[c^2 \boldsymbol{\nabla}\cdot(\rho_0 \mathbf{v}) + \frac{p_0}{c_v}(\mathbf{v}\cdot\boldsymbol{\nabla})s_0\right] + \frac{1}{\rho_0}\mathbf{g}_0(\boldsymbol{\nabla}\cdot(\rho_0\mathbf{v})) \,, \tag{2.90}$$

$$\mathbf{N} = \frac{1}{\rho_0}\frac{\partial \mathbf{f}}{\partial t} - \frac{1}{\rho_0}\boldsymbol{\nabla}\left(\frac{\partial e}{\partial t}\right) - \frac{1}{\rho_0}\boldsymbol{\nabla}\left(\frac{p_0}{c_v}h\right) \,, \tag{2.91}$$

and

$$\mathbf{f} = -\boldsymbol{\nabla} \cdot \left(\frac{\rho_0^2}{\rho} \mathbf{v}\mathbf{v} \right) , \tag{2.92}$$

$$e = \frac{\Gamma_1 - 1}{2} \frac{c^2}{\rho_0} \rho_1^2 + \frac{\rho_0}{2c_v^2} s_1^2 + \frac{c^2}{c_v} \rho_1 s_1 , \tag{2.93}$$

$$h = \frac{\rho_1}{\rho_0} (\mathbf{v} \cdot \boldsymbol{\nabla}) s_0 - (\mathbf{v} \cdot \boldsymbol{\nabla}) s_1 , \tag{2.94}$$

the subscript 0 refers to equilibrium values, and the subscript 1 denotes perturbations around the equilibrium values. In writing Equation 2.89, the authors separated the linear part $\mathcal{L}$ – which they expressed solely as a function of the velocity wave variable – from all other, non-linear contributions $\mathbf{N}$. They identified these non-linear terms to inhomogeneous forcing terms (akin to the driving force $f(t)$ in the Section 2.2.1). The three terms in the definition of $\mathbf{N}$ can be categorised according to the multipolar expansion one usually encounters, for instance, in electromagnetism, depending on the spatial structure of the acoustic emission each term produces. The emission can either be monopolar (stemming from isotropic gas expansion and contraction), dipolar (stemming from fluctuations of a body force locally exerted on the fluid, in which case the direction of the force corresponds to the axis of the dipole) or quadrupolar (stemming from fluctuations in a stress force locally exerted on the fluid). For instance, the first term on the right-hand side of Equation 2.91 is a quadrupolar source (where the emitting stress force is the Reynolds stress force), while the third term is predominantly dipolar (where the emitting body force is the buoyancy force, directed in the local direction of $\mathbf{g}_0$).

Then, the authors derived scaling relations for each of the non-linear terms. To evaluate the amplitude of the fluctuating quantities, they used 1) the Kolmogorov scaling relations relevant in the inertial subrange of the turbulent cascade, 2) the standard MLT description of convection to relate the entropy, pressure and density fluctuations to the velocity fluctuations, and 3) the hypothesis that the turbulent eddies whose typical size should be used in the scaling relations are those with lifetimes comparable to the period of the mode – i.e. the *resonant* eddies. The authors found that for modes whose period is shorter than the local lifetime of the energy-bearing eddies, the quadrupolar contribution from the Reynolds stress dominates, while it is the dipolar contribution from the buoyancy force that prevails for modes whose period is longer. The latter condition is only verified close to the surface of the star, and only for the lowest order modes: they concluded that Reynolds stress fluctuations are responsible for most of the mode driving. Finally, they derived an expression for the excitation rate due to Reynolds stress force fluctuations, using the same kind of analysis as the one I very crudely presented in Section 2.2.1. In particular, as I hinted above, the two-time, two-point correlation product of $\mathbf{N}$ is of crucial importance for mode driving. For want a better representation of these correlations, the authors chose to describe the two-time correlation as Gaussian, with a typical width given by the lifetime of the resonant eddies, and to get rid of two-point correlations by integrating over the corresponding space difference. Eventually, they obtained an integral expression for the excitation rates of solar radial p-modes of order $n = 0$ to $n = 21$, and therefore could infer the velocity amplitude of these modes, which they could compare to observations. They found values ranging from ~ 1 to ~ 6 cm.s^{-1}. While these values are several times lower than the actual observed amplitudes (which can reach as high as ~ 30 cm.s^{-1} for the Sun), their analysis still provided with the right order of magnitude for excitation rates.

The approach of Goldreich and Keeley (1977b) was later refined by other studies (e.g. Dolginov and Muslimov 1984; Balmforth 1992c; Goldreich et al. 1994; Samadi and Goupil 2001; Samadi et al. 2003; Chaplin et al. 2005; Belkacem et al. 2006, 2008, 2010). The question of the relative importance of the quadrupolar excitation by the Reynolds stress force and the dipolar excitation by the buoyancy force was, at some point, the subject of some disagreement (Stein and Nordlund 1991; Goldreich et al. 1994). The current accepted picture, however, is that the former contribution is indeed dominant. In that case, the two-time, two-point correlation of $\mathbf{N}$, being equivalent to its Fourier spectrum in time and space, is directly related to the turbulent velocity spectrum, which is defined as

$$\phi_{ij}(\mathbf{k}, \omega, \mathbf{X}) \equiv \frac{1}{\sqrt{2\pi}} \int \mathrm{d}^3\mathbf{x} \int \mathrm{d}\tau \, \langle u_i(\mathbf{X}, t) u_j(\mathbf{X} + \mathbf{x}, t + \tau) \rangle \exp^{j(\omega\tau + \mathbf{k}\cdot\mathbf{x})} , \tag{2.95}$$

with the understanding that the turbulent velocity $\mathbf{u}$ has stationary statistical properties, which therefore do not depend on t, but only on τ. As a result, solar-like p-mode excitation rates can be used as a way to constrain the properties of the turbulent spectrum ϕ_{ij} (Balmforth 1992c; Samadi and Goupil 2001). In particular, Samadi and Goupil (2001) built on the formalism of Goldreich and Keeley (1977b) to include both quadrupolar and dipolar

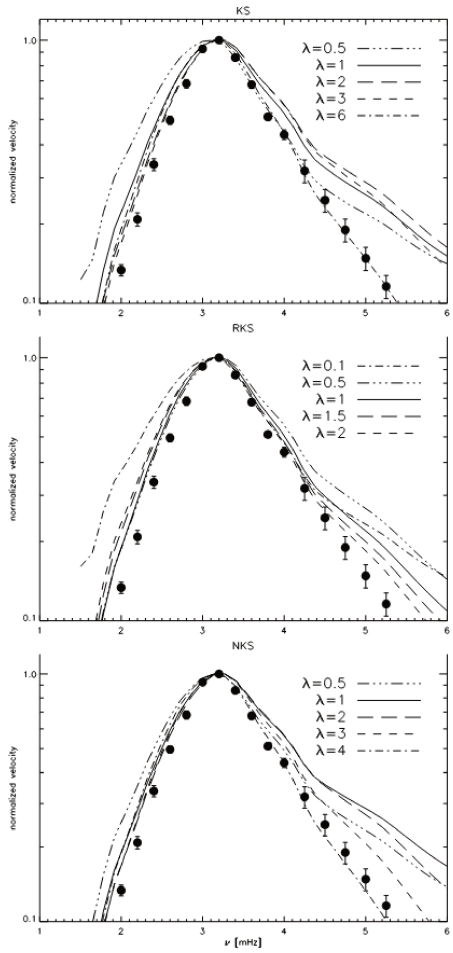

Figure 2.5: Comparison between the solar radial p-mode amplitudes inferred from the velocity solar power spectrum observed from the ground at the Big Bear Solar Observatory (Libbrecht 1988), and theoretical predictions computed through the model of Samadi and Goupil (2001), for three different forms of the spatial part of the turbulent velocity power spectrum (from top to bottom), and different values of the free parameters in the model. Comparison between the two allows to constrain the values of these parameters. Credits: Samadi et al. (2001).

emission, and more importantly, to include the turbulent velocity spectrum in both space and time in the most general way possible. This allowed them to constrain the various non-dimensional parameters of order unity usually introduced in turbulent spectrum models to account for the uncertainty on the time and length scales associated to the energy bearing eddies. They applied this formalism to the Sun in Samadi et al. (2001), and found very good agreement with solar data, as illustrated in Figure 2.5, with the adoption of a Kolmogorov spectrum extended to small wave vectors outside the universal range by different power laws. However, they found that the amplitude of the low-frequency modes is systematically overestimated. As regards the temporal spectrum, they argued that a Gaussian form is preferable to a decaying exponential. It was later argued by Belkacem et al. (2010), on more physical grounds, that a mixed Lorentzian-Gaussian form should be adopted, which allowed them to correct the low-frequency overestimation of mode amplitude.

By contrast with damping rates (see Section 2.3) or surface effects (see Section 2.4), the mechanism responsible for the excitation of solar-like p-modes is therefore fairly well understood, and the theoretical predictions match the observations quite satisfactorily. As such, mode driving is probably the most well understood mechanism arising from oscillation–turbulence coupling. I will have the opportunity, in Chapter 5 in particular, to come back to the details of the theoretical modelling of stochastic driving for solar-like oscillations.

2.3 Mode damping

2.3.1 Foreword

On the stable nature of solar-like oscillations

Historically, the coupling between solar-like oscillations and turbulent convection was studied for the purpose of accurate determination of mode frequencies in stellar models, as I will show in detail in Section 2.4. The question of the energetic aspects of these modes was at first only secondary, and mainly aimed at determining whether or not solar oscillations are linearly stable. In other words: do these oscillations behave as damped and

forced harmonic oscillators, or do their amplitude grow exponentially due to some instability process? Some stars do indeed exhibit such unstable modes, which develop in the interior through the advent of self-excited instabilities. Two such important instabilities, for instance, are the κ-mechanism and the γ-mechanism (e.g. Samadi et al. 2015). In the κ-mechanism, the key ingredient is the dependence of the Rosseland mean opacity on temperature: if the local equation of state is such that a small local increase in temperature, due to local random fluctuations, leads to a corresponding increase in opacity, then the matter absorbs the outwards photon flux more efficiently, which heats up the gas, thus leading to a further increase in temperature, etc. This runaway mechanism constitutes an instability, and translates into global modes of oscillation being self-excited, and therefore having considerable amplitudes. By nature of the κ-mechanism, however, the perturbation of the radiative flux plays a crucial role in the behaviour of the mode, so that this mechanism cannot possibly arise from the adiabatic framework we introduced in Section 2.1: a non-adiabatic framework is necessary. This is also the case of the γ-mechanism, whereby the variation of the radiative flux is responsible for the instability, through its dependence on the adiabatic exponents. The mechanism is based on the fact that the adiabatic exponents are lower inside ionisation regions (where part of the energy brought to the gas serves for ionisation, rather than for heating) than outside. As a result, during a compression phase, the radiative flux is increased by a smaller amount inside the ionisation region than outside. This creates a gradient of the radiative flux perturbation at the boundary of the ionisation region, and if the gradient is in the correct direction – i.e. directed inwards –, this leads to a local heating of the gas. Ultimately, as for the κ-mechanism, the temperature increase also runs away. Once again, the γ-mechanism cannot arise from an adiabatic framework for the pulsations. Both mechanisms arise in or close to ionisation regions, where the $\kappa(T)$ relation or the dependence of radiative flux variation on the adiabatic exponents allows for the instability to develop. Even though other mechanisms exist – like the convective flux blocking mechanism, or the ϵ-mechanism for instance–, these two are primarily responsible for *classical pulsators*, which encompasses all classes of stars that exhibit large-amplitude, linearly overstable modes of oscillation. Because of their large amplitudes, these oscillations, which are also sometimes called *opacity-driven oscillations*, were historically the first to be discovered – hence the term 'classical' –, for instance in Mira stars, or the classical Cepheids that are still used, as they were more than a century ago, for the measure of distances in the Universe[16].

Comparatively, the discovery of solar oscillations – and, *a fortiori*, oscillations in other solar-like stars – is much more recent, with the 5-minute oscillations measured on the surface of the Sun (Leighton et al. 1962) only having been ascribed to global modes of oscillation in the 1970's by Ulrich (1970) and Leibacher and Stein (1971). The question of their stability was tackled shortly thereafter, for example by Ando and Osaki (1975) or Antia et al. (1982), with an early consensus on the unstable nature of solar oscillations. On the contrary, other studies (Goldreich and Keeley 1977a; Balmforth 1992a), including the effect of turbulent pressure and dissipation of turbulent kinetic energy into heat, predicted that solar oscillations should be stable. Once the instrumental capabilities allowed for the resolution of the line profile of the resonant peaks in the p-mode spectrum, it became clear that they feature the Lorentzian profile characteristic of linearly stable oscillators (see Section 2.2.1). The characteristic of such oscillations is that the background in which they develop takes more energy from it than it provides during a cycle of the mode. From the point of view of the mode, this leads to a net loss of energy each cycle, and in the long run, to a decay – or damping – that is only counterbalanced by the forcing of the waves (see Section 2.2 for more details). To this decay of mode energy is associated a decay rate – or damping rate – η, which is defined as half the e-folding time of energy loss. The inverse of the damping rate corresponds to the typical lifetime of the mode[17], and therefore corresponds, in the observed p-mode spectrum of the star, to the linewidth associated to the resonant mode: if the resolution is sufficient, it can therefore be directly inferred from observations. The dependence of the solar damping rates with frequency is illustrated by Figure 2.6, where the observed linewidths of the solar p-modes are plotted against frequency – each dot representing one mode. More precisely, the top panel represents the linewidth at half maximum $\Gamma_{nl} \equiv \eta/\pi$ (Baudin et al. 2005) (where n and l are the radial order and angular degree of the modes), while the bottom panel represents the linewidths *weighted by a factor Q_{nl}, which depends on the radial order n and the angular degree l of the modes, and defined*

[16]It was indeed discovered that the intrinsic luminosity of Cepheid pulsators is tightly correlated with the period of their pulsation. Therefore, measuring their period gives a measure of their luminosity, which can then be combined with the measurement of their apparent luminosity – which goes as the inverse square of the distance between the object and the observer – to yield an estimate of their distance.

[17]That is, the time it would take for a mode to be reduced to a negligible amplitude *if the mode energy was not constantly replenished by the forcing processes*.

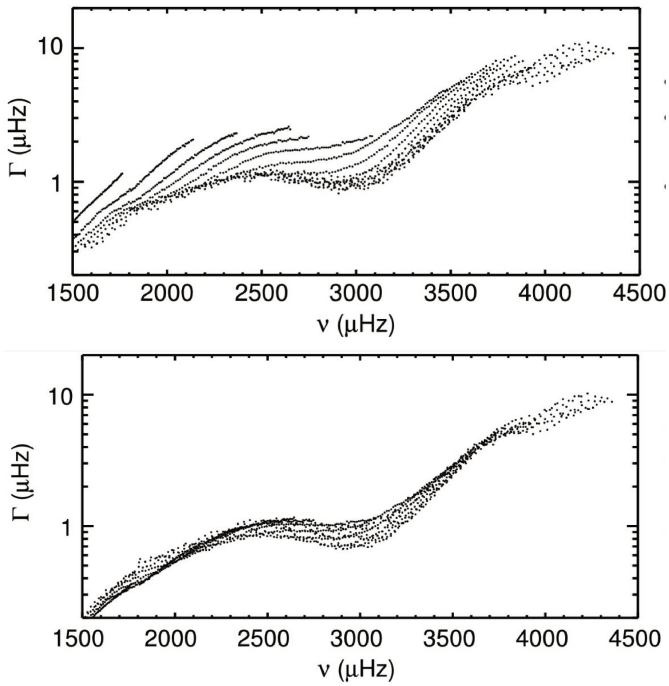

Figure 2.6: **Top**: Linewidths of individual p-modes in the solar velocity power spectrum, inferred from observations by the GONG network, for angular degrees $l = 0 - 150$, as a function of frequency. Each symbol represents one mode. **Bottom**: Same as top panel, but linewidths are scaled by the factor $Q_{n,l}$ defined in Equation 2.96. Credits: Kiefer et al. (2018).

as (Christensen-Dalsgaard and Thompson 1997)

$$Q_{nl} \equiv \frac{\mathcal{M}_{nl}}{\mathcal{M}_{\text{rad}}} = \frac{\mathcal{I}_{nl}\,|\boldsymbol{\xi}_{\text{rad}}(R)|^2}{\mathcal{I}_{\text{rad}}\,|\boldsymbol{\xi}_{nl}(R)|^2}\,, \tag{2.96}$$

where $\mathcal{M}$ is the mode mass, R is the radius of the star – where the modes are observed –, the subscript 'rad' refers to the radial mode that has the same frequency as the (n, l) mode under consideration (so that, in particular, $Q_{n=0,l} = 1$), and $\mathcal{I}$ is the mode inertia, defined as

$$\mathcal{I} = \int_{\mathcal{V}} \mathrm{d}^3\mathbf{x}\,\rho_0(\mathbf{x})\,|\boldsymbol{\xi}_{nl}(\mathbf{x})|^2\ . \tag{2.97}$$

The scaled linewidth $Q_{nl}\Gamma_{nl}$ is a more relevant quantity to compare between different modes than the raw linewidth. Indeed, the mode mass corresponds to the mass of gas that would need to be put in motion across the entire volume of the star if it were to be displaced everywhere with the amplitude actually observed on the surface, while keeping the same kinetic energy. Because high-angular-degree modes are trapped in a much narrower region than radial modes (see Section 2.1.2), they naturally have a much smaller mass, and are comparatively much more affected by convection than radial modes, regardless of the intrinsic properties of convection. Correcting for the mode mass therefore allows for the comparison of the linewidths of modes that have the same frequency but different values of l. This is particularly visible upon comparing the two panels of Figure 2.6: the top panel is clearly comprised of different 'continuous' curves that are offset with respect to one another, while all these curves collapse to a unique, slowly-varying function of frequency in the bottom panel. Furthermore, Figure 2.6 shows that the damping rate of the modes increases with frequency, going from ~ 0.1 μHz to ~ 10 μHz throughout the solar p-mode spectrum. An interesting feature of Figure 2.6, in particular, is the plateau between ~ 2.5 and ~ 3 mHz, whose existence means that some destabilising process decreases the damping rate in this frequency range. The most probable cause is the κ-mechanism described above, associated to hydrogen ionisation, and which still exists in solar-like oscillators, even though it is not strong enough to overcompensate the stabilising effect of convection-oscillation coupling (e.g. Samadi et al. 2015).

Once the stable nature of solar-like oscillations had been established, the focus shifted towards the determination of the dominant physical processes responsible for the damping of the modes, and to the development of

predictive theoretical models. This became more important, in particular, with the advent of space-borne missions that considerably increased the amount of asteroseismic observations at our disposal, like the CoRoT (Baglin et al. 2006) or the *Kepler* missions (Borucki et al. 2010). It became apparent that the properties of the modes, including their damping rate, follow distinct trends with global parameters, such as effective temperature and surface gravity for instance. These trends constitute valuable clues as to the nature of the underlying physical processes responsible for mode damping; on the other hand, they give observed mode damping the potential to serve as a way to constrain stellar global parameters. Both require an accurate and precise theoretical knowledge of the coupling between the turbulent convection and solar-like oscillations.

On the difficulty of modelling p-mode damping

The fact that it is necessary to include the effect of turbulent pressure and turbulent dissipation to explain even the stable nature of the modes shows that the turbulence–oscillation coupling is crucial in understanding why the modes are damped instead of being self-excited, and are *a fortiori* essential in predicting to what extent they are damped. More precisely, it is this coupling *close to the surface of the star* that is responsible, because this is the region where it is at its most efficient. The reason has to do with characteristic timescales, and coincidence thereof. Here, three timescales are relevant to the problem: the typical period of the modes Π, the local thermal timescale $\tau_{\rm th}$, and the eddy turn-over timescale $\tau_{\rm to}$ associated to the turbulent convection. I already mentioned the coincidence between Π and $\tau_{\rm th}$ in Section 2.1.1, when I discussed the validity of the adiabatic approximation for oscillations. I remarked that while they are very different throughout most of the star, they become similar close to its surface, with typical timescales of ~ 5 minutes. As for $\tau_{\rm to}$, it represents the time it takes for a turbulent eddy to be dissolved into the neighbouring background once it has been born from random fluctuations at its birth location (see Section 1.2.2 for more details), and it is also related to the typical dissipation timescale for turbulent kinetic energy. In the MLT picture, it is given by the ratio of the mixing length l to the convective velocity (Equation 1.59). In most of the convective zone, the convection is extremely efficient, so that the eddies can live a long time before they die: their turn-over timescale is much longer than the period of the modes. However, close to the surface, convection becomes superadiabatic, and therefore much less efficient. As a result, the lifetime of the eddies is much shorter, and happens to be comparable with the period of the modes.

We therefore have three timescales that are very different from one another in most of the stellar interior, but which converge towards one another in its superficial layers. This assertion is true not only of the Sun, but of solar-like oscillators in general. The fact that $\Pi \sim \tau_{\rm to}$ explains why the coupling between turbulent convection and solar-like oscillations is so strong in the superadiabatic region. On the other hand, the fact that $\Pi \sim \tau_{\rm th}$ explains why non-adiabatic effects become prominent in this region, and why they must necessarily be accounted for to understand the properties of the modes therein. In addition, the typical length scales associated with convection (i.e the mixing length l), oscillations (i.e. the wavelength λ) and stratification (i.e. the pressure scale height H_p) also coincide in the superficial layers of the star. As a result, understanding the physical processes responsible for the damping of the modes requires not only a time-dependent treatment of turbulent convection, but also a non-adiabatic one. This makes the task of theoretically prescribing these processes an immensely complicated one, as I will show in the remainder of this section.

2.3.2 The work integral

Mode damping as a counterpart of mode frequency

In Section 2.1.2, I introduced the mode frequencies as the eigenvalues associated to a boundary value problem comprised of Equations 2.50 and 2.51, to which I added the boundary conditions at the center and on the surface. The wave variables are complex functions of the radial coordinate r, and therefore the eigenvalues themselves are complex, a point that I have left aside until now. In writing the temporal Ansatz for the wave variables in the form of Equation 2.18, it is customary to denote it as $\exp^{j\sigma t}$, and to reserve the notation ω to the real part of σ. Then ω does indeed correspond to the angular frequency at which the mode oscillates, while the imaginary part of σ corresponds to the e-folding time of either the decay or the growth of the wave amplitude, depending on its sign. As such, we see that it corresponds to the damping rate η defined in Section 2.3.1, and we have

$$\sigma = \omega + j\eta \,, \tag{2.98}$$

so that a positive value of η corresponds to a decaying mode, and a negative value to an unstable, linearly growing mode. From a theoretical point of view, mode damping and mode frequency are therefore one and the same, and in particular the question: how does turbulent convection affect mode damping? is the same as the question: how does it affect mode frequency? In other words, modelling mode damping and modal surface effects is the same task; I will come back to this statement upon introducing surface effects, in Section 2.4.

I also take this opportunity to remark that, while the importance of adopting a non-adiabatic framework to study mode damping is made clear by the coincidence between the period of the mode and the local thermal timescale in the superadiabatic region, it could actually have been outlined as early as in Section 2.1. Indeed, I briefly discussed in Section 2.1.2 the nature of the boundary value problem associated to the oscillations in the adiabatic framework, and remarked that while the full problem was not of Sturm-Liouville type, it becomes of Sturm-Liouville type in both asymptotic limits $\sigma \to 0$ and $\sigma \to +\infty$, i.e. both high-order g-modes and high-order p-modes. One of the key characteristics of a Sturm-Liouville problem is the fact that *all of its eigenvalues are real*. I recall that the eigenvalue associated to the boundary value problem associated to stellar oscillations is σ^2: if σ^2 is real, then σ is either real or purely imaginary. The solution has an oscillating behaviour only in the first case, in which case $\sigma = \omega$, and $\eta = 0$. Otherwise stated, *in the adiabatic framework presented in Section 2.1, and in the asymptotic limit, neither p-modes nor g-modes can be damped.* Therefore, the stability of solar-like p-modes can only stem from either the effect of turbulent convection (which we also discarded in Section 2.1), or from non-adiabatic effects. As I will now show, both are responsible.

Definition and interpretation of the work integral

In general, the correct computation of the damping rate of a mode requires the full non-adiabatic linear eigenvalue problem to be solved, where, as I remarked above, the imaginary part of the complex eigenvalues corresponds to the damping rates. This would be the correct, rigorous way to obtain them; however, there is a more practical and convenient way to proceed, based on the *work integral*, which I introduce now. For the sake of simplicity, I will only consider radial modes in this discussion. Multiplying the perturbed vertical displacement equation (Equation 2.22) by $\xi_r^\star$, integrating over the entire stellar volume, and taking the imaginary part, one finds the work integral in the form (e.g. Samadi et al. 2015)

$$\eta = \frac{1}{2\omega \mathcal{I}} \int_0^M \mathrm{d}m \, \mathrm{Im}\left[\frac{\delta\rho^\star}{\rho_0^2}\delta p\right] , \tag{2.99}$$

where the mass variable m is defined through its differential form

$$\mathrm{d}m = 4\pi r^2 \rho_0 \, \mathrm{d}r , \tag{2.100}$$

and the inertia $\mathcal{I}$ of the mode is defined by Equation 2.97. Equation 2.99 yields the damping rate η of the mode, provided the oscillatory angular frequency ω and the inertia $\mathcal{I}$ of the mode are known, in addition to its complex eigenfunctions written in terms of density and pressure. Here, δp refers to the Lagrangian perturbation of the *total* pressure: with the inclusion of turbulent convection, it contains both the gas pressure p_g and the turbulent pressure p_t. It is immediately seen that the damping rate depends on the phase difference between the pressure fluctuations and the gas expansion due to the modes, and is intimately related to the total pressure work exerted on the mode by the background. Let me interpret this relation further. The quantity under the integral can be rewritten in terms of the change in the material volume $\mathrm{d}\mathcal{V}$ occupied by the layer $\mathrm{d}m$

$$\mathrm{d}m \frac{\delta\rho^\star}{\rho_0^2} = -\,\mathrm{d}m\delta\left(\frac{1}{\rho}\right)^\star = -\delta\left(\frac{\mathrm{d}m}{\rho}\right)^\star = -\delta\,\mathrm{d}\mathcal{V}^\star , \tag{2.101}$$

so that the quantity under the integral is simply $-\mathrm{Re}\left(-j\omega\delta\,\mathrm{d}\mathcal{V}^\star\delta p\right)/\omega$. I made $-j\omega$ appear on purpose inside the real part: indeed, the quantity $-j\omega\delta\,\mathrm{d}\mathcal{V}^\star$ is the (conjugated) complex representation of the rate of change of the local material volume, and *the entire real part is the real representation of the power transferred by the background to the mode in the layer* $\mathrm{d}m$ *through the pressure mechanical work* $-p\,\mathrm{d}V$. Integrating over m, and taking the extra minus sign into account, yields the total power transferred *by* the mode *to* the background through pressure work, which I will denote as $\mathcal{P}_p$. With these new quantities in mind, Equation 2.99 is simply (e.g. Samadi et al. 2015)

$$\eta = \frac{\mathcal{P}_p}{2\omega^2 \mathcal{I}} . \tag{2.102}$$

It can immediately be seen that η has the same sign as $\mathcal{P}_p$, which is consistent with the idea that $\eta > 0$ if the mode loses energy to the background each cycle – i.e. if it is damped. Furthermore, $\omega^2 \mathcal{I}$ corresponds to the total kinetic energy contained in the mode (this can be seen by inserting ω inside the integral defining the inertia in Equation 2.97, and remarking that $|\omega \xi_r|^2$ is the modulus squared of the modal velocity). As such, the ratio $\mathcal{P}_p/(\omega^2 \mathcal{I})$ is the ratio of the mode energy loss rate to the mode energy itself, and does indeed correspond to the inverse time scale associated to the energy loss. Finally, the factor $1/2$ stems from the fact that the square of a decaying quantity decreases twice as fast as the quantity itself: if the amplitude of the mode decreases at a rate η, the energy does so at a rate 2η.

One can go one step further and break down the pressure perturbation into its different components. This is done by expressing the gas pressure perturbation in terms of density and entropy perturbations through Equation 2.34, and replacing the entropy perturbation with its expression given by Equation 2.26. One finds (Samadi et al. 2015)

$$\begin{aligned} \eta &= \frac{1}{2\omega \mathcal{I}} \int_0^M \mathrm{d}m \, \mathrm{Im}\left[\frac{\delta\rho^\star}{\rho_0}\left(\frac{\delta p_t}{\rho_0} + \frac{\nabla_{\mathrm{ad}}\Gamma_1}{j\omega}\left(\frac{\mathrm{d}\delta L^{\mathrm{rad}}}{\mathrm{d}m} + \frac{\mathrm{d}\delta L^{\mathrm{conv}}}{\mathrm{d}m} + \delta\epsilon_2\right)\right)\right] \\ &= \eta_{\mathrm{pt}} + \eta_{\mathrm{rad}} + \eta_{\mathrm{conv}} + \eta_{\mathrm{diss}} \,, \end{aligned} \tag{2.103}$$

where the *radiative* and *convective luminosities* are defined by

$$L^{\mathrm{rad}} \equiv 4\pi r^2 F_r^{\mathrm{rad}} \,, \tag{2.104}$$

$$L^{\mathrm{conv}} \equiv 4\pi r^2 F_r^{\mathrm{conv}} \,. \tag{2.105}$$

In addition to the extra contributions from turbulent pressure and convective flux, the inclusion of convection in this expression also yields a modification of the dissipation in the entropy equation, which now takes the form $\epsilon_2 \equiv \epsilon + \overline{\mathbf{v}_{\mathrm{conv}} \cdot \boldsymbol{\nabla} p_g}$, where the second term corresponds to the mechanical work exerted by the gas pressure force on the fluid moving with the convective velocity.

The form of the work integral given by Equation 2.103 makes it clear that mode damping can come from two different processes: the work of turbulent pressure, and the work of the non-adiabatic part of the fluctuating pressure. The adiabatic pressure perturbation, being in phase with the density perturbation, yields a vanishing imaginary part, and therefore does not contribute to the work integral. This is easily interpreted: the adiabatic pressure fluctuations being perfectly in phase with the volume changes, the amount of work exerted in the expansion phases exactly compensates the work exerted in the contracting phases, so that no net work is done during an entire cycle of the mode. As for the other contributions, there are four: one from turbulent pressure, one from the radiative flux (which contains, among other things, the κ-mechanism mentioned above), one from the convective flux, and one from the turbulent dissipation rate[18]. The last three contributions collectively correspond to the effect of the non-adiabatic pressure perturbation. In general, an extra contribution should come from the perturbation of the energy generation rate in the core. Since I am only concerned with processes happening close to the surface of the star, I do not include this contribution here. Equation 2.103 is only valid for radial modes, but a generalised expression valid for radial and non-radial modes alike can be derived (e.g. Grigahcène et al. 2005).

For completeness, I should also add two more contributions that do not arise directly from the work integral formalism. One is the leaking of the acoustic waves into the evanescent region above the upper turning point, especially for high-frequency modes close to the acoustic cut-off frequency ν_{ac} (Balmforth and Gough 1990). The other is the incoherent scattering of the waves in the superadiabatic layer (Goldreich and Murray 1994). The authors showed that this layer is subjected to large density inhomogeneities in the horizontal direction, with the RMS value of the density fluctuations being proportional to the turbulent Mach number[19] squared. These inhomogeneities scatter the waves, which the authors showed leads to a coupling between modes of similar frequencies and different angular degrees. They further showed that the energy exchange stemming from this coupling between different modes is unfavorable to the p-modes, thus creating, in effect, an additional source of p-mode damping. It is usually recognised, however, that these two additional sources of damping are negligible compared to the ones included in Equation 2.103.

[18] This denomination is perhaps a bit of a misnomer, seeing as ϵ_2 contains the turbulent dissipation rate ϵ *in addition to the buoyancy work* $\overline{\mathbf{v}_{\mathrm{conv}} \cdot \boldsymbol{\nabla} p_g}$. Nevertheless, I will conserve this designation in the following.

[19] The turbulent Mach number is defined as the ratio between the RMS turbulent velocities to the local sound speed, the former being given, for instance, by Equation 1.59 in standard MLT.

2.3.3 Solar mode damping predictions

Equation 2.103 is both very simple in its form, and extremely complicated to apply. The reason is that the complexity is hidden behind the different modal perturbations appearing in the expression of the damping rate, and that are not directly related to the wave variables $\delta\rho$ or ξ_r for instance. The reason is that they pertain to the turbulent convection, and their accurate assessment requires a time-dependent *and* non-adiabatic treatment of convection. If one wishes to better understand solar-like mode damping, and to answer the questions: what are the dominant contributions?, and: can we predict the damping rates in a given stellar model?, one encounters the exact same obstacles and has to face the exact same challenges as for stellar turbulent convection modelling, which I have discussed in detail in Chapter 1.

Naturally, the work integral is useful not only for solar-like oscillators, but for stellar oscillations in general. It can be used to predict the stable or unstable nature of global modes of oscillation in a given star, thus allowing for a determination of the physical processes responsible for self-excitation in classical pulsators, as well as the boundaries of the instability strips in the HR diagram. As such, the wealth of results produced by mode stability analysis far outstrips the realm of solar-like oscillators. Here, however, I am only concerned with this realm, and I will leave aside the question of classical pulsators entirely. I refer the reader who wishes a more general discussion to the review by Houdek and Dupret (2015) for more details.

Predictions based on MLT

Balmforth (1992a) made use of the time-dependent, non-local, non-adiabatic formalism of Gough (1977a) to compute complex eigenfrequencies for a solar model. His model is such that the only contributions to η that he considered are $\eta_{\rm pt}$, $\eta_{\rm rad}$ and $\eta_{\rm conv}$ (see Equation 2.103), where the radiative flux is described in the Eddington approximation, and the quasi-adiabatic approximation was adopted. The author found the solar modes to be stable – with the exception of a few low-frequency modes –, in agreement with observations. He also found orders of magnitude similar to the observations, as illustrated in Figure 2.7. However, the high-frequency modes are found to be much less stable than observed. Furthermore, while for low-frequency modes the predicted damping rate do not depend too much on the free parameters chosen in the MLT treatment of convection – unsurprisingly, since low frequency modes are reflected in deeper layers of the star, and are therefore much less sensitive on the physics of the surface –, by contrast this is not the case for higher-frequency modes. This work was extended by Houdek et al. (1999) for other solar-like oscillators on the main-sequence. The authors found that the contribution $\eta_{\rm rad}+\eta_{\rm conv}$ has a destabilising effect (except for high-frequency modes), while $\eta_{\rm pt}$ has a stronger stabilising effect, which explains the overall stability of the modes. In particular, they predicted that the compensation peaks just below 3 mHz, thus explaining the damping plateau. Chaplin et al. (2005) used the same model, but allowed the Reynolds stress tensor to be anisotropic; this requires the introduction of yet another free parameter, in the form of an anisotropy factor defined as the ratio of the vertical-vertical Reynolds stress component to the trace of the Reynolds stress tensor. They adjusted all the free parameters to fit the data, which led them to a somewhat reasonable agreement.

On the other hand, Dupret et al. (2004) used the formalism of Unno (1967) in the form presented by Grigahcène et al. (2005) to perform similar calculations. However, they also considered the contribution of turbulent dissipation $\eta_{\rm diss}$. In addition to the usual free parameters inherent to MLT, the authors needed to introduce an additional free parameter β, which is a *complex* non-dimensional damping time for the entropy perturbation[20]. The results of this study are very different from the ones of Balmforth (1992a) or Houdek et al. (1999): the authors found that it is $\eta_{\rm conv}$ that has a stabilising effect, while $\eta_{\rm pt}$ has a destabilising effect. Furthermore, they found that the contribution $\eta_{\rm diss}$ cancels out with $\eta_{\rm pt}$ to a large extent, with the cancellation being exact in the limit of adiabatic, isotropic turbulence. They also found an agreement with observations, but the agreement is found for completely different reasons than in Chaplin et al. (2005) for instance. This is particularly illuminating, because it shows that the resulting stability analysis largely depends on the MLT empirical prescription used in the pulsation computations. Belkacem et al. (2012) extended these calculations to a non-local treatment of convection (although they still retained β as a model parameter, but constrained its value by matching the resulting frequency of maximum spectral height $\nu_{\rm max}$ with the value yielded by scaling relations), and applied their model on a variety of solar-like oscillators

[20]This parameter is necessary to remove the non-physical fast spatial oscillations of the eigenfunction δL that otherwise arise. This happens when the typical entropy perturbation have a typical length scale that is much smaller than the mixing length: in a purely local treatment of convection such as considered here, this leads to abnormally fast entropy eigenfunctions. This can otherwise be avoided by treating convection non-locally.

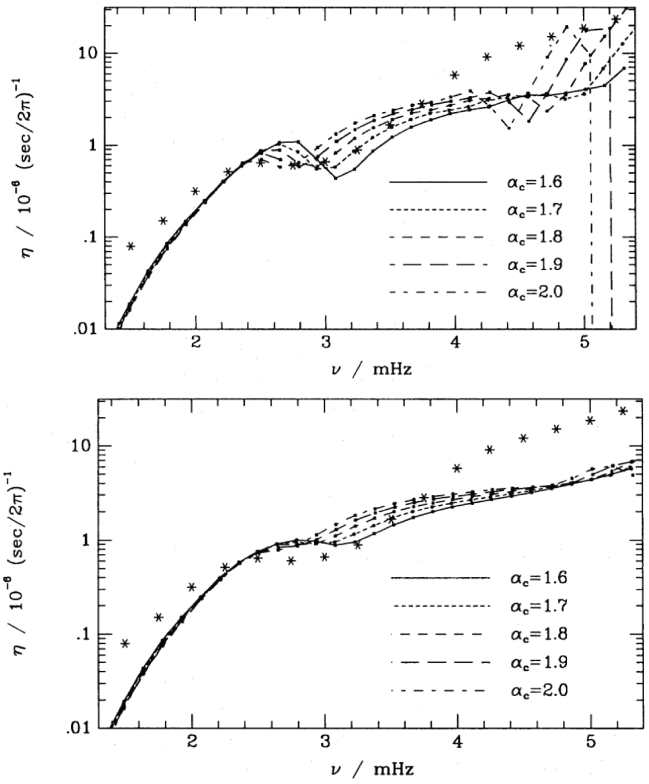

Figure 2.7: Comparison between the observed solar linewidths (symbols) and theoretically predicted linewidths (solid lines), with quasi-adiabatic pulsation calculations in a non-local MLT equilibrium solar model, for different values of the mixing-length parameter $\alpha_{\rm MLT}$ and **top**: $a^2 = b^2 = c^2 = 600$, or **bottom**: $a^2 = b^2 = c^2 = 300$. Credits: Balmforth (1992a).

for confrontation with observations made by CoRoT and *Kepler*. They found, in a perhaps closer agreement with the prior results of Balmforth (1992a), that the turbulent pressure has a stabilising effect, while the non-adiabatic gas pressure perturbations have a destabilising effect. However, the authors found a much more pronounced cancellation between the two, with overall damping rates being much smaller than the individual contributions. They also found the damping plateau to be caused by a peak in the mutual cancellation.

The early studies on the subject clearly formulated the hope that the comparison between theoretically predicted and observationally inferred damping rates could serve as a mean to calibrate the free parameters pertaining to MLT formalisms. Unfortunately, the absence of consensus not only on the quantitative predictions of damping rates, but also on the determination of the dominant physical processes, makes it doubtful that this can be done. The reason lies in the large number of free parameters inherent to this approach, but also – as we already point out for surface effects – in the simplistic nature of the mixing length hypothesis, which introduces a large uncertainty in the model in the first place. Even from this limited account, it becomes apparent that alternative methods must be employed.

Predictions based on alternative methods

In Section 1.2.3, I presented Reynolds-stress models of turbulent convection as a natural extension of the MLT formalism, whereby closure relations are prescribed not for second-order correlation products, but at higher order. Xiong et al. (2000) made use of the Reynolds stress model of Canuto (1992) to carry out linear stability analysis and predict mode damping rates in the Sun. They did so alternatively with and without any effect from convection. In agreement with the prior studies mentioned above, the authors found that convection stabilises the modes: without convection, they found all modes of radial order smaller than $n = 10$ to be unstable, while the range of unstable modes is narrower with convection. However, the agreement stopped there, because even with the full effect of convection–oscillation coupling, the authors predicted all radial modes of order $11 \lesssim n \lesssim 24$ to be unstable, in direct disagreement with observations, which show that the Sun does not feature any unstable oscillations. As I had the opportunity to outline in Section 1.2.3, while the Reynolds-stress approach indeed constitutes a better

representation of reality than MLT, it still suffers from the same overall problems, in particular the wealth of free parameters, and the reliance on the Boussinesq approximation, and more importantly, on the mixing length hypothesis. As such, the Reynolds-stress approach does not address the core issues posed by MLT treatments of turbulent convection.

The invaluable input of 3D hydrodynamic simulations in this context has become apparent more recently, and its potential for calibrating turbulent convection models – and in particular MLT – was outlined, for instance, by Stein and Nordlund (2001) – although their focus was mainly on the excitation rate of the modes –, or more recently by Houdek et al. (2017) or Aarslev et al. (2018). While the procedure provides with an agreement with observations, there still remains the problem that the agreement is obtained after fitting a certain number of free parameters. For instance, Houdek et al. (2017) chose to calibrate the non-local parameter a for turbulent pressure so that the maximum of the equilibrium turbulent pressure in the 3D atmosphere and in the 1D model coincide, while the other non-local parameters b and c are fitted to obtain the best possible agreement between theoretical and observed linewidths, the anisotropy of the Reynolds stress tensor is approximated with an analytical function designed to agree as best as possible with the anisotropy 'observed' in 3D simulations, and the mixing-length parameter is calibrated so that the depth of the convective zone matches the value inferred from helioseismic measurements. Because of these numerous free parameters, and the multiple ways in which each is calibrated, these models do not allow for any theoretical predictions, nor do they shed light on the physical processes at stake. Building on the idea of using 3D hydrodynamic simulations, Belkacem et al. (2019) suggested to investigate directly the normal modes that develop in a 3D LES of stellar superficial layers, and whose properties can be extracted directly from the simulation. They applied this idea to a solar model, and managed to extract three different radial modes, which they identified with corresponding non-radial modes in the actual Sun, having a node at the layer corresponding to the bottom of the simulation, and whose angular degree matches the boundary conditions on the lateral sides of the simulation box. They compared the measured linewidths with the predictions from the work integral (Equation 2.103), and found reasonable agreement for the only two modes they managed to resolve. Using the work integral, they also managed to split the 'observed' linewidths of the simulated modes into their different physical contributions, and furthermore identified the damping regions (where the work integral is positive) and the driving regions (where it is negative). Their results are in stark contrast with those presented above in the MLT framework: they found that it is the radiative and convective contributions $\eta_{\rm rad}$ and $\eta_{\rm conv}$ that nearly cancel each other, with the former having a destabilising effect, and the latter a stabilising effect of similar importance. Furthermore, also in contrast with previous results, they found that the overall non-adiabatic gas pressure perturbation and the turbulent pressure perturbation were both stabilising factors, and equally contribute to the stability of the modes.

Zhou et al. (2019) followed a similar path, with the notable difference that they found a way to enhance the visibility of any given normal mode of the box in the simulation. To do so, they modified the bottom boundary condition of their simulation to introduce a forced sinusoidal oscillation of thermal pressure while at the same time ensuring that the entropy remains constant. In effect, this injects energy into the Fourier component of the spectrum that coincides with the imposed frequency, so that the target mode has a much larger amplitude than any other mode, or than the convective noise. This procedure allowed the authors to extract the eigenfunctions of the mode directly from the simulation; and what is more, this gave them access to many more modes in the simulation than if they were 'observed' without artificial excitation. The authors then used the work integral to obtain the different contributions to the damping rate of the modes. For the Sun, they found a perhaps slightly less obvious agreement with observations, which still reproduces the qualitative behaviour of damping rate with frequency – in particular the damping plateau –, and, in contrast with all MLT-based approaches, is independent of any free parameters. In contrast with Belkacem et al. (2019), however, they found that the non-adiabatic gas pressure perturbation has a destabilising effect, and the turbulent pressure perturbation a stabilising effect, in accordance with Balmforth (1992a) for instance. This approach was then extended to other stellar models by Zhou et al. (2020).

While the input of 3D simulations is indeed valuable, and makes it possible to disentangle the various physical contributions to mode damping, this kind of approach still has its own limitations. First, it is absolutely impossible to assess the contribution $\eta_{\rm diss}$ from a 3D simulation, because in such LES, the turbulent dissipation is either completely dominated by numerical dissipation (which cannot be controlled, and is completely non-physical), or explicitly described by equally non-physical models (see Section 1.2.1 for more details). Secondly, this approach requires a considerable simulation running time, so as to resolve the modes and be able to measure their linewidths.

This precludes the use of such simulations for a parametric study, for instance. Finally, the results are much more dependent on the boundary conditions, and in particular at the top boundary of the box, than in full stellar models, primarily because of the relative size of the regions under consideration. These observations, and the discussion I conducted in this section in general, showcase what I already hinted in Section 2.3.1, namely that theoretical efforts to prescribe the relation between the properties of turbulent convection and solar-like damping rates are met with considerable difficulties, directly stemming from our lack of knowledge on turbulent convection itself, and illustrated by the lack of consensus, still lingering to this day, concerning the dominant physical process for mode damping. It would therefore be of much interest to go beyond these approaches, whether they be based on MLT, Reynolds-stress models or LES: I will come back to this last point in Chapter 3.

2.4 Surface effects

2.4.1 Definition and observed properties

In Section 2.1, I introduced the stellar global modes of oscillation in a framework that discarded a certain number of aspects in the physics of stellar interiors. While this allowed me to conduct a simple discussion, adapted to the brevity called for in the context of this introduction, one must realise that each approximation, each discarded phenomenon, increases the inaccuracy of the model. On the contrary, if one wishes to accurately predict the properties of the modes in a given star, one has to include much more realistic physics in the stellar model. Many studies have been devoted to the inclusion of better physics in stellar models for more accurate eigenfrequency predictions: rotation, whether it be slow (e.g. Cowling and Newing 1949; Hansen et al. 1977; Dziembowski and Goode 1992; Goupil et al. 1996; Soufi et al. 1998; Townsend 2003) or fast (e.g. Dintrans and Rieutord 2000; Lignières et al. 2006; Reese et al. 2006, 2009; Ouazzani et al. 2015); magnetic fields (e.g. Kurtz 1982; Dziembowski and Goupil 1998; Bigot and Dziembowski 2002); the non-adiabaticity of the oscillations (e.g. Christensen-Dalsgaard and Gough 1975; Dziembowski 1977; Saio and Cox 1980; Christensen-Dalsgaard 1981; Pesnell 1990; Balmforth 1992a; Rosenthal et al. 1995; Houdek 1996; Dupret 2001; Dupret et al. 2002; Reese et al. 2017); or the impact of element diffusion (e.g. Guzik and Cox 1993; Günther 1994; Guzik and Swenson 1997; Deal et al. 2017), are several examples. Each step helps close the gap between the predicted frequencies and the observed frequencies.

But despite these refinements to stellar modelling, their still remains a substantial discrepancy, and what is more, one that largely dominates the errors stemming from the observational techniques or the reduction of the observational data (Christensen-Dalsgaard et al. 1996). This discrepancy has been given the name *surface effects*, for reasons that will become clear in an instant. Since these surface effects do not originate from uncertainties in the observations, they must come from uncertainties in the models. In a large part, this discrepancy is due to the fact that the effect of convection was ignored in the analysis conducted in Section 2.1. Figure 2.8 shows, as a function of frequency, the difference between the p-mode frequencies inferred from solar observations by the GONG network, and those computed through an adiabatic standard solar model, without convection – i.e. in the framework presented in Section 2.1.1. More precisely, the frequency differences are weighted by the same factor $\mathcal{Q}_{nl}$ that we introduced for damping rates in Section 2.3, and defined by Equation 2.96. For the same reasons detailed in Section 2.3.1, the scaled frequency difference $\mathcal{Q}_{nl}\left(\nu_{nl,\mathrm{obs}} - \nu_{nl,\mathrm{th}}\right)$ is a more relevant quantity to compare between different modes than the raw frequency differences.

Figure 2.8 presents some striking features: it shows that the scaled frequency differences are very small for frequencies $\lesssim 2$ mHz, but start rising significantly for higher frequency modes, and ends up reaching as far high as ~ 15 mHz at the high-frequency end of the p-mode spectrum. Furthermore, the frequency differences always have the same sign, with the theoretically predicted frequencies being systematically overestimated compared to the observed frequencies. Finally, the scaled frequency difference is quite independent of angular degree, and collapses to a unique, slowly varying function of frequency only. These features tend to support the hypothesis that the frequency discrepancy is primarily due to the uncertainties in the modelling of convection *close to the surface of the star*, where the convective motions are at their most turbulent – hence the name: surface effects. Indeed, at the surface, modes with lower frequencies have their upper turning point[21] more deeply located than high frequency modes, which means that they are much less affected by the phenomena occurring at the surface

[21] We recall, from Section 2.1.2, that the upper turning point r_u of solar-like p-modes is defined by the implicit relation $\omega^2 = N^2(r_u)$. With N^2 rapidly increasing with r in the superficial layers of the star, r_u does indeed increase with ω.

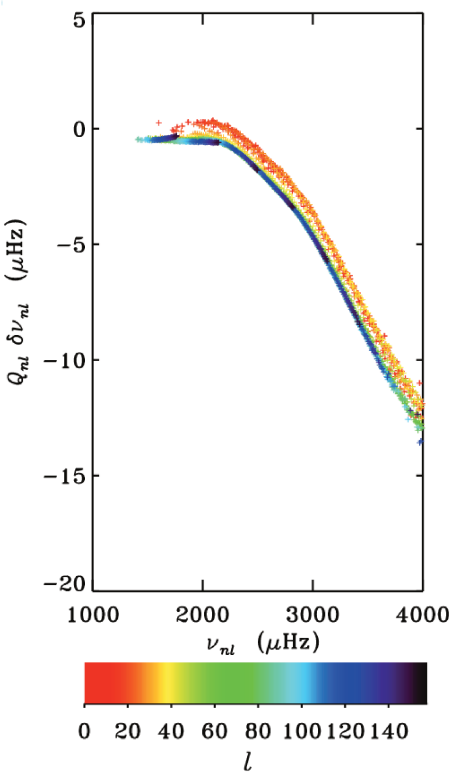

Figure 2.8: Frequency difference between observed frequencies (inferred from GONG observations) and theoretical predictions for adiabatic oscillations in a standard solar model. The frequency difference is scaled by the factor given by Equation 2.96. The color scale refers to angular degree l. Credits: Christensen-Dalsgaard et al. (1996).

of the star. This is why the frequency difference is much larger for high frequency modes. Additionally, the wave vectors associated to the p-modes are almost vertical close to the surface[22], and therefore the behaviour of the mode there is almost independent of angular degree. This is why the surface effects themselves, like the damping rates (see Section 2.3), are almost independent of angular degree.

Unsurprisingly, these properties are very similar to the properties of the mode damping rates, given in Section 2.3.1. This is because, as I had the opportunity to point out then, not only do surface effects and damping processes for solar-like oscillations both arise from the coupling with turbulent convection, but also, perhaps more fundamentally, because both phenomena are actually two faces of the same complicated coin, since the damping rate and the frequency of the modes are simply the real and imaginary part of the same complex eigenvalue. Therefore, in attempting to explain surface effects from a theoretical point of view, one runs into the exact same difficulties as for mode damping, and all of the conclusions drawn for mode damping in Section 2.3 remain valid for surface effects, in particular regarding the difficulties inherent to the theoretical modelling of turbulence–oscillation coupling, and the as-of-yet still lingering absence of consensus concerning the dominant physical processes. This is particularly problematic when it comes to surface effects: indeed, the use of p-mode eigenfrequencies to infer the structure of stellar interiors requires that the frequencies be accurately, and without bias, predicted from stellar modelling. Consequently, it is necessary to correct modelled frequencies from these surface effects, and one way to do this, which I outline below, is through a better theoretical modelling of the surface layers, and particularly of the interplay between the convection and the oscillations.

2.4.2 Theoretical modelling of surface effects

The surface effects are commonly separated into two distinct classes of effects: those pertaining to the modification of the equilibrium state, and those pertaining to the modification of the mode physics. The former are referred to as *structural* or *extrinsic effects*, the latter as *modal* or *intrinsic effects* (Balmforth 1992b). In fact, the separation is rather artificial, as we will see in a moment: one actually depends on the other, and vice versa.

[22]This statement might, at first glance, seem to be at odds with the dispersion relation presented in Section 2.1.2, according to which we should have $k_r^2 = 0$ at the upper turning point (where $\omega^2 = N^2$). However, this is not so: the increase of the Brünt-Väisälä frequency with r is so sudden at the surface that ω^2 actually remains non-negligibly larger than N^2 until just below the upper turning point. Therefore, the factor $\omega^2 - N^2$ in the dispersion relation remains of the order of ω^2 itself, and since, in addition, $L_l^2 \ll \omega^2$, the dispersion relation yields $k_h \ll k_r$. The radial wave vector only becomes zero – and therefore the p-modes only become horizontal – in an extremely narrow region around their upper turning point (which is why, incidentally, the acoustic waves are said to be *reflected* at the surface).

Nevertheless, for the sake of this discussion, I will introduce them separately.

Structural surface effects

Turbulent convection acts on the momentum equation through the additional Reynolds stress force, which represents the diffusive transport of momentum by the small scale turbulent motions of the gas (see Chapter 1). In general, it is assumed to be isotropic, and in analogy with the viscous stress force, this isotropic part is characterised by the scalar quantity p_t, referred to as the turbulent pressure. The turbulent pressure thus adds up with the gas pressure, so that in the momentum equation, the gas pressure p must be replaced by the total pressure[23] $p_{\rm tot} \equiv p + p_t$. While a majority of stellar models disregard the effect of p_t altogether, it actually does become non-negligible in the superficial layers of the star, and especially in the superadiabatic region, as shown by 3D hydrodynamic simulations (Stein and Nordlund 2001). In fact, the ratio p_t/p can reach as high as ~ 0.15 in the Sun (Rosenthal et al. 1999): turbulent pressure must therefore be accounted for in the oscillation analysis. It is common to separate the contributions of turbulent pressure to the surface effects into two components: one due to the equilibrium turbulent pressure $p_{t,0}$, and one due to the perturbation of the turbulent pressure δp_t.

The time-averaged, equilibrium turbulent pressure modifies the hydrostatic equilibrium condition, and with it the state around which the equations are perturbed. Then the hydrostatic equilibrium condition must be modified to

$$\frac{\partial p_{\rm tot,0}}{\partial x_i} + \rho_0 \frac{\partial \Phi_0}{\partial x_i} = 0 \,, \tag{2.106}$$

where $p_{\rm tot,0} \equiv p_0 + p_{t,0}$ is the equilibrium total pressure. Essentially, the extra pressure term elevates the radius of the star, and therefore increases the size of the resonant cavity associated to the p-modes. With the increase of the cavity size comes a decrease in the eigenfrequencies: this partially explains why the frequencies are overestimated when turbulent pressure is not accounted for. The effect of the equilibrium turbulent pressure was investigated, for example, by Rosenthal et al. (1995). The authors considered several treatments of convection-oscillation coupling. Their model number 2, in particular, focuses solely on the effect of the equilibrium turbulent pressure, and discards the perturbation to the turbulent pressure. They computed the interior of the model, excluding the superficial layers, by treating convection in the standard MLT approach (see Section 1.2.2), but without turbulent pressure. In parallel, they used a 3D hydrodynamic simulation of solar convection, and averaged all quantities horizontally and temporally for each horizontal layer in the simulation, in order to obtain a more realistic equilibrium model for the outer 2% of the Sun. In particular, by averaging the quantity ρu_r^2 (ρ being the density and u_r the vertical velocity), they obtained $p_{t,0}$ as a function of radius in the superficial layers of their model. The authors then patched the averaged surface layers on top of the more crudely modelled interior, making sure, in doing so, that the sound speed profile remained continuous at the transition, thus obtaining what is commonly referred to as a *patched model*. While this procedure yields a much more realistic equilibrium turbulent pressure than the standard MLT for instance, it tells us nothing of the turbulent pressure perturbations δp_t. The authors argued, on the basis of results obtained with non-local MLT (see Section 1.2.2) as well as hydrodynamic simulations, that δp_t varies in quadrature with the other forces, and in particular with δp. As such, they considered that this perturbation only impacts the imaginary part of the eigenfrequency, and not its real part – in other words, not the oscillatory frequency. For the sake of computing the real part of the frequencies, the authors therefore considered $\delta p_t = 0$. In the linearly perturbed equations, everything remains the same, except that $\delta p/p_0$ now actually refers to $\delta p_{\rm tot}/p_{\rm tot,0}$, with

$$\frac{\delta p_{\rm tot}}{p_{\rm tot,0}} = \frac{\delta p}{p_0}\frac{p_0}{p_{\rm tot,0}} = \frac{\Gamma_1 p_0}{p_{\rm tot,0}}\frac{\delta \rho}{\rho_0} \,. \tag{2.107}$$

In other words, *the linear analysis presented in Section 2.1 remains exactly the same, with the first adiabatic exponent being replaced by an effective exponent Γ_1^r, called the reduced adiabatic exponent.* Because of the averaging process performed to obtain the model, the reduced exponent must also be carefully averaged, and the authors found

$$\Gamma_1^r \equiv \frac{\langle \Gamma_1 p \rangle_0}{p_{\rm tot,0}} \,, \tag{2.108}$$

[23] Since I do not account for the radiative pressure here, this is actually not really the total pressure. For the sake of this discussion, however, I will disregard this point.

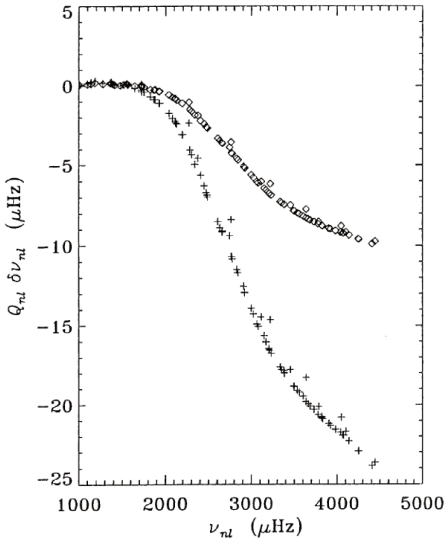

Figure 2.9: Scaled frequency differences between an adiabatic oscillation model with and without equilibrium turbulent pressure. The two sets of symbols correspond to two distinct models for the equilibrium turbulent pressure, derived respectively by Rosenthal et al. (1995) and Canuto and Mazzitelli (1991). Turbulent pressure perturbations are included in the scope of the RGM. This frequency difference is directly comparable to the scaled frequency differences between observations and the standard model (i.e. without equilibrium turbulent pressure), as shown in Figure 2.8. One can see that the qualitative behaviour is similar. Credits: Rosenthal et al. (1995).

where $\langle . \rangle_0$ denotes a horizontal and temporal average. This approximation is accordingly referred to as the *Reduced*-Γ_1 *Model* (or RGM). The authors computed the frequencies of the model, and compared them to a standard solar model, as computed according to the model presented in Section 2.1. The resulting scaled frequency differences are shown in Figure 2.9, which shows that the inclusion of the equilibrium turbulent pressure in the model decreases the predicted mode frequencies, and that the latter are therefore brought closer to the observed values. In particular, Figure 2.9 must be compared with its observational counterpart Figure 2.8: the difference between observed and reference frequencies, on the one hand, and the difference between frequencies computed with equilibrium turbulent pressure and reference frequencies, on the other hand, have qualitatively similar dependence on mode frequency. It can be seen that the turbulent pressure decreases the predicted frequencies, and furthermore, the behaviour of the difference closely resembles the observed surface effects illustrated in Figure 2.8.

This path was further investigated by Rosenthal et al. (1999), with a focus on the treatment of the turbulent pressure perturbation δp_t. In addition to the RGM approximation described above, the authors also considered the possibility that the perturbation of turbulent pressure might be proportional to the gas pressure perturbations, so that $\delta p_t / p_{t,0} = \delta p / p_0$. In that case, one simply has

$$\frac{\delta p_{\rm tot}}{p_{\rm tot,0}} = \Gamma_1 \frac{\delta \rho}{\rho_0} \,. \tag{2.109}$$

The frequencies are computed as in the RGM, but this time the effective first adiabatic component is given by $\langle \Gamma_1 \rangle_0$. This alternative approximation was dubbed *Gas*-Γ_1 *Model* (or GGM) by the authors. This time around, the turbulent pressure was also included in the interior of the model, with a prescription given by the standard MLT and adjusted for turbulent pressure continuity at the transition between the interior model and the averaged surface layers. The authors concluded that the GGM leads to a better agreement of the predicted frequencies with observations than the RGM. Scaled frequency differences between the GGM and GONG observations are shown in Figure 2.10. There still exist discrepancies, which are now either positive or negative depending on the frequency; however, the difference is considerably smaller than those shown in Figure 2.8.

Other studies aiming at assessing the structural surface effects followed, with further and further refinements brought to the equilibrium state, but most of which rely on either the RGM or the GGM. For instance, Li et al. (2002), and later Robinson et al. (2003), also included the anisotropy of the equilibrium Reynolds stress tensor in their model, as well as the turbulent contribution to entropy and kinetic energy. However, the pulsation calculations were still carried out in an adiabatic framework, and the relative perturbation of total pressure assumed equal to the relative perturbation of gas pressure, thus amounting to adopting the GGM. The authors found a better agreement with observed frequencies than with the sole inclusion of an isotropic turbulent pressure, and underlined the importance of the turbulent kinetic energy in the solar model. In later studies, the patching procedure described above was used to study the dependence of the structural surface effects on the stellar model under consideration. Sonoi et al. (2015) used 3D hydrodynamic simulations performed with the CO^{5}BOLD code to construct several stellar patched models for various values of the effective temperature and surface gravity, and showed that the dependence of surface effects with frequency largely varies across the HR diagram. They also considered the

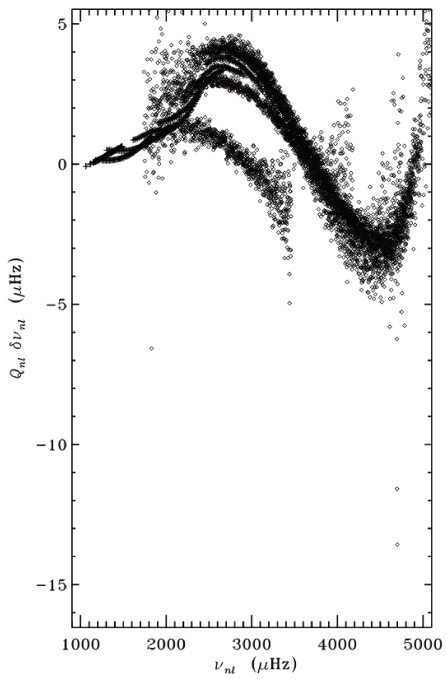

Figure 2.10: Same as Figure 2.8, but the model used to theoretically predict mode frequencies accounts for the equilibrium turbulent pressure throughout the entire star, and the turbulent pressure perturbations are included in the scope of the GGM. The remaining residuals are either due to non-adiabatic effects, or to a poor modelling of δp_t. Credits: Rosenthal et al. (1999).

GGM. Ball et al. (2016) performed a similar study with the `MURaM` code, but with a complementary set of stellar models: while the grid of models used by Sonoi et al. (2015) extended to more evolved models, the one used by Ball et al. (2016) contained cooler stars on the main sequence. The results found by both studies were relatively similar, with structural surface effects being more prominent for hotter stars. Trampedach et al. (2017) conducted a similar analysis, but adopted the RGM instead of the GGM. Magic and Weiss (2016) focused on a solar model, but investigated the influence of the averaging process used to construct the patched model, alternatively averaging over layers of fixed geometrical depth or fixed column mass density, separating the upflows from the downflows or not, and correcting the column mass density for turbulent pressure or not. They concluded that the latter effect is very important in obtaining accurate frequencies from 1D models. The authors elected to use the GGM[24]. They also investigated the effect of chemical composition and magnetic field on the p-mode frequencies. Metallicity, in particular, was later shown by Manchon et al. (2018) to significantly affect structural surface effects, through the surface value of the Rosseland mean opacity. The authors considered the GGM.

While a more and more consistent light is shed on the structural part of the surface effects, a significant part of the frequency difference between models and observations remains unaccounted for. As we can see from the approximations adopted by all the above mentioned studies, there are two different potential reasons for that. First, all the aforementioned studies carry out pulsation computations in an adiabatic framework, which means that neither the perturbation of the radiative flux, nor that of the convective flux, are considered. Second, the turbulent pressure perturbations are consistently modelled through either the GGM or the RGM, neither of which have any real physical ground. Indeed, the argument for adopting the RGM is the assumption that the turbulent pressure perturbations vary in quadrature with respect to the gas pressure perturbations. Figure 2 from Houdek et al. (2017) shows, for a particular solar radial mode around 3 mHz, that the phase difference actually never exceeds 50 degrees. To assert that the perturbations are $\pi/2$-phased therefore seems like a questionable leap to take, especially when it comes to modelling such subtle frequency differences. This assumption was further disproved by Schou and Birch (2020). The authors extracted p-mode eigenfunctions directly from a 3D hydrodynamic simulation of the surface layers of the Sun, in terms of displacement, density, gas pressure and turbulent pressure. They computed, among other things, the phase difference between the density and turbulent pressure eigenfunctions (which is close to the phase difference between gas pressure and turbulent pressure, since most of the gas pressure perturbation are adiabatic, and therefore in phase with the density perturbations). Their Figure 5 clearly shows that the two are not in quadrature. As for the GGM, it is openly admitted that it has absolutely no physical grounds, and is only adopted because it happens, for whatever reason, to give better results. The physical assumptions underlying these two widely used approximations were recently investigated by Belkacem et al. (2021), who concluded that

[24]They indicate having also tried the RGM, and report that the reduced first adiabatic exponent is very close to the actual Γ_1. However, they defined the reduced Γ_1 as $\Gamma_1^r = \langle p\Gamma_1\rangle/p_0$ instead of $\langle p\Gamma_1\rangle/p_{\mathrm{tot},0}$, so this may have played a role.

they both amount not only to considering adiabatic oscillations, but additionally to neglecting two effects in the linear perturbation of the equations of hydrodynamics that are *a priori* not negligible, namely the mechanical work exerted by the buoyancy force, and the dissipation of turbulent kinetic energy into heat. In order to account for the entirety of the surface effects, it is therefore necessary to go beyond both approximations – the adiabaticity, and the GGM/RGM treatment of δp_t.

Modal surface effects

The combined effect of non-adiabaticity and δp_t on the p-mode frequencies is usually considered to correspond to the *modal surface effects*, i.e. the part of the surface effects that are due to a poor modelling of the perturbation of turbulent pressure and convective flux (or even absent, in the standard adiabatic approach introduced in Section 2.1). However, this simplified picture of structural and modal surface effects being separate effects, and the subsequent hope that one may be able to study them in a completely separate manner, does not exactly correspond to reality. Indeed, in studies focusing on the structural surface effects, the very assumptions made about δp_t entail that part of the modal surface effects are also included. Therefore, the two kinds of surface effects are only artificially separated, and as a result, including both non-adiabaticity and realistic turbulent pressure perturbations must be seen not as a way to add modal surface effects to otherwise purely structural effects, but simply as a way to model the entirety of the surface effects.

To this end, it is necessary to use a description of the turbulent convection that is both non-adiabatic and time-dependent. One of the first use of a time-dependent, non-adiabatic MLT formalism to describe the full extent of the surface effects is due to Balmforth (1992b). The author used a formalism that he presented in Balmforth (1992a), which is a hybrid between the time-dependent formalism of Gough (1977b) and the non-local formalism of Spiegel (1963), both of which I introduced in Section 1.2.2. This entails the presence of several free parameters in the model, more specifically the MLT non-dimensional parameter $\alpha_{\rm MLT}$, and the three parameters of non-locality a, b and c. The author showed that the influence of both the entropy perturbation and turbulent pressure perturbation – which he referred to as *intrinsic surface effects* – is heavily dependent on the values taken by these free parameters, as shown in Figure 2.11. For instance, for $a^2 = b^2 = c^2 = 300$ (all three then being exactly 10 times higher than their counterpart in the radiative transfer equation), varying $\alpha_{\rm MLT}$ even moderately (between 1.6 and 2.0 in Figure 2.11) entails frequency differences that can go from ~ 0.5 to ~ 2 μHz for frequencies above 3 mHz, and can even change sign for higher-frequency modes. Predicted surface effects are equally impacted by the values taken by the parameters of non-locality, as illustrated by the difference between the two panels of Figure 2.11, where the parameters of non-locality are only multiplied by a factor $\sqrt{2}$. Throughout most of the p-mode spectrum, and almost independently of the values taken by the various free parameters of the model, the author found that the intrinsic surface effect to be positive, in the sense that the obtained frequencies are larger than those obtained without either δs or δp_t. Therefore, the intrinsic surface effects partially compensate the effect of the modified equilibrium state – or, in the vocabulary of the author, *extrinsic surface effects* –, so that the non-adiabatic frequencies actually get closer to the standard adiabatic frequencies without equilibrium turbulent pressure than the adiabatic frequencies with the extrinsic effect. However, the extrinsic effect still largely dominates, so that this compensation is only limited. A similar result was found by Rosenthal et al. (1995), except that the compensation is much more important, and the frequency shift with both extrinsic and intrinsic effects is much smaller (with values not exceeding 5 μmHz, while Balmforth (1992b) predicted values close to 10 μmHz). Balmforth (1992b) was further able to separate the frequency shift ascribed to entropy perturbations from those attributed to turbulent stress perturbations, and showed that while the turbulent stress part is larger for low-frequency modes, neither dominates the other from $\sim$ 3 mHz onwards. Similar conclusions were reached for the hotter and more evolved star η Boo by Christensen-Dalsgaard et al. (1995), and later by Straka et al. (2006), although the equilibrium turbulent pressure and kinetic energy used to assess the structural surface effects were extracted from a solar model.

Other uses of time-dependent convection theories to describe the modal surface effects include the work of Grigahcène et al. (2012), who used the time-dependent mixing length formalism developed by Unno (1967), later refined by Gabriel (1996) and Grigahcène et al. (2005), and implemented in the `MAD` pulsation code Dupret (2001). The authors used this local, time-dependent convection model to compute non-adiabatic pulsation frequencies for the Sun as well as 3 other stars. They then compared them to adiabatic frequencies obtained in the same equilibrium state, and investigated whether or not the time-dependent treatment of convection gives better results than adiabatic frequencies corrected through empirical formulations of the surface effects (see Section 2.4.3). They concluded that this is indeed the case, but that the frequency differences still remain significantly larger than the

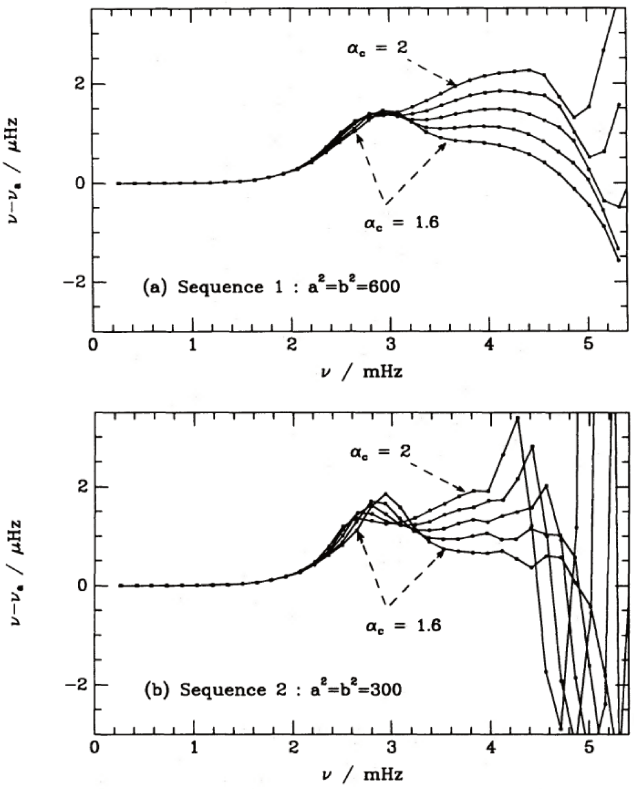

Figure 2.11: Frequency difference between theoretical predictions made with adiabatic calculations and the non-adiabatic, non-local calculations of Balmforth (1992a). Both panels show a strong dependence of the predicted surface effects with the mixing length parameter $\alpha_{\rm MLT}$ and the parameters of non-locality a, b and c. Credits: Balmforth (1992b).

observational uncertainties, so that the time-dependent, non-adiabatic treatment of convection must be refined. Let me remark, for the sake of completeness, that while their model is local, and therefore does not contain any free parameters for non-locality, it includes another free parameter β, related to the filtering of fast spatial oscillations in the non-adiabatic luminosity eigenfunctions (see the above section on extrinsic surface effects). Later on, Sonoi et al. (2017) used the same time-dependent treatment of convection to study solar surface effects, but this time in the adiabatic limit. As such, their study purposefully neglects the effect of the entropy perturbation in the modal surface effects, and focuses on the effect of the turbulent pressure perturbation. They compare the resulting frequency shift in a solar model to the corresponding frequency shift obtained through the GGM and RGM, and find that while the GGM does indeed give better results than the RGM (in accordance with the conclusions of Rosenthal et al. (1999)), the agreement with observations is much better with the time-dependent convection model than with either the GGM or RGM approximations. Furthermore, they find that a significant part of the modal surface effects could be ascribed to the perturbation of the turbulent pressure – a different conclusion compared to Balmforth (1992b), who found that the entropy perturbation plays a role of similar importance for high frequency modes –, and more particularly to the contribution of the density perturbation and advection effect thereon. The authors also treated the parameters of non-locality differently: instead of leaving them as free parameters, they used a 3D hydrodynamic simulation to calibrate their value (Dupret et al. 2006). In doing so, they found $a = 6.975$ and $b = 1.697$, which is also at odds with the much higher values adopted by Balmforth (1992b): in other words, Sonoi et al. (2017) found the convection to be much less local. The same path was also pursued by Houdek et al. (2017), but this time through the use of the same time-dependent treatment of convection as Balmforth (1992b) (based on the formalism developed by Gough (1977a)), and only for radial modes. The authors compared a) the purely adiabatic frequencies obtained in the standard MLT framework with b) the adiabatic frequencies of a patched model obtained in the RGM, c) the adiabatic frequencies obtained in a non-local MLT framework, still in the RGM, and d) the non-adiabatic frequencies obtained in the non-local, time-independent MLT framework of Balmforth (1992b). The authors concluded that the fourth model gives a better agreement with observed frequencies, with scaled differences not exceeding 3 μHz. One must remark, however, that the two components of the surface effects were not computed with the same equilibrium model, and furthermore, the agreement was found at the expense of having to adjust a number of free parameters – mixing-length parameter, anisotropy parameter for the equilibrium Reynolds stress tensor, parameters of non-locality, with the addition of a different non-local parameter for the convective flux and the turbulent pressure. What is more, the authors calibrated part of these free parameters on 3D simulations, while others were adjusted to give the best agreement possible between the observed and

predicted linewidths (see Section 2.3.3). The authors report that the agreement with observations is the result of a large compensation of the structural effects (which lower the frequencies) and the non-adiabatic modal effects (which increase them). While this is in accordance with the conclusions of Balmforth (1992b), it is directly at odds with the conclusions of Grigahcène et al. (2012) or Sonoi et al. (2017), where the effect of the turbulent pressure perturbation is dominant.

Final note on the theoretical modelling of surface effects

Even this brief and non-exhaustive review of the treatment of surface effects through theoretical modelling, whether it be structural or modal effects, allows me to make this general observation: that there is currently no real consensus, and that this is due to the uncertainty in the treatment of convection-oscillation coupling itself. The underlying assumptions are either too crude – as is illustrated by the GGM and RGM –, or, to the best of our current capabilities, impossible to constrain physically, and therefore too heavily parameterised. This prevents us from making real predictions when it comes to surface effects. As a result of this uncertainty, the conclusions drawn in different studies, through different treatments of convection, are at odds with each other, and when agreements are found, it is seldom for the same physical reasons, even for a star as well known as the Sun. For this reason, in most asteroseismic diagnosis where accurate frequencies are needed, two alternative approaches are adopted. First, it is possible to study not the observed frequencies individually, but combinations of these frequencies that happen to not be affected by the physics at the surface of the star. For instance, Roxburgh and Vorontsov (2003) proposed to use the ratio of the small to large separations, instead of both quantities separately. They showed that the ratio was much less impacted by the structure of the outer layers of the Sun, and therefore does not need surface effect correction to be used for seismic diagnosis purposes. Roxburgh (2005) later extended this conclusion to other solar-like stars (see also Otí Floranes et al. 2005). While this prevents us from having to treat surface effects, it presents the distinct disadvantage of reducing the amount of information at our disposal in the p-mode spectrum, and therefore decreases the precision of the ensuing seismic diagnosis. Secondly, the other alternative approach for the correction of surface effects is the use of purely empirical formulations, which I introduce now.

2.4.3 Empirical formulations

Let me denote as $\nu_{\rm obs}(n)$ the observed eigenfrequency associated to the radial p-mode of order n in a given star; and let me suppose that a best-fit stellar model[25] has been constructed for this star, whose radial eigenfrequencies I denote as $\nu_{\rm best}(n)$. Then to design an empirical formula for the surface effects is to answer this question: can one find a simple function $f(n, \Theta)$, where Θ is a limited set of free parameters, which closely fits the frequency difference $\nu_{\rm obs}(n) - \nu_{\rm best}(n)$ regardless of the star under consideration *for the same value of* Θ? If this last condition can be reached, then the situation would be ideal: the values of the free parameters could be constrained with observations of a very well known star – like the Sun for instance –, and could then be used to predict – and therefore correct – the surface effects in any other star, or at least any other star of the same type. Unfortunately, while several functions have been proposed by different studies, the free parameters associated to these functions are never even remotely universal. For instance, Kjeldsen et al. (2008) proposed a simple power law

$$f(n, (a, b, \nu_0)) = a \left(\frac{\nu_{\rm obs}(n)}{\nu_0} \right)^b , \tag{2.110}$$

with three free parameters in the form of a characteristic frequency ν_0, an exponent b and a prefactor a. This was proposed on the basis of an analysis conducted by Christensen-Dalsgaard and Gough (1980), who quantified, in the case of a polytropic atmospheric model, the frequency discrepancy entailed by neglecting the phase shift incurred by the waves whose frequency is similar to the acoustic cut-off frequency ν_{ac} of the star, and can therefore penetrate further into the upper layers before being reflected. In this simplified polytropic model, they found the discrepancy to be larger as frequency is increased (because higher-frequency modes are reflected higher in the atmosphere), and to take the form of a power law, with an exponent directly related to the average polytropic index considered in the atmospheric model. In the analysis conducted by Kjeldsen et al. (2008), the parameters a, b and ν_0 are supplemented by an additional parameter r used to modify the stellar model to yield a more accurate estimation of the mean density of the star, under the assumption that the structure of the star is homologous. The

[25] By that, I mean a standard model – in particular, where the convection is treated in the standard MLT – that most closely matches the global parameters of the star, such as its mass, radius and effective temperature.

parameters b and r are in fact degenerate, as the value of one constrains the value of the other. The authors first determined the best-fit parameter values for a, b, ν_0 and r for the Sun. Then they used the same procedure on other stars, where they fixed a value of ν_0 for each star, used the solar value of b to constrain r for each star, and finally left a as a free parameter. The authors found that the large separations $\Delta\nu$ – i.e. the mean star density – were accurately recovered after this surface effect correction for the sample of stellar models considered.

As I mentioned in Section 2.4.1, the surface effects become increasingly prominent as the frequency of the modes get closer to the acoustic cut-off frequency ν_{ac} of the star. Building on this observation, Christensen-Dalsgaard (2012) proposed that the surface effects be a self-similar function of frequency, with the frequency of reference being chosen as ν_{ac}. The author hypothesised the existence of a somewhat universal function $\mathcal{G}_\odot(x)$ such that

$$f\left(n, (\widetilde{a}, \mathcal{G}_\odot)\right) = \widetilde{a}\mathcal{G}_\odot\left(\frac{\nu_{\text{obs}}(n)}{\nu_{ac}}\right) . \tag{2.111}$$

The notation $\mathcal{G}_\odot$ stems from the fact that this function is calibrated on the Sun, and then assumed to be the same for all stars. The factor $\widetilde{a}$ still needs to be adjusted, in addition to the same homology factor r as in Kjeldsen et al. (2008). The agreement found with observation, once the frequencies are surface-effect-corrected, is better than with the simpler power law, which is understandable, as a functional form such as Equation 2.111 is much more flexible than the one given by Equation 2.110. On the other hand, the assumption that $\mathcal{G}$ is universal is more of a leap to take than the assumption that the exponent b is universal, because one is a function, and the other a simple scalar. An alternative empirical relation was proposed by Sonoi et al. (2015), to alleviate the fact that Equation 2.110 overestimates surface effects for high frequencies, in the form

$$f\left(n, (\alpha, \beta)\right) = \alpha\nu_{\text{max}}\left[1 - \frac{1}{1 + (\nu_{\text{best}}(n)/\nu_{\text{max}})^\beta}\right] , \tag{2.112}$$

where ν_{max} is the frequency of maximum spectral height in the p-mode spectrum of the star.

These empirical relations pertain to the raw frequency differences, which may seem incompatible with the observation I made in Section 2.4.1 that the modes with a high angular degree, having a much smaller mode mass, are associated with a much larger surface effect than radial modes of similar frequencies, and therefore scaled frequency differences should be considered instead. So long as only low angular degrees are considered (or even exclusively radial modes), this is not a problem. However, this ceases to be true for stars featuring mixed modes, in which case it is necessary to include mode inertia in the empirical relation. This was done by Ball and Gizon (2014), who proposed both a cubic law

$$f\left(n, l, (a_3, \nu_0)\right) = \frac{a_3}{\mathcal{I}_{n,l}}\left(\frac{\nu_{\text{obs}}(n,l)}{\nu_0}\right)^3 , \tag{2.113}$$

and a composite cubic and inverse law

$$f\left(n, l, (a_3, a_{-1}, \nu_0)\right) = \frac{a_3}{\mathcal{I}_{n,l}}\left(\frac{\nu_{\text{obs}}(n,l)}{\nu_0}\right)^3 + \frac{a_{-1}}{\mathcal{I}_{n,l}}\left(\frac{\nu_{\text{obs}}(n,l)}{\nu_0}\right)^{-1} , \tag{2.114}$$

where $\mathcal{I}_{n,l}$ is the inertia of the mode of radial order n and angular degree l, defined by Equation 2.97. The authors found that including the inertia of the modes in the empirical relation considerably improves the fit, and that the second formulation in particular gives better results than a simple power law.

All these empirical relations provide accurate frequency corrections, which can be used, for instance, for the correct determination of stellar parameters from the observed frequencies. They perform differently depending on the type of star considered, and more importantly yield global stellar parameters that can be degenerate (meaning that several equally probable solutions can be found). Another problem of these approach is that even if surface effects are indeed corrected, there is no way to relate the correction to physical arguments, which becomes problematic when extending the corrective formula to a vaster sample of stars. Indeed, it is impossible to assess how adequate the extrapolation of a given surface effect empirical formula is to stars for which it has not been tested, and in particular, to assess the degree of universality of the coefficients in said formula. Finally, in extrapolating these relations to other stars, it is implicitly assumed that the discrepancy between the observed and modelled frequencies remain solely attributed to surface effects. In reality, all sources of uncertainties from the modelling

point of view are corrected simultaneously, and the assumption that it only comes from surface effects leads to an 'overcorrection' of the frequencies, if other modelling inaccuracies are present in the analysis. As a result, there is absolutely no guarantee that the corrected frequencies can be safely compared with observations. Although these relations have subsequently been used in numerous asteroseismic analysis (Metcalfe et al. (2012); Mathur et al. (2012); Metcalfe et al. (2014) for the formulation of Kjeldsen et al. (2008); Bellinger et al. (2017); Ball and Gizon (2017); Compton et al. (2018); Di Mauro et al. (2018) for the composite formulation of Ball and Gizon (2014), perhaps the mostly widely used; Buldgen et al. (2019); Farnir et al. (2019) for the formulation of Sonoi et al. (2015)), there is to this day no consensus on which form should be adopted, and no way to assess the accuracy of the resulting correction.

On a final note, Gruberbauer et al. (2012) advocated for the use of Bayesian inference to treat the systematic frequency bias entailed by surface effects, with the idea that no *ad hoc* empirical relation is needed in this approach. The improved flexibility, and the fact that the frequencies do not need to be corrected beforehand, is certainly an improvement compared to the other approaches presented above. However, this kind of Bayesian approach is fundamentally based on the assumption that the asteroseismic grid used for the stellar parameter inference is only impacted by the uncertainty related to the surface effects. But since the results of such Bayesian analysis are model-dependent, there is, once again, no reason why additional model deficiencies could not arise elsewhere, and significantly bias the results. Furthermore, as noted by the authors, enough low-order modes, less impacted by surface effects, are needed to obtain less biased results.

3 Motivations and issues tackled by this thesis

Contents

3.1 A summary of the context

In this introductory discussion, I presented the current state-of-the-art regarding our theoretical knowledge of the main aspects of the coupling between solar-like oscillations and turbulent convection, namely mode driving (Section 2.2), mode damping (Section 2.3), and surface effects (Section 2.4). The amount of asteroseismic data provided by ground-based observations, and more recently space-borne missions (with the huge impact of CoRoT and *Kepler* in particular) has grown exponentially, and this led to a much better and more refined understanding of the processes underlying these aspects of mode physics. In solar-like oscillations, this is important for two mutually complementary reasons. First, the properties of the modes are tightly related to the physics of the turbulent convection close to the surface of the star, which means that the observed mode properties can serve as a way to constrain the behaviour of turbulent convection. This is of paramount importance, because, as I outlined in Chapter 1, the way convection is modelled in stellar evolutionary models heavily impacts the results. Secondly, asteroseismic indices, such as the frequency of maximum spectral height $\nu_{\max}$, the acoustic cut-off frequency $\nu_{\rm ac}$, the damping and excitation rates, and the velocity and bolometric amplitudes for instance, are subjected to scaling relations, meaning that they follow somewhat universal trends with the stellar parameters (radius, mass, effective temperature, surface gravity). As such, measuring the former can give an estimate for the latter, especially when large samples are used, in the scope of *ensemble asteroseismology*.

But all of these challenges require an accurate and realistic theoretical knowledge of the mechanisms at play concerning the interaction between turbulent convection and solar-like oscillations. While the stochastic driving of the modes by turbulence is, to this day, fairly well understood, this is not the case of surface effects or damping mechanisms, and this lack of understanding, which has been more and more clearly revealed by the wealth of seismic data on this age of ensemble asteroseismology, prevents us from using the full potential of asteroseismic measurements – whether it be frequencies for internal probing, or energetic aspects of solar-like modes for the use of realistic scaling relations. This lack of understanding is related to the absence of a satisfactory description of stellar turbulent convection, a point which I attempted to make clear in Section 1.2. The most widely used prescriptions are based on Mixing-Length Theory, which leaves to be desired on a certain number of points (Section 1.2.2), especially in that it overly simplifies the description of the turbulent cascade – a simplification that directly impacts predictions on turbulence–oscillation coupling, since the large range of sizes and life times of turbulent eddies close to the star surface has, as we saw, an important role to play. We also mentioned Reynolds-stress models as an alternative approach (Section 1.2.3); however, its use has remained limited in the present context, and the predictions stemming from it have not necessarily done well when confronted to observations (Section 2.3.3). Another very important avenue of research in this area is the use of 3D simulations to constrain turbulent convection prescriptions, or more directly mode properties (Section 1.2.1). Compared to other approaches, this has only become possible recently, with the ever increasing[1] computational capabilities of our computers. In particular, the possibility to use properly averaged 3D simulations to replace the outer layers of 1D models has considerably

[1] but for how long still?

improved the physics of the superficial layers in stellar evolutionary models and pulsation calculations. However, from the point of view of turbulence–oscillation coupling, there is only so much that we can learn from these simulations. This is primarily because of the artificial treatment of unresolved small scales, which is unavoidable with our current computational power, and has an important impact on the behaviour of the turbulent cascade. On another point, *3D simulations can only serve to constrain preestablished analytical prescriptions: they do not provide with the prescriptions themselves*. In particular, they are, more often than not, used to constrain the free parameters in such or such MLT formalism, thus circling back to the weaknesses of MLT itself. Lastly, these simulations remain, to this day, very heavy to run, so that they cannot be reasonably used in parametric studies designed to explore the physics of turbulence–oscillation coupling. In summary, our theoretical understanding of this coupling still leaves to be desired, and this shows in the large uncertainties surrounding our understanding of mode physics itself, and in particular the surface effects, as well as the damping mechanisms responsible for the stabilisation of solar-like oscillations.

3.2 Structure of this manuscript

It is in this very open context that I undertook the work that I present in the rest of this manuscript. It was done in two stages, seemingly independent from one another, but nevertheless related, and which are the subject of the two remaining parts of this work.

3.2.1 Part II: Solar-like p-mode asymmetries

The first part of my work has to do with an aspect of turbulence-oscillation coupling that I deliberately left behind until now: the asymmetry shown by the line profile of solar-like p-modes in the observed power spectrum. This asymmetry skews the line profile in such a way that they feature slightly more power on their left side than their right side in velocity observations, while it is reversed in intensity observations. In essence, this is tightly related to the stochastic excitation of the mode, just like the observed amplitude; unlike the observed amplitudes, however, the depth of the driving region is very important in explaining the observed asymmetries. Historically, observed asymmetries have been used to infer to position of the excitation region inside the star, with mitigated success, primarily because of the lack of realism of the prescriptions that were used. I summarise these efforts in much more details in Chapter 4. My motivation, by contrast, consisted in using a more realistic excitation model, coupled with a 3D hydrodynamic simulation of the superficial layers of the star, to constrain the prescription of the turbulent velocity spectrum – with the same philosophy as Samadi and Goupil (2001). I present this model, and apply it to the observed solar asymmetries in velocity data, in Chapter 5. I also present how I adapted this model to intensity measurements, thus shedding light on the physical origin of the asymmetry reversal between the two observables, in Chapter 6. Chapters 5 and 6 are the subject of two articles that were published in Astronomy and Astrophysics (Philidet et al. 2020a,b).

Even though many details still need some consideration, the question of mode driving, and the subsequent asymmetry it entails in solar-like p-mode line profiles, is quite satisfactorily understood. However, the other aspects of turbulence-oscillation coupling that constitute mode damping and surface effects are, as I showed in Sections 2.3 and 2.4, much more sensitive to the specific properties of the coupling. Further theoretical investigation was therefore needed on this subject, which led me to the second part of my PhD.

3.2.2 Part III: A combined stochastic Lagrangian/SPH approach to turbulence–oscillation coupling

In the second part, I will interest myself with a new approach designed to theoretically describe the turbulent convection in the presence of oscillations, with the short-term goal of describing the impact of the former on the latter 1) without having to rely on the hypotheses inherent to MLT prescriptions or Reynolds-stress models, i.e. the mixing-length hypothesis and the reduction of the entire range of timescales relevant in the turbulent cascade to a unique typical turbulence timescale, and 2) in a way that allows to relate the underlying properties of turbulence to the observed properties of the modes, in a direct and physical manner. To that effect, I investigate turbulence models based on the evolution of the joint-Probability Density Function (or PDF) associated to the turbulent quantities, and more particularly, I investigate the possibility of modelling this evolution by representing turbulence as a large set of individual fluid particles, evolving according to stochastic differential equations (or SDE) – a class of

models referred to as *Lagrangian stochastic models*. I will first introduce the subject of stochastic processes and SDE – a necessary mathematical tool in these models –, as well as PDF methods, and in particular Lagrangian stochastic models and their use in the context of turbulent flow modelling, in Chapter 7. The motivation, in Part III, is to propose an alternative to both MLT formalisms, Reynolds-stress formalisms, and the use of 3D LES for our description of the aspects of turbulence-oscillation coupling that we presented in this chapter. In practice, I followed two different avenues, one analytical, one numerical, which, while distinct in their implementation, are nevertheless related to each other, and benefit from being developed alongside one another

- in Chapter 8, I will present how a Lagrangian stochastic model can be handled analytically to yield a wave equation that is stochastic in nature, and consistently encompasses the full effect of turbulent convection. I will then show how this stochastic wave equation can serve as a baseline framework where surface effects, damping mechanisms and driving mechanisms alike can be studied, from an analytical point of view. This formalism offers a way to physically construct analytical prescriptions for the relation between turbulence properties and observed mode properties. Furthermore, it can be used to help disentangle the various physical contributions to turbulence-oscillation coupling, and therefore shed light into the results obtained numerically;

- in Chapter 9, I will present a direct, numerical implementation of the Lagrangian stochastic model itself, in a simplified 1D framework. More particularly, I will show how normal modes of oscillations can be extracted from the resulting simulation, and their coupling with turbulence studied efficiently. This numerical approach may become preferable over the analytical approach for more complex Lagrangian stochastic models, and can also serve as a more efficient way to quantify the prescription offered by the analytical formalism presented in Chapter 8.

The work presented in Chapter 8 is the subject of an article that was published in Astronomy and Astrophysics (Philidet et al. 2021), as well as another article in preparation. By contrast, the work presented in Chapter 9 is only in its first stages, and the only results I detail in this chapter are preliminary results, aiming at validating the numerical approach.

Part II

Asymmetries of solar-like oscillations

4 Mode asymmetry: history and context

Contents

> - Permettez-moi de vous dire que ce soir, je ne suis pas le Premier ministre, et vous n'êtes pas le président de la République, nous sommes deux candidats à égalité [...], vous me permettrez donc de vous appeler monsieur Mitterrand.
> - Mais vous avez tout à fait raison, monsieur le Premier ministre.
>
> François Mitterrand à Jacques Chirac

I had the opportunity, in Sections 2.2 to 2.4, to show that stochastically excited and damped oscillations, such as solar-like oscillations, are characterised, in their observed power spectrum, by a Lorentzian line profile. However, as the resolution reached in helioseismic measurements (both ground-based and space-borne) have increased, it has become apparent that, just as French politics, the observed line profiles are actually skewed and asymmetric, in such a way that one side of the line profile has more power than the other. This was first measured in the solar spectrum, but later confirmed in other stars as well. More precisely, the line profiles in the velocity power spectrum have more power on their left side than right side, while the opposite occurs in the intensity power spectrum. This last result, in particular, was particularly puzzling at the time, as one would assume the two power spectra to be simply proportional to one another: it was quickly dubbed the *asymmetry reversal puzzle*.

This phenomenon was quickly ascribed to several physical mechanisms. First, it was recognised that the asymmetries had to do with the *p*-mode excitation process, and more particularly to the localisation of the source of excitation in a narrow layer just beneath the surface of the star. This constitutes the dominant mechanism at play for mode asymmetry, but alternative processes were proposed to explain the asymmetry reversal puzzle: non-adiabatic effects, correlation of the mode with incoherent convective noise, or opacity effects for instance.

The subject of *p*-mode asymmetries has been studied through the prism of mainly two different questions. The first question concerns exclusively the asymmetries in velocity data. Since they are caused by the localisation of the excitation source, it was not long after their discovery before several authors attempted to constrain the position of the source using observed asymmetries, in the hope of bringing a better understanding of driving mechanisms. The second question concerns the asymmetry reversal puzzle, and is twofold: what is the underlying mechanism at play? and what does observed asymmetry reversal tell us about the physics of the mode? This introduction is therefore structured in two parts. I first give an account of the observational aspects of solar-like *p*-mode asymmetry; after which, in a second part, I present the efforts already made to bring answers to the set of questions raised above, and why there is still much to be done. As I will show, while considerable progress has been made, these questions still remain very open.

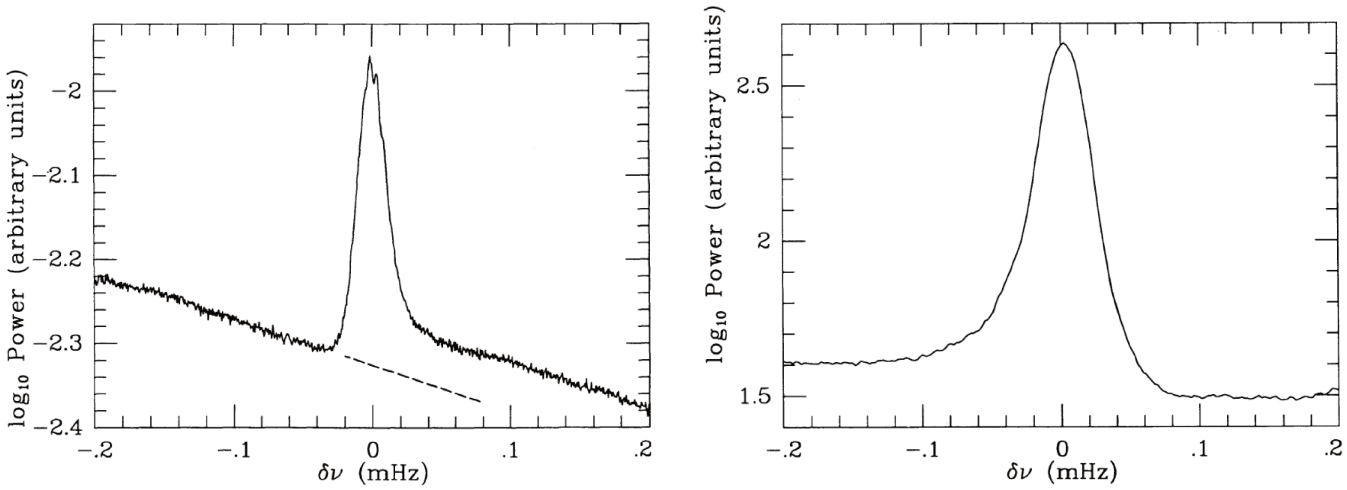

Figure 4.1: **Left**: Solar intensity power spectrum of the $n = 2$ modes, averaged over values of the angular degree $l = 157 - 221$ and over all values of m, as inferred from observational data taken from the ground at the South Pole. The eigenfrequency dependence for different values of l and m was removed before averaging. The dashed line represent a linear extrapolation of the low-frequency background slope. The line profile is distinctly skewed. **Right**: Same as left panel, but with the velocity data of GONG. The asymmetry is clearly reversed compared to the intensity measurements shown in the left panel. Credits: Duvall et al. (1993).

4.1 Observation of solar-like p-mode asymmetries

Asymmetries of solar p-modes were first reported by Duvall et al. (1993), using ground-based observations made at the geographical South Pole during a period of 16 days. Those consisted in full-disk observations of the Sun, onto which a narrow pass band filter centered on the Ca II K absorption spectral line was applied, thus isolating the minimum temperature region of the Sun. This allowed them to measure the solar intensity power spectrum. In parallel, they used spectroscopic data from the Global Oscillations Network Group (GONG) to obtain, in a similar fashion, the velocity power spectrum. They investigated the asymmetries in both observables, although their focus was on the intensity data. The authors resolved p-modes of angular degrees between $l = 0$ and $l = 250$, and with frequencies ranging from ~ 2 mHz to ~ 4.5 mHz. Averaging each (n, l) multiplet over all values of the azimuthal order m, they found the line profiles to be distinctly skewed, with asymmetries barely depending on l at all. This l-independence allowed them to further average the line profiles over all measured l for any given radial order n (recentering the frequencies beforehand) to obtain a clearer picture of the asymmetries. This is illustrated for the modes of radial order $n = 2$ in the left panel of Figure 4.1 for instance, which shows quite clearly an offset of the sloped background between the two sides of the line profile, with the high-frequency end of the line being elevated with respect to the low-frequency end. On the other hand, the authors conducted a similar investigation on the velocity power spectrum. The results are shown, also for the modes of radial order $n = 2$, in the right panel of Figure 4.1, which shows two main differences compared to the left panel: first, the background is no longer sloped; secondly, it is now the low-frequency side of the spectrum that is elevated with respect to the high-frequency side. The asymmetry difference is, of course, more general than just the $n = 2$ modes. For instance, Figure 4.2 shows the asymmetric line profiles featured in both observables (velocity for the top panel, intensity for the bottom panel) for $l = 200$ modes of various radial orders $n = 1 - 21$. The asymmetry reversal between the two observables is clearly general, throughout the entire p-mode spectrum.

In order to measure mode asymmetry more consistently, Duvall et al. (1993) proposed an asymmetric form of the line profiles that they could then use to fit the observations. They used an analogy with a Fabry-Pérot interferometer with a light source outside the resonant cavity: then the total observed wave is the result of the interference between 1) the direct wave, 2) the wave that reflects on the upper turning point of the cavity, without ever entering it, and 3) the multiple echoes of the wave trapped inside the cavity. The situation is illustrated in Figure 4.3.

Duvall et al. (1993) obtained the following formula

$$P(\theta) = P_0 \frac{1 + R^2 + D^2 - 2R\cos 2\theta + 2D\cos 2(\theta + \delta\theta) - 2RD\cos\delta\theta}{1 + R^2 - 2R\cos 2\theta}, \tag{4.1}$$

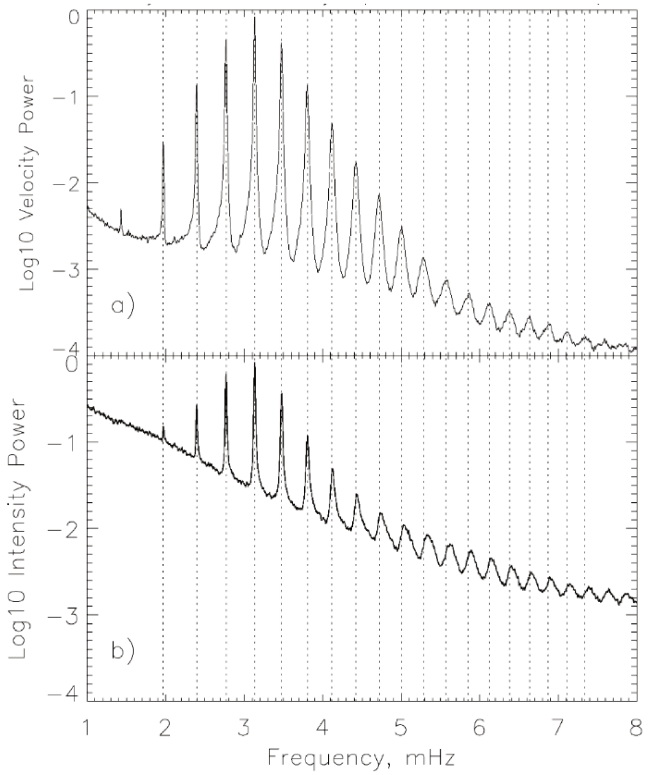

Figure 4.2: $l = 200$ solar power spectrum, measured with the Michelson Doppler Imager (MDI) in velocity (**top**) and intensity (**bottom**), during the same 3-day period. The vertical dashed lines correspond to the local maxima in the velocity power spectrum. Credits: Nigam et al. (1998).

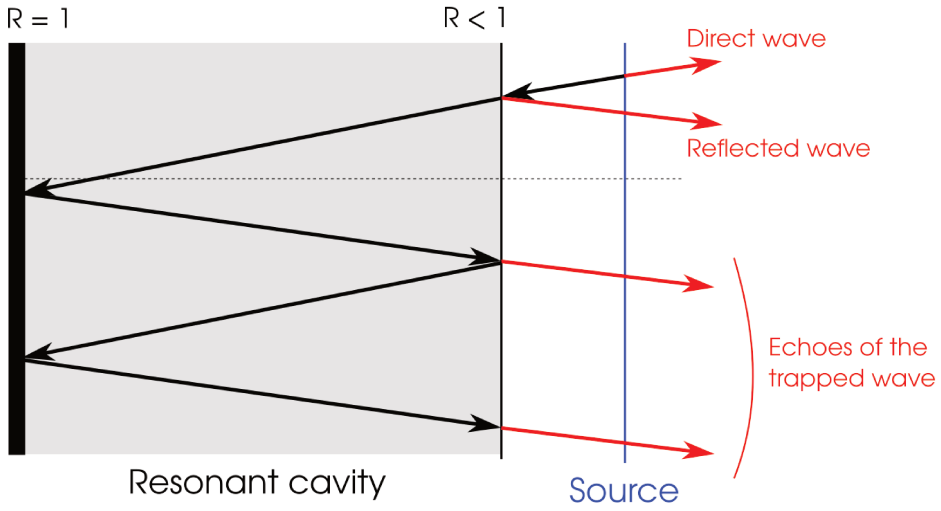

Figure 4.3: Illustrative picture of the analogy between the solar-like p-modes and light waves in a Fabry-Pérot interferometer. The source of the waves (represented in blue) is located outside the resonant cavity (represented in grey), characterised by a perfect reflection boundary (black rectangle) on one side, and a slightly transmitting boundary (black vertical line) on the other. The total observed wave – where the observer is located on the right side of the picture – is the superposition of all components represented in red: a direct wave going directly towards the observer; a wave that travels the other way but reflects on the boundary of the cavity without entering it, and travels the other way towards the observer; and finally, the multiple echoes of the part of the wave that did enter the cavity, and lets a small portion of its energy leak out of the cavity upon each reflection.

where R is the reflection coefficient in amplitude associated to the upper turning point; D is the amplitude reduction factor undergone by the wave after it has traveled in the evanescent region between the source outside the cavity to the cavity itself; the frequency variable is recast in the form of the phase shift θ of the wave after a trip back and forth in the cavity

$$\theta \equiv \int_{r_1(\nu)}^{r_2(\nu)} \mathrm{d}r \, k_r(\nu) \, , \tag{4.2}$$

where r_1, r_2 and k_r are the lower turning point, upper turning point and radial wave vector, all dependent on ν (see Section 2.1.2), and $\delta\theta$ is an additional phase shift incurred by the waves upon each reflection. *This latter quantity is a measure of the asymmetry of the modes*. Indeed, the resonant modes correspond to values of θ that are multiples of π, and in the neighbourhood of such a resonant mode, one has approximately

$$\theta = \frac{\pi(\nu - \nu_0)}{\Delta\nu} + n\pi \, , \tag{4.3}$$

where ν_0 is the eigenfrequency of the mode, and $\Delta\nu$ is the difference between the eigenfrequencies of two consecutive resonant modes. Plugging this into Equation 4.1, and Taylor-developing the cosines around $\delta\theta = 0$ and $\theta = n\pi$, one finds

$$P(\theta) \sim P_0 \frac{(1 - R + D)^2 + Rx^2 - D(x - 2\delta\theta)^2 + RD\delta\theta^2}{(1 - R)^2 + Rx^2} \, , \tag{4.4}$$

with

$$x = \frac{2\pi(\nu - \nu_0)}{\Delta\nu} \, . \tag{4.5}$$

As such, it is immediately seen that the line profile $P(\nu)$ is symmetric if and only if $\delta\theta = 0$. In fact, the line profile then takes the form of a combination between a flat background and a peaked Lorentzian profile, centered around $x = 0$ (i.e. $\nu = \nu_0$), and whose linewidth is given by

$$\Gamma = \frac{\Delta\nu(1 - R)}{\pi\sqrt{R}} \, . \tag{4.6}$$

As a result, the better the reflection, the narrower the resonant peak. This is not surprising, given the analogy with a Fabry-Perot interferometer whence this analysis stems. If, on the other hand, $\delta\theta \neq 0$, the line profile features asymmetry: *the parameter $\delta\theta$ therefore constitutes an asymmetry parameter for the line profile*. The authors fitted the observed line profiles with Equation 4.1, the free parameters of the fit being R, D, ν_0, $\delta\theta$ and P_0. This allowed the authors to extract values of $\delta\theta$ for each mode, among other things. The results are shown in Figure 4.4, where each point represents one mode. This plot has several interesting features. First, the asymmetry parameter $\delta\theta$ seems to only be weakly dependent on l, and all dots seem to collapse to a unique, slowly varying function of frequency only. This is very similar to the behaviour of surface effects (see Section 2.4.1), and suggests that the asymmetries are yet another marker of the physics of the superficial layers of the star. Secondly, the authors found that $\delta\theta$ takes non-zero, positive values for low-frequency modes, but vanishes around $\nu_{\max} \sim 3$ mHz. Concerning frequencies higher than ~ 3 mHz, the authors argued that the formula given by Equation 4.1 is no longer valid, because then the upper turning point becomes higher than the driving source, meaning that the latter ends up inside the cavity instead of outside.

Nigam and Kosovichev (1998) proposed an alternative fitting formula for asymmetric line profiles, based on a polynomial expansion of the profile obtained for an oscillating mode in a non-stratified equilibrium background, and excited by a point-like driving source (i.e. characterised by a Dirac spatial distribution). They found

$$P(x) = A\frac{(1 + Bx)^2 + B^2}{1 + x^2} + B_l \, , \tag{4.7}$$

where

$$x = \frac{2(\nu - \nu_0)}{\gamma} \, . \tag{4.8}$$

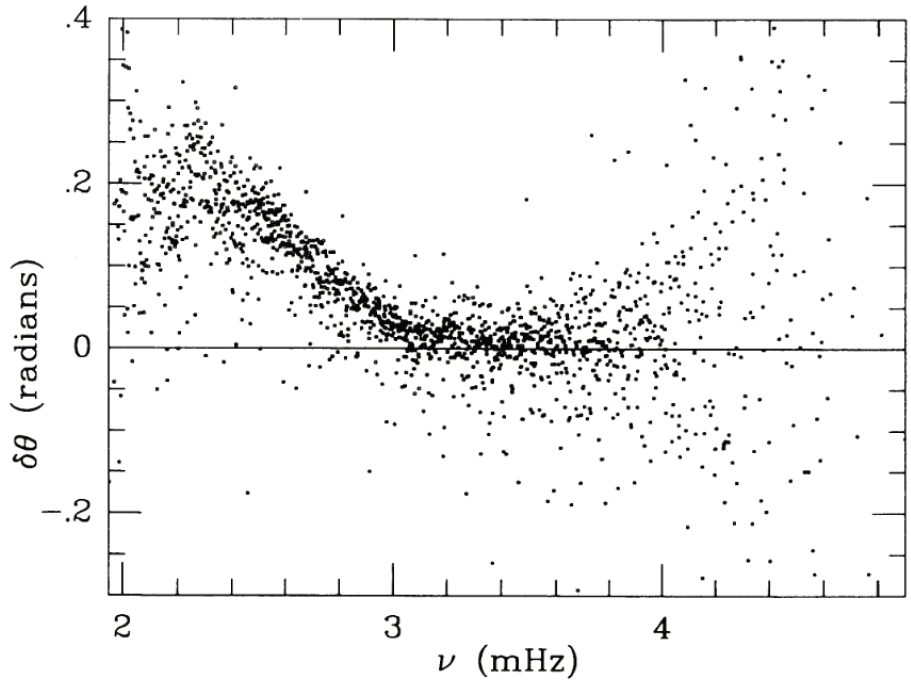

Figure 4.4: Value of the asymmetry parameter $\delta\theta$ for individual modes, obtained by fitting individual line profiles in the observed intensity power spectrum of the Sun with Equation 4.1, as a function of mode frequency. Each dot represents one mode. Credits: Duvall et al. (1993).

Fitting observed line profiles to this formula requires the adjustment of 5 free parameters, in the form of A, ν_0, γ, B_l and B. The first four are the height of the mode, its eigenfrequency, its linewidth and its background. If $B = 0$, one obtains a Lorentzian line profile, perfectly symmetric. A non-zero value of this fifth, non-dimensional parameter, on the other hand, leads to an asymmetric line profile. If $B > 0$, the power is higher on the high-frequency side of the mode than the low-frequency side, and vice-versa if $B < 0$. The former case corresponds to a mode having *positive asymmetry*, and the latter to a mode having *negative asymmetry*. The authors fitted solar p-mode line profiles observed with the Michelson Doppler Interferometer (MDI), aboard the Solar and Heliospheric Observatory (SoHO) spacecraft, both in velocity and intensity. They showed that Equation 4.7 provides with a good fit to the data in both observables, and applied the fit to modes of radial order $n = 3$ to 8, for angular degree $l = 75$. Even though the asymmetry is quantified by the parameter B instead of $\delta\theta$, they still found the same qualitative behaviour of solar p-mode asymmetry as Duvall et al. (1993), with asymmetries being positive in intensity, negative in velocity, and both vanishing for frequencies higher than ~ 3 mHz.

Fits to observed solar p-mode line profiles were subsequently performed by several authors, using more and more precise and resolved data as time went by, thus leading to more and more accurate inference of the mode asymmetry across the solar p-mode spectrum (e.g. Toutain et al. 1998; Korzennik 1998; Rosenthal 1998; Chaplin et al. 1999; Thiery et al. 2000; Basu and Antia 2000; Gelly et al. 2002; Oliviero et al. 2002; Korzennik 2005; Vorontsov and Jefferies 2013; Howe et al. 2013; Korzennik et al. 2013). Equation 4.7 found the most use in asymmetric line profile fitting to solar data, although several alternative forms were also used, among which Korzennik (1998, 2005); Korzennik et al. (2013)

$$P_{n,l,m}(\nu) = \frac{1 + \alpha_{n,l}\left(x_{n,l,m} - \dfrac{\alpha_{n,l}}{2}\right)}{x^2_{n,l,m} + 1}\,, \qquad (4.9)$$

$$x_{n,l,m} = \frac{\nu - \nu_{n,l,m}}{\Gamma_{n,l}/2}\,,$$

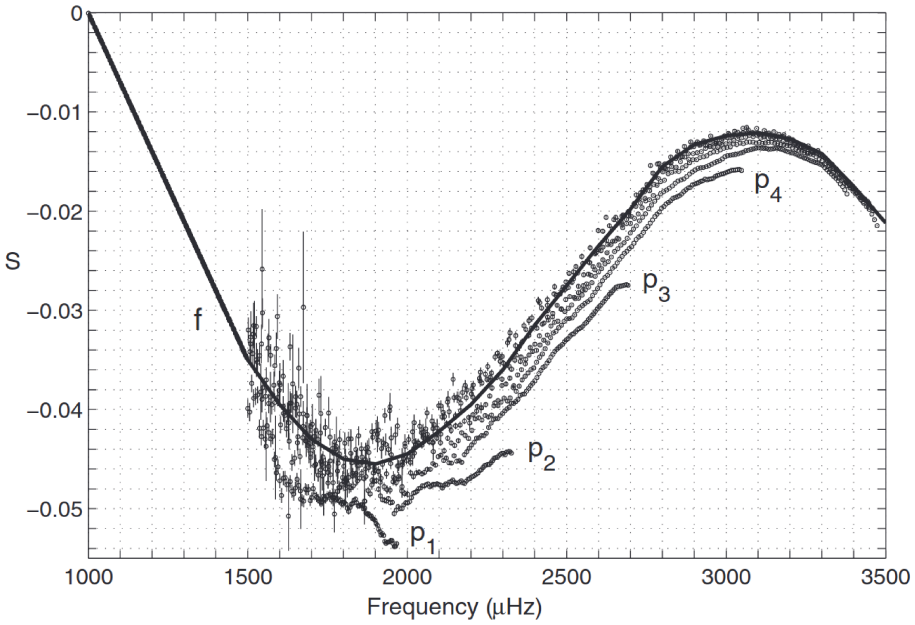

Figure 4.5: Asymmetry parameter S obtained by fitting individual line profiles in the solar velocity power spectrum measured by MDI with Equation 4.11. Each dot represents one mode, and the uncertainty stemming from the fit is shown. The solid line shows an approximation of the data with a function of frequency only, except below $\sim$ 1.5 mHz, where it is a simple linear extrapolation. The dots are arranged along different lines marked p_i, where i refers to the radial order of the p-modes. Credits: Vorontsov and Jefferies (2013).

where the asymmetry parameter is $\alpha_{n,l}$; Rosenthal (1998)

$$P(x) = \alpha_2 + \alpha_3 \times \left(\sin^2 x \cosh^2 \alpha_1 + \cos^2 x \sinh^2 \alpha_1\right)^{-1} \times \left([(\alpha_4 \cos x - \sin x) \sinh \alpha_1 - \alpha_5 \sin x \sinh \alpha_1]^2 + [(\alpha_4 \sin x + \cos x) \sinh \alpha_1 + \alpha_5 \cos x \cosh \alpha_1]^2 \right) , \tag{4.10}$$

$$x = \frac{\pi(\nu - \nu_0)}{\delta} ,$$

where the asymmetry parameter is α_4; or Vorontsov and Jefferies (2013)

$$P(\phi) = P_0 \left(\left[\frac{A \cos(\phi - S)}{1 - R^2} \right]^2 + B^2 \right) , \tag{4.11}$$

$$\tan \phi = \frac{1 + R}{1 - R} \tan \theta ,$$

where θ and R are the same quantities as in Duvall et al. (1993), and the asymmetry parameter is S. The asymmetry parameters $\delta\theta$, B, α, α_4 and S are all perfectly equivalent to one another, in particular if the asymmetry is small (which is the case for the Sun). In this limit, these various asymmetric line profiles all perform equivalently, so that there is no reason to choose one over the other. For instance, in the small asymmetry limit, one has $S \sim B \sim \alpha/2$ (Vorontsov and Jefferies 2013). We now have very good measurements of solar p-mode asymmetries in both observables, which support the early conclusions of Duvall et al. (1993). For instance, Figure 4.5 shows the asymmetry parameter S defined by Equation 4.11 as a function of mode frequency, for low-frequency solar p-modes in the velocity power spectrum (below $\sim \nu_{\max}$). The figure shows that the asymmetry remains negative over this entire range of frequencies. It also shows that, in terms of absolute values, the asymmetry reaches a minimum at $\sim \nu_{\max}$, after which it increases again for higher frequencies.

Asymmetry measurements performed at different moments in the solar activity cycle revealed that the asymmetry parameter varies between the quiet phases and active phases (Jiménez-Reyes et al. 2007; Howe et al. 2015). This is primarily due to the fact that the asymmetry parameters defined above, like the parameter B for instance,

scales with the linewidth of the mode, which itself vary with the solar activity cycle. To avoid the linewidth-dependence of the asymmetry parameter, Gizon (2006) proposed to recast it as

$$\chi = \frac{2B\nu_0}{\Gamma} \,. \tag{4.12}$$

This definition also has the advantage of relating the asymmetry directly to the relative position of the peaks (local maxima) and valleys (local minima) in the power spectrum. Indeed, if ν_1 is the frequency of the nearest valley and ν_2 the frequency of the nearest peak, then one has $\chi = \nu_2/(\nu_2 - \nu_1)$: the closer the consecutive peak and valley are to each other, the more pronounced the asymmetry. Because the linewidths of the solar-like p-modes depend so much on frequency (see Section 2.3.1), it is perhaps more relevant to measure mode asymmetry with the parameter χ rather than with B.

An alternative fitting model for asymmetric line profiles was used by Severino et al. (2001) on the $n = 10$, $l = 17$ solar p-mode, and later extended to a larger frequency range in the solar p-mode spectrum by Barban et al. (2004). Their model is based on the assumption that the asymmetries are caused by the presence of convective noise partially correlated to the coherent, resonant modes (see Section 4.2.2 for more details on the matter). Although the model can be used regardless of the actual physical origin of p-mode asymmetry, the interpretation of the best-fit parameter values as representing the properties of the correlated convective noise is of course contingent on the validity of this assumption. The novelty of their approach is to fit simultaneously the p-mode spectra in both observables – velocity and intensity –, in addition to the amplitude and phase of the coherent velocity-intensity cross-spectrum. Each observable is decomposed into a p-mode component ($V_p(\nu)$ and $I_p(\nu)$), a coherent, correlated background component (V_{cc} and I_{cc}), a coherent uncorrelated background component (V_{cu} and I_{cu}), and an incoherent, uncorrelated background component (V_n and I_n). The p-mode component is assumed to be the only one that depends on frequency over a given line profile frequency range: if the mode under consideration is thin enough in the power spectrum, the behaviour of all background components can indeed be considered frequency-independent. Each component is written thus

$$\begin{aligned}
&V_p(\nu) = \left|V_p(\nu)\right| \exp^{j\Phi_{V_p}(\nu)} \,, && I_p(\nu) = \left|I_p(\nu)\right| \exp^{j\Phi_{I_p}(\nu)} \,, && V_{cc} = |V_{cc}| \exp^{j\Phi_{V_{cc}}} \,, \\
&I_{cc} = |I_{cc}| \exp^{j\Phi_{I_{cc}}} \,, && V_{cu} = |V_{cu}| \exp^{j\Phi_{V_{cu}}} \,, && I_{cu} = |I_{cu}| \exp^{j\Phi_{I_{cu}}} \,, \\
&V_n = |V_n| \,, && I_n = |I_n| \,,
\end{aligned} \tag{4.13}$$

where V_n and I_n only impact the observed spectra through their modulus square, so that their phase is irrelevant to the model. The p-mode components are assumed Lorentzian, and are characterised by an amplitude, a phase, a central frequency and a linewidth. Naturally, phases are only defined in terms of phase differences, and the time origin can be set such that

$$\left|V_p(\nu)\right|^2 = \frac{\left|V_p(\nu - \nu_0)\right|^2 \eta^2}{(\nu - \nu_0)^2 + \eta^2} \,, \tag{4.14}$$

$$\left|I_p(\nu)\right|^2 = \frac{\left|I_p(\nu - \nu_0)\right|^2 \eta^2}{(\nu - \nu_0)^2 + \eta^2} \,, \tag{4.15}$$

$$\Phi_{V_p}(\nu) = -\arctan\left(\frac{\eta}{\nu - \nu_0}\right) \,, \tag{4.16}$$

$$\Phi_{I_p}(\nu) = -\arctan\left(\frac{\eta}{\nu - \nu_0}\right) + \Phi_{I_p - V_p} \,. \tag{4.17}$$

Then the four observed spectra (velocity power spectrum, intensity power spectrum, coherence I-V cross-spectrum and phase of the I-V cross-spectrum respectively) are fitted with the following formulae

$$P_V(\nu) = \left|V_p(\nu) + V_{cc}\right|^2 + |V_{cu}|^2 + |V_n|^2 \,, \tag{4.18}$$

$$P_I(\nu) = \left|I_p(\nu) + I_{cc}\right|^2 + |I_{cu}|^2 + |I_n|^2 \,, \tag{4.19}$$

$$\mathrm{COH}(\nu) = \frac{\left(I_p(\nu) + I_{cc}\right)\left(V_p(\nu) + V_{cc}\right)^\star + I_{cu}V_{cu}^\star}{\sqrt{P_I(\nu)P_V(\nu)}} \,, \tag{4.20}$$

$$\Phi_{I-V}(\nu) = \mathrm{Arg}\left[\left(I_p(\nu) + I_{cc}\right)\left(V_p(\nu) + V_{cc}\right)^\star + I_{cu}V_{cu}^\star\right] \,, \tag{4.21}$$

where * denotes a complex conjugate. The fit has 14 different parameters for each mode, in the form of 8 amplitudes ($V_p(\nu = \nu_0)$, $I_p(\nu = \nu_0)$, $|V_{cc}|$, $|I_{cc}|$, $|V_{cu}|$, $|I_{cu}|$, $|V_n|$ and $|I_n|$), 4 phase differences ($\Phi_{I_p - V_p}$, $\Phi_{V_{cc}}$, $\Phi_{I_{cc}-V_{cc}}$ and $\Phi_{I_{cu}-V_{cu}}$), the central frequency ν_0 and the linewidth η. The authors showed, in particular, that the resulting fit is more robust when all four spectra are fitted simultaneously than when each observable is treated separately.

It was noted as early as Duvall et al. (1993) that neglecting asymmetry in the fit leads to a systematic error in the measurement of mode frequency. The authors remarked that using a fitting formula with and without asymmetry yields a frequency difference $\Delta\nu \sim 1.7\,\delta\theta$, where $\delta\theta$ is their asymmetry parameter. Similar scalings were found for the Sun by Abrams and Kumar (1996) or Chaplin et al. (1999) for instance – provided the frequency differences are normalised by the linewidth of the modes –, as well as for other solar-like oscillators by Benomar et al. (2018). Frequencies obtained with a symmetric fit are systematically found to be higher than those obtained with an asymmetric fit if $B > 0$, and vice-versa if $B < 0$. This is fairly easily understood: a symmetric fit will compensate the impossibility of giving more power to the wing that deserves it by shifting the central frequency towards it. It can also be understood in terms of the maximum of the line profile. Indeed, taking Equation 4.7 for instance, one easily finds that, to leading order in B, the maximum is reached for $x \sim B$, i.e for $\nu = \nu_0 + B\Gamma/2$. Assuming that the symmetric fit places the central frequency at the maximum of the line profile, while the asymmetric fit places it correctly at ν_0, then the frequency difference normalised by the linewidth becomes

$$\frac{\nu_0^{B=0} - \nu_0^{B\neq 0}}{\Gamma} \sim \frac{B}{2}\,. \tag{4.22}$$

For the Sun, where $B \sim 0.05$ and the linewidth reaches $\sim 10\,\mu$Hz for the highest frequencies (see Section 2.3.1), the frequency bias can reach values as high as $\sim 0.5\,\mu$Hz. While this is negligible compared with the frequency bias entailed by surface effects (see Section 2.4), it remains largely superior to the spectral resolution attained in solar observations, and more importantly to the statistical error stemming from the fitting procedure that yields the inferred value of the mode frequencies, so that it is important to account for the asymmetry of the p-mode line profiles for an accurate determination of mode frequency, especially for higher frequency modes, characterised by a larger linewidth. However, as noted by Roxburgh and Vorontsov (2003), frequency differences are less affected by this bias than absolute frequencies, especially close to the damping plateau, so that seismic indices such as the large or small separation are likely to constitute less biased diagnosis tools than indices based on absolute frequencies. Accounting for mode asymmetry is also important so as not to mix observational and theoretical biases together: as it stands, the surface effect correction applied on frequencies obtained by symmetric fitting formulae actually correct for both surface effects and the effect of asymmetry at the same time, meaning that any conclusion drawn on surface effects is biased.

For a long time, asymmetry measurements were limited to the solar spectrum. The reason is that the spectrum needs to be very well resolved in order for p-mode asymmetries to be accurately inferred. This only became possible for other solar-like oscillators with *Kepler* data, once the observation duration was sufficient. Recently, asymmetries were inferred by Benomar et al. (2018) from the intensity power spectrum of 43 stars from the *Kepler* LEGACY sample (whose signal-to-noise ratio is highest). They used Equation 4.7 to fit the observed line profiles, and quantified the asymmetry parameter with χ (see Equation 4.12). Even though their targets were chosen to have the highest possible signal-to-noise ratio, it was necessary, in order to improve the robustness of the fit, to assume a unique asymmetry parameter over the entire measured frequency range for any given star. As I showed for solar measurements, this assumption is an oversimplification; nevertheless, the authors tested the consistency of this assumption by comparing the solar asymmetries measured in the different photometric channels (red, green and blue) of the SPM/Virgo instrument aboard the SoHO spacecraft. They found that the best-fit value of χ is similar in all channels for high-frequency and high-signal-to-noise ratio modes, but that it is no longer the case for lower frequency modes, whose signal-to-noise ratio is much smaller. The authors chose to consider an average of χ over all three channels, banking on the fact that the strong assumption that a unique value of χ exists for all modes under consideration in a given star is sufficient to compare the asymmetries across the HR diagram. Their results are shown in Figure 4.6. Shown in the figure is the asymmetry χ as a function of the stellar parameters $T_{\rm eff}$ (effective temperature) in the right panel, and g (surface gravity) in the left panel, where each point represents one star. The figure shows a clear trend, with intensity asymmetries being negative for hotter and more massive stars and positive for colder and less massive stars. They place the limit at $T_{\rm eff} \sim 5700$ K, and $\log(g) \sim 4.4$, which is incidentally not too far from the solar parameters. The authors also investigated, as it had been done for the Sun, the effect on the frequency determination of not accounting for mode asymmetry. They found that, because of

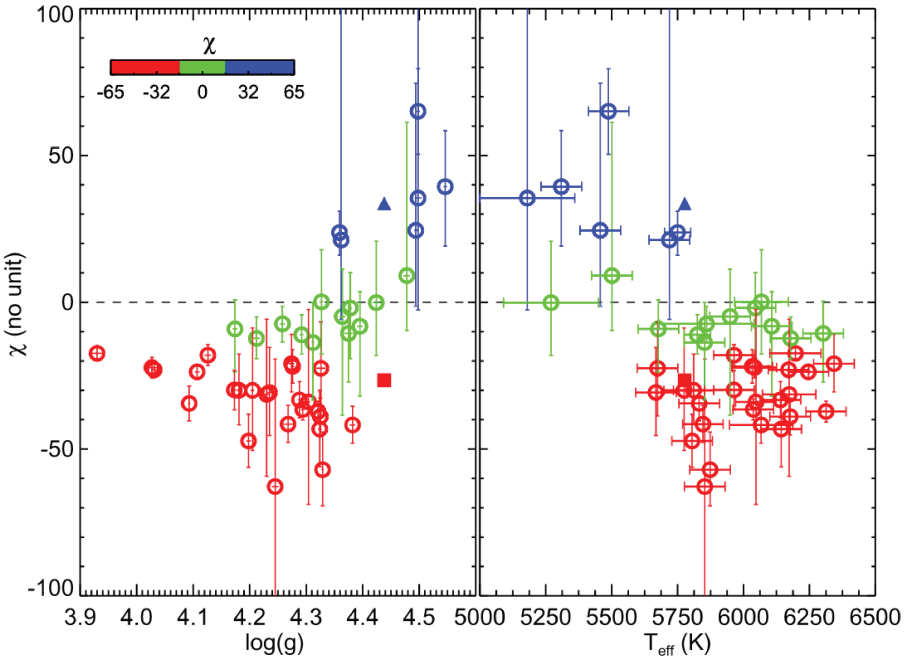

Figure 4.6: Asymmetry parameter χ inferred from Kepler observations for a set of main-sequence solar-like oscillators, as a function of surface gravity (**left**) and effective temperature (**right**). The parameter χ was obtained by fitting all observed modes with Equation 4.10, where B and χ are related to each other through Equation 4.12. χ was assumed to be unique for any given star. Each dot represents one star, error bars stemming from the fit to the data are shown. The Sun is represented, for comparison, by the filled square (for velocity asymmetry) and the filled triangle (for intensity asymmetry). The sample is divided into three categories, depending on the value of χ: red for negative asymmetry, green for negligible asymmetry, blue for positive asymmetry. The figure shows a clear trend of χ with stellar parameters. Credits: Benomar et al. (2018).

the high quality of the *Kepler* data, the frequency bias often exceeds the 1σ-difference, with the differences being more pronounced for modes with a larger linewidth.

4.2 Physical origin of p-mode asymmetry

4.2.1 Source localisation

The first physical mechanism to which mode asymmetry was ascribed is the localisation of the source of excitation of the modes within a thin layer located close to the surface of the star. As I showed in Section 2.2.2, mode driving is indeed primarily due to turbulent acoustic emission, which is particularly efficient at the top of the convective envelope in solar-like oscillators, where the gas advected upwards by the convective instability suddenly has to go back down. The fact that locally-driven modes feature an asymmetric line profile was recognised in the context of solar-like p-modes even before the asymmetries were observed (e.g. Gabriel 1992, 1993, 1995; Roxburgh and Vorontsov 1995; Abrams and Kumar 1996).

Physical mechanism

In order to understand why a localised source leads to an asymmetric profile, let me briefly consider a very simple situation. In the adiabatic framework presented in Section 2.1, and with the Cowling approximation, I had obtained two first-order ordinary differential equations in the form of Equations 2.62 and 2.63, for the two variables $\widetilde{\xi_r}$ and $\widetilde{\eta}$. These two equations can be transformed into a single second-order equation. Let me differentiate Equation 2.62 with respect to r, and then replace $\mathrm{d}\widetilde{\eta}/\,\mathrm{d}r$ and $\widetilde{\eta}$ by their expressions as functions of $\widetilde{\xi_r}$ and $\mathrm{d}\widetilde{\xi_r}/\,\mathrm{d}r$ using Equations 2.62 and 2.63 itself respectively. We obtain, for a radial mode

$$\frac{\mathrm{d}^2\widetilde{\xi_r}}{\mathrm{d}r^2} = \frac{\mathrm{d}}{\mathrm{d}r}\left[\ln\left(\frac{hr^2}{c^2}\right)\right]\frac{\mathrm{d}\widetilde{\xi_r}}{\mathrm{d}r} - \frac{\omega^2 - N^2}{c^2}\widetilde{\xi_r}\,, \tag{4.23}$$

where c is the speed of sound, N the Brünt-Väisälä frequency, and h is defined by Equation 2.64. The first-derivative-term can be eliminated by introducing the new wave variable

$$\Psi(r) \equiv \frac{c}{rh^{1/2}}\widetilde{\xi_r}(r) \equiv \frac{\widetilde{\xi_r}}{x} \,, \tag{4.24}$$

in which case one gets a Schrödinger-type equation

$$\frac{\mathrm{d}^2\Psi}{\mathrm{d}r^2} + \left[\frac{\omega^2}{c^2} - V(r)\right]\Psi = 0 \,, \tag{4.25}$$

with an acoustic potential given by

$$V(r) \equiv -\frac{1}{x}\frac{\mathrm{d}^2 x}{\mathrm{d}r^2} + \frac{2}{x^2}\left(\frac{\mathrm{d}x}{\mathrm{d}r}\right)^2 + \frac{N^2}{c^2} \,. \tag{4.26}$$

The shape of the acoustic potential defines the cavity within which the modes develop: in particular, for a mode of angular frequency ω, the regions where $\omega^2/c^2 > V$ form the resonant cavity (where the eigenfunction $\Psi(r)$ has an oscillatory behaviour), whereas the regions where $\omega^2/c^2 < V$ form the evanescent regions (where the eigenfunction has a decaying exponential behaviour). With this in mind, let me consider the simplest case where the acoustic potential forms a square well. Since I consider a radial mode, the inner turning point is at the center of the star, while the upper turning point is almost at the surface. The boundary condition at the center imposes perfect reflection, but this is not the case at the surface, where part of the energy of the mode is lost through the evanescent region. Therefore, the well should have a wall of infinite height at the center, and a wall of finite height at the surface. Furthermore, I will consider that the equilibrium sound speed is uniform throughout the entire star, so that I can replace the radial variable r with an acoustic depth variable τ, defined through its differential form $\mathrm{d}\tau \equiv \mathrm{d}r/c$. Finally, I will add, 'by hand', the effect of the linear damping as an additional linear term on the left-hand side of the wave equation (Equation 4.25), and the effect of the localised driving as a point-like source with no frequency dependence. Piecing all these ingredients together yields the following toy model wave equation

$$\frac{\mathrm{d}^2\Psi}{\mathrm{d}\tau^2} + \Big(\omega^2 - V(\tau) + j\omega\gamma\Big)\Psi = \delta(\tau - \tau_s) \,, \tag{4.27}$$

where γ is the damping rate of the mode, δ is the Dirac distribution, τ_s is the acoustic depth of the point-like source, and the acoustic potential has a square-well shape

$$\begin{aligned} V(r) = \quad & +\infty \ \text{ if } \ \tau < 0 \,, \\ & 0 \ \text{ if } \ 0 < \tau < a \,, \\ & \alpha^2 \ \text{ if } \ a < \tau \,. \end{aligned} \tag{4.28}$$

In this model, a represents the acoustic length of the cavity, and corresponds to the time it takes for the sound waves to travel from one side of the stellar radius to the other. As for α, it represents the acoustic cut-off frequency, above which waves are no longer confined within the square well. This toy model corresponds to the wave equation considered, for instance, in Section II of Abrams and Kumar (1996). The wave equation, together with appropriate boundary conditions (namely that Ψ should vanish at the center, and the growing exponential solution should be filtered out at the surface) is straightforwardly solved: the detailed calculations can be found in Appendix C of Philidet et al. (2020a). The value of the acoustic depth related to the layer at which the modes are observed (which we will denote as τ_{obs}) being fixed, the *observed* wave variable becomes a function of angular frequency ω alone, and depending on whether the source is inside or outside the well, one finds[1] (Abrams and Kumar 1996)

$$\Psi_{\mathrm{obs}}(\omega) = -\frac{N(\omega)}{D(\omega)}\exp^{-\omega_o(\tau_{\mathrm{obs}}-a)} \,, \tag{4.29}$$

with

$$D(\omega) = \omega_i \cos\omega_i a + \omega_o \sin\omega_i a \,, \tag{4.30}$$

[1]The solution given here is only valid if $a, \tau_s < \tau$, meaning the layer at which the mode is observed is located higher than both the upper turning point of the mode and the point-like source of excitation. This corresponds to what happens in practice, since modes are observed in the atmosphere of the star, outside the acoustic cavity of the modes.

and

$$N(\omega) = \begin{cases} \sin \omega_i \tau_s & \text{if} \quad \tau_s < a \quad (4.31) \\ \omega_i \cos \omega_i a \sinh \omega_o(\tau_s - a) + \omega_o \sin \omega_i a \cosh \omega_o(\tau_s - a) & \text{if} \quad a < \tau_s \, . \quad (4.32) \end{cases}$$

(see also Philidet et al. 2020a, Appendix C), where $\omega_i^2 \equiv \omega^2 + j\omega\gamma$ and $\omega_o^2 \equiv \alpha^2 - \omega^2 - j\omega\gamma$. The observed quantity, then, is $|\Psi_{\text{obs}}(\omega)|^2$.

Naturally, because I considered an inhomogeneous wave equation with a forcing term, non-trivial solutions are found for every value of ω, not just for the eigenvalues of the corresponding homogeneous system. This solution can be split three ways

- the denominator $D(\omega)$ of the fraction, which is the same whether the source is inside or outside the mode cavity, corresponds to the Wronskian[2] of two homogeneous solution of the wave equation, one verifying the boundary solution at the center, the other verifying the boundary solution at the surface. I plot $1/|D(\omega)|^2$ as a function of ω in the left panel of Figure 4.7. In the absence of damping (i.e. if $\gamma = 0$), D would vanish for all values of the angular frequency ω that coincides with an eigenvalue of the homogeneous system, so that $1/|D(\omega)|^2$ would diverge for all eigenfrequencies. This is due to the definition of the Wronskian: if ω is an eigenfrequency, then the solution to the homogeneous system verifies both boundary conditions, and the Wronskian of two identical solutions if obviously zero. In the presence of a linear damping contribution, such as in the case of Equation 4.27, $1/|D(\omega)|^2$ does not diverge, and instead takes the form of a set of Lorentzian profiles centered on each eigenfrequency of the system, each having a width at half maximum equal to γ. As such, the corresponding spectrum feature regularly spaced resonant peaks, so long as $\omega < \alpha$. For $\omega > \alpha$, one still finds peaks in the spectrum, but they are much less pronounced, because these waves are no longer confined modes, and do not undergo any reflection at the surface. Regardless of whether ω is smaller and greater than the acoustic cut-off frequency, $1/|D(\omega)|^2$ *alone yields symmetric line profiles*;

- the exponential factor simply represents the evanescent nature of the region outside the cavity: the higher in the atmosphere the mode is observed, the lower its apparent amplitude. This factor is almost independent of ω, and does not participate in the shape of the line profiles, except in the sense that it decreases its overall amplitude;

- the numerator $N(\omega)$ of the fraction is the only component that depends on the position of the source τ_s. I plot the quantity $|N(\omega)/D(\omega)|^2$ in the right panel of Figure 4.7. The difference with the left panel is striking: the line profiles are now distinctly asymmetric. The reason is that $N(\omega)$ is not symmetric around an eigenfrequency of the system. More specifically, if $N(\omega)$ increases with ω in the vicinity of an angular eigenfrequency ω_0, then $|\Psi_{\text{obs}}(\omega)|^2$ takes slightly higher values for $\omega > \omega_0$ than for $\omega < \omega_0$, and the line profile will feature positive asymmetry. The argument is reversed if $N(\omega)$ decreases with ω in the vicinity of ω_0: then the line profile will feature negative asymmetry. The right-panel of Figure 4.7 also shows that the amplitude of the modes drastically vary from mode to mode: this is also due to the fact that $N(\omega)$ can take very different values depending on ω_0.

The asymmetry of a given mode, therefore, is primarily determined by the direction of variation of $|N(\omega)|^2$ with ω. But it can be seen from the calculations carried out in Appendix C of Philidet et al. (2020a) that $N(\omega)$ corresponds to the value of the wave variable $\Psi_\omega(\tau)$ at $\tau = \tau_s$ (to a ω-independent factor), i.e. at the position of the point-like source of excitation. Since, in these expression, ω and τ systematically appear together in the form of the product $\omega_i\tau$, *the direction of variation of* $|N(\omega)|^2$ *with* ω *is exactly the same as the direction of variation of the wave variable* $|\Psi_\omega(\tau)|$ *with* τ *around the source position.* Since the wave variable has an oscillatory behaviour for $0 < \tau < a$, and behaves as an evanescent wave for $a < \tau$, the following conclusions can be drawn

1) if $\tau_s < a$ (i.e. if the source is inside the cavity), then the sign of the asymmetry of a mode depends on the location of the source compared to the nodes and antinodes of the associated eigenfunction. More specifically, if the source is located between a node below and an antinode above, then the modulus square

[2] In general, given a n-th order system of linear differential equations, and n solutions to the homogeneous system, then the *Wronskian* of these n solutions is the determinant of the $n \times n$ matrix consisting of the n first derivatives of each solution. One of its fundamental properties is that it does not depend on the variable of the linear system. If, in addition, the solutions are linearly degenerate (i.e. if one can be written as a linear combination of the others), then the Wronskian vanishes.

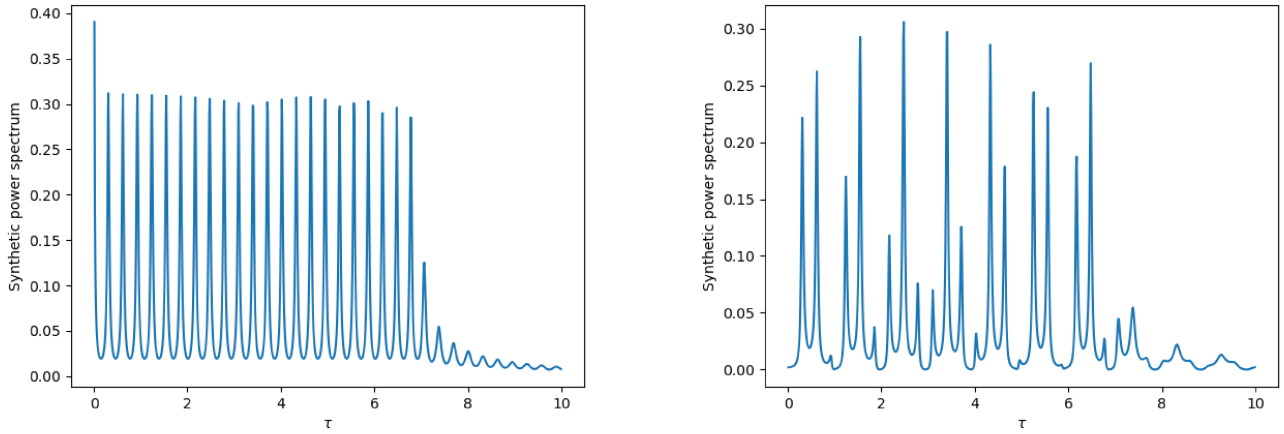

Figure 4.7: **Left**: Inverse square of the Wronskian $1/|D(\omega)|^2$, where $D(\omega)$ is defined by Equation 4.30. Arbitrary values $\alpha = 7$, $a = 10$, $\gamma = 0.05$, and $\tau_s = 3.2$ were chosen. All line profiles are symmetric. **Right**: Same as left panel, but with the quantity $|N(\omega)/D(\omega)|^2$, also including the numerator defined by Equation 4.31. The line profiles are now asymmetric, and their amplitude varies significantly from mode to mode.

of the eigenfunction increases with τ in the vicinity of the source: the mode features positive asymmetry. On the other hand, if the source is located between an antinode below and a node above, the mode features negative asymmetry. Additionally, the relative amplitude of the modes also depends on whether τ_s is located close to a node or not;

2) if $a < \tau_s$ (i.e. if the source is outside the cavity), then the eigenfunction associated to any mode is evanescent, so that its modulus square decreases with τ in the vicinity of the source. Therefore, all modes feature a negative asymmetry.

These conclusions, which I drew from a simplified toy model, are actually very general, which can be understood through the perhaps more intuitive argument illustrated in Figure 4.8. I plot an asymmetric line profile in the left panel, with three different frequencies highlighted green, red and blue respectively. One is the eigenfrequency of the mode, the other two are slightly lower and slightly larger respectively, while still remaining within the frequency range of the mode line profile. On the right panel are plotted (in an illustrative manner) the spatial profiles $\Psi_\omega(\tau)$ associated to these three frequencies, and I add the position of the point-like source of excitation. It is clear from this illustration that the relative amplitude of the wave variable profile at the position of the source is not the same for all three frequencies, which impacts the efficiency of the excitation of a given frequency-component by the point-like source. More specifically, if a component ω is associated with a wave variable profile that features a node at the position of the source, then the source will not be able to excite this component of the spectrum. On the contrary, the efficiency of the excitation will be maximal if the source coincides with an antinode of the frequency-component under consideration. Otherwise stated, in perhaps more familiar terms, the driving efficiency does not only depend on the amplitude of the driving source itself, but also on the modulus squared of the local compressibility $|\partial\xi_r/\partial r|^2$ of the mode. In the example illustrated in Figure 4.8, the source 'sees' a much larger amplitude for the green frequency than for the blue frequency, which explains why the green frequency has slightly more power than the blue one. From this example, it is clear why, in the most general case, the sign of the asymmetry is tightly related to the direction of variation of the eigenfunction of the mode in the vicinity of the source of excitation.

Other interpretations of the asymmetry caused by source localisation have been proposed as well. Gabriel (1992) or Abrams and Kumar (1996), for instance, remarked that one could reason in terms of interference patterns between the multiple reflections undergone by the waves. A localised source of excitation creates a certain difference between the travel time of the outwards-travelling waves and the inwards-travelling ones, thus entailing a certain phase difference, which leads to a frequency-dependent interference pattern that can create asymmetry. In fact, this interpretation is already contained in Equation 4.29, which can be rewritten, as was remarked by Abrams and Kumar (1996), in the form of an infinite series of travelling waves precisely corresponding to the multiple reflections constituting the resonant mode, in addition (in the case of a source outside the cavity) to the original

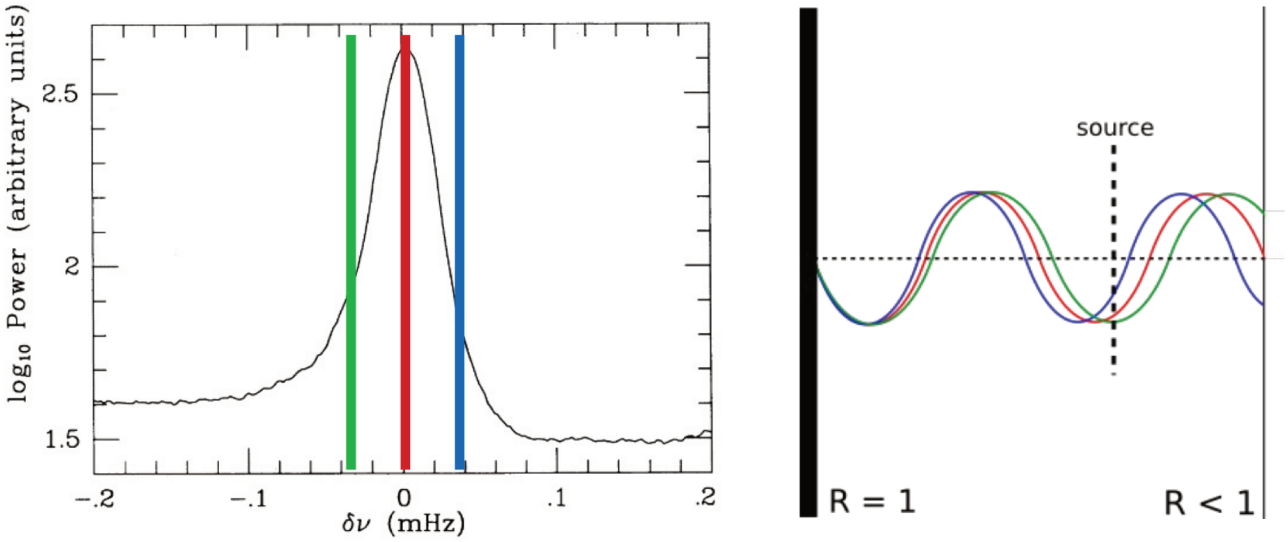

Figure 4.8: Schematic illustration of mode asymmetry caused by a localised source of excitation.

outwards-travelling wave that never entered the cavity in the first place. Let me note that a similar argument was used by Duvall et al. (1993), except that they considered that the phase difference was not caused by a localised source, but by non-adiabatic effects influencing the phase of the waves upon reflection on the surface. However, the influence of non-adiabaticity on mode asymmetry was later shown to be negligible by Rast and Bogdan (1998). This may sound surprising, seeing as the oscillations are notoriously non-adiabatic close to the surface of the star, as we saw in Section 2.1; however, I recall that mode asymmetry is a differential effect, not subjected to overall changes to the mode line profile, so that certain effects affecting the amplitude of the mode can leave the asymmetries unscathed. Another, alternative interpretation of the asymmetry caused by source localisation was proposed by Rosenthal (1998). In his view, he measured the asymmetry of the mode as a non-equidistance between the consecutive peaks and troughs in the power spectrum. He remarked that while the peaks correspond to the eigenfrequencies of the whole solar cavity, the troughs correspond to the eigenfrequencies of the upper part of the cavity only, truncated at the position of the source. Then, if a mode has a node on the source, the peaks and troughs are superimposed, and the asymmetry is maximal; if the mode has an antinode on the source, each trough is located exactly in between the two adjacent peaks, and there is no asymmetry. These conclusions are identical to those reached above: all these alternative representations of source localisation as a source of mode asymmetry are perfectly equivalent to the one I presented in more details earlier.

Constraints on the depth of excitation of solar p-modes

Since p-mode asymmetry carry the signature of the position of the driving region of the modes, observed solar asymmetries have been used by several authors to try and constrain this position in the Sun. Abrams and Kumar (1996) used a solar model calculated by Christensen-Dalsgaard (1991) to extract a realistic radial profile $V(r)$ for the acoustic potential, and used it to compute theoretical asymmetries for a grid of source positions, located between the photosphere and a point 2000 km below the photosphere. Comparing their results to the observed solar asymmetries reported by Duvall et al. (1993), they concluded that the point-like source of excitation of the solar p-modes should be located between 325 and 525 km beneath the photosphere. They remarked that any deeper source of excitation would cause some modes to feature a strong positive asymmetry (in direct disagreement with observations), because the source would then have passed one of their radial nodes. Nigam et al. (1998) performed a similar study, but used asymmetries observed in both velocity and intensity. Their goal was to determine both the position of the source and its multipolar nature. For the latter, they considered that the right-hand side of the wave equation can be written as a combination of monopolar ($\propto \delta(\tau - \tau_s)$) and dipolar ($\propto \mathrm{d}\,\delta(\tau - \tau_s)/\,\mathrm{d}\tau$) sources. The authors reported that they could only explain the observed asymmetries by including both components at the same time, and constrained the location of the source between 25 and 125 km below the photosphere, in stark disagreement with the results of Abrams and Kumar (1996). Kumar and Basu (1999a) later also considered different source types, but focused on low-frequency modes in velocity. They found that in order for theoretically

predicted asymmetries in the velocity power spectrum to agree as best as possible with observations, quadrupolar sources have to be located between 700 and 1050 km below the photosphere, while the depth only has to be between 120 and 350 km for dipolar sources. However, they did not consider the possibility of a mix between the two kinds of sources, and could not discriminate between a purely dipolar and purely quadrupolar source using observed asymmetries. Kumar and Basu (2000) extended this analysis to both low- and high-frequency modes. Using this wider frequency range, they discarded the possibility that the high-frequency modes be excited by a dipolar source, thus leaving only the possibility of a quadrupolar source. They further concluded that a quadrupolar source should be located between 60 and 250 km below the photosphere to reproduce the observed asymmetries for high-frequency modes. Chaplin and Appourchaux (1999) followed a slightly different approach. They considered only modes of low angular degree l, observed both in velocity with 3 years worth of solar data from BiSON, and in intensity with the full-disk intensity observations made with SPM/Virgo aboard the SoHO spacecraft, and extracted their line profiles. In parallel, they computed theoretical line profiles by using the same inhomogeneous wave equation presented above (Equation 4.27). Then they adjusted the model to match each observed line profile individually, resulting in a best-fit value for the position of the source for each mode individually. They found that all modes are excited by sources located between $\sim$ 50 km and $\sim$ 400 km. However, they considered the same simplified square-well potential as I did above, instead of a more realistic solar potential.

This account strikes by the variety of results obtained by different, independent studies, as regards the depth of the excitation source for solar p-modes. The results either disagree too much with each other, or are subjected to uncertainties that are too large, which prevents the inferred source position from providing with a realistic picture of solar-like p-mode excitation, even in the case of the Sun. This begs the question: can the properties of the source actually be inferred from observations? This question was investigated by Jefferies et al. (2003), by using the model of Severino et al. (2001) described in Section 4.1 (making use simultaneously of the velocity and intensity power spectra, as well as the coherence velocity-intensity cross-spectrum, and their relative phase difference), to fit the observed line profiles, by including both the effect of the source localisation, and the correlation of the resonant mode with the convective noise, which can also lead to some sense of mode asymmetry (see Section 4.2.2 for more details). They concluded that the depth of the acoustic source cannot be uniquely determined, despite the simultaneous use of the information contained in all four spectra, thus replying to the above question with a resounding 'no'. The exact same conclusion was reached by Wachter and Kosovichev (2005) as well. To conclude on the subject of source position inference from observed asymmetries, we point out that all the studies presented above either consider a point-like source of excitation, without any spatial extent, or include the spatial extent of the source as an additional free parameter, but systematically simplify the spatial profile of the source to be Gaussian (e.g. Gabriel 1992; Abrams and Kumar 1996; Chaplin and Appourchaux 1999). As I will show in Chapter 5, these constitute oversimplifying assumptions, and the lack of a realistic description of the spatial profile of the excitation source is a major drawback of these models, preventing them from enabling the inference of accurate source properties through the use of observed p-mode asymmetries.

4.2.2 Correlated background

Another source of asymmetry is the partial statistical correlation of the resonant mode with the convective noise in the background. The correlation stems from the fact that the modes are precisely excited by the turbulent motions at the top of the convective zone: therefore, there can be interference between the mode and the background noise, which, as I will now show, can skew the line profile of the modes. This is perfectly equivalent to another phenomenon occurring in atomic spectroscopy: when a given atomic bound-bound transition can be subjected to auto-ionisation (i.e. when an electron can be excited or deexcited through interaction with a continuum of free-free or bound-free transitions of similar energy), then the resulting resonant spectral line can interfere with the continuum, and the spectral line becomes asymmetric. Such asymmetric atomic line profiles are referred to as Fano profiles (Fano 1961). The similarity between this phenomenon and the asymmetry of solar-like p-modes was noted by Gabriel et al. (2001), and gives an invaluable insight into the physical mechanism at play in the realm of helioseismology.

Physical mechanism

Let us assume that the resonant mode is intrinsically characterised by a Lorentzian line profile, without asymmetry[3]. Then the amplitude of the Fourier transform in time of the signal associated to the mode can be written as

$$f_{\text{mode}}(\omega) = \frac{A_m}{x + j} \,, \tag{4.33}$$

where A_m is a complex constant representing the amplitude and phase of the mode (although one can always redefine the time origin so that A_m is real), and

$$x = \frac{2(\omega - \omega_0)}{\Gamma} \,, \tag{4.34}$$

ω_0 is the angular eigenfrequency of the mode, and Γ its linewidth. If only the mode itself were observed, the modulus squared of this signal would yield a symmetric, Lorentzian profile. However, there is also noise, part of which is correlated to the mode, and part of which is not. Denoting the former as $A_c \exp(j\Phi_c)$ and the latter as $A_u \exp(j\Phi_u)$ (where A_c and A_u are the real amplitude of the correlated and uncorrelated background respectively, and Φ_c and Φ_u their phase difference with the mode), then the total, observed power spectrum is

$$P(\omega) = \left| \frac{A_m}{x + j} + A_c \exp^{j\Phi_c} \right|^2 + A_u^2 \,. \tag{4.35}$$

After some algebra, one finds

$$P(\omega) = \frac{A_m^2}{1 + x^2} + \frac{2A_m A_c}{\sqrt{1 + x^2}} \sin\left(\arctan x + \Phi_c\right) + A_c^2 + A_u^2 \,. \tag{4.36}$$

The first term corresponds to the Lorentzian profile one would have obtained if only the mode were there, and the last two terms correspond to the frequency-independent background. Both these contributions are symmetric about the angular eigenfrequency ω_0 (i.e. around $x = 0$). But the second term, in general, is not: unless the mode and the correlated background are in quadrature (i.e. their phase difference $\Phi_c = \pm\pi/2$), this interference term is clearly not an even function of x. In fact, if $\Phi_c = 0$ or π, this term is an odd function of x. In other words, the interference between the mode and the correlated background is either destructive for $x < 0$ and constructive for $x > 0$, or the other way around. As a result, one of the wings of the mode is elevated by the interference pattern, and the other is lowered: the mode has an asymmetric line profile. It is apparent, then, that while the degree of asymmetry depends on a number of properties of the background, including its overall amplitude and its degree of correlation with the mode, the sign of the asymmetry, on the other hand, only depends on the phase difference between the mode and the correlated background – that is, between the mode and its source of excitation. Let me remark, before going further, that a similarity can be drawn between the asymmetries caused by source localisation (see Section 4.2.1) and the asymmetries caused by the correlated background: they can both be described in terms of an interference pattern. This begs the question: is there a physical reason for separating the two? or is this distinction purely artificial, and these two mechanisms really two sides of the same process? Gabriel et al. (2001) hinted that this was indeed the case. Here, I content myself with remarking that as a result of this similarity, both mechanisms have the same formal effect on the line profiles: *it is therefore rigorously impossible to disentangle the contribution of source localisation from the contribution of the correlated background using only observations*.

Constraints on the solar correlated background

Originally, this mechanism was proposed by Nigam et al. (1998) to explain the asymmetry reversal puzzle between the velocity and intensity observables. The authors included the correlated background into their model in the following manner: they considered different source types – monopolar, dipolar, quadrupolar –, and for each

[3]Of course, that is not true, since we just saw that the localisation of the mode driving source also creates an intrinsic asymmetry. However, for the sake of this discussion, I will consider that the correlated background is the only source of asymmetry.

source type computed the *Green's function*[4] associated to the wave equation

$$\frac{\mathrm{d}^2\Psi}{\mathrm{d}r^2} + \left[\frac{\omega^2}{c^2} - V(r)\right]\Psi = S(r)\,, \tag{4.38}$$

$$V(r) = \frac{1}{c^2}\left[\omega_c^2 + L_l^2\left(1 - \frac{N^2}{\omega^2}\right)\right]\,, \tag{4.39}$$

where ω_c is the acoustic cut-off frequency. They considered that the Green's function is the same for the velocity and intensity observables. They then expressed the full observed signal by adding an arbitrary frequency-dependence for the point-like source $S(\nu)$, the correlated background $C(\nu)$ and the uncorrelated background $U(\nu)$

$$P(\nu) \equiv S(\nu, r_s)\,(C(\nu) + G(\nu)) + U(\nu)\,, \tag{4.40}$$

where the position of the source r_s and the position at which the modes are observed r_{obs} are fixed in advance. The authors then tweaked the position of the source, the relative weight of each source type, as well as the amplitude of both the correlated and uncorrelated background in each observables, to reproduce the observed power spectra as best they could. They found that they could only explain the asymmetry reversal between the two observables if the amplitude of the correlated background was different in velocity than in intensity; varying any other parameter also changes the sign of the asymmetries, but does so in both observables simultaneously. As a result, the authors argued that the asymmetry reversal is caused by a much higher correlated background in intensity (where it can be so high as to reverse the sign of the asymmetries) than in velocity (where it cannot). They remarked, as I did earlier, that the presence of a correlated background can be explained by the presence of granulation overshoot, which is responsible both for part of the noise and for the excitation of the modes. However, they offer no explanation as to why it should be higher in one observable than in the other. Around the same time, Roxburgh and Vorontsov (1997) proposed the same explanation, except they considered that the correlated background is more important in velocity rather than in intensity. They argued that the kinematic velocity of the turbulent eddies shooting upwards while exciting the modes is responsible for the correlated noise signal. On the other hand, Nigam and Kosovichev (1999) proposed that the higher degree of correlation between the background and the modes in intensity is due to the slight local photospheric darkening occurring before an acoustic emission event in the superadiabatic layer, as observed on the surface of the Sun by Goode et al. (1998), as well as in 3D simulations (Stein and Nordlund 1991). Although Rast and Bogdan (1998) only considered uncorrelated, additive background, they remarked that another explanation for the noise impacting asymmetries differently in both observables could stem from the fact that modes stand out above noise level much more significantly in velocity than in intensity. They argued that, as a result, one observes the wings of the modes much further away from the center in velocity than in intensity, so that the line profiles in velocity are more sensitive to the frequency-dependence of the noise than the line profile in intensity.

Regardless of the exact physical origin of the difference between the correlated noise levels in velocity and intensity, observed solar asymmetry reversal was used by several authors to constrain the properties of the correlated background. Kumar and Basu (1999b), for instance, considered that the correlated background could be neglected in velocity, and only included it in the intensity spectrum. More specifically, they parameterised it through two different parameters, namely the relative amplitude β of the correlated background compared to the amplitude of the mode, and their phase difference ϕ. They computed theoretical asymmetries in velocity (i.e. with $\beta = 0$) and in intensity (i.e. with $\beta \neq 0$) for dipolar and quadrupolar sources, and found that they could explain the asymmetry reversal provided the parameter $\beta' \equiv \beta\exp(-\eta)$ (where η is the acoustic depth difference between the upper turning point of the modes and the layer at which the observations are performed) exceeds ~ 0.1. However, they considered the oversimplified toy model that I presented in the Section 4.2.1, instead of a more realistic solar acoustic potential, which makes this figure a somewhat rough approximation. Nevertheless, they computed the expected

[4]For any given linear differential equation $\mathcal{L}(\Psi) = S$, where $\mathcal{L}$ is a linear operator, Ψ the variable of the equation, and S the inhomogeneous source term, the Green's function $G(r, r_s)$ is defined as the unique solution to the differential equation, with its associated boundary conditions, when $S(r) = \delta(r - r_s)$. Knowing the Green's function for every value of r and r_s is sufficient to solve the full equation with an arbitrary source term $S(r)$, because the general solution is simply

$$\Psi(r) = \int \mathrm{d}r_s\, G(r, r_s)S(r_s)\,. \tag{4.37}$$

value of β for the Sun, using a more realistic wave equation, and found the values to be in the range leading to a reversal of asymmetry. A more systematic determination of this parameter was performed by Chaplin and Appourchaux (1999), who also included it only in intensity measurements, but adjusted its value for a set of observed solar p-modes individually. They found that the ratio α_{correl} between the correlated background and the maximum of the real part of the Green's function of the modes reaches a minimum around $\nu_{\max}$, and a maximum for very low and very high frequency modes, with values ranging from $\sim 2\%$ to $\sim 5\%$. However, the authors remarked that the frequency dependence of α_{correl} was primarily due to the difference in the amplitude of the modes themselves. Considering instead the product of α_{correl} and the amplitude of the modes in intensity – in other words, the absolute amplitude of the correlated background in intensity –, they found a much less pronounced, monotonously decreasing frequency dependence.

The idea that only the intensity signal should contain correlated noise was then challenged by Skartlien and Rast (2000), who used both observed asymmetries in intensity and velocity as well as observed phase differences between the two spectra to conclude that *both observables* contain a certain measure of correlated background. They argued that this was in agreement with the observation that acoustic emission event are systematically accompanied not only by a local darkening of the photosphere, but also by the creation of a local downdraft, quickly followed by a subsequent upflow to take the place of the evacuating gas (Stein and Nordlund 1991; Rast and Toomre 1993; Rast 1999). The same conclusion was reached by Severino et al. (2001), and later by Barban et al. (2004), who used the information contained in all four observed spectra (velocity, intensity, and amplitude and phase velocity-intensity cross-spectra) and fitted the observations with their model consisting of Equations 4.18 to 4.21. However, by construction, their model ascribes the entirety of the asymmetry of the modes and the observed velocity-intensity phase difference to the correlated background, whereas, as I showed in the Section 4.2.1, part of it is due to the localisation of the source. This analysis was improved by Wachter and Kosovichev (2005), who included the non-adiabatic effects due to radiative transfer into their model, thus freeing them from having to include an *ad hoc* intensity-velocity p-mode phase difference as a free parameter in the fit, and also included the effect of source localisation on the asymmetry of the modes. Instead of focusing on the dependence of the noise on frequency, like Severino et al. (2001) and Barban et al. (2004), the authors focused on the simultaneous determination of source properties (position and multipolar decomposition) and noise properties (amplitude and phase). While they did not manage to constrain the properties of the source, they did succeed in determining those of the correlated and uncorrelated background. More specifically, they found that the fraction of the noise that is correlated to the oscillations is indeed higher in intensity ($\sim 4\%$), but still exists in velocity ($< 3\%$). As for the phase difference, the authors found it to be almost in phase opposition (between -155° and -162°). However, these results are considerably tainted by the uncertainty surrounding the source properties. The idea that the velocity signal should also contain a correlated background component is also supported by the findings of Tripathy et al. (2003) or Sánchez Cuberes et al. (2003) for instance, who reported that the asymmetry reversal is stronger when the asymmetries are observed locally close to the center of the solar disk than when they are observed near its limb. The only explanation is that the velocity field we observe is radial in the center and horizontal in the limb; but only the radial velocity is correlated with the oscillations, so that the correlated background component in the velocity signal is lower near the limb than near the center. Naturally, this only works if the velocity signal contains a correlated noise component in the first place. However, these results were contradicted by Tripathy et al. (2009), who concluded, at complete odds with these earlier results, that their is no difference between measurements near the limb and near the center, and that therefore only the intensity signal contains a contribution from the correlated background.

Attempts were also made at *predicting* the effect of the correlated background on mode asymmetry, for instance by Chaplin et al. (2008). The authors managed to give a theoretical prescription for the asymmetry parameter B caused by the correlated background, for any given observable and any given geometrical factor related to the observational technique. However, they still need to leave the fraction of noise correlated to the source of excitation as a free parameter, which is precisely that part of the calculations on which concentrates a large part of the modelling complexity. They also assume that the noise level is the same for all modes. Were these obstacles to be lifted, however, one could find out what portion of B is caused by the correlated background, with the understanding that the leftover, compared to observations, is due to source localisation alone, and can therefore be used for a more accurate determination of the source properties. I conclude on the matter by remarking that in the absence of such a predictive model, and as I hinted in the beginning of this section, it is extremely complicated to disentangle the various contributions to mode asymmetry, and therefore it is very complicated to infer properties

of either the excitation source or the correlated background from observed asymmetries. This is illustrated, in particular, by the absence of consensus concerning the question of which mode observable is correlated with the convective noise, an absence of consensus that mirrors the one I already mentioned regarding the properties of the source (see Section 4.2.1), and that still lingers to this day.

4.2.3 Opacity effect

Physical mechanism

A third physical mechanism that is susceptible to be responsible for mode asymmetry, and more specifically for asymmetry reversal between velocity and intensity, was proposed by Georgobiani et al. (2003), and has to do with the modulation of the radiative flux by the oscillations, and more specifically the modulation of the optical depth that they bring about. The authors used a 3D hydrodynamic simulation of the solar atmosphere calculated with the `STAGGER` code (Stein and Nordlund 1998), which they had already used in Georgobiani et al. (2000) to directly extract normal modes of oscillation from the simulation, and to 'observe' the asymmetry reversal directly in the simulation. This approach presents the distinct advantage of allowing for a precise exploration of the physical mechanisms at hand, since they are all contained in the output of the simulation[5]. The authors isolated one normal mode of oscillation in their simulation box, and 'observed' it alternatively at fixed geometrical depth r_0 (chosen such that the horizontal and time average of the optical depth τ at r_0 equals unity), and at fixed optical depth $\tau = 1$. In the following, I will refer to the former as the r-frame, and to the latter as the τ-frame. Because of the fluctuations due to the noise *and* to the modes, the layer of optical depth $\tau = 1$ depends on both time and horizontal coordinates. In particular, one sees deeper in the cooler – and therefore more transparent – intergranular lanes than in the hotter granules. Therefore, the r-frame and the τ-frame are different. First, the authors remarked that the amplitude of the modes in temperature was considerably reduced in the τ-frame compared to the r-frame, while the amplitude in velocity remains unaffected. Furthermore, they remarked that the asymmetry of the line profile was the same in velocity and temperature in the r-frame, but that the asymmetry in temperature became opposite in sign in the τ-frame. They also observed the line profile in the emergent intensity spectrum, which features the same reversed asymmetry as temperature in the τ-frame. Real solar observations are done in the τ-frame: indeed, the emergent intensity is observed at the $\tau = 2/3$ layer (due to the Eddington-Barbier relations, Mihalas and Mihalas 1984), and the Doppler measurements are made at the formation height of the spectral absorption line under consideration, which is also τ-dependent. Based on this observation, the authors proposed the following picture: modal fluctuations of the temperature entail fluctuations of the opacity; opacity fluctuations perturb the geometrical depth at which modes are observed; because of the steep background temperature gradient at the photosphere, the *observed* background temperature undergoes fluctuations in phase with the observation height fluctuations; the background temperature fluctuations adds up with the modal temperature fluctuations, thus modifying the observed intensity spectrum. Because the background temperature fluctuations are in phase opposition with the modal temperature fluctuations, the τ-frame intensity spectrum has a reduced amplitude compared to the r-frame intensity spectrum. Because there is no background mean velocity gradient at the photosphere (at least in their simulation), the τ-frame velocity spectrum is identical to the r-frame velocity spectrum. Finally, because the $\kappa - T$ relation is non-linear, the intensity spectrum reduction between the two frames depends on the amplitude of the starting modal fluctuations, which explains why the wing of the temperature line profile that has more power in the r-frame is more drastically reduced than the other once observed in the τ-frame, so much so that the asymmetry is reversed.

A toy-model for the opacity effect

In the simulation studied by Georgobiani et al. (2003), the authors showed that the opacity effect described above is responsible for the asymmetry reversal between velocity and intensity observables. However, their explanation is based on an intrinsically non-linear mechanism. This begs the question: while this effect might be important in a 3D simulation, where modes have a very high amplitude, does it remain important in the real solar case, where the modes have much smaller amplitudes? In order to answer this question, I propose the following toy-model to quantify the extent to which the opacity effect impacts the shape of the line profile of a resonant mode

[5] On the other hand, the simulation presents the distinct disadvantage of not being the Sun, which, as will become clear later on, makes the transposition of these results to the real solar case complicated.

in the temperature power spectrum, both in terms of its overall amplitude and of its asymmetry. It is similar, at least in its spirit, to the model presented by Severino et al. (2008), although they applied it to the numerical results of Georgobiani et al. (2003) rather to the actual Sun.

In the following, I denote the Lagrangian temperature perturbation as δT in the r-frame, and the τ-frame temperature perturbation as δT_τ. The two kinds of fluctuations are related through

$$\delta T_\tau = \delta T - \frac{\mathrm{d}T_0}{\mathrm{d}\tau}\delta\tau \,, \tag{4.41}$$

where $\delta\tau$ refers to the Lagrangian perturbation of the optical depth, and $T_0(\tau)$ is the unperturbed, equilibrium temperature. I recall that the optical depth is defined through its differential form by

$$\mathrm{d}\tau \equiv -\rho\kappa_R \,\mathrm{d}r \,, \tag{4.42}$$

where ρ is the density and κ_R the mean Rosseland opacity per unit mass. The minus sign ensures that the optical depth is zero far away from the star, and increases as one goes deeper into it. Perturbing this linearly, one finds

$$\mathrm{d}\delta\tau = -\delta\rho\kappa_R \,\mathrm{d}r - \rho\delta\kappa_R \,\mathrm{d}r - \rho\kappa_R \,\mathrm{d}\xi_r \,, \tag{4.43}$$

where ξ_r is the radial fluid displacement. Integrating this between the radius r_o at which the mode is observed and infinity (where $\delta\tau = 0$), one finds

$$\delta\tau = -\int_{r_o}^{+\infty} \mathrm{d}r \,\rho\kappa_R \left(\frac{\delta\kappa_R}{\kappa_R} + \frac{\delta\rho}{\rho} + \frac{\mathrm{d}\xi_r}{\mathrm{d}r}\right) . \tag{4.44}$$

There is a bit of a subtlety here. Indeed, I argued only moments ago that the modes are observed in the τ-frame, which means that the geometrical height at which the observations are done is not fixed: in other words, r_o depends on time. However, the difference between the instantaneous and average values of r_o can be treated as a first-order quantity in the perturbative framework of the oscillations. Since the integral is already first-order, accounting for the perturbation of r_o would only add a second-order correction to this expression, which can therefore be neglected. As such, the value of r_o that appears in Equation 4.44 is actually the *average* geometrical height of observation, and is constant. Plugging Equation 4.44 into Equation 4.41, one obtains

$$\delta T_\tau = \delta T + \frac{1}{\kappa_{R,o}\rho_o}\frac{\mathrm{d}T_0}{\mathrm{d}r}\int_{r_o}^{+\infty} \kappa_R\rho\left(\frac{\delta\kappa_R}{\kappa_R} + \frac{\delta\rho}{\rho} + \frac{\mathrm{d}\xi_r}{\mathrm{d}r}\right)\mathrm{d}r \,, \tag{4.45}$$

where $\kappa_{R,o}$ and ρ_o are the equilibrium opacity and density at the average height of observation r_o.

To close this relation, one has to express the density, opacity and displacement perturbations $\delta\kappa_R$, $\delta\rho$ and ξ_r as a function of the temperature perturbation δT. Using the perturbed continuity equation, one can write $\delta\rho/\rho + \mathrm{d}\xi_r/\,\mathrm{d}r = -2\xi_r/r$. Because the modes are observed in the atmosphere of the star, this curvature term is negligible[6]. As such, only the opacity perturbation need be retained in Equation 4.45. Assuming an equation of state of the form $\kappa_R \propto T^\beta$, one easily derives

$$\frac{\delta\kappa_R}{\kappa_R} = \frac{\delta\left(T^\beta\right)}{T^\beta} = \left(1 + \frac{\delta T}{T}\right)^\beta - 1 \,. \tag{4.46}$$

Note that I do not linearise this expression, because the asymmetry change between the r-frame and τ-frame intensity spectra are precisely brought about by the non-linearity of this relation (Georgobiani et al. 2003). Close to the photosphere, the opacity is mainly due to H^- absorption, for which the exponent in the $\kappa - T$ relation is approximately $\beta \sim 7.5$ for the Sun (Kippenhahn and Weigert 1994). One can then combine Equations 4.45 and 4.46 to obtain the following relationship between Lagrangian and τ-frame temperature perturbations

$$\delta T_\tau = \delta T - \frac{T_o}{H_T\kappa_{R,o}\rho_o}\int_{r_o}^{+\infty} \kappa\rho\left[\left(1 + \frac{\delta T}{T}\right)^\beta - 1\right] \mathrm{d}r \,, \tag{4.47}$$

[6]For an order of magnitude: in the Sun ξ_r is typically of the order of a few tens of meters, while r refers to the radius of the Sun, $\sim 700,000$ km. The ratio between the two is $\sim 10^{-8}$, which is indeed negligible compared to the few parts per million of the relative opacity perturbation entailed by the modes.

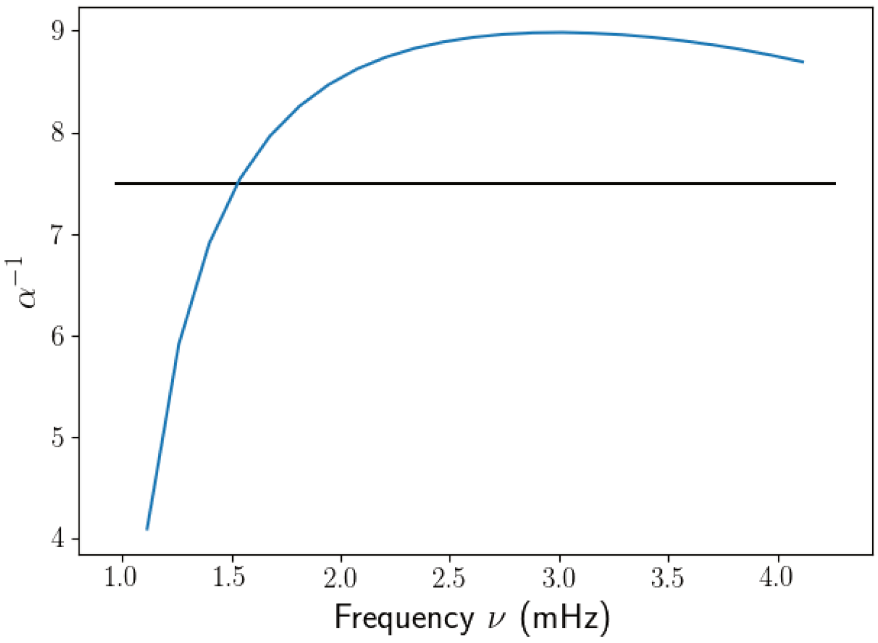

Figure 4.9: Inverse of the dimensionless parameter $\alpha \equiv l/H_T$, where l is defined by Equation 4.48, as a function of frequency, for a solar model. The horizontal solid black line corresponds to $\alpha^{-1} = \beta$.

where T_o is the equilibrium temperature at the average observation height, and I have introduced the temperature scale height H_T such that $\mathrm{d}T_0/\,\mathrm{d}r = -T_o/H_T$. This expression can be simplified greatly if one introduces the integral spatial scale related to the integral over r

$$l \equiv \frac{\displaystyle\int_{r_o}^{+\infty} \kappa_R \rho \left[\left(1 + \frac{\delta T}{T}\right)^{\beta} - 1\right] \mathrm{d}r}{\kappa_{R,o}\rho_o \left[\left(1 + \frac{\delta T}{T_o}\right)^{\beta} - 1\right]} \,. \tag{4.48}$$

In order to render this integral scale dimensionless, I introduce the parameter α such that $l = \alpha H_T$, in which case Equation 4.47 reduces to

$$\frac{\delta T_\tau}{T_o} = \frac{\delta T}{T_o} - \alpha \left[\left(1 + \frac{\delta T}{T_o}\right)^{\beta} - 1\right] , \tag{4.49}$$

where the parameter α only depends on the temperature eigenfunction associated to the mode in the atmosphere, as well as the equilibrium state of the stellar atmosphere. In order to apply this toy model to the solar case, I used an equilibrium patched model of the Sun computed with the CO^{5}BOLD hydrodynamic code to extract the equilibrium quantities appearing in Equation 4.48, and the adiabatic pulsation code ADIPLS[7] to extract the temperature eigenfunction δT associated to the solar radial p-modes of radial order $n = 6$ to $n = 30$. This allowed me to compute the values of the dimensionless parameter α for each of these modes. I show the results in Figure 4.9. It can be seen that, except for very low-frequency modes, the parameter α^{-1} remains slightly above β, which will prove of crucial importance in the following.

Equation 4.49 provides with a closed relation between the temperature perturbations as observed in the Lagrangian and τ-frames. It can therefore be used to analytically derive a relation between the properties of a given p-mode in both frames. Denoting the eigenfrequency of the mode as ν_0, its linewidth as Γ, its height as H_r and its asymmetry as B_r in the r-frame, then the *complex* Fourier transform in time associated to the mode reads

$$\widehat{y_r}(\nu) = \sqrt{H_r}\left(\frac{1}{1 + jx} - jB_r\right) , \tag{4.50}$$

[7] I am getting slightly ahead of myself here, as the numerical tools I use in this toy model are the same I used for the bulk of my work, which I present in the next few chapters. As such, for the moment, I deliberately give no further details as regards either of these codes or how I used them. These details can be found in the Chapter 5.

where $x = 2(\nu - \nu_0)/\Gamma$ is the reduced frequency, the notation y refers to $\delta T/T_o$, the subscript r refers, as before, to quantities measured in the Lagrangian frame, and j is the imaginary unit. The modulus squared of the above expression, which corresponds to the power spectrum of the quantity y, indeed yields an asymmetric line profile corresponding to Equation 4.7

$$\left|\widehat{y_r}\right|^2(\nu) = H_r \frac{(1 + B_r x)^2 + B_r^2}{1 + x^2} \,. \tag{4.51}$$

Naturally, the same is true for the τ-frame counterpart of y, where the eigenfrequency ν_0 and the linewidth Γ remain the same, but the height and asymmetry may differ. The inverse Fourier transform of Equation 4.50 is readily derived, and one finds

$$y_r(t) = A_r \exp^{-\pi\Gamma t + 2\pi j \nu_0 t}\,\Theta(t) + j\frac{A_r B_r}{\pi\Gamma}\delta(t) \tag{4.52}$$

$$y_\tau(t) = A_\tau \exp^{-\pi\Gamma t + 2\pi j \nu_0 t}\,\Theta(t) + j\frac{A_\tau B_\tau}{\pi\Gamma}\delta(t) \,, \tag{4.53}$$

where the functions Θ and δ are the Heaviside and Dirac distributions respectively, A_r refers to the amplitude of the mode in the Lagrangian frame: $A_r \equiv \sqrt{\pi\Gamma H_r}$, and A_τ is its τ-frame counterpart. Note that the time series derived from the Fourier transform should be subjected to a normalising factor, depending both on the convention used for the definition of the Fourier transform and the total observation time. However, since this factor is identical for y_r and y_τ, it is not relevant to the following calculations, and we take it as unity. Plugging Equation 4.52 into Equation 4.49 and expanding the β-th power, one finds

$$y_\tau(t) = (1 - \alpha\beta)\left(A_r \exp^{-\pi\Gamma t + 2\pi j \nu_0 t}\,\Theta(t) + j\frac{A_r B_r}{\pi\Gamma}\delta(t)\right) - \alpha \sum_{i=2}^{\infty} C_\beta^i \left(A_r \exp^{-\pi\Gamma t + 2\pi j \nu_0 t}\,\Theta(t) + j\frac{A_r B_r}{\pi\Gamma}\delta(t)\right)^i \,, \tag{4.54}$$

where I simply separated the terms $i = 0$ and $i = 1$ from all others in the expansion, and C_n^k refers to the 'k among n' binomial coefficient. Among the many terms arising from the expansion in the second term on the right-hand side, only the term $i = 2$ affects the mode under consideration. Indeed, it can be seen that all other terms are either proportional to $\exp(2\pi n j \nu_0 t)$, with $n \geqslant 2$, in which case its influence on the $\nu = \nu_0$ mode is negligible, or it is of second or higher order in B_r, in which case, given the small typical values of the asymmetry, it is also negligible. For the same reason, in the $i = 2$ term, only the crossed term in the expansion of the square is retained. As such, one finds

$$y_\tau(t) = (1 - \alpha\beta)\left(A_r \exp^{-\pi\Gamma t + 2\pi j \nu_0 t}\,\Theta(t) + j\frac{A_r B_r}{\pi\Gamma}\delta(t)\right) - \alpha\frac{\beta(\beta - 1)}{2} \times 2j\frac{A_r^2 B_r}{\pi\Gamma}\delta(t) \,. \tag{4.55}$$

Finally, identifying the $\Theta(t)$ and $\delta(t)$ terms in Equation 4.55 with those of Equation 4.53, one finds

$$A_\tau = (1 - \alpha\beta)A_r \,, \tag{4.56}$$

$$B_\tau = B_r\left(1 - \frac{\alpha\beta(\beta - 1)}{1 - \alpha\beta}\right) \,, \tag{4.57}$$

which gives the amplitude and asymmetry of the τ-frame intensity spectrum as a function of their Lagrangian-frame counterparts.

Equations 4.56 and 4.57 encompass every qualitative aspect of the opacity effect as I described them above. Let me consider separately the effect on mode amplitude and the effect on mode asymmetry

- it can be seen from Equation 4.56 that the amplitude reduction due to the opacity effect is a purely linear phenomenon, as the ratio A_τ/A_r does not depend on the amplitude of the oscillation. This is further supported by the fact that it only depends on the $i = 0$ and $i = 1$ terms in the expansion of Equation 4.54, which are precisely the terms that would have been retained, had I linearised the expression from the start. Since both α and β are positive, we further have $A_\tau < A_r$; if, in addition, the product $\alpha\beta$ is sufficiently close to unity – which, as can be seen from Figure 4.9, is the case throughout the entire p-mode spectrum –, the amplitude reduction becomes quite significant. As a crude estimate, for instance, taking $\beta = 7.5$ and $\alpha^{-1} \sim 8.5$, one finds $A_\tau/A_r \sim 0.1$. This is in agreement with the results of Georgobiani et al. (2003), who report in their

simulation a temperature amplitude reduction from ~ 30 K to ~ 2 K (see their Figures 6 and 7 respectively). Since this ratio does not depend on the amplitude of the modes, a similar amplitude reduction is to be expected in the real solar case. What this means, therefore, is that *the Lagrangian temperature perturbation is not an appropriate proxy for the emergent intensity spectrum*: adopting δT as proxy would lead to a severe overestimation of the mode amplitude in intensity. I will have the opportunity to elaborate on this point in Chapter 6, and more specifically in Section 6.3;

- on the other hand, Equation 4.57 shows that the asymmetry change due to the opacity effect is a non-linear effect, as the ratio B_τ/B_r does depend on the mode amplitude A_r. This is further supported by the fact that, had I linearised the expression for δT_τ given by Equation 4.49 from the start, the $i > 1$ terms in the above expansion would have vanished, and I would simply have obtained $B_\tau = B_r$. As such, in the limit $A_r \to 0$, the asymmetry remains unchanged by the opacity effect. Equation 4.57 gives us an estimate for the amplitude threshold above which B_τ starts significantly departing from B_r

$$A_{\text{threshold}} \sim \frac{1-\alpha\beta}{\alpha\beta(\beta-1)} \,. \tag{4.58}$$

  Again, because the product $\alpha\beta$ is fairly close to unity, this threshold is substantially smaller than unity. Adopting the same crude estimates as above ($\beta = 7.5$, $\alpha^{-1} \sim 8.5$), one finds $A_{\text{threshold}} \sim 0.02$. In the 3D simulation studied by Georgobiani et al. (2003), plugging in visually-estimated values of the spectral height and linewidth of the r-frame modal temperature line profile as illustrated in their Figure 6, one finds $A_r \sim 5 \times 10^{-3}$, which is only slightly below the predicted value of $A_{\text{threshold}}$. This explains why their τ-frame asymmetry B_τ differs from its Lagrangian frame counterpart, but not so much as to have a reversed sign, as can be visually inferred from their Figure 7. Actual solar modes are, however, of much smaller amplitude: indeed, they are of the order of several parts per million (ppm) in intensity, meaning that, in terms of temperature fluctuations, $A_r \sim 10^{-6} \ll A_{\text{threshold}}$. The solar p-mode asymmetries in intensity therefore need not be corrected for the non-linear opacity effect, which is negligible at such low amplitudes.

I conclude from this toy model that while the opacity effect is likely to have a drastic impact on the amplitude of the modes observed in the intensity power spectrum, its effect on mode asymmetry is completely negligible in the real solar case, and cannot explain the observed asymmetry reversal puzzle. The reason is that the impact of opacity effects on mode asymmetry is non-linear, and therefore negligible for low-amplitude modes such as the solar p-modes.

4.3 My work in the context of solar-like p-mode asymmetry

There are two main questions surrounding the subject of solar-like p-mode asymmetry, both of which I tackle in the scope of this thesis

1) how can the observed asymmetries help us constrain the properties of the source of excitation of the modes, as well as the properties of the part of the background convective noise that is correlated with the modes?

2) to what physical mechanism is due the asymmetry reversal between the velocity and intensity observables? and how can we use it to further constrain the properties of the source of excitation and the correlated background?

As I showed during the course of this introduction, these two questions have been extensively investigated in the past, but still remain open. Furthermore, the recent observation of skewed line profiles in the power spectrum of solar-like oscillators other than the Sun (Benomar et al. 2018) not only calls for a revisiting of these two questions, but also opens up a third one

3) how can the observed scaling law for asymmetry as a function of the stellar parameters (effective temperature or surface gravity) be used as a tool for seismic diagnosis?

Concerning the first question: as I showed in Section 4.2.1 (for the localised source) and Section 4.2.2 (for the correlated background), our ability to infer their properties from observations is tightly related to the degree of realism that goes in the modelled p-mode power spectrum. It is clear from the account given above that all

attempts, so far, are either based on overly simplified models (in particular concerning the spatial extent of the source of excitation – which is assumed to follow either a Dirac or a Gaussian distribution –, but also the frequency or wavelength dependence of the driving source or the correlated background), or on models that contain so many free parameters that best-fit solutions cannot be uniquely determined (more particularly, since the effect of the localised source and of the correlated background on mode asymmetry takes rigorously the same form, there is a strong degeneracy between the inferred properties of both these components). Using observed asymmetries as a way to constrain these properties therefore requires two things: a model for p-mode excitation that is much more realistic than what has been tried in the context of mode asymmetry so far; and one, what is more, that contains much fewer free parameters – in other words, not an empirical prescription, but a physically-grounded model. In the larger context of solar-like p-mode excitation, several such realistic and physically-grounded models have been proposed and applied to constrain the properties of the source from observed amplitudes – as I showed in Section 2.2.2. But these models have so far found very few uses in the context of p-mode asymmetry.

The first task I undertook, in the beginning of my PhD, was therefore to develop a realistic oscillation synthetic power spectrum model, largely based on the p-mode excitation formalism of Samadi and Goupil (2001). The model contains a *limited* number of *physical* parameters, which allowed me to successfully predict not simply the amplitude of the modes, but also the full shape of their line profiles, and in particular their asymmetry, while providing with useful constraints on the few physical parameters present in the model, pertaining to the spatial and temporal properties of the turbulent velocity spectrum. In the next two chapters, I only concern myself with radial modes (since, as I had the opportunity to point out in Section 4.1, the observed asymmetry are relatively independent of the angular degree l, and mainly depend on the frequency of the modes). Furthermore, the work presented in this first part concerns new theoretical developments, and the short-term goal of this work was to test the validity of these developments. As such, for the moment, I have only applied it to the case of the most finely understood solar-like oscillator: the Sun. Chapter 5, then, is devoted to presenting this synthetic power spectrum model, as well as the results it yielded when applied to the case of solar radial p-modes, with a focus on the velocity power spectrum only.

Answering the second question requires a model with the same qualities as mentioned above. Having at my disposal a synthetic power spectrum model for the solar-like radial p-modes in velocity, it was only natural that I should investigate whether the model could be adapted to intensity observations as well. The short-term goal, in doing so, was to investigated the second question. But the longer-term motivation was to prepare for an investigation of the third question. Indeed, at the present time, for stars other than the Sun, only photometric measurements are resolved enough to allow for a determination of mode asymmetry. Otherwise stated, velocity asymmetry are only observationally available for the Sun, not for other stars. As such, fully understanding question 2) is actually a prerequisite to even starting to consider question 3). The adaptation of my model to photometric measurements is the subject of Chapter 6.

5 Solar radial *p*-mode line profile asymmetry: a realistic predictive model

Contents

> Indulge your passion for science... but let your science be human, and such as may have a direct reference to action and society. Be a philosopher; but amidst all your philosophy, be still a man.
>
> David Hume

This chapter is devoted to the work of Philidet et al. (2020a). All the details of this work are presented in this article, which I reproduce in the end of this chapter. I will not present all these details in the body of the thesis, as this would be redundant. Instead, I focus on the main building steps of my formalism, after which I present the main results of the application of this model to the solar case.

5.1 The formalism

I showed in Chapter 4 that solar-like *p*-mode asymmetry stems primarily from two physical sources: the localisation of the source of excitation, and the convective background correlated with the oscillations. In this chapter, I build on the excitation formalism of Samadi and Goupil (2001) to describe the shape of the *p*-mode line profiles as a function of the turbulent velocity spectrum Φ_{ij} (see Equation 2.95), in such a way that both sources of asymmetry are contained in the model. The first step is to express the observed power spectrum in terms of the Fourier transform in time of the fluid velocity. To do this, I decompose the flow velocity in an oscillatory component $\mathbf{v}_{\rm osc}$ corresponding to the modes, and a background component $\mathbf{u_n}$ corresponding to the turbulent convection. The total velocity is then Fourier transformed in time, projected along the observer line of sight, and integrated over the entire solar disk. Then the modulus squared is expanded, yielding three components in the synthetic power spectrum: one due to the oscillatory component alone, one due to the turbulent background alone, and a crossed term. Neglecting the turbulent background, on account of its small amplitude compared to the resonant mode, and the fact that it constitutes an additive noise, and therefore cannot impact the asymmetry of the modes, one finds (see Philidet et al. 2020a, Eq. 4)

$$P(\omega) = \left(\int \mathrm{d}\Omega \, \mu \widetilde{h}(\mu) \right)^2 \left\langle \left| \widehat{v_{\rm osc}}(\omega) \right|^2 \right\rangle + 2 \int \mathrm{d}\Omega \, \mu \widetilde{h}(\mu) \mathrm{Re} \left(\int \mathrm{d}\Omega \, \widetilde{h}(\mu) \left\langle \widehat{v_{\rm osc}}(\omega) \widehat{u_n}^\star(\omega) \right\rangle \right) , \tag{5.1}$$

where the integrals span over the observed solar disk, and represent the variable visibility of the radial fluid velocity between the center and the limb, weighted by the reduced limb-darkening factor $\widetilde{h}(\mu)$, and $\widehat{v_{\rm osc}}$ and $\widehat{u_n}$ are the Fourier transform in time of the oscillatory and background components of the velocity respectively. The observed power spectrum $P(\omega)$ contains two terms. The first term is the contribution of the *p*-modes to the total observed velocity: the mode line profiles due to this term only contain the asymmetry due to the source localisation. On the other hand, the second term is the contribution of the correlated background to the total observed velocity: this

additional term is susceptible to modify the shape of the mode line profiles, and contains the aforementioned effect of the correlated background on mode asymmetry.

I now need to model $\widehat{v_{\rm osc}}(\omega)$. To this end, I use the adiabatic wave equation that I presented in Chapter 2, with three modifications

- the first modification has to do with the fact that I only consider radial p-modes, so that the Lamb frequency $L_{l=0}$ vanishes. This also means that the Cowling approximation becomes useless, as the perturbation Φ' of the gravitational potential is now easily related to the fluid radial displacement ξ_r. This is done by plugging Equation 2.24 into Equation 2.25, and discarding all horizontal gradients of the wave variables and the equilibrium quantities. One finds (Unno et al. 1989)

$$-\frac{\mathrm{d}\Phi'}{\mathrm{d}r} = 4\pi G\rho_0\xi_r \,. \tag{5.2}$$

  Because of this simple relation, the order of the system is not increased by taking Φ' into account, and the wave equation remains of second-order in the radial coordinate;

- the second modification consists in not discarding the convective velocity in the wave equation any longer. More precisely, I retain the non-homogeneous forcing term stemming from the non-linear advection term in the momentum equation. This results in a source term in the wave equation, which represents turbulent emission from the perturbation of the Reynolds stress force which I introduced in Section 2.2.2;

- the third modification consists in including the effect of linear damping by adding, by hand, a damping contribution in the wave equation, similarly to what I did in Equation 4.27 (see also Abrams and Kumar 1996). This extra damping term is characterised by a damping rate γ, for which I use observed solar values (see Philidet et al. 2020a, Table 1).

With these three modifications, the inhomogeneous wave equation becomes (see Philidet et al. 2020a, Eq. 8)

$$\frac{\mathrm{d}^2\Psi_\omega}{\mathrm{d}r^2} + \left(\frac{\omega^2 + j\omega\Gamma_\omega}{c^2} - V(r)\right)\Psi_\omega = S(r) \,, \tag{5.3}$$

where the wave variable $\Psi_\omega(r)$ is related to $\widehat{v_{\rm osc}}(r,\omega)$ through (see Philidet et al. 2020a, Eq. A.28)

$$\Psi_\omega(r) = \frac{rc(r)\sqrt{\rho_0(r)}}{j\omega}\widehat{v_{\rm osc}}(r,\omega) \,, \tag{5.4}$$

the acoustic potential is slightly modified compared to Equation 4.26 (because of the inclusion of the perturbed gravitational potential) to

$$V(r) = \frac{N(r)^2 - 4\pi G\rho_0(r)}{c(r)^2} + \frac{2}{x(r)^2}\left(\frac{\mathrm{d}x}{\mathrm{d}r}\right)^2 - \frac{1}{x(r)}\frac{\mathrm{d}^2x}{\mathrm{d}r^2} \,, \tag{5.5}$$

and the source term is given by (see Philidet et al. 2020a, Eq. 7)

$$S(r) \equiv \frac{r}{c(r)\sqrt{\rho_0(r)}}\frac{\mathrm{d}p_t'}{\mathrm{d}r} = \frac{r}{c(r)\sqrt{\rho_0(r)}}\frac{\mathrm{d}}{\mathrm{d}r}\left[\rho u_r u_r - \langle\rho u_r u_r\rangle\right] \,, \tag{5.6}$$

where p_t' is the Eulerian perturbation of the turbulent pressure, and u_r the turbulent part of the radial velocity. As I mentioned in Section 4.2.1, the general solution of this inhomogeneous wave equation is

$$\Psi_\omega(r) = \int \mathrm{d}r_s G_\omega(r,r_s)S(r_s) \,, \tag{5.7}$$

where $G_\omega(r,r_s)$ is the Green's function associated to the wave equation, i.e. its solution when the source term is replaced by a Dirac distribution centered on $r = r_s$

$$S(r) = \delta(r - r_s) \,. \tag{5.8}$$

It becomes apparent, then, that modelling the wave variable $\Psi_\omega(r)$ – and therefore, through Equations 5.1 and 5.4, modelling the observed power spectrum – requires two ingredients: the Green's function and the source term.

The first ingredient is obtained numerically, according to the procedure described in Section 3.2 of Philidet et al. (2020a). In broad lines, I use a solar equilibrium model constructed with the 1D evolutionary code CESTAM, on top of which a solar atmosphere computed with the CO^{5}BOLD code, averaged temporally and horizontally, is patched. This provides with the equilibrium quantities appearing in the homogeneous part of the wave equation (Equation 5.3). The total inhomogeneous wave equation, where the source term is given by Equation 5.8, is then integrated numerically using a fourth-order Runge-Kutta scheme, with boundary conditions imposing a null radial displacement at the center, and a vanishing Lagrangian pressure perturbation at the surface. This procedure allows me to compute the radial profile of the Green's function $G_\omega(r, r_s)$ for any given angular frequency ω *and* any source position r_s: it can be considered completely known.

The second ingredient is the statistical properties of the turbulent source of excitation $S(r)$, i.e. those of the turbulent velocity field. It is precisely those properties that I strive to constrain. More precisely, the first term in the right-hand side of Equation 5.1 depends on the fourth-order correlation product of the turbulent velocity, while the second term in the right-hand side depends on its third-order correlation product. The challenge, therefore, consists in prescribing the form taken by these high-order correlations in the case of stellar turbulent convection. First, they must be expressed in terms of second-order correlations, through adapted closure relations. This is done, for fourth-order terms, by adopting the Quasi-Normal Approximation[1] (see Philidet et al. 2020a, Eq. 14), and for third-order terms, by adopting the closure relation of Belkacem et al. (2006), in the scope of the Plume Closure Model (see Philidet et al. 2020a, Eq. 15). The core idea behind the Plume Closure Model (PCM thereafter) is the assumption that the gas close to the surface of the star is organised in separate upflows and downflows, each being characterised by a turbulent velocity that follows a Gaussian distribution. The total velocity field is therefore characterised by a bi-Gaussian distribution, and the asymmetry between the upflows and downflows – the latter being more turbulent – skews the total distribution, thus yielding non-zero third-order moments[2]

Once this is done, only the second-order moment of the turbulent velocity – i.e. its two-point, two-time covariance – needs to be prescribed. I adopt exactly the same prescription as Samadi and Goupil (2001), and details of this prescription can be found both in their paper or in the one reproduced in the end of this chapter. In short, the second-order moment is described in terms of its Fourier transform in space and time Φ_{ij} (see Equation 2.95), which takes the form (see Philidet et al. 2020a, Eqs. 17 and 18)

$$\begin{aligned}\Phi_{ij}(\mathbf{k},\omega) &\equiv \int \mathrm{d}^3\mathbf{k} \int \mathrm{d}\omega \, \left\langle u_i(\mathbf{R},t) u_j(\mathbf{R}+\mathbf{r},t+\tau)\right\rangle \exp^{j(\omega\tau+\mathbf{k}\cdot\mathbf{r})} \\ &= \frac{E(k)}{4\pi k^2}\left(\delta_{ij} - \frac{k_i k_j}{k^2}\right) \times G \times \chi_k(\omega) \,, \end{aligned} \tag{5.9}$$

where the first factor on the right-hand side of Equation 5.9 is the spatial part, written in the case of isotropic incompressible turbulence, and only depends on the energy spectrum $E(k)$; the second factor G is an anisotropy factor, relevant in the stellar context where the turbulent eddies are distorted in the radial direction, and given by (see Philidet et al. 2020a, Eq. B.10)

$$G \equiv \int_{-1}^{1} \mathrm{d}\mu \left(1 - \frac{Q^2\mu^2}{(Q^2-1)\mu^2+1}\right) , \tag{5.10}$$

$$Q^2 \equiv \frac{\left\langle u_\theta^2\right\rangle}{\left\langle u_r^2\right\rangle} = \frac{\left\langle u_\phi^2\right\rangle}{\left\langle u_r^2\right\rangle} , \tag{5.11}$$

where u_θ and u_ϕ are the two horizontal components of the turbulent velocity; and the third factor is the temporal turbulent spectrum. The spatial turbulent energy spectrum $E(k)$ is then given by the Kolmogorov spectrum,

[1] I already discussed the shortcomings of this approximation in Section 1.2.3, and it may seem odd that I should adopt it here. But these shortcomings were related, as I showed, to the third-order moments of the turbulent velocity. By contrast, the dependence of the two-point, fourth-order moment on space increment is relatively well reproduced by the QNA, as shown by Belkacem et al. (2006). As far as mode asymmetry is concerned, therefore, the QNA is acceptable to model the fourth-order moment of the turbulent velocity.

[2] Let me note that the PCM also yields fourth-order moments that are different than in the QNA, so that, strictly speaking, it would have been more consistent to adopt the PCM for both third- and fourth-order moments at the same time. However, the fourth-order moments yielded by the PCM and the QNA are not too dissimilar from one another, in particular when it comes to the dependence of the two-point correlation products on the space increment. Since it is precisely this dependence that is primarily important for mode asymmetry, as the rest of the derivation presented in this Chapter shows, this apparent inconsistency has, in reality, no bearing on the resulting asymmetries.

extended to small wavevectors by a constant function, so that (see Philidet et al. 2020a, Eq. 19)

$$E(k) = 0.652\,\frac{u_0^2}{k_0} \text{ if } 0.2\,k_0 < k < k_0 \tag{5.12}$$

$$0.652\,\frac{u_0^2}{k_0}\left(\frac{k}{k_0}\right)^{-5/3} \text{ if } k_0 < k\,, \tag{5.13}$$

where $u_0^2 \equiv \left(u_r^2 + u_\theta^2 + u_\phi^2\right)/3$, the factor 0.652 is introduced so that the turbulent energy spectrum is properly normalised, and k_0 is the *injection scale*, i.e. the norm of the wavevectors at which the turbulent kinetic energy is injected into the turbulent cascade (see Section 1.2.1). The turbulent energy spectrum, in this prescription, only depends on k_0 and u_0. As for the temporal spectrum, we follow Belkacem et al. (2010) and write it as a truncated Lorentzian function (see Philidet et al. 2020a, Eq. 23)

$$\chi_k(\omega) = \begin{cases} \dfrac{1}{2\omega_k \arctan(\omega_E/\omega_k)}\,\dfrac{1}{1+(\omega/\omega_k)^2} & \text{if } \omega < \omega_E\,, \\ 0 & \text{if } \omega_E < \omega\,, \end{cases} \tag{5.14}$$

where ω_E is the frequency at which the spectrum is truncated, and ω_k is a typical angular frequency associated to the turbulent eddies of size k. The first factor in the right-hand side of Equation 5.14 is introduced so that the spectrum is properly normalised. This form is justified by the following arguments: large eddies, having a long lifetime – i.e. a small value of ω_k – have an evolution in time that is dominated by the intrinsic processes happening inside these eddies, which makes them decay exponentially, thus leading to a Lorentzian spectrum; on the other hand, the evolution of the small eddies is dominated by their advection by large eddies – an assumption referred to as the *sweeping hypothesis* –, thus leading to a Gaussian spectrum (Belkacem et al. 2010). Since the Gaussian function decreases much more rapidly with frequency than the Lorentzian function, the Lorentzian part of the temporal spectrum largely dominates the Gaussian part, so that I neglect the latter, and set it to zero. In the scope of the Kolmogorov hypotheses (Kolmogorov 1941), the typical angular frequency ω_k associated to the turbulent eddies of size k scales as ku_k, where u_k is the typical velocity of these eddies, given by (Stein 1967)

$$u_k^2 = \int_k^{2k} \mathrm{d}k\; E(k)\,. \tag{5.15}$$

However, following Balmforth (1992a), I account for the uncertainty in this scaling relation by introducing a dimensionless parameter λ such that

$$\omega_k = \frac{2ku_k}{\lambda}\,. \tag{5.16}$$

As for the cut-off frequency ω_E in the spectrum, it is related to the timescale over which the eddies of size k are advected, or swept, by the energy-bearing eddies. It is also referred to as the Eulerian microscale, and is given by (Belkacem et al. 2010)

$$\omega_E = ku_0\,. \tag{5.17}$$

The temporal spectrum therefore only depends on u_0 and λ.

Putting these two ingredients together – the Green's function and the statistical properties of the turbulent velocity – for a set of possible source positions r_s located in the region covered by the 3D CO^{5}BOLD simulation yields, through Equation 5.7, an expression for $\Psi_\omega(r)$ for any given angular frequency ω. Then, using Equations 5.1 and 5.4, I obtain the observed power spectrum $P(\omega)$ for any given angular frequency ω, and for any observation radius I want. Once the computation is performed for a set of different angular frequencies ω, this provides with an analytical expression for the velocity p-mode spectrum, containing both the effect of the modes themselves *and* the effect of the correlated background, and whose shape can be reconstructed point by point. Naturally, this synthetic spectrum features resonant peaks centered on the eigenfrequencies of the problem, and if the power spectrum is computed for a sufficient number of angular frequencies within the linewidth of such a mode, its line profile can be 'resolved', and adjusted with Equation 4.7. This entire procedure yields a value of the asymmetry parameter B for any given solar radial p-mode.

However, the implementation of this procedure is contingent on the estimation of the various parameters introduced in the statistical model for the turbulent velocity (i.e. u_0, k_0, Q^2 and λ). Some of these parameters are accessible directly through the 3D hydrodynamic simulation of the solar atmosphere mentioned above: this is the case for all one-point statistics of the turbulent velocity, i.e. u_0 and Q^2. However, k_0 and λ depend on the two-point statistics of the turbulent velocity, and are not as easily extracted from the simulation. I followed two different models

- in the 'numerical spectrum' model, I extracted $E(k)$ directly from the simulation, with the idea that the relevant part of the energy spectrum pertains to the large, resolved scales of motion, so that the spectrum in the simulation is a realistic depiction of the actual large-scale spectrum in the Sun. I isolated each horizontal slice in the simulation, and computed a 2D power spectrum of turbulent velocity in each of them. Integrating over the angular variable gave me a numerical estimation of $E(k)$ in the simulation. In this model, k_0 is no longer needed, and λ is the only free parameter that remains;

- in the 'theoretical spectrum' model, I left k_0 as a free parameter, but assumed that it could only take two values, one below the photosphere and one above. This assumption stems from a similar behaviour observed for the vertical profile of k_0 in 3D simulations (Samadi et al. 2003). The injection scale, therefore, is described in terms of its value above the photosphere $k_{0,\mathrm{atm}}$ as well as the ratio $R_k \equiv k_{0,\mathrm{int}}/k_{0,\mathrm{atm}}$ between the injection scale in the two regions. In this model, the only free parameters that remain are λ, $k_{0,\mathrm{atm}}$ and R_k.

These two models are complementary. The 'theoretical spectrum' model contains multiple free parameters, so that no prediction can be made with it; but since they are physical parameters, they can act as control parameters allowing us to *explore the effect of the physics of turbulence on p-mode asymmetry*. On the other hand, the 'numerical spectrum' model only contains one free parameter, and since this parameter can be related to its physical role (i.e. the how the lifetime of the turbulent eddies depend on their size), it can actually be constrained by other means (see for instance Samadi et al. (2001) who constrained it using observed solar p-mode amplitudes); this model allows me to *give quantitative predictions regarding the p-mode asymmetries in any stellar model*.

As I warned the reader in the beginning of this chapter, I have not detailed all the calculations leading to this formalism. However, it is important, for more clarity, to explicitly spell out the hypotheses and assumptions I made in the course of these derivations. While the prescription for the turbulent spectrum is similar to the choice of Samadi and Goupil (2001), this approach significantly diverges from their, in the sense that they were only interested in the overall amplitude of the modes, while I explicitly solve for their entire line profile, through the derivation of the Green's function for all individual frequencies within the line profile of the modes, and its convolution with the source term. Nevertheless, several underlying hypotheses are common to their work, namely

(H1) I assumed that *the length scale of turbulence (i.e. the energy-bearing eddy size) is separated from the scale of stratification (i.e. the pressure scale height) as well as the scale of the modes (i.e. their wavelength).* This scale separation is not valid in the subsurface layers of the star, where, in particular, the mode wavelength becomes comparable to the eddy size responsible for the driving of the p-modes. For want of a better alternative, I nevertheless adopt this approximation;

(H2) I assumed a *plane-parallel geometry* for the atmosphere of the star. Since I only consider radial modes, which have radial wavevectors, this assumption is physically justified;

(H3) I considered *adiabatic oscillations*. As I showed in Section 2.1, this assumption is not verified in the superficial layers of the star. Nevertheless, as I am interested in the velocity power spectrum, and that velocity is a dynamical variable rather than a thermal variable, non-adiabatic effects are much less likely to significantly impact the properties of the modes;

(H4) in prescribing the second-order correlation product of turbulent velocity, I assumed *a stationary, homogeneous and incompressible turbulence*. The stationarity is a consequence of the mechanical and thermal equilibrium conditions. The homogeneity is justified by the fact that the stratification of the equilibrium medium has very little impact on the driving of the modes (Stein 1967). The incompressible limit requires a bit more thought, but can ultimately be justified by the fact that the flow remains subsonic in the entire superficial region of the star, as shown, for instance, by Stein and Nordlund (2001);

(H5) the one-point statistical properties of the turbulent velocity field – i.e. u_0 and Q^2 – are extracted from the CO^{5}BOLD 3D hydrodynamic simulation. Therefore, I only have access to these quantities in the superficial layers overlapping with the simulation box, meaning that *I only considered mode driving in the first outer 2% of the Sun.* This assumption is not restrictive, seeing as this is where most of the stochastic excitation occurs.

Hypotheses (H2) to (H5) are physically justified. This is not so much the case for hypothesis (H1), more specifically for high-frequency modes that have smaller wavelengths, so that the scale separation assumption becomes questionable[3]. Nevertheless, observed p-mode excitation rates are correctly reproduced theoretically under hypothesis (H1), so that I adopt the latter throughout the entire p-mode spectrum.

5.2 Results and discussion

In the 'theoretical spectrum' model, I tweaked every control parameter to observe how the asymmetry profile[4] $B(\nu)$ varies with the physics of the solar surface turbulence. The results are collected in Figures 5, 6 and 7 of Philidet et al. (2020a), which I reproduce in Figure 5.1. In broad strokes, I find that 1) the asymmetry profile hardly depends on the absolute value of the injection scale k_0, but instead 2) it largely depends on the relative value of the injection scale between the regions located above and below the photosphere, especially for high-frequency modes; and 3) the asymmetry profile only starts depending on λ if the latter is decreased below ~ 1.

The first two points show that the relative contribution of the subsurface layers (below the photosphere) and of the atmospheric layers (above the photosphere) to mode driving is of primary importance for p-mode asymmetry, more particularly for high-frequency modes. This is in accordance with the introductory discussion proposed in Section 4.2.1, where I remarked that a source located within the acoustic cavity of the modes creates asymmetry depending on its position relative to the nodes and antinodes of the eigenfunctions of the cavity, whereas a source located outside always creates negative asymmetry. When the spatial extent of the driving region is correctly accounted for, the total asymmetry is a combination of both cases, and it is only natural that it should drastically depend on the relative weight with which each region contributes to the total driving of the modes. A logical corollary is that any model for p-mode asymmetry that either considers point-like driving sources, or accounts for the spatial extent of the source in a non-physical manner – and, to the best of my knowledge, all preexisting models until now fell into one of these categories–, *cannot possibly hope to make any correct inference of the source properties using observed p-mode asymmetries.* I insist, however, on the fact that in the present study, unlike prior studies on the subject, the goal is not to *infer* the position or spatial extent of the source: rather, I use an analytical prescription for the turbulent velocity spectrum to *input* the position and spatial extent of the source, and it is the parameters of the turbulence prescription that I *infer* from the model.

The third point listed above is not as straightforwardly interpreted, but can be ascribed to the two limiting behaviour of the temporal turbulent velocity spectrum $\chi_k(\omega)$. It is flat for low angular frequencies, and follows an inverse square law for high angular frequencies. The threshold between the two regimes is $\omega \sim \omega_k$: depending on whether the angular frequency of the modes is smaller or greater than ω_k, the properties of mode driving – and therefore, those of the asymmetry profile – are susceptible to be different in the two regimes. Equation 5.16, with typical solar values of $k \sim 10^{-6}$ m^{-1}, $u_k \sim 10^3$ m.s^{-1} and $\omega \sim 10^{-3}$ rad.s^{-1}, shows that this threshold in ω_k translates into a threshold for $\lambda \sim 1$, which corresponds to the observation I made earlier. Finally, to the results listed above, I add 4) that the effect of the correlated background on p-mode asymmetry – in the velocity power spectrum – is negligible compared to the effect of the source localisation, with a relative weight never exceeding $\sim 3\%$.

Concerning the 'numerical spectrum' model, the resulting asymmetry profile is shown in Figure 12 of Philidet et al. (2020a), which I reproduce in Figure 5.2, and where the value $\lambda = 0.5$ constrained by Samadi et al. (2001) is

[3] If the scale separation is no longer valid, then it is no longer the $\mathbf{k} = \mathbf{0}$ component of the Fourier transform of the *fourth-order moment* of the turbulent velocity that interacts with the mode, but a finite $\mathbf{k}$-component instead, where $\mathbf{k}$ is the wavevector of the mode. In turn, this means that the driving of the modes involves two-wavevector-interaction of the turbulent cascade between pairs of wavevectors $\mathbf{p}$ and $\mathbf{q}$ such that $\mathbf{p} + \mathbf{q} = \mathbf{k}$ instead of $\mathbf{0}$. But two such wavevectors $\mathbf{p}$ and $\mathbf{q}$ are much less likely to be simultaneously characterised by a high energy in the turbulent cascade if $\mathbf{p} + \mathbf{q} = \mathbf{k}$ than if $\mathbf{p} + \mathbf{q} = \mathbf{0}$: mode driving becomes much less efficient.

[4] In the following, I will use the phrase *asymmetry profile* to refer to the curve obtained when the asymmetry parameter B of the radial modes are plotted against the frequency of the modes. Since, as I mentioned in Section 4.1, p-mode asymmetry hardly depends on angular degree, the asymmetry profile corresponds to the slowly varying function of frequency onto which the asymmetry of all solar p-modes collapses.

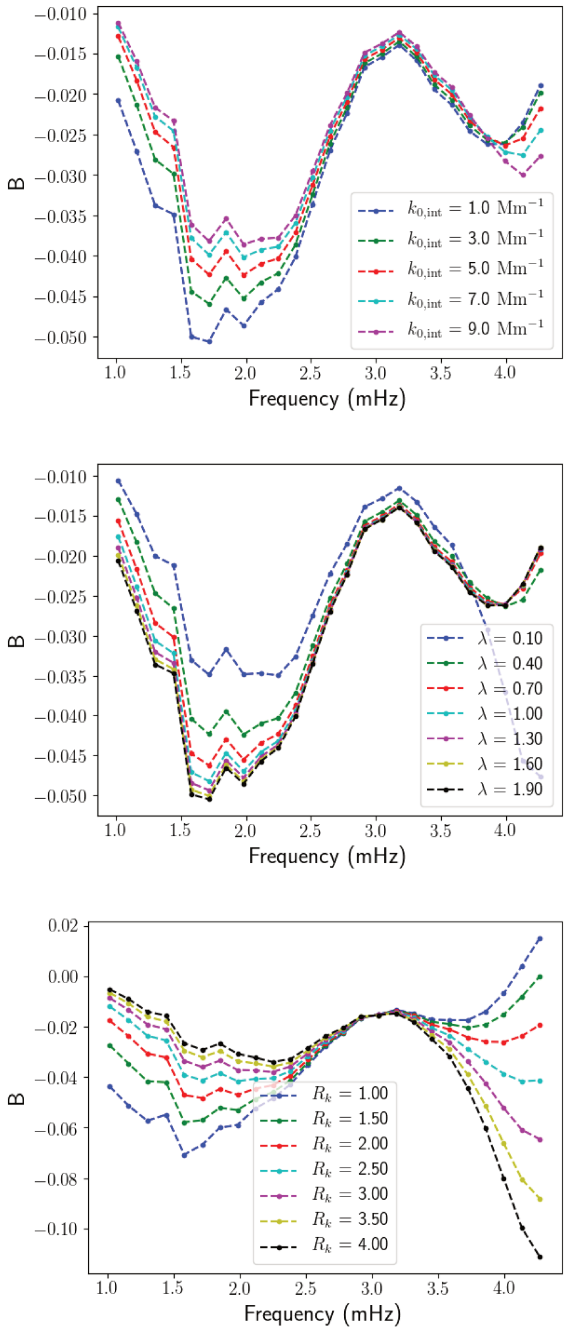

Figure 5.1: **Top**: Asymmetry parameter B as a function of frequency, obtained in the scope of the 'theoretical spectrum' model, for different values of $k_{0,\mathrm{atm}}$, with $\lambda = 1$ and $R_k = 2$ (see text for the definitions of these parameters). **Middle**: Same, but for different values of λ, and $k_{0,\mathrm{atm}} = 2$ Mm^{-1}. **Bottom**: Same, but for different values of R_k, and $k0,\mathrm{atm} = 2$ Mm^{-1} and $\lambda = 1$. Credits: Philidet et al. (2020a).

adopted. Very good quantitative agreement is found across the entire p-mode spectrum, from which I conclude that the approach presented here is valid for the inference of p-mode asymmetries in solar-like oscillators. However, as I mentioned in the last section of Chapter 4, asymmetries are only observed in the intensity power spectrum for solar-like oscillators other than the Sun. Therefore, this model alone is only of limited use until it is adapted to photometric measurements. This is the subject of the next chapter.

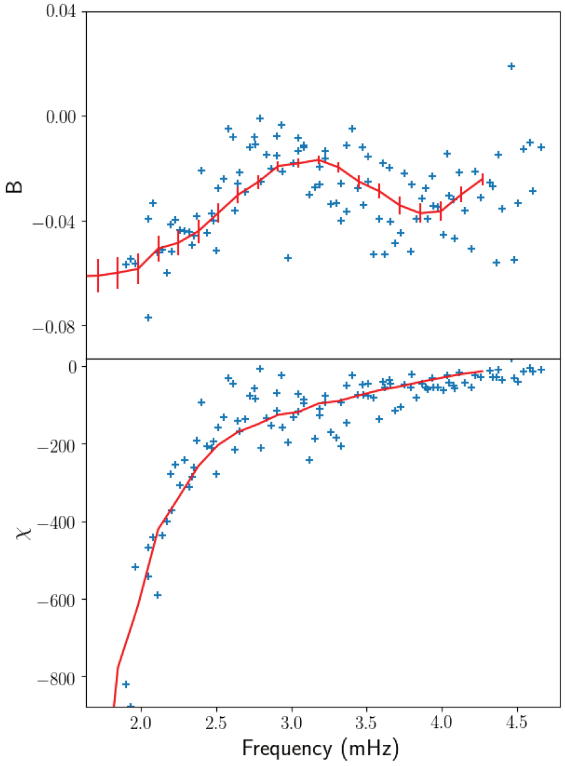

Figure 5.2: Asymmetry profile obtained through the 'numerical spectrum' model (solid red line), with $\lambda = 0.5$, compared to the observed asymmetry profile (blue crosses). The data points are taken from Barban et al. (2004). For more readability, only data points corresponding to modes with angular degrees $15 \leqslant l \leqslant 20$ have been retained. The asymmetry profile is given in terms of the parameter B defined by Equation 4.7 **(top)**, and in terms of the asymmetry parameter χ defined by Equation 4.12 **(bottom)**. The error bars in the top panel correspond to the uncertainty on the observed values of the mode linewidths, which propagates to the asymmetry parameter B. Credits: Philidet et al. (2020a).

A&A 635, A81 (2020)
https://doi.org/10.1051/0004-6361/201936847

Astronomy & Astrophysics

Modelling the asymmetries of the Sun's radial *p*-mode line profiles

J. Philidet[1], K. Belkacem[1], R. Samadi[1], C. Barban[1], and H.-G. Ludwig[2,3]

[1] LESIA, Observatoire de Paris, PSL Research University, CNRS, Université Pierre et Marie Curie, Université Paris Diderot, 92195 Meudon, France
e-mail: jordan.philidet@obspm.fr
[2] Zentrum für Astronomie der Universität Heidelberg, Landessternwarte, Königstuhl 12, 69117 Heidelberg, Germany
[3] GEPI, Observatoire de Paris, PSL Research University, CNRS, Université Pierre et Marie Curie, Université Paris Diderot, 92195 Meudon, France

Received 5 October 2019 / Accepted 16 January 2020

ABSTRACT

Context. The advent of space-borne missions has substantially increased the number and quality of the measured power spectrum of solar-like oscillators. It now allows for the *p*-mode line profiles to be resolved and facilitates an estimation of their asymmetry. The fact that this asymmetry can be measured for a variety of stars other than the Sun calls for a revisiting of acoustic mode asymmetry modelling. This asymmetry has been shown to be related to a highly localised source of stochastic driving in layers just beneath the surface. However, existing models assume a very simplified, point-like source of excitation. Furthermore, mode asymmetry could also be impacted by a correlation between the acoustic noise and the oscillating mode. Prior studies have modelled this impact, but only in a parametrised fashion, which deprives them of their predictive power.

Aims. In this paper, we aim to develop a predictive model for solar radial *p*-mode line profiles in the velocity spectrum. Unlike the approach favoured by prior studies, this model is not described by free parameters and we do not use fitting procedures to match the observations. Instead, we use an analytical turbulence model coupled with constraints extracted from a 3D hydrodynamic simulation of the solar atmosphere. We then compare the resulting asymmetries with their observationally derived counterpart.

Methods. We model the velocity power spectral density by convolving a realistic stochastic source term with the Green's function associated with the radial homogeneous wave equation. We compute the Green's function by numerically integrating the wave equation and we use theoretical considerations to model the source term. We reconstruct the velocity power spectral density and extract the line profile of radial *p*-modes as well as their asymmetry.

Results. We find that stochastic excitation localised beneath the mode upper turning point generates negative asymmetry for $\nu < \nu_{\max}$ and positive asymmetry for $\nu > \nu_{\max}$. On the other hand, stochastic excitation localised above this limit generates negative asymmetry throughout the *p*-mode spectrum. As a result of the spatial extent of the source of excitation, both cases play a role in the total observed asymmetries. By taking this spatial extent into account and using a realistic description of the spectrum of turbulent kinetic energy, both a qualitative and quantitative agreement can be found with solar observations performed by the GONG network. We also find that the impact of the correlation between acoustic noise and oscillation is negligible for mode asymmetry in the velocity spectrum.

Key words. methods: numerical – turbulence – Sun: helioseismology – Sun: oscillations – line: profiles

1. Introduction

Solar-like oscillations are known to be stochastically excited and damped by turbulence occurring close to the surface of low-mass stars (see e.g. Goldreich & Keeley 1977a,b or Samadi et al. 2015 for a review). The power spectral density of such oscillations is expected to feature a Lorentzian-shaped peak centred around their eigenfrequencies. This idealised line profile has been extensively used to fit observations (see e.g. Jefferies et al. 1991). However, as the resolution reached in helioseismic measurements (both ground-based and space-borne) has increased, it has become apparent that the observed line profiles feature a certain degree of asymmetry (see e.g. Duvall et al. 1993 for observations made at the geographic South Pole; Toutain et al. 1998 for data from the MDI and SPM instruments aboard the SOHO spacecraft).

Since the discovery of this skew symmetry in solar *p*-mode line profiles, several studies have been devoted to explaining this feature. In particular, it had been recognised early on that a source of excitation that is highly localised compared to the mode wavelength (which we refer in the rest of the paper as "source localisation") could lead to a certain degree of mode asymmetry, depending on the position of the source (Gabriel 1992, 1993; Duvall et al. 1993; Abrams & Kumar 1996; Roxburgh & Vorontsov 1995, 1997). Line profile asymmetries have then been used to infer some properties of the turbulent source, especially its radial location and its multipolar nature (see e.g. Roxburgh & Vorontsov 1997; Nigam et al. 1998).

Furthermore, Duvall et al. (1993) noticed an inversion of the sense of asymmetry between spectrometric and photometric measurements, with line profiles in the velocity spectrum featuring more power in their low-frequency wing than in their high-frequency wing and vice-versa for line profiles in the intensity spectrum. Since intensity perturbations were expected to be proportional to velocity perturbations, one would have expected the asymmetries to be the same. Many hypotheses were posited to explain this puzzling result. Duvall et al. (1993) suggested that it was due to non-adiabatic effects lifting the proportionality relationship between the two kinds of perturbations (fluid displacement and temperature) but this hypothesis was later contradicted by Rast & Bogdan (1998). Non-adiabaticity was brought up again later on by Georgobiani et al. (2003) who suggested

that the explanation resided in radiative transfer between the mode and the medium. Indeed, the observed radiation temperature corresponds to the gas temperature at local optical depth $\tau = 1$. But optical depth depends on opacity, which non-linearly depends on temperature. Therefore, the temperature fluctuations due to the oscillating mode entails opacity fluctuations, which in turn impacts the "observed" radiation temperature. Given the non-linear nature of the $\kappa - T$ relation, this modulation decreases the observed temperature fluctuations more significantly in the low-frequency wing of the mode than in its high-frequency wing. Since this radiative transfer does not impact the velocity measurements, this could explain the asymmetry reversal between velocity and intensity spectra. Using 3D simulations, Georgobiani et al. (2003) computed mode line profiles in both the velocity and the intensity power spectrum alternatively at mean unity optical depth and instantaneous unity optical depth. Their results indeed show that the modulation of the "observed" intensity fluctuations due to radiative transfer could be significant enough to reverse the sense of mode asymmetry. One of the hypothesis enjoying the most support for asymmetry reversal, however, is based on the effect of turbulent perturbations partially correlated with the mode, which thus impact its line profile (Nigam et al. 1998; Roxburgh & Vorontsov 1997; Rast & Bogdan 1998; Kumar & Basu 1999). Indeed, a part of these perturbations is coherent with the mode and, thus, leads to interference. This interference term may be constructive or destructive, depending on the phase difference between the mode and the coherent turbulent perturbations. For frequencies at which the interference is constructive, the power spectral density is slightly elevated, whereas it drops slightly for frequencies at which it is destructive. Typically, in the vicinity of a resonant mode, the dependence of the phase difference between mode and turbulent perturbation is such that the interference term is constructive for frequencies located in one wing of the mode and destructive in the other. Therefore, as a result of this interference behaviour, one of the wings falls off more slowly and the other more rapidly, leading to mode asymmetry. It has been suggested that the degree of correlation between the turbulent perturbations and the oscillation it excites is higher in intensity than in velocity, so that it changes the sign of mode asymmetry only in the intensity spectrum. While it is widely accepted that correlated turbulent perturbations must be taken into account to explain asymmetries in the intensity spectrum, the question of whether it has a significant impact on the velocity spectrum remains an open issue (see e.g. Jefferies et al. 2003).

The possibility that correlated turbulent fluctuations have an affect on mode asymmetry has led many authors to include them in their models for the power spectrum. Even though correlated noise was introduced to explain the particular puzzle of asymmetry reversal between velocity and intensity measurements, several models include correlated noise in the velocity spectrum as well as in the intensity spectrum. This is the case for the model developed by Severino et al. (2001) and later used, for instance, by Barban et al. (2004), which includes three types of noise (coherent-correlated, coherent-uncorrelated and incoherent) in both the velocity spectrum, the intensity spectrum, and the velocity-intensity cross-spectrum. They considered, however, that the "pure oscillation" (without the noise) has a Lorentzian shape, thus discarding the contribution of source localisation. This model was later refined by Wachter & Kosovichev (2005) to take this contribution into account.

These prior studies have one thing in common, however, and that is that they all treat the various sources of asymmetry (mainly source localisation and correlated noise) in a simplified, parametrised fashion. Indeed, the excitation is consistently modelled as a point-like source, with radial position and multipolar development left as free parameters. This prescription remains somewhat unsatisfactory in the sense that it does not take into account the finer properties of the source of excitation, such as its spatial extent or its dependence on frequency, for instance. As such, these prior models lack a realistic description of the source of excitation. Likewise, for models including the effect of noise on the power spectrum, the various relative amplitudes and phase differences between modal oscillation and correlated noise in both spectra are also left as free parameters. The approach followed by these studies is to find best-fit values for all their free parameters by fitting their model to observations in order to localise the source.

In contrast, in the present paper, we follow a different approach: we model both the source of excitation and the correlated background by constraining their properties using an analytical model of stochastic excitation, coupled with a 3D simulation of the solar atmosphere. The novelty of our approach lies in the fact that we do not fit a parametrised model to the observations but, instead, we predict the dependence of mode asymmetry on frequency, which we then compare to observations in order to validate our model. Our model of mode asymmetry is, therefore, both more realistic (in its description of the source of excitation) and more complete (in its lack of freely adjustable parameters). It can then be used to deepen our understanding of the underlying physical mechanisms behind mode asymmetry by exploring how varying a given physical constraint impacts the results yielded by our model. Finally, our model allows for a much higher predictability of mode asymmetry, which is essential when it comes to applying these results to other solar-like oscillators. We note that this paper is devoted to the modelling of the velocity power spectrum only and, as a result, we do not address the problem of asymmetry reversal, which is a separate challenge altogether.

These efforts to model the line profiles of solar-like oscillations are also necessary in order to correctly infer mode properties from observations. Indeed, it was discovered early on that using a Lorentzian shape to fit skew symmetric line profiles led to a significant bias in the eigenfrequency determination, which may be higher than the frequency resolution achieved by helioseismic measurements (Duvall et al. 1993; Abrams & Kumar 1996; Chaplin et al. 1999; Thiery et al. 2000; Toutain et al. 1998). Such eigenfrequency determination bias has also been revealed for solar-like oscillations in stars other than the Sun by Benomar et al. (2018). Inversion methods used to infer the internal structure of solar-like oscillators, whether they be analytical or numerical, require a very accurate determination of the mode eigenfrequencies. For spectra extracted from very long time series, the resolution is high enough that this bias in eigenfrequencies impacts the results obtained by inversion methods (see e.g. Toutain et al. 1998, who show that the difference between the sound speed squared inferred from symmetric and asymmetric fits can reach 0.3% in the core). When fitting these observations, mode asymmetry must, therefore, be taken into account. Since it has proven very difficult to determine accurate mode eigenfrequency without prior knowledge on its line shape, obtaining an a priori model of p-mode line profiles is of primary importance.

In this paper, we present a predictive model of solar radial p-mode line profile in the velocity spectrum. In particular, we use a realistic model for stochastic excitation, following a method similar to that of Samadi & Goupil (2001). Furthermore, we include the effect of correlated turbulent perturbations in the

model in a non-parametrised way, unlike what was done in previous works (see e.g. Severino et al. 2001). The paper is structured as follows: we present the analytical model of the Sun's velocity power spectral density in Sect. 2 and its numerical implementation in Sect. 3. We then present the results yielded by our model concerning mode asymmetry in Sect. 4. In Sect. 5, we briefly describe the development of a toy model to describe the impact of source localisation on mode asymmetry and use it to interpret our results; we also investigate the matter of the influence of correlated turbulent perturbations. We then confront our results with the related observations in Sect. 6 and discuss the issue of eigenfrequency determination bias entailed by the skewness of the mode line profiles.

2. Modelling the p-mode line profiles

To extract the asymmetries of solar radial p-modes, we first need to model their line profile in the velocity power spectrum. In this section, we present the analytical developments that led us to this model. First, we define the disc-integrated velocity power spectrum in terms of the radial fluid displacement. We then present the inhomogeneous, radial wave equation associated to the acoustic modes and detail how convolving its Green's function with its inhomogeneous part gives us access to the velocity power spectral density.

2.1. Definition of the velocity power spectral density

Before embarking on a discussion of the actual modelling of the line profiles, the spectrum from which they are extracted needs to be defined. In this paper, we restrict ourselves to the study of radial acoustic modes in the Sun. Furthermore, as part of the definition of the spectrum, we include the effect of limb-darkening and of disk integration that affect the Sun-as-a-star measurements. We note, however, that other instrumental effects – in particular mode leakage – are not accounted for.

To derive an expression for the observed power spectral density, we separate the total surface velocity into an oscillatory part $\boldsymbol{v}_{\rm osc}$ and a turbulent part $\boldsymbol{u}$, where it is understood that the modes are described by the oscillatory part. The observations made for the Sun-as-a-star are obtained by integrating the velocities over the entire solar disk. Neither the mode velocity (for radial modes), nor the turbulent perturbations depend on the point of the disk at which it is estimated; however, the projection on the line of sight $\boldsymbol{n}$ does. This integration over the solar disk is affected by limb-darkening $h(\mu)$ (where μ refers to the cosine of the angle between the local radial direction and the line of sight). Furthermore, since it is the turbulent perturbations that excite the mode, a certain fraction of the former must be correlated with the latter, so that the contribution of turbulent perturbations to the velocity spectrum must be considered.

With these considerations, the observed velocity power spectral density can be expressed as

$$P(\omega) = \frac{1}{\int \mathrm{d}\Omega\, h(\mu)} \left\langle \left| \int \mathrm{d}\Omega\, h(\mu) \left(\widehat{\boldsymbol{v}_{\rm osc}}(\omega) + \widehat{\boldsymbol{u}}(\omega)\right) . \boldsymbol{n} \right|^2 \right\rangle, \tag{1}$$

where the integration is performed over the solar disk, Ω refers to the solid angle, $\boldsymbol{n}$ is the unit vector along the line of sight, $\boldsymbol{v}_{\rm osc}$ is the mode velocity, $\boldsymbol{u}$ represents the fluctuations of the turbulent velocity around its mean value, ω is the angular frequency, the notation $\widehat{.}$ refers to temporal Fourier transform, and $\langle . \rangle$ refers to ensemble average. Since we are only considering radial modes, $\boldsymbol{v}_{\rm osc}$ is exclusively radial. Thus, Eq. (1) becomes

$$P(\omega) = \left\langle \left| \widehat{v_{\rm osc}}(\omega) \int \mathrm{d}\Omega\, \mu \widetilde{h}(\mu) + \int \mathrm{d}\Omega\, \widetilde{h}(\mu) \widehat{u_n}(\omega) \right|^2 \right\rangle, \tag{2}$$

where u_n is the component of the turbulent velocity along the line of sight. We introduced the reduced limb-darkening $\widetilde{h}(\mu)$ so that its integral over the solar disk is normalised to unity.

We expand the square in the above expression and we consider that the term containing $\langle |\widehat{u_n}|^2 \rangle$ is negligible compared to the terms that contain $\langle |\widehat{v_{\rm osc}}|^2 \rangle$ and $\mathrm{Re}\left(\langle \widehat{u_n} \widehat{v_{\rm osc}}^\star \rangle\right)$, respectively. Indeed, the power spectral density is several orders of magnitude higher for the mode velocity than for the turbulent velocity (typically, the former is of order $10^5\,\mathrm{m^2\,s^{-2}\,Hz^{-1}}$, while the latter is of order $10\,\mathrm{m^2\,s^{-2}\,Hz^{-1}}$, e.g. Turck-Chièze et al. 2004, Fig. 2), so that

$$\langle |\widehat{u_n}|^2 \rangle \ll \mathrm{Re}\left(\langle \widehat{u_n} \widehat{v_{\rm osc}}^\star \rangle\right) \ll \langle |\widehat{v_{\rm osc}}|^2 \rangle, \tag{3}$$

where the notation Re refers to the real part of a complex quantity, and $\star$ refers to its complex conjugate. Finally, we obtain

$$\begin{aligned} P(\omega) = &\left(\int \mathrm{d}\Omega\, \mu\, \widetilde{h}(\mu) \right)^2 \left\langle \left| \widehat{v_{\rm osc}}(\omega) \right|^2 \right\rangle \\ &+ 2 \int \mathrm{d}\Omega\, \mu\, \widetilde{h}(\mu) \mathrm{Re}\left(\int \mathrm{d}\Omega\, \widetilde{h}(\mu) \left\langle \widehat{v_{\rm osc}}(\omega) \widehat{u_n}^\star(\omega) \right\rangle \right). \end{aligned} \tag{4}$$

The first term corresponds to the spectral power density of the mode velocity $v_{\rm osc}$. In itself, the line profile generated by this term is already asymmetric; indeed, it has been known for a long time that source localisation can generate line profile asymmetry (see e.g. Abrams & Kumar 1996; Roxburgh & Vorontsov 1997; Chaplin & Appourchaux 1999). The second term corresponds to what the literature commonly refers to as correlated turbulent perturbations and which is also expected to significantly impact mode asymmetry in photometric measurements (see e.g. Nigam et al. 1998; Roxburgh & Vorontsov 1997; Kumar & Basu 1999), although its importance in velocity measurements is not as clear.

2.2. The inhomogeneous wave equation

Going further, we write the radial wave equation associated to $v_{\rm osc}$ with the same formalism as Unno et al. (1989). We detail its derivation in Appendix A. Although we included both the source terms due to Reynolds stress fluctuations and non-adiabatic pressure fluctuations in the computation detailed in Appendix A, we only consider the former in the following. Indeed, it is the dominant source of excitation for acoustic modes in the Sun (e.g. Belkacem et al. 2008). When it is temporally Fourier transformed, the inhomogeneous wave equation for radial modes reads:

$$\frac{\mathrm{d}^2 \Psi_\omega}{\mathrm{d}r^2} + \left(\frac{\omega^2}{c^2} - V(r) \right) \Psi_\omega = S(r), \tag{5}$$

where c is the sound speed, the wave variable $\Psi_\omega(r)$ is related to the radial fluid displacement $\xi_r(r)$ through

$$\Psi_\omega(r) = rc(r) \sqrt{\rho_0(r)} \xi_r(r), \tag{6}$$

and the acoustic potential and source term are given by

$$\begin{aligned} V(r) &= \frac{N^2 - 4\pi G\rho_0}{c^2} + \frac{2}{x^2}\left(\frac{\mathrm{d}x}{\mathrm{d}r}\right)^2 - \frac{1}{x}\frac{\mathrm{d}^2x}{\mathrm{d}r^2}, \\ x(r) &= \frac{r\sqrt{I}}{c}, \\ S(r) &= \frac{r}{c\sqrt{\rho_0(r)}}\frac{\mathrm{d}p_t'}{\mathrm{d}r}, \\ I(r) &= \exp\left(\int_0^r \frac{N^2}{g_0} - \frac{g_0}{c^2}\,\mathrm{d}r'\right), \end{aligned} \tag{7}$$

where r is the radial coordinate, ρ_0 is the density, N is the Brunt-Väisälä frequency, g_0 is the gravitational acceleration, G is the gravitational constant, and p_t' refers to the fluctuations of the Reynolds stress around its mean value. Indeed, only the fluctuating part of the Reynolds stress contributes to the source term $S(r)$ and its mean value only modifies the equilibrium structure. The subscript 0 refers to the equilibrium structure and all the above quantities are dependent on the radius at which they are estimated, even when not explicitly specified. We note that we only model radial modes in this paper, so that the wave equation (Eq. (5)) is of the second order despite the fact that we did not use the Cowling approximation.

Mode damping is not included in Eq. (5). Indeed, we did not take into account the feedback of modal oscillations on the equilibrium state through modulations in the fluid density, pressure, opacity, etc. Such feedback allows mechanical work and thermal transfer to occur from the mode to the medium in which it develops; depending on the phase-lag between these different modulations energy can be exchanged with the surrounding medium. However, the modelling of damping rates of solar-like oscillations is extremely difficult (Samadi et al. 2015). Thus, we directly introduce damping in the wave equation in the form of a mode lifetime, or, equivalently, by a (frequency-dependent) linewidth Γ_ω, so that the wave equation takes the following form

$$\frac{\mathrm{d}^2\Psi_\omega}{\mathrm{d}r^2} + \left(\frac{\omega^2 + j\omega\Gamma_\omega}{c^2} - V(r)\right)\Psi_\omega = S(r), \tag{8}$$

where j denotes the imaginary unit and the linewidths Γ_ω are inferred from observations. We used the line-widths presented in Baudin et al. (2005) (see their Table 2), which were inferred from GOLF data. Note, however, that our definition of Γ_ω corresponds to their Γ multiplied by 2π, or equivalently to twice their damping rate η. We completed these data with low-frequency line-widths obtained by Davies et al. (2014) through BiSON, which go as low as $\sim$900 μHz (see their Table 1). We reproduce the dependence of the linewidth we used on frequency in Table 1. We note that damping can potentially be a source of mode asymmetry. However, the impact of damping on mode asymmetry is very weak compared to the other sources of asymmetry (Abrams & Kumar 1996), so that the direct introduction of observed linewidths in our model is unlikely to have an impact on our results.

2.3. Expression of the velocity power spectral density

By definition, the Green's function $G_\omega(r_\mathrm{o}, r_\mathrm{s})$ is the value taken by the function Ψ_ω at the radius $r = r_\mathrm{o}$ (the variable r_o refers to the height in the atmosphere at which the spectrum is observed and the variable r_s refers to the position of the point-like source term), where Ψ_ω is the solution to the inhomogeneous wave equation,

$$\frac{\mathrm{d}^2\Psi_\omega}{\mathrm{d}r^2} + \left(\frac{\omega^2 + j\omega\Gamma_\omega}{c^2} - V(r)\right)\Psi_\omega = \delta(r - r_\mathrm{s}), \tag{9}$$

Table 1. Observational linewidth Γ_ω used in Eq. (8) as a function of frequency ν.

ν (μHz)	Γ_ω (μHz)	ν (μHz)	Γ_ω (μHz)
972.615	0.0055	2828.15	0.94
1117.993	0.0091	2963.29	0.80
1263.198	0.022	3098.16	1.08
1407.472	0.033	3233.13	1.12
1548.336	0.082	3368.56	1.84
1686.594	0.20	3504.07	2.83
1749.33	0.26	3640.39	3.85
1885.10	0.28	3776.61	5.90
2020.83	0.47	3913.49	8.09
2156.79	0.54	4049.46	10.73
2292.03	0.74	4186.98	12.69
2425.57	0.88	4324.79	16.39
2559.24	0.94	4462.08	17.35
2693.39	0.92	4599.96	26.42

Notes. The data are extracted from Baudin et al. (2005) for frequencies higher than 1750 μHz, and from Davies et al. (2014) below. When a frequency laid between these points, linear interpolation was used.

and δ refers to the Dirac function. Once the Green's function is known, it can be used to express explicitly v_osc in Eq. (4). Indeed, on the one hand, the general solution to the inhomogeneous wave equation with a source term $S(r_\mathrm{s})$ is

$$\Psi_\omega(r_\mathrm{o}) = \int \mathrm{d}r_\mathrm{s}\; G_\omega(r_\mathrm{o}, r_\mathrm{s}) S(r_\mathrm{s}), \tag{10}$$

where the source term is given by Eq. (7). The pulsational velocity v_osc is related to the variable Ψ_ω through

$$v_\mathrm{osc}(r_\mathrm{o}) = \frac{j\omega}{r_\mathrm{o} c(r_\mathrm{o})\sqrt{\rho_0(r_\mathrm{o})}}\Psi_\omega(r_\mathrm{o})\,. \tag{11}$$

Using the source term given by Eq. (7) in Eqs. (10) and (11) and after finally performing an integration by part, we write the velocity Fourier transform at angular frequency ω as

$$\begin{aligned} \widehat{v_\mathrm{osc}}(\omega, r_\mathrm{o}) = &-\frac{j\omega}{r_\mathrm{o} c(r_\mathrm{o})\sqrt{\rho_0(r_\mathrm{o})}} \\ &\times \int \mathrm{d}^3\boldsymbol{r}_\mathrm{s}\; \boldsymbol{\nabla}\left(G_\omega(\boldsymbol{r}_\mathrm{s}, r_\mathrm{o})\frac{\|\boldsymbol{r}_\mathrm{s}\|}{c(\boldsymbol{r}_\mathrm{s})\sqrt{\rho_0(\boldsymbol{r}_\mathrm{s})}}\right).(\rho_0\widehat{u_r\boldsymbol{u}})(\boldsymbol{r}_\mathrm{s}))\,. \end{aligned} \tag{12}$$

In the following, the observation height r_o will be fixed, so that we drop it for ease of notation. However, since the observation height depends on the transition line used for the observations and on whether the observations rely on spectrometric or photometric measurements, it significantly varies from instrument to instrument (see Sect. 6 for more details).

Using Eq. (12) in Eq. (4) then gives an expression for the velocity power spectral density in terms of Green's function $G_\omega(r_\mathrm{s})$:

$$P(\omega) = \left(\int \mathrm{d}\Omega\,\mu\,\widetilde{h}(\mu)\right)^2\left[\left\langle\left|\widehat{v_\mathrm{osc}}(\omega)\right|^2\right\rangle + C(\omega)\right], \tag{13}$$

where $\left\langle\left|\widehat{v_\mathrm{osc}}(\omega)\right|^2\right\rangle$ and $C(\omega)$ are given, respectively, by Eqs. (B.19) and (B.28). We note that the effects of limb-darkening and disk integration are now contained in a single factor and, thus, these will only have an effect on mode amplitude.

Since the asymmetry of a mode does not depend on its amplitude, it is not impacted by such a factor.

The calculations leading from Eqs. (4)–(13) are detailed in Appendix B. In the following, we only provide the main steps and assumptions. We split the calculations two ways, focussing separately on the first term inside the brackets of Eq. (13), which we hereby refer to as the leading term, and on its second term, which we hereby refer to as the cross term.

2.3.1. Closure models

The calculations leading from Eqs. (4)–(13) involve the evaluation of fourth-order and third-order two-point correlation moments of the turbulent velocity. Therefore, an appropriate closure model is needed to express these high-order moments as a function of second-order moments. We devote the following subsection to presenting and developing these closure models.

Fourth-order moments. To describe the fourth-order correlation moments of the turbulent velocity, we make use of the quasi-normal approximation (QNA). This closure model consists in considering that all turbulent quantities are normally distributed, in which case fourth-order moments can be analytically expressed as a combination of second-order moments (Lesieur 2008):

$$\langle abcd\rangle = \langle ab\rangle\langle cd\rangle + \langle ac\rangle\langle bd\rangle + \langle ad\rangle\langle bc\rangle, \tag{14}$$

where a, b, c, and d refer to any turbulent scalar quantity. Applying the QNA to isotropic, homogeneous turbulence inhibits energy transfers among modes of different wave numbers, thus leading to violations of the energy conservation principle (Kraichnan 1957). This is due to the fact the QNA entails vanishing third-order correlation moments. When it comes to estimating the fourth-order moments, however, the picture is different. Belkacem et al. (2006a) have studied the validity of the QNA for two-points, fourth-order correlation moments of the vertical turbulent velocity, in the form of $\langle u_{r,1}^2 u_{r,2}^2\rangle$ (where the indices 1 and 2 refer to two different points in space), using 3D simulations of the solar atmosphere. They found that the dependence of this correlation moment on the distance ΔX between the two points is correctly estimated by the QNA but that its absolute value (which can be taken as the corresponding one-point moment) is not. Consequently, the amplitude of the modes are largely underestimated when the QNA is used. However, the asymmetry of the modes does not depend on their amplitude, so that mode asymmetry will be unaffected by a discrepancy in the absolute value of the two-points, fourth-order moments. As such, the decomposition given by Eq. (14) can be considered valid when it comes to studying mode asymmetry.

Third-order moments. While the QNA provides an adequate closure relation for fourth-order moments, as mentioned above, it assumes vanishing third-order moments. Therefore, in order to estimate these third-order moments, we make use of another closure model, the Plume closure model (PCM), which was developed by Belkacem et al. (2006b). The idea behind this closure model is to separate the flows directed upwards from those directed downwards (the latter being referred to as plumes) and to apply the QNA to both separately. The anisotropy between the two types of flow – in particular, turbulence is more prominent in the downwards plumes (e.g. Goode et al. 1998) – yields non-vanishing third-order correlation moments:

$$\begin{aligned}\langle u_r(\boldsymbol{R},t)^2 u_r(\boldsymbol{R}+\boldsymbol{r},t+\tau)\rangle = {} & \Big[a(1-a)^3 - a^3(1-a)\Big]\delta u^3 \\ & - a(1-a)\Big[2\langle \widetilde{u_d}(\boldsymbol{R},t)\widetilde{u_d}(\boldsymbol{R}+\boldsymbol{r},t+\tau)\rangle \\ & + \langle \widetilde{u_d}(\boldsymbol{R},t)^2\rangle\Big]\delta u,\end{aligned} \tag{15}$$

where u_r is the vertical component of the turbulent velocity, a is the relative horizontal section of the upflows, δu is the difference between the mean velocity of the two types of flows (considering their respective signs, it actually is the sum of their absolute values), and $\widetilde{u_d}$ is the fluctuation of the vertical velocity around its mean value in the downflows.

We note that, strictly speaking, the third-order moment given by Eq. (15) and yielded by the PCM are centred. However, we consider that the mean value of the overall vertical velocity of the flow is sufficiently low (compared to its standard deviation for instance) to be neglected. Therefore, these moments may interchangeably refer here either to centred or non-centred moments.

We also note that this closure relation is written here in terms of $\widetilde{u_d}$ (i.e. the turbulent fluctuations in the downflows only). It would be more practical to rewrite it in terms of u_r (i.e. the total turbulent fluctuations). The two are related through

$$\langle \widetilde{u_d}(\boldsymbol{R},t)\widetilde{u_d}(\boldsymbol{R}+\boldsymbol{r},t+\tau)\rangle = \frac{1}{1-a}\langle u_r(\boldsymbol{R},t)u_r(\boldsymbol{R}+\boldsymbol{r},t+\tau)\rangle - a\delta u^2. \tag{16}$$

2.3.2. The leading term

In the following, we detail the derivation of the first term of Eq. (13). This term corresponds to the pulsational velocity itself, without correlated turbulent perturbations. As such, any asymmetry featured by this term alone represents the effect of source localisation. The first step consists in separating the scales relevant to the turbulent velocity $\boldsymbol{u}$ from the scales relevant to both the medium stratification and the oscillating mode (respectively, the pressure scale height and the mode wavelength). The scale separation approximation is not realistic in the subsurface layers (in particular, the mode wavelength is comparable to the typical correlation length associated with turbulence); however, for want of a better alternative, we are led to use this approximation in the following.

Since the integral defining $\widehat{v_{\rm osc}}(\omega)$ in Eq. (12) contains the turbulent velocity fluctuations squared, expanding the square of its modulus will raise these fluctuations to the fourth. The contribution of turbulence to the expression of $v_{\rm osc}$ thus takes the form of two-points, fourth-order correlation moments of the turbulent velocity. We use the closure relation presented and detailed in Sect. 2.3.1 to express them as a function of second-order moments.

We then use analytical expressions for the second-order moments of the turbulent velocity. We describe the second-order moment of the ith and jth component of the turbulent velocity in terms of its spatial and temporal Fourier transform $\phi_{ij}(\boldsymbol{k},\omega)$. For isotropic turbulence, it reads (Batchelor 1953):

$$\phi_{ij}(\boldsymbol{k},\omega) = \frac{E(k,\omega)}{4\pi k^2}\left(\delta_{ij} - \frac{k_i k_j}{k^2}\right), \tag{17}$$

where $E(k,\omega)$ is the specific turbulent kinetic energy spectrum, k is the norm of the wavevector $\boldsymbol{k}$, k_i and k_j are its ith and jth component, and δ_{ij} is the Kronecker symbol. The integration over the solid angle of wave vectors $\boldsymbol{k}$ is straightforward, and only an integral over the norm of $\boldsymbol{k}$ remains. However, solar turbulence close to the photosphere is known to be highly anisotropic.

To take this anisotropy into account, we follow the formalism developed by Gough (1977). In this formalism, the integral over the solid angle of $\boldsymbol{k}$ is simply readjusted by adding an anisotropy factor given by Eq. (B.10) (see Appendix B in Samadi & Goupil 2001).

Following Stein (1967), we then decompose $E(k, \omega)$ into a spatial part $E(k)$, which describes how the turbulent kinetic energy is distributed among modes of different wave numbers, and a temporal part $\chi_k(\omega)$, which describes the statistical distribution of the life-time of eddies of wavenumber k

$$E(k, \omega) = E(k)\chi_k(\omega). \tag{18}$$

In order to model the spatial and temporal part of the spectrum of turbulent kinetic energy, we followed two different approaches, described in the following.

The "theoretical spectrum" model. We use theoretical prescriptions to model both the spatial spectrum $E(k)$ and the temporal spectrum $\chi_k(\omega)$ of turbulent velocity. Based on the assumption that turbulent flows are self-similar, Kolmogorov's theory of turbulence leads to a spatial spectrum $E(k) \propto k^{-5/3}$ in the inertial range, between $k = k_0$ (where k_0 is the scale at which the kinetic energy is injected in the turbulent cascade, and is henceforth referred to as the injection scale) and the dissipation scale (at which the turbulent kinetic energy is converted into heat). Given the very high Reynolds number characterising solar turbulence ($\mathrm{Re} \sim 10^{14}$), we cast the dissipation scale to infinity. Then, following Musielak et al. (1994), we extend the turbulent spectrum below the injection scale by considering that $E(k)$ takes a constant value for $k < k_0$. This extended spectrum, referred to as the broadened Kolmogorov spectrum (BKS) was introduced to account for the broadness of the maximum of $E(k)$. The BKS can be written as

$$E(k) = \begin{cases} 0.652\dfrac{u_0^2}{k_0} & \text{if } 0.2\ k_0 < k < k_0 \\ 0.652\dfrac{u_0^2}{k_0}\left(\dfrac{k}{k_0}\right)^{-5/3} & \text{if } k_0 < k, \end{cases} \tag{19}$$

where $u_0^2 \equiv \langle \boldsymbol{u}^2(\boldsymbol{r})\rangle/3$ and the 0.652 factor is introduced so that the total specific kinetic energy of the turbulent spectrum matches $u_0^2/2$. Therefore, the spatial spectrum is parametrised solely by the injection scale k_0. However, the injection scale varies significantly between the sub-surface layers and the atmosphere (Samadi et al. 2003), so that we keep it free in our model and allow for it to depend on the radial coordinate r.

Following Samadi et al. (2003), we consider a Lorentzian shape for the temporal spectrum $\chi_k(\omega)$, which is supported both by numerical simulations (Samadi et al. 2003) and by theoretical arguments. Indeed, a noise described by a stationary, Gaussian Markov process in time is expected to relax exponentially, meaning that the resulting eddy-time correlation is expected to be a decreasing exponential, and its Fourier transform a Lorentzian function (Belkacem et al. 2011). The width ω_k associated to eddy-time correlation is linked to the life-time of the eddies of wavenumber k. Dimensional arguments would suggest that $\omega_k \propto k u_k$, where u_k is the typical velocity associated to the eddies of wavenumber k. However, there remains a substantial indetermination on the actual value of ω_k, so that, following Balmforth (1992), we consider:

$$\omega_k = 2ku_k/\lambda, \tag{20}$$

where λ is a dimensionless, constant parameter. Overall, the only input parameters of this model are $k_0(r)$ and λ.

The "numerical spectrum" model. In the second model, we extract the spatial spectrum $E(k)$ from a 3D hydrodynamic simulation of the solar atmosphere, provided by the CO^{5}BOLD code (see Sect. 3 for details). This simulation gives us access to the velocity field as a function of all three spatial coordinates and time. In order to extract the turbulent spectrum $E(k)$, we average the velocity field temporally, then isolate each horizontal slice in the simulated cube and perform a 2D Fourier transform of each slice separately, thereof which we only retain the radial part. This gives us a spectrum $E(k)$ for each vertical point in the simulation. Finally, we renormalise each spectrum so that

$$\int_0^{+\infty} \mathrm{d}k\ E(k) = \frac{u_0^2}{2}, \tag{21}$$

where u_0 is also extracted from the 3D atmospheric simulation, by averaging the fluid velocity squared temporally and horizontally, and using the definition $u_0^2 = \langle \boldsymbol{u}^2(\boldsymbol{r})\rangle/3$.

The temporal spectrum $\chi_k(\omega)$ is also treated in a slightly different manner than in the "theoretical model" above. Indeed, the arguments invoked above to justify the Lorentzian shape of the spectrum, while valid for most of the relevant time scales associated to turbulent eddies, are no longer valid for shorter time scales, that is, for higher angular frequencies. Belkacem et al. (2010) argued that if the time correlation associated to small eddies indeed originates from their advection by larger, energy-bearing eddies – a hypothesis referred to as the sweeping assumption – one recovers a Gaussian spectrum instead of a Lorentzian one. The transition between a Lorentzian spectrum, valid for low angular frequencies, and a Gaussian spectrum, valid for high angular frequencies, occurs at the cut-off angular frequency ω_E, which is given by the curvature of the eddy-time correlation function at $\tau = 0$ (Belkacem et al. 2010):

$$\omega_E = ku_0. \tag{22}$$

Since a Gaussian spectrum would fall off much more rapidly than a Lorentzian spectrum, we simply consider that χ_k vanishes entirely for $\omega > \omega_E$,

$$\chi_k(\omega) = \begin{cases} \dfrac{1}{2\arctan(\omega_E/\omega_k)\omega_k}\dfrac{1}{1+(\omega/\omega_k)^2} & \text{if } \omega < \omega_E \\ 0 & \text{if } \omega_E < \omega. \end{cases} \tag{23}$$

We modified the prefactor so that χ_k meets the normalisation condition. The typical life time of eddies of wavenumber k, parametrised by ω_k, is still given by Eq. (20). We note that the convolution of the function $\chi_k(\omega)$ with itself must be computed to evaluate the leading term (see Eq. (B.13)). While the convolution of a Lorentzian function with itself straightforwardly yields a Lorentzian function with a width twice as large, the convolution of the modified spectrum above with itself is slightly different, but can be obtained analytically as

$$(\chi_k * \chi_k)(\omega) = \frac{1}{2\pi\omega_k}\frac{1}{1+(\omega/2\omega_k)^2} \times \frac{\pi\left(\arctan\left(\dfrac{\omega_E}{\omega_k}\right) - \arctan\left(\dfrac{\omega-\omega_E}{\omega_k}\right)\right)}{4\arctan^2\left(\dfrac{\omega_E}{\omega_k}\right)}. \tag{24}$$

Physically, taking the cut-off frequency into account significantly decreases the predicted amplitudes for high frequency modes. As far as mode asymmetry is concerned, we found that it did not have a significant impact in the "theoretical spectrum"

model. In contrast, it substantially changes mode asymmetry at high frequency in the "numerical spectrum" model, which is why we only introduce it in the latter. The reason is the following: the spatial spectrum of turbulent energy falls off much more rapidly with k in the "theoretical spectrum" than in the "numerical spectrum". Therefore, small spatial scales play a more important role in the latter. Since the cut-off frequency only impacts these small scales, it is natural that taking it into account should only have a significant impact on the "numerical spectrum" model.

2.3.3. The cross term

The derivation of the cross term follows essentially the same steps as for the leading term. The main difference is that the turbulent velocity correlation moments that appear are now two-point, third-order moments. We use the closure relation presented in Sect. 2.3.1 to express them, as we did with the fourth-order moments, as a function of two-point, second-order moments of the turbulent velocity. We then use the same analytical description of second-order moments as the one we used for the leading term. The rest of the calculations is very similar to those described in Sect. 2.3.2 and leads to the second term in Eq. (13).

These two models – the "theoretical spectrum" and "numerical spectrum" models – are complementary in the sense that the first one allows us to explore the impact of the properties of turbulence on mode asymmetries and gives physical insight into this problem, whereas the second one relies on fewer input parameters and, therefore, has more predictive capability (we recall here that the former requires the parameters λ and $k_0(r)$ to be set, while the latter only requires λ). Consequently, in the following, we present and develop the results yielded by both.

3. Numerical implementation

In this section, we detail how we numerically implemented the model presented in Sect. 2. We describe how we obtained the solar equilibrium state in which the acoustic modes develop and how we integrated the inhomogeneous wave equation given by Eq. (8). Having obtained the solar radial p-mode line profiles, we then detail how we extracted their asymmetries and perform several tests to validate our model and its numerical implementation.

3.1. The solar equilibrium state

The acoustic potential given by Eq. (7) depends only on the equilibrium structure of the Sun. We extracted the potential from a 1D solar model provided by the evolutionary code CESTAM (Morel 1997; Marques et al. 2013). The 1D model includes treatment of the convective flux (using standard mixing-length theory with no overshoot) and of the radiative flux (using the Eddington approximation). On the other hand, turbulent pressure, rotation, and diffusion processes are ignored.

However, 1D stellar models do not fully take into account the more complex physical phenomena taking place in the uppermost layers of a star; in particular, the rapid transition between the convective zone and the superficial radiative region (Kupka & Muthsam 2017). This leads to significant biases in the equilibrium structure. Since the excitation of solar oscillations precisely takes place in these layers, it is essential that we model them more accurately. To do so, we use a 3D hydrodynamic simulation of the solar atmosphere computed using the CO^{5}BOLD code

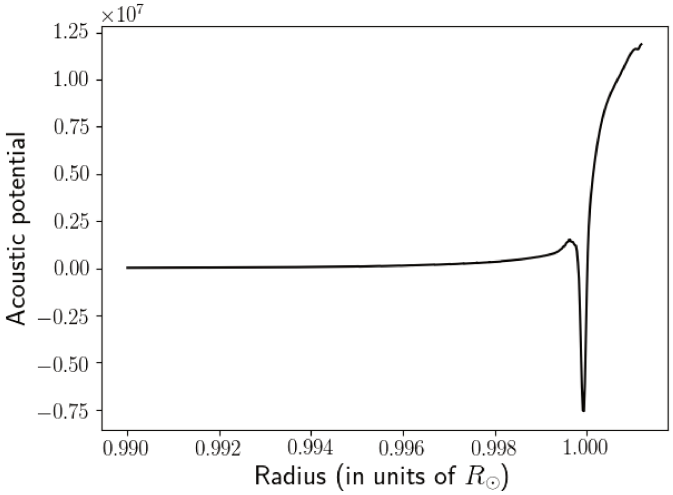

Fig. 1. Acoustic potential $V(r)$ used in Eq. (8), calculated using Eq. (7) and the equilibrium state of the Sun given by the solar patched model described in the text. The radius is normalised by the photospheric radius $R_\odot$, and only the outermost region is shown. We note that the acoustic potential is normalised by $R_\odot^{-2}$ here (where $R_\odot$ is the radius of the solar photosphere) so that it is dimensionless.

(Freytag et al. 2012). The modelled region includes the superadiabatic peak just below the photosphere and goes up to the lower atmosphere of the star.

It is now possible to construct a "patched" model of the solar interior. We use the solar patched model computed by Manchon et al. (2018). The process of constructing patched models has been extensively discussed (e.g. Trampedach 1997; Samadi et al. 2008) and the particular case of the patched model used in this paper is described in much detail in Manchon et al. (2018). The basic idea is to transform the 3D atmosphere into a 1D atmosphere through temporal and horizontal averaging and then to replace the surface layers of the 1D stellar interior with this 1D atmosphere. We note that the input parameters of the CESTAM model used to describe the solar interior (age, total stellar mass, mixing-length parameter $\alpha_{\rm MLT}$, and helium abundance) are chosen so that the top layers match the bottom layers of the CO^{5}BOLD atmosphere. Here the model was computed with the mixing-length parameter $\alpha_{\rm MLT} = 1.65$, an initial helium abundance of $Y_{\rm init} = 0.249$, and an initial metallicity of $Z_{\rm init} = 0.0135$. Figure 1 shows the acoustic potential profile $V(r)$ given by this solar patched model, computed using Eq. (7).

Finally, we use the same simulation of the solar atmosphere to extract the various parameters appearing in the analytical description of the source term; in particular, the standard deviation u_0 associated to turbulent velocities, the anisotropy factor G given by Eq. (B.10), as well as the parameters used in the Plume closure model (see Eq. (15)). Specifically, the ensemble average appearing in the definition of u_0 was computed by performing a temporal and horizontal average of the norm of the velocity squared in the 3D simulation of the solar atmosphere. We also used this same simulation to extract the spatial spectrum of turbulent kinetic energy in the "numerical spectrum" model (see Sect. 2).

3.2. Integration of the inhomogeneous wave equation

To compute one value of $P(\omega)$ for one value of the angular frequency ω (i.e. one point in the velocity power spectrum), we convolve the Green's function $G_\omega(r_{\rm s})$ associated to Eq. (8) with the

stochastic source term $S(r_s)$ (see Sect. 2). It is then possible to reconstruct the velocity power spectral density, and in particular the line profile of the resonant modes, point by point (typically, we only need 10 points regularly spaced between $\omega_0 - \Gamma_{\omega_0}$ and $\omega_0 + \Gamma_{\omega_0}$, where ω_0 is the angular eigenfrequency of the mode and Γ_{ω_0} its linewidth). In the following, we describe how the wave equation was integrated and how we extracted its Green's function.

For a given angular frequency ω, we carry out the integration using a 4th-order Runge-Kutta scheme (Press et al. 1986) with the acoustic potential $V(r)$ given by the solar equilibrium state (see Sect. 3.1). Given that radial modes develop in the entire solar volume, we perform this integration over the entire solar radius, between $r = 0$ and $r = r_{\max}$. We note that $r_{\max}$ refers not to the photospheric radius, but to the maximum radial extent of the solar model described in Sect. 3.1, so that $r_{\max} > r_{\text{photosphere}}$.

We imposed Dirichlet boundary conditions on the wave equation. The condition at the centre is straightforward: by definition, $\Psi_\omega(r = 0) = 0$. At $r_{\max}$, we impose a vanishing Lagrangian pressure perturbation (which physically means that the atmosphere of the Sun is force-free). The continuity equation and the equation of state allow us to rewrite this latter condition in terms of Ψ_ω:

$$\frac{\mathrm{d}\Psi_\omega}{\mathrm{d}r} + \frac{\mathrm{d}}{\mathrm{d}r}\left[\ln\left(\frac{r}{c\sqrt{\rho_0}}\right)\right]\Psi_\omega = 0. \tag{25}$$

The use of Dirichlet boundary conditions leads us to implement a shooting method: we perform the integration with $\Psi_\omega(r = 0) = 0$, and tune the initial slope (i.e. the value of $\mathrm{d}\Psi_\omega/\mathrm{d}r$ at $r = 0$) until the other boundary condition is met. Note that this method is not similar to the shooting method usually implemented to solve the eigenvalue problem associated to the determination of acoustic mode eigenfrequencies: here, the pulsation ω is fixed, and it is the initial slope that is tuned to meet the boundary condition at the surface. The difference between these two methods is that in the inhomogeneous problem, the initial slope (or, alternatively, the amplitude of the mode) is fixed by the amplitude of the source of excitation. The shape of the eigenfunction, however, remains the same as in the homogeneous problem.

This method enables us to extract the Green's function associated to the wave equation (Eq. (8)). To obtain one value of the Green's function $G_\omega(r_s)$, for one value of the pulsation ω and one value of the source position r_s, we carry out the integration of the inhomogeneous equation as described above, adding a point-like source term to the numerical scheme. The source is normalised in such a way that the right-hand side equals $1/h$ when the source falls within the integration radial step, and 0 otherwise (h is the radial step of the integration).

This integration gives us the radial oscillation profile $\Psi_\omega(r)$, and we simply extract its value at a fixed radius r_o, which corresponds to the height in the atmosphere at which the spectrum is measured. We note that the presence of damping in the wave equation implies that it is complex-valued. As such, the Green's function is complex-valued as well.

Finally, to calculate the integrals over source positions which appear in Eqs. (B.19) and (B.28), we compute the Green's function using the above method for a grid of source positions r_s, while ω is kept constant. This grid corresponds to the radial grid provided by the 3D atmospheric model described in Sect. 3.1.

We also use the aforementioned 3D model to extract the physical quantities appearing in both the leading term of Eq. (13) (the anisotropy factor G, the turbulent velocity fluctuations u_0), and the cross term (the parameters a and δw in the PCM; see Sect. 2 for a definition of these parameters).

Using Eq. (13) provided by the model developed in Sect. 2 and the radial grid of Green's functions computed using the above method finally allows us to extract the value of $P(\omega)$ for each value of ω.

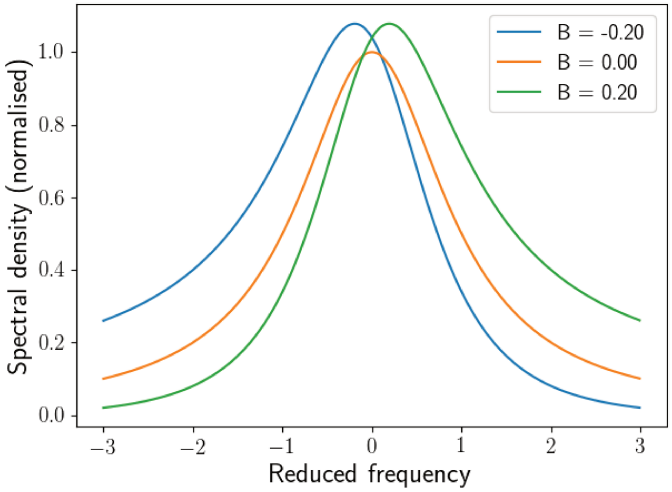

Fig. 2. Dependence of the line profile given by Eq. (26) on the asymmetry parameter B. The line profiles are normalised with $H_0 = 1$.

3.3. Fitting of the mode asymmetries

We fit the line profile of the modes following Nigam & Kosovichev (1998) with the formula

$$P(\omega) = H_0 \frac{(1 + Bx)^2 + B^2}{1 + x^2}, \tag{26}$$

where $x = 2(\omega - \omega_0)/\Gamma_{\omega_0}$ is the reduced pulsation frequency. The fit contains three free parameters (H_0, ν_0 and B), the last of which is defined as the asymmetry parameter. We illustrate the dependence of the line profile on B in Fig. 2. In particular, $B < 0$ means that the peak contains more power in the low-frequency side (that corresponds to negative asymmetry), $B > 0$ means that the high-frequency side contains more power (that corresponds to positive asymmetry), while with $B = 0$ we recover a classic, Lorentzian profile. Figure 2 also shows that the mode does not peak exactly at the eigenfrequency, but rather at a slightly higher (for $B > 0$) or lower value (for $B < 0$). This can have important repercussions for the determination of the mode eigenfrequencies from observations, as we discuss in Sect. 6.3.

Note that several other definitions of the asymmetry parameters can be found in the literature. Korzennik (2005) prefers to adjust the mode line profiles with

$$P(\omega) \propto \frac{1 + \alpha(x - \alpha/2)}{x^2 + 1}, \tag{27}$$

and defines the asymmetry parameter as $\alpha_{n,l}$. Meanwhile, Vorontsov & Jefferies (2013) use the following formula:

$$P = H\left[\left(\frac{A\cos(\phi - S)}{1 - R^2}\right)^2 + B^2\right], \tag{28}$$

where the frequency variable is ϕ, and the asymmetry parameter is defined as S. While these three formulas have been derived in

different ways, they are perfectly equivalent close to the eigenfrequency (for $x \ll 1$, or equivalently for $\phi \equiv 0 \pmod{\pi}$), with $S \sim B \sim \alpha/2$.

Finally, Gizon (2006) provides the asymmetry parameter defined as (see also Benomar et al. 2018):

$$\chi = 2B\omega_0/\Gamma_\omega. \tag{29}$$

The author quantified the mode asymmetry by means of the relative positions of the local maxima (peaks) and minima (troughs) in the power spectral density: minima located half-way between the neighbouring maxima lead to symmetric line profiles, while a deviation from this behaviour leads to asymmetric line profiles. The parameter χ derived from these considerations is independent from both the amplitude and the line-widths of the modes.

The formulas presented above only lead to different line profiles far from the central frequency, whereas they are equivalent in our range of interest. We opted for the definition given by Nigam & Kosovichev (1998) (Eq. (26)) because it is the most commonly used.

To ensure the significance of fitting an asymmetric profile to the mode obtained through our model, we compared the results produced by the fitting formula Eq. (26) and by a symmetric, Lorentzian profile (that is, imposing $B = 0$ in Eq. (26)). The asymmetric fits led to excellent agreement with the modelled line profiles; however, the symmetric fits led to substantial discrepancies, with one wing consistently falling off more rapidly than the numerical line profile and the other too slowly. Finally, it should be noted that the excellent fit given by Eq. (26) to the numerical line profile is independent from the number of points used for the adjustment; we have indeed performed a similar fit with thrice the number of points, without any loss of accuracy and the resulting asymmetry parameter B was the same to an excellent approximation.

3.4. Validation of the method

Using the method presented above, we extracted solar radial modes of radial orders $n = 6$ to $n = 30$. Indeed, the formula used for the fit and given by Eq. (26) does not converge properly for higher-order modes (because the increasing linewidths lead to mode overlapping), while we did not have access to observed linewidths for lower-order modes. In addition to their line profile asymmetries, we also extract other fundamental properties, namely their eigenfrequencies, amplitudes, and eigenfunctions. In the following, to support the validity of our model, we compare the mode properties we obtained with similar properties obtained through other methods.

First, we compare the eigenfrequencies obtained through our model to the eigenfrequencies of the 1D adiabatic oscillations calculated using the ADIPLS code (Christensen-Dalsgaard 2011). For this validation, we did not make use of the patched model described in Sect. 3.1 but, rather, the corresponding unpatched model. The reason is that the patching procedure produces a small discontinuity of the physical quantities at the patching point, which can affect the eigenfrequencies calculated by ADIPLS. We recover the correct eigenfrequencies, with errors not exceeding ~0.1%. Since mode asymmetry is only expected to vary on the scale of ~mHz, modelled asymmetries will not be significantly affected by such small discrepancies of the eigenfrequencies.

Our numerical method also allows us to extract the radial profile $\Psi(r)$ of the eigenmodes. We compare them in Fig. 3 to the eigenfunctions calculated using the same 1D adiabatic oscillations obtained through the ADIPLS code and presented above. The figure shows that the modes obtained through our model have eigenfunctions that are very similar to those obtained through this dedicated code, which further supports the validity of the model we have used.

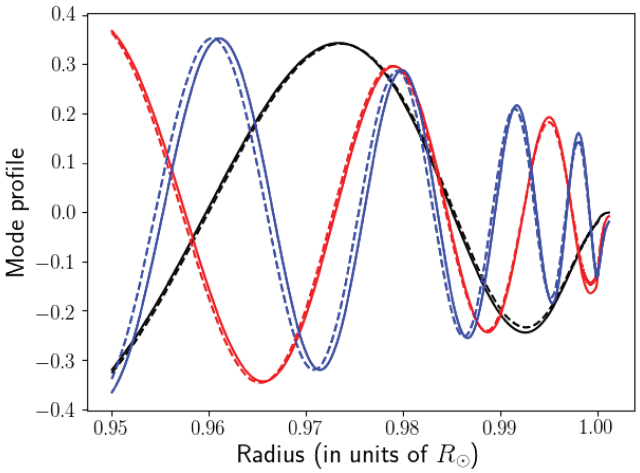

Fig. 3. Eigenfunction $\Psi(r)$ of several radial acoustic modes (black: $n = 10$ ($\nu_0 = 1.580$ mHz); red: $n = 20$ ($\nu_0 = 2.912$ mHz); blue: $n = 30$ ($\nu_0 = 4.267$ mHz)) as computed by our model (solid lines), and calculated using the ADIPLS code (dashed lines). The radial axis is zoomed to show only the outermost region. The eigenfunctions have been normalised so that their maximum over the entire solar interior equals 1.

Finally, we compare the mode amplitudes obtained through our model to the observed ones. To that end, we estimated the velocity power spectrum at an observation height of 340 km, which corresponds to the observation height of the GOLF instrument as estimated by Baudin et al. (2005), following Bruls et al. (1992). By definition, the velocity amplitude squared is the total area under the mode peak, so that it depends both on its maximum H and on its width Γ,

$$\nu_{\mathrm{osc}} = \sqrt{\pi H \Gamma}. \tag{30}$$

We note that when it is used to treat observational data, this formula also contains a geometric factor to account for instrumental effects, including mode visibility. This factor is, however, irrelevant in our case.

We show in Fig. 4 the comparison between the mode amplitudes ν_{osc} obtained through our "numerical spectrum" model and the mode amplitudes inferred from observations performed by the GOLF instrument (Baudin et al. 2005). The free parameter λ of our model (cf. Sect. 2) has been adjusted so as to obtain the best possible agreement. As a consequence, our model does not hold any predictive power when it comes to mode amplitudes. However, the fact that we manage to retrieve a very good agreement with observational data by using reasonable values of the input parameters is still a solid sign that our model is valid. In particular, we correctly recover the frequency at maximum amplitude ν_{max}, as well as the slopes on both the low-frequency and the high frequency limit. To conclude on the matter, we emphasise that the asymmetry parameter B is independent from the mode amplitude, so that potential discrepancies concerning the latter should not affect the former.

4. Results for the asymmetry profile $B(\nu)$

Using the model presented in Sect. 2, numerically implemented using the method presented in Sect. 3, we extract the solar

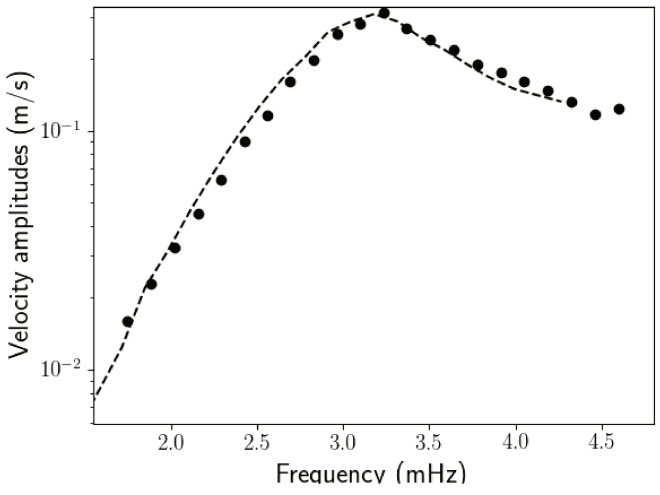

Fig. 4. Velocity amplitudes of radial acoustic modes as computed by our model, using Eq. (30) (black dashed line), and as observed by GOLF (black points). The data points are taken from Baudin et al. (2005). The free parameters in the model have been tuned to obtain the best possible agreement with observational data.

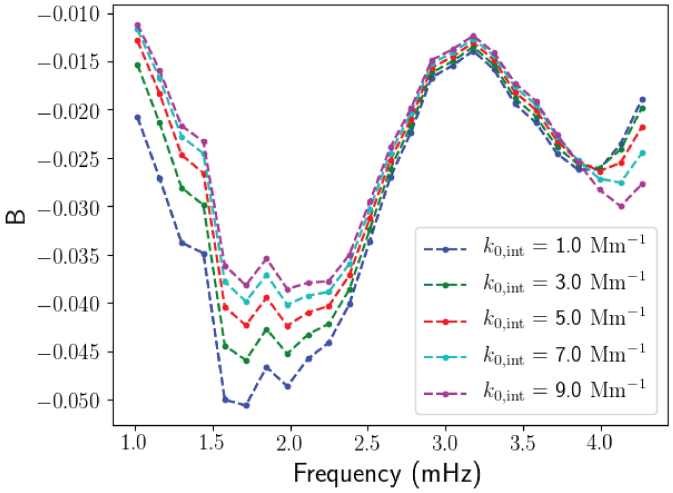

Fig. 5. Asymmetry parameter B as a function of frequency obtained by the "theoretical spectrum" model, for different values of $k_{0,\mathrm{int}}$, with $\lambda = 1$ and $R_k = 2$ fixed. The sub-photospheric injection scale $k_{0,\mathrm{int}}$ is expressed in Mm^{-1}.

p-modes line profile asymmetries $B(\nu)$ throughout a large part of the spectrum, between $n = 6$ ($\nu \sim 1$ mHz) and $n = 30$ ($\nu \sim 4.3$ mHz). In this section, we present the results yielded by our model, focusing on the dependence of the asymmetry parameter B on frequency (which we hereafter shorten to the expression "asymmetry profile") and on the impact of our different input parameters on the asymmetry profile.

As we detailed in Sect. 2, we followed two different approaches to model the turbulent kinetic energy spectrum. The first one, which we refer to as the "theoretical spectrum" model, uses the prescription given by Kolmogorov's theory of turbulence and which we have described in detail in Sect. 2. The second approach, which we refer to as the "numerical spectrum" model, uses the turbulent spectrum extracted from the 3D hydrodynamic simulation of the solar atmosphere described in Sect. 3. In this section, we present separately the asymmetry profile $B(\nu)$ yielded by both models.

4.1. The "theoretical spectrum" model

This model relies on a prescription for the properties of turbulence. It contains the following input parameters: the temporal spectrum of turbulent kinetic energy, parametrised by the dimensionless quantity λ, which is defined by Eq. (20), and its spatial spectrum, parametrised by $k_0(r)$, which is defined as the (radius-dependent) injection wavenumber of turbulent kinetic energy. We let the latter depend on r in order to account for the fact that the typical size of turbulent eddies drastically depends on where they are located with respect to the photosphere. It is known that the size of the energy-bearing eddies increases with height, so that the injection scale k_0 decreases with r (Samadi et al. 2003). We simplify the situation by considering that the injection rate only takes two values: $k_0(r) = k_{0,\mathrm{int}}$ below the photosphere, and $k_0(r) = k_{0,\mathrm{atm}}$ above the photosphere. This picture crudely corresponds to what is observed in 3D atmospheric simulations (Samadi et al. 2003). In the following, we denote the ratio between the two as $R_k \equiv k_{0,\mathrm{int}}/k_{0,\mathrm{atm}}$. This leaves only three input parameters in our model: λ, $k_{0,\mathrm{int}}$, and $k_{0,\mathrm{atm}}$; or equivalently λ, $k_{0,\mathrm{int}}$, and R_k.

In Fig. 5, we keep λ and R_k constant, and we show the asymmetry profile $B(\nu)$ for several values of $k_{0,\mathrm{int}}$. Despite the fact that we vary $k_{0,\mathrm{int}}$ across almost one order of magnitude, the asymmetry profile $B(\nu)$ does not depend significantly on the absolute value of k_0, except close to $\nu \sim 1.7$ mHz. By comparison, its dependence on both R_k and λ is more substantial, especially at high frequencies (cf. Figs. 6 and 7). Since $k_{0,\mathrm{int}}$ does not seem to play an important role, we keep it fixed in the following, and focus on the impact of the other two input parameters, λ and R_k.

Figure 5 illustrates the main qualitative features of the asymmetry profile $B(\nu)$. In fact, together with Figs. 6 and 7, it shows that the qualitative behaviour of the asymmetry profile is largely model-independent. Thus the asymmetries of the solar radial p-mode line profiles are negative across a large part of the spectrum, in agreement with solar observations (see for instance Duvall et al. 1993). Furthermore, the asymmetry profile $B(\nu)$ exhibits three distinct local extrema: the absolute value of B increases below ∼1.7 mHz, decreases between ∼1.7 and ∼3 mHz, increases again between ∼3 mHz and ∼4 mHz, and finally decreases again above ∼4 mHz. Note, however, that this last extremum is, unlike the other ones, somewhat impacted by the values given to the different input parameters of the model.

The first two local extrema (∼1.7 and ∼3 mHz) correspond respectively to the beginning and end of the damping rate plateau. Indeed, the asymmetry parameter B depends on the linewidth of the modes, so it is natural that a sudden change in the behaviour of the latter should reflect on the former. The third extrema is not so easily explained and it will be discussed in Sect. 5.

Figure 6 shows how the asymmetry profile $B(\nu)$ depends on R_k. An increase of this parameter attenuates low-frequency mode asymmetries (below $\nu_{\max} \sim 3$ mHz), while on the contrary, the high-frequency modes (above $\nu_{\max}$) become more asymmetric. The effect is significantly more substantial for the latter than for the former. Asymmetries close to $\nu_{\max}$, however, are not affected by the parameter R_k whatsoever.

Figure 7 shows that the impact of λ on the asymmetry profile $B(\nu)$ is quite similar, albeit inverted, in the sense that $|B|$ increases with λ for low-frequency modes and decreases for high-frequency modes. Similarly, B is barely impacted by a change of λ close to $\nu_{\max}$. Furthermore, the asymmetry profile

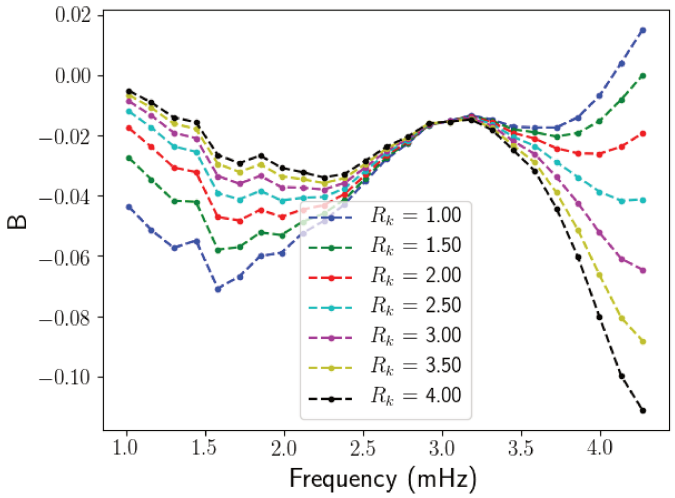

Fig. 6. Same as Fig. 5, but only R_k varies, $\lambda = 1$ and $k_{0,\mathrm{int}} = 2\,\mathrm{Mm}^{-1}$.

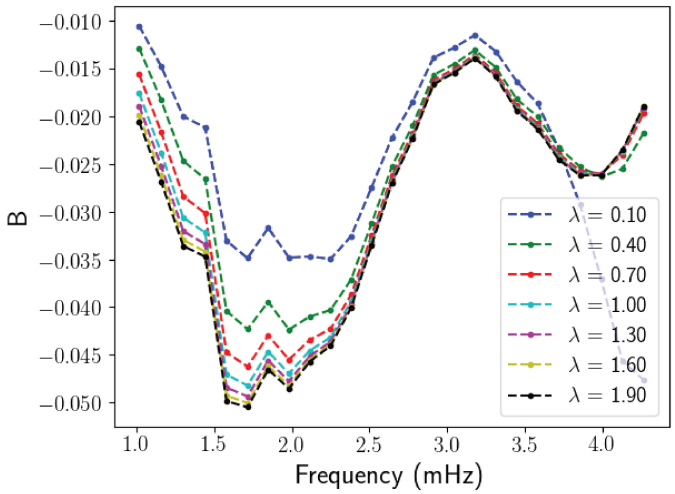

Fig. 7. Same as Fig. 5, but only λ varies, $R_k = 2$ and $k_{0,\mathrm{int}} = 2\,\mathrm{Mm}^{-1}$.

$B(\nu)$ undergoes saturation, in the sense that it ceases to depend on λ when it is increased above a certain value. In the following, we denote this threshold as λ_{sat}. Figure 7 shows that $\lambda_{\mathrm{sat}} \sim 1$. This dichotomy between $\lambda \lesssim 1$ and $\lambda \gtrsim 1$ originates in the Lorentzian nature of the temporal turbulent spectrum: depending on the value of λ, the angular frequencies relevant to solar p-modes are either in the low frequency part or in the high frequency part of the spectrum. We do not go into too much detail here as we discuss this matter further in Sect. 5.

4.2. The "numerical spectrum" model

In the "numerical spectrum" model, which describes the properties of turbulence more realistically, there is only one input parameter left, λ. In this sense, it has a greater predictive power than the previous model. The qualitative behaviour of the asymmetry profile $B(\nu)$ and, in particular, the positions of the different local extrema featured by $B(\nu)$, are, in this model, rather independent from λ and in agreement with what we observed in the scope of the previous model.

However, the input parameter λ does have an impact on the quantitative behaviour of the asymmetry profile $B(\nu)$. We show in Fig. 8 the asymmetry profile $B(\nu)$ obtained with the "numerical spectrum" model (see Sect. 2) for several values of λ. As

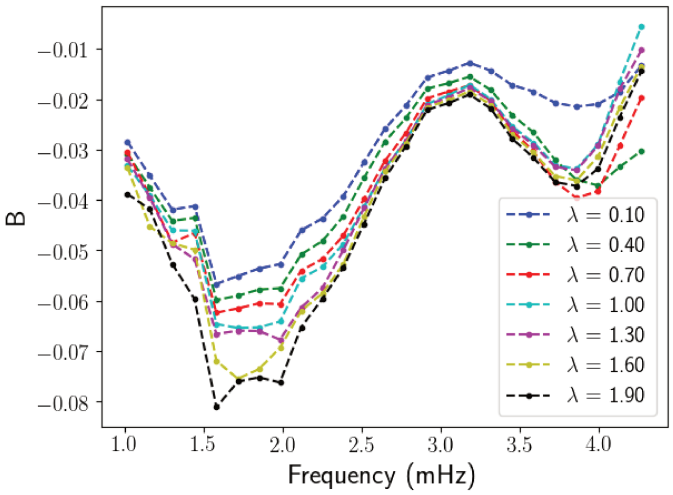

Fig. 8. Asymmetry parameter B as a function of frequency obtained by the "numerical spectrum" model, for several values of λ.

for the "theoretical spectrum" model, B is always negative and features several local extrema at $\nu \sim 1.7$, 3 and 4 mHz.

As for the dependence of $B(\nu)$ on λ, two distinct regimes can be separated. Below $\nu_{\mathrm{max}} \sim 3$ mHz, we recover the same dependence of the asymmetry parameter B with λ as we obtained in the scope of the "theoretical spectrum" model, with absolute values of B increasing with λ. The picture at frequencies higher than ν_{max} is, however, somewhat different. The asymmetry profile $B(\nu)$ features a local minimum at $\nu \sim 4$ mHz; the curve inflexion grows sharper as λ increases up to $\lambda \sim 1$, after which this part of the asymmetry profile does not significantly depend on λ. In this sense, the asymmetry profile $B(\nu)$ seems to undergo the same saturation behaviour as in the "theoretical spectrum" model (see Sect. 4.1), for the same value $\lambda_{\mathrm{sat}} \sim 1$. The fact that we recover approximately the same threshold gives us confidence that this particular feature of the asymmetry profile $B(\nu)$ is not a mere artefact of one model or the other but, rather, it is a genuine effect based on a physical origin. Again, we postpone the discussion of the physical origin of this behaviour to Sect. 5.

5. Impact of the properties of turbulence on mode asymmetry

Line profile asymmetry of solar-like oscillations have two main causes: localisation of the source of excitation (see for instance Duvall et al. 1993) and correlation with the turbulent perturbations (see for instance Nigam et al. 1998). In the following, we investigate both contributions in light of the results yielded by the "theoretical spectrum" model and presented in Sect. 4.1. With its various input parameters, the "theoretical spectrum" model allows us to understand the physical origin of mode asymmetry. In this section, then we only consider this model, although the conclusions are valid for the "numerical spectrum" model as well. We first discuss how source localisation and correlated turbulent perturbations can skew the mode line profiles. In particular, we support the discussion concerning source localisation with a simplified toy-model of mode excitation, which we describe in Appendix C. We then use this discussion to interpret the results yielded by our model. Additionally, we show that the contribution of the correlated turbulent perturbations to the mode asymmetries is negligible in the velocity power spectrum.

5.1. Origin of mode asymmetry

5.1.1. Effect of source localisation on mode asymmetry: generic arguments

The fact that the source of excitation of a mode is spatially localised can affect the skewness of the mode line profile in Fourier space. There are several ways of describing the impact of source localisation on mode asymmetry.

One way is to make use of the analogy between the development of acoustic modes in the stellar cavity and the phenomenon of optical interference in a Fabry-Pérot cavity. This analogy was used to account for the acoustic mode asymmetry in the Sun by Gabriel (1992), Duvall et al. (1993), among others. The idea is that acoustic, stationary modes in the Sun can be described by means of two progressing waves, propagating in opposite directions. Each of these waves follows the same cycle: they propagate one way, get refracted on the lower turning point of the acoustic cavity, then propagate backwards, get reflected on the upper turning point, and so forth. As a result of these multiple reflections and refractions on both turning points, the acoustic waves pass multiple times through the same regions and, therefore, interfere with each other (and with themselves). This interference pattern leads to the development of resonant modes in the cavity. What we observe then is the evanescent tail of these modes in the atmosphere, which lies outside the resonant cavity.

Let us now consider that the source of the waves is located at a certain point within the cavity. The waves propagating outwards and inwards will have travelled over different distances before interfering with one another and this difference of travel times will depend on the location of the source. The shape of the mode line profile is directly related to the dependence of the phase difference between the outwards and inwards interfering waves on frequency. Since this phase difference is not exactly symmetric about the mode eigenfrequency, neither is its line profile; and given that it depends on the source location, mode asymmetry is indeed a marker of source localisation.

Another physical interpretation of how source localisation can bring about mode asymmetry has been proposed by Rast & Bogdan (1998), and later refined by Rosenthal (1998). They remarked that mode asymmetry could be mathematically described by the relative position of local maxima (or peaks) and local minima (or troughs) in the power spectrum. Peaks located exactly halfway between their neighbouring troughs feature symmetric, Lorentzian line profiles. However, if one of the neighbouring trough is closer than the other, the peak in question appears skewed and, depending on which trough is closest, its asymmetry parameter is either positive or negative.

The position of the peaks are simply related to the eigenmodes of the solar acoustic cavity. As for the position of the troughs, in the special case of a point-like source of excitation, with a given multipolar decomposition, the authors showed that it is related to the eigenmodes of the atmosphere truncated at the source position, with a vanishing external boundary condition depending on the multipolar nature of the source. In that interpretation, the position of the troughs thus depends on both the position and the multipolar decomposition of the source.

Yet another way to describe the impact of source localisation on mode asymmetry is to consider the eigenfunction of the mode. In order to illustrate this, we present in Appendix C a very simplified toy-model of mode excitation, where the source is considered point-like and the acoustic cavity is simplified to a square well potential. From this toy-model we draw the following conclusion: for a given frequency, the amplitude of the wave is proportional to the eigenfunction associated with the wave at the source of excitation. In particular, excitation at a mode's antinode is much more efficient than at a mode's node.

With this conclusion in mind, let us consider the situation illustrated by Fig. 9. The blue and red curves represent the radial profile of the acoustic wave for two different angular frequencies. It can be seen that an increase of ω causes the radial profile of the oscillation to "shrink" radially. Therefore, the amplitude of the oscillation as seen by the source will either increase or decrease with ω, depending on its position. More specifically, a source at $r = r_1$ (see illustration in Fig. 9) will see the amplitude of the oscillation increase with ω, and a source at $r = r_2$ will see it decrease. In light of the conclusion presented in the previous paragraph, it can be deduced that if the source is located at $r = r_1$, the right wing of the mode line profile will be slightly elevated compared to the left wing, thus leading to positive asymmetry. Likewise, the asymmetry generated by a source at $r = r_2$ will be negative.

From the illustration in Fig. 9, it is straightforward to see that the dichotomy between the $r = r_1$ case and the $r = r_2$ case is based on the relative position of the source and the nodes and antinodes of the mode, or, in other words, on the sign of the derivative of the absolute value of the eigenfunction. To be more specific, one has to separate the case of a source inside and outside the acoustic cavity. If the source is inside the cavity, the $r = r_1$ case (i.e. case where source localisation entails positive asymmetry) corresponds to any source position located above a node and below an antinode of the oscillation profile, whereas the $r = r_2$ case (i.e. the case where source localisation entails negative asymmetry) corresponds to any source position located above an antinode and below a node. Here we recall that a node is a point at which the wave amplitude is zero and an antinode is a point at which it is maximal. If the source is outside the cavity, however, it is always as in the $r = r_2$ case and, thus, it always generates negative asymmetry: indeed, the outside of the cavity corresponds to an evanescent zone for the acoustic waves so that the absolute value of the eigenfunction always decreases in this region.

It should be noted that we only consider this toy-model in the present subsection. In the following sections, we return to the discussion of our model, simply using the conclusions drawn above to interpret the results which it yields.

5.1.2. Correlated turbulent fluctuations

Acoustic modes in the Sun are excited by fluctuations of turbulent nature – more specifically by turbulent fluctuations of the Reynolds stress or non-adiabatic pressure perturbations. It is therefore natural that a part of the turbulent fluctuations should be not only coherent, but statistically correlated with the oscillating mode.

The resulting interference between the mode and the turbulent fluctuations leads, in turn, to mode asymmetry. In order to illustrate this, let us consider a mode whose line profile is intrinsically Lorentzian and turbulent fluctuations whose power spectral density is constant over the width of the mode under consideration. We then have

$$P(x) = \left| \frac{A_m}{x + j} + A_n e^{j\phi_n} \right|^2 , \tag{31}$$

where P is the total power spectral density, $x = 2(\omega - \omega_0)/\Gamma_\omega$ is the reduced frequency (ω_0 is the angular eigenfrequency of the mode, and Γ_ω its linewidth), A_m and A_n are the (real) amplitudes associated to the mode and the noise respectively, ϕ_n is the

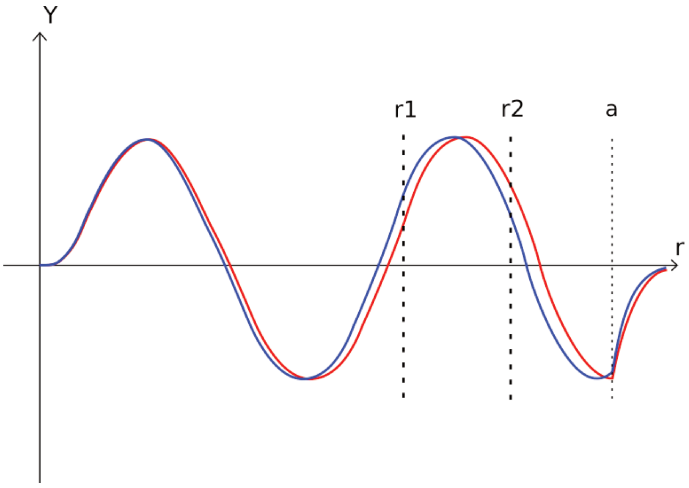

Fig. 9. Illustration of the importance of source position with respect to nodes and antinodes of the eigenfunction associated to a mode to explain its asymmetry. The blue and red lines show the radial profile of the oscillation for two angular frequencies very close to one another ($\omega_{\rm red} < \omega_{\rm blue}$). The bold vertical dashed lines show two source positions generating opposite mode asymmetries: positive for r_1, negative for r_2. The third vertical dashed line marks the edge of the acoustic cavity $r = a$.

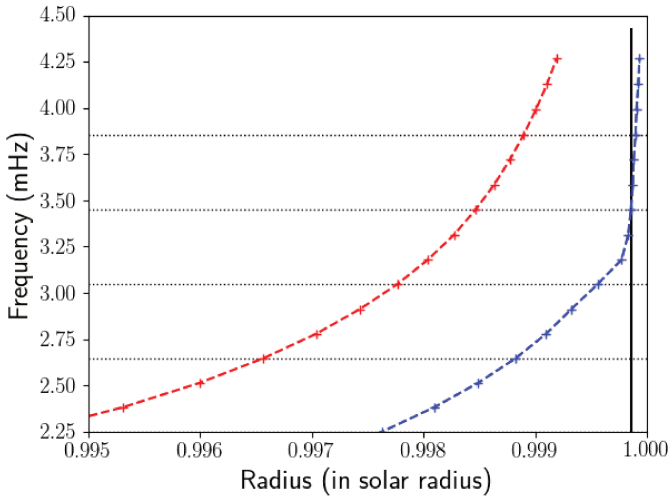

Fig. 10. Radial location of the nodes (red symbols connected by a dashed line) and anti-nodes (blue symbols connected by a dashed line) that are closest to the super-adiabatic peak, for each radial mode between $n = 16$ and $n = 30$. The vertical black line represents the maximum of the super-adiabatic peak, where the excitation is most efficient. Horizontal black dotted lines are added for readability only.

phase difference between the mode and the noise, and j is the imaginary unit. Expanding the module squared, we obtain

$$P(x) = \frac{A_m^2}{1+x^2} + \frac{2A_mA_n}{\sqrt{1+x^2}} \sin\left(\arctan x + \phi_n\right) + A_n^2. \tag{32}$$

The first term of the right-hand side of Eq. (32) corresponds to a Lorentzian profile and is symmetric about $x = 0$. The third term simply acts as an offset and does not introduce any mode asymmetry. The second term, however, is clearly not symmetric at $x = 0$, unless $\phi_n = \pm\pi/2$. For instance, if $\phi_n = 0$, this term is even antisymmetric. In other words, the interference between the mode and the noise is destructive in the left wing of the mode and constructive in its right wing. As such, the power spectral density $P(x)$ is higher than the Lorentzian profile in the right wing and lower in the left wing, thus entailing positive mode asymmetry. The sign and magnitude of the mode asymmetry depends on the amplitude A_n, that is, on the degree of correlation between the mode and the turbulent fluctuations, as well as on the phase difference ϕ_n, both of which are included in the model we developed in Sect. 2.

5.2. Contribution of source localisation to $B(\nu)$

In the previous subsection, we summarised the impact of source localisation on mode asymmetry by stating the following: a source within the resonant cavity of a mode entails negative asymmetry if it is located above an antinode and below a node of the associated eigenfunction and positive asymmetry otherwise; a source outside the resonant cavity always entails negative mode asymmetry. With this in mind, we set out to interpret the results obtained in Sect. 4 in the scope of the "theoretical spectrum" model.

Once applied to the case of solar p-mode excitation, this rule can be rephrased in the following way. There is a dichotomy between the effect of the turbulent eddies located below the upper turning point of the mode and those located above. The former skew the mode line profile one way or the other depending on their height relative to the nodes and antinodes of the mode eigenfunction. The latter always skew the mode line profile so that it feature negative asymmetry. Until now, we have only discussed the case of a point-like source of excitation. However, the driving region of the solar p-modes, while localised around the super-adiabatic peak just below the photosphere, has a certain spatial extent. As such, driving turbulent eddies can be found both below and above the upper turning point of the modes and the observed mode asymmetry is due to the combination of both.

As we mention above, the sense of asymmetry created by turbulent eddies below the upper turning point depends on their position with respect to the nodes and antinodes of the modes. Since the wavelength of the modes is much larger than the spatial extent of the driving region, it is sufficient to study the position of the super-adiabatic peak with respect to the nodes and antinodes of the mode eigenfunction. We illustrate this in Fig. 10, which shows the position of the node and antinode of the radial modes obtained through our model, with respect to the super-adiabatic peak, where the stochastic excitation is mainly located. Below $\nu \sim 3.5$ mHz, the super-adiabatic peak lies above the closest antinode (dashed blue line in Fig. 10), thus generating negative asymmetries. Above the aforementioned threshold, the closest antinode is above the super-adiabatic peak and it generates positive asymmetry. Close to 3.5 mHz, the super-adiabatic peak coincides with an antinode, so that the asymmetry is very low.

The dichotomy between turbulent eddies below and above the upper turning point stands thus: excitation localised below the upper turning point makes modes with $\nu \lesssim \nu_{\rm max}$ negatively asymmetric and modes with $\nu \gtrsim \nu_{\rm max}$ positively asymmetric; excitation localised above the upper turning point makes all modes negatively asymmetric; since the source of excitation has a certain spatial extent, the total asymmetry is a combination of both cases. This is in perfect accordance with the dashed blue curve of Fig. 6 which shows the asymmetry profile $B(\nu)$ with $R_k = \lambda = 1$ (i.e. imposing the same turbulent spectrum everywhere). Indeed, this curve shows that B is negative for low frequencies, and positive for high frequencies. If the source of excitation was only located below the upper

turning point of the modes, the threshold between the two regimes would be ∼3.5 mHz; however, turbulent eddies above the upper turning point generate additional negative asymmetry, thus shifting the curve downwards and increasing the threshold between the $B < 0$ and the $B > 0$ regimes.

The results presented in Figs. 5 and 6 are also easily interpreted. Indeed, Eqs. (B.19) and (B.28) show that the efficiency of stochastic excitation scales as k_0^{-4}, where k_0 is the injection wavenumber of turbulent kinetic energy. Therefore, keeping R_k constant does not change the contribution of atmospheric turbulence relatively to the contribution of turbulence below the upper turning point, and consequently only impacts the mode amplitude, not its asymmetry.

However, decreasing $k_{0,\mathrm{atm}}$ with respect to $k_{0,\mathrm{int}}$ increases the contribution of atmospheric eddies relatively to eddies below the upper turning point. Therefore, increasing R_k makes asymmetries at high frequencies decrease, and the frequency above which $B > 0$ increases. The ratio R_k needed for the asymmetry profile to be negative throughout the entire spectrum is only $R_k \sim 2$, which is explained by the high sensitivity of the excitation efficiency on k_0 (since it scales to k_0^{-4}).

The physical interpretation of the influence of λ on the asymmetry profile $B(\nu)$ is not as straightforward. It cannot be interpreted in the same way as the influence of $k_0(r)$, since we consider λ to be uniform throughout the region of excitation. Furthermore, it cannot be interpreted in terms of the relative contribution of the leading and cross term (see Eq. (13)), because both terms scale to λ. The existence of the threshold λ_{sat} can be explained as follows: depending on λ, the typical period of solar p-modes compares differently to the typical turbulent eddy-time correlation, that is, ω compares differently to ω_k, which indeed depends on λ. Depending on whether $\omega < \omega_k$ or $\omega > \omega_k$, the temporal turbulent spectrum $\chi_k(\omega)$ vary differently with ω: indeed, χ_k is almost flat for very low frequencies, whereas it decreases as ω^{-2} for high frequencies. As such, as λ is increased, it is expected that the qualitative behaviour of the mode properties – including mode asymmetry – changes when $\omega \sim \omega_k$. This explanation is supported by the value found for λ_{sat}. Indeed, if we take $k \sim 10^{-6}\,\mathrm{m}^{-1}$, $u_k \sim 10^3\,\mathrm{m\,s}^{-1}$ and $\omega \sim 10^{-3}\,\mathrm{rad\,s}^{-1}$, we obtain $\omega/\omega_k \sim \lambda$. Consequently, $\lambda \sim 1$ does correspond to the threshold at which ω and ω_k have the same order of magnitude.

5.3. Contribution of correlated turbulent perturbations to $B(\nu)$

Earlier in this paper, we illustrate how a certain degree of correlation between the oscillating modes and the turbulent fluctuations can create mode asymmetry. Furthermore, it has been claimed (Nigam et al. 1998) that correlation between pulsational velocity and acoustic turbulent perturbations is at the root of the inversion of the sign of mode asymmetry between spectrometric and photometric measurements. This suggests that this correlation plays a crucial role when it comes to interpreting photometric data, although other explanations exist (Duvall et al. 1993; Georgobiani et al. 2003). However, determining whether or not this role can be disregarded in the velocity spectrum or if it must be taken into account at all (even if it is not so significant as to change the sign of the mode asymmetries) remains an open question.

Our model allows us to shed some light upon this issue. In the following, we compute the asymmetry profile $B(\nu)$ alternatively with and without the cross term $C(\omega)$ in Eq. (13). In terms of amplitude, the leading term will, unsurprisingly, dominate over the correlation term $C(\omega)$; however, one must keep in mind that the asymmetry of the mode line profile is a subtle effect, and it is possible that, albeit negligible in amplitude, $C(\omega)$ impacts the asymmetry as much as the leading term.

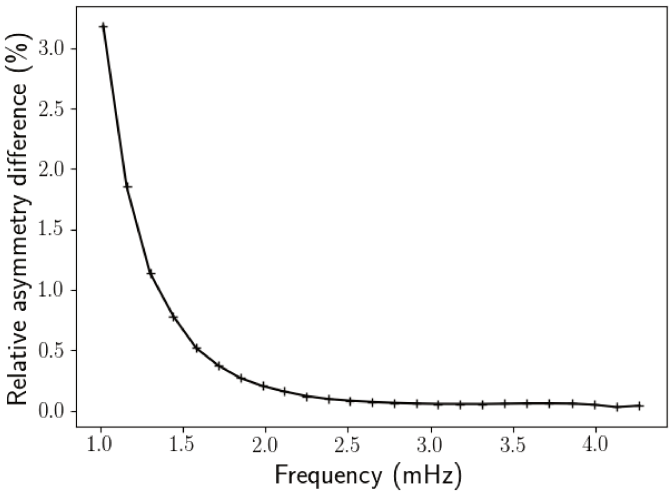

Fig. 11. Relative difference (in percentages) between the asymmetry parameter B obtained by respectively taking into account and discarding the cross term $C(\omega)$ ($k_{0,\mathrm{int}} = 2\,\mathrm{Mm}^{-1}$, $R_k = 2$ and $\lambda = 1$), as a function of frequency.

Figure 11 shows the relative difference between the asymmetry profile $B(\nu)$ when the cross term is respectively taken into account and discarded. This relative difference is highest at low frequency, and almost vanishes when $\nu > \nu_{\mathrm{max}}$. This can be easily explained by the fact that low-frequency modes have the smallest power spectral density, while power spectral density associated to the noise is higher: in contrast, the effect of correlated turbulent perturbations is at its most substantial at the lowest frequencies. Nevertheless, even in the lowest part of the spectrum, the relative difference in asymmetry between a model with and without the cross term does not exceed 3%, which is much smaller than the dispersion characterising observed asymmetries. We therefore conclude that the dominant source of asymmetry in velocity data is the source localisation and that the effect of correlated turbulent perturbations can be disregarded.

It is possible to support this conclusion with a simple order of magnitude estimation. Indeed, B is of order 10^{-2}, which means it is necessary for the cross term to represent at least 1% of the leading term to have a significant impact on the asymmetry profile. The Cauchy-Schwarz inequality provides an upper bound to the cross term: $C(\omega) \leqslant \widehat{v}_{\mathrm{rms}}(\omega)\widehat{u}_{\mathrm{rms}}(\omega)$, where the case of equality happens when the correlation between the mode v and the turbulence u is optimal. Therefore

$$\frac{\left\langle \left|\widetilde{v}(\omega)\right|^2 \right\rangle}{C(\omega)} \gtrsim \frac{\widehat{v}_{\mathrm{rms}}(\omega)}{\widehat{u}_{\mathrm{rms}}(\omega)}, \tag{33}$$

where $C(\omega)$ corresponds to the second term in Eq. (13), and is defined by Eq. (B.28).

If we estimate the power spectral density of the mode as $\widehat{v}^2_{\mathrm{rms}} \sim 10^5\,\mathrm{m^2\,s^{-2}\,Hz^{-1}}$ and that of the turbulent fluctuations as $\widehat{u}^2_{\mathrm{rms}} \sim 10\,\mathrm{m^2\,s^{-2}\,Hz^{-1}}$ (Fig. 2 Turck-Chièze et al. 2004), the above ratio becomes $\sqrt{10^5/10} \sim 10^2$. We note that at this stage, the correlation term is about 1% of the leading term, which is barely enough to impact the asymmetries significantly. However, by considering the limiting case in the Cauchy-Schwarz inequality, we assumed that the mode velocity and the turbulent velocity were both optimally coherent and completely independent. This

is not, however, the case; consequently we probably overestimated the importance of $C(\omega)$ by at least an order of magnitude. Therefore, this crude order of magnitude estimation indeed tends to support the conclusion that correlated turbulent perturbations can be disregarded when interpreting mode asymmetries in the velocity spectrum.

6. Comparison with observations

Observed properties of solar-like oscillations depend not only on the observable (velocity or intensity), but also on the specifics of each instruments. As far as velocity measurements are concerned, all instruments do not perform their Doppler observations on the same spectral line. Since different spectral lines form at different altitudes in the atmosphere, and since the properties of turbulence change throughout the atmosphere, mode properties, and especially mode asymmetries, may depend on the instrument.

In the following, we compare the results of our model to observations performed with the GONG network. We then focus on the dependence of the asymmetry profile $B(\nu)$ on the height at which the velocity spectrum is observed. We use the "numerical spectrum" model (see Sect. 2) to compare the asymmetry profiles $B(\nu)$ as observed by several instruments performing solar velocity spectrum measurements. Finally, we focus on the bias in the determination of mode eigenfrequencies entailed by mode asymmetry, whose understanding is of primary importance for accurate inference of mode properties.

6.1. Comparison with GONG observations

First – and in order to support the validity of our model in terms of mode asymmetry – we compare the asymmetries yielded by our model to those inferred from observations. We use the data points extracted from the spectrum analysis of Barban et al. (2004). The authors chose an equivalent, albeit different, set of parameters to fit the acoustic modes observed by the GONG network. Therefore, we reconstructed the shape of the modes point by point using the parameters extracted from their fit and fitted them again with the formula given by Eq. (26). We note that the modes analysed in their study are not radial, but have angular degrees ranging from $l = 15$ to $l = 50$. It is known, however, that the dependence of mode asymmetry on the angular degree is very weak (see for instance Duvall et al. 1993), who studied modes of angular degree up to $l = 170$) because the eigenfunctions associated to the acoustic modes are very weakly dependent on l close to the photosphere, as long as l is not too high. Thus, comparing our radial study to their non-radial observations remains relevant.

We showcase this comparison in Fig. 12. The parameter λ was adjusted for a better agreement with the observations. We obtained $\lambda = 0.5$ (see Eq. (20) for a definition of this parameter), which is approximately the value obtained by constraining mode amplitudes (Samadi & Goupil 2001). It is rather clear that we reproduce the main features of the asymmetry profile $B(\nu)$, especially its sense of variation on the different intervals (when the frequency range of the observations overlaps ours), as well as the positions and values of its local extrema. Alternatively, we show the same comparison in terms of the asymmetry parameter χ in the bottom panel of Fig. 12. This parameter is defined by Eq. (29), and is more robust when it comes to comparing theory and observations because it does not depend on the determination of the mode linewidths, which may introduce extra uncertainty in the determination of the observed asymmetries.

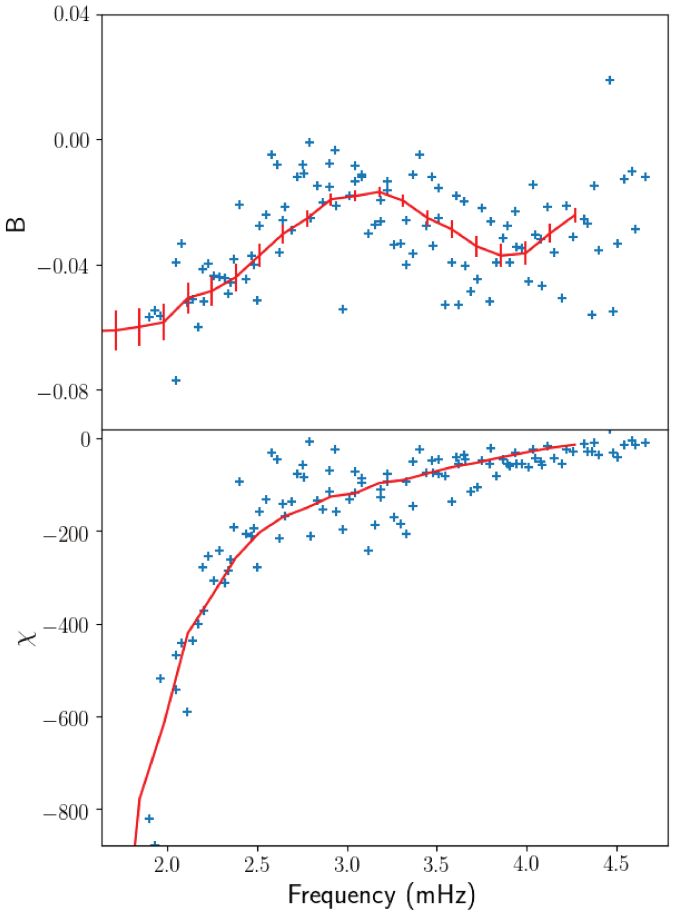

Fig. 12. Asymmetry profile obtained by the "numerical spectrum" model (solid red line), compared to the observed asymmetry profile (blue crosses). The data points are taken from Barban et al. (2004). For more readability, only data points corresponding to modes with angular degrees $15 \leq l \leq 20$ have been retained. The asymmetry profile is given in terms of the parameter B (*top panel*), and alternatively in terms of the parameter χ (*bottom panel*), which is defined by Eq. (29). The error bars in the top panel correspond to the uncertainty on the observed values of the mode linewidths, which propagates to the asymmetry parameter B.

In conclusion, the good agreement obtained between our model and observations show that the model developed in this paper is relevant to account for acoustic mode asymmetry quantitatively.

6.2. Dependence of asymmetry profile $B(\nu)$ on observation height

We consider three different observation heights in this paper associated, respectively, with the *Michelson* Doppler Imager (MDI), the GOLF instrument (both onboard the SOHO spacecraft), the Global Oscillation Network Group (ground-based), and the Helioseismic and Magnetic Imager (HMI; onboard the SDO spacecraft). We provide further information on the observation height of each of these instruments in Table 2. However, determining the formation height of a given absorption line is extremely difficult in that it does not depend only on the nature of the line (Fleck et al. 2011). Therefore, the values given in Table 2 are not to be considered as precise estimates but, rather, as approximate figures.

In Fig. 13, we compare the asymmetry profile $B(\nu)$ as it would be observed by the various instruments listed in Table 2. We control the height by tuning the radial coordinate r_o at which

Table 2. Summary of the nature, wavelength, and formation height of the absorption line used by the instruments considered in this paper.

Instrument	Line	λ (Å)	Height (km)
MDI/GONG	Ni I	6768	170
GOLF	Na I D1/D2	5896/5890	340
HMI	Fe I	6173	100

Notes. The formation heights are given with respect to the photosphere. References: Fleck et al. (2011; MDI/GONG, HMI) and Baudin et al. (2005; GOLF). Note that the MDI instrument and the GONG network use the same spectral line and therefore observe the modes at the same altitude.

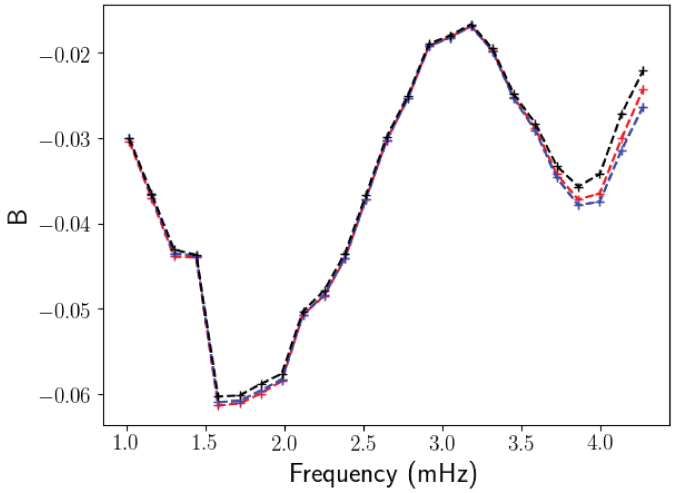

Fig. 13. Asymmetry profile $B(\nu)$ obtained by the "numerical spectrum" model (with $\lambda = 0.5$), as would be observed at three different heights in the atmosphere, corresponding respectively to the observation heights of GOLF (dashed red line), MDI/GONG (dashed blue line) and HMI (dashed black line).

the Green's function of the homogeneous wave equation is calculated (see Sect. 2 for more details). Mode asymmetry is only slightly dependent on the observation height. This is not so surprising since mode asymmetry is a global property of the modes. It is noticeable, however, that the difference between these asymmetry profiles is most prominent at high frequency ($\gtrsim$3.5 mHz). This is because by observing the modes at a lower height in the atmosphere, we effectively increase the contribution of atmospheric turbulence compared to the contribution of sub-photospheric turbulence on mode asymmetry. As we discussed in Sect. 5, it is at high frequency that the atmospheric turbulence has a more significant impact on mode asymmetry. Therefore, changing the observation height has more impact at high frequency than at low frequency.

6.3. Bias in eigenfrequency determination

In order to infer the stellar internal structure from asteroseismic measurements, it is important to determine the eigenfrequencies of the observed modes not only precisely, but also accurately. As was noted early on (Duvall et al. 1993; Abrams & Kumar 1996; Chaplin et al. 1999; Thiery et al. 2000; Toutain et al. 1998), using a symmetric, Lorentzian model to fit asymmetric line profiles results in an appreciable bias in the best-fit parameters, thus rendering inaccurate the frequency determination.

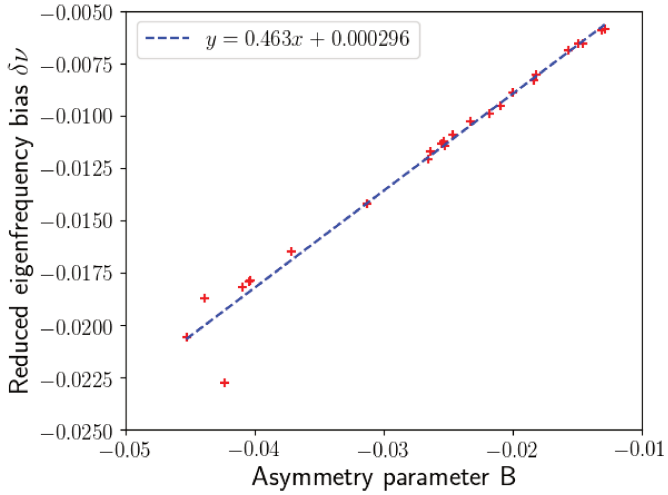

Fig. 14. Reduced frequency bias $\delta\nu$, defined by Eq. (34), as a function of the asymmetry parameter B for each radial p-mode between $n = 6$ and $n = 30$. The blue dashed line shows the best linear fit.

We illustrate this bias in the following. We fit the line profiles we obtained numerically with a formula given either by Eq. (26) or by the symmetric version (i.e. fixing $B = 0$). Following Abrams & Kumar (1996), we denote the reduced frequency bias as

$$\delta\nu = \frac{\nu_0^{B=0} - \nu_0^{B\neq 0}}{\Gamma_{\nu_0}}. \tag{34}$$

Figure 14 shows the results obtained for all radial modes described in Sect. 4. Given that the asymmetry of solar p-modes in the velocity spectrum are all negative, using a symmetric fit introduces an underestimation of ν_0. It is very clear that this underestimation grows linearly with the asymmetry B of the modes. We superimpose on Fig. 14 the best linear fit to the numerical data, given by: $\delta\nu = 0.463\ B + 0.000296$. Given the typical values of $\delta\nu$, it is safe to say that the intercept of this linear regression is negligible.

This result can be easily interpreted by taking a closer look to the asymmetric fitting formula given by Eq. (26). Indeed, after applying elementary algebra, it becomes clear that for leading order in B, this expression reaches its maximum at $x \sim B$ (or $\nu_{\max} = \nu_0 + B\Gamma_{\nu_0}/2$). Therefore, while the asymmetric fit accurately finds the eigenfrequency at $\nu_0^{B\neq 0} = \nu_0$, the symmetric fit finds it at $\nu_0^{B=0} = \nu_{\max}$. One can therefore derive the simple expression $\delta\nu = B/2$, which is in accordance with the linear fit shown in Fig. 14.

The frequency bias introduced when not taking the line profile asymmetry into account can easily reach several percents of the mode linewidth. This bias largely exceeds the frequency resolution achievable in current solar measurements, especially for high-frequency modes, which are the widest.

7. Summary and conclusion

In this paper, we detail the development of a realistic and predictive model for the asymmetry displayed by solar radial p-modes in the velocity spectrum. The basic idea behind this model is to compute the Green's function associated to the radial acoustic wave equation, as well as its inhomogeneous part (which corresponds to the source of excitation) and to convolve the two to reconstruct the velocity power spectral density point by point.

Once the power spectral density is reconstructed, we extract its resonant modes and study their asymmetry. In particular, and unlike previous attempts to such modelling, we included in our model the correlation of the oscillating modes with the fluctuations associated to turbulent velocity.

First, the Green's function associated with the wave equation was computed numerically. We put the wave equation in the form of a 1D stationary Schrödinger equation, whose potential only depends on the equilibrium structure of the Sun. We extracted the acoustic potential from a solar patched model: the solar interior is calculated using the 1D evolutionary code CESTAM and the solar atmosphere is calculated using the 3D hydrodynamic code CO^{5}BOLD and horizontally averaged. We integrated the wave equation along the solar radius, and added a point-like, normalised source to the integration scheme in order to compute the Green's function.

Secondly, the source term of the wave equation being of stochastic nature, we modelled the statistical properties of the source by means of theoretical developments. We made use of the adequate closure relation to express the third and fourth-order correlation products of the turbulent velocity as functions of second-order products; more specifically on their spatial and temporal Fourier transform. We developed two distinct models: one is based on theoretical prescriptions for the spatial and temporal spectrum of turbulent kinetic energy; the other is based on theoretical modelling of the temporal spectrum only, whereas the spatial spectrum is extracted from a 3D hydrodynamic simulation of the solar atmosphere. We refer to the former as the "theoretical spectrum" model, and to the latter as the "numerical spectrum" model.

The asymmetry B displayed by the modes in our model drastically depends on their frequency ν. This is because the shape of the eigenfunctions close to the photosphere is very dependent on ν. We find that B is negative throughout the p-mode spectrum, and that its behaviour weakly depends on the input parameters of our model. It drops from -0.01 to -0.05 between 1 mHz and 1.7 mHz, then rises to 0.015 at 3 mHz, and decreases again from 3 mHz to 4 mHz. Above 4 mHz, the behaviour of $B(\nu)$ is much more dependent on the value given to our input parameters and, in particular, on the injection scale associated to the turbulent cascade above the photosphere, compared to below the photosphere. This is related to the fact that the contribution of atmospheric turbulence to mode excitation only becomes significant at high frequency, so that only in this part of the spectrum it may have an impact on mode asymmetry.

The asymmetry of the modes can have two different origins: localisation of their source of excitation within a region of lesser spatial extent than the mode wavelength and correlation between the oscillating modes and the fluctuations associated to turbulent velocity. Formally, these two phenomena have the same impact on mode asymmetry, so that they cannot be separated using observational data only. Our model allows us to make this distinction and to study their relative weight in the total mode asymmetry. We find that the correlation with turbulent fluctuations is negligible in the velocity spectrum, and that the observed asymmetries are exclusively due to source localisation. More precisely, we interpret the results of our model in terms of the source position with respect to the various nodes and antinodes featured by the eigenfunctions of the modes. In the case of a point-like source of excitation, mode asymmetry drastically depends on whether it is located within or outside the mode acoustic cavity. In our model, however, the source of excitation has a certain spatial extent, so that the total asymmetry is a combination of the contributions from the source outside and inside the mode acoustic cavity.

We find that it is impossible to interpret even the qualitative behaviour of the asymmetry profile $B(\nu)$ by considering that the source of excitation is point-like (either outside or inside the modes cavity). On the contrary, taking into account the spatial extent of the source allows us to reproduce the observed asymmetries, not only qualitatively, but also quantitatively. This positive result shows that our model is indeed relevant to describe – and, more importantly, to predict – acoustic mode asymmetry in solar-like oscillators. It also shows that any model that assumes a point-like source of excitation cannot give reliable results as far as mode asymmetry is concerned. In particular, such a model would predict positive asymmetries for high-frequency modes, whereas observations show that all asymmetries are negative when measured in terms of velocity power spectral density.

Finally, we study the eigenfrequency bias entailed by neglecting to fit observations with an asymmetric profile. We find that for the most asymmetric modes, this bias can reach several percent of the mode linewidth. Therefore, this bias is higher for high frequency modes, which are the widest. In particular, for $\nu \sim 4$ mHz, the asymmetry parameter is of order $B \sim -0.04$, and the linewidth is of order $\Gamma \sim 10\,\mu$Hz, so that the eigenfrequency bias is of order $\delta\nu \sim 0.2\,\mu$Hz. This is in perfect accordance with actual biases obtained from observation fit of the solar spectrum (see Benomar et al. 2018, Fig. 6, topmost panel). Since the eigenfrequency bias is most pronounced for higher frequency (because it is proportional to the mode line-width, which is widest at high frequency), it is likely to have a non-negligible impact on inversion methods, especially those based on asymptotic formulae. One must keep in mind, however, that the deviation of the modelled eigenfrequencies from the observed ones, induced by surface effects, largely dominates the eigenfrequency bias entailed by symmetric fits.

In this paper, we have restricted ourselves to the study of solar radial p-modes. Our formalism can be easily adapted to the study of non-radial modes simply by using a non-radial wave equation instead of the radial one. However, since the eigenfunction associated to p-modes in solar-like oscillators are very weakly independent on angular degree l close to the photosphere, which is precisely where the excitation takes place, the mode asymmetry is not expected to vary significantly with l, at least as long as l remains reasonably small. Observational data tend to confirm this (see e.g. Vorontsov & Jefferies 2013, who report that the spectral parameters of individual modes collapse to slowly varying functions of frequency only for modes with $l \lesssim 100$).

We only considered one type of acoustic source in this study, that is, the turbulent fluctuations of the Reynolds stress. Indeed, it has been shown by Stein & Nordlund (2001) that this is the dominant source of excitation of solar acoustic modes (see also Chaplin et al. 2005; Samadi et al. 2007; Nordlund et al. 2009). Therefore, our objective was to start by considering only this source. However, further refinements of the model will have to include other sources of excitation, in the form of non-adiabatic, turbulent pressure fluctuations.

Our formalism can also be easily applied to other solar-like oscillators. Comparing the asymmetries featured by the velocity spectra of several solar-like oscillators as modelled by the method presented in this paper and, in particular, the trend followed by mode asymmetry with stellar parameters such as effective temperature or surface gravity, undoubtedly constitutes the next step of this study. In the long run, mode asymmetry may serve as a useful tool for seismic diagnoses of solar-like oscillators. However, the one major difference that remains between the solar case and other stars is that the Sun is the only solar-like

oscillator for which spectra obtained by spectrometric measurements are sufficiently resolved to allow for a determination of their mode asymmetry. The asymmetry of acoustic modes of all other stars can only be observed in intensity spectra. As has been reported numerous times (see e.g. Duvall et al. 1993), asymmetry in intensity and in velocity spectra are drastically different. It is, therefore, necessary to adapt our formalism to the intensity spectrum, which is another key element of any further considerations on the matter treated here.

Acknowledgements. J.P. wishes to warmly thank Louis Manchon for having provided us with the solar patched model we used in this paper. J.P. and K.B. would also like to thank Marie-Jo Goupil for her thorough reading of the manuscript, as well as John Leibacher for useful discussions. J.P. and K.B. acknowledge financial support from the "Programme National de Physique Stellaire" (PNPS) of CNRS/INSU. H.G.L. acknowledges financial support by the Sonderforschungsbereich SFB 881 "The Milky Way System" (subprojects A4) of the German Research Foundation (DFG).

References

Abrams, D., & Kumar, P. 1996, ApJ, 472, 882
Balmforth, N. J. 1992, MNRAS, 255, 639
Barban, C., Hill, F., & Kras, S. 2004, ApJ, 602, 516
Batchelor, G. K. 1953, The Theory of Homogeneous Turbulence (Cambridge: Cambridge University Press)
Baudin, F., Samadi, R., Goupil, M.-J., et al. 2005, A&A, 433, 349
Belkacem, K., Samadi, R., Goupil, M. J., Kupka, F., & Baudin, F. 2006a, A&A, 460, 183
Belkacem, K., Samadi, R., Goupil, M. J., & Kupka, F. 2006b, A&A, 460, 173
Belkacem, K., Samadi, R., Goupil, M.-J., & Dupret, M.-A. 2008, A&A, 478, 163
Belkacem, K., Samadi, R., Goupil, M. J., et al. 2010, A&A, 522, L2
Belkacem, K., Samadi, R., & Goupil, M. J. 2011, GONG-SoHO 24: A New Era of Seismology of the Sun and Solar-Like Stars, 271, 012047
Benomar, O., Goupil, M., Belkacem, K., et al. 2018, ApJ, 857, 119
Bruls, J. H. M. J., Rutten, R. J., & Shchukina, N. G. 1992, A&A, 265, 237
Chaplin, W. J., & Appourchaux, T. 1999, MNRAS, 309, 761
Chaplin, W. J., Elsworth, Y., Isaak, G. R., Miller, B. A., & New, R. 1999, MNRAS, 308, 424
Chaplin, W. J., Houdek, G., Elsworth, Y., et al. 2005, MNRAS, 360, 859
Christensen-Dalsgaard, J. 2011, Astrophysics Source Code Library [record ascl:1109.002]
Davies, G. R., Broomhall, A. M., Chaplin, W. J., Elsworth, Y., & Hale, S. J. 2014, MNRAS, 439, 2025
Duvall, Jr., T. L., Jefferies, S. M., Harvey, J. W., Osaki, Y., & Pomerantz, M. A. 1993, ApJ, 410, 829
Fleck, B., Couvidat, S., & Straus, T. 2011, Sol. Phys., 271, 27
Freytag, B., Steffen, M., Ludwig, H.-G., et al. 2012, J. Comput. Phys., 231, 919
Gabriel, M. 1992, A&A, 265, 771
Gabriel, M. 1993, A&A, 274, 935
Georgobiani, D., Stein, R. F., & Nordlund, Å. 2003, ApJ, 596, 698
Gizon, L. 2006, Cent. Eur. Astrophys. Bull., 30, 1
Goldreich, P., & Keeley, D. A. 1977a, ApJ, 211, 934
Goldreich, P., & Keeley, D. A. 1977b, ApJ, 212, 243
Goode, P. R., Strous, L. H., Rimmele, T. R., & Stebbins, R. T. 1998, ApJ, 495, L27
Gough, D. O. 1977, ApJ, 214, 196
Jefferies, S. M., Duvall, Jr., T. L., Harvey, J. W., Osaki, Y., & Pomerantz, M. A. 1991, ApJ, 377, 330
Jefferies, S. M., Severino, G., Moretti, P.-F., Oliviero, M., & Giebink, C. 2003, ApJ, 596, L117
Korzennik, S. G. 2005, ApJ, 626, 585
Kraichnan, R. H. 1957, Phys. Rev., 107, 1485
Kumar, P., & Basu, S. 1999, ApJ, 519, 389
Kupka, F., & Muthsam, H. J. 2017, Liv. Rev. Comput. Astrophys., 3, 1
Lesieur, M. 2008, Turbulence in Fluids (Berlin: Springer)
Manchon, L., Belkacem, K., Samadi, R., et al. 2018, A&A, 620, A107
Marques, J. P., Goupil, M. J., Lebreton, Y., et al. 2013, A&A, 549, A74
Morel, P. 1997, A&AS, 124, 597
Musielak, Z. E., Rosner, R., Stein, R. F., & Ulmschneider, P. 1994, ApJ, 423, 474
Nigam, R., & Kosovichev, A. G. 1998, ApJ, 505, L51
Nigam, R., Kosovichev, A. G., Scherrer, P. H., & Schou, J. 1998, ApJ, 495, L115
Nordlund, Å., Stein, R. F., & Asplund, M. 2009, Liv. Rev. Sol. Phys., 6, 2
Press, W. H., Flannery, B. P., & Teukolsky, S. A. 1986, Numerical Recipes. The Art of Scientific Computing (Cambridge: University Press)
Rast, M. P., & Bogdan, T. J. 1998, ApJ, 496, 527
Rosenthal, C. S. 1998, ApJ, 508, 864
Roxburgh, I. W., & Vorontsov, S. V. 1995, MNRAS, 272, 850
Roxburgh, I. W., & Vorontsov, S. V. 1997, MNRAS, 292, L33
Samadi, R., & Goupil, M.-J. 2001, A&A, 370, 136
Samadi, R., Nordlund, Å., Stein, R. F., Goupil, M. J., & Roxburgh, I. 2003, A&A, 403, 303
Samadi, R., Georgobiani, D., Trampedach, R., et al. 2007, A&A, 463, 297
Samadi, R., Belkacem, K., Goupil, M. J., Dupret, M.-A., & Kupka, F. 2008, A&A, 489, 291
Samadi, R., Belkacem, K., & Sonoi, T. 2015, EAS Publ. Ser., 73, 111
Severino, G., Magrì, M., Oliviero, M., Straus, T., & Jefferies, S. M. 2001, ApJ, 561, 444
Stein, R. F. 1967, Sol. Phys., 2, 385
Stein, R. F., & Nordlund, Å. 2001, ApJ, 546, 585
Thiery, S., Boumier, P., Gabriel, A. H., et al. 2000, A&A, 355, 743
Toutain, T., Appourchaux, T., Fröhlich, C., et al. 1998, ApJ, 506, L147
Trampedach, R. 1997, Master's Thesis, Aarhus University, Denmark
Turck-Chièze, S., García, R. A., Couvidat, S., et al. 2004, ApJ, 604, 455
Unno, W., Osaki, Y., Ando, H., Saio, H., & Shibahashi, H. 1989, Nonradial Oscillations of Stars (Tokyo: University of Tokyo Press)
Vorontsov, S. V., & Jefferies, S. M. 2013, ApJ, 778, 75
Wachter, R., & Kosovichev, A. G. 2005, ApJ, 627, 550

Appendix A: The inhomogeneous wave equation (Eq. (8))

A.1. Hydrodynamic equations and their linearisation

We linearise the governing, hydrodynamic equations in order to derive the wave equation with its source term. We consider that the mode velocity and the turbulent velocity obey separately their own continuity equation. Furthermore, we only consider radial modes, such that the mode velocity may we written in terms of the radial fluid displacement as $\boldsymbol{v}_{\rm osc} = \mathrm{d}\xi_r/\mathrm{d}t\, \boldsymbol{e_r}$. In this context, the governing equations are as follows:

– the continuity equation associated to the mode velocity can be written as

$$\frac{\partial \rho}{\partial t} + \boldsymbol{\nabla}(\rho \boldsymbol{v}_{\rm osc}) = 0. \tag{A.1}$$

Writing $\rho = \rho_0 + \rho'$ (where ρ' is the Eulerian density perturbation corresponding to the mode), linearising this equation around a motionless state, and integrating with respect to time yields

$$\rho' + \boldsymbol{\nabla}(\rho_0 \boldsymbol{\xi}) = 0. \tag{A.2}$$

We then introduce the Lagrangian density perturbation $\delta\rho = \rho' + (\boldsymbol{\xi}.\boldsymbol{\nabla})\rho_0$, which allows us to write the linearised continuity equation in its final form:

$$\frac{\delta\rho}{\rho_0} + \frac{1}{r^2}\frac{\mathrm{d}(r^2\xi_r)}{\mathrm{d}r} = 0; \tag{A.3}$$

– the Euler equation:

$$\frac{\partial \rho \boldsymbol{v}}{\partial t} + \boldsymbol{\nabla}{:}(\rho \boldsymbol{v}\boldsymbol{v}) = -\boldsymbol{\nabla}P + \rho \boldsymbol{g}. \tag{A.4}$$

Unlike what we did for the continuity equation, the velocity $\boldsymbol{v}$ now includes the mode velocity $\boldsymbol{v}_{\rm osc}$ as well as the turbulent velocity $\boldsymbol{u}_{\rm turb}$. We further decompose the latter into a mean value $\boldsymbol{U} \equiv \langle \boldsymbol{u}_{\rm turb} \rangle$ (where the notation $\langle . \rangle$ refers to an ensemble average) and fluctuations around this mean value $\boldsymbol{u} \equiv \boldsymbol{u}_{\rm turb} - \boldsymbol{U}$. As such, we have

$$\boldsymbol{v} = \boldsymbol{U} + \boldsymbol{v}_{\rm osc} + \boldsymbol{u} = \boldsymbol{U} + \mathrm{d}\xi_r/\mathrm{d}t\, \boldsymbol{e_r} + \boldsymbol{u}. \tag{A.5}$$

The last two terms are treated as small perturbations compared to the first one. In the term $\partial\rho\boldsymbol{v}/\partial t$, the contribution of $\boldsymbol{U}$ vanishes because we consider that $\boldsymbol{U}$ is independent of time (in other words, we consider a stationary turbulence), and the contribution of $\boldsymbol{u}$ vanishes after ensemble averaging. Concerning the advection term, among the 9 terms of its development, only 2 survive after the linearisation and ensemble averaging, namely $\boldsymbol{\nabla} : (\rho \boldsymbol{U}\boldsymbol{U})$ and $\boldsymbol{\nabla} : (\rho \boldsymbol{u}\boldsymbol{u})$. The first one can be rewritten as $\boldsymbol{\nabla} p_t$, where p_t is the turbulent pressure, and is of order zero, so that it will only impact the equilibrium structure. The second one can be equivalently rewritten as $\boldsymbol{\nabla} p'_t$, where p'_t refers to the perturbation of the turbulent pressure. Finally, performing a Fourier transform with respect to time, the radial component of the Euler equation reads:

$$-\omega^2 \xi_r + \frac{1}{\rho_0}\frac{\mathrm{d}p'}{\mathrm{d}r} + \frac{\rho'}{\rho_0} g_0 - g' = -\frac{1}{\rho_0}\frac{\mathrm{d}p'_t}{\mathrm{d}r}, \tag{A.6}$$

where p' is the Eulerian pressure perturbation, g_0 is the mean gravitational acceleration, g' is its Eulerian perturbation and $\mathrm{d}p'_t/\mathrm{d}r$ refers to the turbulent fluctuations of the Reynolds stress around its mean value. Since we only aim at modelling radial modes, using the Cowling approximation to eliminate g' would not reduce the order of the final wave equation, and is therefore of no particular use. Instead, we follow Unno et al. (1989) and express g' as a function of the radial fluid displacement (see their Eq. (14.36)):

$$g' = -\frac{\mathrm{d}\phi'}{\mathrm{d}r} = 4\pi G \rho_0 \xi_r. \tag{A.7}$$

One can note that this is equivalent to saying that the Lagrangian perturbation of the gravitational potential is zero.

– the equation of state we will use to close the system: after some algebra, a linearised version of the equation of state in terms of the Lagrangian perturbations can be derived:

$$\frac{\delta\rho}{\rho_0} = \frac{1}{\Gamma_1}\frac{\delta p}{p_0} - \frac{\rho_0 T_0}{p_0}\nabla_{\rm ad}\delta s, \tag{A.8}$$

where δs corresponds to the turbulent fluctuation of the specific entropy of the fluid and we define the various thermodynamic coefficients as

$$\Gamma_1 \equiv \left(\frac{\partial \ln p}{\partial \ln \rho}\right)_s$$
$$\nabla_{\rm ad} \equiv \left(\frac{\partial \ln T}{\partial \ln p}\right)_s. \tag{A.9}$$

In order to facilitate the following calculations, we replace the Lagrangian pressure perturbation δp with the Eulerian one p', and we derive two versions of the linearised equation of state, one with the Lagrangian density perturbation, one with the Eulerian one. Noting that the hydrostatic equilibrium gives us

$$\frac{\mathrm{d}p_0}{\mathrm{d}r} = -\rho_0 g_0\,, \tag{A.10}$$

and that by definition of the Brunt-Väisälä frequency, we have

$$\frac{N^2}{g_0} = \frac{1}{\Gamma_1}\frac{\mathrm{d}\ln p_0}{\mathrm{d}r} - \frac{\mathrm{d}\ln \rho_0}{\mathrm{d}r}, \tag{A.11}$$

and we finally obtain

$$\frac{\delta\rho}{\rho_0} = \frac{1}{\Gamma_1}\frac{p'}{p_0} - \frac{g_0\rho_0}{\Gamma_1 p_0}\xi_r - \frac{\rho_0 T_0}{p_0}\nabla_{\rm ad}\delta s$$
$$\frac{\rho'}{\rho_0} = \frac{1}{\Gamma_1}\frac{p'}{p_0} + \frac{N^2}{g_0}\xi_r - \frac{\rho_0 T_0}{p_0}\nabla_{\rm ad}\delta s. \tag{A.12}$$

A.2. Changing variables

The two variables that we wish to keep in these equations are ξ_r and p'. We first make use of Eq. (A.12) to eliminate the density fluctuations. Noting that $c^2 = \Gamma_1 p_0/\rho_0$ (where c is the sound speed), the continuity and Euler equations then yield:

$$\frac{\mathrm{d}(r^2\xi_r)}{\mathrm{d}r} - g_0\frac{r^2}{c^2}\xi_r + \frac{r^2}{\rho_0 c^2}p' = r^2\nabla_{\rm ad}\frac{\rho_0 T_0}{p_0}\delta s$$
$$\frac{1}{\rho_0}\frac{\mathrm{d}p'}{\mathrm{d}r} + \frac{g_0}{c^2}\frac{p'}{\rho_0} + (N^2 - \omega^2 - 4\pi G\rho_0)\xi_r = \frac{\rho_0 g_0 T_0}{p_0}\nabla_{\rm ad}\delta s - \frac{1}{\rho_0}\frac{\mathrm{d}p'_t}{\mathrm{d}r}. \tag{A.13}$$

In order to remove ξ_r from the 0th order term in the ξ_r equation, and same for p', the required variable change is then (Unno et al. 1989):

$$r^2\xi_r(r) = \widetilde{\xi}(r)\exp\left(\int_0^r \frac{g_0}{c^2}\,\mathrm{d}r'\right)$$
$$p' = \rho_0\widetilde{\eta}(r)\exp\left(\int_0^r \frac{N^2}{g_0}\,\mathrm{d}r'\right). \tag{A.14}$$

Plugging this into Eq. ((A.13)), we obtain

$$\frac{\mathrm{d}\widetilde{\xi}}{\mathrm{d}r} + \frac{r^2}{c^2}\exp\left(\int_0^r \frac{N^2}{g_0} - \frac{g_0}{c^2}\,\mathrm{d}r'\right)\widetilde{\eta} = r^2\exp\left(-\int_0^r \frac{g_0}{c^2}\,\mathrm{d}r'\right)\nabla_{\mathrm{ad}}\frac{\rho_0 T_0}{p_0}\delta s, \tag{A.15}$$

and

$$\frac{\mathrm{d}\widetilde{\eta}}{\mathrm{d}r} + \frac{1}{r^2}\exp\left(\int_0^r \frac{g_0}{c^2} - \frac{N^2}{g_0}\,\mathrm{d}r'\right)(N^2 - \omega^2 - 4\pi G\rho_0)\widetilde{\xi} = \exp\left(-\int_0^r \frac{N^2}{g_0}\,\mathrm{d}r'\right)\left[\nabla_{\mathrm{ad}}\frac{\rho_0 g_0 T_0}{p_0}\delta s - \frac{1}{\rho_0}\frac{\mathrm{d}p_t'}{\mathrm{d}r}\right], \tag{A.16}$$

where we denote the right-hand side terms of Eqs. (A.15) and (A.16) as S_0 and S_1 respectively in the following. We also define

$$I(r) \equiv \exp\left(\int_0^r \frac{N^2}{g_0} - \frac{g_0}{c^2}\,\mathrm{d}r'\right)$$
$$x(r) \equiv \frac{r\sqrt{I}}{c}$$
$$k^2 \equiv \frac{\omega^2 - N^2 + 4\pi G\rho_0}{c^2}. \tag{A.17}$$

The above set of equations can be rewritten as

$$\frac{\mathrm{d}\widetilde{\xi}}{\mathrm{d}r} + x^2\widetilde{\eta} = S_0$$
$$\frac{\mathrm{d}\widetilde{\eta}}{\mathrm{d}r} - \frac{k^2}{x^2}\widetilde{\xi} = S_1. \tag{A.18}$$

We can now eliminate $\widetilde{\eta}$ to get a single second-order wave equation. Using the first of Eq. (A.18) to express $\widetilde{\eta}$ as a function of $\widetilde{\xi}$, and plugging it in the second equation, we get the following equation:

$$\frac{\mathrm{d}^2\widetilde{\xi}}{\mathrm{d}r^2} - \frac{2}{x}\frac{\mathrm{d}x}{\mathrm{d}r}\frac{\mathrm{d}\widetilde{\xi}}{\mathrm{d}r} + k^2\widetilde{\xi} = \frac{\mathrm{d}S_0}{\mathrm{d}r} - \frac{2}{x}\frac{\mathrm{d}x}{\mathrm{d}r}S_0 - x^2 S_1. \tag{A.19}$$

Similarly to what has been done for the first change of variables, we wish for the left-hand side to contain no first-order term, but only second-order and 0th-order ones. Thus we introduce yet another variable: $\Psi(r) \equiv \widetilde{\xi}/x$. Plugging this new variable into Eq. (A.19), we easily obtain a wave equation that assumes the form of a 1D stationary Schrödinger equation

$$\frac{\mathrm{d}^2\Psi}{\mathrm{d}r^2} + \left(\frac{\omega^2}{c^2} - V(r)\right)\Psi = \frac{1}{x}\left(\frac{\mathrm{d}S_0}{\mathrm{d}r} - \frac{2}{x}\frac{\mathrm{d}x}{\mathrm{d}r}S_0 - x^2 S_1\right), \tag{A.20}$$

with an acoustic potential $V(r)$ that only depends on the star's equilibrium state:

$$V(r) = \frac{N^2 - 4\pi G\rho_0}{c^2} + \frac{2}{x^2}\left(\frac{\mathrm{d}x}{\mathrm{d}r}\right)^2 - \frac{1}{x}\frac{\mathrm{d}^2 x}{\mathrm{d}r^2}. \tag{A.21}$$

A.3. The source term

With the above notations, the parameters intervening in the source term of Eq. (A.20) have the following expressions:

$$S_0(r) = r^2\exp\left(-\int_0^r \frac{g_0}{c^2}\,\mathrm{d}r'\right)\nabla_{\mathrm{ad}}\frac{\rho_0 T_0}{p_0}\delta s$$
$$S_1(r) = \exp\left(-\int_0^r \frac{N^2}{g_0}\,\mathrm{d}r'\right)\left[\nabla_{\mathrm{ad}}\frac{\rho_0 g_0 T_0}{p_0}\delta s - \frac{1}{\rho_0}\frac{\mathrm{d}p_t'}{\mathrm{d}r}\right]$$
$$x(r) = \frac{r}{c}\exp\left(\frac{1}{2}\int_0^r \frac{N^2}{g_0} - \frac{g_0}{c^2}\,\mathrm{d}r'\right). \tag{A.22}$$

Furthermore, one can easily derive the following relationship between ∇_{ad} and $\alpha_s \equiv (\partial P/\partial s)_\rho$ by means of the adequate Schwarz relation:

$$\nabla_{\mathrm{ad}}\frac{\rho_0 T_0}{p_0} = \frac{\alpha_s}{\rho_0 c^2}. \tag{A.23}$$

After some manipulations, one finally obtain the source term in the form:

$$S(r) = \frac{r}{c\rho_0}\exp\left(-\frac{1}{2}\int_0^r \frac{N^2}{g_0} + \frac{g_0}{c^2}\,\mathrm{d}r'\right) \times\left[\alpha_s\delta s\frac{\mathrm{d}}{\mathrm{d}r}\ln\left(\frac{\alpha_s\delta s}{\rho_0}\right) - \alpha_s\delta s\left(\frac{N^2}{g_0} + \frac{g_0}{c^2}\right) + \frac{\mathrm{d}p_t'}{\mathrm{d}r}\right]. \tag{A.24}$$

Finally, since

$$\frac{N^2}{g_0} + \frac{g_0}{c^2} = -\frac{\mathrm{d}\ln\rho_0}{\mathrm{d}r}, \tag{A.25}$$

this expression can be drastically simplified to

$$S(r) = \frac{r}{c\sqrt{\rho_0(r=0)\rho_0(r)}}\left(\frac{\mathrm{d}(\alpha_s\delta s)}{\mathrm{d}r} + \frac{\mathrm{d}p_t'}{\mathrm{d}r}\right). \tag{A.26}$$

This form clearly shows that the source term can be split three ways: a monopolar source term (proportional to $\delta s\mathrm{d}\alpha_s/\mathrm{d}r$) due to non-adiabatic pressure fluctuations in a stratified environment, a dipolar term (proportional to $\alpha_s\mathrm{d}\delta s/\mathrm{d}r$) due to a stratification in the non-adiabatic pressure fluctuations themselves, and a quadripolar term (proportional to $\mathrm{d}p_t'/\mathrm{d}r$) due to Reynolds stress fluctuations. In the following, we only consider this last term but we also show here how the effect of non-adiabaticity can be introduced as well.

To conclude, note that the value of the fluid density at the centre of the star $\rho_0(r = 0)$ appears both in the definition of the variable Ψ and in the source term $S(r)$. This is due to the particular change of variable we have performed, and it can be factored out of the wave equation. Finally, we can put the wave equation in the following form:

$$\frac{\mathrm{d}^2\Psi}{\mathrm{d}r^2} + \left(\frac{\omega^2}{c^2} - V(r)\right)\Psi = S(r), \tag{A.27}$$

with $V(r)$ given by Eq. (A.21), and the source term and wave variable are given by

$$S(r) = \frac{r}{c\sqrt{\rho_0(r)}}\left(\frac{\mathrm{d}(\alpha_s\delta s)}{\mathrm{d}r} + \frac{\mathrm{d}p_t'}{\mathrm{d}r}\right)$$
$$\Psi(r) = rc(r)\sqrt{\rho_0(r)}\xi_r(r). \tag{A.28}$$

Appendix B: From the Green's function to the power spectral density

Here we detail the calculations carried out to obtain the expression of the velocity power spectral density (Eq. (13)) as a function of the Green's function associated with the homogeneous wave Eq. (8). Note that these calculations correspond to the "theoretical spectrum" model described in Sect. 2.3.2. The calculations in the "numerical spectrum" model being fairly similar, we do not detail it. We start with the development given by Eq. (4), with the expression of $\widehat{v_{\rm osc}}$ given by Eq. (12). We detail the treatment of both terms in the development (4) (leading term and cross term) separately.

B.1. The leading term

For more clarity, in the following, we introduce

$$X_\omega(\boldsymbol{r}) \equiv G_\omega(\boldsymbol{r}) \frac{\|\boldsymbol{r}\|}{c(\boldsymbol{r})\sqrt{\rho_0(\boldsymbol{r})}}. \tag{B.1}$$

We then have

$$\begin{aligned}\left\langle \left|\widehat{v_{\rm osc}}(\omega)\right|^2 \right\rangle &= \left\langle \frac{\omega^2}{r_{\rm o}^2 c_{\rm o}^2 \rho_0(r_{\rm o})} \times \iint \mathrm{d}^3\boldsymbol{r}_{s1}\mathrm{d}^3\boldsymbol{r}_{s2}\ \left(\boldsymbol{\nabla} X_\omega . \rho_0 \widehat{u_r \boldsymbol{u}}\right)(\boldsymbol{r}_{s1}) \right. \\ &\left. \times \left(\boldsymbol{\nabla} X_\omega^\star . \rho_0 \widehat{u_r \boldsymbol{u}}^\star\right)(\boldsymbol{r}_{s2}) \right\rangle, \end{aligned} \tag{B.2}$$

where $r_{\rm o}$ is the radius at which the spectrum is observed, $c_{\rm o}$ is the speed of sound at that radius, and the notation $\star$ refers to the complex conjugate.

We then perform the following change of variable: $\boldsymbol{R} = (\boldsymbol{r}_{s1} + \boldsymbol{r}_{s2})/2$ and $\boldsymbol{r} = (\boldsymbol{r}_{s1} - \boldsymbol{r}_{s2})/2$, the former being a "slow" variable, and the latter a "fast" variable. This allows us to separate the scales relevant to the turbulent velocity $\boldsymbol{u}$ from the scales relevant to the medium stratification and the mode wavelength, with turbulent quantities only relevant in the $\boldsymbol{r}$ scale and the stratification and Green function only relevant in the $\boldsymbol{R}$ scale. The scale separation approximation is not realistic in the subsurface layers (in particular, the mode wavelength is comparable to the typical correlation length associated with turbulence); however, for want of a better alternative, we are led to use this approximation in the following.

Therefore, we make the assumption that the second-order correlation product of the turbulent velocity vanishes for lengths much shorter than the scale associated to the variations of the equilibrium structure. Being able to separate the two scales, as well as the fact that, for radial modes, X_ω only depends on the radial coordinate, allows us to rewrite the leading term as

$$\begin{aligned}\left\langle \left|\widehat{v_{\rm osc}}(\omega)\right|^2 \right\rangle &= \frac{\omega^2}{r_{\rm o}^2 c_{\rm o}^2 \rho_0(r_{\rm o})} \\ &\times \int \mathrm{d}m \left|\frac{\mathrm{d}X_\omega}{\mathrm{d}R}\right|^2 \rho_0(R) \int \mathrm{d}^3\boldsymbol{r} \left\langle \widehat{u_r^2}(\boldsymbol{0},\omega)\widehat{u_r^2}^\star(\boldsymbol{r},\omega)\right\rangle, \end{aligned} \tag{B.3}$$

where we have dropped the variable $\boldsymbol{R}$ in favor of the more practical mass variable m. We note that we can only perform this change of variable because the wave equation is radial so that the function $X_\omega(\boldsymbol{r})$ only depends on the radial coordinate.

In the following, we focus on establishing the expression of the integral over the fast variable $\boldsymbol{r}$. By definition of the temporal Fourier transform appearing in said integral, we have

$$\begin{aligned}&\int \mathrm{d}^3\boldsymbol{r} \left\langle \widehat{u_r^2}(\boldsymbol{0},\omega)\ \widehat{u_r^2}^\star(\boldsymbol{r},\omega)\right\rangle \\ &\qquad = \frac{1}{(2\pi)^2} \iint \mathrm{d}^3\boldsymbol{r}\mathrm{d}\tau\ e^{-j\omega\tau} \left\langle u_r^2(\boldsymbol{0},0)\ u_r^2(\boldsymbol{r},\tau)\right\rangle. \end{aligned} \tag{B.4}$$

We then use the Quasi-Normal Approximation (hereby abbreviated QNA), under which any fourth-order correlation product can be decomposed into a sum of three second-order correlation products, so that (Lesieur 2008)

$$\left\langle u_r^2(\boldsymbol{0},0)u_r^2(\boldsymbol{r},\tau)\right\rangle = 2\left\langle u_r(\boldsymbol{0},0)u_r(\boldsymbol{r},\tau)\right\rangle^2 + \left\langle u_r(\boldsymbol{0},0)\right\rangle^2 \left\langle u_r(\boldsymbol{r},\tau)\right\rangle^2. \tag{B.5}$$

The last term does not depend on τ or $\boldsymbol{r}$ if the turbulence is homogeneous and uniform, and thus yields zero when the Fourier transform is performed. We can then write

$$\begin{aligned}&\int \mathrm{d}^3\boldsymbol{r} \left\langle \widehat{u_r^2}(\boldsymbol{0},\omega)\widehat{u_r^2}^\star(\boldsymbol{r},\omega)\right\rangle \\ &\qquad = \frac{2}{(2\pi)^2} \iint \mathrm{d}^3\boldsymbol{r}\mathrm{d}\tau\ \mathrm{e}^{-j\omega\tau} \left\langle u_r(\boldsymbol{0},0)u_r(\boldsymbol{r},\tau)\right\rangle^2. \end{aligned} \tag{B.6}$$

Using the Parseval identity, we can express this as an integral over wave vectors $\boldsymbol{k}$ and angular frequencies ω

$$\begin{aligned}&\int \mathrm{d}^3\boldsymbol{r} \left\langle \widehat{u_r^2}(\boldsymbol{0},\omega)\widehat{u_r^2}^\star(\boldsymbol{r},\omega)\right\rangle \\ &\qquad = 2\times(2\pi)^2 \\ &\qquad\quad \times \iint \mathrm{d}^3\boldsymbol{k}\mathrm{d}\omega'\ \mathrm{TF}\left[\mathrm{e}^{-j\omega\tau}\left\langle u_r(\boldsymbol{0},0)u_r(\boldsymbol{r},\tau)\right\rangle\right] \\ &\qquad\quad \times \mathrm{TF}\left[\left\langle u_r(\boldsymbol{0},0)u_r(\boldsymbol{r},\tau)\right\rangle\right], \end{aligned} \tag{B.7}$$

where the notation TF[.] refers to temporal and spatial Fourier transform.

We then proceed to describe the second-order correlation product not in terms of time and space increments, but in terms of angular frequencies ω and spatial modes $\boldsymbol{k}$. We denote the temporal and spatial Fourier transform of the second-order correlation product of the ith and jth component of the turbulent velocity as $\phi_{ij}(\boldsymbol{k},\omega)$, so that

$$\begin{aligned}&\int \mathrm{d}^3\boldsymbol{r} \left\langle \widehat{u_r^2}(\boldsymbol{0},\omega)\widehat{u_r^2}^\star(\boldsymbol{r},\omega)\right\rangle \\ &\qquad = 8\pi^2 \iint \mathrm{d}^3\boldsymbol{k}\mathrm{d}\omega'\ \phi_{rr}\left(\boldsymbol{k},\omega'-\omega\right)\phi_{rr}\left(\boldsymbol{k},\omega'\right). \end{aligned} \tag{B.8}$$

For isotropic turbulence, ϕ_{ij} can be expressed analytically (Batchelor 1953) as

$$\phi_{ij} = \frac{E(k,\omega)}{4\pi k^2}\left(\delta_{ij} - \frac{k_i k_j}{k^2}\right), \tag{B.9}$$

where $E(k,\omega)$ is the specific turbulent kinetic energy spectrum, k, k_i and k_j are the norm, ith component and jth component of the wave vector $\boldsymbol{k}$, and δ_{ij} is the Kronecker symbol. The integration over the solid angle of $\boldsymbol{k}$ is straightforward and only an integral over its norm remains. However, solar turbulence close to the photosphere is known to be highly anisotropic. To take this anisotropy into account, we follow the formalism developed by Gough (1977). In this formalism, the integral over the solid

angle of $\boldsymbol{k}$ is simply readjusted by adding an anisotropy factor G, given by (see Appendix B in Samadi & Goupil 2001)

$$G = \int_{-1}^{1} \mathrm{d}\mu \left(1 - \frac{Q^2\mu^2}{(Q^2-1)\mu^2+1}\right)^2, \tag{B.10}$$

where

$$Q^2 = \frac{\left\langle u_x^2 \right\rangle}{\left\langle u_r^2 \right\rangle} = \frac{\left\langle u_y^2 \right\rangle}{\left\langle u_r^2 \right\rangle}, \tag{B.11}$$

u_x and u_y referring to the two horizontal components of the turbulent velocity.

This anisotropy factor depends on the ratio between horizontal and vertical turbulent velocities, and therefore depends on the slow $\boldsymbol{R}$ variable – or equivalently, on the mass variable m. Under this formalism, the integral over k and ω remains the same as in the isotropic case.

Following Stein (1967), we decompose $E(k,\omega)$ into a spatial part $E(k)$, which describes how the turbulent kinetic energy is distributed among modes of different wave numbers, and a temporal part $\chi_k(\omega)$, which describes the statistical life-time distribution of eddies of wavenumber k

$$E(k,\omega) = E(k)\chi_k(\omega). \tag{B.12}$$

Finally, the integral given by Eq. (B.8) can be rewritten as

$$\int \mathrm{d}^3\boldsymbol{r} \left\langle \widehat{u_r^2}(\boldsymbol{0},\omega)\widehat{u_r^2}^{\star}(\boldsymbol{r},\omega)\right\rangle = 2\pi G \int \mathrm{d}k \, \frac{E(k)^2}{k^2} \int \mathrm{d}\omega' \, \chi_k(\omega'-\omega)\chi_k(\omega'). \tag{B.13}$$

As mentioned in the main body of the paper, we have followed two different leads to model the functions $E(k)$ and $\chi_k(\omega)$ in this study. In the following, we only detail what we refer to as the "theoretical spectrum" model, which is based on theoretical prescriptions.

Based on the assumption that turbulent flows are self-similar, Kolmogorov's theory of turbulence leads to a spatial spectrum $E(k) \propto k^{-5/3}$ in the inertial range, between $k = k_0$ (where k_0 is the scale at which the kinetic energy is injected in the turbulent cascade, and is henceforth referred to as the injection scale) and the dissipation scale (at which the turbulent kinetic energy is converted into heat). Given the very high Reynolds number characterising solar turbulence ($\mathrm{Re} \sim 10^{14}$), we cast the dissipation scale to infinity. Then, following Musielak et al. (1994), we extend the turbulent spectrum below the injection scale by considering that $E(k)$ takes a constant value for $k < k_0$. This extended spectrum, referred to as the BKS was introduced to account for the broadness of the maximum of $E(k)$. Finally, the BKS can be written thus:

$$E(k) = \begin{cases} 0.652\dfrac{u_0^2}{k_0} & \text{if } 0.2\ k_0 < k < k_0 \\ 0.652\dfrac{u_0^2}{k_0}\left(\dfrac{k}{k_0}\right)^{-5/3} & \text{if } k_0 < k, \end{cases} \tag{B.14}$$

where $u_0^2 \equiv \left\langle \boldsymbol{u}^2(\boldsymbol{r})\right\rangle/3$ and the 0.652 factor is introduced so that the total specific kinetic energy of the turbulent spectrum matches $u_0^2/2$.

Following Samadi et al. (2003), we consider a Lorentzian shape for the temporal spectrum $\chi_k(\omega)$, which is supported both by numerical simulations (Samadi et al. 2003) and by theoretical arguments (if the noise is characterised by a time-correlation function which decays exponentially, its spectrum is Lorentzian). Thus:

$$\chi_k(\omega) = \frac{1}{\pi\omega_k}\frac{1}{1+(\omega/\omega_k)^2}. \tag{B.15}$$

The width of the Lorentzian is the inverse of the typical correlation time-scale and by dimensional arguments, it is proportional to ku_k, where u_k is the typical velocity of eddies of wavenumber k. However, there remains a substantial indetermination on the actual value of ω_k. To account for this indetermination, we follow Balmforth (1992) and introduce the dimensionless parameter λ, so that

$$\omega_k = 2ku_k/\lambda. \tag{B.16}$$

For a Kolmogorov spectrum, u_k scales as $k^{-1/3}$, which means that we have

$$\omega_k = \omega_{k_0}\left(\frac{k}{k_0}\right)^{2/3} \equiv \frac{2k_0u_{k_0}}{\lambda}\left(\frac{k}{k_0}\right)^{2/3}, \tag{B.17}$$

There is a temptation to approximate the typical velocities of eddies of wavenumber k_0 with u_0. This assumption requires some discussion, however. Indeed, Stein (1967) has pointed out that eddies of all sizes have the same Eulerian velocity fluctuations u_0. As far as Lagrangian fluctuations go, the fluctuations u_k can be expressed as (Stein 1967)

$$u_k^2 = \int_k^{2k} \mathrm{d}k\ E(k). \tag{B.18}$$

Using the expression of $E(k)$ given in Eq. (B.14) and applying it to $k = k_0$, we finally find $u_{k_0} = 0.602u_0$. Under all these assumptions, all further calculations being carried out, we ultimately obtain the leading term,

$$\left\langle \left|\widehat{v_{\mathrm{osc}}}(\omega)\right|^2\right\rangle = \frac{0.353\lambda\omega^2}{r_{\mathrm{o}}^2c_{\mathrm{o}}^2\rho_0(r_{\mathrm{o}})}\int \mathrm{d}m \left[\rho_0 G\left|\frac{\mathrm{d}X_\omega}{\mathrm{d}r}\right|^2\frac{u_0^3}{k_0^4}\left(\int_{0.2}^{1} f_1(K)\mathrm{d}K + \int_1^{\infty} f_2(K)\mathrm{d}K\right)\right], \tag{B.19}$$

with

$$f_1(K) = \frac{K^{-8/3}}{1+\left(\dfrac{\lambda\omega}{2.408u_0k_0}\right)^2 K^{-4/3}}$$
$$f_2(K) = \frac{K^{-6}}{1+\left(\dfrac{\lambda\omega}{2.408u_0k_0}\right)^2 K^{-4/3}}, \tag{B.20}$$

and where K is the reduced inverse eddy scale ($K \equiv k/k_0$). We note that all the terms appearing in the integrand depend on the mass variable m, particularly u_0 and k_0, even when the dependence does not appear explicitly. Free parameters are left in this description of the leading term in the form of λ and $k_0(m)$; solar turbulence close to the photosphere being as poorly constrained as it is today, we cannot hope to achieve a non-parametrised description of stochastically excited modes of oscillation.

B.2. The cross term

Similarly to the leading term, the cross term in the development of $P(\omega)$ shown in Eq. (4) can be written as

$$\mathrm{Re}\left(\int \mathrm{d}\Omega\, \widetilde{h}(\mu)\left\langle \widehat{v_{\mathrm{osc}}}(\omega)\widehat{u_n}^{\star}(\omega)\right\rangle\right) = -\frac{\omega}{r_{\mathrm{o}}c_{\mathrm{o}}\sqrt{\rho_0(r_{\mathrm{o}})}} \times \int \mathrm{d}\Omega\, \widetilde{h}(\mu)\mathrm{Re}\left(j\int \mathrm{d}^3\boldsymbol{r}_{\mathrm{s}}\, \rho_0 \frac{\mathrm{d}X_\omega}{\mathrm{d}r}\left\langle \widehat{u_r^2(\boldsymbol{r}_{\mathrm{s}})}\widehat{u_n(\boldsymbol{r}_{\mathrm{o}})}^{\star}\right\rangle\right), \tag{B.21}$$

where μ is the cosine of the angle between the local vertical direction and the direction of the line of sight.

We note that this time, one of the velocities in the correlation product is estimated at a fixed location corresponding to the observation height, so that only one variable is left. Expressing the line-of-sight component of $\boldsymbol{u}$ as $u_n = u_r\cos\theta - u_\theta\sin\theta$, this transforms into

$$\mathrm{Re}\left(\int \mathrm{d}\Omega\, \widetilde{h}(\mu)\left\langle \widehat{v_{\mathrm{osc}}}(\omega)\widehat{u_n}^{\star}(\omega)\right\rangle\right) = -\frac{\omega}{r_{\mathrm{o}}c_{\mathrm{o}}\sqrt{\rho_0(r_{\mathrm{o}})}} \times \left[\mathrm{Re}\left(j\int \mathrm{d}m\, \frac{\mathrm{d}X_\omega}{\mathrm{d}r}\left\langle \widehat{u_r^2(\boldsymbol{r}_{\mathrm{s}})}\widehat{u_r(\boldsymbol{r}_{\mathrm{o}})}^{\star}\right\rangle\right)\int \mathrm{d}\Omega\, \widetilde{h}(\mu)\mu + \mathrm{Re}\left(j\int \mathrm{d}m\, \frac{\mathrm{d}X_\omega}{\mathrm{d}r}\left\langle \widehat{u_r^2(\boldsymbol{r}_{\mathrm{s}})}\widehat{u_\theta(\boldsymbol{r}_{\mathrm{o}})}^{\star}\right\rangle\right)\int \mathrm{d}\Omega\, \widetilde{h}(\mu)\sqrt{1-\mu^2}\right]. \tag{B.22}$$

Since u_θ is a horizontal component of the turbulent velocity, if we consider there is no preferential horizontal direction as far as turbulence goes, the third-order correlation product appearing in the second integral cancels out, so that we are left with the first integral only. The latter can be rewritten thus:

$$\int \mathrm{d}m\, \frac{\mathrm{d}X}{\mathrm{d}r}\left\langle \widehat{u_r^2(\boldsymbol{r}_{\mathrm{s}})}\widehat{u_r(\boldsymbol{r}_{\mathrm{o}})}^{\star}\right\rangle = \int \mathrm{d}^3\boldsymbol{r}_{\mathrm{s}1}\mathrm{d}^3\boldsymbol{r}_{\mathrm{s}2}\, \rho_0(\boldsymbol{r}_{\mathrm{s}1})\frac{\mathrm{d}X}{\mathrm{d}r}(\boldsymbol{r}_{\mathrm{s}1})\left\langle \widehat{u_r^2(\boldsymbol{r}_{\mathrm{s}1})}\widehat{u_r(\boldsymbol{r}_{\mathrm{s}2})}^{\star}\right\rangle\delta(\boldsymbol{r}_{\mathrm{s}2}-\boldsymbol{r}_{\mathrm{o}}), \tag{B.23}$$

where we have artificially introduced a second spatial variable $\boldsymbol{r}_{\mathrm{s}2}$, so as to get an expression formally similar to that of the leading term above. Performing the same change of variables, and plugging the definition of the temporal Fourier transform, we have

$$\int \mathrm{d}m\, \frac{\mathrm{d}X}{\mathrm{d}r}\left\langle \widehat{u_r^2(\boldsymbol{r}_{\mathrm{s}})}\widehat{u_r(\boldsymbol{r}_{\mathrm{o}})}^{\star}\right\rangle = \frac{1}{(2\pi)^2}\rho_0(\boldsymbol{r}_{\mathrm{o}})\frac{\mathrm{d}X}{\mathrm{d}r}(\boldsymbol{r}_{\mathrm{o}})\int \mathrm{d}\tau\mathrm{d}^3\boldsymbol{r}\, e^{-j\omega\tau}\left\langle u_r^2(0,\boldsymbol{0})u_r(\tau,\boldsymbol{r})\right\rangle. \tag{B.24}$$

The challenge in estimating the contribution of correlated turbulent perturbations fundamentally lies in the correct determination of non-local, third-order correlation products. While the QNA provides an adequate closure relationship for fourth-order moments, it yields vanishing third-order moments, which is known to lead to serious violations of the energy conservation principle, as well as an impossibility for the turbulent cascade to develop (see Kraichnan 1957).

In order to estimate the third-order moments, we follow Belkacem et al. (2006b) and use the Plume closure model, which consists of separating the flow into upward flows and downward plumes, each normally distributed, with different mean values and standard deviations. In addition, we consider that the downflows are much more turbulent than the upflows (which is supported by Goode et al. 1998, according to whom the intergranular lanes harbour stronger turbulence than the granules themselves at the Sun's surface), and that the two types of flows considered separately have zero third-order correlation products. In Belkacem et al. (2006b), the authors use the same approximations but focused on one-point correlation products; however, the calculations can be easily extended to the two-point correlation products that we need and the model yields

$$\begin{aligned}\langle u_r(\boldsymbol{R},t)^2 u_r(\boldsymbol{R}+\boldsymbol{r},t+\tau)\rangle = {} & \left[a(1-a)^3 - a^3(1-a)\right]\delta u^3 \\ & - a(1-a)\left[2\langle \widetilde{u_d}(\boldsymbol{R},t)\widetilde{u_d}(\boldsymbol{R}+\boldsymbol{r},t+\tau)\rangle\right. \\ & \left.+\langle \widetilde{u_d}(\boldsymbol{R},t)^2\rangle\right]\delta u,\end{aligned} \tag{B.25}$$

where a is the relative horizontal section of the upflows, δu is the difference between the mean velocity of the two types of flows (considering their respective signs, it actually is the sum of their absolute values), and $\widetilde{u_d}$ is the fluctuation of the downflow velocity around its mean value. The only additional approximation we make to adapt these calculations to two-point correlation products is that the parameters of the model a and δu vary on scales much greater than the typical correlation length, which is another illustration of the scale separation approximation, which we have already used for the leading term (see above).

Note that strictly speaking, the third-order moment appearing in Eq. (B.25) and yielded by the PCM are centred. However, we consider that the mean value of the overall vertical velocity of the flow is sufficiently low (compared to its standard deviation for instance) to be neglected. Therefore, the moment described by Eq. (B.25) may interchangeably refer either to a centred or non-centred moment.

Also note that this closure relation is written here in terms of $\widetilde{u_d}$ (i.e. the turbulent fluctuations in the downflows only). It would be more practical to rewrite it in terms of u_r (i.e. the total turbulent fluctuations). The two are related through

$$\langle \widetilde{u_d}(\boldsymbol{R},t)\widetilde{u_d}(\boldsymbol{R}+\boldsymbol{r},t+\tau)\rangle = \frac{1}{1-a}\langle u_r(\boldsymbol{R},t)u_r(\boldsymbol{R}+\boldsymbol{r},t+\tau)\rangle - a\delta u^2\,. \tag{B.26}$$

Plugging Eq. (B.26) into Eq. (B.25), we obtain a closure model that allows us to write the third-order moments as a function of second-order moments only, after which we can use the same prescriptions for turbulence as we did for the leading term. We note that while this closure relation contains many terms, not many survive the Fourier transform in Eq. (B.24) as all terms not depending on $\boldsymbol{r}$ or τ will not contribute to the Fourier transform. The integral over m appearing in Eq. (B.21) becomes

$$\int \mathrm{d}m\, \frac{\mathrm{d}X}{\mathrm{d}r}\left\langle \widehat{u_r^2(\boldsymbol{r_s})}\widehat{u_r(\boldsymbol{r_o})}^{\star}\right\rangle = -8\pi^2 a\delta u\rho_0(r_o)\frac{\mathrm{d}X}{\mathrm{d}r}(r_o)\phi_{rr}(\boldsymbol{0},\omega). \tag{B.27}$$

Formally, the integration over $\boldsymbol{r}$ makes the value of ϕ_{rr} at $\boldsymbol{k}=\boldsymbol{0}$ appear. Physically, that means only the largest eddies have a significant impact on the correlation between the mode and the turbulent perturbations. Since considering eddies characterised by $\boldsymbol{k}=\boldsymbol{0}$ does not actually make physical sense, we considered a comprise by assuming that the largest contributing eddies are those at the injection scale k_0, so that the correlated turbulent perturbations term finally becomes

$$\mathrm{Re}\left(\int \mathrm{d}\Omega\, \widetilde{h}(\mu)\left\langle \widehat{v_{\mathrm{osc}}}(\omega)\widehat{u_n}^{\star}(\omega)\right\rangle\right) = C(\omega)\int \mathrm{d}\Omega\, \widetilde{h}(\mu)\mu$$

$$C(\omega) = -\frac{1.083\lambda a\omega u_0\delta u}{r_{\mathrm{o}}c_{\mathrm{o}}k_0^4}$$

$$\times \sqrt{\rho_0(r_o)}\left.\frac{\mathrm{d}\mathrm{Im}X_\omega}{\mathrm{d}r}\right|_{r_o} \times \left(1+\left(\frac{\lambda\omega}{1.204k_0u_0}\right)^2\right)^{-1}, \quad \text{(B.28)}$$

where every parameter is estimated at the observation height r_o, even when not specified explicitly. Note that we introduce no new free parameter compared to those used for the leading term, as the parameters a and δu appearing in the PCM are extracted from numerical hydrodynamic simulations of the stellar atmosphere. Plugging Eqs. (B.19) and (B.28) in the expression of the velocity power spectral density given by Eq. (4), we obtain Eq. (13).

Appendix C: A simplified toy model

Here we consider a simplified model of solar acoustic mode excitation, which has already been developed, used, and analysed in previous works (see e.g. Abrams & Kumar 1996; Chaplin & Appourchaux 1999). In the scope of this toy-model, the acoustic potential appearing in Eq. (8) takes the form of a square well, and the sound speed c is considered constant throughout the entire stellar radius. The latter approximation allows us to substitute the radial coordinate r in the wave equation for the acoustic depth τ, defined such that $\mathrm{d}\tau = \mathrm{d}r/c$. In this approximation, the wave equation simply yields

$$\frac{\mathrm{d}^2\Psi}{\mathrm{d}\tau^2} + (\omega^2 - V(\tau) + j\omega\gamma)\Psi = \delta(\tau-\tau_s), \quad \text{(C.1)}$$

where we have introduced a point-like source at acoustic depth τ_s, and the acoustic potential is

$$V(\tau) = \begin{cases} +\infty & \text{if } \tau < 0 \\ 0 & \text{if } 0 \le \tau \le a \\ \alpha^2 & \text{if } a < \tau. \end{cases} \quad \text{(C.2)}$$

In this model, a represents the acoustic length of the cavity (for radial modes, it corresponds to the time it takes for sound waves to propagate throughout the entire stellar radius) and α is the acoustic cut-off angular frequency above which waves are no longer confined. We added an infinite step at $\tau = 0$ to force the wave variable Ψ to vanish at the centre.

C.1. Analytic solution of Eq. (C.1)

In order to solve the wave equation, it should be rewritten in terms of matrices:

$$\frac{\mathrm{d}X}{\mathrm{d}\tau} = AX + B, \quad \text{(C.3)}$$

where

$$X = \begin{bmatrix} \Psi \\ \mathrm{d}\Psi/\mathrm{d}\tau \end{bmatrix}$$
$$A = \begin{bmatrix} 0 & 1 \\ V(\tau) - \omega^2 - j\omega\gamma & 0 \end{bmatrix} \quad \text{(C.4)}$$
$$B = \begin{bmatrix} 0 \\ \delta(\tau-\tau_s) \end{bmatrix}.$$

The general solution to the homogeneous equation is $X_h(\tau) = \exp(A\tau)C$, where C is a constant vector. A particular solution to the inhomogeneous equation can then be sought in the form $X_p(\tau) = \exp(A\tau)C(\tau)$. For each domain in which the matrix A is constant, injecting this form in Eq. (C.3) yields

$$C(\tau) = \begin{cases} \begin{bmatrix} 0 \\ 0 \end{bmatrix} & \text{if } \tau < \tau_s \\ \\ \begin{bmatrix} 0 \\ \exp(-A\tau_s) \end{bmatrix} & \text{if } \tau_s \leqslant \tau. \end{cases} \quad \text{(C.5)}$$

A being piecewise constant, we can thus write the general solution to Eq. (C.3) as

$$X(\tau) = \begin{cases} \exp(A\tau)C & \text{if } \tau < \tau_s \\ \exp(A\tau)\left(C + \begin{bmatrix} 0 \\ \exp(-A\tau_s) \end{bmatrix}\right) & \text{if } \tau_s \leqslant \tau, \end{cases} \quad \text{(C.6)}$$

where the integration constant C is constant on whichever domain A is; in other words, C is piecewise constant on the same domains as A, that is, between 0 and a, and above a separately. In the following, we denote the column vector C as $[A_i\ B_i]$ in the former domain, and $[A_o\ B_o]$ in the latter, the indices i and o referring to the inner and outer regions, respectively.

The simple form of A allows for a straightforward computation of its exponential. We obtain

$$\exp(A\tau) = \begin{cases} \begin{bmatrix} \cos\omega_i\tau & \dfrac{\sin\omega_i\tau}{\omega_i} \\ -\omega_i\sin\omega_i\tau & \cos\omega_i\tau \end{bmatrix} & \text{if } 0 < \tau < a \\ \\ \begin{bmatrix} \cosh\omega_o\tau & \dfrac{\sinh\omega_o\tau}{\omega_o} \\ \omega_o\sinh\omega_o\tau & \cosh\omega_o\tau \end{bmatrix} & \text{if } a < \tau, \end{cases} \quad \text{(C.7)}$$

where $\omega_i^2 = \omega^2 + j\omega\gamma$ and $\omega_o^2 = \alpha^2 - \omega^2 - j\omega\gamma$ (with the understanding that $0 < \omega < \alpha$).

Finally, injecting this into the general solution (C.6) and only keeping the first line (at this point, the second one only gives the derivative of the solution and is redundant with the solution itself) yields the following expression, depending on whether the source is inside the cavity or not:

$$\Psi_i(\tau) = \begin{cases} A_i\cos\omega_i\tau + \dfrac{B_i}{\omega_i}\sin\omega_i\tau & \text{if } \tau < \tau_s \\ A_i\cos\omega_i\tau + \dfrac{B_i}{\omega_i}\sin\omega_i\tau & \\ \quad + \dfrac{1}{\omega_i}\sin\omega_i(\tau-\tau_s) & \text{if } \tau_s < \tau < a \\ A_o\cosh\omega_o\tau + \dfrac{B_o}{\omega_o}\sinh\omega_o\tau & \text{if } a < \tau_s, \end{cases} \quad \text{(C.8)}$$

and

$$\Psi_o(\tau) = \begin{cases} A_i\cos\omega_i\tau + \dfrac{B_i}{\omega_i}\sin\omega_i\tau & \text{if } \tau < a \\ A_o\cosh\omega_o\tau + \dfrac{B_o}{\omega_o}\sinh\omega_o\tau & \text{if } a < \tau < \tau_s \\ A_o\cosh\omega_o\tau + \dfrac{B_o}{\omega_o}\sinh\omega_o\tau & \\ \quad + \dfrac{1}{\omega_o}\sinh\omega_o(\tau-\tau_s) & \text{if } \tau_s < \tau, \end{cases} \quad \text{(C.9)}$$

where Ψ_i is the solution if the source is inside the cavity ($\tau_s < a$) and Ψ_o is the solution if the source is outside ($a < \tau_s$). Predictably, this general solution contains 4 constants of integration (in the form of A_i, B_i, A_o and B_o), and we therefore need 4 boundary conditions to find Ψ_i and Ψ_o. We impose that $\Psi(\tau = 0) = 0$ and that the solution do not diverge when $\tau \to +\infty$; furthermore,

we impose that both Ψ and its derivative be continuous at $\tau = a$. With all calculations having been carried out, this set of boundary conditions finally gives us:

$$\begin{aligned}
\Psi_{\mathrm{i,o}}(\tau) &= -\frac{f_{\mathrm{i,o}}(\tau_\mathrm{s})}{\omega_\mathrm{i}\cos\omega_\mathrm{i}a + \omega_\mathrm{o}\sin\omega_\mathrm{i}a}\exp^{-\omega_\mathrm{o}(\tau-a)} \\
f_\mathrm{i}(\tau_\mathrm{s}) &= \sin\omega_\mathrm{i}\tau_\mathrm{s} \\
f_\mathrm{o}(\tau_\mathrm{s}) &= \omega_\mathrm{i}\cos\omega_\mathrm{i}a\sinh\omega_\mathrm{o}(\tau_\mathrm{s}-a) \\
&\quad + \omega_\mathrm{o}\sin\omega_\mathrm{i}a\cosh\omega_\mathrm{o}(\tau_\mathrm{s}-a).
\end{aligned} \tag{C.10}$$

We note that the above expression is only valid if $\tau > a$ and $\tau > \tau_\mathrm{s}$. Since the first condition means that we observe the mode of oscillation above the upper turning point (which is always the case in practice) and since the second condition means that the excitation of the mode occurs in layers located deeper than the observation height in the atmosphere (which is also always the case in practice, at least for spectrometric measurements), these are not restrictive conditions.

C.2. Discussion

In each case (source inside or outside the cavity), the solution $\Psi_{\mathrm{i,o}}$ can be decomposed into three parts:

- the denominator corresponds to the Wronskian $W(\omega)$ of the wave equation. $|1/W(\omega)|^2$ peaks at the eigenfrequencies associated to the acoustic cavity and is responsible for the presence of resonant modes in the spectrum. The line profile it generates have a Lorentzian profile, so long as the damping rate of the modes are much smaller than their frequency;
- the exponential part accounts for the fact that the modes are evanescent outside the acoustic cavity, so that the higher in the atmosphere the mode is observed, the lower its amplitude as we observe it. Therefore, it only affects the observed amplitude of the mode, not its line profile;
- the numerator $f_{\mathrm{o,i}}(\tau_\mathrm{s})$ is responsible for the mode line profile asymmetry. Because it is the only term that depends on the source position τ_s, it is commonly said that mode asymmetry is caused by source localisation.

Regardless of whether the source is located inside or outside the cavity, it can be seen from Eqs. (C.8) and (C.9) that the third term $f_{\mathrm{o,i}}(\tau_\mathrm{s})$ actually corresponds to the amplitude of the solution $\Psi_{\mathrm{i,o}}$ at $\tau = \tau_\mathrm{s}$. This leads us to the following conclusion, which we reproduce in the main body of the paper: for a given frequency, the amplitude of the excited wave is proportional to the radial profile associated with the wave at the source of excitation.

6 Velocity-Intensity asymmetry reversal: insight from our model

Contents

> Oh ! Il y a certes dans ma maison toutes les choses inutiles. Il n'y manque que le nécessaire, un grand morceau de ciel comme ici. Tâchez de garder toujours un morceau de ciel au-dessus de votre vie.
>
> Marcel Proust, à propos de Paris

This chapter is devoted to the work of Philidet et al. (2020b). All the details of this work are presented in this article, which I reproduce in the end of this chapter. I will not present all these details in the body of the thesis, as this would be redundant. Instead, I focus on the main steps of the adaptation of the model presented in Chapter 5 to intensity measurements, and on the results yielded by the application of this adapted model to the solar case.

6.1 Adaptation of the formalism to intensity measurements

In Chapter 5, I described how I modelled the wave variable $\Psi_\omega(r)$ for any angular frequency ω. I then used Equation 5.4 to relate this wave variable to the oscillatory component of the velocity $\widehat{v_{\rm osc}}(\omega)$. In order to adapt this model to intensity measurements, the challenge is therefore to find a similar relation between the modelled $\Psi_\omega(r)$ and the oscillatory component of the luminosity perturbation $\widehat{\delta L}(\omega)/L$. This is done in Sections 2.1 and 2.2 of Philidet et al. (2020b). I do not detail the calculations here; however, let me list the approximations I adopted and the assumptions I made in order to carry them out. In addition to hypotheses (H1) to (H5) listed in Section 5.1, those are the following

(H6) following Dupret et al. (2002), I treat the superficial layers responsible for the driving of the modes as a *grey atmosphere*. This assumption is justified by the fact that the photometric measurements leading to the observed intensity power spectrum correspond to the continuum intensity, on which the atomic absorption lines that form in the atmosphere have almost no impact. As a result of this assumption, the gas temperature becomes a function of optical depth and effective temperature only[1], in the form (see Philidet et al. 2020b, Eq. 3)

$$T(\tau, T_{\rm eff}) = \left(\frac{3}{4}(\tau + q(\tau))\right)^{1/4} T_{\rm eff}\,, \tag{6.1}$$

[1] In general, it is also a function of the surface gravity. However, as I mentioned in Section 2.1.1, the perturbation of the gravitational acceleration by the oscillations is negligible, thus leading to the well-established Cowling approximation. The surface gravity remaining constant, it can be discarded from the list of variables on which the gas temperature depends.

where $q(\tau)$ is the Hopf function (Mihalas and Mihalas 1984). I adopt a *solar-calibrated Hopf function*, based on solar spectroscopic measurements performed by Vernazza et al. (1981). The Hopf function reads (Sonoi et al. 2019)

$$q(\tau) = 1.036 - \ 0.3134 \ \exp^{-2.448\ \tau} - 0.2959 \ \exp^{-30.0\ \tau} \ . \tag{6.2}$$

(see also Philidet et al. 2020b, Eq. 16).

(H7) I consider that the atmosphere is in *radiative equilibrium*, so that the perturbed emergent radiative flux is the same as the perturbed radiative flux at the photosphere;

(H8) I consider that the *convective flux is frozen*, meaning that its Lagrangian perturbation vanishes. This is typically the case when the convective timescale τ_{to} (i.e. the turnover time of the turbulent eddies) is much greater than the modal timescale Π (i.e. the period of the modes). Indeed, in that case, the convective flux never has time to adapt to the continuously changing physical conditions, and the effect of the modes over an entire cycle cancels out, so that the convective luminosity always remains the same. Unfortunately, as I made abundantly clear in Section 2.3, the two timescales become similar close to the surface of the star, so that the convective flux must be treated in a time-dependent manner. Nevertheless, until the model is refined, and as a first step, I will neglect the perturbation of the convective flux. This allows me to write $\delta L = \delta L^{\text{rad}}$, where L^{rad} is the radiative luminosity defined by Equation 2.104;

(H9) I place myself in the *quasi-adiabatic approximation*, in the sense that I neglect the Lagrangian perturbation of entropy in the expression of the temperature fluctuations. This allows me to write

$$\frac{\delta T}{T} = \Gamma_1 \nabla_{\text{ad}} \frac{\delta \rho}{\rho} \ . \tag{6.3}$$

Similarly to hypothesis (H3), the quasi-adiabatic approximation is not valid close to the surface of the star (see Section 2.1.1). But going beyond this approximation would require adopting a fully non-adiabatic framework for the oscillations, which would drastically increase the complexity of the formalism. Furthermore, as I hinted in Section 4.1, since the asymmetries are only affected by differential effects – i.e. processes that affect the line profiles differently in one wing than in the other –, non-adiabatic effects are likely to only have a weak impact on mode asymmetry. Therefore, as a first step, I adopt this approximation in the following;

(H10) I *discard the effect of the correlated background* on the synthetic intensity power spectrum, meaning that I only retain the first term on the right-hand side of Equation 5.1 (or rather its intensity equivalent). While this contribution is negligible in the velocity power spectrum (as was showed in Philidet et al. (2020a)), it does not necessarily have the same impact in the intensity power spectrum, where it can have a higher relative amplitude, as I showed in Section 4.2.2. However, the same way including the effect of the correlated background in the velocity p-mode spectrum required describing the third-order moment of the turbulent velocity (see Chapter 5), including this contribution in the intensity p-mode spectrum would require modelling third-order moments involving both the turbulent velocity and the turbulent entropy fluctuations. For lack of an appropriate closure relation for these third-order moments, I do not include this contribution in the synthetic intensity power spectrum model. As a result of this approximation, the intensity asymmetries I obtain only contain the effect of source localisation;

(H11) as in Philidet et al. (2020a), I consider that *the driving of the modes is primarily due to perturbations of the Reynolds stress force*, and in particular, I do not account for the non-adiabatic perturbation of the pressure force. As shown by Samadi et al. (2003), the Reynolds stress force is the dominant contribution to p-mode excitation, meaning that this hypothesis is justified.

These hypotheses do not share the same degree of validity. More specifically, hypotheses (H6), (H7) and (H11) are valid to a satisfactory degree, and are not restrictive assumptions. On the other hand, hypotheses (H8), (H9) and (H10) are strong approximations, which I only adopt as a first step, because circumventing them would require a considerably more complex approach. Nevertheless, with all these assumptions in mind, the formalism described in Chapter 5 can be adapted to photometric measurements, thus yielding a synthetic intensity power spectrum

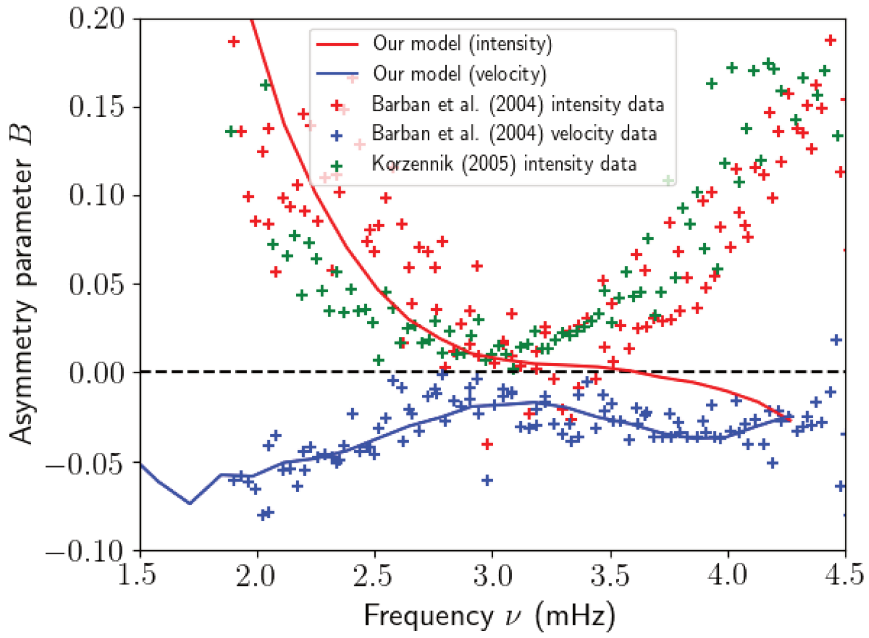

Figure 6.1: Asymmetry profile $B(\nu)$ obtained through the 'numerical spectrum' model with $\lambda = 0.5$, in the intensity power spectrum (solid red line) and in the velocity power spectrum (solid blue line). Both are compared to the asymmetry profile inferred from observations by Barban et al. (2004) in the intensity and velocity power spectra (red and blue crosses respectively), as well as the asymmetry profile inferred from intensity observations by Korzennik (2005) (green crosses). Credits: Philidet et al. (2020b).

model, in the form of Eqs. (23), (24) and (25) in Philidet et al. (2020b). From this synthetic power spectrum, radial p-mode asymmetries can be extracted in terms of intensity through the exact same procedure described in Chapter 5 for velocity measurements. Of particular importance is the fact that *under the extra hypotheses listed above, no additional free parameter is needed, so that the velocity and intensity power spectra are modelled simultaneously.*

6.2 Results and discussion

My goal here is to assess whether the model presented here, which was already validated for velocity measurements in Philidet et al. (2020a), is also able to make equally accurate predictions in terms of intensity measurements. Therefore, I will only interest myself with the 'numerical spectrum' model (see Chapter 5) – i.e. the model that has predictive capabilities. Moreover, instead of leaving the only parameter of the model (λ) free, I retain the exact same value already adopted in Philidet et al. (2020a): $\lambda = 0.5$. Indeed, it does not make sense to use different values of the same physical quantity in the same model, under the pretext that different observables are considered. Only by adopting a unique value is it possible assess whether or not the predictions made by this model are accurate for velocity and intensity measurements simultaneously. The results are shown in Figure 2 of Philidet et al. (2020b), which we reproduce in Figure 6.1, and where the predictions of the model are shown in both observables at the same time – in the form of the blue (velocity) and red (intensity) solid lines –, while the observed values are represented by the blue (velocity), red and green (intensity) crosses. I insist on remarking that this is simply a superposition of theoretical predictions and observations, not the result of an adjustment. There are two main results to be kept in mind: 1) that the observed asymmetry reversal is accurately predicted by our model throughout a significant portion of the solar p-mode spectrum – more specifically for $\nu \lesssim 3$ mHz, but that 2) our model fails to predict asymmetry reversal for modes with a higher frequency.

The first point has to do with the specific form of the relation between $\widehat{\delta L}(\omega)/L$ and Ψ_ω, whose derivation concentrates all the efforts deployed in adapting the model to intensity measurements, as I mentioned in the very

first lines of Section 6.1. This relation is given by (see Philidet et al. 2020b, Eq. 20)

$$\frac{\widehat{\delta L}}{L} = \frac{L^{\rm rad}}{L}\left(A_L\Psi_\omega + B_L\frac{\mathrm{d}\Psi_\omega}{\mathrm{d}r} + C_L\frac{\mathrm{d}^2\Psi_\omega}{\mathrm{d}r^2}\right), \tag{6.4}$$

where $L^{\rm rad}$ is the equilibrium radiative luminosity (see Equation 2.104 for a definition), L is the total equilibrium luminosity, and A_L, B_L and C_L are coefficients given by Eqs. (21) and (22) in Philidet et al. (2020b), and only depend on the equilibrium structure of the star. Instead of the simple proportionality relation between $\widehat{v_{\rm osc}}(\omega)$ and Ψ_ω given by Equation 5.4, one now obtains a much more complex relation involving not only Ψ_ω, but also its first and second derivatives with respect to the radial coordinate[2]. Since Ψ_ω and its derivatives do not have the same ω-dependence, the total line profiles does not necessarily have the same shape in intensity as it does in velocity. It is therefore not overly surprising to obtain different asymmetries between the two, and even a reversal in sign. To further establish that it is the presence of several terms in the right-hand side of Equation 6.4 that entails the asymmetry reversal, I performed the exact same calculations by adopting the following, overly simplified relation instead

$$\frac{\delta T}{T} = \frac{\delta T_{\rm eff}}{T_{\rm eff}}\,. \tag{6.5}$$

The asymmetry profile $B(\nu)$ obtained in this approximation is shown in Figure 3 of Philidet et al. (2020b), where it is apparent that no asymmetry reversal is observed in that case. It is clear, therefore, that the key in understanding the asymmetry reversal puzzle does not lie in an extra physical mechanism, like the presence of a high amplitude correlated background in one of the observables for instance, but instead *in the complicated relation between the Green's functions in intensity and temperature*. In many studies on the subject of asymmetry reversal, this relation is assumed to be extremely simple: either they are considered identical, which amounts to adopting Equation 6.5 (e.g. Duvall et al. 1993; Rast and Bogdan 1998; Nigam et al. 1998; Kumar and Basu 1999b), or it is the velocity and intensity Green's function that are considered identical (e.g. Roxburgh and Vorontsov 1997; Chaplin and Appourchaux 1999). All these studies share this common point, that they do not fully account for the more complicated relation given, for instance, by Equation 6.4: this is the reason why an alternative mechanism has always been invoked to explain the asymmetry reversal puzzle.

On the other hand, the second key point mentioned above – about the quantitative predictions no longer being accurate for frequencies higher than ~ 3 mHz – shows that this picture has its limits. For higher-frequency modes, Figure 6.1 shows that there is some ingredient missing in this model. A number of explanations can be given to explain this discrepancy: it could be due to a failure of the quasi-adiabatic approximation (see hypothesis H9); or another physical process could become non-negligible at these higher frequencies – a contribution from the perturbed convective flux (see hypothesis H8), or from the correlated background (see hypothesis H10) for instance. This may also be due to the fact that the scales of oscillation and turbulence are no longer separable for high-frequency modes (see hypothesis H1). Answering this question would require getting rid of at least one of these simplifying approximations – something which would require more work.

6.3 What about mode amplitudes?

The formalism developed in Chapter 5 for velocity measurements and extended in this chapter for intensity measurements gives access to the shape of the radial p-mode line profiles for a given stellar model. So far, I have focused on the asymmetry displayed by these line profiles, but of course one also has access to their amplitude. This naturally begs the question: do the amplitudes predicted by this model accurately agree with the observed amplitudes? I delve into this question in this section.

[2]It may seem odd that the second derivative of Ψ_ω should appear in this relation, seeing as the wave equation (Equation 5.3) is of second order, and therefore relates $\mathrm{d}^2\Psi_\omega/\,\mathrm{d}r^2$ to lower derivatives. However, because the wave equation is inhomogeneous, it would also relate it to the source term, which would therefore appear in Equation 6.4 if I were to eliminate the second derivative of the wave variable. It is therefore much more practical to retain this second derivative in Equation 6.4.

6.3.1 Extraction of mode amplitude

The procedure described above involves the adjustment of the synthetic line profiles with the formula given by Equation 4.7, which I recall here for clarity

$$P(\omega) = H\frac{(1+Bx)^2+B^2}{1+x^2}\,, \tag{6.6}$$

where

$$x = 2(\omega-\omega_0)/\Gamma\,. \tag{6.7}$$

The adjustment of an individual line profile provides with four quantities: its height H, corresponding to the maximum reached by its spectral height; its angular eigenfrequency ω_0; its linewidth Γ; and its asymmetry parameter B. Then, the physical amplitude A of the mode is obtained by integrating the area under the line profile – corresponding to the energy of the mode –, and then taking the square root. For low values of the asymmetry parameter, the amplitude barely depends on asymmetry, and it can be estimated by assuming $B = 0$, in which case one finds the integral of a simple Lorentzian function. This yields[3]

$$A_{V,I} = \sqrt{\pi\Gamma H_{V,I}}\,, \tag{6.8}$$

where the subscripts V and I refer to velocity and intensity respectively: while the two spectra feature the same linewidths, they have different spectral heights, and therefore different amplitudes. The velocity amplitude is expressed in $\mathrm{m.s^{-1}}$, and the intensity amplitude in ppm (parts per million).

The velocity amplitudes are straightforwardly extracted from the model. This is not the case for the intensity amplitudes. The reason has to do with the fact, which I already mentioned in Section 6.1, that the quasi-adiabatic approximation (see hypothesis H8) severely overestimates the intensity amplitudes: this is illustrated in Figure 4 of Philidet et al. (2020b), where the observed velocity amplitudes are fairly well reproduced by the model predictions, but there is a factor ~ 5 between intensity predictions and observations. One of the reasons for this discrepancy is the fact that in the formalism presented in Section 6.1, the intensity power spectrum is rather sensitive to the τ-derivative of the eigenfunctions associated to the mode. Therefore, to alleviate the impact of adopting the quasi-adiabatic approximation on amplitude predictions, an alternative approach would be to replace the differential form of the optical depth perturbation

$$\frac{\mathrm{d}\delta\tau}{\mathrm{d}\tau} = \frac{\delta\kappa}{\kappa}+\frac{\delta\rho}{\rho}+\frac{\partial\xi_r}{\partial r}\,, \tag{6.9}$$

by its τ-integrated counterpart

$$\delta\tau = \int_0^\tau \mathrm{d}\tau\left(\frac{\delta\kappa}{\kappa}+\frac{\delta\rho}{\rho}+\frac{\partial\xi_r}{\partial r}\right)\,. \tag{6.10}$$

The good news is that the resulting expression of the intensity power spectrum no longer relies on τ-derivatives, so that the predicted intensity line profiles stemming from it are much less sensitive on the effects of non-adiabaticity. The bad news is that the expression of the intensity power spectrum now takes an integral form, and becomes drastically inconvenient to use. However, while this precludes me from extracting the exact shape of the line profiles in intensity, it is possible to extract their overall amplitude. This is done in two steps.

First, I compute the *temperature power spectrum*. This is done by adopting the following adiabatic relation between temperature and density Lagrangian perturbations

$$\frac{\delta T}{T} = \nabla_{\mathrm{ad}}\Gamma_1\frac{\delta\rho}{\rho}\,, \tag{6.11}$$

[3] This is in contrast with the usual formula $A = \sqrt{\pi C_{\mathrm{obs}}\Gamma H}$ (e.g. Baudin et al. 2005), where C_{obs} is a factor encompassing the effect due to the observational techniques as well as the geometrical effects. In our case, the power spectrum is not inferred from observations, and the geometrical effects are encompassed in the limb-darkening factor in Equation 5.1 (in the form of the integral over solid angle Ω). Therefore, I can discard C_{obs} *so long as this limb-darkening factor is also discarded from the model presented above*.

which is rewritten in terms of the wave variable Ψ_ω

$$\frac{\delta T}{T} = \underbrace{-\frac{\nabla_{\rm ad}\Gamma_1}{r^2}\frac{\mathrm{d}}{\mathrm{d}r}\left(\frac{r}{c\sqrt{\rho}}\right)}_{\equiv A_T}\Psi_\omega \underbrace{-\frac{\nabla_{\rm ad}\Gamma_1}{rc\sqrt{\rho}}}_{\equiv B_T}\frac{\mathrm{d}\Psi_\omega}{\mathrm{d}r} \,. \tag{6.12}$$

From there on out, the calculations are the same as those detailed in Philidet et al. (2020b), and one finds

$$\left\langle \left| \widehat{\frac{\delta T}{T}} \right|^2 \right\rangle = A_T^2 I_\omega(X_\omega, X_\omega) + 2A_T B_T I_\omega(X_\omega, X'_\omega) + B_T^2 I_\omega(X'_\omega, X'_\omega) \,, \tag{6.13}$$

where the function I and the quantities X_ω and X'_ω are given by Eqs. (24) and (25) of Philidet et al. (2020b). This provides with the power spectrum in terms of relative temperature perturbations, the same way the procedure described in Chapter 5 provided with the velocity power spectrum, and the one described in Section 6.1 with the intensity power spectrum. In particular, I can extract the *temperature mode amplitudes* A_T for each solar radial p-mode under consideration, expressed in ppm. This is completely independent of τ-derivatives, because those appear when relating the temperature perturbation with the radiative flux perturbation.

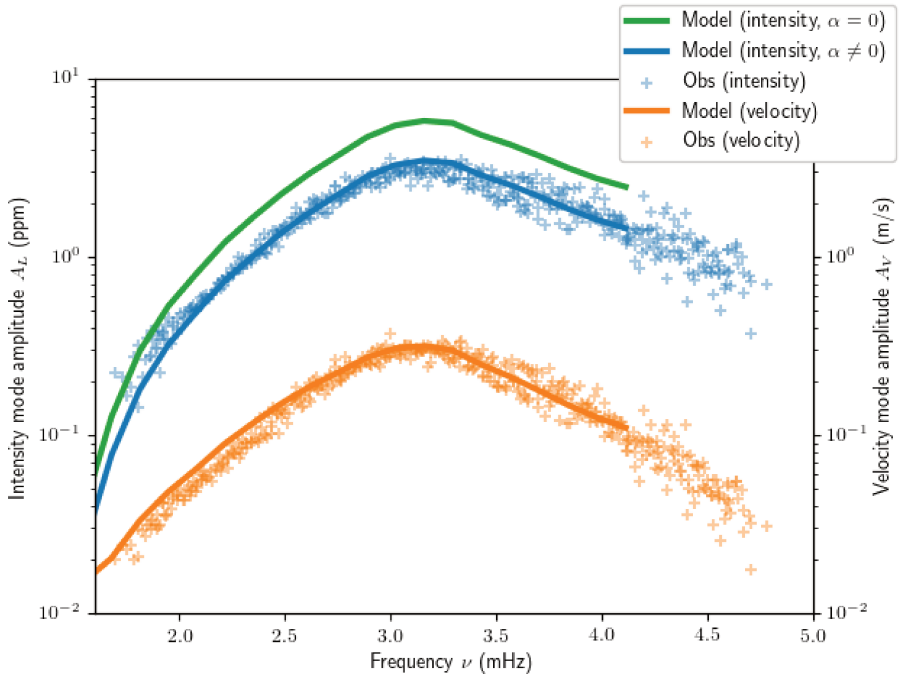

Figure 6.2: Comparison between the observed solar p-mode amplitudes inferred by Barban et al. (2004) from GONG observations (orange crosses for velocity, blue crosses for intensity) and our predictions obtained through the formalism described in the text. The orange solid line represents the velocity prediction. The blue solid line represents the intensity prediction with the parameter α given by Equation 6.24. The green solid line represents the intensity prediction with $\alpha = 0$, corresponding to the approximation $\delta T/T = \delta T_{\rm eff}/T_{\rm eff}$ at the photosphere. The agreement between the two is relatively good throughout the solar p-mode spectrum, both in velocity and intensity. By contrast, adopting $\alpha = 0$ leads to an overestimation of the intensity amplitudes compared to observations.

In a second step, I relate A_I to A_T. To do this, I start from the linear perturbation of the grey atmosphere model, given by (see Philidet et al. 2020b, Eq. 4)

$$\frac{\delta T}{T} = \left(\frac{\partial \ln T}{\partial \ln T_{\rm eff}}\right)_\tau \frac{\delta T_{\rm eff}}{T_{\rm eff}} + \left(\frac{\partial \ln T}{\partial \ln \tau}\right)_{T_{\rm eff}} \frac{\delta \tau}{\tau} \,. \tag{6.14}$$

The partial derivatives are computed from the unperturbed equation (see Philidet et al. 2020b, Eq. 3)

$$T(\tau, T_{\rm eff}) = \left(\frac{3}{4} r(\tau)\right)^{1/4} T_{\rm eff} \,, \tag{6.15}$$

where

$$r(\tau) \equiv \tau + q(\tau) \,, \tag{6.16}$$

and $q(\tau)$ is the Hopf function associated with the grey atmosphere model, so that

$$\left(\frac{\partial \ln T}{\partial \ln T_{\rm eff}}\right)_{\tau} = 1 \,, \tag{6.17}$$

$$\left(\frac{\partial \ln T}{\partial \ln \tau}\right)_{T_{\rm eff}} = \frac{\tau r'(\tau)}{4r} \,. \tag{6.18}$$

The optical depth perturbation is given by Equation 6.10, which can be rewritten by using the continuity equation and discarding its curvature term (see the toy-model in Section 4.2.3, where I performed the exact same simplification). One finds

$$\frac{\delta\tau}{\tau} = \frac{1}{\tau}\int_0^{\tau} {\rm d}\tau' \, \frac{\delta\kappa}{\kappa} \,. \tag{6.19}$$

As for the effective temperature perturbation, it is directly related to the desired luminosity fluctuations through

$$\frac{\delta L}{L} = 4\frac{\delta T_{\rm eff}}{T_{\rm eff}} + 2\frac{\xi_r}{r} \,. \tag{6.20}$$

I will again neglect the curvature term. Finally, isolating the luminosity perturbation in Equation 6.14 yields

$$\frac{\delta L}{L} = 4\frac{\delta T}{T} - \frac{r'(\tau_o)}{r(\tau_o)}\int_0^{\tau_o} {\rm d}\tau \, \frac{\delta\kappa}{\kappa} \,, \tag{6.21}$$

where τ_o refers to the optical depth at which the modes are observed.

Then, I express the opacity fluctuations in terms of temperature and density fluctuations, thus

$$\frac{\delta\kappa}{\kappa} = \kappa_T \frac{\delta T}{T} + \kappa_\rho \frac{\delta\rho}{\rho} = \left(\kappa_T + \frac{\kappa_\rho}{\nabla_{\rm ad}\Gamma_1}\right)\frac{\delta T}{T} \,, \tag{6.22}$$

where $\kappa_T \equiv (\partial \ln\kappa / \partial \ln T)_\rho$ and $\kappa_\rho \equiv (\partial \ln\kappa / \partial \ln\rho)_T$. Equation 6.21 can finally be rewritten

$$\left.\frac{\delta L}{L}\right|_{\tau_o} = 4\left(1 - \frac{\alpha r'(\tau_o)}{4r(\tau_o)}\right)\left.\frac{\delta T}{T}\right|_{\tau_o} \,, \tag{6.23}$$

where I have defined

$$\alpha \equiv \frac{\displaystyle\int_0^{\tau_o} {\rm d}\tau \left(\kappa_T + \frac{\kappa_\rho}{\nabla_{\rm ad}\Gamma_1}\right)\frac{\delta T}{T}}{(\delta T/T)|_{\tau_o}} \,. \tag{6.24}$$

By construction, the parameter α does not depend on the amplitude of the mode, but only on the radial profile of its temperature eigenfunction. Ultimately, the temperature and intensity amplitudes are related through

$$A_I = F \times A_T \,, \tag{6.25}$$

where

$$F = 4\left|1 - \frac{\alpha r'(\tau_o)}{4r(\tau_o)}\right| \,, \tag{6.26}$$

α is given by Equation 6.24, and the function $r(\tau)$ only depends on the Hopf function characterising the grey atmosphere.

6.3.2 Results

I compile the velocity and intensity amplitudes yielded by the 'numerical spectrum' model, and compare them to solar observations, in Figure 6.2. Velocity amplitudes are shown in blue, and intensity amplitudes in orange. Specifically, I show two predicted intensity amplitudes, both of them computed with the procedure previously described, but with two different values of the parameter α in Equation 6.26: one given by Equation 6.24 (in orange), and one given by $\alpha = 0$ (in green). The intensity amplitudes are computed by assuming that the observation height is the layer at which the equilibrium temperature is equal to the effective temperature of the Sun $T_{\rm eff} = 5780$ K. I used the same CO^{5}BOLD 3D simulation of the solar atmosphere that I considered in Chapter 5 to estimate the optical depth corresponding to this observation height, and found $\tau_o = 0.45$. The parameter α appearing in the factor F was computed from ADIPLS eigenfunctions for a solar model.

Figure 6.2 shows that the velocity amplitudes, as I mentioned earlier, are correctly predicted by this model. In addition, it shows that the intensity amplitudes are also correctly predicted, so long as a realistic value of α is adopted. The $\alpha = 0$ case is particularly illuminating, because then one simply obtains $F = 4$: this amounts to assuming that the gas temperature at the observation height is always equal to the instantaneous effective temperature. As I showed in Section 6.2, this oversimplifying approximation has a severe impact on the intensity asymmetries, and therefore on the velocity–intensity asymmetry reversal. Figure 6.2 shows that it also has a drastic impact on intensity amplitude: *assuming that the gas temperature at the photosphere equals the effective temperature leads to an overestimation of the photometric amplitudes by a factor of* ~ 2. I conclude, therefore, that a realistic treatment of the radiative transfer is absolutely necessary to understand the properties of the observed intensity power spectrum of solar-like oscillators, including both the amplitude and asymmetry exhibited by their p-mode line profiles. Mistaking the actual gas temperature at the photosphere for the effective temperature is too crude an approximation, and precludes us from using intensity observations to constrain the physics of the modes, or those of the turbulence at the top of the convective zone. The question still requires some investigation however; in particular, the temperature power spectrum is still computed in the adiabatic limit, and a full, consistent picture on the subject would require going beyond this approximation (i.e. including the entropy Lagrangian perturbation in Equation 6.11).

A&A 644, A171 (2020)
https://doi.org/10.1051/0004-6361/202038222

Astronomy & Astrophysics

Velocity-intensity asymmetry reversal of solar radial *p*-modes

J. Philidet[1], K. Belkacem[1], H.-G. Ludwig[2,3], R. Samadi[1], and C. Barban[1]

[1] LESIA, Observatoire de Paris, PSL Research University, CNRS, Université Pierre et Marie Curie, Université Paris Diderot, 92195 Meudon, France
e-mail: jordan.philidet@obspm.fr
[2] Zentrum für Astronomie der Universität Heidelberg, Landessternwarte, Königstuhl 12, 69117 Heidelberg, Germany
[3] GEPI, Observatoire de Paris, PSL Research University, CNRS, Université Pierre et Marie Curie, Université Paris Diderot, 92195 Meudon, France

Received 21 April 2020 / Accepted 28 October 2020

ABSTRACT

The development of space-borne missions has significantly improved the quality of the measured spectra of solar-like oscillators. Their *p*-mode line profiles can now be resolved, and the asymmetries inferred for a variety of stars other than the Sun. However, it has been known for a long time that the asymmetries of solar *p*-modes are reversed between the velocity and the intensity spectra. Understanding the origin of this reversal is necessary in order to use asymmetries as a tool for seismic diagnosis. For stars other than the Sun, only the intensity power spectrum is sufficiently resolved to allow for an estimation of mode asymmetries. We recently developed an approach designed to model and predict these asymmetries in the velocity power spectrum of the Sun and to successfully compare them to their observationally derived counterpart. In this paper we expand our model and predict the asymmetries featured in the intensity power spectrum. We find that the shape of the mode line profiles in intensity is largely dependent on how the oscillation-induced variations of the radiative flux are treated, and that modelling it realistically is crucial to understanding asymmetry reversal. Perturbing a solar-calibrated grey atmosphere model, and adopting the quasi-adiabatic framework as a first step, we reproduce the asymmetries observed in the solar intensity spectrum for low-frequency modes. We conclude that, unlike previously thought, it is not necessary to invoke an additional mechanism (e.g. non-adiabatic effects, coherent non-resonant background signal) to explain asymmetry reversal. This additional mechanism is necessary, however, to explain asymmetry reversal for higher-order modes.

Key words. methods: analytical – Sun: helioseismology – Sun: oscillations – stars: atmospheres – stars: oscillations – stars: solar-type

1. Introduction

The power spectral density of solar-like oscillations is expected to feature Lorentzian peaks centred on their eigenfrequencies. However, observations show that their line profiles are slightly asymmetric (Duvall et al. 1993). This asymmetry is primarily due to the fact that stochastic excitation occurs in a localised region just beneath the surface of the star. Several studies have consequently used observed line profile asymmetries to infer properties of the turbulent source of excitation of solar *p*-modes, in particular its radial position and its multipolar nature (see e.g. Roxburgh & Vorontsov 1997; Nigam et al. 1998). These prior studies used parametrised models, and aimed to find best-fit values for their free parameters by applying fitting procedures to individual peaks in the observed spectrum. Philidet et al. (2020) followed a different approach, which consisted in modelling mode asymmetry without fitting any free parameters to the available observational data. Instead, they developed an analytical model of stochastic excitation, coupled with a 3D hydrodynamical simulation of the stellar atmosphere. This allowed the authors to reproduce the asymmetries of solar *p*-modes as measured in the observed velocity power spectrum, and to subsequently demonstrate the role of the spatial extent of the mode driving region, together with the differential properties of turbulent convection (namely the variation of the injection length-scale below and above the photosphere).

The recent measurement of *p*-mode asymmetries in solar-like oscillators by Benomar et al. (2018), using *Kepler* observations, opened the way to constrain the properties of stochastic excitation, and therefore of turbulent convection, throughout the HR diagram. Unlike in the solar case, however, only observations made by *Kepler* in intensity have the resolution necessary for mode asymmetry to be inferred. But it is well known that asymmetries are very different between velocity and intensity observations (Duvall et al. 1993; Toutain et al. 1997). More precisely, line profiles in the velocity power spectrum have more power on their low-frequency side, whereas line profiles in the intensity power spectrum have more power on their high-frequency side. This is known as the asymmetry reversal puzzle.

Several hypotheses have been proposed to explain this reversal, but no consensus has emerged. Duvall et al. (1993) suggested that modal entropy fluctuations could affect intensity asymmetries while leaving asymmetries in velocity unaffected. Following this argument, Rast & Bogdan (1998) quantified these non-adiabatic effects, and found that radiative cooling has a negligible impact on line profile asymmetry, so that it can hardly explain the asymmetry reversal. Gabriel (1998) then remarked that in order for such heat transfers to impact line asymmetry, it is necessary that they affect the wave equation beyond the second order, which was not the case in the model of Rast & Bogdan (1998).

Shortly afterwards, another candidate was found to explain the asymmetry reversal puzzle. Roxburgh & Vorontsov (1997) remarked that adding a coherent, non-resonant background (i.e. a signal with a very broad spectrum but whose Fourier component close to an oscillating mode would be coherent with it, and

would therefore be able to interfere with it) to a resonant signal could affect its line profile, and thus its asymmetry. They argued that the overshooting of turbulent eddies into the lower layers of the atmosphere should act as a coherent non-resonant background in the velocity signal, while keeping the intensity signal unaffected, thus explaining the asymmetry reversal. On the other hand, Nigam et al. (1998) argued that both signals contain a coherent background component, and that the asymmetry reversal stems from the fact that it is much stronger in the intensity signal than in the velocity signal. Subsequently, several studies have undertaken the task of estimating the level of correlated background in the intensity signal using the observed asymmetry reversal (e.g. Kumar & Basu 1999; Chaplin & Appourchaux 1999; Severino et al. 2001; Barban et al. 2004).

Yet another candidate to explain asymmetry reversal was recognised by Georgobiani et al. (2003). They noticed that p-modes featured in the velocity and intensity power spectra of 3D hydrodynamic simulations of the stellar uppermost layers have opposite asymmetries when they are computed at fixed optical depth, but identical asymmetries when they are computed at fixed geometrical depth. They therefore proposed the following picture: the velocity and intensity line profiles are intrinsically proportional to one another, but the height of unity optical depth, at which the intensity fluctuations are observed, oscillates with the mode. Since there is a strong temperature gradient there, the observed background temperature also oscillates, which adds a component to the resonant intensity signal. They showed that this added component tends to reduce the amplitude of the intensity fluctuations. However, because the $\kappa - T$ relation is highly non-linear at the photosphere, this reduction is not uniform over the entire line profile, and thus it changes its asymmetry. Since there is no equilibrium velocity gradient, there is no corresponding additional component in the velocity signal, and the velocity asymmetry remains unaffected.

At the core of these models lies the assumption that the gas temperature at the photosphere and the effective temperature are equal, and therefore have equal relative fluctuations. This assumption means that the velocity and intensity line profiles should have the same asymmetry, so that the key to understanding the asymmetry reversal puzzle must be sought elsewhere. While this assumption is not problematic when it is used as a photospheric boundary condition in the framework of fully non-adiabatic calculations (Dupret et al. 2002), it becomes more questionable when used to justify that luminosity and temperature eigenfunctions are simply proportional to one another. In this context, our objective is to question this assumption, and to show that the radiative flux reacts in a more complex way to temperature variations, which has a crucial impact on line profile asymmetry in the intensity spectra. To this end, we extend the model of Philidet et al. (2020) for intensity observations. We show that, unlike previously thought, source localisation impacts velocity and intensity observations differently, so that an additional physical mechanism is not necessary to account for asymmetry reversal, except maybe at high frequency.

This paper is structured as follows. In Sect. 2 we describe the steps necessary for the adaptation of our model to intensity observations. We then present its predictions pertaining to asymmetry reversal in Sect. 3, and discuss these results in Sect. 4.

2. Modelling the intensity power spectrum

In order to adapt our p-mode stochastic excitation model to intensity observations, it is first necessary to model the intensity Green's function associated with radial p-modes. In Philidet et al. (2020), the wave equation was written in terms of a wave variable Ψ_ω, related to the velocity fluctuations through

$$\widehat{v_{\rm osc}}(r) = \frac{j\omega}{rc\sqrt{\rho}}\Psi_\omega(r)\,, \tag{1}$$

where ρ is the equilibrium density, c is the sound speed, ω the angular frequency, j the imaginary unit. The notation $\widehat{.}$ refers to Fourier transform in time. The radial inhomogeneous wave equation then reads

$$\frac{\mathrm{d}^2\Psi_\omega}{\mathrm{d}r^2} + \left(\frac{\omega^2 + j\omega\Gamma_\omega}{c^2} - V(r)\right)\Psi_\omega = S(r)\,, \tag{2}$$

where $V(r)$ is the acoustic potential, Γ_ω is the frequency-dependent damping rate of the oscillations, and $S(r)$ is a source term proportional to the divergence of the fluctuating Reynolds stresses. The damping rates Γ_ω are inferred from observations; we use the same values as those presented in Table 1 of Philidet et al. (2020).

For a given value of ω, convolving the Green's function in Eq. (2) with the source term $S(r)$ allows us to predict the value of the power spectrum in terms of Ψ_ω. Then the velocity power spectrum is given by Eq. (1). Following the same approach, the goal of this section is to relate the intensity fluctuations to the wave variable Ψ_ω, so that from the Ψ_ω power spectrum we have access to the intensity power spectrum.

2.1. Intensity fluctuations in a grey atmosphere

Because the p-mode intensity power spectrum is observed close to the photosphere, we only need to model the oscillation-induced intensity variations in this region. In order to model these variations, we treat the atmosphere as a grey atmosphere. This is justified, in part, by the fact that the observed intensity power spectrum corresponds to the continuum intensity, on which absorption spectral lines have little impact.

A grey atmosphere is, by definition, in radiative equilibrium. When studying p-mode-driven intensity fluctuations, working under the radiative equilibrium assumption is justified by the large gap existing between the modal period and the local thermal timescale. The period of the modes is of the order of several minutes, while the thermal timescale is about ten seconds at the photosphere. As such, the radiative flux reacts almost instantly to the oscillations induced by the p-modes, and the atmosphere remains at radiative equilibrium at all times. One of the consequences of radiative equilibrium is that the radiative flux is uniform, and its relative fluctuations are proportional to the relative fluctuations of the effective temperature $T_{\rm eff}$. The equality between the relative luminosity fluctuations at the photosphere and at the observation height of the modes is further supported by the fact that the modes are observed very close to the photosphere. The goal of the present section is therefore to relate the variations of $T_{\rm eff}$ to the gas fluctuations brought about by the oscillating modes, and in particular to the gas temperature fluctuations. In doing so, we follow the same treatment of p-mode-induced atmospheric perturbation as Dupret et al. (2002).

In a grey atmosphere, the temperature of the gas is given by a unique function of the optical depth τ and effective temperature $T_{\rm eff}$, expressed by means of the Hopf function $q(\tau)$ (Mihalas 1978)

$$T(\tau, T_{\rm eff}) = \left(\frac{3}{4}(\tau + q(\tau))\right)^{1/4} T_{\rm eff}\,. \tag{3}$$

An arbitrary relation $T = T(\tau, T_{\rm eff})$ can be perturbed as

$$\frac{\delta T}{T} = \left(\frac{\partial \ln T}{\partial \ln T_{\rm eff}}\right)_{\tau} \frac{\delta T_{\rm eff}}{T_{\rm eff}} + \left(\frac{\partial \ln T}{\partial \ln \tau}\right)_{T_{\rm eff}} \frac{\delta \tau}{\tau} , \tag{4}$$

where the fluctuations of the optical depth can be expressed as

$$\frac{{\rm d}\delta\tau}{{\rm d}\tau} = \frac{\delta\kappa}{\kappa} + \frac{\delta\rho}{\rho} + \frac{\partial \xi_r}{\partial r} , \tag{5}$$

where κ is the Rosseland mean opacity and ξ_r the radial displacement of the gas.

Taking the partial derivative of Eq. (4) with respect to τ, and eliminating ${\rm d}\delta\tau/{\rm d}\tau$ alternatively through Eqs. (4) and (5), we find

$$\begin{aligned}\frac{\partial(\delta T/T)}{\partial \ln \tau} = {} & \frac{\partial \ln T}{\partial \ln \tau}\left(\frac{\delta\kappa}{\kappa} + \frac{\delta\rho}{\rho} + \frac{\partial \xi_r}{\partial r}\right) \\ & - \left(1 - \frac{\partial^2 \ln T/\partial \ln \tau^2}{\partial \ln T/\partial \ln \tau}\right)\left(\frac{\delta T}{T} - \frac{\partial \ln T}{\partial \ln T_{\rm eff}}\frac{\delta T_{\rm eff}}{T_{\rm eff}}\right) \\ & + \frac{\partial^2 \ln T}{\partial \ln \tau \partial \ln T_{\rm eff}}\frac{\delta T_{\rm eff}}{T_{\rm eff}} .\end{aligned} \tag{6}$$

Isolating the perturbation of the effective temperature, this can be rearranged as

$$\begin{aligned}\frac{\delta T_{\rm eff}}{T_{\rm eff}} = {} & \left(\frac{\partial^2 \ln T}{\partial \ln \tau \partial \ln T_{\rm eff}} + \frac{\partial \ln T}{\partial \ln T_{\rm eff}}\left(1 - \frac{\partial^2 \ln T/\partial \ln \tau^2}{\partial \ln T/\partial \ln \tau}\right)\right)^{-1} \\ & \times \left[\frac{\partial(\delta T/T)}{\partial \ln \tau} - \frac{\partial \ln T}{\partial \ln \tau}\left(\frac{\delta\kappa}{\kappa} + \frac{\delta\rho}{\rho} + \frac{\partial \xi_r}{\partial r}\right)\right. \\ & \left. + \frac{\delta T}{T}\left(1 - \frac{\partial^2 \ln T/\partial \ln \tau^2}{\partial \ln T/\partial \ln \tau}\right)\right] .\end{aligned} \tag{7}$$

When the temperature law as given by Eq. (3) is used, Eq. (7) reduces to

$$\begin{aligned}\frac{\delta T_{\rm eff}}{T_{\rm eff}} = {} & \left(\frac{\tau r'(\tau)}{r(\tau)} - \frac{\tau r''(\tau)}{r'(\tau)}\right)^{-1}\left[\frac{\partial(\delta T/T)}{\partial \ln \tau}\right. \\ & \left. - \frac{\tau r'(\tau)}{4r(\tau)}\left(\frac{\delta\kappa}{\kappa} + \frac{\delta\rho}{\rho} + \frac{\partial \xi_r}{\partial r}\right) + \frac{\delta T}{T}\left(\frac{\tau r'(\tau)}{r(\tau)} - \frac{\tau r''(\tau)}{r'(\tau)}\right)\right] ,\end{aligned} \tag{8}$$

where we have introduced

$$r(\tau) \equiv \tau + q(\tau) , \tag{9}$$

and $'$ and $''$ respectively refer to the first and second derivatives with respect to τ. The first term in the brackets can be rearranged as

$$\frac{\partial(\delta T/T)}{\partial \ln \tau} = \frac{\tau r'(\tau)}{4r(\tau)}\left(\frac{\partial \delta T/\partial r}{{\rm d}T/{\rm d}r} - \frac{\delta T}{T}\right) . \tag{10}$$

Finally, using Eqs. (8) and (10), the fluctuations of the effective temperature can be written

$$\begin{aligned}\frac{\delta T_{\rm eff}}{T_{\rm eff}} = {} & \frac{1}{4}\left(1 - \frac{r(\tau)r''(\tau)}{r'(\tau)^2}\right)^{-1}\left[\left(3 - \frac{r(\tau)r''(\tau)}{r'(\tau)^2}\right)\frac{\delta T}{T}\right. \\ & \left. + \frac{\partial \delta T/\partial r}{{\rm d}T/{\rm d}r} - \frac{\delta\kappa}{\kappa} - \frac{\delta\rho}{\rho} - \frac{\partial \xi_r}{\partial r}\right] .\end{aligned} \tag{11}$$

The fluctuations in the effective temperature do not depend on τ, and therefore neither does the right-hand side of Eq. (11), even though its individual terms do. The atmosphere being in radiative equilibrium, and the height of observation being fairly close to the photosphere, the radiative flux is uniform and equal to its value at the photosphere. This also holds true for the fluctuations of the radiative luminosity, which, by definition of the effective temperature, are therefore given by

$$\frac{\delta L_R}{L_R} = 4\frac{\delta T_{\rm eff}}{T_{\rm eff}} + 2\frac{\xi_r}{r} , \tag{12}$$

which, thanks to Eq. (11), becomes

$$\frac{\delta L_R}{L_R} = 2\frac{\xi_r}{r} + \frac{1}{1 - x(\tau)}\left[(3 - x(\tau))\frac{\delta T}{T} + \frac{\partial \delta T/\partial r}{{\rm d}T/{\rm d}r} - \frac{\delta\kappa}{\kappa} - \frac{\delta\rho}{\rho} - \frac{\partial \xi_r}{\partial r}\right] , \tag{13}$$

where we have introduced

$$x(\tau) \equiv \frac{r(\tau)r''(\tau)}{r'(\tau)^2} = \frac{(\tau + q(\tau))q''(\tau)}{(1 + q(\tau))^2} . \tag{14}$$

Finally, we neglect the Lagrangian perturbations of the convective luminosity L_C compared to those of the radiative luminosity L_R. Including the convective contribution in this model would require a non-local, time-dependent treatment of turbulent convection; furthermore, the oscillations would have to be treated in a non-adiabatic framework. Until subsequent refinements are made to this model, and as a first approximation, we therefore consider $\delta L = \delta L_R$, in which case we have

$$\begin{aligned}\frac{\delta L}{L} = {} & \frac{L_R}{L}\left(2\frac{\xi_r}{r} + \frac{1}{1 - x(\tau)}\left[(3 - x(\tau))\frac{\delta T}{T}\right.\right. \\ & \left.\left. + \frac{\partial \delta T/\partial r}{{\rm d}T/{\rm d}r} - \frac{\delta\kappa}{\kappa} - \frac{\delta\rho}{\rho} - \frac{\partial \xi_r}{\partial r}\right]\right) .\end{aligned} \tag{15}$$

In the following we adopt a solar-calibrated Hopf function, which is based on a numerical solution to the non-LTE radiative transfer equation derived by Vernazza et al. (1981) to match the observed solar spectrum. This Hopf function is furthermore consistent with 3D hydrodynamic atmospheric simulations provided by CO^{5}BOLD, which we use to model the source term in Eq. (2). The Hopf function reads (see Sonoi et al. 2019)

$$q(\tau) = 1.036 - 0.3134\exp(-2.448\tau) - 0.2959\exp(-30.0\tau) . \tag{16}$$

In Fig. 1, we plot the quantity $x(\tau)$ against τ, where the Hopf function given by Eq. (16) is adopted. As expected, $x(\tau)$ is much smaller than unity at high optical depth. This is in accordance with the condition that the Hopf function must reduce to a constant in the deeper layers of the star. At lower optical depth, however, $x(\tau)$ is no longer negligible. The height of observation of the continuum intensity power spectrum ($\tau \sim 2/3$, vertical dashed line in Fig. 1) lies halfway between these two extreme cases; we therefore account for the quantity $x(\tau)$ in the following, even though it should not be of much significance.

On a side note, comparing Eq. (15) to the perturbed radiative diffusion equation (see Eq. (21.15) of Unno et al. 1989)

$$\frac{\delta L}{L} = \frac{L_R}{L}\left(2\frac{\xi_r}{r} + 3\frac{\delta T}{T} - \frac{\delta\kappa}{\kappa} - \frac{\delta\rho}{\rho} + \frac{\partial \delta T/\partial r}{{\rm d}T/{\rm d}r} - \frac{\partial \xi_r}{\partial r}\right) , \tag{17}$$

it can be seen that the intensity fluctuations of a grey atmosphere with an arbitrary Hopf function $q(\tau)$ reduce to their diffusive counterpart when the following condition is met:

$$x(\tau) \ll 1 . \tag{18}$$

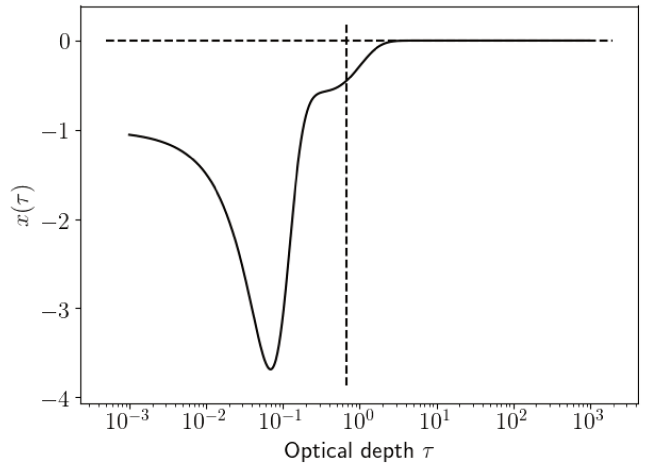

Fig. 1. Quantity $x(\tau)$ defined by Eq. (14) as a function of optical depth τ, when the Hopf function given by Eq. (16) is adopted. The vertical dashed line corresponds to the radius of the photosphere ($\tau = 2/3$), where the intensity power spectrum is observed. The τ-axis is oriented *from left to right*, so that the surface is on the left side of the figure, and the deeper layers on the right side.

In particular, in the limit where the Hopf function is linear in τ (another common approximation in stellar atmospheres, leading to the widely used Eddington-Barbier relations, for instance), $x(\tau)$ strictly vanishes, and the luminosity fluctuations of the grey atmosphere are identical to the expression obtained in the diffusion approximation. We note, however, that this is only true of the fluctuating part of the luminosity. Even if $x(\tau)$ vanishes, the total luminosity of the grey atmosphere is not equal to the total luminosity obtained in the diffusion approximation.

2.2. Relating the intensity fluctuations to the Ψ_ω variable

Using the perturbed equation of state and the perturbed continuity equation, Eq. (15) can be rewritten in terms of fluid displacement and temperature fluctuations:

$$\frac{\delta L}{L} = \frac{L_R}{L}\left(\left(2+\frac{2+3\kappa_\rho}{1-x}\right)\frac{\xi_r}{r} + \frac{4-x-\kappa_T}{1-x}\frac{\delta T}{T} + \frac{r\kappa_\rho}{1-x}\frac{\mathrm{d}(\xi_r/r)}{\mathrm{d}r} - \frac{H_T}{1-x}\frac{\mathrm{d}(\delta T/T)}{\mathrm{d}r}\right) . \tag{19}$$

Here $H_T \equiv |\mathrm{d}\ln T/\mathrm{d}r|^{-1}$ is the temperature scale height, $\kappa_\rho \equiv (\partial \ln\kappa/\partial\ln\rho)_T$, $\kappa_T \equiv (\partial\ln\kappa/\partial\ln T)_\rho$, and x is the value of the quantity $x(\tau)$, defined by Eq. (14), at the considered optical depth.

We can then write the temperature fluctuations as a function of fluid displacement. While it is known that non-adiabatic effects are important at the top of the convection zone, they are considerably complicated to account for in the treatment of solar-like oscillations (in particular, including them in this formalism would require going beyond the second order in Eq. (2)). As a first step we therefore choose to neglect their impact on p-mode asymmetry, and we place ourselves in the quasi-adiabatic approximation. Further discussion regarding the validity of this assumption can be found in Sect. 4.2. In this approximation, the relative temperature fluctuations are proportional to the relative density fluctuations, which are related to the fluid displacement through the perturbed continuity equation. In turn, the fluid displacement is related to the velocity variable through $\widehat{v_{\rm osc}}(r) = j\omega\xi_r(r)$, and the velocity variable to the variable Ψ_ω through Eq. (1). This finally leads to

$$\frac{\delta L}{L} = \frac{L_R}{L}\left(A_L\Psi_\omega + B_L\frac{\mathrm{d}\Psi_\omega}{\mathrm{d}r} + C_L\frac{\mathrm{d}^2\Psi_\omega}{\mathrm{d}r^2}\right) , \tag{20}$$

with

$$\begin{aligned} A_L &= \left(2+\frac{2+3\kappa_\rho}{1-x}\right)A_\xi + \frac{4-x-\kappa_T}{1-x}A_T + \frac{r\kappa_\rho}{1-x}\frac{\mathrm{d}A_\xi}{\mathrm{d}r} - \frac{H_T}{1-x}\frac{\mathrm{d}A_T}{\mathrm{d}r} \\ B_L &= \frac{4-x-\kappa_T}{1-x}B_T + \frac{r\kappa_\rho}{1-x}A_\xi - \frac{H_T}{1-x}\left(A_T + \frac{\mathrm{d}B_T}{\mathrm{d}r}\right) \\ C_L &= -\frac{H_T}{1-x}B_T , \end{aligned} \tag{21}$$

and

$$\begin{aligned} A_T &= -\frac{\nabla_{\rm ad}\Gamma_1}{r^2}\frac{\mathrm{d}}{\mathrm{d}r}\left(\frac{r}{c\sqrt{\rho}}\right) \\ B_T &= -\frac{\nabla_{\rm ad}\Gamma_1}{rc\sqrt{\rho}} \\ A_\xi &= \frac{1}{r^2 c\sqrt{\rho}} , \end{aligned} \tag{22}$$

where $\nabla_{\rm ad}$ is the adiabatic gradient and Γ_1 is the gas adiabatic index.

Equation (20) shows that the intensity fluctuations cannot be described as being simply proportional to the wave equation variable Ψ_ω, but that they also depend on its first and second derivatives. It can be seen, for instance from the last two terms in the right-hand side of Eq. (19), that this is because the radiative flux is sensitive to the temperature gradient. In prior studies tackling the issue of asymmetry reversal, it is always either explicitly argued, or implicitly assumed, that the Green's function associated with intensity (or its pressure proxy) and velocity are proportional to one another (see e.g. Kumar & Basu 1999). This relation would, with the above notations, correspond to a case where only one of the coefficients A_L, B_L, or C_L is non-zero. In particular, synthetic spectrum models usually assume that the effective temperature fluctuations are equal to the actual temperature fluctuations, in which case only $B_L \neq 0$ (see Sect. 4.1 for a more detailed discussion).

2.3. Intensity power spectral density

The remainder of the procedure is identical to the one detailed in Philidet et al. (2020). More precisely, to derive Ψ_ω we convolve the Green's function G_ω and the source term S associated with the inhomogeneous wave equation (Eq. (2)). This is done by considering only the contribution of source localisation to the p-mode asymmetries; in particular, we do not account for the contribution of correlated noise, although it was in our previous study. We also assume that the only source term in Eq. (2) stems from fluctuations of the turbulent pressure. Finally, using the resulting Ψ_ω in Eq. (20) leads to

$$\begin{aligned} \left\langle\left|\widehat{\frac{\delta L}{L}}\right|^2\right\rangle = \left(\frac{L_R}{L}\right)^2\Big(&A_L^2 I_\omega(X_\omega, X_\omega) + B_L^2 I_\omega(X'_\omega, X'_\omega) \\ &+ C_L^2 I_\omega(X''_\omega, X''_\omega) + 2A_L B_L I_\omega(X_\omega, X'_\omega) + 2A_L C_L I_\omega(X_\omega, X''_\omega) \\ &+ 2B_L C_L I_\omega(X'_\omega, X''_\omega)\Big) , \end{aligned} \tag{23}$$

where $\langle\rangle$ denotes ensemble average, and the function I_ω is defined as

$$\begin{aligned} I_\omega(f_1, f_2) = \iint \mathrm{d}^3\boldsymbol{r}_{s1}\mathrm{d}^3\boldsymbol{r}_{s2}\,\mathrm{Re}\left(\partial_i f_1(\boldsymbol{r}_{s1})\partial_j f_2^\star(\boldsymbol{r}_{s2})\right) \\ \times\left\langle(\rho_0\widehat{u_r u_i})\big|_{\boldsymbol{r}_{s1}}\,(\rho_0\widehat{u_r u_j}^\star)\big|_{\boldsymbol{r}_{s2}}\right\rangle , \end{aligned} \tag{24}$$

where the Einstein convention on index summation is used for the indices i and j, the superscript star (*) denotes complex conjugation, Re denotes the real part of a complex quantity, and X_ω, X'_ω and X''_ω are defined in terms of the Green's function as

$$\begin{aligned} X_\omega(\boldsymbol{r}_s) &= \frac{r}{c\sqrt{\rho}} G_\omega(\boldsymbol{r}_o;\boldsymbol{r}_s)\,, \\ X'_\omega(\boldsymbol{r}_s) &= \frac{r}{c\sqrt{\rho}} \left.\frac{\partial G_\omega}{\partial r_o}\right|_{\boldsymbol{r}_o;\boldsymbol{r}_s}\,, \\ X''_\omega(\boldsymbol{r}_s) &= \frac{r}{c\sqrt{\rho}} \left.\frac{\partial^2 G_\omega}{\partial r_o^2}\right|_{\boldsymbol{r}_o;\boldsymbol{r}_s}\,, \end{aligned} \tag{25}$$

where the variables r_o and r_s in the Green's function refer to the radius of observation and the radius of the source respectively. We note that the coefficients A_L, B_L, and C_L in Eq. (23) are only evaluated at the height of observation of the modes. This means, as we pointed out above, that we only need to model the oscillation-induced radiative flux variations at the photosphere, whereas the effect of the spatial extent of the source is entirely contained within the function I_ω. In particular, this is the reason why the value of the quantity $x(\tau)$ is only important at the height of observation (illustrated by the vertical dashed line in Fig. 1).

It is worth mentioning that Eq. (23) does not involve any further modelling than when the velocity power spectrum is calculated. Except for additional equilibrium thermodynamic quantities, both the Green's function and the fourth-order correlation term in Eq. (24) were already modelled in Philidet et al. (2020). In other words, this means that modelling the contribution of source localisation to asymmetries in intensity does not require additional physical constraints, nor does it require new input parameters to be introduced, provided the non-adiabatic terms (not accounted for in this model) indeed remain small in the stellar superficial layers.

3. Results for intensity asymmetries and comparison with observations

3.1. Numerical computation of intensity asymmetries

The system comprised of (23) to (25) constitutes a closed, semi-analytical form of the intensity power spectrum. The equilibrium quantities involved, as well as the turbulent quantities needed as inputs for the analytical model of turbulence, are all extracted from a 3D hydrodynamic simulation of the solar atmosphere computed using the CO^{5}BOLD code, which, after horizontal and time average, we patched on top of a 1D solar model provided by the evolutionary code CESTAM (for more details, see Manchon et al. 2018). Once the intensity power spectrum is calculated, we fit the obtained synthetic line profiles using the following formula (Nigam & Kosovichev 1998):

$$P(\omega) = H_0 \frac{(1+Bx)^2 + B^2}{1+x^2}\,. \tag{26}$$

Here $x = 2(\omega-\omega_0)/\Gamma_{\omega_0}$ is the reduced pulsation frequency, ω_0 the angular eigenfrequency, and Γ_{ω_0} the linewidth of the mode. The parameter B corresponds to the asymmetry parameter. The terms positive and negative asymmetry refer to the sign of B, and in the special case $B = 0$ we recover a Lorentzian line profile.

In order to compare our results to observational data, we used the numerical spectrum model developed in Philidet et al. (2020). It contains only one parameter in the form of λ (see their Sect. 2.3.2 for a definition), which illustrates the relative uncertainty pertaining to the temporal spectrum associated with the turbulent cascade in the solar superficial layers. Physical arguments allow us to constrain the value of this parameter (see e.g. Samadi & Goupil 2001); to be consistent with these constraints, they retained the value $\lambda = 0.5$. This led to a satisfactory quantitative agreement between their model and observations in the velocity spectrum. Here, we retain the same value for λ, and compare the resulting intensity asymmetries to observations; there is therefore no parameter adjustment in what follows.

3.2. Observational datasets

To compare the asymmetries predicted by the model with observations, we use the same observational data as for the velocity power spectrum in Philidet et al. (2020). These data points were extracted from the spectrum analysis conducted by Barban et al. (2004) on observations made by the *GONG* network. We used these observations because they are particularly fitting for the study of asymmetry reversal; the *GONG* network provides velocity and intensity measurements simultaneously. We recall that the spectral analysis of Barban et al. (2004) considers non-radial modes ($15 < l < 50$), whereas our model was developed for radial modes. However, the dependence of asymmetry on angular degree is very weak, and the asymmetry observations collapse to a slowly varying function of frequency, so long as $l \lesssim 100$ (see e.g. Vorontsov & Jefferies 2013) Therefore, the frequency-dependence of asymmetry for the modes observed by *GONG* is expected to be almost identical to that of radial modes.

To obtain the asymmetries in the intensity spectrum, Barban et al. (2004) used approximately one year of *GONG* data, allowing us to resolve about 600 modes. Following Severino et al. (2001), they simultaneously fitted the velocity spectrum, intensity spectrum, and I–V cross spectrum (both coherence and phase difference), which is known to yield more reliable results. The observed asymmetries we used in velocity and intensity are not obtained independently, but through the same fitting procedure. The model used for the spectral analysis, however, considered that the asymmetry was entirely due to a coherent non-resonant background component, so that their results were presented in terms of noise level and phase differences. This is a different mathematical description for the same line profile shape as given by Eq. (26). In order to extract the asymmetry parameter B as defined by Eq. (26), we reconstructed the line profiles using the best-fit values obtained by Barban et al. (2004), and then fitted these reconstructed line profiles using Eq. (26) instead.

We also consider intensity asymmetries inferred from *HMI* observations, and extracted from the spectral analysis procedure described in Korzennik (2005). The asymmetry profile $B(\nu)$ resulting from this spectral analysis, while in agreement with the values inferred by Barban et al. (2004), shows less dispersion, and thus allows for a more robust comparison of our results with observations. The dataset used contains four periods of 72 days each. In Korzennik (2005) the asymmetries are already directly given in terms of a parameter α, which is easily related to the parameter B through $B = \alpha/2$. We only considered angular degrees between $l = 0$ and $l = 20$, and we averaged the values of B over bins of width 30 μHz.

3.3. Modelled asymmetries compared with observations

Our model allows us to predict the mode asymmetries in both the velocity and intensity spectra simultaneously. However,

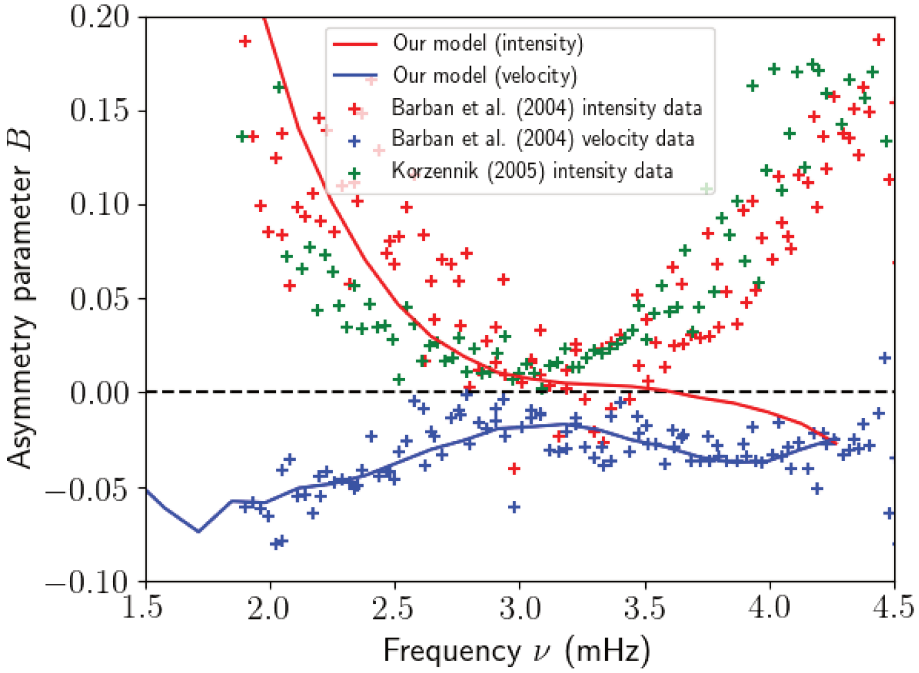

Fig. 2. Asymmetry profile $B(\nu)$ obtained by the numerical spectrum model with $\lambda = 0.5$, in the intensity power spectrum (*solid red line*) and in the velocity power spectrum (*solid blue line*). Both are compared to the asymmetry profile $B(\nu)$ inferred from observations by Barban et al. (2004) in the intensity (*red crosses*) and the velocity power spectra (*blue crosses*), respectively. The green crosses correspond to the asymmetry measured by Korzennik (2005) in the intensity power spectrum.

since we focus on the results pertaining to the Sun's velocity power spectrum in Philidet et al. (2020), in this paper we focus on the subsequent analysis of the Sun's intensity power spectrum.

Figure 2 showcases the comparison between the asymmetries predicted by our model and those inferred from observations, both in velocity and intensity. It is clear that our model predicts a reversal of the asymmetries between these two observables, except for the higher order modes ($\nu \gtrsim 3.6$ mHz). It is also clear that a quantitative agreement is found with observations for modes with $\nu \lesssim \nu_{\max}$, where $\nu_{\max} \sim 3$ mHz is the frequency of maximum height in the p-mode power spectrum. This shows that the localisation of the source, which is the primary cause of asymmetry in the velocity spectrum, is sufficient to explain a large portion of the asymmetry reversal.

However, our model fails to account for the intensity asymmetry of the higher order modes, with $\nu \gtrsim \nu_{\max}$. While it consistently predicts slightly negative asymmetries for these modes, observations tend to show that they actually feature strong positive asymmetry. This shows that other mechanisms must be invoked to fully explain the asymmetry reversal throughout the entire p-mode spectrum. For instance, unlike the velocity power spectrum, our intensity power spectrum model does not contain the contribution of the correlated background. It is widely thought that this contribution is negligible in velocity data; in turn, the results presented in Fig. 2 indicate that it is also negligible in intensity data for low-frequency modes, but that it may no longer be the case for high-frequency modes. Furthermore, the non-adiabaticity of the oscillations is not taken into account in our study; we discuss this approximation in Sect. 4.2. The opacity effect, as it was called by Severino et al. (2008), could also play a role. Finally, the fluctuations of the convective flux may add a non-negligible contribution to the total intensity fluctuations, whereas we only considered the fluctuations of the radiative flux in Eq. (17). The relative importance of both kinds of fluxes depends on the height at which the modes are observed. In particular, the higher the radius of observation, the more prominent the radiative flux.

4. Discussion

4.1. Understanding the asymmetry reversal puzzle

As already mentioned in Sect. 2, the reason why source localisation leads to different asymmetries in the intensity and velocity power spectra is the fact that the relation that links the intensity fluctuations to the velocity fluctuations (or, equivalently, to the variable Ψ_ω) is not a simple linear relation, but involves its first and second derivatives as well. As we also mentioned above, this is because the radiative flux depends primarily on the temperature gradient, and not only on the absolute value of the temperature. There can be partial cancellation between the three terms on the right-hand side of Eq. (20), leading to line profiles that are not simply proportional to each other.

In contrast, using simpler approximations to model the intensity fluctuations leads to much simpler relations between $\delta L/L$ and $v_{\rm osc}$, which, precisely because of their simplicity, are unable to predict any asymmetry reversal. In the following we illustrate this by considering that $\delta T_{\rm eff}/T_{\rm eff} = \delta T/T$ at the photosphere. In that simple case the intensity fluctuations can be written

$$\frac{\delta L}{L} = 4\frac{\delta T}{T} + 2\frac{\xi_r}{r} \,. \tag{27}$$

It is readily shown that the second term on the right-hand side of Eq. (27) is negligible for solar p-modes close to the surface. In turn, the temperature fluctuations are, in the quasi-adiabatic approximation, proportional to the pressure fluctuations. In this simple model pressure fluctuations are therefore a suitable proxy for intensity fluctuations. Then, using the perturbed continuity equation, the intensity fluctuations are related to the variable Ψ_ω through a relation similar to Eq. (20), but with

$$B_L = -\frac{4\nabla_{\rm ad}\Gamma_1}{rc\sqrt{\rho}} \,, \qquad A_L = C_L = 0 \,. \tag{28}$$

We compare in Fig. 3 the velocity and intensity asymmetry profiles $B(\nu)$ obtained when the relation $\delta T_{\rm eff}/T_{\rm eff} = \delta T/T$ is

adopted at the photosphere. As can readily be seen, the asymmetries are not reversed. This is because in this simplified model only one term is retained in the relation between the two types of fluctuations.

The relation between the intensity and velocity Green's functions is therefore a crucial key to tackling the issue of asymmetry reversal. In many studies on the subject, various approximations were made to model this relation. For instance, when dealing with asymmetry reversal, Duvall et al. (1993) split the wave variables into dynamical variables, such as velocity, and thermal variables, such as temperature or brightness. They then implicitly consider that each set of variables is characterised by one Green's function, and in particular that temperature and intensity fluctuations are proportional to one another, which is analogous to Eq. (27). Adopting Eq. (27), as shown by Dupret et al. (2002), does not substantially alter predictions regarding intensity fluctuations, provided temperature fluctuations are described in a fully non-adiabatic framework. However, the use of a simple Newton's cooling law to model non-adiabaticity renders it invalid. Rast & Bogdan (1998), Nigam et al. (1998), Kumar & Basu (1999) made similar assumptions regarding the intensity fluctuations, all of which are equivalent to considering the approximation $\delta T_{\rm eff}/T_{\rm eff} = \delta T/T$, without the necessary non-adiabatic framework.

On the other hand, Roxburgh & Vorontsov (1997) used the same Green's function for velocity and intensity, but considered different source terms. More specifically, they added a frequency-independent source term for the velocity fluctuations, which they did not consider for the intensity fluctuations. In other words, they considered that the only difference between the velocity and intensity fluctuations is the addition of a coherent, non-resonant background component in the velocity signal. Likewise, in Chaplin & Appourchaux (1999), the authors considered proportional Green's functions for velocity and intensity. All these assumptions are equivalent to considering that the coefficients B_L and C_L in Eq. (20) are zero, thus only retaining the coefficient A_L.

Prior studies on asymmetry reversal thus have this in common; they use simplifying approximations to model the intensity fluctuations, so that their equivalent of Eq. (20) only contains one non-vanishing coefficient (either A_L or B_L, depending on the authors). This is the reason why, in their models, source localisation alone was not able to explain the different sense of asymmetry observed in velocity and intensity.

4.2. Quasi-adiabatic approximation

As we mentioned above, our model describes the oscillations in the quasi-adiabatic framework, in the sense that, in establishing the wave equation given by Eq. (2), we neglect all heat transfers, both in the homogeneous part (the full, non-adiabatic wave equation is of fourth order, whereas ours is only second-order) and in the source term (we only considered mechanical work exerted by fluctuations of the turbulent pressure, and left out the effect of turbulent entropy fluctuations). As pointed out by Gabriel (1998), increasing the order of the wave equation is likely to cause asymmetries in different observables to drift further apart. Thus, in order to predict the shape of the mode line profiles as realistically as possible, one should go beyond the quasi-adiabatic approximation and perform fully non-adiabatic computations. However, as a first step, we adopted this approximation in this study.

The quasi-adiabatic approximation is notoriously questionable in the superficial layers of solar-like oscillators, and more specifically in the super-adiabatic region (Samadi et al. 2015; Houdek & Dupret 2015), because the thermal timescale over which heat transfers typically occur in this region is neither much smaller, nor much greater than the period of the oscillations, but rather coincide with it. Thus, modal entropy fluctuations are non-zero, and should, in a fully non-adiabatic framework, be included in the equation of state along with their corresponding evolution equation. The difference is seen, for example, in the phase difference between velocity and intensity modal fluctuations; while the quasi-adiabatic approximation yields a phase difference of $\pi/2$ between the two, the observed phase difference varies significantly with frequency (Barban et al. 2004).

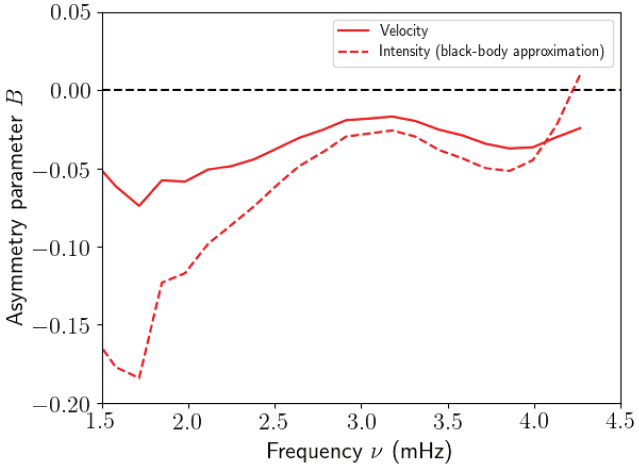

Fig. 3. Predicted asymmetry profiles $B(\nu)$ when the relation $\delta T_{\rm eff} = \delta T$ is assumed. The solid red line shows the velocity asymmetries (since they are unaffected by the intensity fluctuation modelling, it is identical to the solid blue line in Fig. 2). The dashed red line corresponds to the intensity asymmetries obtained by using Eq. (27) in place of Eq. (20).

Therefore, in adopting the quasi-adiabatic approximation, we do not overlook its shortcomings, but rather consider this a first step to a novel approach, which is still likely to shed light on the issue of asymmetry reversal. The impact of non-adiabaticity is perhaps best illustrated with mode amplitudes. In discarding modal entropy fluctuations from the oscillation model, predicted intensity amplitudes are severely overestimated compared to their observed counterparts.

This is illustrated in Fig. 4, where we show the amplitudes predicted by our model as well as the observed solar mode amplitudes, both for velocity and intensity. Predicted mode amplitudes are accessed from the same fitting procedure described in Sect. 3; the amplitude squared of a mode indeed corresponds to the area under the curve of its spectral power density, and is therefore given by

$$A^2 = \pi \Gamma_\omega H_0 \,, \tag{29}$$

where A is the mode amplitude and Γ_ω its linewidth, and H_0 is defined by Eq. (26). We note that mode amplitudes defined in this way are intrinsic amplitudes, and do not account for visibility factors. As for the observed amplitudes, we use the results of the same spectral analysis conducted by Barban et al. (2004) that we used to compare asymmetries in Sect. 3.

It can be seen from Fig. 4 that while our model reproduces the amplitudes in velocity to a satisfactory extent, the intensity amplitudes are overestimated by an order of magnitude (approximately a factor of 5). In particular, it appears that the overestimation factor only slightly depends on frequency. This

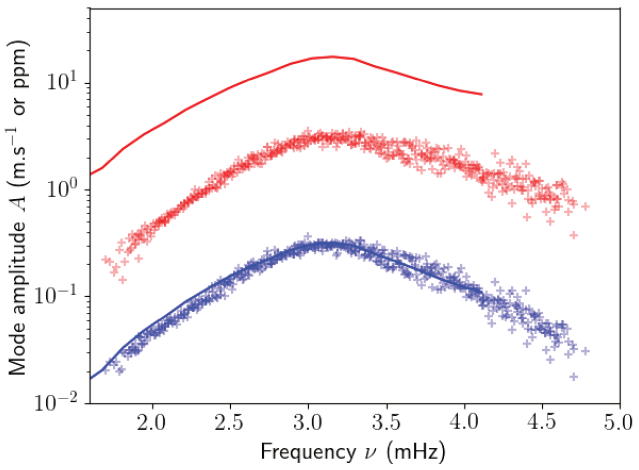

Fig. 4. p-mode amplitudes A, as defined by Eq. (29), as a function of mode frequency ν. The legend is identical to that of Fig. 2: crosses correspond to amplitudes inferred from observations, using the spectral analysis of Barban et al. (2004) (each cross represents an individual doublet (n, l)), whereas solid lines correspond to the prediction of our model; blue element pertain to velocity, red elements to intensity. The amplitudes are given in m.s^{-1} for velocity, and in ppm for intensity.

overestimation is a known shortcoming of the quasi-adiabatic approximation, whose alleviation, as we mentioned above, would require going beyond a second-order wave equation. We note, however, that simply because non-adiabatic effects have an important impact on mode amplitude does not mean that the impact on asymmetries is as critical. Asymmetries are only sensitive to differential, frequency-dependent alterations of the line profiles, and remain unchanged under an overall reduction factor. An alternative approach would be to obtain an equivalent of Eq. (11) by replacing $\delta\tau/\tau$ in Eq. (4) by its integral expression obtained through Eq. (5). Since this method does not rely on τ-derivatives, it is likely to be less affected by departure from adiabaticity; however, the integral form of $\delta\tau/\tau$ renders the resulting equivalent of Eq. (23) impractical to use.

5. Conclusion

In this paper we extended the semi-analytical synthetic power spectrum model developed in Philidet et al. (2020) to predict the radial p-mode asymmetries in intensity observations. We treated the p-mode-induced fluctuations of the radiative flux by perturbing a grey atmosphere model with a solar-calibrated Hopf function. We showed that the dependence of the radiative flux on the temperature gradient, and not simply on the absolute value of the temperature, has a profound impact on the shape of the line profiles in the intensity spectrum. We find quantitative agreement between our predicted asymmetries and the corresponding observations for low-frequency modes, both in velocity and intensity simultaneously. We conclude that no secondary physical mechanism is necessary to explain the reversal between asymmetries in velocity and intensity, at least for $\nu \lesssim \nu_{\max}$.

Our model is unable, however, to explain asymmetry reversal for higher order modes. Secondary mechanisms can be invoked there. The non-adiabatic effects invoked by Duvall et al. (1993), the correlated background effect invoked by Nigam et al. (1998), and the impact of the convective flux fluctuations are all viable candidates. The fact that these discrepancies are restricted to high-frequency modes in intensity suggests that non-adiabaticity is at least partly responsible. As a concluding remark, we point out that radiative transfers, even if they are not sufficient to reverse asymmetries at the high-frequency end of the p-mode spectrum, still have a significant impact on the line profiles. As a result, in investigating the impact of any other physical mechanism on asymmetry reversal, this intrinsic difference between velocity and intensity line profiles must still be accounted for.

The main limitation of the model presented in this study is the quasi-adiabatic approximation, which is not valid in the superficial layers of the star. Although it sheds some light on the asymmetry reversal problem, any further improvement of this model will therefore need to go beyond this approximation and consider a non-adiabatic wave equation instead. We postpone this refinement to a later study.

Acknowledgements. The authors wish to thank the anonymous referee for his/her useful comments, which helped considerably improve this manuscript. J.P, K.B and R.S acknowledge financial support from the "Programme National de Physique Stellaire" (PNPS) of CNRS/INSU and from the "Axe Fédérateur Etoiles" of Paris Observatory. H.G.L. acknowledges financial support by the Sonderforschungsbereich SFB 881 "The Milky Way System" (subprojects A4) of the German Research Foundation (DFG).

References

Barban, C., Hill, F., & Kras, S. 2004, ApJ, 602, 516
Benomar, O., Goupil, M., Belkacem, K., et al. 2018, ApJ, 857, 119
Chaplin, W. J., & Appourchaux, T. 1999, MNRAS, 309, 761
Dupret, M. A., De Ridder, J., Neuforge, C., Aerts, C., & Scuflaire, R. 2002, A&A, 385, 563
Duvall, T. L., Jr, Jefferies, S. M., Harvey, J. W., Osaki, Y., & Pomerantz, M. A. 1993, ApJ, 410, 829
Gabriel, M. 1998, A&A, 330, 359
Georgobiani, D., Stein, R. F., & Nordlund, Å. 2003, ApJ, 596, 698
Houdek, G., & Dupret, M.-A. 2015, Liv. Rev. Sol. Phys., 12, 8
Korzennik, S. G. 2005, ApJ, 626, 585
Kumar, P., & Basu, S. 1999, ApJ, 519, 389
Manchon, L., Belkacem, K., Samadi, R., et al. 2018, A&A, 620, A107
Mihalas, D. 1978, Stellar Atmospheres
Nigam, R., & Kosovichev, A. G. 1998, ApJ, 505, L51
Nigam, R., Kosovichev, A. G., Scherrer, P. H., & Schou, J. 1998, ApJ, 495, L115
Philidet, J., Belkacem, K., Samadi, R., Barban, C., & Ludwig, H. G. 2020, A&A, 635, A81
Rast, M. P., & Bogdan, T. J. 1998, ApJ, 496, 527
Roxburgh, I. W., & Vorontsov, S. V. 1997, MNRAS, 292, L33
Samadi, R., & Goupil, M.-J. 2001, A&A, 370, 136
Samadi, R., Belkacem, K., & Sonoi, T. 2015, EAS Publ. Ser., 73–74, 111
Severino, G., Magrì, M., Oliviero, M., Straus, T., & Jefferies, S. M. 2001, ApJ, 561, 444
Severino, G., Straus, T., & Steffen, M. 2008, Sol. Phys., 251, 549
Sonoi, T., Ludwig, H. G., Dupret, M. A., et al. 2019, A&A, 621, A84
Toutain, T., Appourchaux, T., Baudin, F., et al. 1997, Sol. Phys., 175, 311
Unno, W., Osaki, Y., Ando, H., Saio, H., & Shibahashi, H. 1989, Nonradial Oscillations of Stars
Vernazza, J. E., Avrett, E. H., & Loeser, R. 1981, ApJS, 45, 635
Vorontsov, S. V., & Jefferies, S. M. 2013, ApJ, 778, 75

Conclusion and perspectives of Part II

Summary

My objective was to develop a realistic and predictive formalism designed to model the shape of the solar radial p-mode line profiles. This constitutes a different approach compared to prior studies, whose goal was to adjust parameterised and simplified synthetic power spectrum models to observations. I first developed this formalism for the velocity power spectrum (Philidet et al. 2020a), and next adapted it to the intensity power spectrum (Philidet et al. 2020b). This formalism, based on the work of Samadi and Goupil (2001), allowed me to include the statistics of the turbulent velocity field responsible for the stochastic driving of the modes – and more specifically the turbulent spectrum – in the most general way possible, while still allowing for quantitative predictions to be made. The model combines analytical derivations with the use of a 3D hydrodynamic simulation of the stellar atmosphere computed with the CO^{5}BOLD code, to extract certain properties of the turbulent motions close to the surface of the star. As a first validating step, I applied this formalism to the case of solar radial p-modes.

For asymmetries in the velocity power spectrum, I used two different models: one with a certain number of free physical parameters, enabling the exploration of the impact of changing the physics of the turbulence on the asymmetry of the modes; and one only containing one free parameter in the form of λ, which can additionally be constrained through other methods, allowing to make quantitative predictions concerning the shape of the mode line profiles. With the first model, which I dubbed 'theoretical spectrum' model, I showed that the spatial extent of the source of stochastic excitation is of primary importance to explain the degree of mode asymmetry. More specifically, the asymmetries of the high-frequency modes are quite sensitive to the relative weight of the region above and below the photosphere in the total excitation rate of the modes. As such, it is impossible to infer any property of the source of excitation using observed asymmetries with a model that does not account for its spatial extent in a realistic manner. Furthermore, I showed that the effect of the source localisation to mode asymmetry is largely dominant, and the effect of the correlated background negligible. The second 'numerical spectrum' model, on the other hand, allowed me to predict the asymmetries in the solar case, and to compare them to observations, in order to validate the model. A good agreement is found throughout the p-mode spectrum, thus supporting the validity of the approximations adopted in this formalism. Furthermore, I was able to shed light on the physical origin of the frequency dependence of mode asymmetry in the Sun. For low-frequency modes $\nu \lesssim 3$ mHz, the direction of variation of the asymmetry profile $B(\nu)$ largely stems from the linewidth dependence on frequency – the parameter B being proportional to the width of the modes. On the other hand, for higher-frequency modes, the dependence of asymmetry on frequency is much more dependent on the relative weight of the contributions to mode driving of the regions located above and below the photosphere respectively, or otherwise stated, on the spatial extent of the source of excitation.

For asymmetries in the intensity power spectrum, I only considered the second model, as my goal was to assess whether this formalism is able to correctly predict the asymmetries in both observables at the same time. I showed that a certain degree of asymmetry reversal can be explained by source localisation alone. This is in stark contrast with all other studies, which had to rely on an additional physical mechanism to explain this puzzle: indeed, under simplified hypotheses concerning the oscillation-induced intensity variations, one should expect the asymmetries in intensity and velocity to be identical. The reason the asymmetry reversal constituted a puzzle in the first place is that these studies consider a simplified expression for the intensity perturbation, thus missing out on the finer details of the intensity mode line profiles, and failing to correctly assessing intensity mode asymmetry. By contrast, not only does the more realistic treatment of Lagrangian luminosity perturbations adopted here make asymmetry reversal occur for low-frequency modes ($\nu \lesssim 3$ mHz), I also find good quantitative agreement. However, the agreement fails for higher-frequency modes, where other physical mechanisms may need to be accounted for to correctly recover asymmetry reversal – correlated background, non-adiabatic effects or a contribution from the convective flux for instance. Nevertheless, the fact that a good agreement is found for all modes in velocity, and

for low-frequency modes in intensity, is a solid indicator that the formalism presented here is valid. In particular, it supports the specific form I adopted for the turbulent velocity spectrum, both spatial and temporal.

Perspectives

I already validated the model for a large part, as abundantly explained above. However, there still remain large discrepancies between predicted and observed asymmetries in intensity for high-frequency modes, which warrants further investigation, either into additional mechanisms as mentioned above, or into the assumptions underlying the formalism presented in Chapters 5 and 6 – in particular the quasi-adiabatic approximation. Furthermore, it is possible to support the formalism more firmly still, by exploring the question of mode amplitude, and in particular the comparison between intensity and velocity amplitudes, which can also be studied in the framework of this model. Beyond the motivation to further validate the model, the comparison between the two kinds of mode amplitude also constitutes an interesting subject of study in itself. Indeed, as I mentioned in Section 2.2, observed mode amplitude form a powerful tool for seismic diagnosis, whether they are used for individual stars to constrain the properties of turbulent convection – the same way I presented in these last two Chapters with mode asymmetry –, or in conjunction with scaling relations in the context of ensemble asteroseismology. At any rate, it is necessary to shed as much light as possible on the driving processes pertaining to solar-like oscillations, and how that translates in terms of mode amplitude. This is especially true for intensity amplitudes, which are less readily predicted by theory than velocity amplitude, as was made apparent in Section 6.3. We began this exploration with solar amplitudes, with a focus on the p-mode amplitudes in intensity, in collaboration with Marc-Antoine Dupret. I already described the first efforts we made in that direction in Section 6.3. However, there is still some work to be done in that regard. More specifically, it would be important to try and apply these calculations to the case of other solar-like oscillators, which would allow, for instance, to physically constrain the scaling relations pertaining to the ratio between the spectrometric and bolometric mode amplitudes, but also to the absolute amplitudes as well.

In the same spirit, I started investigating, in collaboration with Hans-Günther Ludwig, the possibility of applying this formalism not to real solar-like oscillators, but to oscillations developing in 3D hydrodynamic simulations. This would help support the validity of this approach even further, but the motivations behind this endeavour are deeper. 3D hydrodynamic simulations present the crucial advantage of offering many more observables than real stars: one has access to all fluid variables at any position in the cube as well as any instant in time – although one is, of course, limited by the time discretisation. Therefore, the simulation provides with fluid properties at any depth, without any observational hurdle, and averages can be performed in any way one could want. In short, the output of a 3D LES is much more controlled, by nature, than the output of the observations of a real solar-like oscillator, even the Sun. As a result, they offer the opportunity to explore more efficiently the relation between the observed properties of mode driving and the underlying physics of turbulence. As a concrete example, such a simulation provides with the 'observed' amplitude of the oscillating modes of the box *at any observational depth*, and *in any frame of reference* (whether it be Eulerian, Lagrangian, or in the fixed-optical-depth frame I already discussed in Section 4.2.3). We hope to be able to develop theoretical tools that are more efficient still for constraining turbulent convection properties from observed mode properties pertaining to mode driving, in particular from the observed velocity/intensity relation.

Last, but certainly not least, now that the validating steps have been successfully taken, it is time to look at the longer-term goals, which were the motivations for this work in the first place. As I explained in the end of Section 4.1, mode asymmetry in intensity is now observed in solar-like oscillators other than the Sun. It is observed, in particular, that the asymmetry of the modes, like their amplitude and their linewidth, follow clear trends with stellar parameters, like surface gravity of effective temperature (Benomar et al. 2018). These trends offer the opportunity to use observed asymmetries for seismic diagnosis purposes. But this requires a thorough theoretical understanding of the relation between stellar parameters and p-mode asymmetry, especially in intensity. Our formalism is prime for use in this context. More concretely, I intend to use a grid of patched stellar models corresponding to an sample of solar-like oscillators – like the CO^{5}BOLD or `Stagger` grid – characterised by different stellar parameters. My goal is to apply the formalism presented in Chapters 5 and 6, and therefore obtain quantitative predictions for the asymmetry profile $B(\nu)$, for each of these stellar models separately. My hope is to be able to use these predictions to shed a brighter light, from a theoretical and physical point of view, on the dependence of $B(\nu)$ on the stellar parameters, in particular close to $\nu_{\max}$. This undoubtedly constitutes the next step in this work.

Another next step, much bigger this time, would be to consider the other aspects of turbulence-oscillation

coupling. So far, I have focused exclusively on one aspect of this coupling: the stochastic driving of the modes by the turbulent motions close to the surface of the star. It is this stochastic driving that is responsible for the asymmetry of the mode line profiles, in addition to their amplitude. The physical processes at play behind mode driving are fairly well understood, and even though there still remain some details to investigate, we have made considerable progress in this context. However, other aspects of turbulence-oscillation coupling – namely mode damping and surface effects – are much more sensitive to the properties of this coupling, and our understanding of these aspects is therefore much less consensual. As was made clear in Sections 2.3 and 2.4, it is necessary to further investigate alternative theoretical approaches to tackle these more sensitive issues, in order to go beyond the Mixing-Length Theory for instance. More particularly, it is necessary to investigate turbulence-oscillation coupling as a whole, instead of focusing on one single aspect at a time, like I did in Part II. This is the subject of Part III, into which I now delve.

Part III

Lagrangian stochastic models for turbulence–oscillation coupling

7 Stochastic models of turbulence: an introduction

Contents

> - Give me a break! That wasn't my fault.
> - Yeah, no. I mean, obviously this was all due to the butterfly effect.
> - The what?
> - Butterfly effect. You know, a butterfly in Africa lands on a giraffe's nose, the giraffe sneezes, that spooks a gazelle, the gazelle bonks into a rhinoceros, and the rhinoceros blindly stampedes into a phone booth, calls New York somehow, and says "Hey, go kill this idiot Ron, for a suitcase", because the rhinoceros speaks English! [...] What's in the suitcase, Ron?
>
> Sterling Archer to Ron Cadillac

In Section 1.2, I presented an overview of the various modelling approaches traditionally followed for the treatment of stellar turbulent convection, either through the use of Large-Eddy Simulations (see Section 1.2.1), through Mixing-Length Theories (see Section 1.2.2), or through Reynolds-stress models (see Section 1.2.3). In particular, I insisted on the difficulties inherent to the theoretical description of convection in a highly turbulent medium, as well as on the shortcomings of these approaches. In Sections 2.2 to 2.4, I described how these approaches are used to tackle the various issues associated with the coupling between the turbulent convection at the top of the convective envelope of solar-type stars and the global acoustic modes of oscillation developing in these stars. In this context, the shortcomings of these methods become more visible still: they require that the turbulent convection and the oscillations be separated into two distinct sets of equations from the start, usually through a separation of timescales, length scales, or between an average and a fluctuating component, which is problematic when it comes to modelling their coupling; the mixing-length hypothesis underlying all versions of MLT oversimplifies the behaviour of convection close to the surface of the star, by reducing the turbulent cascade to a unique time and length scale, thus only crudely modelling turbulent dissipation; closure relations, whether introduced in MLT or Reynolds-averaged Navier-Stokes (RANS) formulations, or implemented in conjunction with 3D LES (like the GGM or RGM for instance) are very difficult to relate to the underlying physical assumptions, which makes it impossible to assess whether they are relevant to the stellar context or not; as a corollary, the free parameters in these models are not physical, and therefore difficult to constrain. As I concluded in Chapter 3, these limitations

are both crippling when it comes to modelling the coupling between turbulent convection and stellar oscillations, and unavoidable, because inherent to these methods. It is therefore necessary to go beyond these approaches, and to propose something new.

To this end, I explore the realm of stochastic models of turbulent media, and its potential for the study of turbulence–oscillation coupling in solar-type stars. The original idea is simple: instead of being described by a set of transport equations for the means (as in MLT formulations), or for the means, variances, and higher-order moments (as in RANS models), the fluid is now described by a transport equation for the joint Probability Density Function (PDF thereafter) associated to every turbulent quantity. This is at the heart of *PDF models* of turbulence, and more specifically, when the PDF is associated to Lagrangian quantities, *Lagrangian PDF models*. Knowing the PDF is equivalent to knowing all the moments of the turbulent quantities. However, its transport equation takes the form of a Fokker-Planck equation, which can prove very complicated to handle both analytically and numerically. To circumvent this problem, the PDF itself can be represented by a large set of individual particles, whose position and physical properties are evolved through time to mimic the evolution of the PDF. When the medium is highly turbulent, the equations used to model the evolution of the fluid particles are no longer ordinary differential equations, but become *stochastic differential equations* (SDE thereafter), i.e. equations containing a random component. Such models are referred to as *Lagrangian stochastic models* of turbulence: the term 'Lagrangian' is called for because the equations pertain to fluid parcels followed along their trajectories, while the term 'stochastic' refers to the nature of the equations. Lagrangian stochastic models have been used to describe turbulent media by the fluid dynamics community for a long time (e.g. Pope 1981; Anand et al. 1989; Haworth and El Tahry 1991; Roekaerts 1991; Hsu et al. 1994; Delarue and Pope 1997; Welton and Pope 1997; Welton 1998; Das and Durbin 2005; Bakosi and Ristorcelli 2011), and have allowed for a considerable improvement of our understanding of high-Reynolds-number flows. These models have also found wide-spread use in the meteorological community, more specifically to model turbulent diffusion in the Convective Planetary Boundary Layer (or CPBL) here on Earth – on the subject, I warmly invite the curious reader to consult the excellent monograph by Rodean (1996). The CPBL is the lowermost layer of the atmosphere, which is in contact with the ground and the bodies of water, and therefore most directly influenced by the solar heating of the Earth's surface. When the heating is strong enough, this layer becomes convectively unstable, and upon arising, the instability entails the onset of turbulent atmospheric motions, responsible for an increased mixing of the scalar properties of the air (like its temperature and density for instance). The CPBL is extremely similar, in its behaviour and its general properties, to the external layers of stellar convective zones[1] Nevertheless, the use of Lagrangian stochastic models has not crossed the seemingly impenetrable barrier separating such distant fields as meteorology and stellar physics, and its use has remained rare in the context of stellar turbulent convection.

My goal, in this context, is to try and remedy this situation, and to show that these methods, that have proved so beneficial in other realms, offer a great potential for deepening our understanding of stellar turbulent convection. In the following chapters, I will focus, more specifically, on the issues related to its coupling with stellar oscillations in solar-type stars. Before I do that, however, it is necessary to offer some background information concerning the basic mathematical tools that I will use throughout the rest of this thesis. This is the goal of this chapter. I start with a short introduction to stochastic processes, stochastic differential equations, and the formalism of Ito calculus that overarches all these mathematical concepts. Then, I present in a non-exhaustive manner the various implementations of Lagrangian stochastic models of turbulent flows that have been developed since the concept of stochastic equations has been invented – which was, after all, only some 60 years ago. The great advantages offered by these models in the context of this thesis will then become apparent.

7.1 Stochastic processes: the basics

Before I show how the concept of stochastic process, and the mathematical artillery that stands behind it, can be used in the context of turbulent flows, it is necessary to give some formal definitions, which I do in the following. These definitions can be found in any textbook on stochastic processes; I refer the reader, for instance, to Gardiner (1994) or Øksendal Bernt Karsten (1992), from which the structure of this section is inspired.

[1] In fact, were it not for the fact that the gas in stellar interiors is at least partially ionised, there would virtually be no qualitative difference between the two.

7.1.1 Stochastic processes: a formal definition

Random variables

Let Ω be a given set, and $\mathcal{F}$ be a family of subsets of Ω which verifies the three following properties: 1) $\mathcal{F}$ contains the empty set, 2) if a subset is contained in $\mathcal{F}$, then so is its complementary – i.e. the subset of all elements of Ω that are not in F –, and 3) the union of any number of elements of $\mathcal{F}$ is also in $\mathcal{F}$. Such a family $\mathcal{F}$ is said to be a *σ-algebra* on Ω. Then a *probability measure* P is defined as a function that maps $\mathcal{F}$ onto $[0, 1]$ in such a way that 1) the empty set is mapped to 0, 2) Ω is mapped to 1, and 3) if A_i is a disjoint subset of $\mathcal{F}$ – i.e. any element of one of the A_i cannot be in any of the other A_j –, then the measure of their union is equal to the sum of their measures. If all of these properties are verified, the triplet $(\Omega, \mathcal{F}, P)$ is called a *probability space*. These definitions may seem a bit formal: what do they intuitively mean? Ω is the Universe in which events can happen in the scope of a given experiment, and $\mathcal{F}$ is the total set of events that can happen within this Universe. As for the function P, it relates any event in the Universe to the probability of its occurrence. In particular, the first property of P means that something impossible is given probability 0, the second property means that an unavoidable outcome is given probability 1, and the third property means that if several outcomes are mutually exclusive, then the probability of either one of them to occur is the sum of their individual probabilities.

In this context, a *random variable* X is defined as a function mapping $\mathcal{F}$ onto $\mathbb{R}^n$ (for a given positive integer n), with the only requirement being that X must be $\mathcal{F}$-measurable – i.e. any open subset of $\mathbb{R}^n$ must be the image by X of a given element of $\mathcal{F}$. In other words, for any given ensemble of real numbers, there should always be at least one event that is associated to this ensemble through the random variable X. In that case, X is invertible, and the function $\mu \equiv P \circ X^{-1}$ (where $\circ$ denotes function composition) is properly defined: it corresponds to the *distribution of the random variable* X. Essentially, it maps the real number associated to a given event to the probability of the event. The *expectation* of the random variable X is defined as

$$E[X] \equiv \int_\Omega X(\omega)\,\mathrm{d}P(\omega) = \int_{\mathbb{R}^n} x\,\mathrm{d}\mu(x)\,, \tag{7.1}$$

where the first equality is the definition, and the second equality stems from the definition of μ. It is easily seen that for any function g of $\mathbb{R}^n$ into $\mathbb{R}^m$, the expectation of $g(X)$ is

$$E[g(X)] = \int_{\mathbb{R}^n} g(x)\,\mathrm{d}\mu(x)\,. \tag{7.2}$$

The differential form of the distribution μ can be rewritten, in the integral defining the expectation, in terms of the infinitesimal element $\mathrm{d}^n x$ over which the integral is performed. Let us write $\mathrm{d}\mu(x) = f(x)\,\mathrm{d}^n x$. Then we have

$$E[g(X)] = \int_{\mathbb{R}^n} g(x) f(x)\,\mathrm{d}^n x\,. \tag{7.3}$$

By construction, $f(x_0)\,\mathrm{d}^n x$ is the probability of all the events that are associated, through the random variable X, to values of x that are located within $\mathrm{d}^n x$ of x_0. Intuitively, it corresponds to a density of probability in the $\mathbb{R}^n$ space onto which the outcomes of the experiment are mapped: it is accordingly referred to as the *Probability Density Function* (PDF thereafter) of the random variable X. Accordingly, the *joint PDF* of two random variables X_1 and X_2 can be defined thus: if $f_{\text{joint}}(x_1, x_2)\,\mathrm{d}^n x_1\,\mathrm{d}^m x_2$ is the probability of all the events that are associated, through X_1 to real values within $\mathrm{d}^n x_1$ of x_1, and, simultaneously, through X_2 to real values within $\mathrm{d}^m x_2$ of x_2, then f_{joint} is the joint PDF of the two random variables. Naturally, the definition can be extended to more than two variables. Finally, the *conditional PDF* $f_{X_2}(X_1)$ of X_1 knowing X_2 is defined as the ratio between their joint PDF and the PDF of X_2 alone. $f_{X_2}(x_1|x_2)\,\mathrm{d}^n x_1$ corresponds, perhaps more intuitively, and as the name 'conditional' suggests, to the probability of all the events associated through X_1 to real values within $\mathrm{d}^n x_1$ of x_1, and through X_2 to exactly x_2.

From random variables to stochastic processes

These notions are undoubtedly familiar to the reader. From there, the leap to stochastic processes is but a small one: indeed, a *stochastic process is simply a parameterised collection $\{X_t\}_{t\in T}$ of random variables.* In general, the set T with which these random variables are indexed can be absolutely anything – finite or infinite, discrete or continuous –, but in the remaining of this manuscript, T will represent the set of all instants in time, and be equal to

$\mathbb{R}$. In that case, a stochastic process can roughly be thought of as a random variable that evolves through time. For any given time t, X_t is a classical random variable, the kind of which everyone is familiar with. On the other hand, for any experiment $\omega \in \Omega$, the function $t \to X_t(\omega)$ that maps $\mathbb{R}$ onto $\mathbb{R}^n$ is called a *sampling path of the stochastic process*. Let me briefly interpret all of these notions if the system under consideration is a turbulent flow. Then for any fixed time t, X_t can be, for instance, a function that associates to a given realisation ω of the flow the velocity of the flow realisation at a predetermined point and time t; and for any given realisation of the flow, the sampling path of X_t is the time evolution of the flow velocity at a predetermined point for this realisation. Then the velocity of the flow at this given point is a set of random variables associated to each instant: we have a stochastic process.

I introduced above the notion of PDF for a random variable. This notion is easily extended to stochastic processes: the PDF $f(x,t)$ of a stochastic process is defined as the PDF of X_t. It now depends both on the real variable x associated to the random variable, and on time t. Let me also extend the definition of the joint PDF of the stochastic process by defining $f(x_1,t_1;x_2,t_2;...)$ as the joint PDF of X_{t_1}, X_{t_2}, ... Note that, in the following, I will drop the subscript 'joint': the context will always make it clear when a PDF is joint and when it is not. Similarly, the conditional PDF of X_{t_1}, X_{t_2}, ..., knowing Y_{τ_1}, Y_{τ_2}, ... is defined as

$$f(x_1,t_1;x_2,t_2;...|y_1,\tau_1:y_2,\tau_2;...) \equiv \frac{f(x_1,t_1;x_2,t_2;...;y_1,\tau_1:y_2,\tau_2;...)}{f(y_1,\tau_1:y_2,\tau_2;...)} \,. \tag{7.4}$$

In the context of stochastic processes, it is useful to remark that the PDF contains the knowledge of the system at one given time, the joint PDF contains the simultaneous knowledge of the state of the system at several different times, and the conditional PDF contains the knowledge of the future state of the system provided its past state is perfectly known. Note that this is only the case if the times are ordered according to $... \leqslant \tau_2 \leqslant \tau_1 \leqslant ... \leqslant t_2 \leqslant t_1$: in the following, I will always assume that this is the case.

7.1.2 Markov processes

Definition

A stochastic process is said to have the Markov property, or to verify the Markov assumption, or to be a *Markov process*, if its conditional PDF verify

$$f(x_1,t_1;x_2,t_2;...|y_1,\tau_1:y_2,\tau_2;...) = f(x_1,t_1;x_2,t_2;...|y_1,\tau_1) \,. \tag{7.5}$$

In common language, *a Markov process is a stochastic process whose future evolution only depends on the present state*. Such a process therefore has absolutely no memory of the past. It is immediately seen that the multi-time joint PDF of a Markov process, whatever its complexity, can always be written in terms of two-times joint PDF only. Indeed, let us consider the three-time joint PDF $f(x_1,t_1;x_2,t_2;y_1,\tau_1)$. By definition of the conditional PDF, one has

$$f(x_1,t_1|x_2,t_2;y_1,\tau_1) = \frac{f(x_1,t_1;x_2,t_2|y_1,\tau_1)}{f(x_2,t_2|y_1,\tau_1)} \,. \tag{7.6}$$

But the Markov property stipulates that $f(x_1,t_1|x_2,t_2;y_1,\tau_1) = f(x_1,t_1|x_2,t_2)$. As such, one obtains

$$f(x_1,t_1;x_2,t_2|y_1,\tau_1) = f(x_1,t_1|x_2,t_2)f(x_2,t_2|y_1,\tau_1) \,. \tag{7.7}$$

Finally, using the definition of the conditional PDF, this can be rewritten

$$f(x_1,t_1;x_2,t_2;y_1,\tau_1) = f(x_1,t_1|x_2,t_2)f(x_2,t_2|y_1,\tau_1)f(y_1,\tau_1) \,. \tag{7.8}$$

This is easily extended to the case of any multi-time joint PDF, and we find the following general property of Markov processes

$$f(x_1,t_1;x_2,t_2;...;x_n,t_n) = f(x_1,t_1|x_2,t_2)f(x_2,t_2|x_3,t_3)...f(x_{n-1},t_{n-1}|x_n,t_n)f(x_n,t_n) \,. \tag{7.9}$$

This property means that the knowledge of the evolution of a Markov process *is only contained in how the system jumps from state to state in short time scales*. This is extremely important, as this is the key property that makes the modelling of Markov processes possible without too much hassle.

By definition of the joint PDF, one has

$$f(x_1, t_1) = \int_{\mathbb{R}^n} \mathrm{d}^n x_2 \; f(x_1, t_1; x_2, t_2) \,, \tag{7.10}$$

which no longer depends on the reference time t_2, because I have integrated over the only variable pertaining to this instant. Similarly, one has

$$f(x_1, t_1|x_3, t_3) = \int_{\mathbb{R}^n} \mathrm{d}^n x_2 \; f(x_1, t_1; x_2, t_2|x_3, t_3) = \int_{\mathbb{R}^n} \mathrm{d}^n x_2 \; \frac{f(x_1, t_1; x_2, t_2; x_3, t_3)}{f(x_3, t_3)} \,. \tag{7.11}$$

For the moment, this is valid for any stochastic process. But using Equation 7.9, this transforms, for Markov processes only, into the *Chapman-Kolmogorov equation*

$$f(x_1, t_1|x_3, t_3) = \int_{\mathbb{R}^n} \mathrm{d}^n x_2 \; f(x_1, t_1|x_2, t_2) f(x_2, t_2|x_3, t_3) \,. \tag{7.12}$$

As will seen in the following, this equation alone contains everything one needs in order to model the evolution of a Markov process.

All of this was the good news. Here is the bad news: there is no such thing as a Markov process in real life. Any system conserves at least a certain amount of memory of the past, even if it is very short, and this memory can be perceived if measurements are made at sufficiently close time intervals. However, if these real memory timescales cannot be perceived, then for all intents and purposes the system can accurately be described by a Markov process. For instance, a fluid parcel in a turbulent flow is subjected to highly fluctuating forces, so that its velocity undergoes unceasing kicks in every directions. But it also has a certain measure of inertia, which means its velocity retains some degree of coherence with the immediate past state of the parcel. In other words, the velocity of the parcel is not strictly speaking a Markov process. However, if the inertia is low enough, and the random forces fluctuating enough, then the memory time of the parcel is very short, and the sample path of its velocity can be approximately considered to have the Markov property. The same can be said of its position: if the velocity itself fluctuates rapidly enough, then the particle is almost never in a uniform rectilinear motion, and its position can be approximated by a Markov process (see Section 12.3.1 of Pope 2000, for a more detailed discussion on the subject).

The differential Chapman-Kolmogorov equation

The Chapman-Kolmogorov equation (Equation 7.12) describes the evolution of a Markov process. But the fact that the times t_1 and t_3 are two completely separated instants, not at all close to one another, makes this equation quite impractical. It would be better to have a form of this evolution equation for arbitrarily close instants t and $t + dt$. This would yield a differential equation, much more practical to model the evolution of the system. Let us suppose that the conditional PDF $f(x_1, t_1|x_2, t_2)$ does not depend on the absolute times t_1 and t_2, but only on the time difference τ between the two[2]

$$f(x_1, t_1|x_2, t_2) \equiv T_\tau(x_1|x_2) \,. \tag{7.13}$$

$T_\tau(x_1|x_2)$ corresponds to the transition probability from the state x_2 to the state x_1 per unit state x_1, during the time interval τ. With this notation, the Chapman-Kolmogorov equation becomes

$$T_{\tau+\tau'}(x_1|x_3) = \int_{\mathbb{R}^n} \mathrm{d}^n x_2 \; T_{\tau'}(x_1|x_2) T_\tau(x_2|x_3) \,. \tag{7.14}$$

Then, as $\tau' \to 0$, one can describe the density of probability for state transition in the following way

$$T_{\tau'}(x_1|x_2) = (1 - a_0\tau')\delta^n(x_2 - x_1) + \tau' J(x_1|x_2) + O(\tau'^2) \,, \tag{7.15}$$

where δ^n is the Dirac distribution on $\mathbb{R}^n$, and $J(x_1|x_2)$ is the *transition probability per unit time* from state x_2 to state x_1. In terms of dimension, both T and the n-dimensional Dirac distribution have the dimension of an inverse volume in the space of random variables, while J has the dimension of an inverse volume (also in random variable

[2]Provided the laws of physics are invariant by translation in time, this is not a very restrictive condition.

space) per unit time, and a_0 is simply an inverse time. The meaning of Equation 7.15 is the following: during a time interval τ', the system either remains in the same state, which happens with probability $1 - a_0\tau'$, where a_0 is the probability per unit time for the system to change state; or the system state changes once, which is represented by the second term on the right-hand side; or the system state changes several times, which happens with a probability that is non-linear in τ', and is represented by the third term on the right-hand side. The quantity a_0 is constrained by the normalisation condition

$$\int_{\mathbb{R}^n} \mathrm{d}^n y \; T_{\tau'}(y|x_2) = 1 \; , \tag{7.16}$$

which immediately yields

$$a_0(x_2) = \int_{\mathbb{R}^n} \mathrm{d}^n y \; J(y|x_2) \; . \tag{7.17}$$

Replacing $T_{\tau'}(x_1|x_2)$ in Equation 7.14 by the expression given by Equation 7.15, one finds

$$T_{\tau+\tau'}(x_1|x_3) = \int_{\mathbb{R}^n} \mathrm{d}^n x_2 \; \left[(1 - a_0(x_2)\tau')\delta^n(x_2 - x_1) + \tau' J(x_1|x_2) + O(\tau'^2)\right] T_\tau(x_2|x_3) \; . \tag{7.18}$$

Then, replacing a_0 by its expression given by Equation 7.17, and using the definition of the Dirac distribution, one finds

$$\begin{aligned} & T_{\tau+\tau'}(x_1|x_3) - T_\tau(x_1|x_3) \\ & = \tau' \left[\int_{\mathbb{R}^n} \mathrm{d}^n x_2 \; J(x_1|x_2) T_\tau(x_2|x_3) - \int_{\mathbb{R}^n} \mathrm{d}^n x_2 \; \int_{\mathbb{R}^n} \mathrm{d}^n y \; J(y|x_2)\delta^n(x_2 - x_1) T_\tau(x_2|x_3) \right] + O(\tau'^2) \\ & = \tau' \left[\int_{\mathbb{R}^n} \mathrm{d}^n x_2 \; J(x_1|x_2) T_\tau(x_2|x_3) - \int_{\mathbb{R}^n} \mathrm{d}^n y \; J(y|x_1) T_\tau(x_1|x_3) \right] + O(\tau'^2) \; . \end{aligned} \tag{7.19}$$

Finally, replacing the variable y by x_2 in the second integral, dividing by τ' and taking the limit $\tau' \to 0$, one finds the *differential Chapman-Kolmogorov equation*, also referred to as the *master equation*

$$\frac{\partial T_\tau(x_1|x_3)}{\partial \tau} = \int_{\mathbb{R}^n} \mathrm{d}^n x_2 \; \left(J(x_1|x_2) T_\tau(x_2|x_3) - J(x_2|x_1) T_\tau(x_1|x_3) \right) \; . \tag{7.20}$$

Considering that the initial state x_3 and the initial time t_3 are both fixed, the master equation can be rewritten in terms of the PDF f in a perhaps more familiar form

$$\frac{\partial f(x,t)}{\partial t} = \int_{\mathbb{R}^n} \mathrm{d}^n x' \; \left(J(x|x') f(x',t) - J(x'|x) f(x,t) \right) \; . \tag{7.21}$$

The physical meaning of the master equation is simply that the rate of change of the probability density associated to the state x is the result of a balance between the probability flow *from* all neighbouring states x' *to* the state x (which increases f) and the probability flow *to* all neighbouring states x' *from* the state x (which decreases f).

The Fokker-Planck equation

From now on, in order to simplify the discussion, let me suppose that the stochastic process X_t is a scalar variable. Usually, J is separated into two components: one due to discontinuous jumps, and one due to continuous transitions. In the context of turbulent flows, I will neglect the contribution from discontinuous jumps, and consider that all the contributions come from continuous transitions: such a Markov process is referred to as a *diffusion process*. Then the function $J(x|x')$ only takes non-zero values for x very close to x'. Rewriting $J(x|x') = J(x', r)$, where $r \equiv x - x'$, it can be stated that J peaks at $r = 0$, and is a slowly varying function of x' (in comparison with its dependence on r). Then Equation 7.21 can be rewritten

$$\frac{\partial f(x,t)}{\partial t} = \int_{\mathbb{R}} \mathrm{d}r \; J(x - r, r) f(x - r, t) - f(x,t) \int_{\mathbb{R}} \mathrm{d}r \; J(x, -r) \; . \tag{7.22}$$

In the first integral on the right-hand side of Equation 7.22, one can consider the Taylor expansion of the integrand in the following form

$$J(x-r,r)f(x-r,t) = \sum_{i=0}^{+\infty} \frac{(-r)^i}{i!} \frac{\partial^i}{\partial x^i} \left[J(x,r)f(x,t) \right] \ , \tag{7.23}$$

in which case Equation 7.22 becomes

$$\frac{\partial f(x,t)}{\partial t} = \int_{\mathbb{R}} \mathrm{d}r \sum_{i=1}^{+\infty} \frac{(-r)^i}{i!} \frac{\partial^i}{\partial x^i} \left[J(x,r)f(x,t) \right] \ , \tag{7.24}$$

where the $i = 0$ term in the Taylor expansion cancels out with the second term on the right-hand side of Equation 7.22. Finally, let me define the moments of the transition probability as

$$\mu_i(x) \equiv \int_{\mathbb{R}} \mathrm{d}r \ r^i J(x,r) \ . \tag{7.25}$$

I recall, in particular, that the first moment of a distribution corresponds to its mean, while the second moment corresponds to the difference between its variance and the square of its mean[3]. Then one finally obtains the *Kramers-Moyal expansion* of the master equation

$$\frac{\partial f(x,t)}{\partial t} = \sum_{i=1}^{+\infty} \frac{(-1)^i}{i!} \frac{\partial^i}{\partial x^i} \left[\mu_i(x) f(x,t) \right] \ . \tag{7.26}$$

In general, one should keep all the orders i in the Kramers-Moyal expansion. However, as it happens, the PDF f is only realisable (i.e. remains positive and normalised to unity at all times) in either one of two cases (Pawula 1967): if all its moments are non-zero, or if only its first two moments are non-zero (in which case it is Gaussian). In addition, Sawford and Borgas (1994) showed, in the context of turbulent flows, that if any $\mu_i \neq 0$ for $i \geqslant 3$, then the sampling paths of the stochastic velocity process is necessarily discontinuous, and additionally ends up violating the Kolmogorov hypotheses (Kolmogorov 1941). As such, any transitional probability density J (also sometimes referred to as *random forcing*) must either be Gaussian, or lead to discontinuous phase-space trajectories (Thomson 1987). If one wishes to retain continuous sampling paths for the flow velocity, J must necessarily be Gaussian, in which case $\mu_i = 0$ for $i \geqslant 3$. Then the Kramers-Moyal expansion of the master equation reduces to the *Fokker-Planck equation*

$$\frac{\partial f(x,t)}{\partial t} = -\frac{\partial}{\partial x} \left[\mu_1(x) f(x,t) \right] + \frac{1}{2} \frac{\partial^2}{\partial x^2} \left[\mu_2(x) f(x,t) \right] \ . \tag{7.27}$$

The Fokker-Planck equation is only an approximation to the master equation, but becomes exact if J is Gaussian – in which case the PDF itself is Gaussian. This equation governs the evolution of the PDF as a function of μ_1 and μ_2 only, and therefore allows for the determination not only of every moment of the statistical distribution of the stochastic process X_t at any time, but also *all multi-time statistics of* X_t – which I recall systematically reduce to two-times statistics, on account of the Markov property verified by X_t.

The physical role played by the two coefficients μ_1 and μ_2 can be inferred from their definition. The first one, μ_1, is defined as the mean of the state transition probability over all possible neighbouring states. If it is non-zero – i.e. if the state transitions towards a given direction are preferred over all other directions –, then, on average, X_t will have a tendency to drift away from its initial value in this preferred direction. On the contrary, if $\mu_1 = 0$, then X_t will tend, on average, to remain in place. This means that μ_1 *tends to make the PDF drift in phase-space in a deterministic manner*: for that reason, μ_1 is referred to as the *drift coefficient*. The second one, μ_2, is defined as the variance of the state transition probability over all possible neighbouring states. It describes how far away from its initial value X_t will tend to travel at ulterior times. If μ_2 is non-zero, then X_t will diffuse away from its initial state. But is $\mu_2 = 0$, there will be no such diffusion; in fact, X_t will only be affected by the deterministic drift, and its evolution will not be random at all. This means that μ_2 *tends to widen the PDF in phase-space, thus increasing the randomness of the variable* X_t: this is why μ_2 is referred to as the *diffusion coefficient*.

[3] It is the *centered* second moment of the distribution that corresponds to its variance. Here, however, I have considered *non-centered* moments.

These results are readily generalised to the case of a multivariate stochastic process, i.e. if X_t maps $\mathcal{F}$ onto $\mathbb{R}^n$. Then the first-order term in the Kramers-Moyal expansion (Equation 7.26) is written in terms of a gradient, and the second-order term in terms of a Hessian matrix. Furthermore, in general, the transition probability J – and therefore the moments μ_1 and μ_2 – can depend on time. Then the Fokker-Planck equation takes the more general form

$$\frac{\partial f(\mathbf{x},t)}{\partial t} = -\frac{\partial}{\partial x_i}\left[A_i(\mathbf{x},t)f(\mathbf{x},t)\right] + \frac{1}{2}\frac{\partial^2}{\partial x_i \partial x_j}\left[B_{ij}(\mathbf{x},t)f(\mathbf{x},t)\right] , \tag{7.28}$$

which now depends on a drift *vector* A_i and a diffusion *matrix* B_{ij}. A particular case is obtained if $A_i = 0$ and $B_{ij} = \delta_{ij}$: then the stochastic process is called a *Wiener process*, and is usually denoted as $\mathbf{W}_t$.

7.1.3 Stochastic differential equations

The Fokker-Planck equation (Equation 7.28) completely describes the statistical properties of the stochastic process X_t. Indeed, if the initial state is known, the solution of this equation provides with the PDF f for any time t, and the PDF at time t contains all the statistical moments of X_t – such as its expectation and variance for instance – through Equation 7.3. However, the Fokker-Planck equation is complicated to solve, whether it be analytically or numerically: this is because the PDF depends on all the random variables described by the stochastic process X_t (for instance, for turbulent flows, at least the three components of velocity), in addition to the time variable t. This is why the Fokker-Planck equation is usually solved through Monte-Carlo methods: different realisations of the stochastic process X_t are integrated forward in time according to a carefully designed evolution equation, in such a way that the set of realisations mimics the PDF at any time t. The question, therefore, is this: what evolution equation should be chosen?

The Langevin equation

For the moment, let me suppose that $X(t)$ is a scalar stochastic process[4]. If $X(t)$ were an ordinary function, it would be associated with a deterministic evolution equation which, in its most general form, would read $\mathrm{d}X/\,\mathrm{d}t = a(X,t)$. But $X(t)$ being a stochastic process, its evolution equation must obviously contain an additional random component. *One can formally write the evolution equation for* $X(t)$ as

$$\frac{\mathrm{d}X}{\mathrm{d}t} = a(X,t) + b(X,t)\,\eta(t) , \tag{7.29}$$

where the stochasticity of the evolution of X is entirely brought about by the second term on the right-hand side. This kind of equation is referred to as a *Langevin equation*. Without loss of generality, one can consider that the fluctuating component $\eta(t)$ is of zero mean: indeed, any non-zero mean can be absorbed in the definition of a. Furthermore, to reflect the fact that the fluctuating term should vary rapidly in time, and not have any memory from the past – i.e. to ensure that X is indeed a Markov process –, it is necessary for $\eta(t)$ and $\eta(t')$ to be statistically independent[5] for $t \neq t'$. The two-time variance of $\eta(t)$ should therefore be proportional to the Dirac distribution. There again, the coefficient of proportionality can be absorbed in the definition of b, and therefore be taken as unity. To summarise, one has

$$E[\eta(t)] = 0 \qquad \text{and} \qquad E[\eta(t)\eta(t')] = \delta(t-t') . \tag{7.30}$$

In particular, setting $t = t'$, it can be seen that $\eta(t)$ as an infinite variance at all times, *so that Equation 7.29, in this naive form, necessarily leads to a pathological behaviour*. Mathematically speaking, the function $\eta(t)$ does not exist, and neither does Equation 7.29. The question, therefore, is this: *how can one give a consistent,*

[4] Starting now, I will occasionally drop the subscript t from the notation X_t, and instead refer to this stochastic process as $X(t)$. Although the notation is less rigorous, it present the advantage of making clear that the random variable is, in a way, a function of time.

[5] Two random variable are said to be *independent* from one another if their joint PDF is equal to the product of their individual, marginal PDF. I already remarked above that in reality, there is always going to be a timescale, however small, on which $\eta(t)$ retains some degree of memory of its past state. If this timescale is much smaller than any other timescale in the system, however, $\eta(t)$ can be safely approximated by this independence property.

mathematically rigorous meaning to Equation 7.29? Instead of considering $\eta(t)$, let me consider its integral, which should exist on account of the fact that the solution X_t to Equation 7.29 itself exists

$$\zeta(t) \equiv \int_0^t \mathrm{d}t' \; \eta(t') \; . \tag{7.31}$$

In order for X_t to be a continuous Markov process (i.e. to have only continuous sampling paths), $\zeta(t)$ itself must be continuous. Then, one has

$$\zeta(t') - \zeta(t) = \int_t^{t'} \mathrm{d}s \; \eta(s) \tag{7.32}$$

$$\zeta(t) = \int_0^t \mathrm{d}s \; \eta(s) = \lim_{\epsilon \to 0} \left[\int_0^{t-\epsilon} \mathrm{d}s \; \eta(s) \right] , \tag{7.33}$$

where the second equality in the second line stems from the continuity of $\zeta(t)$. But all the $\eta(s)$ in the integral on the right-hand side of Equation 7.32 are independent from the $\eta(s)$ in the integral on the rightmost-hand side of Equation 7.33, since $\eta(t)$ is a Markov process and the time intervals involved in the two integrals do not overlap. Therefore, the two terms are statistically independent. Otherwise stated, $\zeta(t') - \zeta(t)$ is independent from $\zeta(t)$. A fortiori, the increment $\zeta(t') - \zeta(t)$ is also independent of any anterior $\zeta(t'')$, which means that $\zeta(t')$ itself is fully determined from the state of $\zeta(t)$. Naturally, t can be chosen arbitrarily close to t', which means that $\zeta(t')$ only depends on the present state of ζ: this is a Markov process.

As such, the PDF of $\zeta(t)$ evolves according to a Fokker-Planck equation. Its coefficients can be computed through their definition given by Equation 7.25: the drift coefficient is the expectation of the increment of ζ per unit time, knowing its initial state

$$A(\zeta_0, t) \equiv \lim_{\Delta t \to 0} \frac{E\left[(\zeta(t + \Delta t) - \zeta_0) \,|\, \zeta_0, t \right]}{\Delta t} = \lim_{\Delta t \to 0} \frac{1}{\Delta t} E\left[\int_t^{t+\Delta t} \mathrm{d}s \; \eta(s) \right] = \lim_{\Delta t \to 0} \frac{1}{\Delta t} \int_t^{t+\Delta t} \mathrm{d}s \; E\left[\eta(s)\right] = 0 \; , \tag{7.34}$$

where the last equality stems from the zero mean of $\eta(s)$. Similarly, the diffusion coefficient is the expectation of the increment squared of ζ per unit time, knowing its initial state

$$\begin{aligned} B(\zeta_0, t) \equiv \lim_{\Delta t \to 0} \frac{E\left[(\zeta(t + \Delta t) - \zeta_0)^2 \,|\, \zeta_0, t \right]}{\Delta t} &= \lim_{\Delta t \to 0} \frac{1}{\Delta t} E\left[\left(\int_t^{t+\Delta t} \mathrm{d}s \; \eta(s) \right)^2 \right] \\ &= \lim_{\Delta t \to 0} \frac{1}{\Delta t} \int_t^{t+\Delta t} \mathrm{d}s \int_t^{t+\Delta t} \mathrm{d}s' \; E\left[\eta(s)\eta(s')\right] = \lim_{\Delta t \to 0} \frac{1}{\Delta t} \int_t^{t+\Delta t} \mathrm{d}s = 1 \; . \end{aligned} \tag{7.35}$$

Therefore, one obtains the important result that, in Equation 7.29, and in order for X_t to be a continuous Markov process, the integral $\zeta(t)$ of the fluctuating term $\eta(t)$ must necessarily coincide with the Wiener process $W(t)$ described in the end of Section 7.1.2. Then let me define

$$\mathrm{d}W(t) \equiv W(t + \mathrm{d}t) - W(t) = \eta(t) \, \mathrm{d}t \; , \tag{7.36}$$

in which case Equation 7.29 can be rewritten in integral form

$$x(t) - x(0) = \int_0^t \mathrm{d}s \; a[x(s), s] + \int_0^t \mathrm{d}W(s) \; b[x(s), s] \; . \tag{7.37}$$

For the moment, Equation 7.37 is only a formal rewriting of Equation 7.29. However, it is possible to give mathematical meaning to the second integral, in which case this integral form is actually the only one that can be interpreted consistently, while Equation 7.29 makes no sense.

Ito stochastic differential equations

In mathematical terms, the second term on the right-hand side of Equation 7.37 constitute a Stieltjes integral[6] where the sample function is the Wiener process $W(t)$. But since $W(t)$ varies over very small timescales, the choice

[6] An ordinary integral, or Riemann integral, is denoted as $I = \int_a^b f(x) \; \mathrm{d}x$, and defined as the limit of the Riemann sum $S = \sum_{i=1}^n f(\tau_i) \, (t_i - t_{i-1})$ when $n \to +\infty$ while $t_0 = a$, $t_n = b$, and each τ_i is restricted to lie between t_i and t_{i-1}. This concept is extended

of the intermediary points τ_i in the sum whose limit defines this integral (Equation 7.38) is very important. Several such choices can be adopted: the choice $\tau_i \equiv t_{i-1}$ defines the *Ito stochastic integral* of the function f

$$\int_0^t f(s)\ \mathrm{d}W(s) \equiv \lim_{n\to\infty} \sum_{i=1}^{n} f(t_{i-1})\left(W(t_i) - W(t_{i-1})\right)\ , \tag{7.39}$$

where the limit is taken so that the $\{t_i\}_{i=1..n}$ are properly ordered between 0 and t, and entirely cover the interval between the two. Then, by definition, the stochastic process X_t is said to follow the *Ito stochastic differential equation* formally written as

$$\mathrm{d}X(t) = a(X(t), t)\,\mathrm{d}t + b(X(t), t)\,\mathrm{d}W(t)\ , \tag{7.40}$$

if it verifies the integral form given above for any time t and initial time t_0

$$X(t) = X(t_0) + \int_{t_0}^{t} a(X(s), s)\ \mathrm{d}s + \int_{t_0}^{t} b(X(s), s)\ \mathrm{d}W(s)\ , \tag{7.41}$$

where the second integral is defined as an Ito stochastic integral. Since $W(s)$ for any $s > t_0$ is independent of $x(s)$ for any $s < t_0$, Equation 7.41 shows that one only needs to know $X(t_0)$ in order to know $X(t)$. But t_0 can be chosen arbitrarily close to t: in other words, the future evolution of X_t is only determined by its present state, meaning that *any solution to an Ito stochastic differential equation is a Markov process.*

Connection between the Ito SDE and the Fokker-Planck equation

Because the solution of Equation 7.40 is a Markov process, its PDF follows a Fokker-Planck equation. Is it possible to relate the coefficients in the Ito SDE to those of the corresponding Fokker-Planck equation? The answer is yes. Before I do this, let me derive an important intermediary result. Let me define, for any given function g, the sum

$$S \equiv \lim_{n\to+\infty} E\left[\left(\sum_{i=1}^{n} g_{i-1}\left(\Delta W_i^2 - \Delta t_i\right)^2\right)\right]\ , \tag{7.42}$$

where $g_i \equiv g(t_i)$, and $\Delta W_i \equiv W(t_i) - W(t_{i-1})$. Expanding the square in the expectation, one finds

$$S = \lim_{n\to+\infty} E\left[\sum_{i=1}^{n} g_{i-1}^2\left(\Delta W_i^2 - \Delta t_i\right)^2 + \sum_{i>j\ ;\ i,j=1}^{n} 2 g_{i-1} g_{j-1}\left(\Delta W_i^2 - \Delta t_i\right)\left(\Delta W_j^2 - \Delta t_j\right)\right]\ . \tag{7.43}$$

In the first sum, g_{i-1}^2 is independent from $\left(\Delta W_i^2 - \Delta t_i\right)^2$, and in the second sum, $g_{i-1}g_{j-1}\left(\Delta W_j^2 - \Delta t_j\right)$ is independent from $\left(\Delta W_i^2 - \Delta t_i\right)$, because of the properties of the Wiener process (in particular the fact that it has the Markov property). Therefore, one has

$$S = \lim_{n\to+\infty}\left(\sum_{i=1}^{n} E\left[g_{i-1}^2\right] E\left[\left(\Delta W_i^2 - \Delta t_i\right)^2\right] + \sum_{i>j\ ;\ i,j=1}^{n} 2E\left[g_{i-1}g_{j-1}\left(\Delta W_j^2 - \Delta t_j\right)\right] E\left[\Delta W_j^2 - \Delta t_j\right]\right)\ . \tag{7.44}$$

But I recall that, according to Equation 7.35, one has $E\left[\Delta W_i^2\right] = \Delta t_i$. Furthermore, since W is a diffusion process, it exhibits a Gaussian PDF, so that its fourth-order moment is equal to three times the square of its variance, and

$$\begin{aligned} E\left[\left(\Delta W_i^2 - \Delta t_i\right)^2\right] &= E\left[\Delta W_i^4\right]^2 - 2\Delta t_i E\left[\Delta W_i^2\right] + \Delta t_i^2 \\ &= 3E\left[\Delta W_i^2\right]^2 - 2\Delta t_i E\left[\Delta W_i^2\right] + \Delta t_i^2 \\ &= 3\Delta t_i^2 - 2\Delta t_i^2 + \Delta t_i^2 \\ &= 2\Delta t_i^2\ . \end{aligned} \tag{7.45}$$

---

to *Stieltjes integrals* denoted as $I = \int_a^b f(x)\ \mathrm{d}g(x)$, and defined as the limit of the sum

$$S = \sum_{i=1}^{n} f(\tau_i)\left(g(t_i) - g(t_{i-1})\right) \tag{7.38}$$

under the same restrictions as for the Riemann integral. If g is differentiable, I is none other than the ordinary integral of $f \times g'$. But the integral is also properly defined if g is not differentiable.

Eventually, the sum S reduces to

$$S = \lim_{n\to+\infty} \sum_{i=1}^{n} 2\Delta t_i^2 E\left[g_{i-1}^2\right] . \tag{7.46}$$

Because the time increment Δt_i appears at second order in the sum, its limit vanishes, and one actually finds $S = 0$. Using the original definition of S, one finds

$$\lim_{n\to+\infty} \sum_{i=1}^{n} 2g_{i-1}\Delta W_i^2 = \lim_{n\to+\infty} \sum_{i=1}^{n} 2g_{i-1}\Delta t_i , \tag{7.47}$$

and using the definitions of the Riemann and Stieltjes integrals respectively, this yields

$$\int_{t_0}^{t} g(s)\ [\mathrm{d}W(s)]^2 = \int_{t_0}^{t} g(s)\ \mathrm{d}s . \tag{7.48}$$

Since this is true for any function g, one can formally write the following, very important identity

$$\mathrm{d}W^2 = \mathrm{d}t . \tag{7.49}$$

Therefore, the increment of a Wiener process is an order $1/2$ in terms of the time increment, which has important implications as regards changes of variable in Ito calculus, as I will now show.

Let me consider any function $g(X(t))$ of the stochastic process X_t. Then, in forming the rate of change of $g(X(t))$ with time at first order in $\mathrm{d}t$, it is actually necessary to go as far as second order in $\mathrm{d}W$. One obtains

$$\begin{aligned}
\mathrm{d}g(X(t)) &= g(X(t) + \mathrm{d}X(t)) - g(X(t)) \\
&\sim g'(X(t))\ \mathrm{d}X(t) + \frac{1}{2} g''(X(t))\ \mathrm{d}X^2(t) \\
&= g'(X(t)) \left[a(X(t),t)\ \mathrm{d}t + b(X(t),t)\ \mathrm{d}W(t)\right] + \frac{1}{2} g''(X(t)) \left[b(X(t),t)\ \mathrm{d}W(t)\right]^2 ,
\end{aligned} \tag{7.50}$$

where I have discarded all terms of order higher than 1 in $\mathrm{d}t$. Injecting Equation 7.49, one finds

$$\mathrm{d}g(X(t)) = \left[a(X(t),t)\ g'(X(t)) + \frac{1}{2} b(X(t),t)^2\ g''(X(t))\right]\mathrm{d}t + b(X(t),t)\ g'(X(t))\ \mathrm{d}W(t) , \tag{7.51}$$

which constitutes the *Ito's formula* for change of variables. Notice the additional term in $g''(X(t))$ compared to the usual chain rule in ordinary calculus, which stems directly from the fact that $\mathrm{d}W$ is a quantity of order $1/2$ in terms of $\mathrm{d}t$. In particular, estimating the expectation of Equation 7.51, one finds

$$\frac{\mathrm{d}}{\mathrm{d}t} E\left[g(X(t))\right] = E\left[a(X(t),t) g'(X(t)) + \frac{1}{2} b(X(t),t)^2 g''(X(t))\right] , \tag{7.52}$$

and, using Equation 7.3, since the stochastic process X_t has a PDF $f(x,t)$, one finds

$$\frac{\mathrm{d}}{\mathrm{d}t}\left(\int_{\mathbb{R}} \mathrm{d}x\ f(x,t)\ g(x)\right) = \int_{\mathbb{R}} \mathrm{d}x\ f(x,t) \left[a(x,t)\ g'(x) + \frac{1}{2} b(x,t)^2\ g''(x)\right] . \tag{7.53}$$

Pulling the time derivative in the integral on the left-hand side, and performing integrations by part on the right-hand side, one finds

$$\int_{\mathbb{R}} \mathrm{d}x\ g(x)\ \frac{\partial f(x,t)}{\partial t} = \int_{\mathbb{R}} \mathrm{d}x\ g(x) \left[-\frac{\partial a(x,t)\ f(x,t)}{\partial x} + \frac{1}{2} \frac{\partial^2 b(x,t)^2\ f(x,t)}{\partial x^2}\right] , \tag{7.54}$$

where I have discarded the surface term, on account of the random variable X_t being bounded (if it is the velocity of the turbulent flow, for instance, this is not a very restrictive condition). Since this equality must be valid for any function g, one necessarily has

$$\frac{\partial f(x,t)}{\partial t} = -\frac{\partial a(x,t) f(x,t)}{\partial x} + \frac{1}{2} \frac{\partial^2 b(x,t)^2 f(x,t)}{\partial x^2} . \tag{7.55}$$

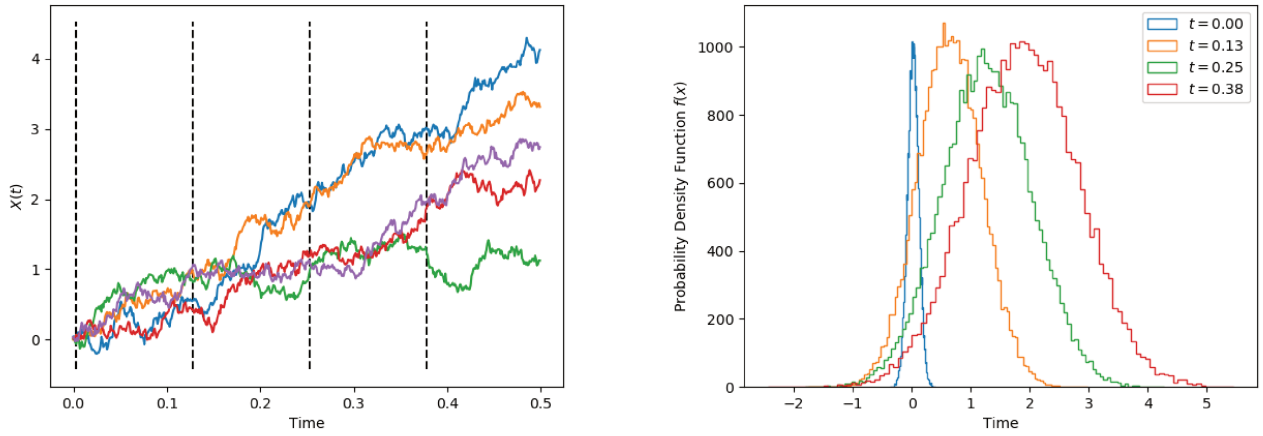

Figure 7.1: **Left**: Different independent realisations of the stochastic process X_t, following the Ito SDE given by Equation 7.40, with $a = 5$ and $b = 1.5$. The vertical dashed lines represent the times at which the PDF are illustrated in the right panel. **Right**: PDF associated to X_t at different times t, reconstructed with $N = 30,000$ independent realisations. *Note that the colour schemes in the two panels are completely unrelated.*

What this means is that *the PDF of a stochastic process that evolves according to the Ito stochastic differential equation given by Equation 7.40 with coefficients a and b follows a Fokker-Planck equation given by Equation 7.28 with coefficients* $A \equiv a$ *and* $B \equiv b^2$. There is a complete equivalence between the Fokker-Planck equation on the PDF of a stochastic process and the Ito SDE on the stochastic process itself: both contain the same statistical information. This does not mean, however, that the correspondence between the two is unique: more specifically, while an Ito SDE corresponds to a unique Fokker-Planck equation, the opposite is not true. I will have the opportunity to come back to this statement in Chapter 8 in more detail.

The relation between a Fokker-Planck equation and its equivalent Ito SDE is illustrated in Figure 7.1, for a case where the drift and diffusion coefficients are constant (arbitrary values $a = 5$ and $b = 1.5$ were chosen). I deliberately leave aside the question of the numerical scheme used to integrate the Ito stochastic differential equations forward in time, as I will be detailing all numerical issues in Chapter 9. I simply warn the reader that the usual deterministic finite-difference schemes cannot be employed, and must be adapted to the stochastic nature of the equation. The left panel of Figure 7.1 showcases trajectories of the stochastic process X_t in time: while the evolution is visibly erratic, the process remains continuous at all times. Furthermore, the figure makes it clear that the process X_t is subjected both to a systematic drift upwards and to some degree of diffusion that spaces the trajectories apart, even when they have the same initial state. The right panel of Figure 7.1 shows how this trajectory behaviour translates in terms of the PDF of X_t: a large number of realisations were calculated in order to reconstruct the PDF at any given time. The drift and diffusion mechanisms are clearly visible there as well: the center of the PDF drifts systematically towards positive values of X, and the PDF also becomes wider and wider as time goes by. It is also apparent that the PDF remains Gaussian at all time.

To conclude with the definitions, let me remark that the derivation performed above for a scalar stochastic process can be extended to the case of a multivariate stochastic process, in which case the Ito SDE takes the form

$$\mathrm{d}X_i(t) = a_i(\mathbf{X}(t), t)\ \mathrm{d}t + b_{ij}(\mathbf{X}(t), t)\ \mathrm{d}W_j(t)\ , \tag{7.56}$$

where the W_j are Wiener processes that are independent from one another. Then the equivalent Fokker-Planck equation is the multivariate version given by Equation 7.28 with

$$A_i = a_i \qquad \text{and} \qquad B_{ij} = b_{ik}b_{kj}\ . \tag{7.57}$$

Since the Ito SDE only has one variable – time –, it is much more practical to integrate than the Fokker-Planck equation, so that the latter is actually often solved through its equivalent stochastic differential equation. This is the case, in particular, when PDF methods are used to model turbulent flows: in this context, the three components of the flow velocity need to be discretised in addition to the space axes, so that, roughly speaking, solving the Fokker-Planck equation numerically would require $O(N^6)$ operations – and the exponent goes further up as more

turbulent quantities are considered. Of course, the caveat is that in using the stochastic differential equation instead, the numerical implementation involves Monte-Carlo methods, which means that a large number of realisations is needed to reconstruct the PDF.

7.2 Lagrangian stochastic models of turbulence

Because high-Reynolds number flows are characterised by turbulent motions that have a random nature[7], stochastic processes and the mathematical formalism that comes with them, introduced in Section 7.1.1, are perfectly suited for their modelling. All modelling approaches of turbulent flows based on this formalism constitute *PDF methods*. In the following, I describe how such models are designed, and how they relate to other models of turbulence, in particular Reynolds-stress models (see Section 1.2.3). This discussion is based on the excellent review of Pope (1994a), to which I refer the reader for further details.

7.2.1 General principles

Eulerian versus Lagrangian flow PDF

How should the PDF of the turbulent flow be defined? This question may seem odd at first glance: as I showed in Chapter 1, the variables describing the flow are readily identified as having to be the density, the velocity and the internal energy of the flow. The difficulty arises because, unlike the stochastic process X_t that I introduced in Section 7.1.1, these variables do not only depend on time, they also depend on space. As I mentioned in the very beginning of Appendix A, there are two different ways of describing the time and space dependence of the flow variables, based on two different representations of the flow: the Eulerian and Lagrangian frames of reference. These two representations accordingly lead to two distinct definitions of the flow PDF.

In the remainder of this section, I will restrict the discussion to incompressible flows. This is done for the sake of simplicity in this introductory discussion. Naturally, this restriction is irrelevant in the stellar context, and I will touch upon the extension of these models to compressible flows in Chapter 8. The first variable to describe, then, is the velocity of the flow. In the Eulerian description, the velocity $\mathbf{u}(\mathbf{x}, t)$ is associated to a fixed position $\mathbf{x}$ at any given time t. The PDF $f_E(\mathbf{V}; (\mathbf{x}, t))$ associated to this quantity[8] is referred to as the *Eulerian PDF of the flow*. On the other hand, in the Lagrangian description, fluid particles[9] are followed along their trajectory. Let me denote as $\mathbf{x}^+(\mathbf{x_0}, t)$ the position at time t of the fluid particle that was located at $\mathbf{x_0}$ at a fixed reference time t_0. Then the Lagrangian velocity is defined by

$$\mathbf{u}^+(\mathbf{x_0}, t) \equiv \mathbf{u}\left(\mathbf{x}^+(\mathbf{x_0}, t), t\right) \ . \tag{7.58}$$

In this description, the PDF considered is the joint PDF associated to $\mathbf{u}^+$ and $\mathbf{x}^+$, conditioned on the initial state of the particle. In other words, it is the joint PDF of the events $\mathbf{u}^+(\mathbf{x_0}, t) = \mathbf{V}$ and $\mathbf{x}^+(\mathbf{x_0}, t) = \mathbf{X}$, conditioned on the events $\mathbf{u}^+(\mathbf{x_0}, t_0) = \mathbf{V_0}$ and $\mathbf{x}^+(\mathbf{x_0}, t_0) = \mathbf{x_0}$. This PDF is denoted as $f_L((\mathbf{V}, \mathbf{X}), t|\mathbf{V_0}, \mathbf{x_0})$, and is referred to as the *Lagrangian PDF of the flow*.

[7] Naturally, the equations of hydrodynamics are deterministic; therefore, the turbulent motions are not intrinsically random. However, very similar starting conditions can lead to drastically different future evolution of the flow – in other words, the flow is subjected to deterministic chaos. As a result, accurately predicting this evolution would require knowing exactly the initial microscopic state of the fluid, like the initial position and velocity of each molecule. But this is impossible, since one only has access to macroscopic quantities (like the velocity of fluid parcels for instance). For all intents and purposes, this inability to predict the future state of the flow is perfectly similar to actual randomness. In other words, *it is our own lack of knowledge on the initial state of the flow that makes its subsequent evolution apparently random, not its intrinsic behaviour.*

[8] Note the difference in notation between the Eulerian velocity of the flow $\mathbf{u}$ and its sampling variable $\mathbf{V}$. The former is a stochastic variable – i.e. a family of functions, indexed by the time variable, each mapping the set of all set of events to an element of $\mathbb{R}^3$ –, while the latter is simply an element of $\mathbb{R}^3$.

[9] In the context of hydrodynamics, there is always a very large separation between the large scales of the flow, or *macroscopic scales* (i.e. the scales on which the flow variables typically vary) and the molecular scales, or *microscopic scales*. This allows for the definition of a whole range of *mesoscopic scales* in between. Then, any portion of fluid whose size lies in the mesoscopic range is called a *fluid particle*. This concept is useful to define the quantity of the flow, because flow quantities can be considered uniform throughout the fluid particle – meaning that the phrase 'temperature of the fluid particle', for instance, makes sense –, while the fluid particle contains a large number of fluid molecules or atoms, so that microscopic processes need not be described exactly.

Different PDF methods

Eulerian PDF methods consist in solving the Fokker-Planck equation associated to either the Eulerian or the Lagrangian PDF of the flow. Let me derive this Fokker-Planck equation in a simple case. Let me suppose that the velocity of the flow is the only variable to model. Then from the Navier-Stokes equation (Equation 1.14) applied to the case of a constant, unity density flow

$$\frac{\partial u_i}{\partial t} + u_j \frac{\partial u_i}{\partial x_j} = -\frac{\partial \overline{p}}{\partial x_i} - \frac{\partial p'}{\partial x_i} + g_i + \frac{\partial \sigma_{ij}}{\partial x_j} \,, \tag{7.59}$$

where I have separated the ensemble averaged pressure $\overline{p}$ from its fluctuations p', and I have made use of Einstein's convention on index contraction, one obtains the following Fokker-Planck equation for the Eulerian PDF (Pope 2000)

$$\frac{\partial f_E}{\partial t} + V_i \frac{\partial f_E}{\partial x_i} + \left(-\frac{\partial \overline{p}}{\partial x_i} + g_i \right) \frac{\partial f_E}{\partial V_i} = \frac{\partial}{\partial V_i} \left(f_E E \left[\frac{\partial p'}{\partial x_i} - \frac{\partial \sigma_{ij}}{\partial x_j} \middle| \mathbf{V} \right] \right) . \tag{7.60}$$

Provided the mean pressure gradient is known, the entire left-hand side is in closed form. This is not the case of the right-hand side, which depends on the expectation of the fluctuating force *conditioned on the local flow velocity*. Modelling these conditional expectations can prove a challenging task, which is why Eulerian PDF methods are seldom implemented in turbulence models.

An entirely different modelling approach consists in considering the Ito stochastic differential equation equivalent to the Fokker-Planck equation, instead of the Fokker-Planck equation itself. This is more readily done in a Lagrangian frame of reference: then, the stochastic model is constructed to simulate the evolution of individual fluid particles – i.e. both their position and their physical properties. Let me denote the position and velocity of one such fluid particle as $\mathbf{x}^\star(t)$ and $\mathbf{u}^\star(t)$ respectively. It is important to realise that these Lagrangian *particle* variables are constructed in a completely different manner than the Lagrangian *flow* variables $\mathbf{x}^+(\mathbf{x_0}, t)$ and $\mathbf{u}^+(\mathbf{x_0}, t)$ defined above. While there is, as I will soon show, a strong connection between the two, they are *a priori* associated to different PDFs. Now, the PDF under consideration is the joint PDF of the events $\mathbf{x}^\star(t) = \mathbf{X}$ and $\mathbf{u}^\star(t) = \mathbf{V}$ conditioned on the joint event $\mathbf{x}^\star(t_0) = \mathbf{X_0}$ and $\mathbf{u}^\star(t_0) = \mathbf{V_0}$. This PDF is denoted as $f_L^\star((\mathbf{V}, \mathbf{X}); t|\mathbf{V_0}, \mathbf{X_0})$, and is referred to as the *Lagrangian PDF of the fluid particles*. The goal, therefore, is *to construct the stochastic model for the two stochastic processes* $\mathbf{x}^\star(t)$ *and* $\mathbf{u}^\star(t)$ *in such a way that the equivalent Fokker-Planck equation for* $f_L^\star$ *accurately mimics the evolution of the actual Lagrangian PDF of the flow* f_L. In other words, one wants

$$f_L((\mathbf{V}, \mathbf{X}), t|\mathbf{V_0}, \mathbf{x_0}) = f_L^\star((\mathbf{V}, \mathbf{X}), t|\mathbf{V_0}, \mathbf{x_0}) \,. \tag{7.61}$$

This class of approaches is referred to as *Lagrangian PDF methods*, and the constructed Ito SDE are called *Lagrangian stochastic models of turbulence*.

To implement Lagrangian PDF methods, Monte-Carlo methods are systematically employed. The idea is to assume a certain initial distribution for the position and velocity of the fluid particles, and then to draw N distinct realisations of this initial state, after which the evolution of each of these fluid particles is computed by integrating the Lagrangian stochastic model forward in time. If N is sufficiently large, the Lagrangian PDF of the fluid particles, and therefore the Lagrangian PDF of the flow, can be reconstructed. From there, the Eulerian PDF of the flow is obtained through

$$f_E(\mathbf{V}; (\mathbf{x}, t)) = \int \mathrm{d}^3\mathbf{x_0} \int \mathrm{d}^3\mathbf{V_0} \; f_E(\mathbf{V_0}; (\mathbf{x_0}, t)) \; f_L((\mathbf{V}, \mathbf{X}), t|\mathbf{V_0}, \mathbf{x_0}) \,, \tag{7.62}$$

provided that the initial Eulerian PDF is known. This relation makes it clear that f_L plays the role of a transitional PDF from a given initial time t_0 to any ulterior time t. The two PDF f_E and f_L are perfectly equivalent to one another, the same way the Eulerian and Lagrangian representation of the flow are perfectly equivalent: one contains just as much statistical information as the other. In particular, Lagrangian PDF methods give access to both PDF indifferently: the dichotomy between Eulerian and Lagrangian PDF has absolutely nothing to do with the dichotomy between Eulerian and Lagrangian PDF methods. Here, it is the method that is Lagrangian, not the PDF. This somewhat complicated picture is summarised in Figure 7.2.

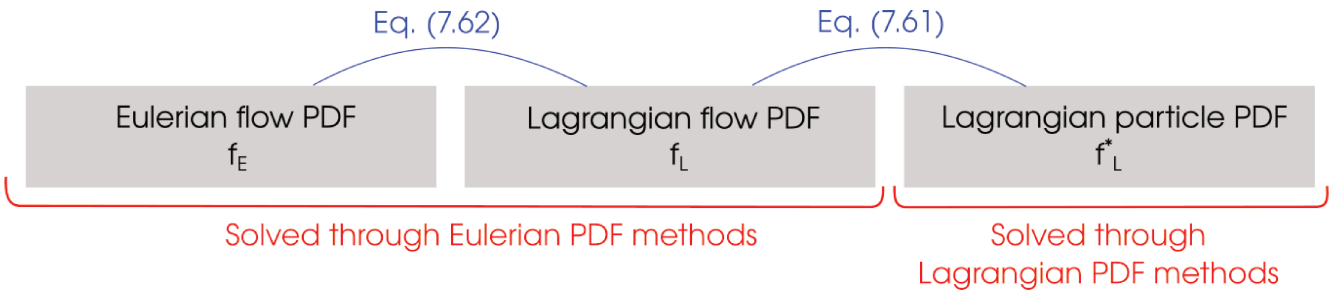

Figure 7.2: Schematic representation of the different PDF for turbulent system, and their mutual relation. The dichotomy between Eulerian and Lagrangian PDF, in particular, is different than the dichotomy between Eulerian and Lagrangian PDF methods.

An illustrative example: the Langevin equation

By construction, the position of the particle evolves according to

$$\frac{\mathrm{d}\mathbf{x}^\star}{\mathrm{d}t} = \mathbf{u}^\star \,. \tag{7.63}$$

The difficulty arises with the velocity equation. Let me consider the most simple case of homogeneous, isotropic, stationary, incompressible turbulence. In statistical terms, the homogeneity means that the moments of the particle velocity, or equivalently, its PDF, is independent of space coordinates; the stationarity means that they are independent of time; and the isotropy means that they are independent of direction. Then, the velocity of the fluid particles evolve according to the *Langevin equation* (Pope 2000)

$$\mathrm{d}\mathbf{u}^\star = -\mathbf{u}^\star \frac{\mathrm{d}t}{T} + \sqrt{\frac{2u'^2}{T}}\,\mathrm{d}\mathbf{W} \,, \tag{7.64}$$

characterised only by the time T and the velocity u', which I will relate to the physics of turbulence in a moment. Physically, the first term on the right-hand side of Equation 7.64 represents a friction term, that tends to make the velocity of the particles decay towards zero, while the second term on the right-hand side represents the random fluctuations of the force acting upon the particle, taking the form of random kicks. While the former makes the turbulence decay, the latter constantly replenishes its energy, so that the total turbulent energy is the result of a balance between the two.

Let me explore several key properties of Equation 7.64. By construction, the stochastic process $\mathbf{u}^\star(t)$ is a Markov process continuous in time. Since the drift coefficient is a linear function of the process $\mathbf{u}^\star$ itself, the particle velocity evolving according to Equation 7.64 is said to be an *Ornstein-Uhlenbeck process* (Uhlenbeck and Ornstein 1930). A general result of Orstein-Uhlenbeck processes is that solutions of their Fokker-Planck equation always asymptotically tend towards a stationary solution when $t \to +\infty$. With the above notation, the stationary PDF for each component of the particle velocity takes the form (Gardiner 1994)

$$f(V) = \frac{1}{\sqrt{2\pi u'^2}} \exp\left(-\frac{V^2}{2u'^2}\right) \,. \tag{7.65}$$

In other words, a direct consequence of Equation 7.64 is that the turbulence is stationary, as well as homogeneous (since nothing in the Langevin equation explicitly depends on $\mathbf{x}^\star$), that it is Gaussian, that the mean velocity is always zero, and that the variance of the velocity (related to the turbulent kinetic energy) is always u'^2. Furthermore, the autocorrelation function of an Ornstein-Uhlenbeck process can be expressed analytically, and with the above notations, one finds (Gardiner 1994)

$$\sigma^\star_{ij}(\tau) \equiv \frac{\overline{u^\star_i(t) u^\star_j(t+\tau)}}{\overline{u^\star_i(t)^2}} = \exp^{-|\tau|/T} \delta_{ij} \,. \tag{7.66}$$

Again, the autocorrelation function is independent of absolute time t, and only depends on the time increment τ, which exactly corresponds to stationary turbulence. Additionally, low- and moderate-Reynolds-number flows

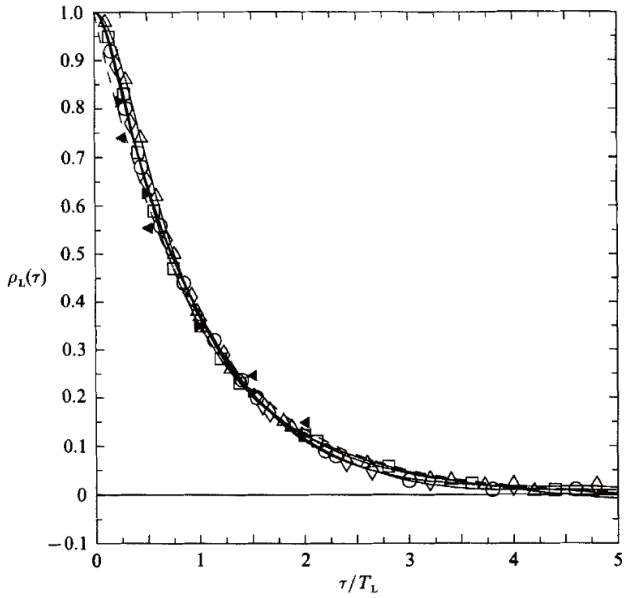

Figure 7.3: Normalised Lagrangian velocity autocorrelation function $\sigma_L(\tau)$ as a function of the normalised time lag τ, for a set of DNS of homogeneous, isotropic, stationary, incompressible turbulence with various Reynolds numbers between 38 and 93 (open symbols), as well as laboratory measurements in the same conditions (filled symbols). The experimental data is from Sato and Yamamoto (1987), the DNS results from Yeung and Pope (1989). The autocorrelation function is normalised by the variance of the velocity, and the time lag with the Lagrangian integral time T. The dashed line is the function $f(x) = \exp(-x)$. Credits: Yeung and Pope (1989).

are accessible to both experiments and direct numerical simulations, where the autocorrelation function can be measured. Under the stationary and homogeneous conditions detailed above, this exponentially decaying time correlation corresponds exactly to the measurements, as illustrated in Figure 7.3. In conclusion, this shows that the Lagrangian stochastic model comprised of Equations 7.63 and 7.64 is perfectly consistent with the physical properties of turbulence listed in the beginning, and yields statistical results that are in accordance with experiments and DNS.

Furthermore, the parameters in the Langevin equation can be related to the physical properties of turbulence: u'^2, as I remarked above, is the variance of the flow velocity, and is related to the turbulent kinetic energy k through

$$u'^2 \equiv \frac{2}{3}k \,, \tag{7.67}$$

while the time T corresponds to the Lagrangian integral time

$$T \equiv \int_0^{+\infty} \mathrm{d}\tau \, \sigma^\star(\tau) \,, \tag{7.68}$$

which can be physically interpreted as the typical correlation time of the turbulent velocity in a Lagrangian frame of reference. Let me now consider that the flow has a high Reynolds number, with a large separation between the Lagrangian integral time T and the Kolmogorov time scale τ_η. Then the Kolmogorov hypotheses, whether original (Kolmogorov 1941) or refined (Kolmogorov 1962), predict that the second-order structure function, defined in terms of Lagrangian velocity by (Monin and Yaglom 1965)

$$D_L(\tau) = \overline{u_i^+(t+\tau)u_i^+(t)} \,, \tag{7.69}$$

should be given by

$$D_L(\tau) = C_0 \epsilon \tau \tag{7.70}$$

for any time lag τ much smaller than T and much greater than the dissipative time scale τ_η, where ϵ is the dissipation rate of turbulent kinetic energy into heat (see Section 1.2.1 for a definition), and C_0 is the Kolmogorov constant.

Using the Langevin equation, and recalling that $\overline{\mathrm{d}W^2} = \mathrm{d}\tau$, one finds

$$D_L^\star(\tau) = \frac{2u'^2\tau}{T} , \tag{7.71}$$

provided $\tau \ll T$. In order for the Langevin equation to be consistent with the Kolmogorov hypotheses, the Lagrangian integral time must be given by

$$T^{-1} = \frac{C_0\epsilon}{2u'^2} = \frac{3C_0\epsilon}{4k} . \tag{7.72}$$

Then the Langevin equation can be rewritten in the following form

$$\mathrm{d}\mathbf{u}^\star = -\frac{3}{4}C_0\frac{\epsilon}{k}\mathbf{u}^\star \ \mathrm{d}t + \sqrt{C_0\epsilon}\ \mathrm{d}W . \tag{7.73}$$

Equation 7.73 only depends on the parameters k and ϵ. The former is a second-order moment of the particle velocity, which is actually in closed form: indeed, the Lagrangian stochastic model contains the information on the PDF, and in turn, on any statistical moment of the flow velocity. I will describe in Section 7.2.4 how the extraction of the moments of the velocity can be performed in practice. As for the other parameter ϵ, it is not in closed form, and one needs a prescription for this quantity. I will describe in Section 7.2.3 how this can be done.

7.2.2 Lagrangian stochastic models for velocity in inhomogeneous flows

The Simplified and Generalised Langevin Models

The first extension of the Langevin equation consists in lifting the condition of homogeneity. This requires the displacement equation (Equation 7.63) to be integrated forward in time alongside the velocity equation (Equation 7.73), because now the instantaneous position of the particles may influence their behaviour – for example through the background felt by the particle, if the medium is stratified. But the velocity equation itself also needs to be modified to take the inhomogeneous nature of turbulence into account. All these modifications pertain to the drift term, because the diffusion term, as I mentioned in Section 7.2.1, is fully determined by the Kolmogorov hypotheses, which remain the same in an inhomogeneous medium. The first modification consists in adding the forces that vanished in the homogeneous limit, namely the mean pressure force and the gravitational force. The second modification concerns the decay contribution in the drift term: it should now make the velocity of the particles decay towards the local mean velocity of the flow, instead of zero. Finally, the third modification consists in modifying the rate at which the particle velocity decays towards the local mean: the reason why this last modification is necessary will become apparent in a moment. The modifications listed above yield the *Simplified Langevin Model* (or SLM)

$$\mathrm{d}x_i^\star = u_i^\star \ \mathrm{d}t , \tag{7.74}$$

$$\mathrm{d}u_i^\star = \left[-\frac{1}{\overline{\rho}}\frac{\partial\overline{p}}{\partial x_i} + g_i - \left(\frac{1}{2}+\frac{3}{4}C_0\right)\frac{\epsilon}{k}\left(u_i^\star - \overline{u_i}\right)\right]\ \mathrm{d}t + \sqrt{C_0\epsilon}\ \mathrm{d}W_i , \tag{7.75}$$

where I recall that $\overline{.}$ refers to ensemble averages of the corresponding Eulerian quantity – namely, in the context of hydrodynamics, Reynolds averages –, and the mean fields $\overline{p}$, $\overline{\rho}$, $\overline{u_i}$, k and ϵ are estimated at the instantaneous position $\mathbf{x}^\star$ of the particle. This constitutes the simplest possible extension of the Langevin model to inhomogeneous turbulence that remains consistent with the basic properties of the flow (i.e. the conservation of momentum and energy). A generalisation of this extension was proposed by Pope (1983), and later more systematically developed by Haworth and Pope (1986, 1987), for *anisotropic*[10] incompressible stationary turbulence, in the form of the *Generalised Langevin Model* (or GLM)

$$\mathrm{d}x_i^\star = u_i^\star \ \mathrm{d}t , \tag{7.76}$$

$$\mathrm{d}u_i^\star = \left[-\frac{1}{\overline{\rho}}\frac{\partial\overline{p}}{\partial x_i} + g_i + G_{ij}\left(u_j^\star - \overline{u_j}\right)\right]\ \mathrm{d}t + \sqrt{C_0\epsilon}\ \mathrm{d}W_i , \tag{7.77}$$

[10]By anisotropic, I mean that the statistical properties of the flow are no longer invariant by arbitrary rotations in space. In particular, the Reynolds stress tensor can be anisotropic. However, the dissipation scales – being much smaller than the large scales of the system in high-Reynolds-number flows, and therefore being insensitive to the particular global geometry of the flow – remain isotropic, in accordance with the Kolmogorov hypotheses (Kolmogorov 1941, 1962). This is the reason why, even when the isotropy condition is lifted, the diffusion term in the stochastic equation remains unchanged.

characterised by the *drift tensor* G_{ij}. In the most general case, G_{ij} is a function of the mean shear tensor $\partial\overline{u_i}/\partial x_j$, the Reynolds stress tensor[11] $\overline{u_i'' u_j''}$ (where $u_i'' \equiv u_i - \overline{u_i}$ denotes the fluctuation of the velocity around its ensemble average), and the turbulent dissipation rate ϵ. The Generalised Langevin Model is therefore a class of Lagrangian stochastic models for incompressible turbulence, specified by the Kolmogorov constant C_0, the functional form of the drift tensor G_{ij}, and an extra model equation for the turbulent dissipation ϵ. The Simplified Langevin Model is contained in this more general class of models, in the form $G_{ij} = -(1/2 + 3C_0/4)\epsilon/k\delta_{ij}$.

In the GLM, the process $\mathbf{u}^\star(t)$ is no longer an Orstein-Uhlenbeck process; however, the Fokker-Planck equation followed by the Lagrangian PDF of the particles can still be determined from Equation 7.57

$$\frac{\partial f_L^\star}{\partial t} = -\frac{\partial V_i f_L^\star}{\partial x_i} + \left(\frac{1}{\rho}\frac{\partial \overline{p}}{\partial x_i} - g_i\right)\frac{\partial f_L^\star}{\partial V_i} - \frac{\partial}{\partial V_i}\left(f_L^\star G_{ij}(V_j - \overline{u_j})\right) + \frac{1}{2}\frac{\partial^2 C_0 \epsilon f_L^\star}{\partial x_i \partial x_i} \,. \tag{7.78}$$

This is the Fokker-Planck equation on $f_L^\star$: the understanding is that if the Lagrangian stochastic model is representative of the flow, then f_L verifies the exact same equation. Then, Equation 7.62 gives the Fokker-Planck equation on the Eulerian PDF of the flow f_E. In fact, because no coefficient in Equation 7.78 depends on $\mathbf{X_0}$, $\mathbf{V_0}$ or t_0, *the Fokker-Planck equation on f_E is exactly the same as the Fokker-Planck equation on f_L.* In that particular case, Equation 7.78 is common to all three PDF. In turn, the Fokker-Planck equation can be used to derive the corresponding evolution equations for any statistical moment of velocity. For instance, multiplying Equation 7.78 by u_i and integrating over all values of $\mathbf{V}$ yields the equation for the mean velocity $\overline{u_i}$, while multiplying it with $(u_i - \overline{u_i})(u_j - \overline{u_j})$ yields the equation for the Reynolds stress tensor $\overline{u_i'' u_j''}$. One finds (Pope 2000)

$$\frac{\overline{D}\,\overline{u_i}}{\overline{D}t} + \frac{\partial \overline{u_i'' u_j''}}{\partial x_j} = -\frac{1}{\rho}\frac{\partial \overline{p}}{\partial x_i} + g_i \,, \tag{7.79}$$

$$\frac{\overline{D}\,\overline{u_i'' u_j''}}{\overline{D}t} + \underbrace{\frac{\partial \overline{u_i'' u_j'' u_k''}}{\partial x_i}}_{\equiv \mathcal{T}_{ij}} = \underbrace{-\overline{u_i'' u_k''}\frac{\partial \overline{u_j}}{\partial x_k} - \overline{u_j'' u_k''}\frac{\partial \overline{u_i}}{\partial x_k}}_{\equiv \mathcal{P}_{ij}} + G_{jk}\overline{u_i'' u_k''} + G_{ik}\overline{u_j'' u_k''} + C_0\epsilon\delta_{ij} \,, \tag{7.80}$$

where $\overline{D}/\overline{D}t \equiv \partial_t + \overline{u_i}\partial_i$ represents the material derivative *following the mean velocity* (and not the actual material derivative). Equation 7.79 reduces to the Reynolds average of the incompressible Navier-Stokes equation in its exact form (i.e. as derived from first principles only). In particular, it includes the Reynolds stress force, without having to include it explicitly in the Lagrangian stochastic model. This is actually a general property of Lagrangian stochastic models of turbulence, that *the transport terms, whether due to large scale advection or to small-scale turbulent transport, are modelled exactly in Lagrangian stochastic models of turbulence*. The right-hand side of Equation 7.79, on the other hand, is modelled exactly because they are included in their exact form in the stochastic equations. By contrast, the Reynolds stress equation (Equation 7.80) depends on the specification for C_0, G_{ij} and ϵ. Let me compare it to the exact form of the Reynolds stress equation, which I derived directly from the Navier-Stokes equation in Section 1.2.3 (see Equation 1.100), and which reduces in the incompressible case to[12]

$$\frac{\overline{D}\,\overline{u_i'' u_j''}}{\overline{D}t} + \frac{\partial \overline{u_i'' u_j'' u_k''}}{\partial x_k} = -\overline{u_i'' u_k''}\frac{\partial \overline{u_j}}{\partial x_k} - \overline{u_j'' u_k''}\frac{\partial \overline{u_i}}{\partial x_k} \underbrace{-\frac{1}{\overline{\rho}}\left(\overline{u_i''\frac{\partial p'}{\partial x_j}} + \overline{u_j''\frac{\partial p'}{\partial x_i}}\right)}_{\equiv \Pi_{ij}} - \frac{2}{3}\epsilon\delta_{ij} \,, \tag{7.81}$$

where Π_{ij} is the *velocity-pressure-gradient tensor*. Comparing the exact and modelled Reynolds stress equations, one can see that, once again, the transport terms represented by the advection term in $\overline{D}/\overline{D}t$ and the turbulent transport tensor $\mathcal{T}_{ij}$ are modelled exactly. It is also the case of the *turbulent production tensor* $\mathcal{P}_{ij}$. However, the acoustic flux – represented by the velocity-pressure-gradient tensor – and the dissipation are not modelled exactly:

[11] Since I only consider incompressible flows in this discussion, the definition of the Reynolds stress tensor given here does not contain ρ inside the ensemble average. I recall from Chapter 1 that, in general, it does.

[12] In the incompressible limit, Favre and Reynolds averages coincide. Furthermore, the compressibility $\overline{u_i''}$ of the turbulent velocity vanishes. Finally, the last term of Equation 1.100 can be rewritten in terms of the turbulent dissipation rate ϵ through Equations 1.36 and 1.37.

they are collectively contained within the last three terms in the right-hand side of Equation 7.80, in such a way that

$$\Pi_{ij} = G_{ik}\overline{u_j'' u_k''} + G_{jk}\overline{u_i'' u_k''} + \left(\frac{2}{3} + C_0\right)\epsilon\delta_{ij} \,. \tag{7.82}$$

One of the fundamental properties of the velocity-pressure-gradient tensor is that, in homogeneous incompressible turbulence, it is traceless, since

$$\frac{1}{2}\Pi_{ii} = -\frac{1}{\overline{\rho}}\left(\overline{\frac{\partial u_i'' p'}{\partial x_i}} - \overline{p'\frac{\partial u_i''}{\partial x_i}}\right) = 0 \,, \tag{7.83}$$

with the first term in the brackets vanishing because the turbulence is homogeneous, and the second term vanishing because it is incompressible. In inhomogeneous turbulence, the first term – i.e. the non-local acoustic flux – is no longer zero, but is usually either explicitly neglected, or implicitly included with the other transport terms in $\mathcal{T}_{ij}$ (Pope 2000) (the exception being near-wall regions, in which I am not interested in this discussion). Neglecting the acoustic flux, *the velocity-pressure-gradient tensor is necessarily traceless*, which physically means that it does not lead to a net creation of turbulent kinetic energy, but instead redistributes the energy among the different components of the Reynolds stress tensor. Taking the trace of Equation 7.82 thus immediately yields the following constraint for the coefficients of the GLM

$$G_{ij}\overline{u_i'' u_j''} = -\left(1 + \frac{3}{2}C_0\right)\epsilon \,. \tag{7.84}$$

In particular, since the trace of the Reynolds stress tensor corresponds to half the turbulent kinetic energy, *if the drift tensor is restricted to be isotropic*, one finds

$$G_{ij}^{\text{isotrop}} = -\left(\frac{1}{2} + \frac{3}{4}C_0\right)\frac{\epsilon}{k}\delta_{ij} \,. \tag{7.85}$$

This corresponds exactly to the prescription of the SLM. The necessity to modify this coefficient compared to Equation 7.73 becomes apparent now: it ensures that the turbulent kinetic energy evolves according to its exact, analytically derived equation in the case of inhomogeneous, incompressible, isotropic turbulence, by contrast with the homogeneous turbulence where the turbulent kinetic energy must not decay at all.

Equivalence between Reynolds-stress models and Lagrangian stochastic models

As illustrated by Equation 7.81, in the incompressible case, a Reynolds-stress model is entirely characterised by the velocity-pressure-gradient tensor Π_{ij} and the turbulent dissipation rate ϵ. Temporarily leaving the question of the prescription of ϵ aside, the modelling efforts are therefore focused on the redistribution tensor, which, in the general case, is written as (Pope 1994b)

$$\Pi_{ij} = \Pi_{ij}^{\star}\left(\frac{\partial \overline{u_j}}{\partial x_i}, \overline{u_i'' u_j''}, \epsilon\right). \tag{7.86}$$

Apart from the restriction, already mentioned above, that this tensor must be traceless, specific forms of the function $\Pi_{ij}^{\star}$ are found empirically – through experimental data or direct numerical simulations. In parallel, as I just mentioned, a given prescription of the GLM is characterised – provided one leaves ϵ aside for the moment – by a specification of the Kolmogorov constant C_0 and the drift tensor G_{ij}. The two approaches may be radically different in their philosophy, but *there exists an equivalence between the Reynolds-stress models and the Lagrangian stochastic models*, in the sense that in certain specifications, both will lead to the same evolution of the statistical properties of the flow. More specifically, to any specification of the drift tensor G_{ij} is associated a unique equivalent redistribution tensor Π_{ij}, through Equation 7.82. However, in general, the opposite is not true: several different drift tensor specifications can lead to the same Reynolds-stress model[13]. In addition, finding the drift tensor(s) equivalent to a given velocity-pressure-gradient tensor can prove challenging, as the corresponding relation is implicit. Pope (1994b) studied in details this relation between Reynolds-stress models and Lagrangian stochastic models. In particular

[13]This is due to the more general fact that while a given Ito stochastic differential equation has a unique corresponding Fokker-Planck equation, a given Fokker-Planck equation can be modelled by multiple distinct Ito SDE (e.g. Gardiner 1994).

- the gas pressure fluctuations p' due to turbulence are usually separated into 'slow', 'rapid', and 'harmonic' fluctuations (Pope 2000): the slow fluctuations are due to the action of the turbulent shear on the turbulent velocity itself (i.e. turbulence-turbulence interaction), while the rapid fluctuations are due to the interaction of the mean shear on the turbulent shear (i.e. mean flow-turbulence interaction). As for the harmonic fluctuations, they represent the decay of pressure fluctuations in the absence of any source. The simplest model for the velocity-pressure-gradient tensor consists in only accounting for the slow pressure fluctuations, and considering that they tend to make the Reynolds stress tensor return to isotropy. This yields the *Rotta's model* (Rotta 1951)

$$\Pi_{ij} = -2C_1\epsilon b_{ij} \,, \tag{7.87}$$

$$b_{ij} \equiv \left(\frac{\overline{u_i'' u_j''}}{\overline{u_i'' u_i''}} - \frac{1}{3}\delta_{ij} \right) , \tag{7.88}$$

  characterised by the constant C_1, and where b_{ij} is the *anisotropy tensor* (in particular, it vanishes if the Reynolds stress tensor is isotropic). The equivalent Lagrangian stochastic model is the SLM, with

$$C_1 = 1 + \frac{3}{2}C_0 \,, \tag{7.89}$$

  so that the standard value of $C_0 = 2.1$ gives $C_1 = 4.15$ (Pope 1994b). However, when Rotta's model for the slow pressure fluctuations is used in conjunction with another model for the rapid fluctuations, a smaller portion of the effect is contained in C_1, so that a lower value is in order for this coefficient;

- in order to model the rapid pressure fluctuations, Naot et al. (1973) proposed the *isotropisation of production model* (or IPM), whereby to the Rotta's term above is added the following contribution

$$\Pi_{ij} = \Pi_{ij}^{\text{Rotta}} - C_2 \left(\mathcal{P}_{ij} - \frac{1}{3}\mathcal{P}_{kk}\delta_{ij} \right) , \tag{7.90}$$

  where $\mathcal{P}_{ij}$ is the turbulent production tensor. The IPM is characterised by the constant C_2, in addition to C_1 in the slow pressure variation term: standard values are $C_1 = 1.8$ and $C_2 = 0.6$ (Pope 1994b). Several specifications for G_{ij} can lead to this Reynolds-stress model; one of them, for instance, is (Pope 1994b)

$$\Pi_{ij} = \frac{\epsilon}{k}\left(\alpha_1\delta_{ij} + \alpha_2 b_{ij} + \alpha_3 b_{ik}b_{kj}\right) + \frac{\partial \overline{u_k}}{\partial x_l}\left(\beta_2\delta_{ik}\delta_{jl} + \beta_3\delta_{il}\delta_{jk} + \gamma_5 b_{ik}\delta_{jl} + \gamma_6 b_{il}\delta_{jk}\right) , \tag{7.91}$$

$$\alpha_2 = 3.5 \quad , \quad \alpha_3 = -10.5 \quad , \quad \beta_2 = 0.8 \quad , \quad \beta_3 = -0.2 \quad , \quad \gamma_5 = -\gamma_6 = 0.6 \,,$$

$$\alpha_1 = -\frac{1}{2} - \frac{3}{4}C_0 + \frac{1}{2}C_2\frac{\mathcal{P}_{ii}}{\epsilon} + 3\alpha_2 b_{ik}b_{kl}b_{kj} \,.$$

  This is therefore an example of a specification of the Generalised Langevin Model (comprised of Equations 7.76 and 7.77) that goes beyond the Simplified Langevin Model (comprised of Equations 7.74 and 7.75).

Numerous other specifications of the velocity-pressure-gradient tensor exist, like the Launder, Reece and Rodi model (or LRR; Launder et al. 1975), the Shih-Lumley model (or SL; Shih and Lumley 1986) or the Speziale, Sarkar and Gatski model (or SSG; Speziale et al. 1991) for instance. Ultimately, they all amount to some specification of the Generalised Langevin Model. The relation between the two approaches makes them mutually beneficial: new advances in Reynolds-stress models can be converted in refinements in Lagrangian stochastic models, and vice versa. However, it can already be seen that Lagrangian stochastic models have an advantage over Reynolds-stress models: by construction, they always lead to *realisable turbulence models* – i.e. the PDF evolving to the equivalent Fokker-Planck equation is necessarily positive and normalised to unity. In other words, *Lagrangian stochastic models constructed through the process described above constitute physical turbulence models: it is much easier to derive closure relations in such models than in Reynolds-stress models*.

7.2.3 Joint velocity-dissipation turbulence models

Lagrangian stochastic model for dissipation

Until now, I have deliberately left aside the question of how to prescribe the turbulent dissipation rate ϵ, in order to focus on the velocity-pressure-gradient tensor Π_{ij}. A possibility is to supplement the Lagrangian

stochastic model on velocity with a model equation for ϵ, in the same form as in $k-\epsilon$ or $k-\omega$ models of turbulence (also referred to as *two-equation models*). An alternative approach, proposed by Pope and Chen (1990), consists in considering the dissipation as being a property of the fluid particles themselves, for which an additional Ito SDE must be developed and integrated forward in time, in conjunction with the position and velocity equations described above. Let me define the *turbulent frequency*

$$\omega_t(\mathbf{x},t) \equiv \frac{\epsilon(\mathbf{x},t)}{k(\mathbf{x},t)}\,, \tag{7.92}$$

where k is the turbulent kinetic energy. The turbulent frequency ω_t has the dimension of an inverse time, and represents the inverse of the typical timescale over which the turbulent kinetic energy is dissipated into heat by the Kolmogorov viscous scales at the end of the turbulent cascade. Pope and Chen (1990) developed a Lagrangian stochastic model for the turbulent frequency associated with a give fluid particle $\omega_t^\star(t)$ on account of observations made in direct numerical simulations of low- and moderate-Reynolds-number flows that 1) the dissipation rate follows a log-normal distribution[14], and 2) the autocorrelation function of its logarithm takes the form of a decaying exponential, with an integral time T_χ which is proportional to the inverse of the mean turbulent frequency itself. In terms of stochastic processes, if we defined

$$\chi^\star(t) \equiv \ln\left(\frac{\omega_t^\star(t)}{\overline{\omega_t}(\mathbf{x}^\star(t),t)}\right)\,, \tag{7.93}$$

then $\chi^\star(t)$ is necessarily an Orstein-Uhlenbeck process, with the integral time $T_\chi \equiv 1/(C_\chi\overline{\omega_t})$, and a certain variance σ

$$\mathrm{d}\chi^\star = -(\chi^\star - \overline{\chi})\frac{\mathrm{d}t}{T_\chi} + \sqrt{\frac{2\sigma^2}{T_\chi}}\,\mathrm{d}W\,. \tag{7.94}$$

Then the turbulent frequency is given by $\omega_t^\star = \overline{\omega_t}\exp(\chi^\star)$. The quantity $\chi^\star$ is already modelled, but if one wants to change variables to $\omega_t^\star$, one also needs a prescription for $\overline{\omega_t}$. This prescription must necessarily be empirical: as I already remarked for turbulent dissipation ϵ in Section 1.2.3, this is the only way to obtain a model equation for dissipation that may be applicable. The standard model equation assumes that $\overline{\omega_t}$ – or equivalently ϵ – decays towards zero at a rate that is itself proportional to $\overline{\omega_t}$. This yields (Pope 2000)

$$\frac{\mathrm{d}\overline{\omega_t}}{\mathrm{d}t} = -\overline{\omega_t}^2 S_\omega\,, \tag{7.95}$$

where S_ω is the non-dimensional rate of change of $\overline{\omega_t}$, given by

$$S_\omega = (C_{\epsilon 2}-1) - (C_{\epsilon 3}-1)\frac{\mathcal{P}_{ii}}{\epsilon}\,. \tag{7.96}$$

Finally, since, by construction, the expectation of $\ln(\chi^\star)$ is unity, and since for any random variable X one has $\overline{\exp(X)} = \exp\overline{X} + \mathrm{Var}(X)/2$ (where $\mathrm{Var}(X)$ denotes the variance of X), the mean value of χ is simply $-\sigma^2/2$. With all these ingredients pieced together, the change of variable from $\chi^\star$ to $\omega_t^\star$ can be performed in Equation 7.94 by means of the Ito's formula (Equation 7.51), and one finds (Pope and Chen 1990)

$$\mathrm{d}\omega_t^\star = -\omega_t^\star\overline{\omega_t}\left[S_\omega + C_\chi\left(\ln\left(\frac{\omega_t^\star}{\overline{\omega_t}}\right) - \frac{1}{2}\sigma^2\right)\right]\,\mathrm{d}t + \omega_t^\star\sqrt{2C_\chi\overline{\omega_t}\sigma^2}\,\mathrm{d}W\,. \tag{7.97}$$

Refined Langevin Model

Combining the velocity stochastic equation introduced in Section 7.2.2 with this dissipation stochastic equation allows for the inclusion of dissipation in the velocity equation in a much more physically realistic manner. But the velocity equation must be modified accordingly. First, the fact that $\omega_t^\star$ is modelled allows to describe the internal

[14] A random variable X is said to follow a *log-normal* distribution if $\ln(X)$ follows a normal distribution.

intermittency[15] inherent to the turbulent motions: under the *refined* Kolmogorov hypotheses (Kolmogorov 1962), the second-order structure function is proportional to $\epsilon^\star \tau$ instead of $\epsilon\tau$. A direct consequence is that ϵ should be replaced with $\epsilon^\star$ in the diffusion term of the velocity SDE. But this cannot be the only modification: indeed, in the Fokker-Planck equation (Equation 7.78), the last term has been substituted thus

$$\frac{1}{2}\frac{\partial^2(C_0\epsilon f_L^\star)}{\partial x_i \partial x_i} \rightarrow \frac{1}{2}\frac{\partial^2(C_0\omega_t^\star k f_L^\star)}{\partial x_i \partial x_i} \,. \tag{7.98}$$

In order to alleviate this substitution, and retain the exact same Fokker-Planck equation, the drift tensor G_{ij} must be replaced with G'_{ij} in such a way that

$$-\frac{\partial(f_L^\star G'_{ij}(V_j - \overline{u_j}))}{\partial V_i} + \frac{1}{2}\frac{\partial^2(C_0\omega_t^\star k f_L^\star)}{\partial x_i \partial x_i} = -\frac{\partial(f_L^\star G_{ij}(V_j - \overline{u_j}))}{\partial V_i} + \frac{1}{2}\frac{\partial^2(C_0\epsilon f_L^\star)}{\partial x_i \partial x_i} \,. \tag{7.99}$$

If one assumes that the marginal velocity PDF is Gaussian, with its mean corresponding to the mean velocity and its covariance matrix corresponding to the Reynolds stress tensor, then this relation can be solved for G'_{ij}, and one finds (Pope and Chen 1990)

$$G'_{ij} = G_{ij} - \frac{3}{4}C_0\left(\omega_t^\star - \overline{\omega_t}\right)A_{ij}^{-1} \,, \tag{7.100}$$

where $A_{ij} \equiv \overline{u_i'' u_j''}/(2k/3)$. Finally, the experimentally constrained value of C_0 being different in the Generalised Langevin Model (~ 2.1) than when a dissipation equation is added (~ 3.5), the drift tensor must also be modified accordingly, with the same goal in mind that the velocity part of the Fokker-Planck equation must remain the same as in the GLM. Finally, the velocity SDE becomes

$$\mathrm{d}u_i^\star = \left[-\frac{1}{\overline{\rho}}\frac{\partial \overline{p}}{\partial x_i} + g_i + L_{ij}\left(u_j^\star - \overline{u_j}\right)\right]\,\mathrm{d}t + \sqrt{C_0\omega_t^\star k}\,\mathrm{d}W \,, \tag{7.101}$$

where

$$L_{ij} = G_{ij} - \frac{3}{4}\left[C_0\left(\omega_t^\star - \overline{\omega_t}\right) + \Delta C_0 \overline{\omega_t}\right]A_{ij}^{-1} \,, \tag{7.102}$$

and $\Delta C_0 = 3.5 - 2.1$. Together, Equations 7.96, 7.97, 7.101 and 7.102 form the *Refined Langevin Model* of turbulence (or RLM), which ensures, in particular, that the PDF associated both to the velocity of the flow and to the turbulent dissipation rate evolves in accordance with numerically and experimentally determined constraints.

The RLM was subsequently extended to inhomogeneous flows by Pope (1991), where the author also discarded the assumed Gaussian form of the velocity PDF and the assumed independence of $u_i^\star$ and $\omega_t^\star$. This allowed him to derive a joint velocity-dissipation Lagrangian stochastic model of turbulence with a much wider range of application. Similarly, the approach can be adapted to a wide range of more complex flows. In particular – and this is of course important in the stellar context –, it can be adapted to *compressible flows* as well. This requires the inclusion of properly defined means in the Lagrangian stochastic model (namely Favre averages), as well as an equation for an additional thermodynamic variable (like temperature, energy, enthalpy or entropy for instance). This will be the subject of a part of the discussion in Chapter 8.

7.2.4 How to evaluate the means?

The Lagrangian stochastic models introduced in Sections 7.2.2 and 7.2.3 explicitly contain the mean fields associated to the flow – like the mean density, gas pressure, velocity, etc. These need to be estimated at the instantaneous positions of the fluid particles at every time step, in order to integrate the SDE forward in time. Furthermore, and perhaps more fundamentally, one is ultimately interested in mean flow quantities, like the mean

[15] The intermittency of turbulence is a vast concept that has many different concrete aspects. Essentially, it refers to the very long tails developed by the PDF associated to the turbulent properties of the flow, so that very strong events are likely to happen at regular intervals. One of the many consequences is the development of strong velocity gradients for instance. But this is in direct and complete contradiction with the concept of a global, average dissipation rate, which would, on the contrary, smooth such strong gradients as soon as they start to develop. Since intermittency is a known experimental fact, the dissipation rate has to be defined locally, as a quantity susceptible to vary over very short length scales.

velocity or the Reynolds stress tensor for instance, rather than the particle properties themselves. Therefore, one needs to be able to evaluate the means. In Eulerian PDF methods, such as those used for studying turbulent dispersion in free turbulence for instance, the means are considered known (either through explicit constraints related to the specific setup under consideration, or computed separately in Large-Eddy Simulations), and plugged in as external inputs in the Lagrangian stochastic model (see Pope 1985, for a review on PDF methods for turbulent reactive flow). However, in the context of my work – i.e. in the context of turbulence-oscillation coupling –, this does not constitute a viable approach. The reason is that the mean fields, being Reynolds or Favre averages, contain the information on the oscillations, while the turbulent quantities correspond to the fluctuation of the flow quantities around these averages. Therefore, by treating the mean fields as external inputs into the Lagrangian stochastic model for turbulence, one effectively decouples the oscillation from the turbulence, which defeats the entire purpose of the model.

Consequently, I deliberately chose to follow an alternative path, which consists in directly using the fluid particles themselves to evaluate the means.

Indeed, it is important to realise that *the mean fields are already in closed form*, since they can be written in terms of the PDF of the flow, whose information is contained in the set of modelled particles. In order to follow that path, one needs to be able to extract the flow PDF – or at least its statistical moments – directly from the set of fluid particles. I describe how this can be done in this section.

Basic particle representation for homogeneous turbulence

As I remarked earlier, Lagrangian stochastic models of turbulence are fundamentally based on the idea that the flow can be represented by a set of N individual fluid particles. This corresponds to the *particle representation* of the system. By contrast, describing the system with flow variables, whether the description be given in a Eulerian or Lagrangian frame, corresponds to the *flow representation* of the system. Ideally, one would like both representations to be equivalent, at least in the limit $N \to +\infty$. An important question, therefore, is this: how are the particle and flow representation related to each other? For instance, how is the set $\left\{\mathbf{u}^{\star\,(i)}\right\}_{i=1..N}$ of all particle velocities related to the Eulerian or Lagrangian velocity PDF of the flow? This question is far from straightforwardly answered, and requires a bit of thought.

Let me denote the velocity of the particle indexed i as $\mathbf{u}^{\star\,(i)}(t)$. I define the *discrete PDF* $f_N(\mathbf{V},t)$ as

$$f_N(\mathbf{V},t) \equiv \frac{1}{N}\sum_{i=1}^{N} \delta^3\left(\mathbf{V} - \mathbf{u}^{\star\,(i)}(t)\right) . \tag{7.103}$$

The expectation of the discrete PDF then follows (Pope 1985)

$$\overline{f_N(\mathbf{V},t)} = f(\mathbf{V},t) , \tag{7.104}$$

where f can refer either to the Lagrangian or Eulerian PDF of the flow, since they are the same for homogeneous flows, and I have substituted the notation E[.] for the notation $\overline{\cdot}$, more familiar in the context of turbulent flows, to represent ensemble averages. The discrete PDF is therefore an accurate, unbiased representation of the flow PDF. Furthermore, this is the case regardless of the value of N: the representation is even valid for $N = 1$. However, a large number of realisations is still needed in order to extract the *expectation* of the discrete PDF.

An alternative procedure would be to estimate the moments of the PDF directly, instead of estimating the PDF itself. By definition of the PDF, one has, for any function $Q(\mathbf{u},t)$ of the velocity

$$\overline{Q(\mathbf{u},t)} = \int_{\mathbb{R}^3} \mathrm{d}^3\mathbf{V}\; f(\mathbf{V})\; Q(\mathbf{V},t) . \tag{7.105}$$

A natural estimator for this statistical expectation is obtained by replacing f by f_N, which leads to the following definition

$$\langle Q(\mathbf{u},t)\rangle_N \equiv \int_{\mathbb{R}^3} \mathrm{d}^3\mathbf{V}\; f_N(\mathbf{V})\; Q(\mathbf{V},t) = \int_{\mathbb{R}^3} \mathrm{d}^3\mathbf{V}\; Q(\mathbf{V},t)\frac{1}{N}\sum_{i=1}^{N} \delta^3\left(\mathbf{V} - \mathbf{u}^{\star\,(i)}(t)\right) = \frac{1}{N}\sum_{i=1}^{N} Q(\mathbf{u}^{\star\,(i)},t) . \tag{7.106}$$

But in parallel, because the expectation of f_N equals f, one has

$$\overline{\langle Q(\mathbf{u},t)\rangle_N} = \overline{Q(\mathbf{u},t)} , \tag{7.107}$$

which means that *averaging the quantity $Q(\mathbf{u}^{\star\,(i)}, t)$ over all particles i yields an unbiased estimator for the ensemble average of $Q(\mathbf{u}, t)$*. Again, this is true for any value of N, but in general, the quantity $\langle Q(\mathbf{u}, t)\rangle_N$ needs to be computed for several independent realisations of the entire set of particles, in order for its expectation to be computed. This ceases to be necessary if N is high enough: indeed, the central limit theorem[16] stipulates that the variance of $\langle Q(\mathbf{u}, t)\rangle_N$ vanishes as $1/\sqrt{N}$ if $N \to +\infty$, in which case this estimator is no longer a random variable. In other words, one has

$$\lim_{N\to+\infty} \langle Q(\mathbf{u}, t)\rangle_N = \overline{Q(\mathbf{u}, t)} \,. \tag{7.108}$$

This is a stronger statement, since it means that *if the number of fluid particles is sufficiently high, one only needs to integrate their Lagrangian stochastic model once*, instead of having to integrate it many times.

Extension to inhomogeneous flows: Smoothed Particle Hydrodynamics

In inhomogeneous flows, the discrete PDF f_N must be modified to account for the position of the particles in addition to their velocity. For incompressible flows, this is done by defining

$$f_N(\mathbf{V}; \mathbf{x}, t) \equiv \frac{\mathcal{V}}{N} \sum_{i=1}^{N} \delta^3\left(\mathbf{x}^{\star\,(i)}(t) - \mathbf{x}\right) \delta^3\left(\mathbf{u}^{\star\,(i)}(t) - \mathbf{u}\right) \,, \tag{7.109}$$

where the constant $\mathcal{V}$ is determined by the following normalisation condition: since the expectation of f_N should equal the actual flow PDF, one has

$$1 = \int_{\mathbb{R}^3} \mathrm{d}^3\mathbf{V}\, \overline{f_N(\mathbf{V}; \mathbf{x}, t)} = \mathcal{V}\overline{\delta^3\left(\mathbf{x}^{\star\,(i)}(t) - \mathbf{x}\right)} \,. \tag{7.110}$$

In order for this condition to be satisfied, it is necessary for $\overline{\delta^3\left(\mathbf{x}^{\star\,(i)}(t) - \mathbf{x}\right)}$ to not depend on $\mathbf{x}$: in other words, the $\mathbf{x}^{\star\,(i)}$ must be uniformly distributed, in which case its PDF equals the inverse of the volume of the domain under consideration. Therefore, *the constant $\mathcal{V}$ in the definition of the discrete PDF is none other than the volume of the domain*. Through the exact same procedure as for homogeneous flows, one finds that the estimator for mean quantities $\overline{Q(\mathbf{u}; \mathbf{x}, t)}$ should be extended to inhomogeneous flows in the following form

$$\langle Q(\mathbf{u}; \mathbf{x}, t)\rangle_N \equiv \frac{\mathcal{V}}{N} \sum_{i=1}^{N} Q\left(\mathbf{u}^{\star\,(i)}, t\right) \delta^3\left(\mathbf{x}^{\star\,(i)}(t) - \mathbf{x}\right) \,. \tag{7.111}$$

In other words, the means are now estimated by averaging the particle-level quantity over all fluid particles *conditioned on their being located exactly at* $\mathbf{x}$. But implementing this estimator in this exact form, does not yield the required result: indeed, for any given position $\mathbf{x}$, any individual fluid particle has exactly zero probability of finding itself at this exact location. Therefore, it is necessary to relax the condition on particle position, and instead of computing means over particles exactly located at $\mathbf{x}$, it is necessary to compute them over particles within a given, compact-support vicinity of $\mathbf{x}$. This is done by replacing the Dirac distribution δ^3 by a wider *kernel function* $K_h(\mathbf{r})$, which serves as a weighting function to implement the particle-position condition in the estimation of the means, thus leading to the following *kernel estimator* for the means

$$\langle Q(\mathbf{u}; \mathbf{x}, t)\rangle_{h,N} \equiv \frac{\mathcal{V}}{N} \sum_{i=1}^{N} Q\left(\mathbf{u}^{\star\,(i)}, t\right) K_h\left(\mathbf{x}^{\star\,(i)}(t) - \mathbf{x}\right) \,, \tag{7.112}$$

where h denotes the size of the compact support of the kernel function K_h. Many different specifications of the kernel function can be chosen, but some properties are mandatory: I already mentioned the fact that it must have a compact support, which ensures that the distant particles cannot impact local means; the kernel function must also be normalised to unity, so that the mean estimates are not biased. One must also have

$$\lim_{h\to 0} K_h = \delta^3 \,. \tag{7.113}$$

[16] Let $\{X_k\}_{k\in\mathbb{N}}$ be a sequence of random variables, independent and identically distributed, each having mean μ and variance σ^2. Defining the random variable $\overline{X_n} \equiv \sum_{k=0}^{n} X_n/n$, it is easily seen that $\overline{X_n}$ has mean μ and variance σ^2/n, so that one can define the reduced and centered random variable $Z_n \equiv (\overline{X_n} - \mu)/(\sigma/\sqrt{n})$, which has mean 0 and variance 1. Then, the *central limit theorem* states that the sequence $\{Z_n\}_{n\in\mathbb{N}}$ converges in law towards a normal distribution of mean 0 and variance 1.

An example is the kernel function used by Welton and Pope (1997)

$$K(\mathbf{r}) = \begin{cases} c\left(1+3\dfrac{|\mathbf{r}|}{h}\right)\left(1-\dfrac{|\mathbf{r}|}{h}\right)^3 & \text{if } |\mathbf{r}| < h\,, \\ 0 & \text{if } |\mathbf{r}| > h\,, \end{cases} \tag{7.114}$$

where $\mathbf{r}$ is the position of the particle with respect to the center of the kernel (where the mean is estimated), and the constant c is given by the normalisation condition[17]. This expression ensures that the kernel function and its first two derivatives are continuous at the surface of its support.

Whichever kernel function is chosen, the choice of h is crucial. Indeed, in the homogeneous case, I mentioned that $\langle Q\rangle_N$ becomes an unbiased estimator of zero variance when $N \to +\infty$. This is no longer true in the inhomogeneous case, where the estimator $\langle Q\rangle_{N,h}$ exhibits both a systematic bias (Pope 1994a)

$$\overline{\langle Q\rangle_{N,h}} - \overline{Q} = \frac{1}{2}h^2\boldsymbol{\nabla}^2\overline{Q} + O(h^4)\,, \tag{7.115}$$

and a statistical error

$$\mathrm{Var}\left(\langle Q\rangle_{N,h}\right) \propto \frac{\mathcal{V}}{Nh^D} = \frac{(L/h)^D}{N}\,, \tag{7.116}$$

where D is the dimension of the domain, and $L \equiv \mathcal{V}^{1/D}$ its typical length. Physically, the systematic bias stems from the inclusion of particles in the mean that are not exactly located at $\mathbf{x}$, and are therefore characterised by a slightly different mean value. The bias grows with h^2, and vanishes as $h \to 0$. On the other hand, the statistical error stems from the limited number of particles used to estimate the mean. It decreases as h^{-D}: indeed, the smaller h is, the fewer particles are used in the mean, the larger the statistical fluctuations of the mean estimate is. It is therefore impossible to have an estimator that is simultaneously accurate and precise: increasing accuracy will always come at the price of a decreased precision, and vice versa. The condition that the best possible compromise between the two must be reached yields an optimal value for h, in the form (Pope 1994a)

$$\frac{h}{L} \sim N^{-1/(4+D)}\,. \tag{7.117}$$

The kernel estimator is readily adapted to compressible flows, where the density is susceptible to vary in time and space, and the particle position PDF is no longer uniform. Then the exact same building procedure leads to

$$\langle Q\rangle_{N,h} \equiv \sum_{i=1}^{N} \mathcal{V}^{\star\,(i)} Q\left(\mathbf{u}^{\star\,(i)}, t\right) K_h\left(\mathbf{x}^{\star\,(i)}(t) - \mathbf{x}\right)\,, \tag{7.118}$$

where this time $\mathcal{V}^{\star\,(i)}$ denotes the lumped volume of fluid represented by the particle i. In the homogeneous limit, this lumped volume equals the total volume of the domain $\mathcal{V}$ divided by the number of particles N, and one recovers Equation 7.112. In inhomogeneous flows, while each particle, by construction, carries a fixed mass $\Delta m^{(i)}$, local fluctuations of the density make the volume occupied by the particle vary, in such a way that

$$\mathcal{V}^{\star\,(i)} \equiv \frac{\Delta m^{(i)}}{\rho^{\star\,(i)}}\,, \tag{7.119}$$

where $\rho^{\star\,(i)}$ denotes the mass density characterising the i-th fluid particle.

Setting $Q = \rho^\star$, $Q = \rho^\star\mathbf{u}^\star$ and $Q = \rho^\star(u_i^\star - \widetilde{u}_i)(u_j^\star - \widetilde{u}_j)$ alternatively in Equation 7.118, one finds a kernel estimator for the local Reynolds-averaged density, mass-averaged velocity, and the Reynolds stress tensor respectively (Welton and Pope 1997)

$$\overline{\rho}(\mathbf{x}, t) = \sum_{i=1}^{N} \Delta m^{(i)} K_h(\mathbf{x}^{\star(i)}(t) - \mathbf{x})\,, \tag{7.120}$$

$$\widetilde{\mathbf{u}}(\mathbf{x}, t) = \frac{1}{\overline{\rho}(\mathbf{x}, t)} \sum_{i=1}^{N} \Delta m^{(i)} \mathbf{u}^{\star(i)}(t) K_h(\mathbf{x}^{\star(i)}(t) - \mathbf{x})\,, \tag{7.121}$$

$$\widetilde{u_i'' u_j''}(\mathbf{x}, t) = \frac{1}{\overline{\rho}(\mathbf{x}, t)} \sum_{i=1}^{N} \Delta m^{(i)} \left(u_i^{\star(i)}(t) - \widetilde{u}_i(\mathbf{x}, t)\right)\left(u_j^{\star(i)}(t) - \widetilde{u}_j(\mathbf{x}, t)\right) K_h(\mathbf{x}^{\star(i)}(t) - \mathbf{x})\,. \tag{7.122}$$

[17] If the model is 1D, one finds (Welton and Pope 1997) $c = 4/(5h)$. In 3D, the normalisation constant becomes $c = 105/(16\pi h^3)$.

In particular, let me remark that the local mean density is computed by 'counting' the particles present in the vicinity. This means that the continuity condition is automatically met in the particle representation, thus lowering the order of the set of equations needed to describe the flow.

The conclusion is that the kernel estimator allows for the estimation of mean fields directly from the particle properties. In order to integrate a Lagrangian stochastic model forward in time, these means must be estimated not at fixed Eulerian positions, but at the instantaneous position of the particles: the use of the kernel estimator to compute mean fields at constantly varying positions is at the heart of *Smoothed Particle Hydrodynamics* (SPH thereafter). The direct computation obviously has $O\left(\frac{h}{L}N^2\right)$ complexity – because it requires the computation of the sum of $\sim hN/L$ terms for each of the N particles separately. However, it is possible to reduce the complexity of the operation to $O(N)$ (Welton 1998), provided the kernel function exhibits some extra properties (namely, it must be expressed as a product of several 1D piecewise polynomial functions involving only one dimension each): I will introduce this algorithm in Section 9.1.2. I refer the reader to Liu and Liu (2010) or Monaghan (1992) for a comprehensive review on the use of SPH in turbulent flow modelling, or to Springel (2010) for its more specific use in the astrophysical context.

7.3 My work in this context

Let me summarise the theoretical basis for Lagrangian stochastic models of turbulence, and their implementation with particle methods like SPH. Instead of considering the evolution in time of the various statistical moments associated to the turbulent flows, one considers the evolution in time of their joint-PDF. This is governed by a Fokker-Planck equation, which is very challenging to solve directly for two reasons, one being of practical nature (the analytical solving of the Fokker-Planck equation is only feasible in a handful of very simple cases, and its numerical solving by grid-based methods – which forms the basis of *Eulerian PDF methods* – requires the discretisation of the entire parameter space), and one being of a more fundamental nature (the Fokker-Planck equation contains the expectation of the force acting on the flow conditioned on the local Eulerian velocity, which is extremely complicated to model). Instead of solving the Fokker-Planck equation directly, it is better to mimic the evolution of the flow PDF by representing the flow as a set of individual fluid particles, each evolving according to a system of Ito stochastic differential equations, carefully constructed to be statistically equivalent to the actual Fokker-Planck equation: this is at the core of *Lagrangian PDF methods*, and the system of SDE used to model the evolution of the fluid particles is referred to as a *Lagrangian stochastic model* of the turbulent flow. A mix of analytical arguments based on the Kolmogorov hypotheses and experimentally and numerically observed behaviour of turbulent flows in certain limits allows for the development of Lagrangian stochastic models on physical grounds, either for velocity only, or for joint velocity and dissipation. Naturally, the account given in this chapter only scratches the surface of this subject. In particular, I have left aside Lagrangian stochastic models for the acceleration of the particles – because they reduce to velocity stochastic models in flows with high Reynolds number (see Heinz 2013, Section 5.1) –, but also the question of the joint modelling of velocity and thermodynamic variables that goes along with the consideration of compressible non-adiabatic flows, upon which I will touch in the next chapter. Finally, central to the implementation of Lagrangian stochastic models of turbulence is the idea of the *particle representation* of the system, i.e. the idea that the information on the PDF of the flow can be directly extracted from the set of fluid particles themselves. The Smoothed Particle Hydrodynamics (SPH) formalism is an example of *particle method* that allows for the estimation of all statistical moments of the turbulent properties of the flow at each particle position, by computing the average of the corresponding particle-level quantity over all neighbouring particles. The conditional mean on particle position is performed through a *kernel estimator* which, if chosen wisely, entails mean field estimates that are neither too biased, nor prone to significant statistical errors. Thanks to this kernel estimator, all mean fields appearing in the Lagrangian stochastic model are in closed form – in addition to being the output in which one was interested in the first place.

This approach in turbulence modelling exhibits several key advantages that make it highly beneficial regarding the modelling of the coupling between stellar turbulent convection and stellar oscillations, and especially allows to circumvent some of the fundamental limitations to the more traditional approaches detailed in Sections 2.2 to 2.4

- the Fokker-Planck equation governing the evolution of the PDF of the flow – whether Eulerian or Lagrangian – *contains the same amount of information as an infinite hierarchy of transport equations on every statistical moments of the turbulent quantities*. *A fortiori*, it contains more information than simply the mean equations

(as in MLT) or the mean and second-order equations (as in Reynolds-stress models);

- the PDF – and, therefore, the set of fluid particles used to represent it – contains the information on both the turbulent motions and the global oscillations at the same time. Therefore, *it also contains the coupling between the two in a naturally consistent manner*. This means there is no longer any need to separate the equations of the flow into turbulence equations and oscillation equations beforehand, which is problematic when one is interested in the interaction between the two components;

- the Lagrangian point of view adopted in the particle representation entails that *all advection processes – whether they be due to the large scale convection, or due to the small-scale turbulent transport – are modelled exactly without having to include them explicitly in the equations*. Lagrangian stochastic models of turbulence therefore completely circumvent the need to adopt the mixing-length hypothesis, which is a crucial asset, seeing as this hypothesis is both almost inescapable in current convection modelling, and very invalid close to the surface of the star;

- the stochastic differential equations are closed at particle level, instead of at mean flow level. Therefore, *it is much easier to relate a given closure relation to the underlying physical assumptions than in MLT or Reynolds-stress models* for instance. As a result, Lagrangian stochastic models do not contain free parameters pertaining to an empirical prescription, but physical parameters, firmly physically grounded, and therefore easier to constrain with the help, for instance, of 3D hydrodynamic simulations;

- the particle representation is, by construction, completely mesh-free, so that it is immune to the grid resolution problem one runs into when dealing with Large-Eddy Simulations. That means *there is no longer any difficulty in including very different length scales in the system*, which significantly improves the description of turbulence;

- the turbulent dissipation rate is also modelled much more realistically than in more traditional approaches, since it is included as a particle-level quantity, and evolves according to its own Ito stochastic differential equation. As a result, Lagrangian stochastic models of turbulence allow for *the inclusion of all turbulent timescales* relevant to the problem – although, unlike length scales, one is still limited by the discretisation of time in numerical implementations.

Naturally, this does not mean this method is ideal: in particular, one still needs an empirical prescription for the turbulent dissipation rate – or equivalently for the mean turbulent frequency. However, Lagrangian stochastic models allow for a better, more realistic representation of the *turbulent fluctuations* of the turbulent frequency, and therefore of intermittency. Furthermore, the use of Ito stochastic differential equations to model the evolution of the fluid particles *presupposes that their PDF is Gaussian*, whereas stellar turbulent convection is much better described by bimodal distributions, due to the skewness between the upflows and downdrafts constituting the structure of the convective motions. There are ways to incorporate this bimodal behaviour in the model however (see Rodean 1996, Chapter 10). Finally, if one wishes to implement these methods in the 3D case, the simulations can become as heavy as the 3D LES traditionally employed in stellar atmosphere modelling. Nevertheless, for all the reasons listed above, Lagrangian stochastic models of turbulence are perfectly suited for the study of turbulence-oscillation coupling, and allow to alleviate some fundamental limitations inherent to Mixing-Length Theories, Reynolds-stress models or the use of Large-Eddy Simulations in that regard. In using this novel modelling approach, the underlying motivation is mainly to answer the following questions

1) how can it help physically relate the observed properties of the modes (i.e. their amplitude and linewidth) to the underlying detailed physical properties of turbulent convection at the top of the convective zone, thus allowing to use the former in order to constrain the latter?

2) how can it help *predict* the frequency correction to apply to theoretically computed eigenfrequencies, in order to obtain surface-effect-free frequencies that can be accurately compared to observations for seismic diagnosis purposes?

Answering these questions is a very long-term motivation; the shorter-term goal I set for myself in this second part of my PhD, therefore, was (and still is) to lay the groundwork for the implementation, both analytical and numerical, of the methods presented in this introductory discussion in the context of solar-like oscillations.

First, I used the kind of procedure outlined in Sections 7.2.2 and 7.2.3 to derive a Lagrangian stochastic model relevant in the context of stellar convective zones. In the rest of this second part, however, and as a first, preliminary step, I only considered a very simplified version of this Lagrangian stochastic model, corresponding to the Simplified Langevin Model described in Section 7.2.2. Using this simplified model, I followed two approaches, one analytical and one numerical, which are different in nature, but perfectly complementary and mutually beneficial.

Concerning the analytical approach, the challenge is to linearly perturb the Lagrangian stochastic model to obtain an intrinsically stochastic linear wave equation, designed to govern the evolution of the stellar oscillations, while simultaneously containing the effect of turbulence in a self-consistent manner. This stochastic wave equation can then be used to derive stochastic differential equations – referred to as *simplified amplitude equations* (Stratonovich 1965) – for the complex amplitudes of any given normal mode of oscillation in the star, including the impact of turbulence. I show that these simplified amplitude equations simultaneously contain the information on the excitation and damping rates of the modes, and also on the shift incurred by the mode frequencies under the influence of turbulence – in other words, surface effects. The motivations behind this analytical model are related to the fact that it allows to obtain a better physical understanding of the interplay between turbulence and oscillations than with the direct numerical implementation of the Lagrangian stochastic model, and additionally, to derive analytical prescriptions for this coupling, something which is, by nature, never possible with numerical methods. Furthermore, the analytical approach can serve to better understand results obtained numerically, or even to validate the numerical approach in some simplified limit cases. Chapter 8 is devoted to these analytical developments.

Concerning the numerical approach, I set out to numerically implement the forward integration in time of the Lagrangian stochastic model, in the simplified case mentioned above, corresponding to the Simplified Langevin Model, in conjunction with the Smoothed Particle Hydrodynamics formalism presented in Section 7.2.4 for the estimation of the mean fields. I show that normal modes of oscillation can be directly extracted from such a simulation, and their line profile resolved in the 'observed' power spectrum. This allows for a direct determination of the frequency, amplitude and linewidth of these modes. The motivations behind this numerical implementation are based on the fact that it allows for the inclusion of much more complex physics than analytical developments; in addition, it allows to properly quantify the analytical prescriptions; not to mention the fact that the numerical approach can help validate the analytical approach: in that regard, both truly benefit from each other. Chapter 9 is devoted to this numerical implementation. I conclude, in the end of this part, on the many perspectives opened by this work.

8 Lagrangian stochastic model for turbulence-oscillation coupling: analytical approach

Contents

> Dip a person into one particular specialty deeply enough and long enough, and he would automatically begin to assume that specialists in all other fields were magicians, judging the depth of their wisdom by the breadth of his own ignorance...
>
> Isaac Asimov

In Section 7.2, I introduced Lagrangian PDF methods as a way to model turbulence through the joint PDF of the random variables describing the flow. More specifically, I showed how these methods can be implemented, in practice, by means of Lagrangian stochastic models, i.e. stochastic differential equations designed to model the evolution of individual fluid particles, which are used to represent the flow. My goal, in this chapter, is to use a Lagrangian stochastic model of turbulence to build a new theoretical formalism specifically tailored to study the impact of turbulent convection on solar-like oscillations. As I mentioned in Section 7.2, this requires the Lagrangian stochastic models introduced in Chapter 7 to be adapted to stellar turbulent convection. In broad strokes, I start from the Refined Langevin Model introduced in Section 7.2.3, and lift several hypotheses pertaining to this model. More specifically, I allow the flow to be compressible, which requires an adaptation of stochastic differential equations (SDE) governing the evolution of the velocity and turbulent frequency associated to the individual fluid particles. In turn, the modification to the velocity equation makes it necessary to add a thermodynamic variable to the quantities required to determine the state of a given fluid particle, in the form of the internal energy. As a result, a new SDE must be derived for the internal energy. Identifying the *modelled* Reynolds-averaged equations

– i.e. the mean equations to which this modified Lagrangian stochastic model reduces – with their *exact* counterparts – i.e. those derived from first principles – allows for the determination of the coefficients appearing in the stochastic equations. These constitute, very schematically, the main step of the derivation; the interesting reader can find all the details in Appendix B. However, for the sake of simplicity, I will base all analytical developments in the remainder of this chapter on a much lighter Lagrangian stochastic model, corresponding to a compressible version of the Simplified Langevin Model (see Section 8.1.1). This is only done as a first step, for illustration purposes.

This new formalism is built in three parts, which constitute the three sections into which this chapter is divided. In Section 8.1, I linearly perturb the starting Lagrangian stochastic model, in order to obtain a linear, stochastic wave equation designed to govern the time evolution of the oscillations, while at the same time directly and consistently containing the effect of the turbulent behaviour of the flow. By construction, such a wave equation naturally contains the information on the turbulence-oscillation coupling. It constitutes the baseline framework in which the rest of the formalism can be developed. This section is the subject of an article that has been published in Astronomy and Astrophysics (Philidet et al. 2021), and which is reproduced in the end of this chapter. As such, I will not present all of the details of the calculations in the body of this thesis, as this would be redundant. Instead, I focus on the main steps of the derivation, and especially the physical assumptions underlying this derivation.

It was shown by Buchler and Goupil (1984) that the partial differential equations governing the physics of stellar oscillations can be dimensionally reduced to a small set of ordinary differential equations governing the complex amplitudes of a limited number of resonant modes, in the scope of the *Amplitude Equation formalism*. The authors later showed, in Buchler et al. (1993), how the effect of the stochastic, convective noise can be included consistently in the Amplitude Equation formalism, thus yielding stochastic differential equations for the complex amplitudes of the modes. In particular, they showed how the exact stochastic amplitude equations can be reduced to a much simpler form, called *simplified amplitude equations*, containing the same statistical information, while being much easier to handle. This is done first by deriving the Fokker-Planck equation equivalent to the stochastic amplitude equations; and then by exploiting the fact that there are an infinity of stochastic models that reduce to the exact same Fokker-Planck equations, so that the original amplitude equations can be replaced by much simpler ones, containing the same amount of one-time statistical information. Originally, this formalism was developed to study the non-linear mode coupling that can occur in classical pulsators, where the oscillations are intrinsically unstable, i.e. self-excited. However, this formalism is also perfectly adapted to the case of non-adiabatic linear oscillations in interaction with turbulence, as is the case of solar-like oscillations. What is more, it allows to extract, from the full wave equation, more specific information regarding the resonant modes, including their amplitude, their damping rate, and the shift undergone by their frequency because of the stochastic noise in the wave equation. I detail the principles behind the Simplified Amplitude Equations formalism, and apply it to the linear case, in Section 8.2. Finally, in Section 8.3, I apply this formalism to the wave equation derived in Section 8.1. The advantages of this method are tightly related to the pros listed in Section 7.3. More specifically, 1) it does not initially rely on a separation between convection equations and oscillation equations, but instead encompasses both components, and therefore naturally contains their coupling, 2) it avoids the reduction of spatial and timescales in the problem to a unique scale, thus allowing for the full description of the turbulent cascade, 3) it simultaneously describes all aspects of the coupling between turbulent convection and solar-like oscillations – their excitation rate stemming from stochastic driving, their linear damping rate, as well as the frequency shift incurred by these modes under the influence of turbulent convection (in other words, the surface effects[1]) –, and 4) it includes the properties of turbulence directly, which allows to easily relate the predicted properties of the modes to the input physics of turbulence. This method will allow, in the long run, to properly infer properties of turbulence-oscillation coupling, and therefore to properly constrain the properties of turbulent convection itself, from asteroseismic observations.

[1] For the moment, because I consider a simplified Lagrangian stochastic model, only the adiabatic part of the surface effects is accounted for, i.e. the contribution from turbulent pressure. This is not a limitation of the method however, and eventually all contributions to surface effects can be described in this formalism.

8.1 The stochastic wave equation for solar-like oscillations

8.1.1 The stochastic model in closed form

A lighter version of the Lagrangian stochastic model

My first short-term goal, in tackling the analytical part of this project, is to prove that the present approach is relevant to the study of turbulence-oscillation coupling. As such, the theoretical developments presented in this chapter serve as a proof of concept for this approach, so that I deliberately choose not to use the most realistic Lagrangian stochastic model possible. Instead, I wish to limit the level of complexity of the model so that the basics of the method may be understood as efficiently as possible. In that spirit, I start not from the Lagrangian stochastic model presented in Appendix B, but from a much lighter version, corresponding to a compressible version of the Generalised Langevin Model, and given by

$$\mathrm{d}x_i^\star = u_i^\star \ \mathrm{d}t \ , \tag{8.1}$$

$$\mathrm{d}u_i^\star = \left[-\frac{1}{\overline{\rho}} \frac{\partial \overline{p}}{\partial x_i} + g_i + G_{ij} \left(u_j^\star - \widetilde{u}_j \right) \right] \mathrm{d}t + \sqrt{C_0 \omega_t k} \ \mathrm{d}W_i \ , \tag{8.2}$$

where I leave the drift tensor unspecified for the moment, and only recall (see Section 7.2.2) that in general it is written as a function of the Reynolds stress tensor, mean shear tensor, and turbulent dissipation rate

$$G_{ij} = f\left(\widetilde{u_i'' u_j''}, \partial_i \widetilde{u}_j, \epsilon \right) \ , \tag{8.3}$$

and I also recall that the turbulent dissipation rate is related to the turbulent frequency through $\epsilon = \omega_t k = \omega_t \ \widetilde{u_i'' u_i''}/2$.

Adopting this model implies two important assumptions. The first one consists in *simplifying the description of the thermodynamic state of the gas by adopting a polytropic relation between the gas pressure and density*. Compared to the model presented in Appendix B, this amounts to replacing the ideal gas law (Equation B.15) by

$$\ln\left(\frac{\overline{p}}{p_0} \right) = \gamma \ln\left(\frac{\overline{\rho}}{\rho_0} \right) \ , \tag{8.4}$$

where γ is the polytropic index associated to the relation, and ρ_0 and p_0 are the equilibrium density and gas pressure, defined as averages of the fluid density and gas pressure over timescales longer than both the turbulent timescale and the period of the oscillations. Such a polytropic relation is relevant, for instance, in regions where the convective transport is very efficient, and the instantaneous temperature gradient can be considered to be equal to the adiabatic gradient at all times (see Section 1.1.1 for definitions). Note that γ is not an intrinsic thermodynamic property of the gas itself, but a property of the thermodynamic transformations undergone by the gas in the specific, extrinsic conditions prevailing in the flow under consideration. For instance, if one considers that these transformations are adiabatic, then one has $\gamma = \Gamma_1$, where the first adiabatic exponent Γ_1, unlike γ, is a thermodynamic property of the gas itself. This was, however, only an example: for the moment, I do not specify γ. On the other hand, both ρ_0 and p_0 are considered known, in which case $\overline{p}$ is a function of $\overline{\rho}$ and γ only. This simplification of the thermodynamic description of the gas also leads me to discard the term proportional to the internal energy fluctuation in the velocity equation, in which case the stochastic quantity $e^\star$, and *a fortiori* the energy SDE, is no longer needed.

The second assumption consists in simplifying the temporal behaviour of turbulence, and in particular discarding internal intermittency, by reducing the turbulent frequency to a fixed, time-independent value of ω_t, externally input in the model. Compared to the model presented in Appendix B, this amounts to replacing every occurrence of $\omega_t^\star$ and $\widetilde{\omega}_t$ by ω_t, in which case the turbulent frequency SDE is no longer needed. However, I still allow the mean turbulent frequency ω_t to depend on $\mathbf{x}$. These two approximations are important ones; I discuss them further in a later part of this section (see hypotheses H6 and H7 below).

From Lagrangian to Eulerian variables

I mentioned earlier, in Section 7.3, that one of the strengths of Lagrangian stochastic models is the fact that the non-linear advection terms are modelled exactly, due to the Lagrangian nature of these models. While this is

extremely important in numerical implementations – as I will show in Chapter 9 –, when it comes to analytically handling this sort of model, it is unfortunately necessary to switch from a Lagrangian point of view to an Eulerian point of view. Indeed, in order to obtain a wave equation where the wave variables can be easily related to the observed properties of the modes, one must ensure that the stochastic variables pertain to the stochastic properties of the flow at a fixed point, and not to fluid particles followed along their trajectories. Otherwise stated, I must perform a change of variables, from the Lagrangian $\mathbf{x}^\star$ and $\mathbf{u}^\star$ to properly defined Eulerian counterparts. The necessity to change variables also shows in the absence of an advection term in Equation 8.2: in the Lagrangian frame, the turbulent pressure does not appear in the momentum equation. But, as I showed in Section 2.2.2, and more generally throughout Part II, the fluctuations of the turbulent pressure gradient is precisely responsible for the stochastic driving of solar-like oscillations. This illustrates the inadequacy of the Lagrangian frame to describe the oscillations[2].

A very general approach to this change of variables is the *Lagrangian-mean trajectories* formalism (Soward 1972; Andrews and McIntyre 1978). Essentially, the Lagrangian position of the fluid particles is decomposed into an average position $\mathbf{x}$ and a fluctuating position $\boldsymbol{\xi}$. Since I am interested in the coupling between the turbulent and oscillatory components of the flow, *it is necessary that both components be simultaneously contained in the fluctuating position* $\boldsymbol{\xi}$*, leaving only the static background state in the average part* $\mathbf{x}$. In that regard, the generality of the Lagrangian-mean trajectories formalism is a crucial asset, because *it allows the averaging process leading to the separation between* $\mathbf{x}$ *and* $\boldsymbol{\xi}$ *to be defined however one wishes*: it can be an ensemble average, a time average, a horizontal average... Seeing as I wish the turbulence *and* the oscillations to be encompassed in the fluctuating part, I chose to use a time average over very long timescales – i.e. long compared both to the period of the modes and to the typical turn-over time of the turbulent eddies. As a result, the mean part does indeed correspond to the static equilibrium state of the star, while the fluctuations contain both the turbulent motions and the oscillations. This decomposition allows me to treat $\mathbf{x}$ as a *fixed, Eulerian position*, with respect to which all the other quantities can be described in the Eulerian frame, while $\boldsymbol{\xi}$ represents a *fluid displacement at* $\mathbf{x}$*, containing both the displacement due to the oscillations and the displacement due to the turbulent motions, and is interpreted as an Eulerian variable*. Furthermore, the velocity of the fluid particles is now regarded as the Eulerian velocity of the flow at $\mathbf{x} + \boldsymbol{\xi}$, and naturally becomes a Eulerian variable. Therefore, the Lagrangian variables $\mathbf{x}^{(i)\star}(t)$ and $\mathbf{u}^{(i)\star}(t)$, indexed by the integer i identifying each fluid particle, are substituted by the Eulerian variables[3] $\boldsymbol{\xi}(\mathbf{x}, t)$ and $\mathbf{u}(\mathbf{x} + \boldsymbol{\xi}(\mathbf{x}, t), t)$, indexed by the Eulerian space variable $\mathbf{x}$. I note, in particular, that by construction, the time average of both these variables is zero, while the fluctuation around the time average *simultaneously* contains the turbulent *and* oscillatory motions. This change of variables must be carried out in Equations 8.1 and 8.2: this is done in details in Section 2.2.1 of Philidet et al. (2021), to which I refer the interested reader if need be. Eventually, I find (see Philidet et al. 2021, Eqs. 25 and 26)

$$\frac{\partial \xi_i}{\partial t} = u_i(\mathbf{x} + \boldsymbol{\xi}, t) \,, \tag{8.5}$$

$$\frac{\partial u_i}{\partial t} + u_j \frac{\partial u_i}{\partial x_j} = -\frac{1}{\overline{\rho}} \frac{\partial \overline{p}}{\partial x_i} + g_i + G_{ij}\left(u_j - \widetilde{u}_j\right) + \sqrt{C_0 \omega_t k}\, \eta_i \,, \tag{8.6}$$

where η_i ($i = 1, 2, 3$) are the "time derivatives" of three independent Wiener processes (see beginning of Section 7.1.3 for more details). It must be noted that while the velocity appearing in the right-hand side of Equation 8.5 is evaluated at the Lagrangian position $\mathbf{x} + \boldsymbol{\xi}(\mathbf{x}, t)$, every mean quantity in Equation 8.6, by contrast, is evaluated at the Eulerian position $\mathbf{x}$. In this new Eulerian version, the velocity SDE now makes the turbulent pressure contribution explicitly appear, in the form of the advection term in the left-hand side of Equation 8.6.

Evaluating the mean fields

The only quantities left to close in this model are the mean density $\overline{\rho}$, the mean velocity $\widetilde{\mathbf{u}}$, and the Reynolds stress tensor $\widetilde{u_i'' u_j''}$ – which appears both in the turbulent kinetic energy k in the velocity diffusion coefficient, and in

[2] This statement may seem odd, as Lagrangian variables are actually often used in the analysis of stellar oscillations (see Section 2.1). However, here, the term Lagrangian refers to a frame of reference attached to the *total velocity* of the flow, including both the turbulent velocity and the oscillation velocity, while the usual sense is rather meant to describe a frame attached to the oscillations alone, and actually only ever refers to a *pseudo-Lagrangian* frame.

[3] Knowing the latter for any position $\mathbf{x}$ is, as I had the opportunity to point out in the very beginning of Appendix A, perfectly equivalent to knowing $\mathbf{u}(\mathbf{x}, t)$ for any position $\mathbf{x}$. Therefore, the new velocity variable is none other than the Eulerian velocity.

the drift tensor G_{ij}. I make use of the Smoothed Particle Hydrodynamics (or SPH) method to evaluate the means, as I explained in the framework of the particle representation in Section 7.2.4. However, this formalism ought to be adapted to the change of variables described above, which is done in Section 2.2.2 of Philidet et al. (2021). This yields

$$\overline{\rho}(\mathbf{x},t) = \int \mathrm{d}^3\mathbf{y}\, \rho_0(\mathbf{y})\, K(\mathbf{y}+\boldsymbol{\xi}(\mathbf{y},t)-\mathbf{x})\,, \tag{8.7}$$

$$\widetilde{\mathbf{u}}(\mathbf{x},t) = \frac{1}{\overline{\rho}(\mathbf{x},t)} \int \mathrm{d}^3\mathbf{y}\, \rho_0(\mathbf{y})\, \mathbf{u}(\mathbf{y}+\boldsymbol{\xi}(\mathbf{y},t),t) K(\mathbf{y}+\boldsymbol{\xi}(\mathbf{y},t)-\mathbf{x})\,, \tag{8.8}$$

$$\widetilde{u_i'' u_j''}(\mathbf{x},t) = \frac{1}{\overline{\rho}(\mathbf{x},t)} \int \mathrm{d}^3\mathbf{y}\, \rho_0(\mathbf{y}) \Big(u_i(\mathbf{y}+\boldsymbol{\xi}(\mathbf{y},t),t) - \widetilde{u_i}(\mathbf{y},t)\Big)\Big(u_j(\mathbf{y}+\boldsymbol{\xi}(\mathbf{y},t),t) - \widetilde{u_j}(\mathbf{y},t)\Big) K(\mathbf{y}+\boldsymbol{\xi}(\mathbf{y},t)-\mathbf{x})\,, \tag{8.9}$$

where the integrals formally span across the entire volume of the star, but actually only involve the compact support vicinity of $\mathbf{x}$ defined by the kernel function K. Equations 8.7 to 8.9 give an estimation of the mean fields as a function of the Eulerian variables $\boldsymbol{\xi}(\mathbf{x},t)$ and $\mathbf{u}(\mathbf{x},t)$ only – in other words, they are now in closed form. I do not specify the explicit form of the kernel function K underlying the SPH formalism; a valid example is given, for instance, by Equation 7.114.

Summary

To summarise, the stochastic variables in the model are the fluid displacement $\boldsymbol{\xi}(\mathbf{x},t)$ and the Eulerian velocity $\mathbf{u}(\mathbf{x},t)$ for every Eulerian position $\mathbf{x}$. The Ito stochastic differential equations governing their evolution are Equations 8.5 and 8.6. The drift tensor G_{ij} is given by Equation 8.3, while the mean gas pressure, density, velocity and Reynolds stress tensor are given by Equations 8.4 and 8.7 to 8.9 respectively. The only external inputs of the model are 1) the equilibrium density $\rho_0(\mathbf{x})$ and gas pressure $p_0(\mathbf{x})$, which can be extracted from an equilibrium model of the star, defined as an average of its structure over a timescale much longer than the turbulent *and* oscillation typical timescales; 2) the polytropic index $\gamma(\mathbf{x})$ (which I allow to depend on space), which is given by specifying the type of thermodynamic transformation undergone by the gas – for instance, in the case of adiabatic transformations, $\gamma = \Gamma_1$, where $\Gamma_1(\mathbf{x})$ can be extracted from an equilibrium model of the star, like ρ_0 and p_0; 3) the functional form of the drift tensor G_{ij} (see Equation 8.3), which I discussed at length in Section 7.2.2; and 4) the equilibrium turbulent frequency $\omega_t(\mathbf{x})$, which acts as a control parameter for turbulence.

8.1.2 Linear perturbation

These equations can then be linearly perturbed around an appropriate zeroth order state, in order to yield a stochastic linear wave equation. This is done in details in Section 3.1 of Philidet et al. (2021). Essentially, I decompose the displacement and velocity variables into a turbulent and an oscillatory components, thus

$$\frac{\partial \boldsymbol{\xi}_{\mathrm{osc}}}{\partial t} - \mathbf{u}_{\mathrm{osc}} - (\boldsymbol{\xi}_{\mathrm{osc}}\cdot\boldsymbol{\nabla})\mathbf{u}_t - (\boldsymbol{\xi}_t\cdot\boldsymbol{\nabla})\mathbf{u}_{\mathrm{osc}} = (\boldsymbol{\xi}_t\cdot\boldsymbol{\nabla})\mathbf{u}_t\,, \tag{8.10}$$

$$\mathbf{u}(\mathbf{x},t) = \mathbf{u}_t(\mathbf{x},t) + \mathbf{u}_{\mathrm{osc}}(\mathbf{x},t)\,. \tag{8.11}$$

Eventually, and under a set of assumptions and approximations that I explicitly discuss below, I find the following wave equation

$$\frac{\partial \boldsymbol{\xi}_{\mathrm{osc}}}{\partial t} - \mathbf{u}_{\mathrm{osc}} - (\boldsymbol{\xi}_{\mathrm{osc}}\cdot\boldsymbol{\nabla})\mathbf{u}_t = \mathbf{0}\,, \tag{8.12}$$

$$\frac{\partial \mathbf{u}_{\mathrm{osc}}}{\partial t} - \mathbf{L}_1^d - \mathbf{L}_1^s = \mathbf{L}_0\,, \tag{8.13}$$

where

$$L_{1,i}^d = \left[\frac{1}{\rho_0}\frac{\partial p_0}{\partial x_i} - \frac{\partial c_0^2}{\partial x_i}\right]\frac{1}{\rho_0}\int \mathrm{d}^3\mathbf{y}\, \rho_0(\mathbf{y})\left(\xi_{\mathrm{osc,j}}\partial_j K^{\mathbf{x}}\right)\Big|_{\mathbf{y},t} + \frac{c_0^2}{\rho_0}\int \mathrm{d}^3\mathbf{y}\, \rho_0(\mathbf{y})\left(\xi_{\mathrm{osc,j}}\partial_j\partial_i K^{\mathbf{x}}\right)\Big|_{\mathbf{y},t}$$
$$+ G_{ij,0}\left(u_{\mathrm{osc,j}} - \frac{1}{\rho_0(\mathbf{x})}\int \mathrm{d}^3\mathbf{y}\, \rho_0(\mathbf{y}) u_{\mathrm{osc,j}}(\mathbf{y}) K^{\mathbf{x}}(\mathbf{y})\right)\,, \tag{8.14}$$

$$L^s_{1,i} = -u_{\mathrm{osc,j}}\partial_j u_{t,i} - u_{t,j}\partial_j u_{\mathrm{osc,i}} - G_{ij,0}\frac{1}{\rho_0}\int \mathrm{d}^3\mathbf{y}\,\rho_0(\mathbf{y})\left(\xi_{\mathrm{osc,k}}\partial_k\left(u_{t,j}K^{\mathbf{x}}\right)\right)\Big|_{\mathbf{y},t} + \left(\frac{\partial G_{ij}}{\partial\widetilde{u''_k u''_l}_1}\widetilde{u''_k u''_l}_1 + \frac{\partial G_{ij}}{\partial(\partial_k\widetilde{u}_l)}\partial_k\widetilde{u}_l + \frac{\partial G_{ij}}{\partial\epsilon}\omega_t k_1\right)u_{t,j} + \frac{1}{2}\sqrt{\frac{C_0\omega_t}{k_0}}k_1\eta_i\,, \tag{8.15}$$

$$L_{0,i} = -\frac{1}{\rho_0}\frac{\partial\left(\rho_0 u_{t,i}u_{t,j} - \rho_0\overline{u_{t,i}u_{t,j}}\right)}{\partial x_j}\,, \tag{8.16}$$

$c_0^2 \equiv \gamma p_0/\rho_0$ is the equilibrium sound speed, $G_{ij,0}$ and k_0 are the equilibrium drift tensor and turbulent kinetic energy respectively, the fluctuation of the Reynolds stress tensor, turbulent kinetic energy and mean shear tensor $\widetilde{u''_k u''_l}_1$, $\partial_k\widetilde{u}_{l1}$ and k_1 are respectively given by Eqs. C.15, C.11 and C.16 in Philidet et al. (2021), and I have introduced the $\mathbf{x}$-centered kernel function $K^{\mathbf{x}}(\mathbf{y}) \equiv K(\mathbf{y}-\mathbf{x})$. Formally, Equations 8.12 and 8.13 take the form of a linear, stochastic, inhomogeneous wave equation in a completely closed form, in the sense that the various terms on their right-hand side are written as explicit functions of the wave variables $\boldsymbol{\xi}_{\mathrm{osc}}$ and $\mathbf{u}_{\mathrm{osc}}$ themselves or the turbulent fields $\boldsymbol{\xi}_t$ and $\mathbf{u}_t$, whose statistical properties are considered known (see hypothesis H4 below). In writing Equation 8.13, I have split the velocity equation into three components. $\mathbf{L}_1^d$ contains all the terms that are linear in $\boldsymbol{\xi}_{\mathrm{osc}}$ and $\mathbf{u}_{\mathrm{osc}}$ but do not explicitly contain either stochastic processes $\boldsymbol{\xi}_t$, $\mathbf{u}_t$ and $\boldsymbol{\eta}$. It represents the deterministic contribution to the homogeneous part of the wave equation, and corresponds to the classical propagation of acoustic waves, without any impact from the turbulence. On the other hand, $\mathbf{L}_1^s$ contains all the terms that are linear in $\boldsymbol{\xi}_{\mathrm{osc}}$ and $\mathbf{u}_{\mathrm{osc}}$ and explicitly depend on $\boldsymbol{\xi}_t$, $\mathbf{u}_t$ or $\boldsymbol{\eta}$. It represents the turbulence-induced perturbation to the linear operator describing the propagation of the waves, and encompasses the effect of turbulent convection on both the damping of the modes and their frequency. Finally, $\mathbf{L}_0$ contains all the terms that are independent from $\boldsymbol{\xi}_{\mathrm{osc}}$ and $\mathbf{u}_{\mathrm{osc}}$. It represents all inhomogeneous forcing terms, and encompasses the driving source of the modes.

8.1.3 Hypotheses and approximations

In order to obtain this linear, stochastic wave equation, a number of hypotheses were assumed. These are extensively discussed in Philidet et al. (2021), but since this is an important part of the discussion, I reproduce them here. (H1) through (H5) pertain to the linearisation process, while (H6) through (H8) concern the elaboration of the stochastic model itself

(H1) I considered $|\mathbf{u}_{\mathrm{osc}}| \ll |\mathbf{u}_t|$. This ordering is justified by the fact that, at the top of the convective envelope of solar-like oscillators, the typical turbulent velocities have much higher amplitudes than the oscillatory velocities, with the former being of the order of a few km.s^{-1}, while the latter are of the order of a few tens of cm.s^{-1}. This allows to treat $\mathbf{u}_{\mathrm{osc}}$ as a first-order perturbation compared to $\mathbf{u}_t$, and any second- or higher-order occurrence of $\mathbf{u}_{\mathrm{osc}}$ will be discarded;

(H2) I considered $|\boldsymbol{\xi}_{\mathrm{osc}}| \ll h, H_p$, where I recall that h is the size of the averaging kernel function K, and $H_p \equiv -(\mathrm{d}\ln p_0/\mathrm{d}r)^{-1}$ is the pressure scale height. In other words, the modal fluid displacement is assumed to be much smaller than the stratification length scale, and the width of the kernel function must be sufficiently large. The first hypothesis is justified by the fact that, in the Sun for instance, the modal displacement is of the order of a few tens of meters, while H_p is of the order of a few hundreds of kilometers. The second hypothesis, on the other hand, constitutes a constraint on h. This allows to treat $\boldsymbol{\xi}_{\mathrm{osc}}$ as a first-order perturbation compared to all length scales relevant to the problem, and any second- or higher-order occurrence of $\boldsymbol{\xi}_{\mathrm{osc}}$ will be discarded;

(H3) I adopted the *anelastic approximation* for turbulence, in the sense that I considered $\rho_t \ll \rho_0$, where ρ_t is the turbulent fluctuation of density, and ρ_0 the equilibrium density. This is the most severe approximation I make in this section. Nevertheless, the anelastic approximation is widely used in analytical models of turbulent convection, on the grounds that the flow is subsonic (with turbulent Mach numbers peaking at around 0.3 in the superadiabatic region), as shown by 3D hydrodynamic simulations of the atmosphere of these stars (Nordlund et al. 2009). Using the continuity equation, this amounts to neglecting the quantity $\boldsymbol{\nabla}\cdot(\rho_0\boldsymbol{\xi}_t)$. As will become apparent in the following, this allows to discard all $\boldsymbol{\xi}_t$-dependent contributions in the linearisation of the ensemble averages in the SPH formalism;

(H4) I considered that the turbulent fields $\boldsymbol{\xi}_t$ and $\mathbf{u}_t$ are the same as what they would be without the presence of an oscillating displacement $\boldsymbol{\xi}_{\text{osc}}$ and velocity $\mathbf{u}_{\text{osc}}$ – in other words, I neglected the back-reaction of the oscillations on the turbulent motions of the gas. I justify this approximation in Appendix B of Philidet et al. (2021). This assumption allows to consider $\boldsymbol{\xi}_t$ and $\mathbf{u}_t$ as an input to the model, whose statistical properties – average, covariance, autocorrelation function – are considered completely known;

(H5) I considered that the gravitational potential is perturbed neither by the turbulent motions of the gas, nor by its oscillatory motions. Those are actually two separate approximations. The first one is justified by the fact that the Reynolds-averaged mass flow through any given horizontal layer due to turbulence is zero, meaning the total mass present beneath this layer is always the same. The second one corresponds to the Cowling approximation, and is justified for modes that feature a large number of radial nodes. These two approximations put together allow to replace the gravitational acceleration $\mathbf{g}$ by its equilibrium value $\mathbf{g}_0$, which only depends on the hydrostatic equilibrium of the star;

(H6) I considered the flow to be adiabatic, in the sense that the only fluid particle properties that need to be described in the Lagrangian stochastic model are the position and velocity of the particles. In the scope of this hypothesis, the energy equation is replaced with a relation between the mean density and pressure that I chose to be polytropic, without specifying the associated polytropic exponent γ. That means that the non-adiabatic effects pertaining to the oscillations are not contained in the formalism presented in this chapter. This includes the perturbation of the convective flux and the radiative flux by the oscillations, which are in reality susceptible to affect the damping rate of the modes as well as the surface effects. Avoiding hypothesis (H6) would allow for the inclusion of all non-adiabatic effects in the model. This can be done, for instance, by starting from the more refined Lagrangian stochastic model presented in Appendix B;

(H7) I considered that the turbulent frequency ω_t – defined as the ratio of the dissipation rate ϵ with the turbulent kinetic energy k – takes a constant value. The turbulent frequency represents the rate at which k would decay towards zero if there was no production of turbulence whatsoever, and can be interpreted as the inverse lifetime of the energy-containing turbulent eddies. In essence, this amounts to assuming the existence of a single timescale associated to the entire turbulent cascade, which is at odds with even the simplest picture of turbulence. Avoiding hypothesis (H7) would allow for a much more realistic modelling of the turbulent dissipation and its perturbation by the oscillations, which is susceptible to play an important role in both mode damping and surface effects. This can be done, for instance, by starting from the more refined Lagrangian stochastic model presented in Appendix B;

(H8) I considered that the time average of the flow velocity over a very long time – in other words the velocity associated to the equilibrium background – is zero. This amounts to neglecting rotation, whether in be global or differential. Taking rotation into account would require either a non-zero velocity field to be included in the Lagrangian-to-Eulerian change of variables described above, or else a Coriolis inertial force to be added in the velocity SDE.

Hypotheses (H1), (H2) and (H4) are fundamental in building the formalism, and cannot be avoided, but they are also firmly and physically grounded. Hypotheses (H3) and (H5) are simplifying assumptions that are not strictly speaking necessary, nor as clearly valid, but which are unavoidable given the current state of our capabilities. Finally, hypotheses (H6), (H7) and (H8) are also simplifying assumptions, and are very much invalid; however, I adopted them here to provide with a simple framework serving as a proof-of-concept for the formalism presented in this chapter. In particular, hypotheses (H6) and (H7) must be discarded as soon as possible if one wishes to adopt a realistic model of turbulence. As regards these hypotheses, I insist on the fact, of particular importance in this model, that *none of them concern the mean fields; indeed, a linearised form of these mean fields naturally arises from the SPH formalism and the hypotheses (H1) through (H4).*

8.2 Simplified amplitude formalism: the general framework

The linear stochastic wave equation comprised of Equations 8.12 and 8.13 forms the baseline framework in which the observed properties of solar-like oscillations can be related to the underlying physics of turbulent convection. More specifically, the inhomogeneous forcing term $\mathbf{L}_0$ given by Equation 8.16 – and its counterpart in

the displacement equation – contains the information on the stochastic driving of the modes, while the stochastic perturbation to the propagative linear operator $\mathbf{L}_1^s$ given by Equation 8.15 contains the joint effect of mode damping and surface effects. However, both are of stochastic nature, so that a large part is actually incoherent or statistically uncorrelated with the oscillating modes themselves[4]. It is therefore necessary to filter the part of these stochastic perturbations to the wave equation that indeed leads to a significant impact on the modes. This can be done in the framework of the *Simplified Amplitude Equation* formalism. It is the goal of this section to introduce this formalism, and in particular to apply it to the case of *linear stellar oscillations*.

The Simplified Amplitude Equation formalism was developed by Stratonovich (1965) (who is one of the founding fathers of stochastic process theory) to describe the effect of noise on harmonic oscillators in the most general case – although his interest in building this formalism was primarily concerned with the effect of noise in electrical circuitry, and its impact on the transfer of information. It was later applied, by Buchler et al. (1993), to the case of stellar pulsations impacted by convective noise. However, the authors' motivation was to study the non-linear coupling between distinct oscillating modes, while in the present case, I am interested in the linear limit of this formalism, where each mode can be studied individually, in isolation from each other. The philosophy behind this formalism can be divided into two distinct parts

- first, the full stochastic wave equation derived in Section 8.1 can be transformed into a finite set of ordinary differential equations governing the evolution of the *complex* amplitudes of a few normal modes of oscillation of the star. This can be done by treating the stochastic part of the wave equation as perturbations to an otherwise deterministic wave equation. This leads to the *amplitude equations* (Buchler and Goupil 1984);

- because the perturbations are stochastic, the amplitude equations are also stochastic. However, they are very impractical to handle, both analytically and numerically. The reason is that the stochastic part of the amplitude equation has a finite memory time which involves a large, continuous range of timescales: the process it describes is therefore not a Markov process (see Section 7.1.2 for a definition). However, the exact stochastic amplitude equation can be transformed into an equivalent *simplified* amplitude equation, which does describe a Markov process, and where the effect of the finite memory time is incorporated in a rigorous manner in the drift and diffusion coefficients of the stochastic amplitude equations. This procedure is carried out in two stages: first the stochastic amplitude equation can be substituted for an equation for the PDF of the complex amplitude of the modes, in the form of a Fokker-Planck equation; then, from this Fokker-Planck equation, another stochastic differential equations on the complex amplitude of the modes can be deduced, under the constraint that it must be equivalent to the exact same Fokker-Planck equation, while only involving Markov processes.

The procedure outlined here can be summarised thus: 1) the full amplitude equations are derived directly from the stochastic model previously described, which is done in Section 8.2.1; then 2) the equivalent Fokker-Planck equation is deduced, whose drift and diffusion coefficients properly encompass the full effect of the finite memory time of the coefficients in the amplitude equations, which is done in Section 8.2.2, after which 3) an alternative set of stochastic differential equations, corresponding to the exact same Fokker-Planck equation, while being much simpler in its form, and only involving Markov stochastic processes, is derived, which is done in Section 8.2.3. The simple form of these simplified amplitude equations makes it possible to derive general analytical results; in particular, I show that their ensemble average directly and simultaneously yields the excitation rate and the damping rate of the mode by the stochastic perturbations, as well as the modal part of the surface effects. This is done in Section 8.2.4.

8.2.1 Amplitude equation for solar-like oscillations

Let me recast the stochastic wave equation in the following, very general form

$$\frac{\mathrm{d}\,|z\rangle}{\mathrm{d}t} = \mathcal{L}(t)\,|z\rangle + |\Theta(t)\rangle \ , \tag{8.17}$$

[4]Here, I mean the word *incoherent* in the wave physics sense of the term, i.e. meaning that two signals operate at lengths or timescales too different from each other to allow for an efficient interaction between the two. Since, as I had the opportunity to point out in Section 1.2.1, high-Reynolds-number flows exhibit a wide range of such scales, it is only natural that only a small portion of it should be able to effectively couple with solar-like p-modes. Likewise, two phenomenon have to be *statistically correlated* to be able to interact with each other.

where $|.\rangle$ denotes a ket in Dirac notation, $\mathcal{L}$ is a stochastic linear operator in the Hilbert space describing the oscillations, and $|\Theta\rangle$ is a stochastic vector in this space, both of which are discussed below. In this section, I do not specify the physical content of the ket $|z\rangle$, the nature of the Hilbert space in which it lies, the linear operator $\mathcal{L}(t)$ or the stochastic ket $|\Theta(t)\rangle$, as this formalism is very general. However, from Section 8.1, the reader should already be aware that the ket $|z\rangle$ contains the fluid displacement $\boldsymbol{\xi}_{\rm osc}$ and oscillatory velocity $\mathbf{u}_{\rm osc}$ at every Eulerian location $\mathbf{x}$ in the star. The Hilbert space in which $|z\rangle$ lies is therefore of infinite dimension. Furthermore, $|z\rangle$ only depends on time, because the space dependence is already contained in the infinite set of Eulerian positions to which pertain each separate component of $|z\rangle$. As a result, $\mathrm{d}/\,\mathrm{d}t$ is a *total* time derivative, not partial. $\mathcal{L}(t)$ is a time-dependent linear operator, which can be further decomposed into an average, deterministic, time-independent part $\mathcal{L}^d$, and a zero-mean, stochastic, fluctuating part $\mathcal{L}^s(t)$, so that

$$\mathcal{L}(t) = \mathcal{L}^d + \mathcal{L}^s(t) \,. \tag{8.18}$$

The term in $\mathcal{L}^d$ corresponds to the unperturbed wave equation, without any turbulent fluctuations. Therefore, it models the classical propagation of sound waves in the stellar medium. In turn, $\mathcal{L}^s(t)$ can be thought of as modelling the impact of turbulence on the propagation of these waves. As for $|\Theta(t)\rangle$, it corresponds to the impact of turbulence on the background equilibrium structure itself, and takes the form of an additive noise component to the wave equation.

The stochastic amplitude equations can then be obtained in two steps (Stratonovich 1965): first, a deterministic amplitude equation can be derived as if there were no stochastic perturbations; then the stochastic part can be treated in a perturbative framework, and stochastic corrections added to the deterministic amplitude equations after the fact. First, let me consider the non-perturbed wave equation (Equation 8.17), which is simply

$$\frac{\mathrm{d}\,|z\rangle}{\mathrm{d}t} = \mathcal{L}^d\,|z\rangle \;, \tag{8.19}$$

where $\langle .|.\rangle$ refers to the scalar product in the $|z\rangle$ Hilbert space, and will be explicitly defined in the beginning of Section 8.3. The linear operator $\mathcal{L}^d$ can be diagonalised, and any vector $|z\rangle$ can be decomposed on a basis of eigenvectors for $\mathcal{L}^d$. Because this linear operator is real, the associated eigenvalues are either real, or come in pairs of complex conjugates. Each such pair of eigenvectors with complex-conjugated eigenvalues correspond to a single mode of oscillation of the system, which can be studied in isolation from every other mode. Therefore, let me denote this pair of eigenvectors as $|\Psi\rangle$ and $|\Psi^\dagger\rangle$, and their associated eigenvalues as $\kappa \pm j\omega$. Without loss of generality, I will consider that both eigenvectors are normalised to unity

$$\langle\Psi|\Psi\rangle = \langle\Psi^\dagger|\Psi^\dagger\rangle = 1 \,. \tag{8.20}$$

Limiting the ket $|z\rangle$ to its projection on this oscillating mode, I can write the solution to Equation 8.19 in the following form (Buchler et al. 1993)

$$|z(t)\rangle = \frac{1}{2}a(t)\exp^{j\omega t}\,|\Psi\rangle + \text{c.c} \,, \tag{8.21}$$

where 'c.c' denotes the complex conjugate. In general, $|z\rangle$ would be written as an arbitrary linear combination of $|\Psi\rangle$ and $|\Psi^\dagger\rangle$; however, if $|z\rangle$ is initially real, it is obvious from Equation 8.19 that it will remain real at all later times (because $\mathcal{L}^d$ is Hermitian), so that the $|\Psi^\dagger\rangle$-component of $|z\rangle$ is necessarily the complex conjugate of its $|\Psi\rangle$-component. As for $a(t)$, it denotes the slowly-varying complex amplitude of the mode. Plugging the solution given by Equation 8.21 into Equation 8.19, one finds the following, very simple amplitude equation for $a(t)$

$$\frac{\mathrm{d}a}{\mathrm{d}t} = \kappa a \,. \tag{8.22}$$

As expected, while the imaginary part ω of the eigenvalue associated with the mode represents its oscillatory angular frequency, its real part κ represents the rate at which its amplitude varies – either a growth rate or a damping rate, depending on the intrinsic stability of the mode in the absence of turbulence. In particular, in the adiabatic case, and as I already mentioned in Section 2.3.1, the boundary value problem associated to stellar oscillations forms a Sturm-Liouville problem, so that its eigenvalues $\sigma^2 = (\kappa + j\omega)^2$ are purely real. This means that either $\omega = 0$, or $\kappa = 0$, so that oscillating modes (with $\omega \neq 0$) are characterised by $\kappa = 0$. Otherwise stated, *in the absence of turbulence, adiabatic oscillations are neither damped nor self-excited, and $a(t)$ remains constant.*

In a non-adiabatic framework, however, one has $\kappa \neq 0$, and this quantity contains, for example, the κ-mechanism, γ-mechanism and ϵ-mechanism.

Turning now to the full, stochastically perturbed wave equation (Equation 8.17), it can be seen that the addition of the two terms $\mathcal{L}^s(t)\,|z\rangle$ and $|\Theta(t)\rangle$ leads to the addition of three terms in the amplitude equation (Buchler and Goupil 1984)

$$\mathrm{d}a = \kappa a \ \mathrm{d}t + c_1(t)\exp^{-j\omega t} \ \mathrm{d}t + c_2(t)\ a \ \mathrm{d}t + c_3(t)\ a^\star \exp^{-2j\omega t} \ \mathrm{d}t \ , \tag{8.23}$$

where

$$c_1(t) = 2\,\langle\Psi|\Theta(t)\rangle \ , \tag{8.24}$$
$$c_2(t) = \langle\Psi|\mathcal{L}^s(t)|\Psi\rangle \ , \tag{8.25}$$
$$c_3(t) = \langle\Psi|\mathcal{L}^s(t)|\Psi^\dagger\rangle \ . \tag{8.26}$$

The form of the stochastic linear operator $\mathcal{L}^s(t)$ and stochastic vector $|\Theta(t)\rangle$ being completely specified by the linear stochastic wave equation derived in Section 8.1, the stochastic processes $c_i(t)$ $(i = 1, 2, 3)$ constitute *knowns* of the system. Therefore, the stochastic differential equation given by Equation 8.23 governing the temporal evolution of the complex amplitude of the mode $a(t)$ is in a closed form. It will be more practical, in the following, to separate the complex amplitude of the mode into its real amplitude $A(t)$ and its phase $\Phi(t)$, both being real functions of time, so that

$$a(t) = A(t)\exp^{j\Phi(t)} \ . \tag{8.27}$$

In place of a single complex stochastic equation for the evolution of $a(t)$, I therefore obtain two distinct, real stochastic equations for the evolution of $A(t)$ and $\Phi(t)$, which take the following form

$$\mathrm{d}A = \kappa A \ \mathrm{d}t + \mathrm{Re}\left(c_1(t)\exp^{-j(\omega t+\Phi)}\right) \ \mathrm{d}t + A\mathrm{Re}\left(c_2(t) + c_3(t)\exp^{-2j(\omega t+\Phi)}\right) \ \mathrm{d}t \equiv G(A,\Phi,t) \ \mathrm{d}t \ , \tag{8.28}$$
$$\mathrm{d}\Phi = \frac{1}{A}\mathrm{Im}\left(c_1(t)\exp^{-j(\omega t+\Phi)}\right) \ \mathrm{d}t + \mathrm{Im}\left(c_2(t) + c_3(t)\exp^{-2j(\omega t+\Phi)}\right) \ \mathrm{d}t \equiv H(A,\Phi,t) \ \mathrm{d}t \ , \tag{8.29}$$

where Re and Im denote the real and imaginary parts respectively. Note that the function $G(A,\Phi,t)$ must not be confused with the drift tensor G_{ij} introduced above; the fact that the two will never appear together in the same equation, and that one is a scalar and the other a tensor, should help keep the confusion to a minimum.

8.2.2 The Fokker-Planck equation for mode amplitude

In this section, I do not yet specify the form or the physical content of either $\mathcal{L}^d$, $\mathcal{L}^s(t)$ or $|\Theta(t)\rangle$. The only hypothesis I make concerning the last two quantities is that their correlation timescale is very small compared to the timescale over which the amplitude and the phase of the mode typically vary. The correlation timescale of these stochastic perturbations correspond to the turnover time of the turbulent eddies, which I argued in Section 2.3 is similar to the period of the modes (i.e. $\sim$ 5 minutes in the superficial layers of the Sun). On the other hand, the amplitude and phase of the modes vary over a typical timescale that corresponds to their lifetime, which is indeed much longer than their period ($\tau \sim \eta^{-1} \sim 3$ hours for the shortest-lived solar modes). As such, this hypothesis is largely verified in solar-like oscillators. A consequence of this assumption is that all turbulent, fluctuating terms in the wave equation (Equation 8.17) can be *approximated* by Markov processes (in the sense that their memory time, while finite, is much smaller than the evolution timescale of the amplitude of the mode), and consequently, so can the stochastic processes $A(t)$ and $\Phi(t)$. It is then possible to replace the two stochastic differential equations on these quantities with an equivalent, single Fokker-Planck equation governing the evolution of their joint PDF $w(A,\Phi,t)$, *but whose coefficients are carefully defined to incorporate in a rigorous manner the effect of the finite memory time of the processes* $A(t)$ *and* $\Phi(t)$. The Fokker-Planck equation takes the general form (see Equation 7.28)

$$\frac{\partial w}{\partial t} = -\frac{\partial w\mathcal{G}}{\partial A} - \frac{\partial w\mathcal{H}}{\partial \Phi} + \frac{1}{2}\frac{\partial^2 w\mathcal{D}}{\partial A^2} + \frac{1}{2}\frac{\partial^2 w\mathcal{E}}{\partial A\partial\Phi} + \frac{1}{2}\frac{\partial^2 w\mathcal{F}}{\partial \Phi^2} \ , \tag{8.30}$$

where $\mathcal{G}$ and $\mathcal{H}$ represent the probability fluxes in (A,Φ) space, $\mathcal{D}$ and $\mathcal{F}$ are the diagonal components of the 2×2 symmetric diffusion matrix associated to these processes, and $\mathcal{E}$ is its off-diagonal component. The explicit

derivation of the probability fluxes and diffusion coefficients is detailed in Appendix C, and these coefficients read

$$\mathcal{G}(A) = A\left(\kappa + \alpha_2^R + \frac{3}{2}\mathrm{Re}(\alpha_3)\right) + \frac{1}{2A}\mathrm{Re}(\alpha_1)\,, \tag{8.31}$$

$$\mathcal{H}(A) = \mathrm{Im}(\alpha_3)\,, \tag{8.32}$$

$$\mathcal{D}(A) = A^2\left(2\alpha_2^R + \mathrm{Re}(\alpha_3)\right) + \mathrm{Re}(\alpha_3)\,, \tag{8.33}$$

$$\mathcal{E}(A) = 0\,, \tag{8.34}$$

$$\mathcal{F}(A) = \frac{1}{A^2}\mathrm{Re}(\alpha_1) + 2\alpha_2^I + \mathrm{Re}(\alpha_3)\,, \tag{8.35}$$

where the α_i correspond to the *autocorrelation spectra of the stochastic processes* $c_i(t)$

$$\alpha_1 = \int_{-\infty}^{0} \mathrm{d}\tau\ \left\langle c_1(t)c_1^\star(t+\tau)\right\rangle \exp^{j\omega\tau}\,, \tag{8.36}$$

$$\alpha_2^R = \int_{-\infty}^{0} \mathrm{d}\tau\ \left\langle \mathrm{Re}(c_2(t))\mathrm{Re}(c_2(t+\tau))\right\rangle\,, \tag{8.37}$$

$$\alpha_2^I = \int_{-\infty}^{0} \mathrm{d}\tau\ \left\langle \mathrm{Im}(c_2(t))\mathrm{Im}(c_2(t+\tau))\right\rangle\,, \tag{8.38}$$

$$\alpha_3 = \int_{-\infty}^{0} \mathrm{d}\tau\ \left\langle c_3(t)c_3^\star(t+\tau)\right\rangle \exp^{2j\omega\tau}\,. \tag{8.39}$$

It can already be seen, without having to specify the stochastic processes $c_i(t)$, that their autocorrelation spectra are independent of the two stochastic variables A and Φ. Furthermore, under the assumption that the turbulence characterising the convective motions at the top of the envelope of solar-like oscillators is stationary, the autocorrelation functions appearing in the definition of these coefficients only depend on the time increment τ, and not on the absolute time t. As such, the α_i are also independent of time t. All things considered, *they are therefore simply complex constants*.

8.2.3 Simplified amplitude equations

As I have mentioned above, either the stochastic differential equations given by Equations 8.28 and 8.29 together, or the Fokker-Planck equation (Equation 8.30), both of which are equivalent to one another, can be used to model the time evolution of the real amplitude and phase of a given mode. However, both are equally impractical to use, albeit for different reasons. Numerically integrating the stochastic equation proves extremely expensive, because a large range of very different timescales must be resolved. Indeed, the total integration time must far exceed the typical timescale of the slowly-varying mode amplitude. But at the same time, the rapidly-varying phase ωt appearing in Equation 8.23 must be accurately resolved. Finally, the whole range of memory timescales associated to the processes $c_i(t)$ must also be resolved, which is problematic, as it corresponds to the range of timescales in the turbulent cascade, and is therefore very wide in high Reynolds number flows (see Section 1.2.1 for more details). Consequently, the numerical integration of Equations 8.28 and 8.29 requires an unreasonably small time step compared to the total integration time. By contrast, the Fokker-Planck equation (Equation 8.30) does not have this timescale problem. Indeed, in computing its probability fluxes and diffusion coefficients, I have filtered out all rapidly-oscillating features (see Appendix C), and as such, the numerical integration of the Fokker-Planck equation does not require these very short timescales to be resolved. However, it poses other difficulties inherent to the integration of Fokker Planck equations in general, and which I already had the opportunity to mention in Chapter 7. In brief, because the PDF w is a function of the entire parameter space (i.e. not only of time, but also of the two stochastic variables A and Φ), its numerical integration would require the discretisation of all three variables. For that reason, it is usually very impractical to directly integrate the Fokker-Planck equation in time.

Fortunately, while a given stochastic differential equation is equivalent to a unique Fokker-Planck equation, the inverse is not true. Indeed, there exists an infinite number of stochastic models for the mode amplitude A and phase Φ which possess the same Fokker-Planck equation (Equation 8.30), and therefore contain the exact same statistical information on A and Φ as Equations 8.28 and 8.29, while having a much simpler form. Those are the

simplified amplitude equations (Stratonovich 1965)

$$\mathrm{d}A = \left(\mathcal{G} - \frac{1}{4}\frac{\partial \mathcal{D}}{\partial A}\right)\,\mathrm{d}t + \sqrt{\mathcal{D}}\,\mathrm{d}W_A\,, \tag{8.40}$$

$$\mathrm{d}\Phi = \left(\mathcal{H} - \frac{1}{4}\frac{\partial \mathcal{F}}{\partial \Phi}\right)\,\mathrm{d}t + \sqrt{\mathcal{F}}\,\mathrm{d}W_\Phi\,, \tag{8.41}$$

where $\mathrm{d}W_A$ and $\mathrm{d}W_\Phi$ are the increments of two independent Wiener processes over the time step $\mathrm{d}t$. Let me remark that in writing Equations 8.40 and 8.41, I made use of Equation 8.34, i.e $\mathcal{E} = 0$, from which stems the fact that the diffusion matrix associated to the set of stochastic variables (A, Φ) is diagonal. Plugging Equations 8.31 to 8.35 into Equations 8.40 and 8.41, one finally finds

$$\mathrm{d}A = \left(A(\kappa + \mathrm{Re}(\alpha_3)) + \frac{\mathrm{Re}(\alpha_1)}{2A}\right)\,\mathrm{d}t + \left(A^2\left(2\alpha_2^R + \mathrm{Re}(\alpha_3)\right) + \mathrm{Re}(\alpha_1)\right)^{1/2}\mathrm{d}W_A\,, \tag{8.42}$$

$$\mathrm{d}\Phi = \mathrm{Im}(\alpha_3)\;\mathrm{d}t + \left(\frac{1}{A^2}\mathrm{Re}(\alpha_1) + 2\alpha_2^I + \mathrm{Re}(\alpha_3)\right)^{1/2}\mathrm{d}W_\Phi\,. \tag{8.43}$$

These equations are much more practical to handle than either the exact amplitude equations derived in Section 8.2.1 or the Fokker-Planck equation derived in Section 8.2.2, in the sense that they allow us to circumvent the problems outlined above. Indeed, as in the Fokker-Planck equation, all rapidly-oscillating terms have been averaged out, which means that the short timescales $\sim \omega^{-1}$ need not be resolved. Furthermore, the stochastic part of these equations now have zero memory – because the effect of the finite width of the turbulent cascade timescale range has been properly and rigorously incorporated in the coefficients of the Fokker-Planck equation –, which also drastically reduces the range of timescales that one needs to resolve. On the other hand, Equations 8.42 and 8.43 are much easier to integrate numerically than the corresponding Fokker-Planck equation, as only the time variable needs to be discretised, with the only cost being that a large number of independent realisations must be integrated in order to reconstruct the moments of the mode amplitude.

8.2.4 General analytical results: driving, damping and frequency correction

In fact, Equations 8.42 and 8.43 are so simple that general analytical results can easily be derived regarding the slow evolution of mode amplitude. In particular, let me denote the mean energy of the mode as $E_m(t) \equiv \langle A(t)^2 \rangle$ and the mean phase of the mode as $\Phi_m(t) \equiv \langle \Phi(t) \rangle$. It must be understood that the word 'mean' here refers to ensemble average, and not time average. As such, E_m and Φ_m are susceptible to depend on time. I derive equations for these quantities by taking the ensemble average of Equation 8.42 (preliminarily multiplied by $2A$) and Equation 8.43. Because $W_A(t)$ and $W_\Phi(t)$ are Wiener processes, the diffusion part of these equations (i.e. the second, stochastic term on their right-hand side) is always of zero-mean, even when the diffusion coefficient depends explicitly on the stochastic variables themselves. The procedure yields

$$\frac{\mathrm{d}E_m}{\mathrm{d}t} = 2E_m\left(\kappa + \mathrm{Re}(\alpha_3)\right) + \mathrm{Re}(\alpha_1)\,, \tag{8.44}$$

$$\frac{\mathrm{d}\Phi_m}{\mathrm{d}t} = \mathrm{Im}(\alpha_3)\,. \tag{8.45}$$

Each of the contributions to the right-hand sides of Equations 8.44 and 8.45 can be interpreted thus

- depending on its sign, the first term on the right-hand side of Equation 8.44 gives either the growth rate or the damping rate of the mode. For solar-like oscillations, which are intrinsically stable, the damping rate of the mode is therefore given by[5]

$$\eta \equiv -\left(\kappa + \mathrm{Re}(\alpha_3)\right)\,. \tag{8.46}$$

  The damping rate is made up of two different contributions. The first corresponds to the non-turbulent, deterministic contribution κ, which, in the case of sound waves, can be attributed to non-adiabatic energy

[5]The notation η, which I have used to denote the damping rate of the modes since Section 2.3, must not be confused with the notation $\eta(t)$, which I have used in Section 7.1.3 to denote the random part of the Langevin equation (see Equation 7.29). Throughout this thesis, the context should make it clear which one is referred to at any given occurrence.

exchanges between the wave and the medium in which it propagates. The second corresponds to the impact of the turbulence-induced, stochastic fluctuations in the wave equation on mode damping. It encompasses a whole array of individual physical contributions from turbulent pressure, turbulent dissipation or convective enthalpy flux for instance (see Section 2.3 for more details);

- the second term on the right-hand side of Equation 8.44 gives the excitation rate of the mode. It can be seen that, unlike the damping rate, the excitation rate only contains contributions from the turbulence-induced stochastic perturbation of the wave equation (Equation 8.17), which is in accordance with the widely acknowledged picture of solar-like oscillations being stochastically excited by highly turbulent motions of the plasma at the top of the convection zone (see Section 2.2 for more details). Furthermore, assuming the mode has reached a stationary state, one can take $\mathrm{d}E_m/\,\mathrm{d}t = 0$ in Equation 8.44. This yields the stationary average energy of the mode

$$E_{\mathrm{stat}} \equiv \frac{\mathrm{Re}(\alpha_1)}{2\eta} \,, \tag{8.47}$$

which is in perfect accordance with Eq. (42) of Goldreich and Keeley (1977b) for instance, or Eq. (40) of Buchler et al. (1993). This result also echoes the discussion in Section 2.2.1, where I mentioned that the energy of the modes results from a balance between driving and damping processes;

- the equation for the evolution of the mean phase is easily integrated to

$$\Phi_m(t) = \mathrm{Im}(\alpha_3)\, t + \Phi_{m,0} \,, \tag{8.48}$$

where $\Phi_{m,0}$ is an arbitrary initial average phase. In turn, this yields the following expression for the *average global phase* of the mode $\phi(t) \equiv \omega t + \Phi_m(t)$

$$\phi(t) = \Big(\omega + \mathrm{Im}(\alpha_3)\Big)\, t + \Phi_{m,0} \,. \tag{8.49}$$

This amounts to a systematic shift in the angular frequency of the mode

$$\delta\omega = \mathrm{Im}(\alpha_3) \,. \tag{8.50}$$

This shift actually represents what is commonly referred to as the modal part of *surface effects*, i.e. the contribution of turbulent convection not to the equilibrium structure, but to the propagation of the waves themselves (see Section 2.4 for more details).

All aspects of turbulence-oscillation coupling – driving and damping processes as well as surface effects – are therefore modelled simultaneously and consistently in this framework. Furthermore, they can be quantified using only the two complex constants α_1 and α_3, which depend on the specific form of the turbulence-induced stochastic perturbation to the linear operator $\mathcal{L}(t)$ in the wave equation, and that of the additive convective noise $|\Theta(t)\rangle$, as well as on the structure of the mode under consideration. Of particular interest is the fact that the part of the damping rate stemming from these turbulent fluctuations, on the one hand, and the frequency shift entailed by these same fluctuations on the other hand, are modelled respectively by the real and imaginary parts of the same complex autocorrelation spectrum α_3. This is not quite surprising: I had already remarked in the beginning of Section 2.3.2 that the damping rate and oscillatory frequency of a mode are themselves simply two sides of the complex eigenvalue associated to the mode – more specifically, its real and imaginary parts.

8.3 Simplified Amplitude Equations for solar-like oscillations

I now set out to apply the very general Simplified Amplitude Equation formalism in its linear form, as introduced in Section 8.2, to the linear stochastic wave equation developed in Section 8.1. In particular, one of the strengths of said stochastic wave equation, on which I have not yet lingered, but which become of crucial importance in this section, is the fact that it contains the turbulent displacement $\boldsymbol{\xi}_t$ and velocity $\mathbf{u}_t$ in their most general form, as an input of the model. Therefore, this formalism allows for *the inclusion of any prescription one could wish for concerning the turbulent velocity spectrum*. As such, in the long run, *this formalism will eventually allow to test any such prescription against asteroseismic observations, by comparing the resulting theoretical excitation*

rate, damping rate or frequency correction by turbulent convection (see Section 8.2.4) with their observationally available counterparts. This will be seen perhaps more clearly later in this section, but I already remark upon it here, because it is one of the key points of this formalism. Before I dive in, however, I wish to warn the reader that this section is the subject of a work that is still very much under way, which is why it may, at times, look incomplete.

I first need to explicitly cast the stochastic wave equation derived in Section 8.1 in the form given by Equation 8.17. A ket $|z\rangle$ can be constructed in such a way that it contains the 6 components of $\omega\,\boldsymbol{\xi}_{\rm osc}$ and $\mathbf{u}_{\rm osc}$ for each Eulerian position $\mathbf{x}$, as follows[6]

$$|z\rangle \equiv \left|\{\omega\boldsymbol{\xi}_{\rm osc}(\mathbf{x}), \mathbf{u}_{\rm osc}(\mathbf{x})\}_{\mathbf{x}\in\mathbb{R}^3}\right\rangle \ , \tag{8.51}$$

where ω refers to the angular frequency of the mode, and must not be confused with the turbulent frequency ω_t introduced in Section 8.1.1. Then the linear operators $\mathcal{L}^d$ and $\mathcal{L}^s(t)$, and the stochastic ket $|\Theta(t)\rangle$ appearing in Equation 8.17 are determined from the vector operators $\mathbf{L}_1^d$, $\mathbf{L}_1^s$ and $\mathbf{L}_0$ defined by Equations 8.14 to 8.16, in the following form

$$\left|\mathcal{L}^d|z\right\rangle = \left|\left\{\omega\mathbf{u}_{\rm osc}\ ;\ \mathbf{L}_1^d\right\}_{\mathbf{x}\in\mathcal{V}}\right\rangle \ , \tag{8.52}$$

$$\left|\mathcal{L}^s(t)|z\right\rangle = \left|\left\{\omega(\boldsymbol{\xi}_{\rm osc}\cdot\boldsymbol{\nabla})\mathbf{u}_t + \omega(\boldsymbol{\xi}_t\cdot\boldsymbol{\nabla})\mathbf{u}_{\rm osc}\ ;\ \mathbf{L}_1^s\right\}_{\mathbf{x}\in\mathcal{V}}\right\rangle \ , \tag{8.53}$$

$$|\Theta(t)\rangle = \left|\{\omega(\boldsymbol{\xi}_t\cdot\boldsymbol{\nabla})\mathbf{u}_t\ ;\ \mathbf{L}_0\}_{\mathbf{x}\in\mathcal{V}}\right\rangle \ , \tag{8.54}$$

where, on the right-hand side of Equations 8.52 to 8.54, the two quantities in the set notation refer to the component of the ket associated to $\omega\boldsymbol{\xi}_{\rm osc}(\mathbf{x})$ and $\mathbf{u}_{\rm osc}(\mathbf{x})$ respectively, and $\mathcal{V}$ refers to the volume of the star. Now that the Hilbert space in which the ket $|z\rangle$ lies is properly defined, I also need to specify the scalar product $\langle .\,|\,.\rangle$ in this Hilbert space. A necessary condition is that distinct eigenvectors $|\Psi\rangle$ of the unperturbed wave equation (Equation 8.19) – i.e. of the linear operator $\mathcal{L}^d$ – must be orthogonal to one another in the sense of this scalar product. For adiabatic, non-radial oscillations, one has (Unno et al. 1989)

$$\int \mathrm{d}^3\mathbf{x}\,\rho_0(\mathbf{x})\,\boldsymbol{\xi}_{n,l,m}(\mathbf{x})\cdot\boldsymbol{\xi}^\star_{n',l',m'}(\mathbf{x}) \propto \delta_{nn'}\delta_{ll'}\delta_{mm'} \ , \tag{8.55}$$

where $\boldsymbol{\xi}_{n,l,m}$ denotes the oscillatory displacement $\boldsymbol{\xi}_{\rm osc}$ associated to the mode of radial order n, angular degree l and azimuthal order m. But the components of $|\Psi\rangle$ are precisely proportional to $\boldsymbol{\xi}_{\rm osc}$ – the displacement part is $\omega\boldsymbol{\xi}_{\rm osc}$, while the velocity part is $\mathbf{u}_{\rm osc} = j\omega\boldsymbol{\xi}_{\rm osc}$. Therefore, the eigenvectors $|\Psi\rangle$ are orthogonal with respect to the scalar product

$$\langle\Psi_1|\Psi_2\rangle \equiv \int \mathrm{d}^3\mathbf{x}\,\rho_0(\mathbf{x})\left(\boldsymbol{\Psi}_{1,\xi}(\mathbf{x})\cdot\boldsymbol{\Psi}^\star_{2,\xi}(\mathbf{x}) + \boldsymbol{\Psi}_{1,u}(\mathbf{x})\cdot\boldsymbol{\Psi}^\star_{2,u}(\mathbf{x})\right) \ , \tag{8.56}$$

where $\boldsymbol{\Psi}_\xi(\mathbf{x})$ (resp. $\boldsymbol{\Psi}_u(\mathbf{x})$) is the part of $|\Psi\rangle$ associated with the oscillatory displacement (resp. velocity) at location $\mathbf{x}$: in other words, they are the space-dependent normalised eigenfunctions written in terms of displacement and velocity. In particular, they are related to each other through

$$\boldsymbol{\Psi}_u = j\boldsymbol{\Psi}_\xi \ . \tag{8.57}$$

In the following, I will adopt the scalar product defined by Equation 8.56, which also corresponds to the scalar product adopted by Buchler and Goupil (1984) – although they included the non-adiabatic component of the oscillations in the ket $|\Psi\rangle$ as well.

8.3.1 Specification of the autocorrelation spectra α_i

In order to exploit the stochastic simplified amplitude equations given by Equations 8.42 and 8.43, or their ensemble average given by Equations 8.44 and 8.45, it is necessary to compute the complex autocorrelation spectra α_i given by Equations 8.36 to 8.39, where the stochastic processes $c_i(t)$ are given by Equations 8.24 to 8.26.

[6] Note that, naturally, the two are simply related through $\mathbf{u}_{\rm osc} = j\omega\boldsymbol{\xi}_{\rm osc}$. The inclusion of both wave variables in $|z\rangle$ allows to keep the wave equation in the form of Equation 8.17, i.e. without any second-derivatives with respect to time. Let me also note that the oscillatory fluid displacement $\boldsymbol{\xi}_{\rm osc}$ is multiplied by the mode frequency ω so that all components of $|z\rangle$ have the same dimension, i.e. that of a velocity.

With the definitions of the ket $|\Psi\rangle$ given by Equation 8.51, and the definition of the scalar product $\langle . | . \rangle$ in the corresponding Hilbert space given by Equation 8.56, I find the following expressions for the stochastic processes $c_i(t)$

$$c_1(t) = 2 \int \mathrm{d}^3\mathbf{x}\, \rho_0 \left[\Psi_{\xi,i} \xi_{t,j}(t) \partial_j u_{t,i}(t) + \Psi_{u,i} L_{0,i}(t) \right] \tag{8.58}$$

$$c_2(t) = \int \mathrm{d}^3\mathbf{x}\, \rho_0 \left[\Psi_{\xi,i} \Psi^\star_{\xi,j} \partial_j u_{t,i}(t) + \omega \Psi_{\xi,i} \xi_{t,j}(t) \partial_j \Psi^\star_{u,i} + \Psi_{u,i} L^{s\star}_{1,i}(t) \right] , \tag{8.59}$$

$$c_3(t) = \int \mathrm{d}^3\mathbf{x}\, \rho_0 \left[\Psi_{\xi,i} \Psi_{\xi,j} \partial_j u_{t,i}(t) + \omega \Psi_{\xi,i} \xi_{t,j}(t) \partial_j \Psi_{u,i} + \Psi_{u,i} L^{s}_{1,i}(t) \right] . \tag{8.60}$$

From there, the coefficients α_i can be computed using the explicit expressions of $\mathbf{L}_1^s$ (Equation 8.15) and $\mathbf{L}_0$ (Equation 8.16). In fact, while all the coefficients α_i appear in Equations 8.42 and 8.43, only α_1 and α_3 play an actual role in the equations on the mean energy and phase of the mode (Equations 8.44 and 8.45), so that I only need to detail the derivation of these two coefficients. Equations 8.36 and 8.39 show that α_1 and α_3 are defined in terms of the second-order correlation product of $c_1(t)$ and $c_3(t)$ respectively. In turn, $c_1(t)$ and $c_3(t)$ depend in the turbulent velocity field $\mathbf{u}_t$. But I already mentioned, in Chapter 5 in particular, that the autocorrelation product of the turbulent velocity, or even the turbulent velocity itself, is best described in terms of its Fourier components in space and time. As a result, *the autocorrelation spectra α_1 and α_3 can be described in terms of the autocorrelation spectrum of the turbulent velocity*, more specifically the second- and fourth-order spectra defined by

$$\phi^2_{ij}(\mathbf{k},\omega) \equiv \int_{-\infty}^{0} \mathrm{d}\tau \int \mathrm{d}^3\delta\mathbf{x} \left\langle u_{t,i}(\mathbf{X})\, u^\tau_{t,j}(\mathbf{X}+\mathbf{x}) \right\rangle \exp^{j(\omega\tau - \mathbf{k}\cdot\delta\mathbf{x})} , \tag{8.61}$$

$$\phi^{4a}_{ijkl}(\mathbf{k},\omega) \equiv \int_{-\infty}^{0} \mathrm{d}\tau \int \mathrm{d}^3\delta\mathbf{x} \left\langle u_{t,i}(\mathbf{X})\, u^\tau_{t,j} u^\tau_{t,k} u^\tau_{t,l}(\mathbf{X}+\mathbf{x}) \right\rangle \exp^{j(\omega\tau - \mathbf{k}\cdot\delta\mathbf{x})} , \tag{8.62}$$

$$\phi^{4b}_{ijkl}(\mathbf{k},\omega) \equiv \int_{-\infty}^{0} \mathrm{d}\tau \int \mathrm{d}^3\delta\mathbf{x} \left\langle u_{t,i} u_{t,j}(\mathbf{X})\, u^\tau_{t,k} u^\tau_{t,l}(\mathbf{X}+\mathbf{x}) \right\rangle \exp^{j(\omega\tau - \mathbf{k}\cdot\delta\mathbf{x})} , \tag{8.63}$$

$$\phi^{4c}_{ijklmn}(\mathbf{k},\omega) \equiv \int_{-\infty}^{0} \mathrm{d}\tau \int \mathrm{d}^3\delta\mathbf{x} \left\langle u_{t,i} \partial_m u_{t,j}(\mathbf{X})\, u^\tau_{t,k} \partial_n u^\tau_{t,l}(\mathbf{X}+\mathbf{x}) \right\rangle \exp^{j(\omega\tau - \mathbf{k}\cdot\delta\mathbf{x})} , \tag{8.64}$$

$$\phi^{4d}_{ijklm}(\mathbf{k},\omega) \equiv \int_{-\infty}^{0} \mathrm{d}\tau \int \mathrm{d}^3\delta\mathbf{x} \left\langle u_{t,i} \partial_m u_{t,j}(\mathbf{X})\, u^\tau_{t,k} u^\tau_{t,l}(\mathbf{X}+\mathbf{x}) \right\rangle \exp^{j(\omega\tau - \mathbf{k}\cdot\delta\mathbf{x})} . \tag{8.65}$$

The derivation of the autocorrelation spectra α_1 and α_3 is detailed in Appendix D, and I eventually obtain

$$\alpha_1 = \frac{2}{\omega^2 \mathcal{I}} \int \mathrm{d}^3\mathbf{X}\, \rho_0^2 k_j k_l u_{\mathrm{osc,i}} u^\star_{\mathrm{osc,k}} \phi^{4b}_{ijkl}(\mathbf{k},\omega) , \tag{8.66}$$

$$\begin{aligned} \alpha_3 = \frac{1}{4\mathcal{I}^2\omega^4} \int \mathrm{d}^3\mathbf{X}\, \rho_0^2 \Big(& F^1_i F^{1\star}_j(\mathbf{X}) \phi^2_{ij}(2\mathbf{k},2\omega) + 2\,\mathrm{Re}\left[F^1_i F^{3b\star}_{jkl}(\mathbf{X}) \phi^{4a}_{ijkl}(2\mathbf{k},2\omega) \right] + F^2_{ij} F^{2\star}_{kl}(\mathbf{X}) \phi^{4b}_{ijkl}(2\mathbf{k},2\omega) \\ & + F^{3a}_{ijm} F^{3a\star}_{kln}(\mathbf{X}) \phi^{4c}_{ijklmn}(2\mathbf{k},2\omega) + 2\,\mathrm{Re}\left[F^{3a}_{ijm} F^{2\star}_{kl}(\mathbf{X}) \phi^{4d}_{ijklm}(2\mathbf{k},2\omega) \right] \Big) , \end{aligned} \tag{8.67}$$

where $\mathbf{k}$ is the (space-dependent) wavevector of the mode, the functions F^1, F^2, F^{3a} and F^{3b} are given by[7]

$$\begin{aligned} F^1_i = {} & 4jk_j u_{\mathrm{osc,i}} u_{\mathrm{osc,j}} + jk_i u_{\mathrm{osc,j}} u_{\mathrm{osc,j}} + \frac{G_{ij,0}}{\omega} k_k u_{\mathrm{osc,j}} u_{\mathrm{osc,k}} + \frac{\partial G_{ij}}{\partial \widetilde{u''_k u''_l}} \frac{\widetilde{u''_k u''_l}_0}{\omega} k_m u_{\mathrm{osc,m}} u_{\mathrm{osc,j}} \\ & + \frac{\partial G_{ij}}{\partial(\partial_k \widetilde{u_l})} jk_k u_{\mathrm{osc,j}} u_{\mathrm{osc,l}} + \frac{\partial G_{ij}}{\partial\epsilon} \frac{\omega_t k_0}{\omega} k_m u_{\mathrm{osc,j}} u_{\mathrm{osc,m}} , \end{aligned} \tag{8.68}$$

$$F^2_{ij} = \left(\frac{\partial G_{ki}}{\partial \widetilde{u''_j u''_l}} + \frac{\partial G_{ki}}{\partial \widetilde{u''_l u''_j}} \right) u_{\mathrm{osc,l}} u_{\mathrm{osc,k}} + \frac{\partial G_{ki}}{\partial\epsilon} \omega_t u_{\mathrm{osc,j}} u_{\mathrm{osc,k}} , \tag{8.69}$$

$$F^{3a}_{ijk} = \frac{\partial G_{li}}{\partial(\partial_k \widetilde{u_j})} \frac{1}{\omega} jk_m u_{\mathrm{osc,l}} u_{\mathrm{osc,m}} , \tag{8.70}$$

$$F^{3b}_{ijk} = -\frac{\partial G_{li}}{\partial \widetilde{u''_j u''_k}} \frac{1}{\omega} k_m u_{\mathrm{osc,l}} u_{\mathrm{osc,m}} - \frac{1}{2} \frac{\partial G_{li}}{\partial\epsilon} \frac{\omega_t}{\omega} k_m u_{\mathrm{osc,l}} u_{\mathrm{osc,m}} \delta_{jk} , \tag{8.71}$$

[7] The subscript $_j$, used as a coordinate index, must not be confused with the in-line notation j, which refers to the imaginary unit.

and the velocity eigenfunction $\mathbf{u}_{\rm osc}$ associated to the mode is no longer normalised – since the normalisation condition $\langle\Psi|\Psi\rangle = 1$ is taken care of in Section D.4 by the inclusion of the inertia $\mathcal{I}$ of the mode, defined by (see Equation 2.97)

$$\mathcal{I} = \int \mathrm{d}^3\mathbf{x}\, \rho_0(\mathbf{x})\, |\boldsymbol{\xi}_{\rm osc}(\mathbf{x})|^2 \ . \tag{8.72}$$

The functions F_1, F_2 and F_3, given by Equations 8.68 to 8.71, are broken down into several contributions, which allows me to separate the effect of each physical process to the turbulence–oscillation coupling. In the present case, of course, seeing as the Lagrangian stochastic model from which I started is extremely simple, there are not many such physical processes: the turbulent pressure, represented by the advection term in the stochastic velocity equation (Equation 8.6), is responsible for the entirety of α_1, as well as the first two terms on the right-hand side of Equation 8.68. On the other hand, all the other contributions to α_3 stem from the G_{ij} term in Equation 8.6, which I recall encompasses the collective effect of the buoyancy force, the fluctuating gas pressure gradient force, and the turbulent dissipation. Let me note, additionally, that Equations 8.66 and 8.67 being written in the form of spatial integrals spanning across the entire volume of the star, this formalism also allows to determine the regions of the star are most responsible for the coupling between the turbulent motions and the oscillatory motions.

8.3.2 Qualitative properties of mode driving, damping and surface effects

In the following, I deduce from the above expressions some basic, qualitative properties of the excitation rate, mean energy, damping rate and intrinsic surface effect of the modes.

Mode driving

In the simplified amplitude equation formalism, the stationary energy of the mode is given by Equation 8.47, which I reproduce here for clarity

$$E_{\rm stat} = \frac{\mathrm{Re}(\alpha_1)}{2\eta} \ . \tag{8.73}$$

In other words, as I mentioned in Section 8.2.4, it is the result of a balance between the rate at which the mode is being damped (namely η) and the rate at which it is being excited by the turbulence. This is in accordance with the commonly accepted picture of energy balance for intrinsically stable modes of oscillation (see Section 2.2.1). Furthermore, it can be seen that the excitation rate $\mathcal{P}$ of the mode is simply equal to the real part of α_1, so that

$$\mathcal{P} = \frac{2}{\mathcal{I}\omega^2} \int \mathrm{d}^3\mathbf{X}\, \rho_0^2 k_j k_l \mathrm{Re}\left(u_{\mathrm{osc,i}} u^\star_{\mathrm{osc,k}} \phi^{4b}_{ijkl}(\mathbf{k},\omega)\right) \ . \tag{8.74}$$

This expression is extremely similar to the formulation obtained by previous models for the excitation of solar-like oscillations (see, for instance Samadi and Goupil 2001; Chaplin et al. 2005), which gives further support to the consistency and validity of the method presented here. First, it is inversely proportional to the inertia of the mode: the larger the mass flow entailed by an oscillating mode, the harder it is to get the flow to actually move. Secondly, it appears that the efficiency of mode driving by turbulence is directly related to the spectrum of the fourth-order moment of turbulent velocity, which must be interpreted as the source of excitation of the mode being of quadrupolar nature. This is in accordance with the widely accepted picture of stochastic driving of solar-like oscillations. Finally, the integrand is weighted by a quantity which takes the form of the product of two different components of the wavevector and two different components of the velocity modal fluctuations. Qualitatively, it can be seen that this is closely related to the square of the mode compressibility $|\boldsymbol{\nabla}\cdot\mathbf{u}_{\rm osc}|$. In other words, the turbulence drives the mode much more efficiently in regions where the compressibility of the mode is high. This is also not surprising, as the turbulent pressure must actually be able to transfer mechanical work to the mode in order to give it energy, and mechanical work is only transferable if the flow undergoes successive compression and dilatation phases.

Mode damping and modal surface effects

Perhaps more interestingly, the simplified amplitude equation also provides with an expression for the damping rate η of the mode, as well as for the frequency shift $\delta\omega$ entailed by turbulence. This is a very interesting aspect

of this model, as mode excitation on the one hand, and mode damping and surface effects on the other hand, are usually modelled through completely separate procedures, while the model presented here encompasses all of them in the same, consistent framework. First, let me remark that in the adiabatic framework considered throughout this chapter, there can be no entropy exchange between the sound waves and the medium, and therefore all loss of energy must come from the interaction of the mode with turbulence. Then, Equations 8.46 and 8.50 yield

$$\eta_{\text{turb}} = -\text{Re}(\alpha_3) \,, \tag{8.75}$$

$$\delta\omega = \text{Im}(\alpha_3) \,. \tag{8.76}$$

As such, it appears that *the damping rate and the intrinsic surface effect are simply two sides of the same effect*, the exact same way the oscillatory frequency of the mode and its growth or damping rate are simply the imaginary and real part of the same complex eigenfrequency. This echoes the same remark I made several times in Sections 2.3 and 2.4. As a result, most of the following qualitative discussion on the damping rate η is also valid for $\delta\omega$. Using the expression for α_3 given by Equation 8.67, one finds

$$\eta = -\frac{1}{4\mathcal{I}^2\omega^4} \int \mathrm{d}^3\mathbf{X}\, \rho_0^2 \text{Re}\left(\underbrace{F_i^1 F_j^{1\star}(\mathbf{X}) \phi_{ij}^2(2\mathbf{k}, 2\omega)}_{\text{dipolar}} + \underbrace{2F_i^1 F_{jkl}^{3b\star}(\mathbf{X}) \phi_{ijkl}^{4a}(2\mathbf{k}, 2\omega)}_{\text{dipolar}} + \underbrace{F_{ij}^2 F_{kl}^{2\star}(\mathbf{X}) \phi_{ijkl}^{4b}(2\mathbf{k}, 2\omega)}_{\text{quadrupolar}} \right.$$
$$\left. + \underbrace{F_{ijm}^{3a} F_{kln}^{3a\star}(\mathbf{X}) \phi_{ijkl}^{4c}(2\mathbf{k}, 2\omega)}_{\text{quadrupolar}} + \underbrace{2F_{ijm}^{3a} F_{kl}^{2\star}(\mathbf{X}) \phi_{ijkl}^{4d}(2\mathbf{k}, 2\omega)}_{\text{quadrupolar}} \right) \tag{8.77}$$

and

$$\delta\omega = \frac{1}{4\mathcal{I}^2\omega^4} \int \mathrm{d}^3\mathbf{X}\, \rho_0^2 \text{Im}\left(\underbrace{F_i^1 F_j^{1\star}(\mathbf{X}) \phi_{ij}^2(2\mathbf{k}, 2\omega)}_{\text{dipolar}} + \underbrace{F_{ij}^2 F_{kl}^{2\star}(\mathbf{X}) \phi_{ijkl}^{4b}(2\mathbf{k}, 2\omega)}_{\text{quadrupolar}} + \underbrace{F_{ijm}^{3a} F_{kln}^{3a\star}(\mathbf{X}) \phi_{ijkl}^{4c}(2\mathbf{k}, 2\omega)}_{\text{quadrupolar}} \right) , \tag{8.78}$$

from which some general results can be unveiled.

First, it can be seen that the damping rate of the mode goes as $\mathcal{I}^{-2}$: similarly to the excitation rate $\mathcal{P}$, the higher the mass flow pertaining to the oscillation, the harder it is to take energy from it. This is in stark contrast with the work integral formulation presented in Section 2.3.2, where the damping rate goes as $\mathcal{I}^{-1}$. The reason is that in the work integral formulation, the damping rate is written as a second-order quantity in the wave variables. By contrast, in the formalism presented here, it is the *instantaneous* damping rate that is a second-order quantity. But in order to derive the *mean, effective* impact of the turbulence-induced damping on the mode, I needed to derive the autocorrelation spectrum of the instantaneous damping – i.e. its Fourier component coinciding with the angular frequency of the mode. This is a fourth-order quantity in terms of the wave variables. The exponent of the scaling of η – or any other mode property for that matter – with inertia is just a by-product of the order with which the wave variables appear in its expression.

Secondly, it can also be seen that the different physical contributions to mode damping and intrinsic surface effect are hidden in F^1, F^2, F^{3a} and F^{3b}, which are given by Equations 8.68 to 8.71 respectively. As indicated above, the first two terms on the right-hand side of Equation 8.68 represent the effect of turbulent pressure, while everything else originates from the combined effect of the buoyancy, the fluctuating gas pressure gradient, and the turbulent dissipation. It is immediately apparent that, depending on the frequency regime, one of these contributions will dominate the other. More precisely, if $\omega \ll G_{ij}$, then the effect of turbulent pressure, which is inertial by nature, acts on timescales much larger than the other contributions, and its impact on mode damping and surface effect will be negligible. On the other hand, if $G_{ij} \ll \omega$, then it is the combined effects of the turbulent dissipation, buoyancy and fluctuating gas pressure gradient on the mechanical work exerted on the mode that will be negligible compared to the contribution of turbulent pressure. The threshold between the two regimes can be easily interpreted by remarking that the different components of the drift tensor G_{ij} are of the order of magnitude of the (inverse) eddy turn-over time, i.e. the turbulent frequency ω_t. Let me remark, however, that this picture is a simplistic one, as it stems primarily from the fact that the Lagrangian stochastic model from which we started in

Section 8.1 only contains one typical turbulent time scale instead of a wide continuous range – otherwise stated, it stems from hypothesis (H7) (see Section 8.1.3). In a more realistic picture, one can assume that within the continuous range of turbulent timescales, the eddies whose turnover time τ_{to} is much larger than the period of the mode would damp it through turbulent pressure, while those a much shorter lifetime would damp it through the other contributions. As a result, depending on the frequency of the modes, it is either the turbulent pressure (for high-frequency modes) or the other mechanical contributions (for low-frequency modes) that dominates. This analysis illustrates how the formalism presented here allows to break down the relative importance of the various physical contributions to mode damping and surface effect, as a function of mode frequency.

Finally, it can be seen that, while the driving source was shown to be of quadrupolar nature (see Equation 8.74 for the excitation rate $\mathcal{P}$), the damping source and the source of frequency shift have both dipolar and quadrupolar contributions, which are explicitly broken down in Equations 8.77 and 8.78. However, in the limit $\omega_t \ll \omega$, the dipolar contribution largely predominates. Note that while the correlation product defining ϕ^{4a}_{ijkl} is fourth-order, its QNA decomposition yields (see Equation 1.103)

$$\left\langle u^A_{t,i} u^B_{t,j} u^B_{t,k} u^B_{t,l} \right\rangle = \left\langle u^A_{t,i} u^B_{t,j} \right\rangle \left\langle u^B_{t,k} u^B_{t,l} \right\rangle + \left\langle u^A_{t,i} u^B_{t,k} \right\rangle \left\langle u^B_{t,j} u^B_{t,l} \right\rangle + \left\langle u^A_{t,i} u^B_{t,l} \right\rangle \left\langle u^B_{t,i} u^B_{t,j} \right\rangle \ , \tag{8.79}$$

where a quantity with the superscript A is evaluated at location $\mathbf{X}$ and time t, and a quantity with the superscript B is evaluated at location $\mathbf{X}+\delta\mathbf{x}$ and time $t+\tau$. In each of these three terms, only the second-order moment involving $u_{t,i}$ is a two-point, two-time correlation product, while the other is simply an element of the one-point, one-time covariance matrix of the turbulent velocity $\mathbf{u}_t$ (i.e. a component of the equilibrium Reynolds stress tensor). This is the reason why the contribution of ϕ^{4a}_{ijkl} is dipolar, and not quadrupolar.

8.4 Concluding remarks

Let me shortly summarise the formalism developed in this chapter. First, a Lagrangian stochastic model of turbulence is linearly perturbed to yield a linear, stochastic wave equation, which governs the behaviour of the solar-like oscillations, while consistently containing the effect of the turbulent convective noise. This stochastic wave equation contains the information on the driving and damping of the modes by the turbulent motions, as well as the shift in frequency due to the convective noise. However, those are present in the wave equation in the form of instantaneous, random fluctuations: by contrast, it is only the long-term effect of these random fluctuations on the modes that are observationally available. Therefore, intuitively, I needed to average the effect of the stochastic perturbation on the wave equation over long time scales, in order to yield the effective impact of turbulence on the observed properties of the modes. This is done through the Simplified Amplitude Equation formalism, which yields two Ito stochastic differential equations on the real amplitude and the phase of the modes, in the form of Equations 8.28 and 8.29. The coefficients in these two equations are directly extracted from the linear stochastic wave equation governing the oscillations, and are given in terms of the complex autocorrelation spectra α_1 and α_3 defined by Equations 8.36 and 8.39, and expressed, in the special case of the stochastic wave equation derived in Section 8.1, by Equations 8.66 and 8.67.

The simplified amplitude equations are fully determined by 1) the equilibrium state of the star, 2) the structure of the mode under consideration, i.e. its velocity eigenfunction, and 3) the statistical properties of the turbulent velocity, and in particular its second- and fourth-order spectra. As I hinted in the beginning of Section 8.3, these expressions are valid regardless of the specific form of the turbulent velocity power spectrum. Different prescriptions of the turbulent spectrum – i.e. of ϕ^2_{ij} and ϕ^{4a}_{ijkl} to ϕ^{4d}_{ijkl}, defined by Equations 8.61 to 8.65 respectively – lead to different theoretical excitation rates, damping rates and modal surface effect, which can then be compared to observations. This will be the subject of a work that is yet to be done. However, one can already see that the qualitative results obtained from this formalism are promising – in particular, I recover the exact same semi-analytical formula for the excitation rate of solar-like p-modes (see Equation 8.74) as the formulation of prior studies on solar-like mode driving Samadi and Goupil (2001); Chaplin et al. (2005). The key difference is that the present formalism, unlike theirs, describes all aspects of turbulence-oscillation coupling at the same time, not simply mode driving. Nevertheless, the fact that this method yields the same mode excitation rates as these other formalisms is a solid support for the validity of this method.

Finally, and I will conclude this chapter on this hopeful note, the analytical developments presented here form a promising lead regarding the motivations I listed in the end of Section 7.3. Indeed, since the properties of turbulence can be input freely in the model, in the form of the second- and fourth-order spectra of the turbulent velocity,

and that all other inputs are easily extracted from appropriate stellar models and 3D hydrodynamic simulations, this formalism allows to relate directly the physics of the turbulent cascade with the observationally available properties of the mode. Therefore, it offers an efficient way of constraining such or such prescription for turbulence, and can also, if sufficiently strong constraints are obtained, help *predict* in a non-empirical manner the surface effects that so inconveniently taint our asteroseismic measurements. A caveat however: the Lagrangian stochastic model from which I started was deliberately oversimplified, in order to serve as a proof-of-concept for this whole approach. Obtaining realistic constraints would obviously require starting from a more realistic stochastic model of turbulence. The subsequent analytical derivation may then prove too challenging to carry out; in that case, numerical integration can help shed some light. This is the subject of the next chapter.

Astronomy & Astrophysics manuscript no. main
September 18, 2021

Coupling between turbulence and solar-like oscillations: A combined Lagrangian PDF/SPH approach

I – The stochastic wave equation

J. Philidet[1], K. Belkacem[1], and M.-J. Goupil[1]

LESIA, Observatoire de Paris, PSL Research University, CNRS, Université Pierre et Marie Curie, Université Paris Diderot, 92195 Meudon, France

September 18, 2021

ABSTRACT

Context. The development of space-borne missions such as CoRoT and *Kepler* now provides us with numerous and precise asteroseismic measurements that allow us to put better constraints on our theoretical knowledge of the physics of stellar interiors. In order to utilise the full potential of these measurements, however, we need a better theoretical understanding of the coupling between stellar oscillations and turbulent convection.

Aims. The aim of this series of papers is to build a new formalism specifically tailored to study the impact of turbulence on the global modes of oscillation in solar-like stars. In building this formalism, we circumvent some fundamental limitations inherent to the more traditional approaches, in particular the need for separate equations for turbulence and oscillations, and the reduction of the turbulent cascade to a unique length and timescale. In this first paper we derive a linear wave equation that directly and consistently contains the turbulence as an input to the model, and therefore naturally contains the information on the coupling between the turbulence and the modes through the stochasticity of the equations.

Methods. We use a Lagrangian stochastic model of turbulence based on probability density function methods to describe the evolution of the properties of individual fluid particles through stochastic differential equations. We then transcribe these stochastic differential equations from a Lagrangian frame to a Eulerian frame more adapted to the analysis of stellar oscillations. We combine this method with smoothed particle hydrodynamics, where all the mean fields appearing in the Lagrangian stochastic model are estimated directly from the set of fluid particles themselves, through the use of a weighting kernel function allowing to filter the particles present in any given vicinity. The resulting stochastic differential equations on Eulerian variables are then linearised. As a first step the gas is considered to follow a polytropic relation, and the turbulence is assumed anelastic.

Results. We obtain a stochastic linear wave equation governing the time evolution of the relevant wave variables, while at the same time containing the effect of turbulence. The wave equation generalises the classical, unperturbed propagation of acoustic waves in a stratified medium (which reduces to the exact deterministic wave equation in the absence of turbulence) to a form that, by construction, accounts for the impact of turbulence on the mode in a consistent way. The effect of turbulence consists of a non-homogeneous forcing term, responsible for the stochastic driving of the mode, and a stochastic perturbation to the homogeneous part of the wave equation, responsible for both the damping of the mode and the modal surface effects.

Conclusions. The stochastic wave equation obtained here represents our baseline framework to properly infer properties of turbulence-oscillation coupling, and can therefore be used to constrain the properties of the turbulence itself with the help of asteroseismic observations. This will be the subject of the rest of the papers in this series.

Key words. Methods: analytical – Stars: oscillations – Stars: solar-type – Turbulence

1. Introduction

Solar-like oscillations are coupled with turbulent convection in a complex manner, especially in the highly turbulent subsurface layers of the star (see Samadi et al. 2015; Houdek & Dupret 2015, for a review). This coupling impacts the behaviour of the modes in several major ways. One of the most prominent effects concerns mode frequencies, and explains in a large part the systematic discrepancy between the theoretical and observed p-mode frequencies (Dziembowski et al. 1988; Christensen-Dalsgaard et al. 1996; Rosenthal et al. 1999). The variety of physical processes responsible for the impact of turbulent convection on p-mode frequencies is collectively referred to as 'surface effects'. These surface effects constitute a major obstacle preventing us from using the full potential of modal frequencies for an accurate probing of stellar interiors or for a precise inference of stellar global parameters.

Many efforts have thus been devoted to the correction of surface effects, either from theoretical modelling (e.g. Gabriel et al. 1975; Balmforth 1992b; Houdek 1996; Rosenthal et al. 1999; Grigahcène et al. 2005) or through empirical formulae (e.g. Kjeldsen et al. 2008; Christensen-Dalsgaard 2012; Ball & Gizon 2014; Sonoi et al. 2015). Some aspects, however, are very complicated to model, and existing models make use of assumptions that can barely be justified, if at all. For instance, turbulent pressure modulations are usually described in the Gas-Γ_1 (GGM) or reduced-Γ_1 (RGM) approximations (Rosenthal et al. 1999), which amounts to neglecting the effects of turbulent dissipation and buoyancy on the mode (Belkacem et al. 2021). Another problem is the use of time-dependent mixing-length formalisms (Unno 1967; Gough 1977) to account for modal surface

effects (e.g. Gabriel et al. 1975; Houdek 1996; Grigahcène et al. 2005; Sonoi et al. 2017; Houdek et al. 2017, 2019). While useful for the bulk of the convective region, the mixing-length hypothesis is no longer valid in the superadiabatic region just beneath the surface of the star, as shown by 3D hydrodynamic simulations of stellar atmospheres (see Nordlund et al. 2009, for a review). Finally, such formalisms require that the oscillations be separated from the convective motions, thus yielding separate equations. This is done either by assuming a cut-off in wavelength space, with oscillations having much shorter wavelengths than turbulent convection (Grigahcène et al. 2005), or by using 3D hydrodynamic simulations and separating the oscillations from convection though horizontal averaging (Nordlund & Stein 2001). The necessity to separate the equations for oscillations and convection is fundamentally problematic as there is no rigorous way to disentangle the two components, mainly because, in solar-type stars, they have the same characteristic lengths and timescales (Samadi et al. 2015). This is even truer if one wishes to model their mutual coupling.

Turbulent convection also has a crucial impact on the energetic aspects of solar-like oscillations. Solar-like p-modes are stochastically excited and damped by turbulent convection at the top of the convective zone. As such, understanding the energetic processes pertaining to the oscillations leads to better constraints on the highly turbulent layers located beneath the surface of these stars. Many theoretical modelling efforts were deployed on the subject of mode driving (e.g. Goldreich & Keeley 1977a,b; Balmforth 1992a,c; Samadi & Goupil 2001; Chaplin et al. 2005; Samadi et al. 2005, 2006; Belkacem et al. 2006, 2008, 2010), as well as mode damping (e.g. Goldreich & Kumar 1991; Balmforth 1992a; Grigahcène et al. 2005; Dupret et al. 2006; Belkacem et al. 2012). The fact that these energetic processes take place in the superadiabatic region, however, makes any predictive model extremely complicated to design as this requires a time-dependent non-adiabatic turbulent convection model able to include the oscillations. Subsequently, modelling attempts have focused on the use of mixing-length formalisms to account for mode damping. This approach, however, presents the considerable disadvantage of reducing the turbulent cascade to a single length scale, and is therefore unable to correctly account for the contribution of turbulent dissipation or turbulent pressure to mode damping. Alternative approaches have been followed in an attempt to go beyond the mixing-length hypothesis, either through a Reynolds stress model (Xiong et al. 2000) or through the use of 3D hydrodynamic simulations of stellar atmospheres to directly measure mode linewidths (Belkacem et al. 2019; Zhou et al. 2020).

These traditional approaches therefore show some fundamental limitations, which prevent them from being able to fully describe the interaction between turbulent convection and oscillations, whether it be to explain the surface effects on mode frequency or the energetic aspects of global modes of oscillation regarding their driving and damping physical processes. Among these limitations, we can include the following.

These approaches require that the turbulent convection and the oscillations be separated into two distinct sets of equations from the start. This is usually justified either by a separation of spatial scales or timescales, or else by performing some averaging process designed to separate an average component from a fluctuating component. The necessity of artificially separating these two intertwined phenomena from the outset is problematic when it comes to modelling their coupling.

Most of these approaches are based on a time-dependent mixing-length formalism, which oversimplifies the behaviour of convection in the superadiabatic region. In addition to poorly describing the structure of the convective motions close to the surface, it reduces the turbulent cascade to a single characteristic length scale, thus only offering a crude understanding of turbulent dissipation, a phenomenon deemed crucial to turbulence–oscillation coupling.

In these approaches, designing a closure relation for the model equations is a complicated process. In particular, it is very difficult to properly relate the chosen closure to the underlying physical assumptions. This is illustrated, for instance, by the wealth of free parameters that need to be adjusted in approaches based on mixing length theory (MLT) or in Reynolds stress approaches where higher-order moments need to be closed at the mean flow level. Approaches based on 3D simulations are not spared, as is illustrated by the need to rely on assumptions like the GGM or RGM, which are not clearly physically grounded.

The multiple free parameters needed in these approaches, and the fact that they are not easily constrained physically, also presents the distinct disadvantage of robbing these models from their predictive power. This becomes problematic when, for example, mode damping rates are used in scaling relations for seismic diagnosis purposes (Houdek et al. 1999; Chaplin et al. 2009; Baudin et al. 2011; Belkacem et al. 2012). The exponent in these scaling relations is difficult to determine, and varies substantially across the Hertzsprung–Russell diagram. Being able to predict the damping rates of stars with different global parameters would go a long way towards a more effective use of this quantity in such scaling relations.

Model parameters for the surface effects on the one hand, and mode damping rates on the other are usually constrained by completely separate adjustment procedures. This is also problematic, as these two quantities are closely related, and are actually just two sides of the same phenomenon: the real and imaginary part of the turbulence-induced shift in the complex eigenfrequency of the modes.

These limitations form substantial hurdles towards a correct turbulence–oscillation coupling model, and circumventing them requires going beyond the methods presented above. Therefore, this series of papers follows a completely different approach. More precisely, the fundamental motivation behind this work is to provide a method that 1) does not initially rely on a separation between convection equations and oscillation equations, but instead encompasses both components at the same time, and therefore naturally contains their coupling; 2) avoids the reduction of length scales in the problem to a unique scale, but instead accounts for the full description of the turbulent cascade; 3) simultaneously describes all effects of turbulent convection on mode properties, including the surface effects and the energetic aspects pertaining to mode driving and damping, in a single consistent framework; and 4) includes the properties of turbulence in such a way that they can be easily related to the observed properties of the modes.

In this paper we therefore build a formalism for the modelling of turbulence–oscillation coupling, which is based on probability density function (PDF) models of turbulence (e.g. O'Brien 1980; Pope 1985; Pope & Chen 1990; Pope 1991, 1994; Van Slooten & Jayesh 1998). The quantity we model is the PDF associated with the random flow variables, whose evolution follows a transport equation that takes the form of a Fokker-Planck equation (Gardiner 1994). Because the Fokker-Planck equation is impractical to handle both analytically and numerically, the PDF is usually represented by a set of fluid particles constituting the flow. The properties of the particles evolve according to stochastic differential equations, and are then used to reconstruct

any given statistics of the flow. This is at the heart of Lagrangian stochastic models of turbulence, which have been used extensively by the fluid dynamics community, first for incompressible flows (e.g. Pope 1981; Anand et al. 1989; Haworth & El Tahry 1991; Roekaerts 1991), and then for compressible flows as well (e.g. Hsu et al. 1994; Delarue & Pope 1997; Welton & Pope 1997; Welton 1998; Das & Durbin 2005; Bakosi & Ristorcelli 2011). In this series of papers we present a general way of using such a Lagrangian stochastic model of turbulence to derive a linear stochastic wave equation applicable to the stellar context. The wave equation is designed to govern the physics of the modes, while simultaneously and consistently encompassing the impact of turbulent convection thereon. This first paper describes how the linear stochastic wave equation is obtained. A subsequent paper will present how this wave equation can be used to simultaneously model the turbulence-induced surface effects, as well as the stochastic driving and damping of the modes by turbulent convection.

This paper is structured as follows. In Section 2 we introduce the stochastic model of turbulence that we will use throughout this study in terms of Lagrangian variables. Then we carry out a variable transformation to obtain stochastic equations on Eulerian quantities, which are more suitable for stellar oscillation analysis. In Section 3 we linearise the Eulerian stochastic equations to obtain a linear stochastic wave equation, and then discuss how it relates to other more familiar forms of the wave equation found in the literature and obtained through more traditional methods. Finally, in Section 4 we return to the various simplifications and approximations adopted in the present derivation, and what they entail as regards the resulting properties of turbulence-oscillation coupling. Conclusions are drawn in Section 5.

Symbol	Definition
$\underline{f_0}$	Time-averaged equilibrium value of the quantity f
$\overline{f}$	Instantaneous Reynolds average of f
$\widetilde{f}$	Instantaneous Favre average of f
$\langle f \rangle_L$	Lagrangian-mean of f
f_1	Fluctuation of f around $\underline{f_0}$
f'	Fluctuation of f around $\overline{f}$
f''	Fluctuation of f around $\widetilde{f}$
a_i, b_{ij}	Drift and diffusion coefficients in velocity stochastic differential equation (SDE)
C_0	Kolmogorov constant
c_0	Equilibrium sound speed
ϵ	Turbulent dissipation rate
η_i	Time derivative of Wiener process
g_i	Gravitational acceleration
G_{ij}	Drift tensor in velocity SDE
γ	Polytropic exponent
Γ_1	First adiabatic exponent
k	Turbulent kinetic energy
K	Kernel weighting function in SPH formalism
p	Gas pressure
ρ	Gas density
u_i	Flow velocity in Eulerian frame
$u_i^\star$	Fluid particle velocity in Lagrangian frame
$u_{i,t}$	Turbulent part of u_i
$u_{i,\mathrm{osc}}$	Oscillatory part of u_i
W_i	Wiener process
x_i	Eulerian average position of fluid particle (used as Eulerian space variable)
$x_i^\star$	Fluid particle position in Lagrangian frame
X_i	Instantaneous fluid particle position, as a function of Eulerian average position
ξ_i	Fluctuation of X_i around x_i
$\xi_{i,t}$	Turbulent part of ξ_i
$\xi_{\mathrm{i,osc}}$	Oscillatory part of ξ_i
ω_t	Turbulent frequency

Table 1: Glossary of the notations used in this paper.

2. Stochastic model of turbulence

In MLT formalisms the modelled quantities pertain to the mean flow (e.g. mean density, velocity, entropy), and the second-order moments appearing in the mean equations must be expressed in terms of the mean flow in order to close the system. In Reynolds stress formalisms the closure at second-order level is replaced by equations on second-order moments, where third-order moments must be similarly closed. These moments are all defined as ensemble averages of stochastic processes such as flow velocity and entropy. The core idea behind PDF models is to replace these numerous equations on various statistical moments of turbulent quantities by a single equation on the PDF of these quantities, in the form of a Fokker-Planck equation. These models present several advantages, which are of special interest given the issues raised in the previous section. By nature, the modelled PDF contains all the required statistical information on the flow, which includes both the turbulent convection and the oscillating modes. As such, this type of model is perfectly suited for the study of turbulence–oscillation coupling. In addition, all the usual quantities can be obtained from the PDF.

However, the direct modelling of the PDF, using its time evolution equation, can quickly become very cumbersome. The reason is that the PDF is a function not only of space and time, but also of each of the turbulent quantities used to represent the flow (starting with the three components of the velocity and the entropy). This makes the PDF equation computationally heavy to integrate, and quite impractical to handle analytically. This is why PDF models are often implemented in a Lagrangian particle framework, where the flow is no longer represented by a set of Eulerian, grid-based fluid quantities, but rather by a set of individual fluid particles whose properties (including their position) are tracked over time. Using Monte Carlo methods, the flow PDF can be reconstructed directly from the set of particles, so that the set contains the exact same statistical information as the PDF itself. In order to represent the turbulent nature of the flow, and to model the PDF accurately, particle properties must evolve according to stochastic differential equations rather than ordinary ones. Therefore, PDF models of turbulence go hand in hand with the implementation of Lagrangian stochastic methods, primarily because it makes their numerical integration much easier and more tractable. In this section we introduce the Lagrangian stochastic model, and we present how it can be rearranged to yield stochastic differential equations for Eulerian quantities instead.

We note that this paper aims to show that the method we present is relevant to the study of turbulence–oscillation coupling, and therefore serves as a proof of concept for this approach. As such, we do not claim to use the most realistic turbulence model possible, but rather we wish to limit the level of complexity so that the basics of this method may be understood in the most efficient way. We leave the use of a more realistic turbulence model for a later paper.

2.1. Lagrangian description: The generalised Langevin model

We consider the simplified case of an adiabatic[1] flow, in the sense that we do not include an energy equation in the system, and instead adopt a polytropic relation between the pressure and the density of the gas. In terms of Eulerian transport equations that would mean only considering the density, the mean velocity, and the Reynolds stress tensor as relevant fluid quantities, with the mean pressure being given, for instance, by the ideal gas law. In the framework of a Lagrangian stochastic model, however, that means that the only fluid particle properties whose evolution we need to put into equations are their position and velocity.

The equation for the particle position is derived by stating that it must evolve according to its own velocity. It reads

$$\mathrm{d}x_i^\star = u_i^\star \,\mathrm{d}t \,, \tag{1}$$

where $\mathbf{x}^\star$ and $\mathbf{u}^\star$ are the position and velocity of the fluid particle, which only depend on the time variable (as well as the initial state). In general, in the following the notation * will denote a stochastic variable. In order to account for the turbulent nature of the flow, the equation on velocity must take the form of a stochastic differential equation (SDE), instead of an ordinary one. In its most general form, an SDE takes the form (Gardiner 1994, Chap. 3)

$$\mathrm{d}u_i^\star = a_i(\mathbf{x}^\star, \mathbf{u}^\star, t)\,\mathrm{d}t + b_{ij}(\mathbf{x}^\star, \mathbf{u}^\star, t)\,\mathrm{d}W_j \,, \tag{2}$$

where we use the Einstein convention on repeated indices, a_i and b_{ij} are functions of the particle properties (and time), and $\mathbf{W}(t)$ is an isotropic Wiener process. The last is a stochastic process (i.e. a random variable whose statistical properties depend on time) whose PDF at any given time t is Gaussian, and which verifies

$$\overline{\mathbf{W}(t)} = \mathbf{0} \,, \tag{3}$$

$$\overline{W_i(t')W_j(t)} = (t' - t)\,\delta_{ij} \,, \tag{4}$$

where δ_{ij} is the Kronecker symbol and the notation $\overline{\cdot}$ refers to an ensemble average. We note that this is not a simplifying assumption regarding the stochastic part of the SDE, but rather a very general property, which is necessary for the resulting particle trajectory in phase-space to be continuous in time (Gardiner 1994). In terms of dimension, the drift vector a_i is an acceleration, while $\mathbf{W}$ is the square root of a time, and the diffusion tensor b_{ij} is a velocity divided by the square root of a time.

On the right-hand side of Eq. (2) the first term corresponds to the deterministic part of the force exerted on the fluid particle, while the randomness of the equation is only brought about by the second term. Physically, the stochastic part of Eq. (2) stems from the fluctuating components of both the pressure and viscous stress forces, which in turn are brought about by the underlying highly fluctuating turbulent velocity field. An illuminating analogy to consider is Brownian motion, which can also be described by means of Eq. (2), and where the stochastic part describes the random collision undergone by the colloidal particle from the water molecules. In the vocabulary of stochastic processes the function $a_i(\mathbf{x}^\star, \mathbf{u}^\star, t)$ is the i-th component of the drift vector, while $b_{ij}(\mathbf{x}^\star, \mathbf{u}^\star, t)$ is the i, j-component of the diffusion tensor. In order to close the system, an explicit expression is needed for these two coefficients.

The specification of the drift and diffusion terms in Eq. (2) is the subject of an abundant amount of literature on turbulence modelling (see Heinz & Buckingham 2004, for a review). It has long been recognised that, in order to be consistent with the Kolmogorov hypotheses, both original (Kolmogorov 1941) and refined (Kolmogorov 1962), the diffusion coefficient has to take the form (Obukhov 1959)

$$b_{ij}(\mathbf{x}^\star, t) = \sqrt{C_0 \epsilon(\mathbf{x}^\star, t)}\,\delta_{ij} \,, \tag{5}$$

where C_0 is a dimensionless constant and ϵ is the local dissipation rate of turbulent kinetic energy into heat. This is especially verified in the high Reynolds number limit (which is relevant in the stellar context), where C_0 then actually corresponds to the Kolmogorov constant. This constant is not universal per se; however, it tends asymptotically to a universal value for very high Reynolds numbers, in which case its value is fairly well constrained. An accepted experimental value is $C_0 = 2.1$ (Haworth & Pope 1986).

For the drift term we adopt the general expression given by the generalised Langevin model (Pope 1983)

$$a_i(\mathbf{x}^\star, \mathbf{u}^\star, t) = -\frac{1}{\overline{\rho}}\frac{\partial \overline{p}}{\partial x_i} + \overline{g_i} + G_{ij}\left(u_j^\star - \widetilde{u_j}\right) \,, \tag{6}$$

where $\overline{\rho}$, $\overline{p}$, and $\overline{\mathbf{g}}$ are the Reynolds average of the fluid density, gas pressure, and gravitational acceleration, respectively; G_{ij} is a second-order tensor that has the dimension of an inverse time, to which we refer as the drift tensor; and $\widetilde{\mathbf{u}}$ is the Favre average of the fluid velocity, with the mass-average (or Favre average) of any quantity ϕ being defined as

$$\widetilde{\phi} \equiv \frac{\overline{\rho\phi}}{\overline{\rho}} \,. \tag{7}$$

All these Reynolds or Favre averages are local and instantaneous quantities, and therefore depend on both time and space. In Eq. (6) they are evaluated at time t and at the position $\mathbf{x}^\star$ of the particle.

The various terms in Eq. (6) can be interpreted in the following way. The first two terms are the mean pressure gradient and the gravitational force exerted on the particle, and correspond to the mean force in the momentum equation, the only ones that remain in the absence of turbulence; we note that rotation and magnetic fields are not accounted for in this model. On the other hand, the last term ensures that, were the turbulent sources to disappear, the particle velocity would decay towards the local mean velocity, thus ensuring that the Reynolds stresses are dissipated. More precisely, the drift tensor can be thought of as the rate at which the various Reynolds stresses decay towards zero. In this paper we need not specify the form of the drift tensor, only to say that in the standard approach it is written as a function of the Reynolds stresses, the mean velocity gradients, and the turbulent dissipation (Haworth & Pope 1986)

$$G_{ij} = f\left(\widetilde{u_i'' u_j''}, \partial_i \widetilde{u_j}, \epsilon\right) \,, \tag{8}$$

where $\mathbf{u}'' \equiv \mathbf{u} - \widetilde{\mathbf{u}}$ denotes the fluctuation of the turbulent velocity around its local Favre average. In particular, G_{ij} only depends on the mean fields and not on the particle properties themselves.

[1] In the vocabulary of asteroseismology, the term 'adiabatic' can sometimes be used to express the absence of energy transfer between the oscillations and the background. We insist that this is not the case here. This term is meant to apply to the thermodynamic transformations undergone by the flow, not to the oscillations. In particular, the background can still inject energy into the modes or take energy from them, allowing the modes to be driven and damped.

Putting together Eqs. (1), (2), (5), and (6), we obtain

$$\mathrm{d}x_i^\star = u_i^\star \,\mathrm{d}t \,, \tag{9}$$

$$\mathrm{d}u_i^\star = \left[-\frac{1}{\overline{\rho}}\frac{\partial \overline{p}}{\partial x_i} + g_i + G_{ij}\left(u_j^\star - \widetilde{u_j}\right)\right]\mathrm{d}t + \sqrt{C_0\epsilon}\,\mathrm{d}W_i \,. \tag{10}$$

The mean fields $\overline{\rho}$, $\overline{p}$, $\widetilde{\mathbf{u}}$, G_{ij}, and ϵ still need to be closed; we return to this matter in Section 2.3.

The stochastic equations (9) and (10) contain more information than the corresponding average equations on the mean velocity and Reynolds stress tensor, the same way the PDF of a distribution carries more statistical information than its first few moments. We do not make use of these corresponding mean equations in the following; nevertheless, we provide them explicitly in Appendix A, to which the reader can refer for a better grasp on the origin of the SDE used in this study.

2.2. From Lagrangian to Eulerian variables

2.2.1. The Lagrangian mean trajectory formalism

By construction, the turbulence model given by Eqs. (9) and (10) is a Lagrangian model as it pertains to the properties of fluid particles followed along their trajectories. By contrast, we would like to obtain equations on stochastic variables pertaining to the stochastic properties of the flow at a fixed point. This would allow us to ultimately obtain a wave equation where the wave variables can be easily related to the known properties of the modes, something for which a purely Lagrangian[2] description is extremely impractical.

A very general approach to this transcription from Lagrangian to Eulerian variables is the Lagrangian mean trajectories formalism (Soward 1972; Andrews & McIntyre 1978). In the following, we give the general ideas and the main steps of the derivation; more detailed calculations are provided in Appendix B, to which we will refer each time an important step is reached. Let us consider a fluid particle whose time-independent average position is denoted by $\mathbf{x}$. Its instantaneous position at time t is written as an explicit function of $\mathbf{x}$ and t

$$\mathbf{X}(\mathbf{x}, t) = \mathbf{x} + \boldsymbol{\xi}(\mathbf{x}, t) \,, \tag{11}$$

where $\boldsymbol{\xi}$ is the particle displacement around its mean position[3], the mean position being interpreted as an Eulerian variable.

For any given Eulerian quantity ϕ, we define its Lagrangian counterpart as

$$\phi_L(\mathbf{x}, t) \equiv \phi(\mathbf{X}(\mathbf{x}, t), t) \,. \tag{12}$$

In particular, we denote by $\mathbf{u}_L$ the velocity field evaluated at $\mathbf{X}$, in other words the Lagrangian velocity, and by $u_{i,L}$ the i-th component of this velocity. Similarly, for any Eulerian averaging process $\langle . \rangle$, we define the corresponding Lagrangian mean $\langle . \rangle_L$ as

$$\langle \phi \rangle_L \equiv \langle \phi(\mathbf{X}(\mathbf{x}, t), t) \rangle \,. \tag{13}$$

[2] This statement may seem odd, as Lagrangian variables are actually often used in the analysis of stellar oscillations. However, in this study the term Lagrangian refers to a frame of reference attached to the total velocity of the flow (including both the turbulent velocity and the oscillation velocity), while the usual sense is rather meant to describe a frame of reference attached to the oscillations alone, and actually only ever refers to a pseudo-Lagrangian frame.

[3] The variable $\boldsymbol{\xi}$ contains the particle displacement due to the oscillations and to the turbulence. As such, it must not be confused with the fluid displacement due to the oscillations only, and to which the notation $\boldsymbol{\xi}$ usually refers.

For the time being, we do not yet specify the averaging process $\langle . \rangle$ as this formalism is very general and can be used regardless of how the means are defined. It is important to note here that the mean position $\mathbf{x}$ of the particle is defined in terms of this yet-to-be-determined averaging process. In the following we simply refer to $\langle . \rangle$ as the 'Eulerian mean', but let us keep in mind that it does not necessarily correspond to an ensemble average.

With the above notations and definitions, the following identity can be derived (Andrews & McIntyre 1978)

$$\left(\frac{D\phi}{Dt}\right)_L = \langle D \rangle_L (\phi_L) \,, \tag{14}$$

where $D/Dt \equiv \partial_t + \mathbf{u} \cdot \boldsymbol{\nabla}$ denotes the particle time derivative, and the operator $\langle D \rangle_L$ is defined by

$$\langle D \rangle_L \equiv \partial_t + \langle \mathbf{u} \rangle_L \cdot \boldsymbol{\nabla} \,, \tag{15}$$

and $\langle \mathbf{u} \rangle_L$ is the Lagrangian mean of the flow velocity. For a detailed derivation of this identity, we refer the reader to Appendix B.1. Because the Lagrangian and Eulerian frames are in motion with respect to one another, the index $_L$ does not commute with either the space or time derivative. For instance, $\partial(\phi_L)/\partial t$ corresponds to the time derivative of the quantity ϕ as seen from the point of view of a fluid parcel (i.e. in the Lagrangian frame), while $(\partial\phi/\partial t)_L$ is the time derivative of the quantity ϕ as seen from an Eulerian point of view, and then evaluated at a given Lagrangian coordinate, after the fact. Essentially, Eq. (14) describes how the material time derivative commutes with the passage from Lagrangian to Eulerian variables, and will therefore be useful for transcribing our Lagrangian model into a Eulerian one.

Applying Eq. (14) on position and velocity respectively yields

$$\frac{\partial \xi_i}{\partial t} = u_{i,L} - \langle u_i \rangle_L - \langle u_j \rangle_L \partial_j \xi_i \,, \tag{16}$$

$$\frac{\partial \left(u_{i,L}\right)}{\partial t} = \left(\frac{\partial u_i}{\partial t}\right)_L + \left[u_{j,L}\delta_{jk} - \langle u_j \rangle_L \delta_{jk} - \langle u_j \rangle_L \partial_j \xi_k\right]\left(\frac{\partial u_i}{\partial x_k}\right)_L \,. \tag{17}$$

The derivation of these two equations is given in detail in Appendix B.2. We note that, for the moment, the displacement $\boldsymbol{\xi}$ and velocity $\mathbf{u}$ are flow variables, which is why they are not denoted with a *. We now relate these flow quantities to the position $\mathbf{x}^\star$ and velocity $\mathbf{u}^\star$ of the fluid particles. Since $\boldsymbol{\xi}$ and $\mathbf{u}_L$ correspond to the displacement and velocity of the particle whose mean position is $\mathbf{x}$, then for any fixed $\mathbf{x}$ we have

$$\mathbf{x}^\star(t) = \mathbf{x} + \boldsymbol{\xi}(\mathbf{x}, t) \,, \tag{18}$$

$$\mathbf{u}^\star(t) = \mathbf{u}_L(\mathbf{x}, t) \,, \tag{19}$$

so that

$$\frac{\mathrm{d}\mathbf{x}^\star}{\mathrm{d}t} = \frac{\partial \boldsymbol{\xi}}{\partial t} \,, \tag{20}$$

$$\frac{\mathrm{d}\mathbf{u}^\star}{\mathrm{d}t} = \frac{\partial \left(\mathbf{u}_L\right)}{\partial t} \,. \tag{21}$$

Putting together Eqs. (10), (17), and (21) we obtain

$$\left(\frac{\partial u_i}{\partial t}\right)_L + \left[u_{j,L} - \langle u_j \rangle_L - \langle u_k \rangle_L \left(\frac{\partial \xi_j}{\partial x_k}\right)_L\right]\left(\frac{\partial u_i}{\partial x_j}\right)_L = -\frac{1}{\overline{\rho}_L}\left(\frac{\partial \overline{p}}{\partial x_i}\right)_L + g_{i,L} + G_{ij,L}\left(u_{j,L} - \widetilde{u}_{j,L}\right) + \sqrt{C_0\epsilon_L}\eta_{i,L} \,. \tag{22}$$

By construction, $\boldsymbol{\eta}(\mathbf{x},t) \equiv \mathrm{d}\mathbf{W}/\mathrm{d}t$ is a multi-variate Gaussian process whose values at two distinct locations are completely uncorrelated, and which verifies[4]

$$\overline{\boldsymbol{\eta}(\mathbf{x},t)} = \mathbf{0}\,, \tag{23}$$

$$\overline{\eta_i(\mathbf{x},t')\eta_j(\mathbf{x},t)} = \delta(t'-t)\delta_{ij}\,, \tag{24}$$

where $\delta(t)$ is the Dirac distribution.

Finally, we note that in this form, all the quantities present in Eq. (22) are evaluated at the instantaneous position $\mathbf{X}$. Insofar as the transformation $\mathbf{x} \mapsto \mathbf{X}$ is invertible (i.e. for any $\mathbf{x}$ and t there exists $\mathbf{y}$ such that $\mathbf{X}(\mathbf{y},t) = \mathbf{x}$), we can drop the notation $_L$ from this equation, except in $\langle\mathbf{u}\rangle_L$, thus yielding a stochastic equation for the evolution of the Eulerian velocity $\mathbf{u}$.

2.2.2. Specification of the averaging process

For the moment, we still have not specified the nature of the mean which defines both the mean particle position $\mathbf{x}$ and the Lagrangian mean velocity $\langle\mathbf{u}\rangle_L$. The specification of this averaging process is crucial, and the fact that this formalism applies to any averaging process is of the utmost importance. Usually, the Lagrangian mean trajectory formalism is used to transform the exact Eulerian hydrodynamics equations into equations on carefully defined Lagrangian means, which happen to be much more suitable to the study of hydrodynamic waves (Andrews & McIntyre 1978). In that context it is customary to consider that $\langle.\rangle$ actually denotes an ensemble average, so that the mean values contain the oscillations as well as the background equilibrium, whereas the fluctuations contain the turbulent fields.

In the present context, however, this is not the picture after which we are. Instead, we want the fluctuating part to contain the waves in addition to the turbulent fluctuations, whereas the means should only contain the background equilibrium. Only then can we obtain a wave equation directly containing turbulence-induced fluctuations, and therefore the turbulence–oscillation coupling. As such, we will define $\langle.\rangle$ as a time average over timescales that are very long compared to the typical turbulent timescale, the period of the oscillations, and their lifetime. This ensures that the mean values only contain the time-independent equilibrium, and the fluctuating part does indeed contain both the waves and the turbulent fields.

The fact that $\langle.\rangle$ denotes a time average also considerably simplifies Eqs. (16) and (22). The Lagrangian mean velocity $\langle\mathbf{u}\rangle_L$ is constructed in such a way that when the fluid velocity at $\mathbf{X}$ is $\mathbf{u}_L$, then the mean position $\mathbf{x}$ is displaced with the velocity $\langle\mathbf{u}\rangle_L$ (Andrews & McIntyre 1978). A perhaps more illustrative way of interpreting the quantities $\boldsymbol{\xi}$, $\mathbf{u}_L$, and $\langle\mathbf{u}\rangle_L$ is given in Fig. (1), in the case where $\langle.\rangle$ is defined as a spatial average in a given direction x. If we isolate a thin tube of fluid lying along this axis, then $\boldsymbol{\xi}$ corresponds to the local deformation of the tube, $\mathbf{u}_L$ corresponds to the instantaneous velocity of the local portion of tube, and $\langle\mathbf{u}\rangle_L$ corresponds to the velocity of the centre of mass of the tube.

In our case where 'average' refers to time average, $\langle\mathbf{u}\rangle_L$ refers to the movement of the centre of mass of a given parcel of fluid in the absence of turbulent convection and oscillations, or

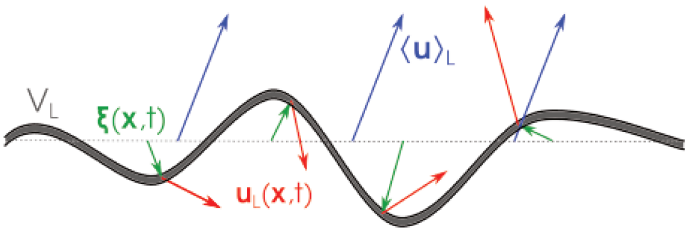

Fig. 1: Visualisation of the fluid displacement $\boldsymbol{\xi}$ (in green), Lagrangian velocity $\mathbf{u}_L$ (in red), and Lagrangian mean velocity $\langle\mathbf{u}\rangle_L$ (in blue), in the case where the mean $\langle.\rangle$ is defined as an average over a given axis (spanning horizontally in the figure). The grey volume V_L represents a thin tube of fluid initially lying along the horizontal direction. The fluid displacement and velocity $\boldsymbol{\xi}$ and $\mathbf{u}_L$ pertain to the deformation and local velocity of the tube, while $\langle\mathbf{u}\rangle_L$ refers to the velocity of the centre of mass of the tube, represented by the dashed horizontal line. This illustration is inspired by Andrews & McIntyre (1978) (see bottom panel of their Figure 1).

in other words, to the background fluid velocity. We note that the effects of rotation, if we were to take them into account, would be encompassed in $\langle\mathbf{u}\rangle_L$. In the absence of rotation, however, we have $\langle\mathbf{u}\rangle_L = \mathbf{0}$, and Eqs. (16) and (22) then reduce to

$$\frac{\partial\xi_i}{\partial t} = u_i(\mathbf{x}+\boldsymbol{\xi},t)\,, \tag{25}$$

$$\frac{\partial u_i}{\partial t} + u_j\frac{\partial u_i}{\partial x_j} = -\frac{1}{\overline{\rho}}\frac{\partial\overline{p}}{\partial x_i} + g_i + G_{ij}\left(u_j - \widetilde{u_j}\right) + \sqrt{C_0\epsilon}\,\eta_i\,. \tag{26}$$

It must be noted that while the velocity appearing on the right-hand side of Eq. (25) is evaluated at the Lagrangian position $\mathbf{x}+\boldsymbol{\xi}(\mathbf{x},t)$, every quantity in Eq. (26), by contrast, is evaluated at the Eulerian position $\mathbf{x}$. Furthermore, it should be noted that everything depends on time, even when not explicitly specified. The key difference between Eqs. (9) and (10), on the one hand, and (25) and (26) on the other, is that the variables whose evolution is described are no longer the Lagrangian quantities $\mathbf{x}^\star(t)$ and $\mathbf{u}^\star(t)$ pertaining to a set of fluid particles, but the Eulerian quantities $\boldsymbol{\xi}(\mathbf{x},t)$ and $\mathbf{u}(\mathbf{x},t)$ pertaining to a set of Eulerian fixed positions $\mathbf{x}$. This description will allow for a much more practical derivation of the wave equation in Section 3.1.

In particular, the momentum equation now makes the contribution of the turbulent pressure explicitly appear, in the form of the advection term on the left-hand side of Eq. (26). The contribution of the turbulent fluctuations of the gas pressure and the turbulent dissipation, on the other hand, are still contained in the last two terms on the right-hand side. Furthermore, the procedure described in this section allowed us to rigorously separate the effect of the equilibrium background (defined by a time average over very long timescales) from the joint contributions of the turbulence and of the oscillations (both of which are contained in the fluctuations around the equilibrium background), and thus will allow us to study their mutual coupling in a consistent framework.

2.3. Evaluating the mean fields: Smoothed particle hydrodynamics

The stochastic model on fluid displacement $\boldsymbol{\xi}$ and velocity $\mathbf{u}$, comprised of Eqs. (25) and (26), is still not in closed form, as it contains several mean quantities (mean density $\overline{\rho}$, gas pressure $\overline{p}$, and velocity $\widetilde{\mathbf{u}}$), as well as the turbulent dissipation ϵ appearing

[4] The stochastic process $\mathbf{W}(t)$ is not defined as an ordinary function of time, and therefore its derivative $\boldsymbol{\eta}$ cannot be defined the classical way; in fact, $\mathbf{W}$ is nowhere differentiable, as can be seen from Eq. (4). However, $\boldsymbol{\eta}$ can be defined formally, with its statistical properties given in the sense of distributions rather than ordinary functions. These definitions are at the heart of Ito stochastic calculus (Gardiner 1994, Chap 4).

in the diffusion tensor, and the Reynolds stress tensor $\widetilde{u_i'' u_j''}$ and shear tensor $\partial_i \widetilde{u_j}$ on which the drift tensor G_{ij} depends. These equations must therefore be supplemented with a model for the mean fields.

One possibility is to make use of a large-eddy simulation (LES) (or direct numerical simulation) to simulate the large-scale flow using the exact equations of hydrodynamics, and then use the mean fields yielded by this simulation as external inputs into the stochastic model. However, the mean fields appearing in Eq. (26) are instantaneous averages (for example, $\overline{\rho}$ is the Reynolds-averaged density at a given time t), not time averages. As a result, the ergodic principle cannot be used to extract the means from a LES. The only way to do this would be to consider that horizontal averages in a 3D LES provide an accurate estimate of instantaneous ensemble averages, and would only work in the scope of a 1D model. Furthermore, this procedure would defeat the purpose of what we are trying to achieve; since the mean fields contain the information on the oscillations, without containing the turbulence, treating them as external inputs would effectively amount to modelling the turbulence and the oscillations in a separate manner, which is what we are trying to avoid.

An alternative method makes use of the particle representation we adopt in Section 2.1. The set of fluid particles used to represent the flow contains all the required statistical information, so that the mean fields can actually be estimated directly from the set of fluid particles themselves (Welton & Pope 1997). This is the core idea behind particle methods, and particularly smoothed particle hydrodynamics (SPH). The reader can refer to Liu & Liu (2010) or Monaghan (1992) for a comprehensive review on the subject, or to Springel (2010) for the use of SPH in the astrophysical context, but we give an outline of this method in the following.

Ideally, we would like to estimate all local means at a given Eulerian position $\mathbf{x}$ by averaging the corresponding particle-level quantity over all fluid particles conditioned on their being located at $\mathbf{x}$. However, implementing this last condition exactly does not yield the required result: for any given position $\mathbf{x}$, any individual fluid particle has exactly zero probability of finding itself at this exact location. Therefore, it is necessary to relax the condition on particle position, and instead of computing means over particles exactly located at $\mathbf{x}$, we compute them over particles within a given compact-support vicinity of $\mathbf{x}$.

Thus, a kernel function $K(\mathbf{r})$ is introduced, which serves as a weighting function to implement the particle-position condition in the estimation of the means. The exact form of K is not important here, but we mention some of its properties, namely that it is a compact-support function, it is normalised to unity, and it is isotropic. The first two properties are mandatory, as the first one ensures that distant particles cannot impact local means, and the second that the estimation of the means is unbiased. The third property makes the subsequent calculations much easier to carry out. A good example is the kernel function used by Welton & Pope (1997)

$$\begin{aligned} K(\mathbf{r}) &= c\left(1+3\frac{|\mathbf{r}|}{h}\right)\left(1-\frac{|\mathbf{r}|}{h}\right)^3 && \text{if } |\mathbf{r}|<h\,, \\ &= 0 && \text{if } |\mathbf{r}|>h\,, \end{aligned} \tag{27}$$

where $\mathbf{r}$ is the position of the particle with respect to the centre of the kernel (where the mean is estimated), $c = 105/(16\pi h^3)$ is defined by the normalisation condition[5], and h is the size of the kernel compact support. This expression ensures that the kernel function and its first two derivatives are continuous at the surface of its support.

The SPH formalism is best formulated if we temporarily return to the representation of the flow as a large set of N particles, whose position and velocity we denote by $\mathbf{x}^{\star(i)}$ and $\mathbf{u}^{\star(i)}$, respectively, where i is the index used to identify each particle. For any quantity Q pertaining to the flow representation, if there is an equivalent quantity $Q^\star$ in the particle representation, we can estimate the mean value of Q at any Eulerian position $\mathbf{x}$ and time t through the following kernel estimator

$$\overline{Q(\mathbf{x},t)} = \sum_{i=1}^{N} \frac{\Delta m^{(i)}}{\rho^{(i)}} Q^{\star(i)}(t) K\left(\mathbf{x}^{\star(i)}(t)-\mathbf{x}\right)\,, \tag{28}$$

where $\Delta m^{(i)}$ is the mass carried by the particle i, and $\rho^{(i)}$ is the mass density characterising particle i. As such, the quantity $\Delta m^{(i)}/\rho^{(i)}$ appearing under the sum corresponds to the lumped volume of fluid that the particle represents.

Setting $Q^\star = \rho$, $Q^\star = \rho\mathbf{u}^\star$, and $Q^\star = \rho(u_i^\star - \widetilde{u_i})(u_j^\star - \widetilde{u_j})$ alternatively in Eq. (28), we find respectively the Reynolds-averaged density, the mass-averaged velocity, and the Reynolds stress tensor

$$\overline{\rho}(\mathbf{x},t) = \sum_{i=1}^{N} \Delta m^{(i)} K(\mathbf{x}^{\star(i)}(t)-\mathbf{x})\,, \tag{29}$$

$$\widetilde{\mathbf{u}}(\mathbf{x},t) = \frac{1}{\overline{\rho}(\mathbf{x},t)} \sum_{i=1}^{N} \Delta m^{(i)} \mathbf{u}^{\star(i)}(t) K(\mathbf{x}^{\star(i)}(t)-\mathbf{x})\,, \tag{30}$$

$$\begin{aligned} \widetilde{u_i'' u_j''}(\mathbf{x},t) = \frac{1}{\overline{\rho}(\mathbf{x},t)} \sum_{i=1}^{N} \Delta m^{(i)} &\left(u_i^{\star(i)}(t) - \widetilde{u_i}(\mathbf{x},t)\right) \\ &\times \left(u_j^{\star(i)}(t) - \widetilde{u_j}(\mathbf{x},t)\right) K(\mathbf{x}^{\star(i)}(t)-\mathbf{x})\,. \end{aligned} \tag{31}$$

In particular, we note that in the SPH formalism, the local mean density is computed by counting the particles present in the vicinity. This means that the continuity condition is automatically met in the particle representation, thus lowering the order of the set of equations needed to describe the flow.

We then rewrite Eqs. (29), (30), and (31) in the representation chosen in Section 2.2, specifically in terms of $\boldsymbol{\xi}(\mathbf{x})$ and $\mathbf{u}(\mathbf{x})$ rather than $\mathbf{x}^{\star(i)}$ and $\mathbf{u}^{\star(i)}$. To do so, we perform the change of variables given by Eqs. (18) and (19). Furthermore, the sum over infinitesimally small masses can be replaced by a continuous integral over $\mathrm{d}m \equiv \rho_0(\mathbf{y})\,\mathrm{d}^3\mathbf{y}$, where ρ_0 is the equilibrium fluid density (which can be thought of as an average of the local fluid density over very long timescales so as to only contain the background value). Finally, in this new representation, the SPH

[5] The reason the value of c given here is different from the value $c = 4/(5h)$ given in Welton & Pope (1997) is that they considered the 1D case, whereas we consider the 3D case.

formalism yields

$$\overline{\rho}(\mathbf{x},t) = \int \mathrm{d}^3\mathbf{y}\, \rho_0(\mathbf{y}) K(\mathbf{y}+\boldsymbol{\xi}(\mathbf{y},t)-\mathbf{x})\,, \tag{32}$$

$$\widetilde{\mathbf{u}}(\mathbf{x},t) = \frac{1}{\overline{\rho}(\mathbf{x},t)} \int \mathrm{d}^3\mathbf{y}\, \rho_0(\mathbf{y}) \mathbf{u}(\mathbf{y}+\boldsymbol{\xi}(\mathbf{y},t),t) K(\mathbf{y}+\boldsymbol{\xi}(\mathbf{y},t)-\mathbf{x})\,, \tag{33}$$

$$\widetilde{u_i'' u_j''}(\mathbf{x},t) = \frac{1}{\overline{\rho}(\mathbf{x},t)} \int \mathrm{d}^3\mathbf{y}\, \rho_0(\mathbf{y}) \Big(u_i(\mathbf{y}+\boldsymbol{\xi}(\mathbf{y},t),t) - \widetilde{u}_i(\mathbf{y},t)\Big) \times \Big(u_j(\mathbf{y}+\boldsymbol{\xi}(\mathbf{y},t),t) - \widetilde{u}_j(\mathbf{y},t)\Big) K(\mathbf{y}+\boldsymbol{\xi}(\mathbf{y},t)-\mathbf{x})\,. \tag{34}$$

While these integrals span across the entire volume of the star, we note that they actually only involve the compact support vicinity of $\mathbf{x}$ defined by the kernel function K.

Two more points need to be addressed here. The first concerns the mean pressure $\overline{p}$. For the sake of simplicity, we consider a polytropic relation between the gas pressure and density in the form

$$\ln\left(\frac{\overline{p}(\mathbf{x},t)}{p_0(\mathbf{x})}\right) = \gamma(\mathbf{x}) \ln\left(\frac{\overline{\rho}(\mathbf{x},t)}{\rho_0(\mathbf{x})}\right)\,, \tag{35}$$

where p_0 is the equilibrium gas pressure (defined in the same way as ρ_0), and we allow the polytropic exponent γ to depend on space. We note that we do not consider the possibility that the oscillations may entail fluctuations in the polytropic index itself. We also note that we can recover the isentropic case at any point by setting $\gamma = \Gamma_1$, where Γ_1 is the equilibrium first adiabatic exponent.

The second point concerns the turbulent dissipation rate ϵ, or equivalently the turbulent frequency ω_t defined through

$$\omega_t \equiv \frac{\epsilon}{k} = \frac{2\epsilon}{\widetilde{u_i'' u_i''}}\,, \tag{36}$$

where k is the turbulent kinetic energy. Physically, ω_t can be interpreted as the inverse of the characteristic lifetime associated with the energy-bearing eddies. The turbulent kinetic energy k is given in closed form by the velocity part of the model (here it is given by half the trace of Eq. 34), and we still need to model ω_t. Usually, this is done either by adding a model equation for the mass-averaged dissipation rate $\widetilde{\omega_t}$, which is very similar to the approach followed in two-equation models of turbulence, such as the $k-\epsilon$ model (Jones & Launder 1972), or else by adding $\omega_t^\star$ to the particle properties in the Lagrangian stochastic model, such as in the refined Langevin model (Pope & Chen 1990). However, in the present work, and in the scope of the generalised Langevin model, we regard ω_t as a time-independent equilibrium quantity, which can still, however, depend on $\mathbf{x}$. Physically, this amounts to assuming that all eddies have the same typical lifetime, regardless of their size, but that it can depend on the depth at which they are located. In the long run, it will be necessary to go beyond this drastic assumption.

To recap Section 2, the model equations are Eqs. (25) and (26), which are stochastic differential equations governing the evolution of the fluid displacement $\boldsymbol{\xi}(\mathbf{x},t)$ and the Eulerian velocity $\mathbf{u}(\mathbf{x},t)$ for any given Eulerian position $\mathbf{x}$. The mean density $\overline{\rho}$, the mass-averaged velocity $\widetilde{\mathbf{u}}$, and the Reynolds stress tensor $\widetilde{u_i'' u_j''}$ are given by Eqs. (32), (33), and (34), respectively, as explicit functions of $\boldsymbol{\xi}(\mathbf{x},t)$ and $\mathbf{u}(\mathbf{x},t)$ only. The mean pressure is given by Eq. (35) as a function of mean density, and the turbulent dissipation rate ϵ is given by Eq. (36). Therefore, all the quantities appearing in the model equations are written explicitly as functions of the modelled variables $\boldsymbol{\xi}(\mathbf{x},t)$ and $\mathbf{u}(\mathbf{x},t)$ themselves: the model is in closed form. The only inputs of the model are 1) the equilibrium density $\rho_0(\mathbf{x})$, gas pressure $p_0(\mathbf{x})$, and polytropic exponent $\gamma(\mathbf{x})$, which can be extracted from an equilibrium model of the star; 2) the functional form of the drift tensor G_{ij} (see Eq. 8), which can be constrained using direct numerical simulations or experimental measurements (Pope 1994); and 3) the equilibrium turbulent frequency $\omega_t(\mathbf{x})$, which can be constrained using a 3D hydrodynamic simulation of the atmosphere of the star, or on the contrary serve as a control parameter for turbulence, which can be varied for a parametric study.

3. The stochastic wave equation

We now set out to linearise the closed set of equations derived in Section 2 to obtain a linear stochastic wave equation that was designed to govern the physics of the mode while simultaneously encompassing the effect of turbulence on the mode. We then discuss the properties of this wave equation, and how it relates to other forms of the wave equation obtained in previous studies.

3.1. Linearisation of the stochastic model

The system to linearise is comprised of Eqs. (25), (26), (32), (33), (34), (35), and (36). The only variables in these equations are the fluid displacement $\boldsymbol{\xi}(\mathbf{x},t)$ and the Eulerian velocity $\mathbf{u}(\mathbf{x},t)$. We define

$$\boldsymbol{\xi}_{\rm osc}(\mathbf{x},t) \equiv \boldsymbol{\xi}(\mathbf{x},t) - \boldsymbol{\xi}_t(\mathbf{x},t)\,, \tag{37}$$

$$\mathbf{u}_{\rm osc}(\mathbf{x},t) \equiv \mathbf{u}(\mathbf{x},t) - \mathbf{u}_t(\mathbf{x},t)\,, \tag{38}$$

where $\boldsymbol{\xi}_t$ and $\mathbf{u}_t$ are the fluid displacement and velocity that would be obtained if there were no oscillations, and that represent the turbulent component of the fluid displacement and velocity, and $\boldsymbol{\xi}_{\rm osc}$ and $\mathbf{u}_{\rm osc}$ are the oscillatory displacement and velocity. We note that while the variables are split into a turbulent and an oscillatory component, the system of equations itself is not split into equations for turbulence and equations for oscillations; instead, there is still only one system of equations containing both components. This is in contrast, for instance, with MLT or Reynolds-Averaged Navier-Stokes (RANS) approaches where the equations are averaged from the start, thus implicitly separating the two components whose coupling we wish to study.

Obtaining a linear wave equation requires the adoption of a certain number of hypotheses regarding the fluid variables, which we itemise here.

(H1) We consider $|\mathbf{u}_{\rm osc}| \ll |\mathbf{u}_t|$. This ordering is justified by the fact that, at the top of the convective envelope of solar-like oscillators, the typical turbulent velocities have much higher amplitudes than the oscillatory velocities; the former are of the order of a few km.s^{-1}, while the latter are of the order of a few tens of cm.s^{-1}. This allows us to treat $\mathbf{u}_{\rm osc}$ as a first-order perturbation compared to $\mathbf{u}_t$, and any second- or higher-order occurrence of $\mathbf{u}_{\rm osc}$ will be discarded.

(H2) We consider $|\boldsymbol{\xi}_{\rm osc}| \ll h, H_p$, where we recall that h is the size of the averaging kernel function K, and $H_p \equiv -(\mathrm{d}\ln p_0/\mathrm{d}r)^{-1}$ is the pressure scale height. In other words, the modal fluid displacement is much smaller than the stratification length scale, and the width of the kernel function must be sufficiently large. The first hypothesis is justified by the fact that, in the Sun for instance, the modal displacement is of the order of a

few tens of meters, while H_p is of the order of a few hundreds of kilometers. The second hypothesis, on the other hand, constitutes a constraint on h. This allows us to treat $\boldsymbol{\xi}_{\rm osc}$ as a first-order perturbation compared to all length scales relevant to the problem, and any second- or higher-order occurrence of $\boldsymbol{\xi}_{\rm osc}$ will be discarded.

(H3) We adopt the anelastic approximation for turbulence, in the sense that we consider $\rho_t \ll \rho_0$, where ρ_t is the turbulent fluctuation of density, and ρ_0 the equilibrium density. This is the most severe approximation we make in this section. Nevertheless, the anelastic approximation is widely used in analytical models of turbulent convection in these regions, on the grounds that the flow is subsonic (with turbulent Mach numbers peaking at around 0.3 in the superadiabatic region), as shown by 3D hydrodynamic simulations of the atmosphere of these stars (Nordlund et al. 2009). Using the continuity equation, this amounts to neglecting the quantity $\boldsymbol{\nabla} \cdot (\rho_0 \boldsymbol{\xi}_t)$. As will become apparent in the following, this allows us to discard all $\boldsymbol{\xi}_t$-dependent contributions in the linearisation of the ensemble averages in the SPH formalism.

(H4) We consider that the turbulent velocity field $\mathbf{u}_t$ is the same as it would be without the presence of an oscillating velocity $\mathbf{u}_{\rm osc}$; in other words, we neglect the back-reaction of the oscillations on the turbulent motions of the gas. We justify this approximation in Appendix C on the basis of a discussion that can be found in Bühler (2009, see their Section 5.1.1). We note that the back-reaction being neglected here concerns both the equilibrium part and the stochastic part (i.e. both the equilibrium structure of the star and the turbulent velocity field). This assumption allows us to consider $\mathbf{u}_t$ as an input to the model, whose statistical properties (average, covariance, autocorrelation function) are considered completely known.

(H5) We consider that the gravitational potential is not perturbed by the turbulent motions of the gas or by its oscillatory motions. These are actually two separate approximations. The first is justified by the fact that the Reynolds-averaged mass flow through any given horizontal layer due to turbulence is zero, meaning the total mass present beneath this layer is always the same. The second corresponds to the Cowling approximation, and is justified for modes that feature a large number of radial nodes. These two approximations put together allow us to replace the gravitational acceleration $\mathbf{g}$ by its equilibrium value $\mathbf{g}_0$, which only depends on the hydrostatic equilibrium of the star.

We insist on the fact that these approximations, with the exception of (H5), only concern the fluid displacement and velocity. By contrast, no specific approximation is adopted concerning the mean fields; a linearised form of these mean fields naturally arises from the SPH formalism and the hypotheses (H1) through (H4). As an example, let us consider the mean density $\overline{\rho}$. Plugging Eq. (37) into Eq. (32), we find

$$\overline{\rho}(\mathbf{x},t) = \int \mathrm{d}^3\mathbf{y}\, \rho_0(\mathbf{y}) K\left(\mathbf{y} + \boldsymbol{\xi}_t(\mathbf{y},t) + \boldsymbol{\xi}_{\rm osc}(\mathbf{y},t) - \mathbf{x}\right) . \tag{39}$$

Then, using (H2) to linearise in terms of the displacement, we find

$$\begin{aligned}\overline{\rho}(\mathbf{x},t) = \int \mathrm{d}^3\mathbf{y}\, \rho_0(\mathbf{y}) K(\mathbf{y}-\mathbf{x}) + \int \mathrm{d}^3\mathbf{y}\, \rho_0(\mathbf{y})\, \left(\boldsymbol{\xi}_{\rm osc}(\mathbf{y},t)\cdot\boldsymbol{\nabla}\right) K\big|_{\mathbf{y}-\mathbf{x}} \\ + \int \mathrm{d}^3\mathbf{y}\, \rho_0(\mathbf{y})\, \left(\boldsymbol{\xi}_t(\mathbf{y},t)\cdot\boldsymbol{\nabla}\right) K\big|_{\mathbf{y}-\mathbf{x}} .\end{aligned} \tag{40}$$

The first term on the right-hand side corresponds to the kernel estimate of ρ_0 at $\mathbf{x}$. By construction, kernel estimation is a representation of ensemble averaging, but ρ_0 is already an equilibrium quantity, and therefore is equal to its own ensemble average. Furthermore, the last term on the right-hand side can be discarded on account of hypothesis (H3). Performing an integration by part makes the quantity $\boldsymbol{\nabla} \cdot (\rho_0 \boldsymbol{\xi}_t)$ appear under the integral sign. Therefore, we eventually find

$$\overline{\rho}(\mathbf{x},t) = \rho_0(\mathbf{x}) + \underbrace{\int \mathrm{d}^3\mathbf{y}\, \rho_0(\mathbf{y})\, \left(\boldsymbol{\xi}_{\rm osc}(\mathbf{y},t)\cdot\boldsymbol{\nabla}\right) K\big|_{\mathbf{y}-\mathbf{x}}}_{\equiv \rho_1(\mathbf{x},t)} . \tag{41}$$

The quantity ρ_1 represents the Eulerian modal fluctuations of density, but of important note is the fact that at no point did we explicitly decompose $\overline{\rho}$ into an equilibrium value ρ_0 and a residual, oscillatory part; instead, the decomposition (41) arises naturally from the SPH formalism, and hypotheses (H2) and (H3).

The linear wave equation is derived in detail in Appendix D using the hypotheses listed above. Ultimately, we obtain

$$\frac{\partial \boldsymbol{\xi}_{\rm osc}}{\partial t} - \mathbf{u}_{\rm osc} - (\boldsymbol{\xi}_{\rm osc}\cdot\boldsymbol{\nabla})\mathbf{u}_t - (\boldsymbol{\xi}_t\cdot\boldsymbol{\nabla})\mathbf{u}_{\rm osc} = (\boldsymbol{\xi}_t\cdot\boldsymbol{\nabla})\mathbf{u}_t , \tag{42}$$

$$\frac{\partial \mathbf{u}_{\rm osc}}{\partial t} - \mathbf{L}_1^d - \mathbf{L}_1^s = \mathbf{L}_0 , \tag{43}$$

where

$$\begin{aligned}L_{1,i}^d = {} & \left[\frac{1}{\rho_0}\frac{\partial p_0}{\partial x_i} - \frac{\partial c_0^2}{\partial x_i}\right]\frac{1}{\rho_0}\int \mathrm{d}^3\mathbf{y}\, \rho_0(\mathbf{y})\left(\xi_{\rm osc,j}\partial_j K^{\mathbf{x}}\right)\Big|_{\mathbf{y},t} \\ & + \frac{c_0^2}{\rho_0}\int \mathrm{d}^3\mathbf{y}\, \rho_0(\mathbf{y})\left(\xi_{\rm osc,j}\partial_j\partial_i K^{\mathbf{x}}\right)\Big|_{\mathbf{y},t} \\ & + G_{ij,0}\left(u_{\rm osc,j} - \frac{1}{\rho_0(\mathbf{x})}\int \mathrm{d}^3\mathbf{y}\, \rho_0(\mathbf{y}) u_{\rm osc,j}(\mathbf{y}) K^{\mathbf{x}}(\mathbf{y})\right) ,\end{aligned} \tag{44}$$

$$\begin{aligned}L_{1,i}^s = {} & -u_{\rm osc,j}\partial_j u_{t,i} - u_{t,j}\partial_j u_{\rm osc,i} \\ & - G_{ij,0}\frac{1}{\rho_0}\int \mathrm{d}^3\mathbf{y}\, \rho_0(\mathbf{y})\left(\xi_{\rm osc,k}\partial_k\left(u_{t,j}K^{\mathbf{x}}\right)\right)\Big|_{\mathbf{y},t} \\ & + \left(\frac{\partial G_{ij}}{\partial \widetilde{u_k'' u_l''}}\widetilde{u_k'' u_l''}_{\,1} + \frac{\partial G_{ij}}{\partial(\partial_k \widetilde{u_l})}\partial_k\widetilde{u_l} + \frac{\partial G_{ij}}{\partial \epsilon}\omega_t k_1\right) u_{t,j} \\ & + \frac{1}{2}\sqrt{\frac{C_0\omega_t}{k_0}} k_1 \eta_i ,\end{aligned} \tag{45}$$

$$L_{0,i} = -\frac{1}{\rho_0}\frac{\partial\left(\rho_0 u_{t,i}u_{t,j} - \rho_0\overline{u_{t,i}u_{t,j}}\right)}{\partial x_j} , \tag{46}$$

$$\begin{aligned}\widetilde{u_i'' u_j''}_{\,1} = {} & -\frac{\widetilde{u_i'' u_j''}_{\,0}}{\rho_0}\int \mathrm{d}^3\mathbf{y}\, \rho_0 \xi_{\rm osc,k}\partial_k K^{\mathbf{x}} \\ & + \frac{1}{\rho_0}\int \mathrm{d}^3\mathbf{y}\, \rho_0 \xi_{\rm osc,k}\partial_k\left(u_{t,i}u_{t,j}K^{\mathbf{x}}\right) \\ & + \frac{1}{\rho_0}\int \mathrm{d}^3\mathbf{y}\, \rho_0 u_{t,i}u_{\rm osc,j}K^{\mathbf{x}} \\ & + \frac{1}{\rho_0}\int \mathrm{d}^3\mathbf{y}\, \rho_0 u_{t,j}u_{\rm osc,i}K^{\mathbf{x}} ,\end{aligned} \tag{47}$$

$$(\partial_i \widetilde{u_j})_1 = -\frac{1}{\rho_0}\int \mathrm{d}^3\mathbf{y}\,\rho_0 u_{\mathrm{osc,j}}\partial_i K^{\mathbf{x}} - \frac{1}{\rho_0}\int \mathrm{d}^3\mathbf{y}\,\rho_0\xi_{\mathrm{osc,k}}\partial_k u_{t,j}\partial_i K^{\mathbf{x}} - \frac{1}{\rho_0^2}\frac{\partial\rho_0}{\partial x_i}\int \mathrm{d}^3\mathbf{y}\,\rho_0 u_{\mathrm{osc,j}}K^{\mathbf{x}} - \frac{1}{\rho_0^2}\frac{\partial\rho_0}{\partial x_i}\int \mathrm{d}^3\mathbf{y}\,\rho_0\xi_{\mathrm{osc,k}}\partial_k\left(u_{t,j}K^{\mathbf{x}}\right)\,, \tag{48}$$

$$k_1 = \frac{1}{2}\widetilde{u_i'' u_i''}\,, \tag{49}$$

where $c_0^2 \equiv p_0\gamma/\rho_0$ is the equilibrium sound speed squared, and we have introduced the **x**-centred kernel function $K^{\mathbf{x}}(\mathbf{y}) \equiv K(\mathbf{y}-\mathbf{x})$. The right-hand sides of Eqs. (42) and (43) constitute inhomogeneous forcing terms (see Section 3.2 for more details), and it was therefore possible to filter out certain negligible contributions. We refer the reader to the details given in Section D.3, where we essentially argue first that the non-stochastic zeroth-order terms in the linearised equations vanish under the unperturbed hydrostatic equilibrium condition, and then that the linear forcing (i.e. the stochastic zeroth-order terms that are linear in the stochastic processes $\boldsymbol{\xi}_t$, $\mathbf{u}_t$ or $\boldsymbol{\eta}$) is negligible. The last point is related to the fact that the turbulent spectrum has most of its power in wavevectors and angular frequencies far removed from those characteristic of the modes, and therefore unable to provide with efficient mode driving.

Formally, Eqs. (42) and (43) take the form of a linear stochastic, inhomogeneous wave equation in a completely closed form, in the sense that the various terms on their right-hand side are written as explicit functions of the wave variables $\boldsymbol{\xi}_{\mathrm{osc}}$ and $\mathbf{u}_{\mathrm{osc}}$ themselves or the turbulent fields $\boldsymbol{\xi}_t$ and $\mathbf{u}_t$, whose statistical properties are considered known (see hypothesis H4). In writing Eq. (43), we split the velocity equation into three components. $\mathbf{L}_1^d$ contains all the terms that are linear in $\boldsymbol{\xi}_{\mathrm{osc}}$ and $\mathbf{u}_{\mathrm{osc}}$, but do not explicitly contain either stochastic processes $\boldsymbol{\xi}_t$, $\mathbf{u}_t$, or $\boldsymbol{\eta}$. It represents the deterministic contribution to the homogeneous part of the wave equation, and corresponds to the classical propagation of acoustic waves, without any impact from the turbulence. On the other hand, $\mathbf{L}_1^s$ contains all the terms that are linear in $\boldsymbol{\xi}_{\mathrm{osc}}$ and $\mathbf{u}_{\mathrm{osc}}$ and explicitly depend on $\boldsymbol{\xi}_t$, $\mathbf{u}_t$, or $\boldsymbol{\eta}$. Finally, $\mathbf{L}_0$ contains all the terms that are independent of $\boldsymbol{\xi}_{\mathrm{osc}}$ and $\mathbf{u}_{\mathrm{osc}}$. The reason for this specific decomposition will become apparent in a moment, when we discuss the physical role played by each term.

3.2. Effects of turbulence on the wave equation

The last term on the left-hand side of Eq. (43), together with its right-hand side, contain the contribution of turbulence to the wave equation, which arises from the action of the turbulent fields on the oscillations. We can see that one effect of turbulence is to add the inhomogeneous part $\mathbf{L}_0$ to the wave equation. This part acts as a forcing term, and Eq. (46) shows that it corresponds to the fluctuations of the turbulent pressure around its ensemble average. This is in perfect accordance with the widely accepted picture that the stochastic excitation of the global modes of oscillation in solar-like stars is due mainly to quadrupolar turbulent acoustic emission (Samadi & Goupil 2001). Furthermore, we note that we only kept the contributions to mode excitation that are not linear in the turbulent velocity field as linear contributions turn out to be negligible (see Section D.3 for a more developed discussion). We note that the non-linear Lagrangian, turbulent fluctuations of entropy, which is widely recognised as another source of stochastic driving for solar-like p-modes, does not arise from the above formalism. The only reason is because we considered a polytropic equation of state from the start, and as such neglected to model entropy fluctuations in both the oscillations and the turbulence.

The second effect of the turbulent fields on the oscillations is to modify the linear part, that is to say the propagation of the waves. This stochastic correction corresponds to the term $\mathbf{L}_1^s$ defined by Eq. (45). This term models two effects that are usually studied as distinct phenomena, but are actually intertwined and cannot be considered separately: a shift in the eigenfrequency of the resonant modes of the system (commonly referred to as the modal or 'intrinsic' part of the surface effects), and the absorption, or damping, of the energy of the waves as they travel through the turbulent medium. Equation (45) shows that these phenomena arise either from the non-linear advection term in the momentum equation, as represented by the first two terms on its right-hand side, or from the joint effect of turbulent dissipation, buoyancy, and pressure-rate-of-strain correlations, as jointly represented by all the other terms. It is apparent, in particular, that while the former is linear in $\mathbf{u}_t$, the latter has a more complicated multipolar decomposition in terms of $\mathbf{u}_t$, with first-, second-, and third-order contributions alike. As a whole, the term $\mathbf{L}_1^s$ in the velocity equation plays the same role, for instance, as $\mathcal{D}(\mathbf{v}_{\mathrm{osc}})$ in Samadi & Goupil (2001) (see their Eq. 26).

3.3. Limiting case: The standard wave equation

We now explore the limiting case where there is no turbulence, in which case the only term that remains in Eq. (43) is $\mathbf{L}_1^d$. In the absence of turbulence the integrals appearing in Eq. (44) are drastically simplified because, in this limit, the wave variables $\boldsymbol{\xi}_{\mathrm{osc}}$ and $\mathbf{u}_{\mathrm{osc}}$ are equal to their own ensemble average, that is to say to their own kernel estimate. This allows us to write, for instance

$$\int \mathrm{d}^3\mathbf{y}\,\rho_0(\mathbf{y})\xi_{\mathrm{osc,i}}(\mathbf{y},t)\left.\frac{\partial K}{\partial x_j}\right|_{\mathbf{y}-\mathbf{x}} = -\frac{\partial\rho_0\xi_{\mathrm{osc,i}}}{\partial x_j}\,. \tag{50}$$

Ultimately, this leads to the following simplification of Eq. (44):

$$L_{1,i}^d = \left[\frac{\partial c_0^2}{\partial x_i} - \frac{1}{\rho_0}\frac{\partial p_0}{\partial x_i}\right]\frac{1}{\rho_0}\frac{\partial\rho_0\xi_{\mathrm{osc,j}}}{\partial x_j} + \frac{c_0^2}{\rho_0}\frac{\partial^2\rho_0\xi_{\mathrm{osc,j}}}{\partial x_i\partial x_j}\,. \tag{51}$$

Hence from Eqs. (42) and (43), which in this limit read

$$\frac{\partial\boldsymbol{\xi}_{\mathrm{osc}}}{\partial t} - \mathbf{u}_{\mathrm{osc}} = \mathbf{0}\,, \tag{52}$$

$$\frac{\partial\mathbf{u}_{\mathrm{osc}}}{\partial t} - \mathbf{L}_1^d = \mathbf{0}\,, \tag{53}$$

we obtain the following homogeneous, second-order wave equation

$$\left(\frac{\partial^2}{\partial t^2} - \mathcal{L}\right)\mathbf{u}_{\mathrm{osc}} = \mathbf{0}\,, \tag{54}$$

with

$$\mathcal{L}(\mathbf{u}_{\mathrm{osc}}) = \frac{1}{\rho_0}\left[\left(\boldsymbol{\nabla}c_0^2(\boldsymbol{\nabla}\cdot\rho_0\mathbf{u}_{\mathrm{osc}})\right) - \frac{1}{\rho_0}\boldsymbol{\nabla}p_0(\boldsymbol{\nabla}\cdot\rho_0\mathbf{u}_{\mathrm{osc}})\right]\,. \tag{55}$$

We recover the equation for free acoustic oscillations in a stratified medium in its exact form, provided the Cowling approximation is adopted (see hypothesis H5). It corresponds exactly

to the homogeneous part of the wave equation derived, for instance by Goldreich & Keeley (1977b) (see their Eq. 16); or, equivalently, to the equation presented in Unno et al. (1989) (see their Eqs. 14.2 and 14.3), although these are written in terms of displacement and pressure fluctuation rather than displacement and velocity (see also Samadi & Goupil 2001, their Eq. 16). The only exception is the absence of the term depending on the entropy gradient (which does not appear here because the gas is polytropic).

4. Discussion

The linear stochastic wave equation comprised of Eqs. (42) and (43) was obtained in the scope of a certain number of hypotheses and approximations, whose validity we now discuss. We can split these hypotheses into two categories: those pertaining to the establishment of the stochastic differential equations, and those pertaining to the linearisation of these equations.

All the hypotheses we adopted in the linearisation are itemised in Section 3.1. Hypotheses (H1) through (H5) are actually of two different natures. Hypotheses (H1) on the smallness of $\mathbf{u}_{\rm osc}$, (H2) on the smallness of $\boldsymbol{\xi}_{\rm osc}$, and (H4) on the absence of back-reaction of the oscillations on the turbulence define the framework in which we performed the linearisation, and are therefore necessary assumptions. On the other hand, hypotheses (H3) on the neglect of $\boldsymbol{\nabla}\cdot(\rho_0\boldsymbol{\xi}_t)$ and (H5) on the neglect of the perturbed gravitational potential are simplifying assumptions that are not necessary, strictly speaking, but help simplify the formalism considerably. Hypothesis (H5) is a common assumption in the analysis of stellar oscillations: without it, because gravity is an unscreened force acting on long distances, the resulting equations would be highly non-local. As we mention in Section 3.1, its domain of validity is the high-radial-order modes of oscillation, but it is usually adopted throughout the entire oscillation spectrum. Hypothesis (H3), on the other hand, may require some more discussion. As we briefly mention above, it corresponds to the anelastic approximation, and amounts to neglecting the turbulent fluctuations of the fluid density ρ_t. Taking these fluctuations into account would require having knowledge of the statistical properties of ρ_t, the same way we consider the properties of $\mathbf{u}_t$ known. However, current models of compressible turbulence are not yet able to fully account for ρ_t without any underlying simplifying assumptions, such as the Boussinesq approximation or the anelastic approximation. It is difficult to assess how sensible to this assumption the results obtained for the behaviour of turbulent convection are, and a fortiori its coupling with oscillations, but for lack of a more realistic treatment of turbulence compressibility, we nevertheless chose to adopt hypothesis (H3).

We have also adopted a number of approximations in order to establish the closed system of equations (Eqs. (25), (26), (32), (33), (34), (35), and (36)) in Section 2. All of them consist in simplifying assumptions, that we adopt not because they are necessary to build the formalism, but because the aim of this paper is to make the basics of this method as clear as possible, rather than adopting the most realistic turbulence model possible. As such, we do not attempt to give a physical justification for the following hypotheses, but instead discuss how they affect the final stochastic wave equation, and how one would go about circumventing these simplifications.

(H6) We consider the flow to be adiabatic, in the sense that the only fluid particle properties that need to be described in the Lagrangian stochastic model are the position and velocity of the particles. In the scope of this hypothesis, the energy equation is replaced with a relation between the mean density and pressure that we chose to be polytropic, without specifying the associated polytropic exponent γ, which means that the non-adiabatic effects pertaining to the oscillations are not contained in the formalism presented in this paper. This includes the perturbation of the convective flux and the radiative flux by the oscillations, which are in reality susceptible to affect the damping rate of the modes as well as the surface effects. Avoiding hypothesis (H6) would allow for the inclusion of all non-adiabatic effects in the model. Essentially, adopting a non-adiabatic framework would require an additional SDE for the internal energy of the fluid particles (or any other alternative thermodynamic variable), thus leading to the introduction of an additional thermodynamic wave variable $e_{\rm osc}$, to be linearised around the turbulence-induced energy fluctuations e_t. This would then increase the order of the system of equations, and would require the statistical properties of the additional turbulent field e_t, including its correlation with $\mathbf{u}_t$, to be known.

(H7) We consider that the turbulent frequency ω_t, defined by Eq. (36) as the ratio of the dissipation rate ϵ to the turbulent kinetic energy k, takes a constant value. The turbulent frequency represents the rate at which k would decay towards zero if there were no production of turbulence whatsoever, and can be interpreted as the inverse lifetime of the energy-containing turbulent eddies. In essence, this amounts to assuming the existence of a single timescale associated with the entire turbulent cascade, which is at odds with even the simplest picture of turbulence. Avoiding hypothesis (H7) would allow a much more realistic modelling of the turbulent dissipation and its perturbation by the oscillations, which is likely to play an important role in both mode damping and surface effects. This would require including the turbulent frequency as a fluid particle property, with its own SDE. As for velocity or internal energy (see hypothesis (H6) above), this would lead to the introduction of $\omega_{t,\rm osc}$ as an additional wave variable, to be linearised around a new turbulent field $\omega_{t,t}$, whose statistical properties would have to be input in the model.

(H8) We consider that the time average of the flow velocity over very long timescale, in other words the velocity associated with the equilibrium background, is zero. This amounts to neglecting rotation, whether it be global or differential. Taking rotation into account would require either a non-zero $\langle\mathbf{u}\rangle_L$ field to be included, or else a Coriolis inertial force to be added in the velocity SDE.

In summary, hypotheses (H1), (H2), and (H4) are fundamental in building the formalism, and cannot be avoided, but they are also firmly and physically grounded. Hypotheses (H3) and (H5) are simplifying assumptions that are not strictly necessary, nor as clearly valid, but which are unavoidable given the current state of our capabilities. Finally, hypotheses (H6), (H7), and (H8) are also simplifying assumptions, and are very much invalid; however, we adopted them here to provide a simple framework serving as a proof of concept for the formalism presented in this paper. In particular, hypotheses (H6) and (H7) must be discarded as soon as possible if a realistic model of turbulence is to be adopted. This is left to a future work in this series.

5. Conclusion

In this series of papers we investigate Lagrangian stochastic models of turbulence as a rigorous way of modelling the various phenomena arising from the interaction between the highly turbulent motions of the gas at the top of the convection zone in solar-like stars and the global acoustic modes of oscillation developing in these stars. These include the stochastic excitation of

the modes, their stochastic damping, and the turbulence-induced shift in their frequency called surface effects.

In this first paper we presented a very simple polytropic Lagrangian stochastic turbulence model, serving as a proof of concept for the novel method presented here, and we showed how it can be used to derive stochastic differential equations (SDEs) governing the evolution of Eulerian fluid variables relevant to the study of oscillations. We then linearised these SDEs to obtain a linear stochastic wave equation containing, in the most self-consistent way possible, the terms arising from the turbulence-oscillation coupling. This wave equation correctly reduces to the classical propagation of free acoustic waves in a stratified medium in the limit where turbulence is neglected. It also exactly models the stochastic forcing term due to turbulent acoustic emission, arising from coherent fluctuations in the turbulent pressure. In addition, the resulting stochastic wave equation contains the turbulent-induced correction to the linear operator governing the propagation of the waves, thus allowing for the modelling of both mode damping and modal surface effects. The method presented here offers multiple, key advantages:

- At no point does it require separating the equations of the flow into a turbulent equation and an oscillation equation, thus allowing the turbulent contribution to naturally and consistently arise in the wave equation. Instead, we leave the statistical properties of the turbulence as known oscillation-independent inputs to the model.
- All aspects of turbulence-oscillation interaction are modelled simultaneously, within the same stochastic wave equation, thus shedding a more consistent light on these intertwined phenomena.
- This method completely circumvents the need to adopt the mixing-length hypothesis, which is crucial as this hypothesis is both almost inescapable in current convection modelling, and very invalid close to the radiative-convective transition zone. The reason we do not need to adopt this assumption stems from the fact that the starting model is at particle level, where equations are much easier to close.
- The parameters appearing in Lagrangian stochastic models are much more easily linked to the underlying physical assumptions, and therefore easier to constrain, with the help of 3D hydrodynamic simulations. They are also more firmly physically grounded.
- In addition, this formalism applies to radial and non-radial oscillations alike.

However, this paper only constitutes a first step. In the following paper in this series we will show how such a stochastic wave equation can be used to yield a set of stochastic differential equations governing the temporal evolution of the complex amplitude of the modes. These simplified amplitude equations (Stratonovich 1965) are much more practical for the study of turbulence-oscillation coupling, and in particular explicitly and simultaneously yield the excitation rates of the modes, their lifetimes, as well as their turbulence-induced frequency corrections. Finally, as we mentioned in Section 4, extending this work to a non-adiabatic model (i.e. discarding hypothesis H6), and with a more realistic treatment of eddy lifetimes (i.e. discarding hypothesis H7), constitutes an essential and unavoidable step to apply this formalism to the actual stellar case, and will be the subject of a subsequent paper.

Acknowledgements. The authors wish to thank the anonymous referee for his/her insightful comments, which helped improve the clarity and quality of this manuscript.

References

Anand, M. S., Mongia, H. C., & Pope, S. B. 1989, A PDF method for turbulent recirculating flows, 672–693
Andrews, D. G. & McIntyre, M. E. 1978, Journal of Fluid Mechanics, 89, 609
Bakosi, J. & Ristorcelli, J. R. 2011, Journal of Turbulence, 12, 19
Ball, W. H. & Gizon, L. 2014, A&A, 568, A123
Balmforth, N. J. 1992a, MNRAS, 255, 603
Balmforth, N. J. 1992b, MNRAS, 255, 632
Balmforth, N. J. 1992c, MNRAS, 255, 639
Baudin, F., Barban, C., Belkacem, K., et al. 2011, A&A, 529, A84
Belkacem, K., Dupret, M. A., Baudin, F., et al. 2012, A&A, 540, L7
Belkacem, K., Dupret, M. A., & Noels, A. 2010, A&A, 510, A6
Belkacem, K., Kupka, F., Philidet, J., & Samadi, R. 2021, A&A, 646, L5
Belkacem, K., Kupka, F., Samadi, R., & Grimm-Strele, H. 2019, A&A, 625, A20
Belkacem, K., Samadi, R., Goupil, M. J., & Dupret, M. A. 2008, A&A, 478, 163
Belkacem, K., Samadi, R., Goupil, M. J., Kupka, F., & Baudin, F. 2006, A&A, 460, 183
Bühler, O. 2009, Waves and Mean Flows
Chaplin, W. J., Houdek, G., Elsworth, Y., et al. 2005, MNRAS, 360, 859
Chaplin, W. J., Houdek, G., Karoff, C., Elsworth, Y., & New, R. 2009, A&A, 500, L21
Christensen-Dalsgaard, J. 2012, Astronomische Nachrichten, 333, 914
Christensen-Dalsgaard, J., Dappen, W., Ajukov, S. V., et al. 1996, Science, 272, 1286
Das, S. K. & Durbin, P. A. 2005, Physics of Fluids, 17, 025109
Delarue, B. J. & Pope, S. B. 1997, Physics of Fluids, 9, 2704
Dupret, M. A., Barban, C., Goupil, M. J., et al. 2006, in ESA Special Publication, Vol. 624, Proceedings of SOHO 18/GONG 2006/HELAS I, Beyond the spherical Sun, ed. K. Fletcher & M. Thompson, 97
Dziembowski, W. A., Paterno, L., & Ventura, R. 1988, A&A, 200, 213
Gabriel, M., Scuflaire, R., Noels, A., & Boury, A. 1975, A&A, 40, 33
Gardiner, C. W. 1994, Handbook of stochastic methods for physics, chemistry and the natural sciences
Goldreich, P. & Keeley, D. A. 1977a, ApJ, 211, 934
Goldreich, P. & Keeley, D. A. 1977b, ApJ, 212, 243
Goldreich, P. & Kumar, P. 1991, ApJ, 374, 366
Gough, D. O. 1977, ApJ, 214, 196
Grigahcène, A., Dupret, M. A., Gabriel, M., Garrido, R., & Scuflaire, R. 2005, A&A, 434, 1055
Haworth, D. C. & El Tahry, S. H. 1991, AIAA Journal, 29, 208
Haworth, D. C. & Pope, S. B. 1986, Physics of Fluids, 29, 387
Heinz, S. & Buckingham, A. 2004, Applied Mechanics Reviews, 57, B28
Houdek, G. 1996, PhD thesis, -
Houdek, G., Balmforth, N. J., Christensen-Dalsgaard, J., & Gough, D. O. 1999, A&A, 351, 582
Houdek, G. & Dupret, M.-A. 2015, Living Reviews in Solar Physics, 12, 8
Houdek, G., Lund, M. N., Trampedach, R., et al. 2019, MNRAS, 487, 595
Houdek, G., Trampedach, R., Aarslev, M. J., & Christensen-Dalsgaard, J. 2017, MNRAS, 464, L124
Hsu, A. T., Tsai, Y. L. P., & Raju, M. S. 1994, AIAA Journal, 32, 1407
Jones, W. & Launder, B. 1972, International Journal of Heat and Mass Transfer, 15, 301
Kjeldsen, H., Bedding, T. R., & Christensen-Dalsgaard, J. 2008, ApJ, 683, L175
Kolmogorov, A. 1941, Akademiia Nauk SSSR Doklady, 30, 301
Kolmogorov, A. N. 1962, Journal of Fluid Mechanics, 13, 82
Liu, M. B. & Liu, G. R. 2010, Arch Computat Methods Eng, 17, 25
Monaghan, J. J. 1992, ARA&A, 30, 543
Nordlund, Å. & Stein, R. F. 2001, ApJ, 546, 576
Nordlund, Å., Stein, R. F., & Asplund, M. 2009, Living Reviews in Solar Physics, 6, 2
O'Brien, E. E. 1980, The probability density function (pdf) approach to reacting turbulent flows, ed. P. A. Libby & F. A. Williams, Vol. 44, 185
Obukhov, A. M. 1959, Advances in Geophysics, 6, 113
Pope, S. B. 1981, Physics of Fluids, 24, 588
Pope, S. B. 1983, Physics of Fluids, 26, 3448
Pope, S. B. 1985, Progress in Energy and Combustion Science, 11, 119
Pope, S. B. 1991, Physics of Fluids A, 3, 1947
Pope, S. B. 1994, Annual Review of Fluid Mechanics, 26, 23
Pope, S. B. 2000, Turbulent Flows
Pope, S. B. & Chen, Y. L. 1990, Physics of Fluids A, 2, 1437
Roekaerts, D. 1991, Appl. Sci. Res., 48, 271
Rosenthal, C. S., Christensen-Dalsgaard, J., Nordlund, Å., Stein, R. F., & Trampedach, R. 1999, A&A, 351, 689
Samadi, R., Belkacem, K., & Sonoi, T. 2015, in EAS Publications Series, Vol. 73-74, EAS Publications Series, 111–191
Samadi, R. & Goupil, M. J. 2001, A&A, 370, 136
Samadi, R., Goupil, M. J., Alecian, E., et al. 2005, Journal of Astrophysics and Astronomy, 26, 171

Samadi, R., Kupka, F., Goupil, M. J., Lebreton, Y., & van't Veer-Menneret, C. 2006, A&A, 445, 233
Sonoi, T., Belkacem, K., Dupret, M. A., et al. 2017, A&A, 600, A31
Sonoi, T., Samadi, R., Belkacem, K., et al. 2015, A&A, 583, A112
Soward, A. M. 1972, Philosophical Transactions of the Royal Society of London Series A, 272, 431
Springel, V. 2010, Annual Review of Astronomy and Astrophysics, 48, 391
Stratonovich, R. L. 1965, Topics in the Theory of Random Noise, Vol. I and II (New York: Gordon and Breach)
Unno, W. 1967, PASJ, 19, 140
Unno, W., Osaki, Y., Ando, H., Saio, H., & Shibahashi, H. 1989, Nonradial oscillations of stars
Van Slooten, P. R. & Jayesh, Pope, S. B. 1998, Physics of Fluids, 10, 246
Welton, W. C. 1998, Journal of Computational Physics, 139, 410
Welton, W. C. & Pope, S. B. 1997, Journal of Computational Physics, 134, 150
Xiong, D. R., Cheng, Q. L., & Deng, L. 2000, MNRAS, 319, 1079
Zhou, Y., Asplund, M., Collet, R., & Joyce, M. 2020, MNRAS, 495, 4904

Appendix A: The equivalent Reynolds stress model

The procedure leading from a given Lagrangian stochastic model to the equivalent Reynolds stress model (i.e. the corresponding transport equations for the first- and second-order moments of the flow velocity) can be found, for instance, in Pope (2000, Chap. 12). For the generalised Langevin model considered in this paper, it yields

$$\frac{D\overline{\rho}}{Dt} + \overline{\rho}\frac{\partial \widetilde{u}_i}{\partial x_i} = 0 \,, \tag{A.1}$$

$$\frac{D\widetilde{u}_i}{Dt} + \frac{1}{\overline{\rho}}\frac{\partial \overline{\rho}\widetilde{u_i''u_j''}}{\partial x_j} = -\frac{1}{\overline{\rho}}\frac{\partial \overline{p}}{\partial x_i} + g_i \,, \tag{A.2}$$

and

$$\frac{D\widetilde{u_i''u_j''}}{Dt} + \frac{1}{\overline{\rho}}\frac{\partial \overline{\rho}\widetilde{u_i''u_j''u_k''}}{\partial x_k} = -\widetilde{u_i''u_j''}\frac{\partial \widetilde{u_k}}{\partial x_k} - \widetilde{u_i''u_k''}\frac{\partial \widetilde{u_j}}{\partial x_k} - \widetilde{u_k''u_j''}\frac{\partial \widetilde{u_i}}{\partial x_k} + G_{ik}\widetilde{u_j''u_k''} + G_{jk}\widetilde{u_i''u_k''} + C_0\epsilon\delta_{ij} \,, \tag{A.3}$$

where δ_{ij} denotes the Kronecker symbol, and we have introduced the pseudo-Lagrangian particle derivative $D/Dt \equiv \partial_t + \widetilde{u}_i\partial_i$.

Equation (A.1) yields the continuity equation in its exact form, without having to include an evolution equation for density at particle level. This is due to the fact that particle positions are advanced through time using their own individual velocities; since each particle carries its own unchanging mass, then by construction there can be no local mass loss or gain.

Equation (A.2) also yields the mean momentum equation in its exact form, primarily because the mean force in the stochastic model is already included in its exact form from the start. We note, however, that the transport term (i.e. the second term on the left-hand side of Eq. A.2) is also modelled exactly, even though it is not explicitly included in any way in Eqs. (9) and (10). This is, once again, because of the Lagrangian nature of the stochastic model, and is incidentally one of its most interesting features: all advection terms are implicitely and exactly modelled because trajectories integrated through Eqs. (9) and (10) coincide with actual fluid particle trajectories.

Equation (A.3) differs slightly from the exact Reynolds stress equation derived directly from the Navier-Stokes equation, which reads

$$\frac{D\widetilde{u_i''u_j''}}{Dt} + \frac{1}{\overline{\rho}}\frac{\partial \overline{\rho}\widetilde{u_i''u_j''u_k''}}{\partial x_k} = -\widetilde{u_i''u_j''}\frac{\partial \widetilde{u_k}}{\partial x_k} - \widetilde{u_i''u_k''}\frac{\partial \widetilde{u_j}}{\partial x_k} - \widetilde{u_k''u_j''}\frac{\partial \widetilde{u_i}}{\partial x_k} \\ \mathrm{sym}\left(-\frac{\overline{u_i''}}{\overline{\rho}}\frac{\partial \overline{p}}{\partial x_j} - \frac{1}{\overline{\rho}}\overline{u_i''\frac{\partial p'}{\partial x_j}} - \epsilon_{ij}\right) \,, \tag{A.4}$$

where 'sym' refers to the symmetric part of the tensor inside the brackets. Several contributions are still modelled in their exact form, including the transport term (the second term on the left-hand side), but also the production term (the first three terms on the right-hand side). However, the last three terms are not modelled exactly, and are (from left to right) the buoyancy contribution, the pressure-rate-of-strain tensor, and the dissipation tensor. Comparing Eqs. (A.3) and (A.4), it can be seen that these contributions are collectively modelled by the last two terms in Eq. (10), which correspond to the fluctuating part of the force acting upon the fluid particle. More specifically, we obtain

$$\mathrm{sym}\left(-\frac{\overline{u_i''}}{\overline{\rho}}\frac{\partial \overline{p}}{\partial x_i} - \frac{1}{\overline{\rho}}\overline{u_i''\frac{\partial p'}{\partial x_i}} - \epsilon_{ij}\right) = G_{ik}\widetilde{u_j''u_k''} + G_{jk}\widetilde{u_i''u_k''} + C_0\epsilon\delta_{ij} \,. \tag{A.5}$$

This equation is more readily interpreted if we remember that, in the high Reynolds number limit, the dissipation tensor is isotropic, which allows for the definition of the scalar dissipation ϵ appearing in the stochastic model:

$$\epsilon_{ij} \equiv \frac{2}{3}\epsilon\delta_{ij} \,. \tag{A.6}$$

Furthermore, the drift tensor is usually decomposed into an isotropic and anisotropic part, according to

$$G_{ij} = -\left(\frac{1}{2} + \frac{3}{4}C_0\right)\frac{\epsilon}{k}\delta_{ij} + G^a_{ij} \,, \tag{A.7}$$

where $k \equiv \widetilde{u_i''u_i''}/2$ is the turbulent kinetic energy. This decomposition ensures that, in the special case of incompressible, homogeneous, isotropic turbulence, if we take $G^a_{ij} = 0$, the evolution of the Reynolds stress tensor reduces to the exact, analytical solution.

Equation (A.5) can be rearranged to yield

$$\mathrm{sym}\left(-\frac{\overline{u_i''}}{\overline{\rho}}\frac{\partial \overline{p}}{\partial x_i} - \frac{1}{\overline{\rho}}\overline{u_i''\frac{\partial p'}{\partial x_i}}\right) = G^a_{ik}\widetilde{u_j''u_k''} + G^a_{jk}\widetilde{u_i''u_k''} \\ -\left(1 + \frac{3}{2}C_0\right)\frac{\epsilon}{k}\left(\widetilde{u_i''u_j''} - \frac{2}{3}k\delta_{ij}\right) \,. \tag{A.8}$$

Equation (A.8) allows us to interpret the collective effect of buoyancy and pressure-rate-of-strain correlation on the evolution of the Reynolds stresses. First, all the terms on the right-hand side are traceless, which means that they only have a redistributive role; they redistribute energy among the different components of the Reynolds stress tensor, without ever resulting in a net loss or gain of energy. By contrast, it is the scalar dissipation ϵ which is responsible for the decay of kinetic turbulent energy, an effect that is only counterbalanced by the shear- and compression-induced production term (i.e. the first three terms on the right-hand side of Eq. (A.4)).

Furthermore, it is readily seen that the last term on the right-hand side of Eq. (A.8) tends to isotropise the Reynolds stress tensor since for isotropic turbulence we would precisely have $\widetilde{u_i''u_j''} = 2k\delta_{ij}/3$. The rate at which this term makes the Reynolds stress decay towards isotropy is equal to $(1+3C_0/2)\omega_t$, where ω_t is the turbulent dissipation rate defined by Eq. (36). On the other hand, the other two terms on the right-hand side of Eq. (A.8) create anisotropy in the Reynolds stress tensor, and we can intuitively understand that the anisotropy of the stationary Reynolds stress results from a balance between these two effects.

Appendix B: A detailed derivation for the Lagrangian-to-Eulerian change of variables

The goal of this appendix is to provide a detailed derivation of the various steps in the procedure described in Section 2.2. We first derive the general identity (14), which is valid for any fluid quantity; we then apply this general identity to the displacement and velocity variables.

Appendix B.1: Derivation of identity (14)

Let us consider, for the moment, that the function $\boldsymbol{\xi}(\mathbf{x}, t)$ is an arbitrary function of space and time, which we do not specify

at first. We recall the following notations

$$\mathbf{X}(\mathbf{x},t) \equiv \mathbf{x} + \boldsymbol{\xi}(\mathbf{x},t)\,, \tag{B.1}$$

$$\phi_L(\mathbf{x},t) \equiv \phi(\mathbf{X}(\mathbf{x},t),t)\,, \tag{B.2}$$

where ϕ is an arbitrary quantity. The usual chain rules for derivation then yield

$$\frac{\partial(\phi_L)}{\partial t} = \left(\frac{\partial\phi}{\partial t}\right)_L + \frac{\partial X_i}{\partial t}\left(\frac{\partial\phi}{\partial x_i}\right)_L\,, \tag{B.3}$$

$$\frac{\partial(\phi_L)}{\partial x_i} = \frac{\partial X_j}{\partial x_i}\left(\frac{\partial\phi}{\partial x_j}\right)_L\,. \tag{B.4}$$

If the function $\mathbf{x} \mapsto \mathbf{X}(\mathbf{x},t)$ (the time t being fixed) is bijective, then for any velocity field $\mathbf{u}(\mathbf{x},t)$, there necessarily exists an associated field $\mathbf{V}(\mathbf{x},t)$ such that, were point $\mathbf{x}$ to move with velocity $\mathbf{V}$, point $\mathbf{X}$ would then move with the actual fluid velocity $\mathbf{u}_L$. Otherwise stated, $\mathbf{V}$ corresponds to the advective velocity in the material derivative of $\mathbf{X}$, so that

$$\frac{\partial X_i}{\partial t} + V_j\frac{\partial X_i}{\partial x_j} = u_{i,L}\,. \tag{B.5}$$

Plugging Eq. (B.5) into Eq. (B.3), we find

$$\begin{aligned}\frac{\partial(\phi_L)}{\partial t} &= \left(\frac{\partial\phi}{\partial t}\right)_L + \left(u_{i,L} - V_j\frac{\partial X_i}{\partial x_j}\right)\left(\frac{\partial\phi}{\partial x_i}\right)_L \\ &= \left(\frac{D\phi}{Dt}\right)_L - V_j\frac{\partial X_i}{\partial x_j}\left(\frac{\partial\phi}{\partial x_i}\right)_L\,,\end{aligned} \tag{B.6}$$

where $D/Dt \equiv \partial_t + u_i\partial_i$. In turn, plugging Eq. (B.4), this transforms into

$$\frac{\partial(\phi_L)}{\partial t} = \left(\frac{D\phi}{Dt}\right)_L - V_j\frac{\partial(\phi_L)}{\partial x_j}\,, \tag{B.7}$$

thus yielding the required identity

$$\left(\frac{D\phi}{Dt}\right)_L = \langle D\rangle_L(\phi_L)\,, \tag{B.8}$$

where $\langle D\rangle_L \equiv \partial_t + V_i\partial_i$.

This is all valid regardless of the definition of the function $\boldsymbol{\xi}(\mathbf{x},t)$. However, let us now consider that $\mathbf{x}$ does actually correspond to a mean[6] position, and that the function $\boldsymbol{\xi}(\mathbf{x},t)$ actually denotes the fluctuating fluid displacement around this mean position $\mathbf{x}$. Then by construction, we have

$$\langle\xi_i\rangle = 0\,. \tag{B.9}$$

Point $\mathbf{x}$ now corresponding to a mean position, the velocity $\mathbf{V}$ at which it is displaced must itself be a mean quantity, so that

$$\langle\mathbf{V}\rangle = \mathbf{V}\,. \tag{B.10}$$

Let us now apply the mean operator $\langle.\rangle$ to Eq. (B.5); since V_j can be pulled out of the mean, we obtain

$$\begin{aligned}\langle u_i\rangle_L &= \frac{\partial\langle X_i\rangle}{\partial t} + V_j\frac{\partial\langle X_i\rangle}{\partial x_j} \\ &= \frac{\partial x_i}{\partial t} + \frac{\partial\langle\xi_i\rangle}{\partial t} + V_j\left(\frac{\partial x_i}{\partial x_j} + \frac{\partial\langle\xi_i\rangle}{\partial x_j}\right) \\ &= 0 + 0 + V_j\left(\delta_{ij} + 0\right)\,,\end{aligned} \tag{B.11}$$

[6] We recall that throughout this discussion, the word 'mean' refers to the as-yet-unspecified averaging process $\langle.\rangle$ (see the main body of the paper for more details).

or in other words

$$\mathbf{V} = \langle\mathbf{u}\rangle_L\,. \tag{B.12}$$

To summarise, the identity (B.8) is always verified, but in general, the velocity $\mathbf{V}$ appearing in the definition of the operator $\langle D\rangle_L$ is not easily specified. Only when the displacement function $\boldsymbol{\xi}$ is judiciously defined as a fluctuating particle displacement does the velocity $\mathbf{V}$ reduce to the mean Lagrangian velocity $\langle\mathbf{u}\rangle_L$.

Appendix B.2: Derivation of Eqs. (16) *and* (17)

Let us apply Eq. (B.8) to $\phi = x_i$ and $\phi = u_i$ alternatively. First, if $\phi = x_i$, then $\phi_L = X_i$, and Eq. (B.8) becomes

$$\left(\frac{\partial x_i}{\partial t}\right)_L + u_{j,L}\left(\frac{\partial x_i}{\partial x_j}\right)_L = \frac{\partial X_i}{\partial t} + \langle u_j\rangle_L\frac{\partial X_i}{\partial x_j}\,. \tag{B.13}$$

The mean position $\mathbf{x}$ having no explicit time dependence, we have $(\partial x_i/\partial t)_L = 0$, $(\partial x_i/\partial x_j)_L = \delta_{ij}$, $\partial X_i/\partial t = \partial\xi_i/\partial t$, and $\partial X_i/\partial x_j = \delta_{ij} + \partial\xi_i/\partial x_j$. The above equation then becomes

$$u_{i,L} = \frac{\partial\xi_i}{\partial t} + \langle u_j\rangle_L\left(\delta_{ij} + \frac{\partial\xi_i}{\partial x_j}\right)\,, \tag{B.14}$$

thus immediately yielding Eq. (16).

Secondly, if $\phi = u_i$, then $\phi_L = u_{i,L}$, and Eq. (B.8) becomes

$$\left(\frac{\partial u_i}{\partial t}\right)_L + u_{j,L}\left(\frac{\partial u_i}{\partial x_j}\right)_L = \frac{\partial(u_{i,L})}{\partial t} + \langle u_j\rangle_L\frac{\partial(u_{i,L})}{\partial x_j}\,. \tag{B.15}$$

But Eq. (B.4) allows us to write

$$\frac{\partial(u_{i,L})}{\partial x_j} = \frac{\partial X_k}{\partial x_j}\left(\frac{\partial u_i}{\partial x_k}\right)_L\,, \tag{B.16}$$

where we recall that

$$\frac{\partial X_k}{\partial x_j} = \delta_{kj} + \frac{\partial\xi_k}{\partial x_j}\,. \tag{B.17}$$

Plugging these into Eq. (B.15), we find

$$\left(\frac{\partial u_i}{\partial t}\right)_L + u_{j,L}\left(\frac{\partial u_i}{\partial x_j}\right)_L = \frac{\partial(u_{i,L})}{\partial t} + \langle u_j\rangle_L\left(\delta_{jk} + \frac{\partial\xi_k}{\partial x_j}\right)\left(\frac{\partial u_i}{\partial x_k}\right)_L\,. \tag{B.18}$$

Isolating the first term on the right-hand side yields Eq. (17).

Appendix C: The insignificance of the back-reaction of the oscillations on the turbulence

Let us formally write the governing equations of the flow in the following abstract form

$$\frac{\partial U}{\partial t} + \mathcal{L}(U) + \mathcal{B}(U,U) = 0\,, \tag{C.1}$$

where U represents the flow variables, $\mathcal{L}$ is a linear operator, and $\mathcal{B}$ a bilinear operator containing the advection terms. In the limit of small amplitudes, which are relevant for solar-like oscillations, the wave variables can be expanded as

$$U = U_0 + aU_1 + a^2U_2\,, \tag{C.2}$$

where a is small ordering parameter. Plugging Eq. (C.2) into Eq. (C.1) and isolating the various orders in a, we obtain the following hierarchy of equations

$$\frac{\partial U_0}{\partial t} + \mathcal{L}(U_0) + \mathcal{B}(U_0, U_0) = 0 \,, \tag{C.3}$$

$$\frac{\partial U_1}{\partial t} + \mathcal{L}(U_1) + \mathcal{B}(U_0, U_1) + \mathcal{B}(U_1, U_0) = 0 \,, \tag{C.4}$$

$$\frac{\partial U_2}{\partial t} + \mathcal{L}(U_2) + \mathcal{B}(U_0, U_2) + \mathcal{B}(U_2, U_0) = -\mathcal{B}(U_1, U_1) \,, \tag{C.5}$$

where the first equation governs the basic flow, the second equation governs the waves, and the third equation governs the back-reaction of the waves on the basic flow. In particular, Eq. (C.5) takes the form of a forced linear wave, where the linear part $\mathcal{L}' \equiv \mathcal{L} + \mathcal{B}(U_0, .) + \mathcal{B}(., U_0)$ is identical to the linear part in the actual wave equation (C.4), and the forcing term is given by the right-hand side of Eq. (C.5). Because $\mathcal{L}'$ is common to both Eqs. (C.4) and (C.5), if we denote the angular frequency of the wave as ω, we can write the homogeneous solution of Eq. (C.5) as

$$U_{2,h}(t) = A \exp^{j\omega t} \,, \tag{C.6}$$

and the total solution (including the forcing, inhomogeneous part) formally reads

$$U_2(t) = -\int_0^t \mathrm{d}t' \;\; \exp^{-j\omega(t'-t)} \, \mathcal{B}\left(U_1(t'), U_1(t')\right) \,. \tag{C.7}$$

The back-reaction of the waves on the turbulence is therefore driven by its resonance with the non-linear oscillation-induced advection. In the limit $t \to +\infty$, this formal solution yields

$$|U_2(t)|^2 \sim \left| \mathrm{TF}\left[\mathcal{B}(U_1, U_1)\right](\omega) \right|^2 \,, \tag{C.8}$$

where 'TF' denotes the Fourier transform. But U_1 refers to the wave, so that its Fourier spectrum only has power around the angular frequency ω of the wave. In turn, this means that the quadratic operator $\mathcal{B}$ applied to the velocity U_1 has a Fourier spectrum whose power is concentrated around $\omega = 0$ (i.e. the continuous component) as well as 2ω (twice the frequency of the waves). By contrast, it contains little to no power around the actual frequency ω of the oscillation, which justifies that the impact of the back-reaction $U_2(t)$ on the mean flow $U_0(t)$ may be neglected.

Appendix D: Derivation of the linear wave equation

In this appendix we linearise the system comprised of Eqs. (25), (26), (32), (33), (34), (35), and (36), using the hypotheses outlined in Section 3.1. We start, in Section D.1, by linearising all the ensemble averages described in the SPH formalism (i.e. Eqs. (32), (33), (34), (35), and (36)). In Section D.2, we then plug these linearised ensemble averages to derive the linearised version of Eqs. (25) and (26). Finally, in Section D.3, we discuss which terms should be retained in the inhomogeneous forcing term of the resulting wave equation. For more clarity in the notations, we dropped all dependence on the space variable $\mathbf{x}$, the space variable $\mathbf{y}$ used inside the integrals, and time t. It must be understood that all the quantities outside the integrals depend on $\mathbf{x}$ and t, and all quantities inside depend on $\mathbf{y}$ and t.

Appendix D.1: Linearising the mean fields

A general remark can be made beforehand concerning all ensemble averages described in the SPH formalism: the occurrence of $\boldsymbol{\xi_t}$ vanishes completely from their linearised version by virtue of hypothesis (H3). We have already shown, in the main body of this paper, that this is the case for the mean density $\overline{\rho}$, but this is also the case for the mean velocity and Reynolds stress tensor. They can both formally be written as

$$\widetilde{Q} = \frac{1}{\overline{\rho}} \int \mathrm{d}^3\mathbf{y} \; \rho_0 Q(\mathbf{y} + \boldsymbol{\xi}) K^{\mathbf{x}}(\mathbf{y} + \boldsymbol{\xi}) \,, \tag{D.1}$$

where Q is a function of velocity only ($Q = \mathbf{u}$ for the mean velocity, and $Q = (u_i - \widetilde{u_i})\left(u_j - \widetilde{u_j}\right)$ for the Reynolds stress tensor), and we have introduced the $\mathbf{x}$-centred kernel function $K^{\mathbf{x}}(\mathbf{y}) \equiv K(\mathbf{y} - \mathbf{x})$. Because Q only depends on the velocity variable $\mathbf{u}$, and not on the displacement variable $\boldsymbol{\xi}$, the only occurrence of $\boldsymbol{\xi_t}$ in the linearisation of $\widetilde{Q}$ comes from the term

$$\widetilde{Q} = [...] + \frac{1}{\overline{\rho}} \int \mathrm{d}^3\mathbf{y} \; \rho_0 \boldsymbol{\xi}_t \cdot \boldsymbol{\nabla} \left(Q K^{\mathbf{x}}\right) \,. \tag{D.2}$$

Performing an integration by part yields

$$\widetilde{Q} = [...] - \frac{1}{\overline{\rho}} \int \mathrm{d}^3\mathbf{y} \; Q K^{\mathbf{x}} \boldsymbol{\nabla} \cdot (\rho_0 \boldsymbol{\xi}_t) \,, \tag{D.3}$$

where the surface term vanishes because of the compact support of the kernel function $K^{\mathbf{x}}$. By virtue of hypothesis (H3), the quantity $\boldsymbol{\nabla} \cdot (\rho_0 \boldsymbol{\xi_t})$ is negligible, and therefore this contribution can be safely discarded.

As we have just shown, this is true of the mean density, mean velocity, and Reynolds stress tensor. In turn, this is also true of the gas pressure $\overline{p}$ (because it is given as a function of the mean density), as well as the turbulent kinetic energy k and the turbulent dissipation rate ϵ (because they are both given as a function of the Reynolds stress tensor). Therefore, $\boldsymbol{\xi}_t$ can indeed be neglected in the linearised version of every single ensemble average appearing in Eqs. (25) and (26).

Appendix D.1.1: Mean density

Using hypotheses (H2) and (H3), Eq. (32) can be linearised as

$$\overline{\rho} = \int \mathrm{d}^3\mathbf{y} \; \rho_0 \left[K^{\mathbf{x}} + \xi_{\mathrm{osc,i}} \partial_i K^{\mathbf{x}}\right] \,. \tag{D.4}$$

The first term on the right-hand side corresponds to the kernel estimator of the equilibrium density ρ_0 at $\mathbf{x}$, and therefore represents the ensemble average of ρ_0 at $\mathbf{x}$. Since ρ_0 is already an equilibrium quantity, it is equal to its own ensemble average, and this term reduces to $\rho_0(\mathbf{x})$ itself. Finally,

$$\overline{\rho} = \rho_0 + \rho_1 \,, \tag{D.5}$$

with

$$\rho_1 = \int \mathrm{d}^3\mathbf{y} \; \rho_0 \xi_{\mathrm{osc,i}} \partial_i K^{\mathbf{x}} \,. \tag{D.6}$$

Appendix D.1.2: Mean gas pressure

The fluctuating mean density ρ_1 is much lower than the equilibrium density ρ_0 on account of hypothesis (H2). Therefore, Eq. (35) can be linearised, immediately yielding

$$\overline{p} = p_0 + p_1 \,, \tag{D.7}$$

with

$$p_1 = \frac{p_0 \gamma}{\rho_0} \rho_1 \equiv c_0^2 \rho_1 \,, \tag{D.8}$$

where c_0^2 is the equilibrium sound speed squared.

Appendix D.1.3: Mean velocity

Using hypotheses (H1), (H2), and (H3), Eq. (33) can be linearised as

$$\begin{aligned} \widetilde{\mathbf{u}} = & \frac{1}{\rho_0} \int \mathrm{d}^3\mathbf{y}\, \rho_0 \mathbf{u}_t K^{\mathbf{x}} - \frac{\rho_1}{\rho_0^2} \int \mathrm{d}^3\mathbf{y}\, \rho_0 \mathbf{u}_t K^{\mathbf{x}} \\ & + \frac{1}{\rho_0} \int \mathrm{d}^3\mathbf{y}\, \rho_0 \mathbf{u}_{\mathrm{osc}} K^{\mathbf{x}} + \frac{1}{\rho_0} \int \mathrm{d}^3\mathbf{y}\, \rho_0 K^{\mathbf{x}} \xi_{\mathrm{osc,i}} \partial_i \mathbf{u}_t \\ & + \frac{1}{\rho_0} \int \mathrm{d}^3\mathbf{y}\, \rho_0 \mathbf{u}_t \xi_{\mathrm{osc,i}} \partial_i K^{\mathbf{x}} \,, \end{aligned} \tag{D.9}$$

where ρ_1 is given by Eq. (D.6). This expression can be simplified by remarking that

$$\int \mathrm{d}^3\mathbf{y}\, \rho_0 \mathbf{u}_t K^{\mathbf{x}} = \overline{\rho} \widetilde{\mathbf{u}_t} \,, \tag{D.10}$$

because kernel averages represent ensemble averages. Since mass is locally conserved by the turbulent velocity field (i.e. the upflows carry as much mass upwards as the turbulent downdrafts carry downwards), it immediately follows that $\widetilde{\mathbf{u}_t} = \mathbf{0}$, and therefore the first two terms in Eq. (D.9) vanish. Rearranging the remaining terms, we obtain

$$\widetilde{\mathbf{u}} = \widetilde{\mathbf{u}}_0 + \widetilde{\mathbf{u}}_1 \,, \tag{D.11}$$

where $\widetilde{\mathbf{u}}_0 = \mathbf{0}$ and

$$\widetilde{\mathbf{u}}_1 = \frac{1}{\rho_0} \int \mathrm{d}^3\mathbf{y}\, \rho_0 \mathbf{u}_{\mathrm{osc}} K^{\mathbf{x}} + \frac{1}{\rho_0} \int \mathrm{d}^3\mathbf{y}\, \rho_0 \xi_{\mathrm{osc,i}} \partial_i \left(\mathbf{u}_t K^{\mathbf{x}} \right) \,. \tag{D.12}$$

Appendix D.1.4: Mean shear tensor

We also need to express the linearised shear tensor $\partial_i \widetilde{u_j}$ because this quantity appears in the drift tensor G_{ij}. Differentiating Eq. (D.12) with respect to x_i, and noting that $\boldsymbol{\nabla}_{\mathbf{x}}(K^{\mathbf{x}}(\mathbf{y})) = -\boldsymbol{\nabla}_{\mathbf{y}}(K^{\mathbf{x}}(\mathbf{y}))$ (because we considered an isotropic kernel function), we obtain

$$\partial_i \widetilde{u_j} = (\partial_i \widetilde{u_j})_0 + (\partial_i \widetilde{u_j})_1 \,, \tag{D.13}$$

where $(\partial_i \widetilde{u_j})_0 = 0$ and

$$\begin{aligned} (\partial_i \widetilde{u_j})_1 = & -\frac{1}{\rho_0} \int \mathrm{d}^3\mathbf{y}\, \rho_0 u_{\mathrm{osc,j}} \partial_i K^{\mathbf{x}} - \frac{1}{\rho_0} \int \mathrm{d}^3\mathbf{y}\, \rho_0 \xi_{\mathrm{osc,k}} \partial_k u_{t,j} \partial_i K^{\mathbf{x}} \\ & - \frac{1}{\rho_0^2} \frac{\partial \rho_0}{\partial x_i} \int \mathrm{d}^3\mathbf{y}\, \rho_0 u_{\mathrm{osc,j}} K^{\mathbf{x}} \\ & - \frac{1}{\rho_0^2} \frac{\partial \rho_0}{\partial x_i} \int \mathrm{d}^3\mathbf{y}\, \rho_0 \xi_{\mathrm{osc,k}} \partial_k \left(u_{t,j} K^{\mathbf{x}} \right) \,. \end{aligned} \tag{D.14}$$

Appendix D.1.5: Reynolds stress tensor

The linearised Reynolds stress tensor is obtain from Eq. (34), using hypotheses (H1), (H2), and (H3). We find

$$\begin{aligned} \widetilde{u_i'' u_j''} = & \frac{1}{\rho_0} \int \mathrm{d}^3\mathbf{y}\, \rho_0 u_{t,i} u_{t,j} K^{\mathbf{x}} - \frac{\rho_1}{\rho_0^2} \int \mathrm{d}^3\mathbf{y}\, \rho_0 u_{t,i} u_{t,j} K^{\mathbf{x}} \\ & + \frac{1}{\rho_0} \int \mathrm{d}^3\mathbf{y}\, \rho_0 u_{t,i} \xi_{\mathrm{osc,k}} \left(\partial_k u_{t,j} \right) K^{\mathbf{x}} \\ & + \frac{1}{\rho_0} \int \mathrm{d}^3\mathbf{y}\, \rho_0 u_{t,j} \xi_{\mathrm{osc,k}} \left(\partial_k u_{t,i} \right) K^{\mathbf{x}} \\ & + \frac{1}{\rho_0} \int \mathrm{d}^3\mathbf{y}\, \rho_0 u_{t,i} u_{t,j} \xi_{\mathrm{osc,k}} \partial_k K^{\mathbf{x}} \\ & - \frac{1}{\rho_0} \int \mathrm{d}^3\mathbf{y}\, \rho_0 u_{t,i} u_{\mathrm{osc,j}} K^{\mathbf{x}} + \frac{1}{\rho_0} \int \mathrm{d}^3\mathbf{y}\, \rho_0 u_{t,j} u_{\mathrm{osc,i}} K^{\mathbf{x}} \\ & - \frac{1}{\rho_0} \int \mathrm{d}^3\mathbf{y}\, \rho_0 u_{t,i} \widetilde{u_{j}}_1 K^{\mathbf{x}} + \frac{1}{\rho_0} \int \mathrm{d}^3\mathbf{y}\, \rho_0 u_{t,j} \widetilde{u_{i}}_1 K^{\mathbf{x}} \,, \end{aligned} \tag{D.15}$$

where ρ_1 is given by Eq. (D.6) and $\widetilde{\mathbf{u}}_1$ by Eq. (D.12). In the last two terms, $\widetilde{u_{i}}_1$ can be pulled from the integral. The kernel estimator is a representation of ensemble averages, and $\widetilde{u_{i}}_1$ is already an ensemble average. Once this quantity is pulled out, we recognise the same integral defined by Eq. (D.10), meaning that these terms vanish. Additionally, the third, fourth, and fifth terms can be conveniently merged together, and ρ_1 can be replaced by its explicit expression (D.6), so that we finally obtain

$$\widetilde{u_i'' u_j''} = \widetilde{u_i'' u_j''}_0 + \widetilde{u_i'' u_j''}_1 \,, \tag{D.16}$$

where

$$\widetilde{u_i'' u_j''}_0 = \frac{1}{\rho_0} \int \mathrm{d}^3\mathbf{y}\, \rho_0 u_{t,i} u_{t,j} K^{\mathbf{x}} \tag{D.17}$$

and

$$\begin{aligned} \widetilde{u_i'' u_j''}_1 = & -\frac{\widetilde{u_i'' u_j''}_0}{\rho_0} \int \mathrm{d}^3\mathbf{y}\, \rho_0 \xi_{\mathrm{osc,k}} \partial_k K^{\mathbf{x}} \\ & + \frac{1}{\rho_0} \int \mathrm{d}^3\mathbf{y}\, \rho_0 \xi_{\mathrm{osc,k}} \partial_k \left(u_{t,i} u_{t,j} K^{\mathbf{x}} \right) \\ & + \frac{1}{\rho_0} \int \mathrm{d}^3\mathbf{y}\, \rho_0 u_{t,i} u_{\mathrm{osc,j}} K^{\mathbf{x}} \\ & + \frac{1}{\rho_0} \int \mathrm{d}^3\mathbf{y}\, \rho_0 u_{t,j} u_{\mathrm{osc,i}} K^{\mathbf{x}} \,. \end{aligned} \tag{D.18}$$

Additionally, we immediately deduce the linearisation of the turbulent kinetic energy, which corresponds to half the trace of the Reynolds stress tensor

$$k = k_0 + k_1 = \frac{\widetilde{u_i'' u_i''}_0}{2} + \frac{\widetilde{u_i'' u_i''}_1}{2} \,. \tag{D.19}$$

Likewise, from Eq. (36), we find the linearised turbulent dissipation

$$\epsilon = \epsilon_0 + \epsilon_1 = \omega_t k_0 + \omega_t k_1 \,. \tag{D.20}$$

Appendix D.1.6: Drift tensor

The drift tensor G_{ij} being dependent on the mean flow, it also needs to be linearised. We recall that, in its most general form, it can be written as an arbitrary function of the Reynolds stress tensor, the shear tensor and the turbulent dissipation

$$G_{ij} = G_{ij}\left(\widetilde{u_k'' u_l''}, \partial_k \widetilde{u_l}, \epsilon\right) , \tag{D.21}$$

and therefore its linearisation reads

$$G_{ij} = G_{ij,0} + G_{ij,1} , \tag{D.22}$$

with

$$G_{ij,0} = G_{ij}\left(\widetilde{u_k'' u_l''}_0, 0, \epsilon_0\right) \tag{D.23}$$

and

$$G_{i,j,1} = \frac{\partial G_{ij}}{\partial \widetilde{u_k'' u_l''}} \widetilde{u_k'' u_l''}_1 + \frac{\partial G_{ij}}{\partial(\partial_k \widetilde{u_l})} (\partial_k \widetilde{u_l})_1 + \frac{\partial G_{ij}}{\partial \epsilon} \epsilon_1 . \tag{D.24}$$

In Eq. (D.23), $\widetilde{u_k'' u_l''}_0$ is given by Eq. (D.17) and ϵ_0 by Eq. (D.20). In Eq. (D.24), the derivatives $\partial G_{ij}/\partial \widetilde{u_k'' u_l''}$, $\partial G_{ij}/\partial(\partial_k \widetilde{u_l})$, and $\partial G_{ij}/\partial\epsilon$ only depend on the functional form of the drift tensor; $\widetilde{u_k'' u_l''}_1$ is given by Eq. (D.18); $(\partial_k \widetilde{u_l})_1$ is given by Eq. (D.14); and ϵ_1 is given by Eq. (D.20).

Appendix D.2: Linearising the displacement and motion equations

Hypotheses (H1) and (H2), in addition to the linearised mean fields computed in the previous section, allow us to write the linearised version of Eqs. (25) and (26) as

$$\frac{\partial \xi_{\mathrm{osc,i}}}{\partial t} = u_{t,i} + u_{\mathrm{osc,i}} + \xi_{\mathrm{osc,j}} \frac{\partial u_{t,i}}{\partial x_j} + \xi_{\mathrm{t,j}} \frac{\partial u_{t,i}}{\partial x_j} + \xi_{\mathrm{t,j}} \frac{\partial u_{\mathrm{osc,i}}}{\partial x_j} \tag{D.25}$$

and

$$\begin{aligned}
&\frac{\partial u_{\mathrm{osc,i}}}{\partial t} + u_{t,j} \frac{\partial u_{t,i}}{\partial x_j} + u_{\mathrm{osc,j}} \frac{\partial u_{t,i}}{\partial x_j} + u_{t,j} \frac{\partial u_{\mathrm{osc,i}}}{\partial x_j} = \\
&- \frac{1}{\rho_0} \frac{\partial p_0}{\partial x_i} + \frac{\rho_1}{\rho_0^2} \frac{\partial p_0}{\partial x_i} - \frac{1}{\rho_0} \frac{\partial p_1}{\partial x_i} + g_{i,0} + G_{ij,0} u_{t,j} \\
&+ G_{ij,0}\left(u_{\mathrm{osc,j}} - \widetilde{u_j}_1\right) + G_{ij,1} u_{t,j} + \left[\sqrt{C_0 \omega_t k_0} + \frac{1}{2}\sqrt{\frac{C_0 \omega_t}{k_0}} k_1\right] \eta_i ,
\end{aligned} \tag{D.26}$$

where ρ_0 and p_0 are the equilibrium density and gas pressure, ρ_1 is given by Eq. (D.6), p_1 by Eq. (D.8), $G_{ij,0}$ by Eq. (D.23), $G_{ij,1}$ by Eq. (D.24), $\widetilde{\mathbf{u}}_1$ by Eq. (D.12), and k_0 and k_1 by (D.19).

Furthermore, we split the right-hand side of Eq. (D.26) three ways: we gather all the terms that do not depend on the oscillatory variables $\mathbf{u}_{\mathrm{osc}}$ and $\boldsymbol{\xi}_{\mathrm{osc}}$ in a quantity $\mathbf{L}_0$, all the terms that depend on $\boldsymbol{\xi}_{\mathrm{osc}}$ and/or $\mathbf{u}_{\mathrm{osc}}$ but not on any of the turbulent fields $\boldsymbol{\xi_t}$ or $\mathbf{u}_t$ in a quantity $\mathbf{L}_1^d$, and all the terms that depend on both the oscillatory variables and the turbulent fields in a quantity $\mathbf{L}_1^s$. This leads us to the following linear equations

$$\frac{\partial \boldsymbol{\xi}_{\mathrm{osc}}}{\partial t} - \mathbf{u}_{\mathrm{osc}} - (\boldsymbol{\xi}_{\mathrm{osc}} \cdot \boldsymbol{\nabla})\mathbf{u}_t - (\boldsymbol{\xi_t} \cdot \boldsymbol{\nabla})\mathbf{u}_{\mathrm{osc}} = \mathbf{u}_t + (\boldsymbol{\xi_t} \cdot \boldsymbol{\nabla})\mathbf{u}_t , \tag{D.27}$$

$$\frac{\partial \mathbf{u}_{\mathrm{osc}}}{\partial t} - \mathbf{L}_1^d - \mathbf{L}_1^s = \mathbf{L}_0 , \tag{D.28}$$

where

$$\begin{aligned}
L_{1,i}^d = &\left[\frac{1}{\rho_0}\frac{\partial p_0}{\partial x_i} - \frac{\partial c_0^2}{\partial x_i}\right] \frac{1}{\rho_0} \int \mathrm{d}^3\mathbf{y}\, \rho_0(\mathbf{y}) \left(\xi_{\mathrm{osc,j}} \partial_j K^{\mathbf{x}}\right)\Big|_{\mathbf{y},t} \\
&+ \frac{c_0^2}{\rho_0} \int \mathrm{d}^3\mathbf{y}\, \rho_0(\mathbf{y}) \left(\xi_{\mathrm{osc,j}} \partial_j \partial_i K^{\mathbf{x}}\right)\Big|_{\mathbf{y},t} \\
&+ G_{ij,0}\left(u_{\mathrm{osc,j}} - \frac{1}{\rho_0(\mathbf{x})} \int \mathrm{d}^3\mathbf{y}\, \rho_0(\mathbf{y}) u_{\mathrm{osc,j}}(\mathbf{y}) K^{\mathbf{x}}(\mathbf{y})\right) ,
\end{aligned} \tag{D.29}$$

$$\begin{aligned}
L_{1,i}^s = &- u_{\mathrm{osc,j}} \partial_j u_{t,i} - u_{t,j} \partial_j u_{\mathrm{osc,i}} \\
&- G_{ij,0} \frac{1}{\rho_0} \int \mathrm{d}^3\mathbf{y}\, \rho_0(\mathbf{y}) \left(\xi_{\mathrm{osc,k}} \partial_k \left(u_{t,j} K^{\mathbf{x}}\right)\right)\Big|_{\mathbf{y},t} \\
&+ \left(\frac{\partial G_{ij}}{\partial \widetilde{u_k'' u_l''}} \widetilde{u_k'' u_l''}_1 + \frac{\partial G_{ij}}{\partial(\partial_k \widetilde{u_l})} \partial_k \widetilde{u_l} + \frac{\partial G_{ij}}{\partial \epsilon} \omega_t k_1\right) u_{t,j} \\
&+ \frac{1}{2}\sqrt{\frac{C_0 \omega_t}{k_0}} k_1 \eta_i ,
\end{aligned} \tag{D.30}$$

$$L_{0,i} = - u_{t,j} \partial_j u_{t,i} - \frac{1}{\rho_0}\frac{\partial p_0}{\partial x_i} + g_{i,0} + G_{ij,0} u_{t,j} + \sqrt{C_0 \omega_t k_0}\, \eta_i , \tag{D.31}$$

where $c_0^2 \equiv p_0 \gamma / \rho_0$ is the equilibrium sound speed squared, and the quantities $\widetilde{u_k'' u_l''}_1$, $\partial_k \widetilde{u_l}_1$, and k_1 are given by Eqs. (D.18), (D.14), and Eq. (D.19) respectively.

Appendix D.3: The forcing term

In Eqs. (D.27) and (D.28) the right-hand side represent inhomogeneous stochastic forcing terms. For the moment we have kept all zeroth order terms (i.e. all the terms that are independent of the wave variables $\boldsymbol{\xi}_{\mathrm{osc}}$ and $\mathbf{u}_{\mathrm{osc}}$) on these right-hand sides, but $\mathbf{L}_0$ can be rearranged into a more compact form, and some terms will in fact prove negligible. Firstly, let us rewrite the first term on the right-hand side of Eq. (D.31). Using hypothesis (H4), we write the continuity equation for $\mathbf{u}_t$ without any contribution from the oscillatory component

$$\frac{\partial \rho}{\partial t} + \rho \frac{\partial u_{t,j}}{\partial x_j} + u_{t,j} \frac{\partial \rho}{\partial x_j} , \tag{D.32}$$

where ρ is the sum of the equilibrium value ρ_0 and the turbulent fluctuations of the density ρ_t. Building on hypothesis (H3), we neglect ρ_t in Eq. (D.32), so that

$$\frac{\partial u_{t,j}}{\partial x_j} = - \frac{u_{t,j}}{\rho_0} \frac{\partial \rho_0}{\partial x_j} , \tag{D.33}$$

finally allowing us to write

$$\begin{aligned}
u_{t,j} \partial_j u_{t,i} &= \partial_j (u_{t,j} u_{t,i}) - u_{t,i} \partial_j u_{t,j} \\
&= \partial_j (u_{t,j} u_{t,i}) - u_{t,i}\left(- \frac{u_{t,j}}{\rho_0} \frac{\partial \rho_0}{\partial x_j}\right) \\
&= \frac{1}{\rho_0} \frac{\partial \rho_0 u_{t,j} u_{t,i}}{\partial x_j} .
\end{aligned} \tag{D.34}$$

Secondly, it does not come as a surprise that the non-stochastic part of Eq. (D.31) corresponds to the hydrostatic equilibrium condition. If radiative pressure is neglected, we have

$$- \frac{1}{\rho_0} \frac{\partial \rho_0 \overline{u_{t,i} u_{t,j}}}{\partial x_j} - \frac{1}{\rho_0} \frac{\partial p_0}{\partial x_i} + g_{i,0} = 0 , \tag{D.35}$$

so that

$$L_{0,i} = -\frac{1}{\rho_0}\frac{\partial(\rho_0 u_{t,i}u_{t,j} - \rho_0\overline{u_{t,i}u_{t,j}})}{\partial x_j} + G_{ij,0}u_{t,j} + \sqrt{C_0\omega_t k_0}\eta_i \ . \tag{D.36}$$

It thus becomes clear that the forcing term contains the usual contribution from the fluctuations of the turbulent pressure, a contribution that is linear in $\mathbf{u}_t$, and a contribution that is linear in $\boldsymbol{\eta}$, and therefore completely uncorrelated in space. Following the discussion from Samadi & Goupil (2001), we argue that all linear contributions are negligible. The contribution of a linear term to the excitation rate of the modes has an efficiency that is based on the resonance between the lifetime of the large-scale energy-bearing eddies and the period of the modes, which the authors showed was negligible. Naturally, the same argument can be used to neglect the third term as well since it has no coherence in either space or time. The non-linear term, on the other hand, is able to couple different length scales together, and therefore leads to a non-negligible contribution to the excitation rate. Finally, after having filtered out those terms we deemed negligible, we obtain

$$L_{0,i} = -\frac{1}{\rho_0}\frac{\partial\left(\rho_0 u_{t,i}u_{t,j} - \rho_0\overline{u_{t,i}u_{t,j}}\right)}{\partial x_j} \ . \tag{D.37}$$

The right-hand side of Eq. (D.27) can be treated similarly: the term $\mathbf{u}_t$ being linear in the turbulent fields, its contribution to mode driving can be neglected, thus only leaving the second term.

9 Lagrangian stochastic model for turbulence-oscillation coupling: numerical implementation

Contents

> Real stupidity beats artificial intelligence every time.
>
> Sir Terry Pratchett

In the previous chapter, I regarded Lagrangian stochastic models as a way to *analytically* determine the relation between the properties of turbulence and the observed properties of the modes in solar-like oscillators. However, as I warned in the concluding remarks therein, should a more complex Lagrangian stochastic model be adopted to start with, this analytical description may quickly become too challenging to build, or may else lead to a formulation that is too impractical to handle in a purely analytical manner. In that case, an alternative would consist in *numerically* implementing these models. More generally, analytical prescriptions for the coupling between turbulent convection and solar-like oscillations, the kind of which is provided by the formalism developed in Chapter 8, are much more efficiently quantified by means of numerical simulations based on the Lagrangian stochastic model itself. For these reasons, and as I already hinted in the end of Section 7.3, the theoretical side of my work largely benefits from a more direct, numerical implementation of the same methods. This is the subject of this chapter.

Fundamentally, the implementation makes use of the exact same mathematical tools presented in Chapters 7 and 8. Except for a few specific numerical points, there is therefore nothing conceptually new in the details of the implementation. It was originally inspired by the work of Welton and Pope (1997), who had already combined Lagrangian stochastic models of turbulence with the Smoothed Particle Hydrodynamics formalism. However, their study was conducted from the point of view of the hydrodynamics community, and they considered the case of a forced flow in an axisymmetric pipe. By contrast, I am interested in free turbulence in the stellar context, and in particular in the oscillations developing in the simulation. I describe the specific procedure designed to extract the oscillations from the output of the simulation, and to determine their properties (frequency, amplitude, linewidth, eigenfunction), in Section 9.2. Finally, in Section 9.3, I conduct the validation of the numerical approach by comparing the output of the simulation with exact analytical results that can be derived in the simple case considered in this chapter, based on the same Lagrangian stochastic model as I considered in Chapter 8, and by showing that the agreement between numerical and exact analytical results is excellent.

9.1 Simulations based on Lagrangian stochastic models of turbulence

In this section, I describe the ways in which the same Lagrangian stochastic model that I considered in Chapter 8 is numerically integrated forward in time. This essentially involves two main issues, namely 1) how are the stochastic differential equations integrated in time for each particle? and 2) how are the means appearing in these stochastic differential equations – and additionally constituting the output of the simulation – evaluated? These two questions are the subjects of Sections 9.1.1 and 9.1.2 respectively. Let me take this opportunity, as I did in Chapter 8, to recall that the Lagrangian stochastic model considered here *is not meant to be a realistic stochastic model in the stellar context*, and is rather meant as a first step to validate the numerical approach.

9.1.1 Integration of the stochastic differential equations

Stochastic Differential Equations in a plane-parallel geometry

I recall here the Lagrangian stochastic model used in Chapter 8, and which I will also consider here

$$\mathrm{d}x_i^{\star(n)} = u_i^{\star(n)}\ \mathrm{d}t\ , \tag{9.1}$$

$$\mathrm{d}u_i^{\star(n)} = \left[-\frac{1}{\overline{\rho}}\frac{\partial \overline{p}}{\partial x_i} + g_i + G_{ij}\left(u_j^{\star(n)} - \widetilde{u}_j\right)\right]\ \mathrm{d}t + \sqrt{C_0\omega_t k}\ \mathrm{d}W_i\ , \tag{9.2}$$

where $\mathbf{x}^{\star(n)}$ and $\mathbf{u}^{\star(n)}$ are the position and velocity of the n-th fluid particle (the system in its entirety being comprised of N such particles), the notation $\mathrm{d}\ \cdot$ denotes an increment over the infinitesimal time interval $\mathrm{d}t$, $\mathbf{W}$ is a vector consisting of three independent Wiener processes (see the end of Section 7.1.2 for a definition), and the mean density $\overline{\rho}$, mean gas pressure $\overline{p}$, gravitational acceleration $\mathbf{g}$, drift tensor G_{ij}, mass-averaged velocity $\widetilde{\mathbf{u}}$ and turbulent kinetic energy k are all evaluated at the position $\mathbf{x}^{\star(n)}$ of the particle. As I described in Section 7.2.4, these mean fields can be estimated directly from the set of N fluid particles used to represent the flow; let me leave aside this aspect of the numerical implementation for the moment, and let me return to it in Section 9.1.2.

Equations 9.1 and 9.2 constitute a three-dimensional form of the stochastic differential equations for the position and velocity of a fluid particle. In the following, however, I will consider the special case of a flow *following a plane-parallel geometry*, exactly as I did in Appendix B, upon deriving a more realistic Lagrangian stochastic model for stellar turbulent convection. I recall that assuming a plane-parallel geometry amounts to considering that the statistics of the flow are invariant by horizontal translations as well as rotations around the vertical axis. Otherwise stated, 1) the moments of the random variables characterising the turbulent flow – in particular the turbulent velocity – only depend on the vertical coordinate, which I will denote as z in the following, 2) the mean fields appearing in Equations 9.1 and 9.2 also only depend on z, and 3) the Reynolds stress tensor is diagonal, and its two horizontal diagonal components are equal. This geometry is relevant in the particular case of radial p-modes, but becomes invalid for non-radial modes, as it does not allow for any horizontal oscillatory motion. At first glance, it may look like the three-dimensional equations given above should be reduced to one-dimensional equations instead, with the vertical position $z^{\star(n)}$ and the vertical velocity $u_v^{\star(n)}$ being the only two quantities needed to describe the state of the n-th fluid particle. However, this is not true: indeed, the evolution of the vertical velocity of the particle still depends on *all* the components of the Reynolds stress tensor, through the dependence of the drift tensor G_{ij} on $\widetilde{u_i'' u_j''}$, but also through the turbulent kinetic energy k appearing in the diffusion coefficient (i.e. the last term on the right-hand side of Equation 9.2). Physically, this is due to the fact that the velocity-pressure-gradient tensor in the Reynolds stress equation redistributes the energy among the various components of the Reynolds stress tensor, meaning that the turbulent fluctuations of the vertical velocity can be fueled by the horizontal motions of the gas. Consequently, it is necessary to keep the horizontal velocity as a variable describing the state of the fluid particles, *although it is not necessary to know their horizontal position*. This leads me to the following 'one-point-five-dimensional' form of the Lagrangian stochastic model

$$\mathrm{d}z^{\star(n)} = u_v^{\star(n)}\ \mathrm{d}t\ , \tag{9.3}$$

$$\mathrm{d}u_v^{\star(n)} = \left[-\frac{1}{\overline{\rho}}\frac{\partial \overline{p}}{\partial z} + g + G_{vv}\left(u_v^{\star(n)} - \widetilde{u_v}\right)\right]\ \mathrm{d}t + \sqrt{C_0\omega_t k}\ \mathrm{d}W_v\ , \tag{9.4}$$

$$\mathrm{d}u_h^{\star(n)} = G_{hh}u_h^{\star(n)}\ \mathrm{d}t + \sqrt{C_0\omega_t k}\ \mathrm{d}W_h\ , \tag{9.5}$$

where $z^{\star(n)}$, $u_v^{\star(n)}$ and $u_h^{\star(n)}$ are the vertical position, the vertical velocity, and *one arbitrary*[1] horizontal component of the horizontal velocity of the n-th fluid particle, g is now the vertical component of $\mathbf{g}$, and G_{vv} and G_{hh} are the vertical and horizontal diagonal components of the drift tensor. Note that in expanding the drift term $G_{ij}\,(u_i - \widetilde{u_i})$, I have discarded all off-diagonal components of the drift tensor: this is another consequence of the plane-parallel geometry.

Numerical scheme for the forward integration in time

One of the main differences between the stochastic differential equations given by Equations 9.3 to 9.5 and the equations of hydrodynamics implemented, for instance, in Large-Eddy Simulations, is that the former involve variables that only depend on time, while the latter involve variables that depend on time *and* space. In the case of LES, establishing a numerical scheme requires taking care of the spatial discretisation in the time scheme. In Lagrangian stochastic models implemented through particle methods, this aspect is completely circumvented, and *the question of the time scheme concerns scalar quantities, not spatial arrays*: this makes the task of designing an appropriate numerical scheme considerably easier. In general, there are mainly three properties that one may wish a numerical scheme to possess: consistency, convergence, stability[2]. In very broad strokes, and without going into the rigorous mathematical definitions of these properties, a numerical scheme is said to be convergent if the solution of the discretised differential equation tends to a fixed function when the time step in the discretisation tends to zero; it is said to be consistent if this fixed solution corresponds to the actual solution of the exact, non-discretised differential equation; and it is said to be stable if similar initial conditions lead to similar solutions, with the ratio between the solution difference and the initial condition difference remaining bounded if the time step is small enough. The issue, in dealing with *stochastic* differential equations, is that numerical schemes that possess one or several of these properties for deterministic equations may lose them upon direct, heuristic application to stochastic equations. Furthermore, the notion of consistency and convergence for time-discretised stochastic equations is not defined as straightforwardly as for deterministic equations. Indeed, assessing the quality, i.e. the accuracy, of a time discrete approximation, heavily depends on the task one wishes to accomplish with the simulation. One can be interested in the individual paths of each realisation of the stochastic process, in which case one should aim for a good *pathwise approximation*. Alternatively, it may happen that one is only interested in the moments of the stochastic process – i.e. its expectation, variance, etc. –, in which case one should instead aim for a good *expectation approximation*. Each objective leads to a different consistency and convergence criterion. In order to obtain a good pathwise approximation, it is necessary that the expectation of the absolute value between the sample path of a stochastic process and its time-discretised counterpart should vanish when the time step tends to zero: this defines the *strong convergence* criterion. If, in addition, the stochastic process in question is a solution of the actual stochastic differential equation, the numerical scheme is said to be *strongly consistent*. On the other hand, in order to obtain a good expectation approximation, it is only necessary that the moments of the solution of the time-discretised stochastic differential equation tend to fixed values when the time step tends to zero (this defines the *weak convergence* criterion), and that the fixed values in question correspond to the moments of the actual solution of the exact stochastic differential solution (this defines the *weak consistency* criterion). In the present context, since I am ultimately interested in the oscillations naturally present in the simulation, I only wish for a good expectation approximation, and would therefore be content with a weakly consistent and convergent scheme.

The vast variety of existing numerical schemes for the time-discretisation of differential equations, the ways in which deterministic schemes can be adapted to the stochastic case, and the respective advantages and drawbacks of these methods as regards their convergence, consistency or stability, stretches far beyond the scope of this thesis. Should the reader be interested in such matters, I would gladly refer them to the textbook by Kloeden and Pletten (1992), and in particular their Parts IV to VI. In the following, I merely present the specific time scheme that I adopted to integrate Equations 9.3 to 9.5 forward in time for each fluid particle individually. Following Welton and Pope (1997), I chose a Predictor-Corrector scheme, which, as its deterministic counterpart, is mainly used for its numerical stability, and happens to be weakly consistent and convergent of order 1.0 – meaning that the difference between the time-discrete solution and the actual solution weakly converges towards zero proportionally to the

[1] In the plane-parallel geometry considered here, all horizontal directions are equivalent, in the sense that the statistical moments of the turbulent quantities are invariant by rotation around the vertical axis. This is the reason why only one horizontal component of the velocity is needed.

[2] Any potential resemblance with the official motto of past political regimes is purely fortuitous.

time step. Let me denote the discrete times used for the numerical integration as t_k, where t_0 is the initial time, and the k-time step as $\Delta_k \equiv t_{k+1} - t_k$. Then for any stochastic process $\{X_t\}_{t\in\mathbb{R}}$, if the corresponding Ito SDE is

$$\mathrm{d}X = a(X,t)\ \mathrm{d}t + b(X,t)\ \mathrm{d}W\ , \tag{9.6}$$

then the value X_{k+1} of the stochastic process at time t_{k+1} is given as a function of its value X_k at time t_k through the corrector

$$X_{k+1} = X_k + \left[\alpha\ \overline{a}_\beta\left(X_k, t_k\right) + (1-\alpha)\ \overline{a}_\beta\left(\overline{X}_{k+1}, t_{k+1}\right)\right]\ \Delta_k + \left[\beta\ b\left(X_k, t_k\right) + (1-\beta)\ b\left(\overline{X}_{k+1}, t_{k+1}\right)\right]\ \Delta W_k\ , \tag{9.7}$$

where the modified drift coefficient $\overline{a}_\beta$ is given by

$$\overline{a}_\beta \equiv a - \beta\ b \frac{\partial b}{\partial X}\ , \tag{9.8}$$

$\overline{X}_{k+1}$ is the value of the stochastic process at time t_{k+1} given by the following predictor (which is simply a first-order, explicit Euler scheme)

$$\overline{X}_{k+1} = X_k + a\left(X_k, t_k\right)\ \Delta_k + b\left(X_k, t_k\right)\ \Delta W_k\ , \tag{9.9}$$

ΔW_k is a random variable drawn at each time step according to a normal distribution of zero mean and variance Δ_k, and $\alpha, \beta \in [0,1]$ are two parameters in the numerical scheme that can be chosen arbitrarily, and control the level of implicitness in the time-difference scheme for the drift and diffusion coefficients respectively. In the following, I have chosen $\alpha = \beta = 0.5$. Of important note is the fact that ΔW_k is only drawn once per time step, with the same value being used in the predictor and the corrector steps.

This numerical scheme is not unconditionally stable, and the time step is subjected to a Courant-Friedrichs-Lewy (or CFL) constraint, i.e. an upper boundary above which the scheme becomes unstable. When combined with the Smoothed Particle Hydrodynamics formalism for the estimation of the means, the CFL constraint becomes[3] Welton and Pope (1997)

$$\Delta_k \leqslant C_t \frac{h}{\max_{n=1..N}\left(\left|u^{\star(n)}_{v,k}\right| + c_s^{(n)}\right)}\ , \tag{9.10}$$

where $c_s^{(n)}$ is the mean sound speed at the location of the n-th particle, h is the size of the kernel function used in the SPH formalism (see Section 7.2.4), and C_t is a non-dimensional empirical constant, for which numerical tests prescribe $C_t \sim 0.75$.

Boundary conditions for the particles

What happens when a fluid particle exits the simulation box? Particle methods, coupled with SPH, offer several ways of enforcing boundary conditions, depending on the situation under consideration (see Liu and Liu 2010, for a review). Periodic boundary conditions are straightforwardly implemented – at least in simple domain geometries –, because one simply has to reinject exiting particles on the other side with the same properties. Solid boundaries are less easy to implement. It is possible to simply keep the exiting particles in the box as if they had been reflected on the boundary; this can be used to implement slip or non-slip boundary conditions alike (e.g. Allen et al. 1989; Frenkel et al. 1997; Revenga et al. 1998, 1999; Willemsen et al. 2000; Duong-Hong et al. 2004; Wang et al. 2006). Other, more refined solid boundary treatments can be implemented, primarily based on the inclusion of *ghost* or *virtual particles* (i.e. artificial fluid particles added on the boundary or even outside the domain), which can be used, for instance, to exert a strong repulsive force on the *real* particles, so as to prevent them from exiting the box (e.g. Campbell 1989; Libersky et al. 1993; Monaghan 1994; Morris et al. 1997; Rapaport 2004). On the other hand, inflow or outflow boundary conditions can be enforced by using buffer zones at each boundary, as in Welton and Pope (1997) for instance. The idea is to 1) compute boundary values for the mean fields, by using both the

[3] It may seem odd that a CFL constraint even exists for Lagrangian stochastic models: indeed, the usual physical interpretation is that a wave should not be able to travel from one grid point to the next during one time step, which presupposes the existence of grid points. In SPH, there are no grid points, but instead the new constraint is that a fluid particle should not be able to see a wave travel through the entire width of the weighting kernel *in its frame of reference* during one time step.

known properties of the inflow and outflow, and the fact that there should not be any outgoing waves at the inlet or ingoing waves at the outlet, then 2) enforcing these boundary mean fields by inserting new particles in buffer zones just outside the domain, drawing their position and velocities according to the mean and variances previously computed, and finally 3) letting the buffer particles evolve as if they were real particles, discarding any particle that has exited the domain after the end of the time step, and retaining any particle that ended the time step inside the domain, regardless of whether it was a real or a buffer particle to begin with.

However, when SPH is used in conjunction with Lagrangian stochastic models – i.e. when the particles are advanced through time using stochastic equations –, an alternative method, particularly interesting for open domain boundaries such as those considered in the context of stellar turbulence, consists in discarding any exiting fluid particle, and resupplying the domain with as many new incoming particles, *whose properties are drawn randomly according to the local Eulerian PDF at the boundary, reconstructed by means of the SPH formalism*. This method was proposed by Meyer and Jenny (2007), and is based on the arguments laid out in the following. Let me consider a boundary located at z_b, such that the region $z > z_b$ is inside the domain, and the region $z < z_b$ is outside. If the time step Δt is small enough that the typical spatial scale of variation of the Eulerian PDF of the flow at the boundary is much larger than the distance travelled by the particles during Δt, then the probability that a particle with vertical velocity u_v and vertical position $z < z_b$ crosses the boundary during Δt is given by

$$\begin{aligned} f_b(u_v|z) = \;& \beta\, f(u_v; z_b) && \text{if} \quad (u_v - \widetilde{u_v}(z_b))\,\Delta t > z_b - z \;\text{ and }\; z < z_b \,, \\ & 0 && \text{otherwise} \,, \end{aligned} \tag{9.11}$$

where β is a normalisation constant. Using the definition of the conditional PDF (see Section 7.1.1), the unconditional PDF of the velocity of the particle entering the domain from the outside during the time interval Δt is then given by

$$\begin{aligned} f_b(u_v) = \;& \int_{-\infty}^{z_b} \mathrm{d}z\; f_b(u_v|z) f(z) && \text{if} \quad u_v > \widetilde{u_v}(z_b) \,, \\ & 0 && \text{otherwise} \,, \end{aligned} \tag{9.12}$$

where $f(z)$ is the PDF of the particle positions. But under the assumption that the PDF does not vary significantly over the typical distances traveled by the particles during Δt, $f(z)$ is uniform, and one obtains

$$\int_{-\infty}^{z_b} \mathrm{d}z\; f_b(u_v|z) f(z) \propto \int_{-\infty}^{z_b} \mathrm{d}z\; f_b(u_v|z) \propto \int_{z_b - u_v \Delta t}^{z_b} \mathrm{d}z\; f(u_v; z) \propto u_v f(u_v; z_b) \,, \tag{9.13}$$

where the first equality stems from the uniformity of the position PDF $f(z)$, the second equality comes from Equation 9.11, and the third equality is a first order expansion in Δt. The proportionality constant is given by the normalisation condition

$$\int_{-\infty}^{+\infty} \mathrm{d}u_v\; f_b(u_v) = 1 \,. \tag{9.14}$$

Therefore, knowing the Eulerian PDF of the flow velocity $f(u_v; z_b)$ at the boundary z_b immediately yields the PDF of the velocity of entering particles. *Assuming the PDF of the vertical velocity of the flow is Gaussian for instance*, with mean $\widetilde{u_v}$ and variance $\widetilde{u_v''^2}$, one obtains

$$\begin{aligned} f_b(u_v) = \;& \frac{u_v}{\widetilde{u_v''^2}} \exp\left(-\frac{(u_v - \widetilde{u_v})^2}{2\widetilde{u_v''^2}} \right) && \text{if} \quad u_v > \widetilde{u_v} \,, \\ & 0 && \text{otherwise} \,. \end{aligned} \tag{9.15}$$

This PDF is clearly not Gaussian: its typical form is given in Figure 9.1. In particular, it can be seen that particles that are too slow cannot penetrate the boundary, while fast particles are favoured by contrast. Note that while Equation 9.15 is only valid if the Eulerian flow PDF is Gaussian, equivalent expressions for non-Gaussian PDF can be derived just as easily, and implemented simply by computing more moments of the PDF through the SPH formalism.

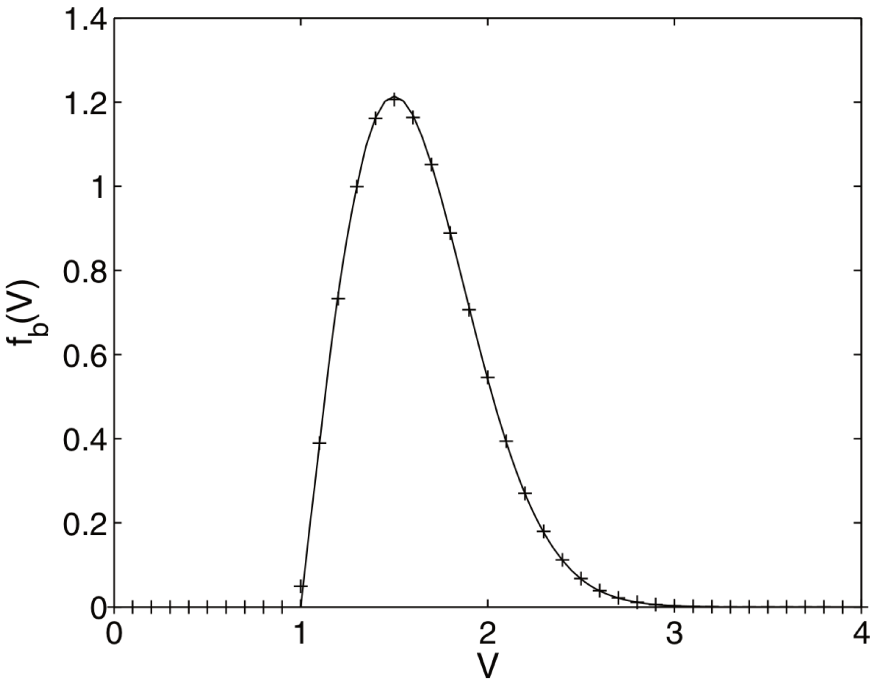

Figure 9.1: PDF of the vertical velocities of the particles entering the domain from the outside during an arbitrary time step Δt. The values $\widetilde{u_v} = 1$ m.s^{-1} and $\sqrt{\widetilde{u_v''^2}} = 0.5$ m.s^{-1} were chosen. The velocity axis is in m.s^{-1}, the PDF axis in s.m^{-1}. The solid line is given by Equation 9.15, and the symbols represent a reconstruction of the PDF from numerical results directly. The agreement is very close. *Credits*: Meyer and Jenny (2007).

The entering particle velocity PDF $f_b(u_v)$ is readily integrated to yield a *Cumulative Density Function*[4] in the form

$$F_b(u_v) = \begin{cases} 1 - \exp\left(-\dfrac{(u_v - \widetilde{u_v})^2}{2\widetilde{u_v''^2}}\right) & \text{if } u_v > \widetilde{u_v}\,, \\ 0 & \text{otherwise}\,. \end{cases} \tag{9.16}$$

In turn, the CDF is readily inverted, so that *the newly entering particles can be assigned a vertical velocity*

$$u_{v,\text{new}} = \sqrt{-2\,\widetilde{u_v''^2}\,\ln(1-\zeta)} + \widetilde{u_v}\,, \tag{9.17}$$

where ζ is uniformly distributed between 0 and 1. Furthermore, the position of the new particles is not initialised exactly at the boundary, but at the position one would have obtained had the particle rebounded on the boundary, and adopted this new velocity $u_{v,\text{new}}$. Concretely, and to summarise, after a given time step, every particle that ends up outside the domain has its vertical position and vertical velocity reassigned according to (Meyer and Jenny 2007)

$$z^{\star(n)} \mapsto z_b - \frac{u_{v,\text{new}} - \widetilde{u_v}}{\widetilde{u_v} - u_v^{\star(n)}}\left(z^{\star(n)} - z_b\right)\,, \tag{9.18}$$

$$u_v^{\star(n)} \mapsto u_{v,\text{new}}\,, \tag{9.19}$$

and the horizontal velocity is also reassigned, this time according to a Gaussian PDF with zero mean – because of the plane-parallel geometry –, and variance $\widetilde{u_h''^2}$, so that

$$u_h^{\star(n)} \mapsto u_{h,\text{new}} \sim \mathcal{N}\left(0, \widetilde{u_h''^2}\right)\,. \tag{9.20}$$

[4]The CDF of a random variable is a function of its sampling variable x, and corresponds to the probability that $X < x$. As a result, the PDF is the derivative of the CDF.

This reassignment of exiting particles only depends on $u_{v,\text{new}}$ and $u_{h,\text{new}}$ (which are drawn randomly from the distributions described by Equations 9.17 and 9.20 respectively, and independently for each particle), as well as the mean fields $\widetilde{u_v}$, $\widetilde{u_v''^2}$ and $\widetilde{u_h''^2}$ at the boundary, all of which are evaluated through the SPH formalism (see Section 9.1.2). Note that the mapping given above is only valid at the bottom boundary of the simulation; a similar mapping is found for particles exiting through the top boundary of the simulation box.

Initial conditions for the particles

In grid-based numerical methods, the initial conditions can be chosen to match a given equilibrium model, and are therefore easily prescribed. In Lagrangian stochastic particle methods, however, the fluid particles are supposed to represent the flow PDF, including the underlying variance of the turbulent quantities. To reflect this, the initial properties of the particles cannot be chosen in a deterministic manner, but instead drawn randomly from a relevant distribution. Concerning their initial velocity, I assume that it is Gaussian, and therefore draw it according to

$$u_v^{\star(n)}(t=0), u_h^{\star(n)}(t=0) \sim \mathcal{N}\left(0, A\, c_s^{2(n)}\right) , \tag{9.21}$$

where $c_s^{2\ (n)}$ is the equilibrium sound speed squared at the initial location of the n-th particle, and A is a non-dimensional constant that I chose to equal unity, *so that the initial standard deviation of the turbulent velocity equals the local sound speed*. The equilibrium sound speed profile is considered to be a known input of the simulation, so that I only need to know the initial position of the particles in order to randomly draw their initial velocity. The initial particle positions are determined in such a way that *the initial mean density $\overline{\rho}$, as determined from the SPH formalism, coincides with the equilibrium density profile ρ_0, which is also considered to be a known input of the simulation*. Otherwise stated, the position of the fluid particles is drawn according to a PDF $f(z, t = 0) \propto \rho_0(z)$ – with the proportionality coefficient being given by the normalisation condition for $f(z, t = 0)$. Since the PDF in question is not in an analytical form, it is necessary to draw the particle positions numerically. This is done through a *rejection algorithm*, which can be summarised thus: for each particle

1) I draw a random position z uniformly distributed in the entire simulated domain;

2) I draw a random variable u uniformly distributed between 0 and $\rho_{0,\text{max}}$, where the latter is the maximum of the equilibrium density profile across the entire simulated domain;

3) I check whether or not $\rho_0(z) < u$. If so, the position z is accepted for the fluid particle. If not, I come back to step 1, and draw a new position for the particle.

Once this is done, I obtained an initial vertical position, vertical velocity and horizontal velocity for each fluid particle, which is sufficient information to initialise the simulation.

9.1.2 Numerical implementation of the Smoothed Particle Hydrodynamics formalism

Expression of the mean fields in SPH

The drift and diffusion coefficients in the velocity SDE given by Equations 9.4 and 9.5, as I had the opportunity to point out in Section 9.1.1, depend on the value of the mean fields at the location of the particle – namely the mean density $\overline{\rho}$, the mean gas pressure gradient $\partial_z \overline{p}$, the mass-averaged vertical velocity $\widetilde{u_v}$, and the vertical and horizontal diagonal components of the Reynolds stress tensor $\widetilde{u_v''^2}$ and $\widetilde{u_h''^2}$. To estimate these mean fields, I use the procedure described in detail in Section 7.2.4, which consists in averaging the corresponding particle-level quantities over all neighbouring particles, the latter being filtered by means of a kernel function K. I recall the

expressions already given in Section 7.2.4 (see Equations 7.120 to 7.122)

$$\overline{\rho}\left(z^{\star(n)}\right) = \sum_{k=1}^{N} \Delta m^{(k)} K\left(z^{\star(k)} - z^{\star(n)}\right) , \tag{9.22}$$

$$\widetilde{u_v}\left(z^{\star(n)}\right) = \frac{1}{\overline{\rho}(z^{\star(n)})} \sum_{k=1}^{N} \Delta m^{(k)} u_v^{\star(k)} K\left(z^{\star(k)} - z^{\star(n)}\right) , \tag{9.23}$$

$$\widetilde{u_v''^2}\left(z^{\star(n)}\right) = \frac{1}{\overline{\rho}(z^{\star(n)})} \sum_{k=1}^{N} \Delta m^{(k)} \left(u_v^{\star(k)} - \widetilde{u_v}(z^{\star(k)})\right)^2 K\left(z^{\star(k)} - z^{\star(n)}\right) , \tag{9.24}$$

$$\widetilde{u_h''^2}\left(z^{\star(n)}\right) = \frac{1}{\overline{\rho}(z^{\star(n)})} \sum_{k=1}^{N} \Delta m^{(k)} \left(u_h^{\star(k)}\right)^2 K\left(z^{\star(k)} - z^{\star(n)}\right) , \tag{9.25}$$

where $\Delta m^{(k)}$ is the mass of fluid carried by the k-th fluid particle. If all particles carry the same mass, then it is given by

$$\Delta m = \frac{1}{N} \int_{z_b}^{z_t} \mathrm{d}z \, \rho_0(z) , \tag{9.26}$$

where z_b and z_t are the vertical coordinates corresponding to the bottom and top boundaries of the simulation box respectively. As far as the mean gas pressure is concerned, I use the same polytropic relation already assumed in Chapter 8 (see Equation 8.4)

$$\overline{p} = p_0 \left(\frac{\overline{\rho}}{\rho_0}\right)^{\gamma} , \tag{9.27}$$

where the equilibrium gas pressure $p_0(z)$ and the polytropic exponent $\gamma(z)$ are treated as known inputs of the simulation. Finally, the turbulent kinetic energy reads, by definition

$$k = \frac{1}{2}\widetilde{u_v''^2} + \widetilde{u_h''^2} . \tag{9.28}$$

Together, Equations 9.22 to 9.28 provide with closed expressions for every mean field appearing in the Lagrangian stochastic model, as a function of the inputs of the simulation – namely $\rho_0(z)$, $p_0(z)$ and $\gamma(z)$ – and the state of the fluid particles themselves – namely $z^{\star(n)}$, $u_v^{\star(n)}$ and $u_h^{\star(n)}$ for each particle n. Note that the SPH formalism also provides with an expression for the gradient of these mean quantities; for instance, the mean density gradient, on which depends the mean gas pressure gradient appearing in the vertical velocity SDE, is given by

$$\left.\frac{\partial \overline{\rho}}{\partial z}\right|_{z^{\star(n)}} = \sum_{k=1}^{N} \Delta m^{(k)} \left.\frac{\mathrm{d}K}{\mathrm{d}z}\right|_{z^{\star(k)} - z^{\star(n)}} . \tag{9.29}$$

In other words, it is obtained by averaging the corresponding particle-level quantity weighted by the gradient of the kernel function instead of the kernel function itself. Since the gradient of the kernel is an analytical function, the estimation of the mean gradients is formally performed in exactly the same way as the mean fields themselves: this is also one of the strengths of the SPH formalism.

O(N) algorithm

Directly using these expressions to compute the mean fields at the location of each particle, however, is quite impractical. Indeed, this requires the computation of N sums containing $\sim hN/L$ terms each, where h/L is the ratio of the kernel size and the domain size – hN/L then representing the average number of particles contributing to each kernel estimate. Using Equation 7.117 for the optimal kernel size h – i.e. the value of h leading to the best compromise between precision and accuracy –, one finds that the direct computations of these sums constitutes an operation of complexity $O\left(N^{9/5}\right)$. In the 1D case, however, it is possible to reduce the complexity to $O(N)$,

provided the kernel function K is piece-wise polynomial, which is the case of the kernel function chosen by Welton and Pope (1997), and that I also choose in the following (see Equation 7.114)

$$K(r) = \begin{cases} c\left(1+3\frac{|r|}{h}\right)\left(1-\frac{|r|}{h}\right)^3 & \text{if } |r|<h\,, \\ 0 & \text{if } |r|>h\,, \end{cases} \tag{9.30}$$

where $c = 5/(4h)$. Let me denote an arbitrary particle-level quantity as $\rho^{\star(n)}Q^{\star(n)}$, and its kernel estimate as $\overline{\rho Q}(z)$. Then the fundamental idea is that *if K is piecewise polynomial, so is* $\overline{\rho Q}(z)$ – since the latter is a linear combination of kernel functions centered on each fluid particle. Therefore, $\overline{\rho Q}\left(z^{\star(n)}\right)$ can be estimated from one particle to the next (provided they are ordered by increasing vertical position) by using *its exact Taylor expansion, which only contains a finite number of terms*.

This idea can be formalised thus. The p-th derivative of $\overline{\rho Q}$ is given, in the SPH formalism, by

$$D^{(p)}(z) = \Delta m \sum_{k=1}^{N} Q^{\star(k)} K^{(p)}\left(z^{\star(k)} - z\right)\,. \tag{9.31}$$

Its Taylor expansion yields, in general, the following infinite series

$$\begin{aligned} D^{(p)}(z+\Delta z) &= \Delta m \sum_{k=1}^{N} Q^{\star(k)} \sum_{q=0}^{+\infty} \frac{\Delta z^q}{q!} K^{(p+q)}\left(z^{\star(k)} - z\right) \\ &= \sum_{q=0}^{+\infty} \frac{\Delta z^q}{q!} D^{(p+q)}(z)\,. \end{aligned} \tag{9.32}$$

If the kernel function is given by Equation 9.30, then $D^{(p)}$ vanishes everywhere for $p > 4$. Therefore, this infinite series becomes a finite sum

$$D^{(p)}(z+\Delta z) = \sum_{q=0}^{4-p} \frac{\Delta z^q}{q!} D^{(p+q)}(z) \quad \text{for } p = 0 \text{ to } 4\,. \tag{9.33}$$

Therefore, knowing $D^{(p)}$ at a particle location for $p = 0$ to 4, this expression yields $D^{(p)}$ at any point in the region located just after the particle *as a sum of only 5 terms* (the computation thereof thus only involving operations of complexity $O(1)$). However, Equation 9.33 is only valid if all derivatives of K are continuous over the range $\left[z^{\star(k)} - z - \Delta z; z^{\star(k)} - z\right]$ for all particles k. By contrast, if there exists a particle k such that $z^{\star(k)} - z - \Delta z$ coincides with a discontinuity of the p-th derivative of K, then $D^{(p)}$ incurs a jump at $z+\Delta z$, which can be explicitly calculated. Denoting the discontinuity in $K^{(p)}$ as $\Delta K^{(p)}$ and the jump incurred by $D^{(p)}$ as $\Delta D^{(p)}$, one simply obtains

$$\Delta D^{(p)} = \Delta m\; Q^{\star(k)} \Delta K^{(p)}\,. \tag{9.34}$$

Then the procedure for computing $\overline{\rho Q}\left(z^{\star(n)}\right)$ for all particles n is the following

1) the particles are ordered by increasing vertical positions, so that $z^{\star(1)} \leqslant z^{\star(2)} \leqslant ... \leqslant z^{\star(N-1)} \leqslant z^{\star(N)}$;

2) the position of every discontinuity of $D^{(p)}$ is computed. For instance, the kernel function K given by Equation 9.30 has three discontinuities: the third and fourth derivatives have discontinuities at $r = \pm h$, with the jumps being given by $\Delta K^{(3)}(h) = \Delta K^{(3)}(-h) = 24\; c/h^3$ and $\Delta K^{(4)}(h) = \Delta K^{(4)}(-h) = 72\; c/h^4$; and the third derivative is also discontinuous at $r = 0$, with a jump $\Delta K^{(3)}(0) = 96\; c/h^3$. Therefore, each location in the box coinciding with $z^{\star(n)} - h$ or $z^{\star(n)} + h$ for any particle n corresponds to a discontinuity for $D^{(3)}$ and $D^{(4)}$, and each particle location also corresponds to a discontinuity for $D^{(3)}$. These discontinuities are also ordered by increasing vertical position;

3) the value of $D^{(p)}$ is explicitly computed for the first particle, and for $p = 0$ to 4, using Equation 9.31. This constitutes an opertion of complexity $O(hN/L)$;

4) the values of $D^{(p)}$ are computed up to the first discontinuity through Equation 9.33;

5) the jumps incurred by $D^{(3)}$ and/or $D^{(4)}$ at the discontinuity are computed through Equation 9.34;

6) steps 4) and 5) are repeated until the position of the second particle is reached. The value of $D^{(0)}$, corresponding to the value of $\overline{\rho Q}$ at the position of the second fluid particle, is saved, along with $D^{(1)}$ if the gradient of the mean field is also needed;

7) steps 4) through 6) are repeated until the last particle has been reached. Each such loop has $O(1)$ complexity, and there are N of them, so that the entire set of loops has $O(N)$ complexity.

Eventually, it can be seen that the entire algorithm indeed has $O(N)$ complexity. In the end of the procedure, one has obtained $\overline{\rho Q}\left(z^{\star(n)}\right)$ for every particle n, as required. Concretely, this procedure must be implemented twice: first, it is used with $Q = 1$, $Q = u_v$ and $Q = u_h^2$ to yield $\overline{\rho}$, $\widetilde{u_v}$ and $\widetilde{u_h''^2}$ at every particle location respectively; then a second round, with $Q = u_v - \widetilde{u_v}$, yields $\widetilde{u_v''^2}$ at every particle location.

Restoring SPH consistency

I briefly mentioned the concept of consistency for the finite-difference scheme in time in Section 9.1.1, whereby the time-discretised solution should converge, when $\Delta t \to 0$, towards an actual solution of the stochastic differential equations. Since the Lagrangian stochastic model is coupled with the kernel estimates obtained through the SPH formalism, it is also necessary for the SPH formalism to be consistent. More specifically, it is said to have *k-th order consistency* if it can reproduce exactly a polynomial function of z up to k-th degree (Liu and Liu 2010, Section 4). The concept of consistency is further divided into two different criteria, namely the *kernel consistency* and the *particle consistency*. The SPH approximation is kernel-consistent of order k if the kernel approximation of any polynomial of degree k is equal to the actual polynomial. For first-order consistency, for instance, one should have

$$\int \mathrm{d}^3\mathbf{x}' \; (c_0 + c_1\mathbf{x}') \; K(\mathbf{x}' - \mathbf{x}) = c_0 + c_1 \, \mathbf{x} \, . \tag{9.35}$$

Setting $c_1 = 0$, one immediately finds the first condition for first-order kernel consistency

$$\int \mathrm{d}^3\mathbf{x}' \; K(\mathbf{x}' - \mathbf{x}) = 1 \, . \tag{9.36}$$

Multiplying Equation 9.36 by $\mathbf{x}$, one finds $\mathbf{x} = \int \mathrm{d}^3\mathbf{x}' \; \mathbf{x} \; K(\mathbf{x}' - \mathbf{x})$, and plugging this in Equation 9.35, one finds the second condition for first-order kernel consistency

$$\int \mathrm{d}^3\mathbf{x}' \; (\mathbf{x}' - \mathbf{x}) \; K(\mathbf{x}' - \mathbf{x}) = \mathbf{0} \, . \tag{9.37}$$

The particle consistency, by contrast, is achieved if the *discrete* kernel estimation exactly reproduces polynomial functions. For first order, this amounts to the following conditions (see Liu and Liu 2010, Eq. 58 and 59)

$$\sum_{k=1}^{N} \frac{\Delta m}{\rho^{\star(k)}} K\left(\mathbf{x}^{\star(k)} - \mathbf{x}\right) = 1 \quad \forall \mathbf{x} \, , \tag{9.38}$$

$$\sum_{k=1}^{N} \frac{\Delta m}{\rho^{\star(k)}} (\mathbf{x}^{\star(k)} - \mathbf{x}) K\left(\mathbf{x}^{\star(k)} - \mathbf{x}\right) = 0 \quad \forall \mathbf{x} \, , \tag{9.39}$$

where $\rho^{\star(k)}$ is the density associated to the k-th particle, i.e. the ration between the mass carried by the particle and the lumped volume that it occupies, and which can be estimated on the fly in the simulation. While the kernel consistency stems from the properties of the kernel function K only, the particle consistency also depends on the specific particle distribution in the system.

There are therefore two sources of inconsistency, illustrated in the 1D case in Figure 9.2: *it is either due to the truncation of the kernel support domain by the boundary of the domain, or to an irregular particle distribution inside the support domain*. In the first case, limited to the boundaries of the domain, both kernel and particle consistency are lost, while in the second case, which can happen at the boundaries or in the bulk of the simulation alike, only the particle consistency is lost. In both cases, it is necessary to restore the consistency of the SPH

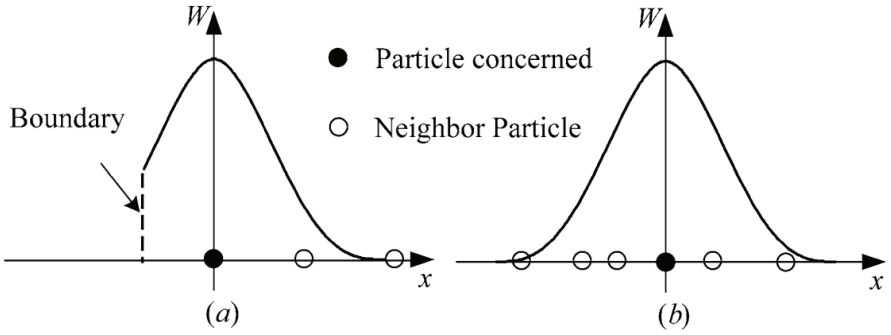

Figure 9.2: Illustration of the two sources of inconsistency in the SPH formalism, namely **(left)** the boundary inconsistency, stemming from the truncation of the kernel function (kernel inconsistency) and the lack of particles outside the domain (particle inconsistency); and **(right)** the irregularity of the particle distribution, which may unduly bias the particle representation of a constant or linear function for instance. *Credits*: Liu and Liu (2010).

formalism. To do this, I make use of the Corrective Smoothed Particle Method (CSPM) suggested by Chen and Beraun (2000), whereby the kernel estimate f_n of a function f at the position of the n-th particle is now given, in the 1D case, by

$$f_n = \frac{\int \mathrm{d}z\, f(z)\, K\left(z - z^{\star(n)}\right)}{\int \mathrm{d}z\, K\left(z - z^{\star(n)}\right)} \,. \tag{9.40}$$

The inclusion of the denominator amounts to renormalising the kernel estimate by the portion of the kernel compact support that lies within the domain of the simulation, in case part of it lies outside. This has no bearing on the kernel estimate in the bulk, because there we have $\int \mathrm{d}z\, K\left(z - z^{\star(n)}\right) = 1$. The corresponding particle approximation is obtained through Liu and Liu (2010, Eq. 68)

$$\overline{\rho Q}\left(z^{\star(n)}\right) = \frac{\sum_{k=1}^{N} Q^{\star(k)} K\left(z^{\star(k)} - z^{\star(n)}\right)}{\sum_{k=1}^{N} \frac{1}{\rho^{\star(k)}} K\left(z^{\star(k)} - z^{\star(n)}\right)} \,. \tag{9.41}$$

Equation 9.41 is only required close to the boundaries – more specifically for particles that are within a distance h of one of the boundaries. There, the $O(N)$ algorithm described above cannot be used, and the kernel estimates must be computed directly; this only involves a limited number of particles however, so that the computational cost of the operation does not suffer too much.

9.2 Extraction of the oscillations from the simulation

Using the procedure detailed in Section 9.1, the trajectories of the fluid particles representing the flow can be integrated forward in time. These trajectories include the turbulent motion of the particle, but also an oscillatory contribution entailed by the normal modes of the simulation box. Ultimately, these modes are what I am interested in. In this section, I describe how the oscillation power spectra are extracted from the simulation, and how the properties of the modes are inferred from the 'observed' power spectra. To illustrate this, and throughout the rest of this chapter, I will consider the following setup

- a number $N = 20,000$ of fluid particles were used to represent the flow. Their trajectories were integrated during $N_t = 500,000$ time steps, and the interval between two time steps was chosen to be $\Delta t = 0.05$ s;
- the Lagrangian stochastic model is comprised of Equations 9.3 to 9.5, where the Kolmogorov constant is $C_0 = 2.1$, the fixed turbulent frequency is $\omega_t = 10^{-4}$ rad.s^{-1}, and the drift tensor is given by the Simplified Langevin Model prescription

$$G_{vv} = G_{hh} = -\left(\frac{1}{2} + \frac{3}{4}C_0\right)\omega_t \,; \tag{9.42}$$

- the size of the compact support of the kernel function was chosen such that $h/L = 0.01$, where L is the total length of the simulation domain;
- the simulation domain corresponds to the region of the Sun located between $r/R_\odot = 0.995$ and $r/R_\odot = 1.002$, where $R_\odot$ denotes the photospheric radius of the Sun. As such the domain contains the superadiabatic region, located just beneath the photosphere, but also the lower layers of the atmosphere;
- I assumed that the polytropic exponent in the pressure-density relation (Equation 9.27) corresponds to the first adiabatic gradient Γ_1. The equilibrium density $\rho_0(z)$, $p_0(z)$ and $\Gamma_1(z)$ are extracted from the exact same solar patched model I already considered in Chapters 5 and 6: all details regarding this patched model can be found in Philidet et al. (2020a). All three equilibrium profiles are shown in Figure 9.3. In particular, the $\Gamma_1(z)$ behaviour originates from the fact that the bottom part of the simulation corresponds to the top of the hydrogen ionisation region, thus explaining the drop in the first adiabatic exponent compared to the top of the domain (see bottom panel of Figure 9.3), and the 'bump' in density at the top of the domain (see top panel of Figure 9.3) stems precisely from this Γ_1 behaviour;
- the initial velocities were drawn according to Equation 9.21, with the non-dimensional constant $A = 1.0$;
- I let the simulation relax before starting to save the output used to extract the oscillations. Concretely, this is done by ensuring that the two modelled components of the Reynolds stress tensor (vertical and horizontal) have reached a somewhat stationary state[5].

9.2.1 Extraction of the raw power spectra

The properties of the oscillations are best described by means of the power spectrum of the flow quantities, i.e. the modulus squared of the time Fourier transform of their kernel estimate. One of the strengths of the SPH formalism is that it allows for the estimation of these flow quantities *at whichever location one wishes*. These locations are not restricted to lie on the nodes of a predefined spatial grid, which not only means that there is no spatial resolution constraint on the positions at which the power spectra are 'observed', but also means that those can be 'observed' *in any frame of reference*. I will consider two different frames of reference for the definition of the time series

1) the most natural way consists in measuring time series in an *Eulerian* frame, so that wave variables measured in this frame correspond to Eulerian perturbations (see Section 2.1). To that effect, I preliminarily define a set of fixed *Eulerian* positions z_i, and I save the value of each of the aforementioned mean field at each of the Eulerian locations z_i at the end of each time step. This results in a set of time series $\overline{\rho}(z_i, t)$, $\widetilde{u_v}(z_i, t)$, etc. for each z_i;

2) it is also possible to extract time series in a *pseudo-Lagrangian* frame, i.e. a frame of reference attached to the mean flow (only to the oscillations), by contrast with the purely Lagrangian frame, which is attached to the total fluid motions, including the oscillations *and the turbulence*. In the absence of turbulence, the two frames are of course identical. Wave variables computed in this frame correspond to Lagrangian perturbations (see Section 2.1 for a definition). To compute time series in the pseudo-Lagrangian frame I preliminarily define a set of fixed mass column densities[6] τ_i, regularly distributed between 0 and M, where M is the total mass of fluid present in the simulation domain. Then, at the end of each time step, I use the instantaneous mean density profile $\overline{\rho}(z, t)$ to compute $\tau(z, t)$, which allows me to numerically determine the positions $z_i(t)$ such that $\tau(z_i(t), t) = \tau_i$. Once this is done, I save the value of each mean field at each $z_i(t)$. This results in a set of time series $\overline{\rho}(\tau_i, t)$, $\widetilde{u_v}(\tau_i, t)$, etc. for each τ_i. Placing oneself in a frame of fixed mass column density amounts to following the mean mass flow, i.e. the mass-averaged velocity $\widetilde{u_v}$. In other words, it does indeed corresponds to a pseudo-Lagrangian frame.

[5] By that I mean the time when the oscillation-induced variations of the Reynolds stress tensor occur around a time-independent state.

[6] In the present context, I define τ such that the mass column density is zero at the bottom boundary. Therefore, one has

$$\tau(z, t) \equiv \int_0^z \mathrm{d}z' \, \overline{\rho}(z', t) \, . \tag{9.43}$$

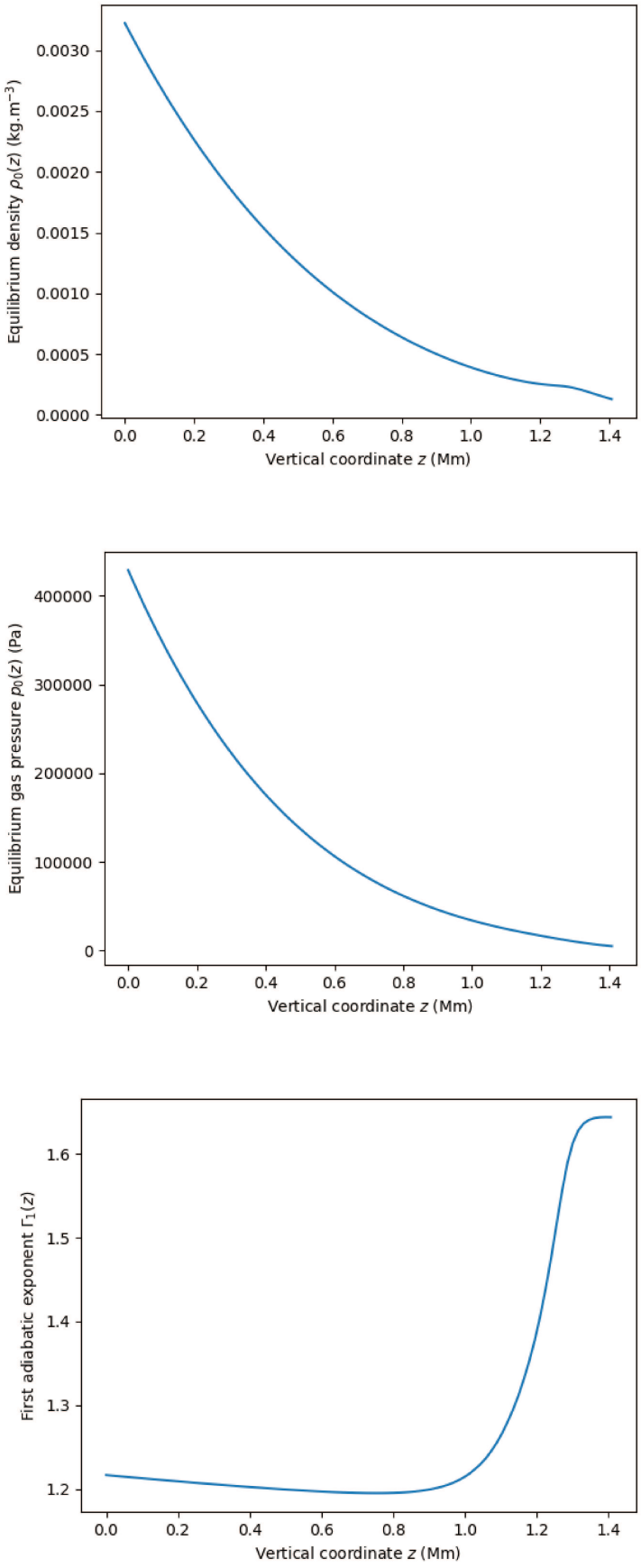

Figure 9.3: Vertical equilibrium profile for density $\rho_0(z)$ **(top)**, gas pressure $p_0(z)$ **(middle)** and first adiabatic exponent $\Gamma_1(z)$ **(bottom)** used as input in the test case simulation presented in this chapter. These profiles are extracted from the patched solar model described in Philidet et al. (2020a), based on a 1D evolutionary model computed with `CESTAM`, on top of which is patched a solar atmosphere computed with the `CO5BOLD` code. Only the region corresponding to the simulation domain is shown.

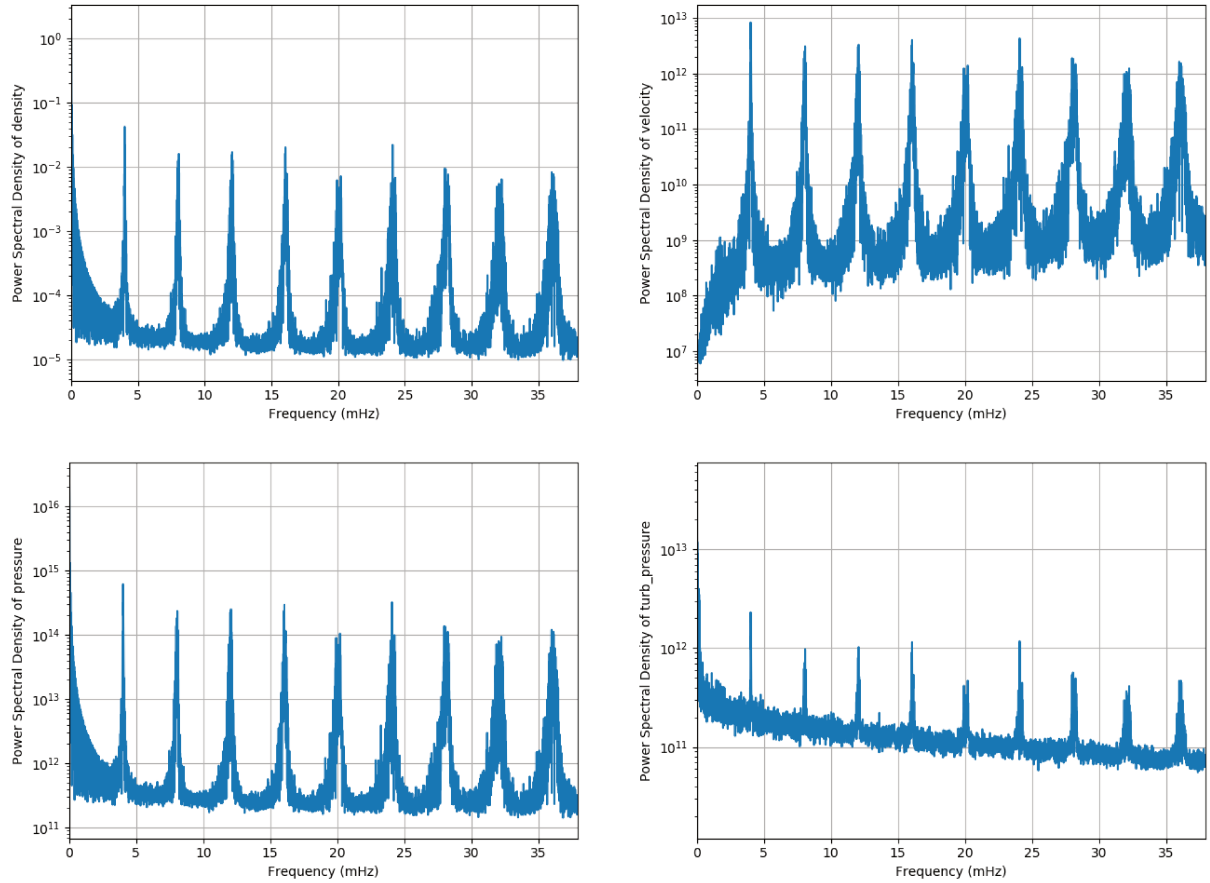

Figure 9.4: Raw power spectrum obtained through the procedure described in the text, in the pseudo-Lagrangian frame, in terms of density ρ **(top-left)**, velocity u_v **(top-right)**, gas pressure p **(bottom-left)** and turbulent pressure p_t **(bottom-right)**. Spectra were averaged over all mass-column-density coordinates τ_i for which spectra were extracted.

Once these time series are obtained, I compute their Fast Fourier Transform in time, which leads to Eulerian power spectra $\left|\widehat{Q}\right|^2(z_i, \nu)$ for each predetermined Eulerian position z_i, and pseudo-Lagrangian power spectra $\left|\widehat{Q}\right|^2(\tau_i, \nu)$ for each predetermined pseudo-Lagrangian coordinate τ_i, and for any quantity Q described in the SPH formalism – i.e. density, gas pressure, velocity, vertical and horizontal components of the Reynolds stress tensor. I will not consider the horizontal component of the Reynolds stress tensor in the following, and will instead focus on the other four quantities. Furthermore, I will consider the *turbulent pressure* $p_t \equiv \widetilde{\overline{\rho} u_v''^2}$ in place of the vertical Reynolds stress tensor itself. Examples of such power spectra are shown in Figure 9.4 for the setup described in the beginning of this section. Resonant modes are clearly visible in each of these spectra, *including in the turbulent pressure spectrum*. One could naively make the remark that the modes in turbulent pressure are narrower than in other variables. In fact, this is not so: the apparent narrowness of the modes actually stems from the fact that the noise level in the turbulent pressure spectrum is much higher than in the other spectra, so that the modes are much more drowned in noise. As such, what we are seeing in the bottom-right panel of Figure 9.4 is only the tip of the resonant peaks. This will also have an impact on the inferred properties of the modes, as I will show in Section 9.2.2.

9.2.2 Mode fitting

Once the various power spectra are extracted from the simulation, for each flow variable, and in the Eulerian and pseudo-Lagrangian frames alike, the properties of the resonant modes can be inferred directly by fitting their line profiles with an appropriate function. In doing so, I assume that the peaks have a Lorentzian shape: then the fitting procedure yields the frequency, linewidth and amplitude of each mode *as a function of 'observation' depth* in the simulation – the latter then giving access to the eigenfunctions of the modes in terms of each wave variable.

The fitting procedure is performed in two steps: first, a Maximum Likelihood Estimator (MLE) is used for a first estimation of mode properties; then, these results are refined by means of a Markov Chain Monte-Carlo (MCMC) method.

Maximum Likelihood Estimator

Let X be a random variable following a PDF $f(x, \boldsymbol{\lambda})$, where x is the sampling variable associated to X, and $\boldsymbol{\lambda}$ is a vector of parameters controlling the form of the PDF. Maximum Likelihood Estimators (MLE) are used when *the form of the PDF f is known, but not the value of the parameters $\boldsymbol{\lambda}$, in which case the aim is to find the best fit values for these parameters*. If N independent random experiments are performed, each yielding a value x_k for X, one can define the *logarithmic likelihood function* (Brandt 1970)

$$l(\boldsymbol{\lambda}) \equiv -\sum_{k=1}^{N} \ln f\left(x_k, \boldsymbol{\lambda}\right) \ . \tag{9.44}$$

Then the fundamental idea behind MLE is that the position of the minimum of l in $\boldsymbol{\lambda}$-space gives an estimate for the most likely value of the parameters; this estimator will be denoted as $\overline{\boldsymbol{\lambda}}$ in the following. In other words, $\overline{\boldsymbol{\lambda}}$ is the solution of

$$\boldsymbol{\nabla}_{\boldsymbol{\lambda}} l = \mathbf{0} \ . \tag{9.45}$$

Furthermore, if $N \rightarrow +\infty$, the central limit theorem states that the estimator $\overline{\boldsymbol{\lambda}}$ of the best-fit parameters value tends to a multivariate Gaussian distribution, uniquely described by its vector mean and covariance matrix. The estimator being unbiased, the mean of the distribution is $\boldsymbol{\lambda}$ itself. As for its covariance matrix, it is given by (Brandt 1970)

$$\sigma_{ij}^2\left(\overline{\boldsymbol{\lambda}}\right) = h_{ij}^{-1} \ , \tag{9.46}$$

where h_{ij}^{-1} is the (i, j)-th component of the inverse Hessian matrix of l, the latter being defined by

$$h_{ij} \equiv E\left[\frac{\partial^2 l}{\partial\lambda_i \partial\lambda_j}\right] \ . \tag{9.47}$$

In particular, the diagonal components σ_{ii}^2 of the covariance matrix provide with the square of the statistical error associated to each parameter λ_i in the Maximum Likelihood estimation procedure. *If f has a known analytical form, so does h_{ij}, and the statistical error in the best-fit value estimation for the PDF parameters can be computed analytically*.

I then follow the work of Toutain and Appourchaux (1994), who argued that the line profile of a solar-like p-mode follows a χ^2 distribution[7] with 2 degrees of freedom and with a Lorentzian-shaped mean, so that the PDF $f(\nu, \boldsymbol{\lambda})$ associated to the random variable $S(\nu)$, where $S(\nu)$ is the value of the observed power spectrum at frequency ν, is given by

$$f(\nu, \boldsymbol{\lambda}) = \frac{1}{S_0(\nu, \boldsymbol{\lambda})} \exp\left(-\frac{S(\nu)}{S_0(\nu, \boldsymbol{\lambda})}\right) \ , \tag{9.48}$$

where $S_0(\nu, \boldsymbol{\lambda})$ is the expected value of the power spectrum at frequency ν, as a function of the parameters defining the line profile. Each frequency bin in the power spectrum is then treated as an independent measurement made according to the same PDF, so that, denoting these frequency bins as ν_k (with $k = 1$ to N), and plugging Equation 9.48 into Equation 9.44, the logarithmic likelihood function becomes

$$l(\boldsymbol{\lambda}) = \sum_{k=1}^{N} \left(\ln S_0(\nu_k, \boldsymbol{\lambda}) + \frac{S(\nu_k)}{S_0(\nu_k, \boldsymbol{\lambda})}\right) \ . \tag{9.49}$$

In the present case, the power spectrum is comprised of a set of Lorentzian-shaped resonant peaks, so that

$$S_0(\nu, \boldsymbol{\lambda}) = \sum_{i=1}^{N_m} \frac{A_i(\Gamma_i/2)^2}{(\nu - \nu_{0,i})^2 + (\Gamma_i/2)^2} + B \ , \tag{9.50}$$

[7] By definition, the χ^2 distribution with k degrees of freedom is the law followed by the sum of the squares of k independent, centered and reduced normal random variables.

where A_i, Γ_i and $\nu_{0,i}$ are the amplitude, linewidth at half maximum and central frequency of the i-th mode, N_m is the number of modes in the spectrum, and B is a background component, which I consider to be flat across the frequency range under consideration. The vector of parameters $\boldsymbol{\lambda}$ is comprised of A_i, Γ_i and $\nu_{0,i}$ for $i = 1$ to N_m, and the background noise B.

As for the Hessian matrix of l, plugging Equation 9.49 into Equation 9.47, one finds

$$h_{ij} = E\left[\sum_{k=1}^{N} \frac{S_0(\nu_k, \boldsymbol{\lambda}) - S(\nu_k)}{S_0^2(\nu_k)} \frac{\partial^2 S_0}{\partial\lambda_i \partial\lambda_j} + \frac{2S(\nu_k) - S_0(\nu_k)}{S_0^3(\nu_k)} \frac{\partial S_0}{\partial\lambda_i} \frac{\partial S_0}{\partial\lambda_j}\right] . \tag{9.51}$$

Toutain and Appourchaux (1994) then argue that while the expected spectrum S_0 and the observed spectrum S differ greatly for any given frequency bin, the expectation of their integral weighted by any arbitrary smooth function of frequency $\phi(\nu)$ is very similar, so that one has, to a very good approximation

$$\sum_{k=1}^{N} S_0\left(\nu_k, \overline{\boldsymbol{\lambda}}\right)\ \phi(\nu_k) \sim \sum_{k=1}^{N} S\ (\nu_k)\ \phi(\nu_k)\ , \tag{9.52}$$

in which case the Hessian matrix reduces to

$$h_{ij} \sim E\left[\sum_{k=1}^{N} \left.\frac{\partial \ln S_0}{\partial\lambda_i}\right|_{\nu_k,\overline{\boldsymbol{\lambda}}} \left.\frac{\partial \ln S_0}{\partial\lambda_j}\right|_{\nu_k,\overline{\boldsymbol{\lambda}}}\right] , \tag{9.53}$$

which can further be considered as an approximation to the corresponding integral (Toutain and Appourchaux 1994)

$$h_{ij} \sim T_{\mathrm{simu}} \int_{\nu_{\min}}^{\nu_{\max}} \mathrm{d}\nu\ \left.\frac{\partial \ln S_0}{\partial\lambda_i}\right|_{\nu,\overline{\boldsymbol{\lambda}}} \left.\frac{\partial \ln S_0}{\partial\lambda_j}\right|_{\nu,\overline{\boldsymbol{\lambda}}} , \tag{9.54}$$

where $\nu_{\min}$ and $\nu_{\max}$ are the lower and upper limits of the frequency range over which the fitting procedure is performed, and T_{simu} is the total duration of the simulation. Plugging Equation 9.50 into Equation 9.54 yields an explicit integral expression for each component of the Hessian matrix – the bounds of which can be considered to be $\pm\infty$, seeing as the contribution of frequencies far away from the resonant peaks are negligible anyway. The analytical Hessian matrix can also be inverted analytically (see for instance Toutain and Appourchaux 1994, Eqs. 19 to 21, for a single resonant mode). However, for the sake of simplicity, and because it yields equally accurate results, I chose to numerically compute the integral defining the Hessian matrix, as well as numerically invert it. The diagonal elements of the Hessian matrix, as I indicated above, correspond to the variance associated to the estimate of each parameter in the fit.

Concretely, for each raw power spectrum $S(\nu)$ extracted from the simulation, I first isolate the part that contains the most visible modes – typically the first ten overtones. I then numerically find the minimum value of the logarithmic likelihood function $l(\boldsymbol{\lambda})$ given by Equation 9.49, with S_0 given by Equation 9.50, by means of a Limited-Memory BFGS algorithm. Essentially, this algorithm starts from a predetermined position in parameter space (provided by hand on the basis of visual estimates), and iteratively walks through parameter space, using the gradient $\boldsymbol{\nabla}_{\boldsymbol{\lambda}} l$ of the function to be minimised in order to determine the direction and amplitude of the steps at each iteration of the process (the algorithm will always go in the direction of the steepest descent of l). The BFGS algorithm does not rely on the Hessian matrix for the iteration; I only need to compute it in the end, once the best-fit parameter values are found. Eventually, this procedure yields best-fit values for the amplitude, linewidth and frequency of each mode *simultaneously*, as well as for the background noise level, and it also yields statistical errors for all these estimates. I provide with an illustration of the fitting procedure in Figure 9.5, where the left panel is a full picture of the power spectrum, showing the entire frequency range over which the fitting procedure was performed, while the right panel is a zoom-in on one of the resonant peaks in the spectrum (more specifically the fifth one from the left). The blue line represents the raw power spectrum; notice the similarity between its jagged, erratic aspect and the typical mode line profiles observed in actual asteroseismic measurements (Figure 2.4). The orange line is the initial guess, obtained by visually inferring approximated values for the properties of the modes, and the green line represents the MLE fit to the spectrum.

Markov Chain Monte-Carlo method

The estimation of mode properties provided by the MLE are then refined by applying a Markov Chain Monte-Carlo (MCMC) method to the problem. I made use of a numerical implementation provided by Réza Samadi; I

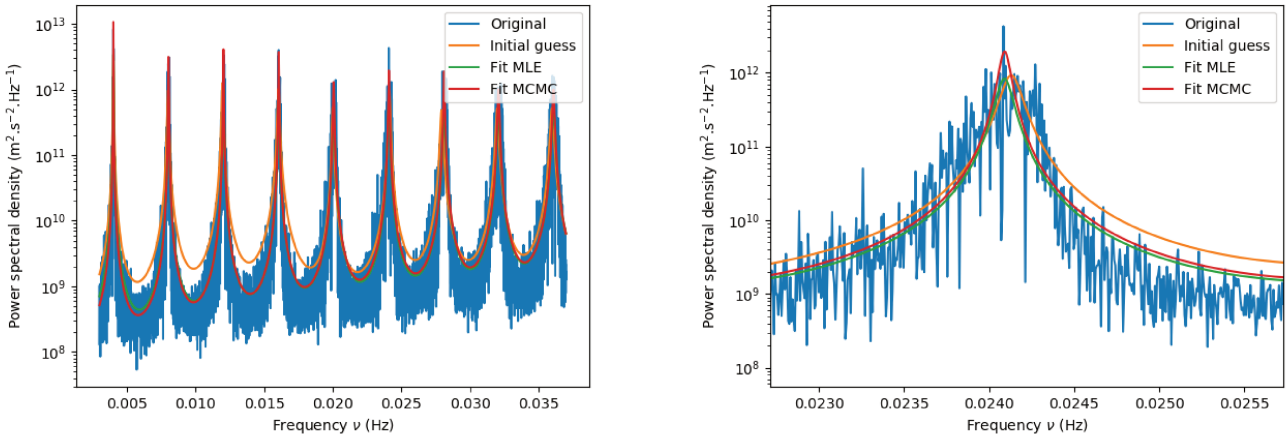

Figure 9.5: Result of the fitting procedure described in the text for the gas pressure power spectrum extracted from the simulation, in the pseudo-Lagrangian frame. A mass-column-density coordinate τ was chosen in such a way that none of the first nine overtones have a node at this location (lest it would have been invisible in the spectrum). The blue jagged line corresponds to the raw spectrum, the orange line to the initial guess (visually inferred from the raw spectrum), the green line corresponds to the fitted spectrum after the first MLE step, and the red line corresponds to the final fitted spectrum, after the Parallel-Tempered MCMC procedure, all of which are described in the text. **Left**: full frequency range over which the fitting procedure was performed. **Right**: zoom-in of the left panel on the $n = 5$ mode. The vertical axis is in logarithmic scale in both panels.

simply applied it to the logarithmic likelihood function given in the previous section. I cannot give a full account of the way it functions, and content myself with describing, in very broad strokes, the idea behind the algorithm. Essentially, the idea is to make the walk through parameter space a *random walk*, by contrast with the procedure described above, where the walk is deterministic. A set of independent 'walkers' are created, which all start from the parameter estimate yielded by the BFGS algorithm described above, but whose trajectories are all independent from each other. Each step of a walker's trajectory is randomly selected from a distribution that only depends on the present state of the walker, so that the resulting stochastic process has the Markov property – hence the name of the method. The set of independent walkers allows to iteratively construct a posterior distribution for the parameters of the fit from the prior Gaussian distribution provided by the MLE, through Bayesian inference.

What is more, the covariance matrix of the prior distribution at each time step is multiplied by a certain factor, referred to as the *temperature* of the Markov chain. Intuitively, a higher temperature will yield wider distributions, which means the walkers will be able to make wider strides in parameter space: this can help them escape an undesired local minimum for instance. On the other hand, a smaller temperature forces the walkers to make tinier steps in parameter space: this can help sampling parameter space more efficiently close to a given region, which may be useful if one knows the solution most probably lies in that region. In the scope of the Parallel-Tempered MCMC (PT-MCMC) method, a set of independent MCMC are run in parallel, each with a different temperature, and the optimal temperature is determined after the fact by comparing the resulting posterior distribution yielded by each chain. The final fit to the raw spectrum obtained through this PT-MCMC procedure is illustrated in Figure 9.5 (solid red line). In this particular instance, the optimal temperature was found to be $T_{\text{opt}} = 0.43$, which is not too far from unity, meaning the walkers had no particular trouble finding the solution in the first place. Notice that the Bayesian PT-MCMC fit is very similar to the MLE fit (green line). Also notice that the line profile shown in the right panel is slightly asymmetric, as illustrated by the apparent overestimation of the right wing of the mode by the fit, compared to the left wing. I discussed in great detail the asymmetry of the solar-like oscillation line profiles in Part II, and it is not altogether surprising to see it in the simulation as well; however, to keep the discussion simple, I will leave this question aside for now.

Extraction of the eigenfunctions

Eventually, the procedure yields a posterior joint-PDF for all parameters in the fit. In particular, the vector mean of the joint distribution provides with the final estimates of the parameters, and the diagonal elements of

the covariance matrix – without the temperature correction, which only serves to enhance or inhibit the diffusion of the walkers in parameter space – provide with a rigorous estimation of the statistical error inherent to the fitting procedure. As I indicated above, the interesting properties are the frequency of the modes $\nu_{0,i} \pm \Delta\nu_{0,i}$, their linewidth at half maximum $\Gamma_i \pm \Delta\Gamma_i$, and their amplitude $A_i \pm \Delta A_i$. The background noise level must be included as a free parameter in the fitting procedure, but its value is not of much interest in the following. Unlike ν_0 and Γ, the amplitude A of a given mode is a function of the Eulerian or pseudo-Lagrangian coordinate at which the power spectrum is 'observed'. Extracting the power spectra for several such coordinates provides with a function of space $A(z)$ or $A(\tau)$ representing the spatial profile of the real amplitude of the mode. However, the phase of the mode must also be accounted for in order to extract the real and imaginary parts of the *eigenfunction* of the mode. The phase of the complex spectrum is extracted in exactly the same way as its modulus squared, for each coordinate z or τ for which a time series was extracted from the simulation, and for every frequency bin. The phase $\Phi(z)$ or $\Phi(\tau)$ of each mode is then evaluated by considering the frequency bin coinciding with its eigenfrequency. Finally, the real and imaginary parts of the eigenfunction are given by $A\cos\Phi$ and $A\sin\Phi$ respectively. In this simplified test case, the density, gas pressure and displacement eigenfunctions are in phase with each other, in accordance with the adiabatic approximation, so that (to within a redefinition of the time origin) only their real part is of interest. As for the turbulent pressure eigenfunction, I redefined the time origin independently, so as to also make it purely real. Note, however, that this does not mean that there is no phase difference *between the turbulent pressure spectrum and the other spectra*. I showcase in Figure 9.6 the numerical eigenfunctions extracted from the simulation described in the beginning of this section for the $n = 5$ mode, where the blue dots represent the velocity eigenfunction, the orange dots represents the gas pressure eigenfunction, and the green dots represent the turbulent pressure eigenfunction, all of which are considered in a pseudo-Lagrangian frame. While the velocity and gas pressure eigenfunctions extracted from the simulation are satisfactorily smooth functions of the mass-column-density coordinate τ, it is not so much the case for the turbulent pressure eigenfunction. The reason is that the modes are much less visible in the turbulent pressure spectrum (bottom-right panel of Figure 9.4) than in the other spectra. This explains, in particular, the apparent discontinuity in the turbulent pressure eigenfunction (green dots in Figure 9.6): because the modes in the turbulent pressure spectrum is partially drowned in the noise level, even at the location of a node of a given mode, a certain amplitude is detected. This non-zero amplitude jumps from positive to negative values – and vice-versa – upon crossing each node, because the phase of the mode itself incurs a $\sim 180°$ jump there. The same numerical eigenfunction discontinuity is exhibited by the gas pressure eigenfunction (orange dots in Figure 9.6), although it is much less visible: this is because the noise level in the gas pressure spectrum is much lower compared to the modes.

9.3 Validation of the numerical implementation

I mentioned, in the beginning of Section 9.1, that the Lagrangian stochastic model used to advanced the fluid particles through time is a very simplified model, not meant to be realistic, but instead to provide with a test case to validate the numerical approach. In order to perform the validation, the numerical results obtained through the procedure detailed in Sections 9.1 and 9.2 must be compared to the exact analytical results to which the test case should reduce. I describe how these exact analytical results are derived in Section 9.3.1, after which I compare them to the output of the simulation in Section 9.3.2.

9.3.1 Exact analytical results

Exact wave equation

The Lagrangian stochastic model comprised of Equations 9.3 to 9.5, is a special case of the more refined version developed in Appendix B. As such, the mean equations stemming from the present model are straightforwardly derived from Equations B.107 to B.110, by setting $G_{vv} = G_{hh} = -(1/2 + 3/4C_0)\omega_t$, $\widetilde{\omega_t} = \omega_t$, $F_e = 0$, and by neglecting the third-order moments in the Reynolds stress equations (on account of the turbulence modelled by

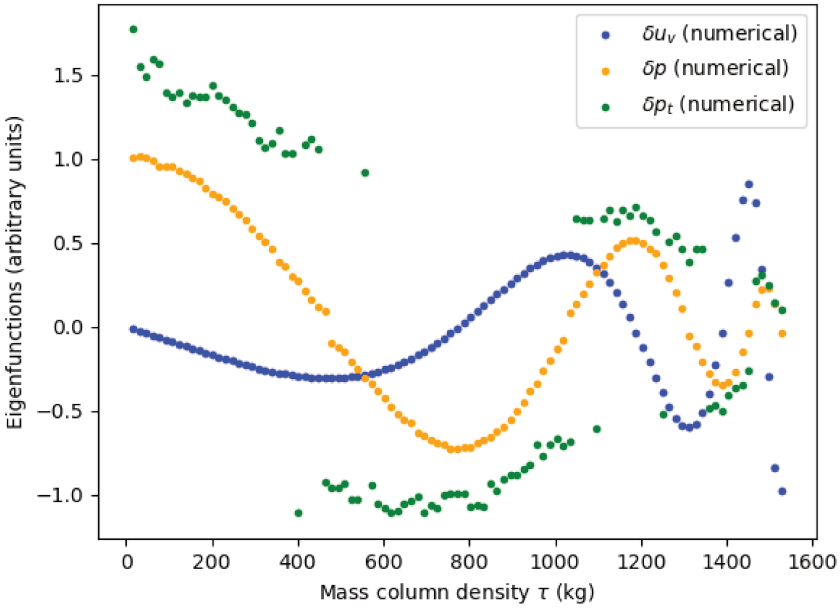

Figure 9.6: Eigenfunction associated to the $n = 5$ mode in the simulation, extracted through the procedure described in the text, in the pseudo-Lagrangian frame, in terms of velocity (blue dots), gas pressure (orange dots) and turbulent pressure (green dots). The velocity and gas pressure eigenfunctions are rather smooth functions of τ, while the turbulent pressure eigenfunction is much more erratic, due to the modes in the turbulent pressure power spectrum being much less visible than in the other spectra.

Equations 9.3 to 9.5 being Gaussian by construction). One obtains

$$\frac{D\overline{\rho}}{Dt} + \overline{\rho}\frac{\partial \widetilde{u_v}}{\partial z} = 0 \,, \tag{9.55}$$

$$\frac{D\widetilde{u_v}}{Dt} + \frac{1}{\overline{\rho}}\frac{\partial \overline{\rho} R_v}{\partial z} = -\frac{1}{\overline{\rho}}\frac{\partial \overline{p}}{\partial z} - g \,, \tag{9.56}$$

$$\frac{DR_v}{Dt} = -2R_v\frac{\partial \widetilde{u_v}}{\partial z} - \left(1 + \frac{3}{2}C_0\right)R_v + C_0\left(\frac{R_v}{2} + R_h\right)\omega_t \,, \tag{9.57}$$

$$\frac{DR_h}{Dt} = -\left(1 + \frac{3}{2}C_0\right)R_h + C_0\left(\frac{R_v}{2} + R_h\right)\omega_t \,, \tag{9.58}$$

where I recall the notations $R_v \equiv \widetilde{u_v''^2}$ and $R_h \equiv \widetilde{u_h''^2}$. In particular, the turbulent pressure is defined as $p_t \equiv \widetilde{\rho u_v''^2} = \overline{\rho} R_v$. Then, the variables $\overline{\rho}$, $\widetilde{u_v}$, R_v and R_h are decomposed into an equilibrium value and a *Lagrangian perturbation*, such that $\overline{\rho} = \rho_0 + \delta\rho$, $\widetilde{u_v} = \delta u_v$, $R_v = R_{v,0} + \delta R_v$ and $R_h = R_{h,0} + \delta R_h$. Remarking that the material derivatives D/Dt of Lagrangian perturbations can be substituted for $j\omega$, where ω is the angular frequency associated to the time dependence of the oscillations, the system of mean equations given above can be linearised thus[8]

$$j\omega\delta\rho + \rho_0\frac{\mathrm{d}\delta u_v}{\mathrm{d}z} = 0 \,, \tag{9.59}$$

$$j\omega\rho_0\delta u_v = -\frac{\mathrm{d}(\delta p_t + \delta p)}{\mathrm{d}z} - g\delta\rho \,, \tag{9.60}$$

$$j\omega\delta R_v = -2R_{v,0}\frac{\mathrm{d}\delta u_v}{\mathrm{d}z} - (1 + C_0)\omega_t\delta R_v + C_0\omega_t\delta R_h \,, \tag{9.61}$$

$$j\omega\delta R_h = \frac{1}{2}C_0\omega_t\delta R_v - \left(1 + \frac{1}{2}C_0\right)\omega_t\delta R_h \,, \tag{9.62}$$

[8]Note that the linearisation in Section 8.1 is performed directly on the equations of the Lagrangian stochastic model, while the present linearisation pertain to mean equations.

where $\delta p_t = R_{v,0}\delta\rho + \rho_0 \delta R_v$. Equations 9.61 and 9.62 can be combined to yield δR_v, and therefore the turbulent pressure perturbation δp_t, in terms of δu_v only. After some elementary algebra, and using Equation 9.59 to rewrite $\mathrm{d}\delta u_v/\,\mathrm{d}z$ in terms of $\delta\rho/\rho_0$, one finds

$$\frac{\delta p_t}{p_{t,0}} = \underbrace{\frac{-3\zeta^2 + j\zeta\left(4+\frac{5}{2}C_0\right)+\left(1+\frac{3}{2}C_0\right)}{-\zeta^2 + j\zeta\left(2+\frac{3}{2}C_0\right)+\left(1+\frac{3}{2}C_0\right)}}_{\equiv\Gamma_t}\frac{\delta\rho}{\rho_0}\,, \tag{9.63}$$

where $\zeta \equiv \omega/\omega_t$ represents the ratio between the turbulent timescale and the period of the oscillation (in that order). Alternatively, one can deduce an expression for the total pressure perturbation as a function of density perturbation

$$\frac{\delta p_{\mathrm{tot}}}{p_{\mathrm{tot},0}} = \frac{\Gamma_1 p_0 + \Gamma_t p_{t,0}}{p_0 + p_{t,0}}\frac{\delta\rho}{\rho_0}\,, \tag{9.64}$$

where I used the fact that $\delta p/p_0 = \Gamma_1 \delta\rho/\rho_0$.

The quantity Γ_t plays for turbulent pressure the role that Γ_1 plays for gas pressure. It reduces to $\Gamma_t = 3$ for $\zeta \gg 1$ (i.e. if the period of the oscillation is much shorter than the turbulent timescale), and to $\Gamma_t = 1$ for $\zeta \ll 1$ (i.e. if the period is much longer). Of particular interest is the fact that the Gas-Γ_1 and Reduced-Γ_1 Models (GGM and RGM respectively) are also recoverable by Equation 9.63. I recall (see Section 2.4.2 for more details) that the RGM amounts to neglecting the turbulent pressure perturbation, which corresponds to the $\Gamma_t = 0$ case. On the other hand, the GGM amounts to equating the relative turbulent and gas pressure perturbations, which corresponds to the $\Gamma_t = \Gamma_1$ case. Notice that neither the GGM nor the RGM seem to correspond to a natural limiting case of Equation 9.63.

Plugging Equation 9.63 into Equations 9.59 and 9.60 yields the following second-order system of differential equations

$$j\omega\delta\rho + \rho_0\frac{\mathrm{d}\delta u_v}{\mathrm{d}z} = 0\,, \tag{9.65}$$

$$j\omega\rho_0\delta u_v = -\frac{\mathrm{d}}{\mathrm{d}z}\left(\frac{p_{t,0}\Gamma_t}{\Gamma_1}\frac{\delta\rho}{\rho_0} + \delta p\right) - g\delta\rho\,, \tag{9.66}$$

from which the density perturbations can be eliminated through the relation

$$\frac{\delta\rho}{\rho_0} = \frac{1}{\Gamma_1}\frac{\delta p}{p_0}\,. \tag{9.67}$$

The system can be rendered non-dimensional by setting

$$y_1 \equiv \frac{\xi}{z} = \frac{\delta u_v}{j\omega z}\,, \qquad y_2 \equiv \frac{\delta p}{p_0}\,, \qquad Z \equiv \ln z\,, \tag{9.68}$$

where ξ is the vertical flow displacement. Then one obtains the linear second-order system

$$\frac{\mathrm{d}y_1}{\mathrm{d}Z} = A_1(Z)\,y_1(Z) + B_1(Z)\,y_2(Z)\,, \tag{9.69}$$

$$\frac{\mathrm{d}y_2}{\mathrm{d}Z} = A_2(Z)\,y_1(Z) + B_2(Z)\,y_2(Z)\,, \tag{9.70}$$

where the coefficients are given by

$$A_1(Z) \equiv -1\,, \qquad B_1(Z) \equiv -\frac{1}{\Gamma_1}\,, \qquad A_2(Z) \equiv \frac{z\rho_0\omega^2}{\widehat{p}}\,, \qquad B_2(Z) \equiv -\frac{\mathrm{d}\ln\widehat{p}}{\mathrm{d}z} + \frac{g\rho_0}{\Gamma_1\widehat{p}}\,, \tag{9.71}$$

and I have introduced

$$\widehat{p} \equiv p_0 + \frac{\Gamma_t}{\Gamma_1}p_{t,0}\,. \tag{9.72}$$

In particular, the quantity $\widehat{p}$ reduces to the gas pressure p_0 in the RGM (since $\Gamma_t = 0$), and to the total pressure $p_0 + p_{t,0}$ in the GGM (since $\Gamma_t = \Gamma_1$).

Shooting algorithm

The system comprised of Equations 9.69 and 9.70, combined with the boundary conditions $y_1(Z_{\rm min}) = y_1(Z_{\rm max}) = 0$, forms a linear eigenvalue problem, because the coefficient $B_2(Z)$ contains the eigenvalue ω^2, which is not known *a priori*. Apart from ω^2, the coefficients $A_1(Z)$, $A_2(Z)$, $B_1(Z)$ and $B_2(Z)$ are completely determined from the equilibrium profile in the simulation, which can be obtained by time-averaging the mean flow quantities. The angular eigenfrequencies ω of the linear problem, as well as the corresponding eigenfunctions $y_1(Z)$ and $y_2(Z)$, can be numerically determined by a *shooting algorithm*. The idea is the following

1) a first guess is chosen for ω, and two values ω_1 and ω_2 are arbitrarily chosen close to this initial value;

2) for each of these angular frequencies, the linear system is numerically integrated from $Z_{\rm min}$ to $Z_{\rm max}$, with initial conditions $y_1(Z_{\rm min}) = 0$ and $y_2(Z_{\rm min}) = 1$ (this last value is arbitrary, I chose unity for convenience). A fourth-order Runge-Kutta scheme is used for the integration;

3) each of the angular frequencies ω_1 and ω_2 yields a value $y_1^{(1)}(Z_{\rm max})$ and $y_1^{(2)}(Z_{\rm max})$ for the function y_1. The goal, naturally, is to find the value of ω that will yield the correct top boundary condition $y_1(Z_{\rm max}) = 0$. Therefore, a new estimate for the target value ω is obtained by replacing

$$\omega_1 \mapsto \omega_1 - \frac{\omega_2 - \omega_1}{y_1^{(2)}(Z_{\rm max}) - y_1^{(1)}(Z_{\rm max})} y_1^{(1)}(Z_{\rm max}) \ . \tag{9.73}$$

   A new arbitrary value for ω_2 is also chosen close to ω_1;

4) the steps 1) to 3) are repeated until the difference between two consecutive values of ω_1 becomes smaller than a preliminarily determined epsilonesque value. When this is the case, I consider that the algorithm has converged: the last value of ω_1 constitutes an estimate for the angular eigenfrequency of the target mode. I integrate the linear system one last time with this final value of ω, so that the solutions $y_1(Z)$ and $y_2(Z)$ constitute the eigenfunctions associated to ω.

The shooting algorithm is used for each mode analysed in the numerical implementation, where I adopt the central frequency $\nu_{0,i}$ from the fitting procedure (multiplied by 2π) as the initial guess for ω_1.

9.3.2 Comparison with numerical results

I start by comparing the frequencies obtained through the shooting procedure, i.e. the exact analytical result, with the frequencies obtained through the fitting procedure described in Section 9.2, i.e. the numerical frequencies. More specifically, I implement the shooting procedure for three different values of Γ_t (see Section 9.3.1 for a definition), namely 1) the exact value given by Equation 9.63, 2) the value $\Gamma_t = 0$ corresponding to the RGM, and 3) the value $\Gamma_t = \Gamma_1$ corresponding to the GGM. This allows me to assess the validity of the GGM and RGM compared to the exact expression in this test case. I compile the results in Figure 9.7, where the exact expression is shown in blue, the GGM in orange and the RGM in green. The right panel, in particular, clearly shows that an agreement is found to a satisfactory extent: the relative error does not exceed $\sim 0.15\%$ for the first nine overtones, and the discrepancy is of the order of the statistical error stemming from the fitting procedure described in Section 9.2 (shown as error bars in both panels of Figure 9.7). On the other hand, the GGM clearly yields biased frequencies, with the *relative* bias being fairly independent of radial order: the analytical frequencies computed in the scope of the GGM systematically underestimate the numerical frequencies by $\sim 2\%$. In the RGM, the discrepancy is even larger, reaching $\sim 4\%$.

In Figure 9.8, I compare the gas pressure and velocity eigenfunctions extracted from the simulation to their exact counterparts, computed with the shooting algorithm described in Section 9.3.1. It can be seen that the agreement is excellent for both variables. However, the agreement becomes slightly less satisfactory for the higher overtones of the simulation box (see in particular the $n = 9$ mode, in the bottom-right panel of Figure 9.8). This is most likely due to the fact that the higher frequency modes also have smaller wavelengths. If the wavelength of a mode *locally* becomes similar to, or smaller than the kernel size h used for the SPH formalism (see Section 9.1.2), then it is to be expected that the structure of the mode in this region will not be accurately recovered. In this setup, I chose $h/L = 0.01$, which indeed starts being non-negligible compare to the $n \sim 10$ mode wavelength close to the top boundary (the modes oscillate faster close to the surface). This is an important point, as this

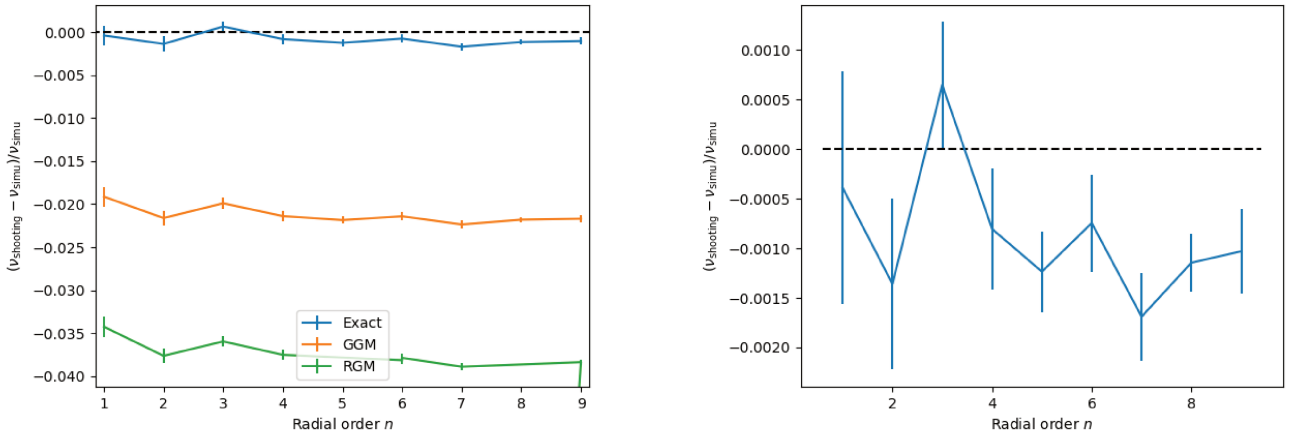

Figure 9.7: **Left**: relative difference between the mode eigenfrequencies extracted from the simulation through the procedure described in Section 9.2, and the analytical frequencies computed with the shooting algorithm described in Section 9.3.1, as a function of radial order n. The color scheme refers to the three prescriptions of the turbulent pressure perturbation, as explained in the text: the blue line corresponds to the exact expression, which happens to be derivable in this test case (see Equation 9.63); the orange line corresponds to the GGM, and the green line to the RGM (see text for more details). Error bars stemming from the fitting procedure for ν_{simu} are shown, but are too small to be clearly visible, compared to the discrepancy between GGM/RGM values of ν_{shooting} and ν_{simu}. The frequency of the last overtone in the RGM was so off that the shooting procedure landed on the previous radial order instead of the target: the corresponding point is much lower in the figure, and not shown. **Right**: same as left panel, but only the results yielded by the exact expression for δp_t (blue line in left-hand side panel) are shown. Error bars are now more clearly visible.

shows a fundamental limitation of the numerical method presented in this chapter, especially considering that the surface effects due to turbulence-oscillation coupling are precisely predominant for high frequency modes (see Section 2.4). However, this shortcoming can potentially be circumvented by assuming a variable kernel size, with h being smaller in regions where the modes have smaller wavelengths.

9.4 Concluding remarks

Let me summarise the main steps of the numerical implementation described in this chapter. In particle methods, the kind of which form the basis of this implementation, the flow is represented by a large set of individual fluid particles, each carrying a certain portion of the total mass of fluid. The core of the algorithm is two-fold, and is comprised of 1) the Lagrangian stochastic model consisting of the Ito stochastic differential equations given by Equations 9.3 to 9.5, which, when integrated forward in time, allow to advance the trajectory of each fluid particles, and 2) the SPH formalism consisting of the kernel estimates given by Equations 9.22 to 9.25 and 9.27, which, when computed at a given time step and at any given location in the box, yield all local mean flow quantities. The latter is used for two purposes: they are estimated at the location of the particles, to be included in the coefficients of the SDE used to advance the particles in time; and they are estimated at predetermined coordinates in the box – Eulerian or pseudo-Lagrangian, i.e. following the mean mass flow –, thus forming the final output of the simulation. The output then consists in time series for all mean flow quantities, either in a Eulerian frame or pseudo-Lagrangian frame, from which power spectra in terms of velocity, density, gas pressure or turbulent pressure can be extracted. These power spectra naturally contain resonant peaks, corresponding to the signal entailed by the various modes of oscillation in the box, and whose properties – frequency, linewidth at half maximum, amplitude – can be inferred by an appropriate fitting procedure.

In this chapter, I presented a test case for the implementation, based on the simplified Lagrangian stochastic model of turbulence that I had already considered in Chapter 8 (thus amounting to considering a compressible version of the Simplified Langevin Model), with the isotropic prescription of the drift tensor G_{ij}. This test case presents the considerable advantage of allowing for exact, analytical results to be derived: comparing these exact

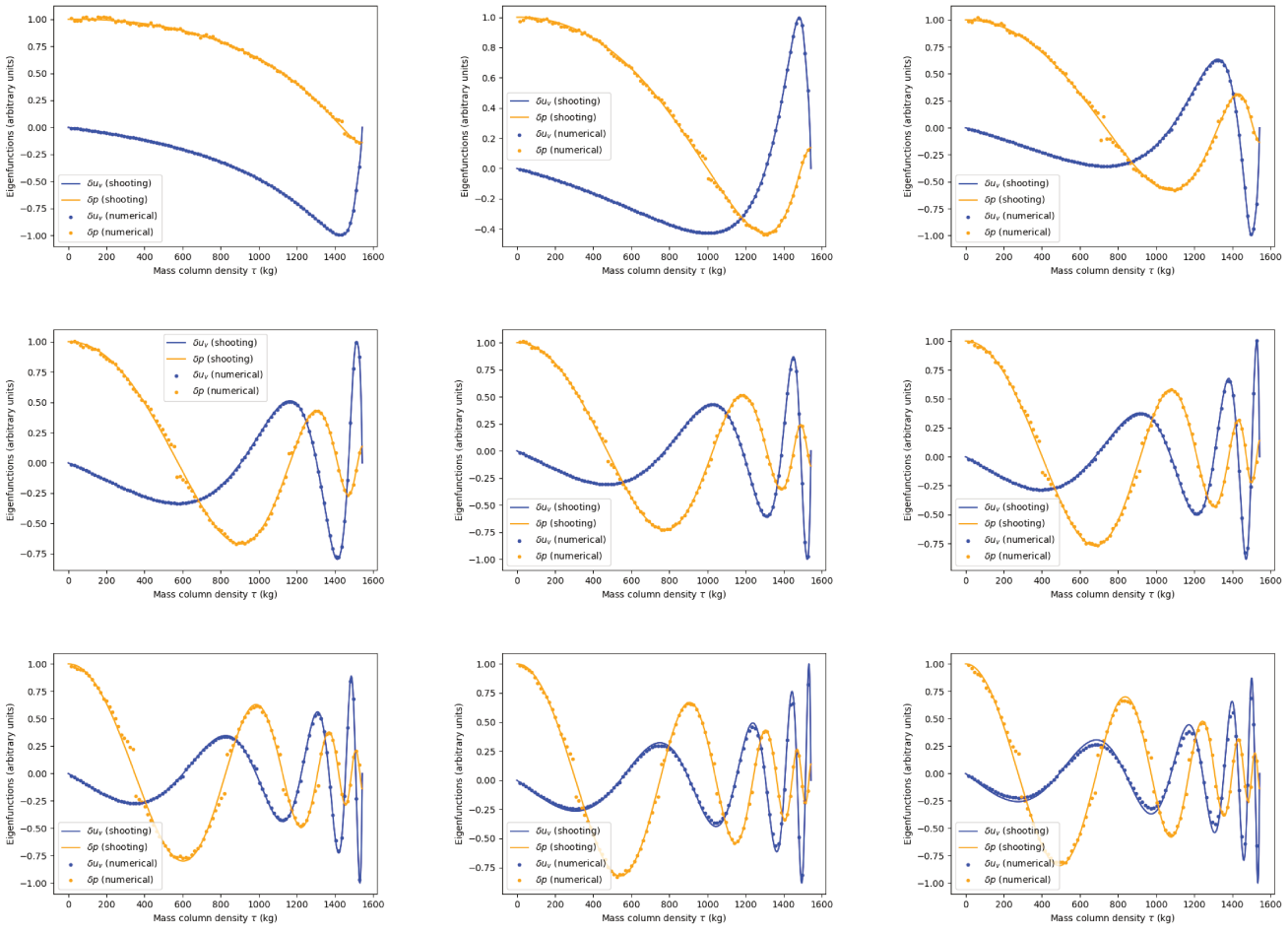

Figure 9.8: Comparison between the eigenfunctions extracted from the simulation through the procedure described in Section 9.2 (dots) and the analytical eigenfunctions obtained through the shooting procedure described in Section 9.3.1 (solid lines). Blue elements pertain to the velocity eigenfunction, and orange ones to the the gas pressure eigenfunction. The eigenfunctions associated to the first nine overtones are shown in separate panels (by increasing radial order n from left to right, and from top to bottom).

results with the output of the simulation therefore serves as a validating step for the numerical approach as a whole. The comparison between the frequencies and eigenfunctions of the modes, as extracted from the simulation, with the setup described in the beginning of Section 9.2, and their exact counterparts as derived through the procedure described in Section 9.3.1, leads to an excellent agreement, as I illustrated in Section 9.3.2. This brings significant support to the consistency of the numerical approach. This, along with the advantages inherent to Lagrangian stochastic models of turbulence and already listed in details in Section 7.3, shows that this implementation does indeed provide with a well-suited method for relating the properties of stellar turbulent convection to the observed properties of solar-like oscillations.

I note, as a concluding remark, that the numerical approach described in this chapter, far from supplanting the analytical approach presented in Chapter 8, actually supplement it. On the one hand, while the application of the analytical approach to more complex – and more realistic – stochastic models might involve convoluted derivations, thus rendering the approach impractical, the numerical implementation described in this chapter is much lighter to carry out: the addition of other stochastic variables to describe the state of the particles, and of other Ito SDE to model their evolution, does not increase the complexity of the implementation in any way; neither does the inclusion of additional mean fields to estimate in the SPH formalism. For example, the implementation of the Lagrangian stochastic model developed in Appendix B would not involve any heavy modifications to the already existing numerical machinery. The transition from 1D to 2D/3D, by contrast, may require a bit more work, in particular as regards the SPH part of the algorithm; it is nevertheless feasible (e.g. Welton 1998). On the other hand, the analytical prescriptions derived by means of the formalism developed in Chapter 8 can help disentangle the numerical results obtained through the method developed here, concerning, for instance, the various physical contributions to mode damping or surface effects. In short, the two approaches can mutually benefit from each other, and much insight can be gained by developing them alongside each other, instead of one after the other. I already had the opportunity to point this out in Section 7.3, but it is perhaps clearer now that the two have been presented in detail.

Conclusion and perspectives of Part III

Summary

In Part III, I investigated *Lagrangian stochastic models* of turbulence as an alternative way to study the coupling between turbulent convection and acoustic modes of oscillations in solar-type stars, compared to the more traditional approaches based on Mixing Length Theory, Reynolds-stress models or Large-Eddy Simulations. The core idea behind these models is to describe the evolution of individual fluid particles, followed along their respective trajectories, instead of the evolution of flow variables. The highly turbulent nature of the flow at the top of the convective zone in solar-type stars entails the stochastic nature of the equations governing the evolution of the fluid particles. I have discussed extensively, in Section 7.2 as well as in Appendix B, the ways in which the relevant form of these stochastic differential equations can be determined, in particular in the context of stellar convection. The evolution of the fluid particles is intrinsically coupled with the instantaneous mean flow – for example, the mean pressure gradient exerts a force on these parcels. In the particle representation, the mean flow can be determined directly from the set of modelled fluid particles themselves, by averaging the corresponding particle-level quantity over all neighbouring parcels of fluid. This is at the heart of *Smoothed Particle Hydrodynamics*, which allows all mean fields in the Lagrangian stochastic model to be put in closed form, and which also allows for the exploitable output of the model to be extracted in an efficient way. Such Lagrangian stochastic models, by contrast with Mixing Length Theory for instance, provide with a method which 1) does not initially rely on a separation between convection equations and oscillation equations, but instead encompasses both components, and therefore naturally contain their mutual coupling; 2) avoids the reduction of spatial scales and timescales in the problem to a unique scale, but instead accounts for the full description of the turbulent cascade; 3) simultaneously describes all effects of turbulent convection on mode properties, namely the surface effects and the energetic aspects pertaining to mode driving and damping, in a single consistent framework; 4) includes the properties of turbulence in the most general way possible, thus allowing to freely investigate the relation between any given prescription for the turbulent velocity field – and, more specifically, for the turbulent spectrum – and the observed properties of the modes. My short-term goal, in this context, and indeed throughout Part III, was (and still is) to provide with a proof-of-concept for the use of the above-described method to study turbulence-oscillation coupling. Consequently, I deliberately investigated a simple Lagrangian stochastic model, which consists of an extension to compressible flows of the Generalised Langevin Model (see Section 7.2.2). I did so both through purely analytical developments – described in Chapter 8 – and through the numerical implementation of these methods – described in Chapter 9 –, in parallel.

Concerning the analytical part, I started by linearly perturbing the Lagrangian stochastic model, in order to extract a wave equation governing the behaviour of the linear oscillations. This is the subject of the work presented in Philidet et al. (2021). Because the model is stochastic, this linear wave equation is itself comprised of stochastic differential equations. By construction, it contains the effect of the turbulent background on the oscillations, based on the closure relation underlying the Lagrangian stochastic model in the first place. Therefore, it naturally contains all aspects of turbulence-oscillation coupling, and within it lies the information after which I am, namely the shift in frequency incurred by the modes under the influence of convection, as well as the rate at which they are excited by the turbulent motions, and finally the contribution of turbulence to the rate at which the modes are damped. However, the stochastic wave equation contains the *instantaneous* information on these quantities, which are not very useful, as one does not have access to them from observations. What one does have access to, by contrast, is the average, effective impact of turbulence on the oscillations, which is the result of an average over long timescales of these instantaneous quantities. Some work was required, therefore, to manipulate the stochastic wave equation in order to extract this *effective* impact of turbulence on the modes. I made use of the *Simplified Amplitude Equation* formalism, originally developed by Stratonovich (1965), and applied to the case of stellar oscillations perturbed by turbulent convection by Buchler et al. (1993). The fundamental idea is to reduce the infinite set of *partial* stochastic differential equations governing the evolution of the fluid variables (infinite

because pertaining to each location in the star) to a finite set of *ordinary* stochastic differential equations governing the evolution of the complex amplitude of a few normal modes of oscillation of the star. In fact, in the linear case relevant to solar-like oscillations, it actually reduces to a *unique* SDE on the complex amplitude of a single mode, which can be described in isolation from every other mode: indeed, mode coupling only arises from non-linearities. This results in a complex *amplitude equation*, which can be further decomposed into two equations on the real amplitude and the phase of the mode under consideration. However, the information after which I am is still not easily extracted from these equations. The reason lies in the nature of the stochastic perturbation in the amplitude equations: because it stems from turbulent motions characterised by a very large Reynolds number, these perturbations act on a very wide range of different timescales. Even from a numerical implementation point of view, this would become a problem, because each of these timescales would have to be resolved – a problem not too dissimilar to that into which one runs with Large-Eddy Simulations for spatial scales. But there is also this more fundamental issue: that it is the *averaged, effective* influence of turbulence on the oscillations in which I am interested, something which is very complicated to extract from an equation with such a wide variety of timescales. In order to circumvent the problem, I transform the amplitude equations into simplified amplitude equations. The idea is to properly and rigorously incorporate all effects of the finite memory time of the stochastic processes at play into *effective* drift and diffusion coefficients in the Ito SDE for the amplitude and phase of the mode, which can be done by computing the Fokker-Planck equation associated to the amplitude equations, and then exploiting the fact that a given Fokker-Planck equation has an infinity of equivalent SDE, some much simpler than the original one. The much simpler form of the simplified amplitude equations, and the fact that their stochastic part is now δ-correlated in time, allows me to extract the effective impact of turbulence on the mode under consideration. The end result consists of semi-analytical expressions for the observationally available properties of the modes that are related to their interaction with stellar turbulent convection – i.e. their excitation rate $\mathcal{P}$, their linewidth η, and the difference $\delta\omega$ between their observed angular eigenfrequency and the value computed in the absence of any turbulence, which constitutes the 'modal' part of the surface effects (see Section 2.4.2 for more details). These are obtained as functions of 1) the equilibrium state of the star, 2) the structure of the mode under consideration in the absence of turbulence, and 3) the statistical properties of the turbulent velocity field, and more particularly its second- and fourth-order autocorrelation spectrum. The first two ingredients are available from 1D stellar evolutionary models or 3D hydrodynamic simulations. As such, this semi-analytical formalism allows to directly relate the observed properties of the modes to the input physics of turbulence: the former can therefore be used to *constrain* the latter, and when it comes to surface effects, good enough constraints on the latter can be used to *predict* the former.

Concerning the numerical part, I implemented directly the same Lagrangian stochastic model considered in Chapter 8, additionally adopting a plane-parallel geometry, thus allowing to reduce the dimension of the simulation to 1D. A large set of N individual fluid particles is used to represent the flow. Each particle is initialised in such a way that the corresponding mean density matches the equilibrium density profile prescribed externally – and extracted from a 1D equilibrium stellar model. Because the particle properties only depend on time, and not explicitly on space, the finite-difference scheme for the time integration is quite light to implement: I chose a Predictor/Corrector scheme *properly adapted to stochastic differential equations*, where the increment of the Wiener processes in the Lagrangian stochastic model is drawn randomly, and independently for each particle, from a normal distribution with zero mean and whose variance is equal to the time step. The coefficients in the finite-difference scheme, as well as the desired output of the simulations, depend on the ensemble average of the flow quantities – density, gas pressure, velocity, Reynolds stress tensor. One of the strengths of Lagrangian stochastic models is that they contain these ensemble averages in closed form at the particle level, and the SPH formalism can be used to estimate them directly from the particle properties, by performing averages over particles weighted by a kernel function designed to filter the neighbouring particles only. I had already used this method in the analytical formalism presented in Chapter 8, but it is also perfectly suited to the present numerical implementation. More specifically, a $O(N)$ algorithm is implemented to efficiently compute the means at every particle location, and also at every location in the box where I wish to save an output. Boundary conditions are enforced by re-injecting exiting particles into the domain, but randomly re-initialising their properties according to the local Eulerian PDF – which can also be reconstructed by way of the SPH formalism – at the boundary. While this may look similar to a reflection of the particles on the boundaries, the old particle must be considered as being lost, while the new particle must be seen as originating either from an upflow coming from below (at the bottom boundary), or a downdraft coming from above (at the top boundary). Eventually, this numerical implementation allows for the extraction of

the power spectral density associated to any output of the simulation – more particularly gas density, gas pressure, turbulent pressure and velocity. Furthermore, the fact that the output can be saved at each time step at arbitrary, time-dependent nodes in the simulations, allows me to 'observe' time series in any given frame of reference: I take this opportunity to measure power spectra in both Eulerian and pseudo-Lagrangian frames – where the latter refers to a frame attached to the mean flow, without the erratic turbulent contribution to the flow. Resonant modes are extracted, and fitted against Lorentzian profiles, in each of these power spectra, which allows for a determination of the frequency, linewidth and amplitude of the modes, directly from the simulation. The mode amplitude also depends on space, and with the help of the phase of the complex spectrum – which is also available from the simulation –, the eigenfunctions of the modes can also be extracted numerically. For the moment, the Lagrangian stochastic model on which this implementation is based is extremely simple, and is not meant to realistically represent stellar turbulence. However, its simplicity allows for exact analytical results to be derived: comparing them to the numerical results is a necessary step to validate the numerical approach as a whole. I perform this validating step in the end of Chapter 9, where I show that the analytical and numerical results are indeed in very good agreement, thus supporting the consistency of the method. Furthermore, I compare these exact results with the GGM and RGM prescriptions, and I show that these systematically yield biased results for the frequency of the modes – with the RGM results exhibiting larger discrepancies than the GGM results. Those only constitute preliminary results, and a considerable amount of refinements still need to be brought to this numerical method – as explained in more detailed in the next section. Nevertheless, the fact that I managed to validate the method makes it a promising lead indeed to study the relation between stellar turbulent convection and the observed properties of the modes.

Perspectives

The analytical developments described in Chapter 8 led me simultaneously, as I explained above, to a semi-analytical formula for the driving and the damping of the modes, as well as the modal part of the surface effects incurred by solar-like oscillations, as a function of the second- and fourth-order autocorrelation spectra of the turbulent velocity field. The immediate follow-up of this work will consist in using specified prescriptions for the autocorrelation spectra, which I will then be able to plug into the expressions for the excitation rate, damping rate and surface effects of any given oscillating mode. In essence, this is very similar to the kind of investigation I performed in Part II of this thesis, except I was then only interested in one of these aspects, i.e. mode driving. This operation will allow me to compare the theoretically computed values of these quantities to their observationally inferred counterparts, which will not only help validate – or invalidate – the chosen turbulence prescription, but will also bring constraints on the parameters introduced in the turbulence prescription. These parameters directly pertain to the turbulent velocity field, and are therefore easily related to the underlying physics of turbulent convection. This is in stark contrast, in particular, with the calibration of the parameters of Mixing Length Theory – starting with the mixing length parameter itself – through similar comparisons between the theoretically computed and observationally inferred mode properties: because the Mixing Length Theory constitutes an empirical prescription not of the turbulent fields themselves, but of their effect on the mean flow, it is much more complicated to relate them to the physics of turbulence, and, *a fortiori*, to assess the range of validity of the constraints put on these parameters. In addition, the present approach is more flexible, as it allows for *any* prescription for turbulence to be tested against observations.

As I have mentioned several times above, for the moment, I applied the analytical formalism presented in Chapter 8 and the numerical implementation described in Chapter 9 to a deliberately oversimplified Lagrangian stochastic model. The goal was to prove the validity of the approach, and to showcase its added value compared to other methods, which I set out to do in these two chapters. But this simplified Lagrangian stochastic model was never intended to realistically describe stellar turbulent convection in the slightest. In particular, it suffers from two major drawbacks, whose circumvention is absolutely necessary, should one wish to consider a model that even remotely begins to accurately represent the properties of the turbulent flow in the convective envelope of solar-type stars. The first one has to do with the fact that *there is no energy equation in this simplified model*. Instead of modelling the evolution of the internal energy associated to each fluid particle, I consider a polytropic relation between the ensemble average of the gas pressure and the density, characterised by a polytropic exponent that acts as an external input in the model (see, in particular, hypothesis H6 in Section 8.1.3). While this frees me from having to include an extra stochastic differential equation for internal energy (or any equivalent thermodynamic

variable), this also amounts to discarding all non-adiabatic effects in the flow – in particular the impact of the radiative flux. This is problematic, as solar-like oscillations are known to exhibit a significant degree of non-adiabaticity (see Section 2.1.1), especially close to the surface of the star, where the coupling with turbulent convection is precisely at its strongest. The second drawback has to do with the fact that *this simplified model assumes the existence of a single timescale for turbulence, in the form of the externally fixed turbulent frequency* ω_t. This is in direct and complete disagreement with the experimentally observed *and* theoretically predicted properties of the turbulent cascade at high Reynolds number, which is known to exhibit a wide range of different timescales, associated to turbulent eddies with very different sizes. Instead of using a fixed unique value for ω_t, it is necessary, therefore, to include the turbulent frequency as a particle property, and to include an extra stochastic differential equation for its evolution. Both these issues are addressed by the more refined Lagrangian stochastic model presented in Appendix B, and a natural next step will be to apply both the analytical formalism of Chapter 8 and the numerical implementation of Chapter 9 to this more realistic model – both components being mutually beneficial, and therefore having to be developed alongside each other.

In addition, it will also be necessary, at some point, to do away with the assumption that the PDF of the turbulent flow is Gaussian. Indeed, the form of the Lagrangian stochastic models, whether it be the simple version considered throughout Chapters 8 and 9 or the more refined version developed in Appendix B, are constructed under the implicit assumption that the equivalent Fokker-Planck equation yields a multivariate Gaussian PDF. By contrast, as shown by 3D hydrodynamic simulations, stellar turbulent convection is characterised by a typical structure comprised of upflows and downdrafts, each separately exhibiting Gaussian turbulence, so that the total flow has a bimodal distribution. Because of the asymmetry between the upflows and the downdrafts – the latter being colder and more turbulent than the former –, the total distribution is not Gaussian. This problem is well-known by meteorologists, because the same situation arises in the Convective Planetary Boundary Layer (CPBL), and their community has come up with ways of taking this 'bi-Gaussianity' of turbulence into account (e.g. Rodean 1996). One such solution is to use a two-flow model, where the distribution is determined by the mean and variance of two Gaussian distributions, or equivalently by the first four moments of the whole distribution. In that case, to the mean and the variance must be added the skewness and the kurtosis of the distribution. It is possible to implement two-flow prescriptions in Lagrangian stochastic models: the idea would be to use different sets of Ito stochastic differential equations to model the evolution of the fluid particles, depending on whether their vertical velocity is positive or negative, and depending on whether their temperature is higher or lower than the local mean temperature. This would also constitute an important task to make the approach more realistic, and its results more applicable to solar-like oscillators.

As I had the opportunity to explain in Section 7.3, the analytical and numerical approaches described in the previous two chapters are mutually beneficial. Indeed, when it comes to prescribing the effect of turbulent convection on solar-like oscillations, only theoretical arguments can provide with the *form of the prescription*, while only the numerical implementation – except in some simple cases – can provide with a *quantification of the parameters in the prescription*. Furthermore, exact analytical results, if they can be obtained, can help validate the numerical approach, while on the other hand, in more complicated cases, the numerical implementation may be the only way to obtain tangible results. Both approaches being mutually beneficial, it is preferable to develop them alongside each other; while I did work on both approaches in parallel, for the moment, I have not truly related them together, which is something towards which I will have to work in the future. In particular, one of the task lying on the path ahead will be to confront the analytical prescriptions derived in Chapter 8 with the results obtained through the numerical implementation of the same Lagrangian stochastic model, which would allow me to assess the self-consistency of the method, but also to quantify said analytical prescriptions. This will involve, for instance, comparing the mode linewidths inferred from the simulation to the theoretically computed value. Furthermore, a considerable insight can be gained by exploring the impact of the different control parameters in the simulation on the subsequent mode properties: this therefore calls for parametric studies based on the numerical implementation presented in Chapter 9. One of the main immediate difficulties, however, concerns the way the turbulent pressure spectrum is extracted from the simulation: as I showed in Chapter 9, the turbulent pressure eigenfunctions, for instance, are subjected to more uncertainty than the other eigenfunctions, a situation which needs remedying.

Those constitute short-term follow-up avenues of research on this project. But once these methods are more firmly established, their potential range of application will far exceed the realm of solar-like oscillations and their coupling with turbulent convection. Another possible application of these methods, for instance, concerns the phenomenon of *convective penetration* or *convective overshoot* (depending on the efficiency of the entropy trans-

fer between the convectively unstable turbulent eddies and the background) that occurs at the transition between convective and radiative regions, i.e. the fact that convective gas elements, upon reaching the transition, do not abruptly stop there, but instead penetrate into the neighbouring radiative zone over a certain distance. This extension of the convective region has an important impact, for example, on the chemical evolution of the star (because the mixing brought about by convection helps refuel the core of the star, thus extending its lifetime), but convective penetration is also partly responsible for the excitation of the internal gravity waves propagating in the radiative zone, and is therefore important as regards the transport of angular momentum (Press 1981; Zahn et al. 1997; Lecoanet and Quataert 2013; Pinçon et al. 2016). Accounting for convective penetration or overshoot requires a non-local model of turbulent convection[9], and is usually incorporated in 1D stellar models through prescriptions based on non-local formulations of the MLT (see Section 1.2.2), or other similar empirical prescriptions. By contrast, Lagrangian stochastic models of turbulence would allow to include a more physical closure relation, at particle level, and would allow for the determination of more physically-grounded prescriptions for the mutual coupling between the convective penetration into the radiative zone, the internal gravity waves, the rotation (global or differential) and the chemical mixing. Essentially, this would require implementing the numerical method described in Chapter 9 in a region straddling the tachocline (i.e. the transition between the radiative core and the convective envelope), so that the bottom of the simulation domain would contain the top of the radiative zone – down to a sufficient depth, so that the convectively unstable eddies can comfortably overshoot once they cross the tachocline –, and the top of the domain would contain the bottom of the convective zone. This would also require a transition from a 1D domain to a multidimensional one. This is not too heavy to do for Lagrangian stochastic models coupled with SPH: the main difficulties would be 1) to extend the Ito SDE for fluid particle evolution beyond the plane-parallel geometry assumed in both Chapter 9 and Appendix B, and 2) to implement a multidimensional version of the $O(N)$ algorithm for the kernel estimate of the means (on this subject, see Welton 1998). Once these obstacles are overcome, the idea would be to use the individual trajectories of the fluid particles to directly *measure* the transport due to convective penetration from the simulation. This exact same approach has already been used in the context of convective penetration on the basis of LES, where the trajectories of artificial trackers are reconstructed from the flow variables in the simulation (e.g Freytag et al. 1996; Cunningham et al. 2019). By construction, however, Lagrangian stochastic models are much more suited to this kind of analysis: the fact that they are implemented with particle methods directly provides with the trackers to be followed. Their trajectory can then be used to estimate the variance of the particle displacement as a function of time, which would directly provide with a diffusion matrix characterising convective penetration – i.e. not only a quantitative estimation of the importance of this transport, as well as of the typical depth of penetration, but also the degree of anisotropy of this phenomenon, which is indeed expected to be non-negligible, seeing as convection obviously has a preferred direction. This avenue of research would constitute an important next step for the numerical part of my work.

Yet another domain of application of this approach would concern not solar-like oscillators, but classical pulsators instead. The Simplified Amplitude Equation formalism described in Section 8.2, as I mentioned in the beginning of Chapter 8, was originally applied by Buchler et al. (1993) to study non-linear mode coupling. Indeed, the global modes of oscillation in classical pulsators are characterised, by contrast with solar-like oscillations, by their intrinsic instability. As such, they are self-excited, in the sense that they systematically lead to the development of a runaway mechanism, which makes their amplitude grow exponentially in time. The amplitude of these modes, therefore, is not limited by a balance between driving and damping processes, like in solar-type stars; instead, their observed amplitude is the result of non-linearities which come into play when they become too large, and which redistribute energy between these modes. The Lagrangian stochastic model approach described in Part III, and its implementation in the scope of the Simplified Amplitude Equation formalism, allows for an investigation of this non-linear coupling. Additionally, it also allows for an investigation of the impact of turbulent convection on the stability of the modes: indeed, an additional stabilising or destabilising contribution from turbulence, however small, can make the difference between a star exhibiting self-excited pulsations and a star only exhibiting stable oscillations. This is susceptible to have an impact on the location of the instability strips in the Hertzsprung-Russell diagram – i.e. the region, in stellar parameter space, occupied by the stars whose

[9] If convection is considered to be purely local, then the behaviour of the convectively unstable gas elements only depends on the flow quantities at their exact, instantaneous location. This means that the moment they enter a region where the Schwarzschild criterion (see Section 1.1.1 for more details) is not verified, they cease to be subjected to the convective instability, and they stop abruptly in their tracks. Of course, in reality, their inertia does not allow for such behaviour: their future evolution depends on their history, i.e. on the properties of the background they traversed before arriving at the boundary of the convective region. Otherwise stated, convection must be described non-locally to explain the convective penetration.

internal structure is precisely in the right range to allow for self-excited pulsations to develop. Finally, turbulent convection is also susceptible to play a role, along with non-linearities, in the saturation of the self-excited mode amplitude, thus impacting the observed amplitude of these modes. Investigating these issues by means of a Lagrangian stochastic model, however, would require going beyond the linear case considered in Chapter 8, and instead considering the higher-order terms in the Taylor expansion of the Ito stochastic differential equations derived in Section 8.1.1. In that case, the wave equation is no longer linear, and the full power of the Simplified Amplitude Equation formalism can be deployed. By contrast with the results of Chapter 8, where each mode had its own independent simplified amplitude equation, and where analytical results could be derived easily, for classical pulsators the Ito SDE for different modes are coupled with each other, and lead to two-mode resonances, three-mode resonances, or more. In that case, it would undoubtedly be necessary to numerically integrate the set of coupled, non-linear stochastic differential equations for the real amplitude and phase of the modes. Solving these equations would provide with a stationary solution for the joint PDF of all these amplitudes – if a stationary solution exists –, which would directly yield the expectations of every mode amplitude under consideration. This would allow to shed light into the saturation process leading to the observed amplitude of these modes.

These last two applications – i.e. the idea to apply this formalism, either analytically or numerically, to the issue of convective penetration, or to extend it to the realm of classical pulsators – undoubtedly constitute longer-term motivations to go further in this project, and still require a significant amount of work. They do show, however, that the ideas presented in Part III are not limited in their range of application, but instead open a good number of doors, each letting the tantalising light of exciting future prospects shine through. Whether or not these doors actually lead somewhere is for time to tell; nevertheless, and allow me to conclude this thesis on this note, I can truthfully assert that it is with as much anticipation and wonderment as I did three years ago, upon starting this PhD, that I contemplate that light.

Appendices

A Equations of hydrodynamics

Contents

Stars, in the broadest definition of the term, are self-gravitating bodies comprised of a more or less ionised gas. In particular, stellar matter is sufficiently dense that it can be described as a continuous medium, and its motion modelled through the equations of hydrodynamics. Those are the fundamental equations governing the behaviour of the plasma constituting the stars, directly derived from first principles, and all phenomena described in this manuscript are, at some point or another, contained within these equations – although some digging may be necessary to unveil them. I present and discuss these fundamental equations in this Appendix.

A.1 Eulerian vs Lagrangian descriptions

There are two possible descriptions of any continuous fluid, equally important and complementary, which set themselves apart through the frame of reference in which the motion of the fluid is measured. In the *Eulerian description*, the flow is viewed in the fixed laboratory frame, and any property Q of the fluid is a function of time t and a fixed position $\mathbf{x}$. On the other hand, in the *Lagrangian description*, a specific parcel of fluid is chosen, and the flow is viewed in the moving frame attached to that parcel[1]. Any property Q^+ of that parcel is only a function of time. The ordinary time derivative of the Lagrangian property Q^+ *defines* a new kind of time derivative for the Eulerian property Q

$$\frac{DQ}{Dt} \equiv \frac{\mathrm{d}Q^+}{\mathrm{d}t} \,, \tag{A.1}$$

where Q is the Eulerian property at time t and at whichever position $\mathbf{x}$ the parcel followed in the Lagrangian description happens to be at that particular time. This new time derivative does not correspond to the actual partial derivative of Q with respect to time, as will become apparent below. It goes by many names: Lagrangian derivative, material derivative, comoving derivative and substantial derivative are some of them.

The two descriptions are perfectly equivalent to one another: knowing the Lagrangian property Q^+ at any time t for any given parcel of fluid gives the same amount of information as knowing the Eulerian property Q at any time t and position $\mathbf{x}$. If the motion of the fluid is non-relativistic, then the choice of description is simply a matter of convenience, and the two can be easily related. In particular, the material derivative in the Lagrangian description can be related to the time and space derivatives in the Eulerian description, in the following way. By virtue of the definition given above, one has

$$\frac{DQ}{Dt} = \lim_{\Delta t \to 0} \frac{Q(\mathbf{x} + \Delta\mathbf{x}, t + \Delta t) - Q(\mathbf{x}, t)}{\Delta t} \,, \tag{A.2}$$

where $\Delta\mathbf{x}$ is the displacement, during the time step Δt, of the parcel of fluid which happens to be located at $\mathbf{x}$ at time t. By definition of the Eulerian velocity $\mathbf{u}$ at location $\mathbf{x}$ and time t, one has $\Delta\mathbf{x} = \mathbf{u}\,\Delta t$, so that one may write

[1] In Heraclitus' words, 'you cannot step into the same river twice, for other waters are continually flowing on'. To which one can reply: yes you can, but only in a Lagrangian frame.

the Taylor expansion of $Q(\mathbf{x} + \Delta\mathbf{x}, t + \Delta t)$ at first order

$$\begin{aligned} Q(\mathbf{x} + \Delta\mathbf{x}, t + \Delta t) &= Q(\mathbf{x}, t) + \frac{\partial Q}{\partial t}\Delta t + \frac{\partial Q}{\partial x_i}\Delta x_i \\ &= Q(\mathbf{x}, t) + \left(\frac{\partial Q}{\partial t} + u_i\frac{\partial Q}{\partial x_i}\right)\Delta t \,, \end{aligned} \tag{A.3}$$

where I have used the Einstein notation for contracted indices. Naturally, any second or higher order term in the expansion will yield a vanishing contribution once $\Delta t \to 0$. Then Equation A.2 yields the following identity

$$\frac{DQ}{Dt} = \frac{\partial Q}{\partial t} + u_i\frac{\partial Q}{\partial x_i} \,. \tag{A.4}$$

Equation A.4 means that there are two contributions to the rate of change of a quantity Q as seen by a given parcel of fluid: the first one is due to the fact that the property Q explicitly depends on time; and the second one is due to the fact that the parcel of fluid travels through regions characterised by different values of the property Q.

A.2 Conservation laws for a fluid

Because the laws of conservation concern material parcels of fluid rather than the flow as seen from a fixed point of view, they are best formulated in a Lagrangian point of view. As I will now show, however, it is possible to transcribe conservation laws in the Eulerian description.

Let me consider a portion of fluid comprised of all parcels of fluid whose position $\mathbf{X}$ is enclosed within the infinitesimal volume $\mathrm{d}V \equiv \mathrm{d}X_1\,\mathrm{d}X_2\,\mathrm{d}X_3$ at an initial time $t = 0$. After a time t, each of these particles will have moved with the flow, so that their position is now $\mathbf{x}$, and they form a new volume $\mathrm{d}V' \equiv \mathrm{d}x_1\,\mathrm{d}x_2\,\mathrm{d}x_3$. The new volume $\mathrm{d}V'$ is given by

$$\mathrm{d}V' = J\,\mathrm{d}V \,, \tag{A.5}$$

where J is the Jacobian of the change of variables $\mathbf{X} \mapsto \mathbf{x}$, that is to say

$$J = \left|\frac{\partial x_i}{\partial X_j}\right| \,. \tag{A.6}$$

In this context, J is also referred to as the *expansion* of the fluid, as it describes how a given element of fluid expands or contracts through time. Let me express the rate of change of this quantity: by multilinearity of the determinant, one has

$$J = \epsilon_{ijk}\frac{\partial x_1}{\partial X_i}\frac{\partial x_2}{\partial X_j}\frac{\partial x_3}{\partial X_k} \,, \tag{A.7}$$

where ϵ_{ijk} is the Levi-Civita tensor defined by

$$\epsilon_{ijk} = \begin{vmatrix} \delta_{i1} & \delta_{i2} & \delta_{i3} \\ \delta_{j1} & \delta_{j2} & \delta_{j3} \\ \delta_{k1} & \delta_{k2} & \delta_{k3} \end{vmatrix} \,. \tag{A.8}$$

The material derivative of the expansion can be expressed thus

$$\begin{aligned} \frac{DJ}{Dt} &= \epsilon_{ijk}\frac{\partial u_1}{\partial X_i}\frac{\partial x_2}{\partial X_j}\frac{\partial x_3}{\partial X_k} + \epsilon_{ijk}\frac{\partial x_1}{\partial X_i}\frac{\partial u_2}{\partial X_j}\frac{\partial x_3}{\partial X_k} + \epsilon_{ijk}\frac{\partial x_1}{\partial X_i}\frac{\partial x_2}{\partial X_j}\frac{\partial u_3}{\partial X_k} \\ &= \epsilon_{ijk}\frac{\partial u_1}{\partial x_l}\frac{\partial x_l}{\partial X_i}\frac{\partial x_2}{\partial X_j}\frac{\partial x_3}{\partial X_k} + \epsilon_{ijk}\frac{\partial x_1}{\partial X_i}\frac{\partial u_2}{\partial x_l}\frac{\partial x_l}{\partial X_j}\frac{\partial x_3}{\partial X_k} + \epsilon_{ijk}\frac{\partial x_1}{\partial X_i}\frac{\partial x_2}{\partial X_j}\frac{\partial u_3}{\partial x_l}\frac{\partial x_l}{\partial X_k} \\ &= \epsilon_{ijk}\frac{\partial u_1}{\partial x_1}\frac{\partial x_1}{\partial X_i}\frac{\partial x_2}{\partial X_j}\frac{\partial x_3}{\partial X_k} + \epsilon_{ijk}\frac{\partial x_1}{\partial X_i}\frac{\partial u_2}{\partial x_2}\frac{\partial x_2}{\partial X_j}\frac{\partial x_3}{\partial X_k} + \epsilon_{ijk}\frac{\partial x_1}{\partial X_i}\frac{\partial x_2}{\partial X_j}\frac{\partial u_3}{\partial x_3}\frac{\partial x_3}{\partial X_k} \\ &= (\boldsymbol{\nabla}\cdot\mathbf{u})J \,. \end{aligned} \tag{A.9}$$

The first equality stems from the fact that the material derivative follows the same product rule as regular derivatives, as can be seen from Equation A.4, as well as the fact that, by construction, the material derivative of a parcel position coincides with its velocity $\mathbf{u}$; the second equality stems from the chain rule for derivation; the third equality is due to the fact that ϵ_{ijk} is an antisymmetric tensor, and therefore its contraction with any symmetric tensor vanishes; and the fourth equality stems from the definition of the divergence operator. The physical interpretation of Equation A.9 is the no doubt familiar notion that the local expansion or contraction of a fluid is the direct result of a growing or decreasing relative distance between the different fluid parcels in the vicinity.

The identity given by Equation A.9 allows the derivation of the following useful result, that for any physical quantity $Q(t)$ written as the integral of an extensive quantity $Q(\mathbf{x}, t)$ over a given material volume $\mathcal{V}$ of fluid

$$Q(t) \equiv \int_{\mathcal{V}} Q(\mathbf{x}, t)\, \mathrm{d}^3\mathbf{x}\,, \tag{A.10}$$

then the material rate of change of Q is

$$\begin{aligned}
\frac{DQ}{Dt} &= \frac{D}{Dt}\left(\int_{\mathcal{V}_0} Q(\mathbf{X}, t) J\, \mathrm{d}^3\mathbf{X}\right) \\
&= \int_{\mathcal{V}_0} \left(\frac{DQ}{Dt} J + Q\frac{DJ}{Dt}\right) \mathrm{d}^3\mathbf{X} \\
&= \int_{\mathcal{V}_0} \left(\frac{DQ}{Dt} + Q\boldsymbol{\nabla}\cdot\mathbf{u}\right) J\, \mathrm{d}^3\mathbf{X} \\
&= \int_{\mathcal{V}} \left(\frac{DQ}{Dt} + Q\boldsymbol{\nabla}\cdot\mathbf{u}\right) \mathrm{d}^3\mathbf{x}\,,
\end{aligned} \tag{A.11}$$

where $\mathcal{V}_0$ is the initial volume of fluid. This identity relates the rate of change of an integral quantity to the rate of change of the more practical, corresponding local quantity, and is invaluable when deriving the equations of hydrodynamics, as will become clear below. One can already see that if Q is a conserved quantity for any given material volume $\mathcal{V}$, then one automatically obtains a *local* equation on Q by setting the integrand to zero.

The interpretation of Equation A.11 as representing the conservation of Q is even clearer when it is rewritten as

$$\begin{aligned}
\frac{DQ}{Dt} &= \int_{\mathcal{V}} \left(\frac{\partial Q}{\partial t} + \boldsymbol{\nabla}\cdot(Q\mathbf{u})\right) \mathrm{d}^3\mathbf{x} \\
&= \int_{\mathcal{V}} \frac{\partial Q}{\partial t}\, \mathrm{d}^3\mathbf{x} + \int_{\mathcal{S}} Q\mathbf{u}\cdot\mathrm{d}\mathbf{S}\,,
\end{aligned} \tag{A.12}$$

with the use of Equation A.4, as well as the divergence theorem, and where $\mathcal{S}$ is the surface enclosing the volume $\mathcal{V}$. Then the physical interpretation of each term is clear: Q can vary in time either because Q varies locally (first term on the right-hand side), or because Q is transported out of the material volume by the flow itself (second term on the right-hand side). While the second form helps physically interpret this identity, its first form given by Equation A.11 is more practical, and I will use this one in the following.

A.3 Continuity equation

The first equation of hydrodynamics stems from the conservation of mass for a given material volume. Indeed, by definition, a given material volume $\mathcal{V}$ is comprised of a set of fluid particles that remains identical through time, and whose mass therefore does not change. Let me denote the mass of the material volume as $\mathcal{M}$, and the local density of the fluid as ρ, then one has

$$\mathcal{M}(t) = \int_{\mathcal{V}} \rho(\mathbf{x}, t)\, \mathrm{d}^3\mathbf{x}\,, \tag{A.13}$$

so that Equation A.11 is applicable and yields

$$0 = \frac{D\mathcal{M}}{Dt} = \int_{\mathcal{V}} \left(\frac{D\rho}{Dt} + \rho\boldsymbol{\nabla}\cdot\mathbf{u}\right) \mathrm{d}^3\mathbf{x}\,. \tag{A.14}$$

Since this is true of any material volume $\mathcal{V}$, the quantity under the integral must vanish everywhere, and one obtains a local equation for the conservation of mass, also referred to as the *continuity equation* (Mihalas and Mihalas 1984)

$$\frac{D\rho}{Dt} + \rho \boldsymbol{\nabla} \cdot \mathbf{u} = 0 \,. \tag{A.15}$$

A.4 Navier-Stokes equation

Equation A.15 features the velocity field $\mathbf{u}$, for which one therefore also needs an equation. Like I did for mass, let me denote the i-th component of the momentum of a material volume of fluid as $\mathcal{P}_i$, so that one has

$$\mathcal{P}_i = \int_{\mathcal{V}} \rho u_i \ \mathrm{d}^3\mathbf{x} \,. \tag{A.16}$$

Unlike mass, however, $\mathcal{P}_i$ is not a conserved quantity, because any material volume of fluid is subjected to external forces. These forces can fall into two different categories. First, there are the *body forces*, which act remotely, and therefore concern the entire material volume. Those contain, for instance, the gravitational force, as well as the Lorentz force exerted by an external magnetic field if the fluid is ionised. All these forces can be written as

$$F_i^b(t) = \int_{\mathcal{V}} f_i(\mathbf{x}, t) \ \mathrm{d}^3\mathbf{x} \,, \tag{A.17}$$

where $\mathbf{f}$ is the force per unit volume acting on the small element of volume $\mathrm{d}^3\mathbf{x}$. Secondly, there are the forces that only act by contact, and therefore only concern the boundary of the material volume. Those are referred to as *stresses*, and contain, for instance, the pressure, the viscous force, as well as radiative pressure if the system is strongly influenced by radiation. All these forces can be written as[2]

$$F_i^s(t) = \int_{\mathcal{S}} T_{ij} n_j \ \mathrm{d}S = \int_{\mathcal{V}} \frac{\partial T_{ij}}{\partial x_j} \ \mathrm{d}^3\mathbf{x} \,, \tag{A.18}$$

where T_{ij} is the *stress tensor* associated to the stress force F^s, $\mathbf{n}$ is the unit vector locally orthogonal to the surface $\mathcal{S}$ and directed outwards, and I have used the divergence theorem for the second equality.

Newton's second law gives $D\mathcal{P}_i/Dt = F_i^b + F_i^s$, so that, using Equation A.11 with $Q = \rho u_i$, one finds

$$\int_{\mathcal{V}} \left(\frac{D\rho u_i}{Dt} + \rho u_i \frac{\partial u_j}{\partial x_j} - f_i - \frac{\partial T_{ij}}{\partial x_j} \right) \mathrm{d}^3\mathbf{x} = 0 \,. \tag{A.19}$$

Since this must be true of any material volume $\mathcal{V}$, the quantity under the integral must vanish everywhere, which gives a local equation for the fluid momentum. More specifically, using Equation A.15 to expand the first term, one finds

$$\rho \frac{Du_i}{Dt} = f_i + \frac{\partial T_{ij}}{\partial x_j} \,. \tag{A.20}$$

In particular, only accounting for the gravitational force in f_i, and for the pressure and viscous forces in T_{ij}, one has

$$f_i = \rho g_i \,, \tag{A.21}$$

$$T_{ij} = -p \, \delta_{ij} + \sigma_{ij} \,, \tag{A.22}$$

where $\mathbf{g}$ is the gravitational acceleration, p is the gas pressure, and σ_{ij} is the viscous stress tensor. The stress tensor T_{ij} has been decomposed into an isotropic part and a deviatoric part, so that p describes the normal part of the stress force per unit surface, while the viscous stress tensor describes the tangential part of the stress force per unit

[2] Here I have implicitly assumed the existence of a second-order tensor T_{ij} defined in such a way that the force per unit surface $\mathbf{f}^s$ acting on an element of surface characterised by a unit orthogonal vector $\mathbf{n}$ verifies $f_i^s = T_{ij} n_j$. The existence of such a tensor is the direct result of the isotropy of space, and has absolutely nothing to do with the specific nature of the stress force per unit surface $\mathbf{f}^s$.

surface. Then the momentum equation takes the well known form of the Navier-Stokes equation (Mihalas and Mihalas 1984)

$$\rho\frac{Du_i}{Dt} = \rho g_i - \frac{\partial p}{\partial x_i} + \frac{\partial \sigma_{ij}}{\partial x_j} \,. \tag{A.23}$$

This equation can be cast in a different but equally useful form by expanding the material derivative on the left-hand side, and using the continuity equation

$$\frac{\partial \rho u_i}{\partial t} + \frac{\partial (p\delta_{ij} + \rho u_i u_j - \sigma_{ij})}{\partial x_j} = \rho g_i \,. \tag{A.24}$$

The momentum equation is therefore almost exclusively in a conservative form (with the exception of the gravitational force, because it is a body force), where the flux of momentum contains a contribution from the fluid pressure, one from the viscous transport of momentum, to which one must add the advection of momentum by the flow itself. From the force budget point of view, advection therefore takes the form of an additional stress force. This is not very surprising, as all stress forces correspond to a local, molecular mode of transport of momentum.

A.5 Energy equation

Equation A.23 features the gas pressure p, for which one therefore needs an equation. Usually, instead of deriving an equation for the evolution of pressure, it is more practical to derive an equation for an alternative thermodynamic variable (for instance entropy, internal energy or enthalpy) and then relate p to the duo of variables formed by this new thermodynamic variable and the density ρ – which is already modelled – through a constitutive equation of state[3].

As I did for mass and momentum, the energy equation can be obtained through the principle of energy conservation for any material volume $\mathcal{V}$. Let me denote the total energy as $\mathcal{E}(t)$, and the local internal energy per unit mass as $e(\mathbf{x}, t)$, then one has

$$\mathcal{E}(t) = \int_{\mathcal{V}} \left(\rho e + \frac{1}{2}\rho \mathbf{u}^2\right) \mathrm{d}^3\mathbf{x} \,, \tag{A.25}$$

which simply amounts to writing that the total energy of the fluid is the sum of its internal and kinetic energy. Like momentum, the energy $\mathcal{E}$ is not conserved *per se*, as the material volume can exchange energy with the fluid on the outside. This energy can be exchanged either through mechanical work from the body forces exerted on the volume

$$P^b = \int_{\mathcal{V}} \mathbf{f}\cdot\mathbf{u} \ \mathrm{d}^3\mathbf{x} \,, \tag{A.26}$$

the mechanical work from the stresses exerted on the surface

$$P^s = \int_{\mathcal{S}} T_{ij} n_j u_i \ \mathrm{d}S = \int_{\mathcal{V}} \frac{\partial T_{ij} u_i}{\partial x_j} \ \mathrm{d}^3\mathbf{x} \,, \tag{A.27}$$

or through heat exchange characterised by a heat flux $\mathbf{F}^h$, so that the heat transfered *to* the material volume *from* the outside is

$$P^Q = -\int_{\mathcal{S}} F^h_i n_i \ \mathrm{d}S = -\int_{\mathcal{V}} \frac{\partial F^h_i}{\partial x_i} \ \mathrm{d}^3\mathbf{x} \,. \tag{A.28}$$

Conservation of energy, stemming from the first principle of thermodynamics, dictates that[4]

$$\frac{D\mathcal{E}}{Dt} = P^b + P^s + P^Q \,, \tag{A.29}$$

[3] This is only possible if the chemical composition of the gas, and therefore its mean molecular weight μ, is known in advance. Otherwise, p is also a function of μ, which also requires its own transport equation. In order to keep the discussion simple, I will not delve into this matter any further in the following, and will consider μ known.

[4] Note that I have not considered the possibility that energy sources may be present within the material volume $\mathcal{V}$. In the stellar context, the source term originates from nuclear fusion reactions in the core of the star, which adds a creation term on the right-hand side of the energy equation. In this entire thesis, however, I will interest myself with more external regions of the star, where there are no such nuclear reactions, and therefore no source term in the energy equation.

so that, using the expressions above and Equation A.11, one finally obtains the *total energy* equation

$$\rho \frac{D}{Dt}\left(e + \frac{1}{2}\mathbf{u}^2\right) = f_i u_i + \frac{\partial T_{ij} u_i}{\partial x_j} - \frac{\partial F_j^h}{\partial x_j} \,, \tag{A.30}$$

where I recall that $f_i = \rho g_i$, $T_{ij} = -p\delta_{ij} + \sigma_{ij}$, and I will consider that the only contribution to the heat flux comes from the radiative transfer (in particular, I neglect the effect of heat conduction). Explicitly expanding the material derivative, and using the continuity equation, the total energy equation becomes (Mihalas and Mihalas 1984)

$$\frac{\partial}{\partial t}\left(\rho e + \frac{1}{2}\rho \mathbf{u}^2\right) + \frac{\partial}{\partial x_i}\left(F_i^{\mathrm{conv}} + F_i^{\mathrm{rad}} + F_i^{\mathrm{kin}} + F_i^{\mathrm{visc}}\right) = \rho g_i u_i \,, \tag{A.31}$$

where the various energy fluxes are given by

$$F_i^{\mathrm{conv}} = (\rho e + p) u_i \equiv \rho h u_i \,, \tag{A.32}$$

$$F_i^{\mathrm{kin}} = \frac{1}{2}\rho \mathbf{u}^2 u_i \,, \tag{A.33}$$

$$F_i^{\mathrm{visc}} = \sigma_{ij} u_j \,, \tag{A.34}$$

and h is the enthalpy per unit mass of the fluid. Similarly to the Navier-Stokes equation, the energy equation takes an almost exclusively conservative form, with the exception of the gravitational term. The keen-eyed reader will have noticed, in particular, that because of the pressure work, the advection term F_i^{conv} in the energy equation corresponds to the enthalpy flux, and not to the internal energy flux. It is this contribution that is commonly referred to as the *convective flux*. I discuss the importance of this mode of energy transport in Section 1.1.1.

One can also derive an equation for the internal energy alone. Forming the dot product of the velocity equation with $\mathbf{u}$ itself, and using the continuity equation, yields the following equation for the specific kinetic energy

$$\frac{\partial}{\partial t}\left(\frac{1}{2}\rho \mathbf{u}^2\right) + \frac{\partial}{\partial x_i}\left(\frac{1}{2}\rho \mathbf{u}^2 u_i\right) = \rho g_i u_i - u_i \frac{\partial p}{\partial x_i} + u_i \frac{\partial \sigma_{ij}}{\partial x_j} \,. \tag{A.35}$$

Subtracting Equation A.35 from Equation A.31, one finds (Mihalas and Mihalas 1984)

$$\frac{\partial \rho e}{\partial t} + \frac{\partial}{\partial x_i}\left(F_i^{\mathrm{conv}} + F_i^{\mathrm{rad}} + F_i^{\mathrm{visc}}\right) = u_i \frac{\partial p}{\partial x_i} - u_i \frac{\partial \sigma_{ij}}{\partial x_j} \,. \tag{A.36}$$

The gravitational term no longer appears in the internal energy equation. This would actually be the case for any other body force: internal energy can only be impacted by stress forces. The convective, radiative and viscous fluxes are still present, whereas the kinetic energy flux, unsurprisingly, appears to only affect the kinetic energy budget, and disappears from the internal energy equation.

Furthermore, two source terms appear on the right-hand side of Equation A.36, so that the internal energy equation is not conservative. Those are related to the mechanical work exerted by the pressure and viscous forces, and actually also appear in the kinetic energy budget given by Equation A.35 with a minus sign. This means that these two terms actually represent the conversion of kinetic energy into heat, and do not have any net effect on the *total* energy budget (as can be seen from the absence of these terms in Equation A.31).

A.6 Entropy equation in the inviscid limit

When I introduce stellar oscillations in Chapter 2, it becomes apparent that an entropy equation is more practical than the energy equation (Equation A.36). I recall the thermodynamic identity $\mathrm{d}U = T\,\mathrm{d}S - p\,\mathrm{d}V$, valid for any *closed* system for any thermodynamic transformation, where U is the internal energy of the system, T its temperature, S its entropy, p its pressure and V its volume. Dividing by the mass of the system yields an equivalent relation where the extensive quantities U, S and V are replaced by the intensive quantities e (internal energy per unit mass), s (entropy per unit mass) and $1/\rho$. This is only valid for a closed system[5]; in particular, if applying this

[5]By definition, a closed system is one that cannot exchange matter with the outside, but is still allowed to exchange energy (by contrast, an *isolated* system can exchange neither). If matter exchanges are allowed, then an additional term must be added, and the more general relation $\mathrm{d}U = T\,\mathrm{d}S - p\,\mathrm{d}V + \mu\,\mathrm{d}N$ must be used instead, where N is the number of particles in the system, and μ its chemical potential.

relation to a material volume, and then dividing it by dt, one obtains a relation between *material time derivatives*, and not partial time derivatives. As such

$$\begin{aligned}\frac{De}{Dt} &= T\frac{Ds}{Dt} - p\frac{D1/\rho}{Dt} \\ &= T\frac{Ds}{Dt} + \frac{p}{\rho^2}\frac{D\rho}{Dt} \\ &= T\frac{Ds}{Dt} - \frac{p}{\rho}\frac{\partial u_i}{\partial x_i}\,,\end{aligned} \tag{A.37}$$

where I have used the continuity equation (Equation A.15) for the last equality. Let me now rearrange the first term on the left-hand side of Equation A.36, as well as the convective flux term

$$\begin{aligned}\frac{\partial \rho e}{\partial t} + \frac{\partial \rho h u_i}{\partial x_i} &= \frac{\partial \rho e}{\partial t} + \frac{\partial \rho e u_i}{\partial x_i} + \frac{\partial p u_i}{\partial x_i} \\ &= \rho\frac{\partial e}{\partial t} + e\frac{\partial \rho}{\partial t} + \rho u_i\frac{\partial e}{\partial x_i} + e\frac{\partial \rho u_i}{\partial x_i} + \frac{\partial p u_i}{\partial x_i} \\ &= \rho\frac{De}{Dt} + e\underbrace{\left(\frac{\partial \rho}{\partial t} + \frac{\partial \rho u_i}{\partial x_i}\right)}_{=0} + \frac{\partial p u_i}{\partial x_i} \\ &= \rho T\frac{Ds}{Dt} - p\frac{\partial u_i}{\partial x_i} + \frac{\partial p u_i}{\partial x_i} \\ &= \rho T\frac{Ds}{Dt} + u_i\frac{\partial p}{\partial x_i}\,.\end{aligned} \tag{A.38}$$

Plugging this into Equation A.36 yields an equation for the entropy per unit mass s. In particular, in the inviscid limit where the viscous tensor σ_{ij} is neglected, one finds

$$\rho T\left(\frac{\partial}{\partial t} + u_i\frac{\partial}{\partial x_i}\right)s = -\frac{\partial F_i^{\mathrm{rad}}}{\partial x_i}\,. \tag{A.39}$$

One sees that the pressure contribution disappears, leaving only a contribution from radiative transfer. This is not surprising, of course, seeing as the rate of change of entropy is only a matter of heat transfer, and does not depend on the mechanical work exerted by the pressure forces.

B Derivation of the Lagrangian stochastic model for stellar turbulent convection

Contents

In this Appendix, I explicitly describe how the Lagrangian stochastic models of turbulence introduced in Section 7.2 can be adapted to the case of stellar turbulent convection. First, in Section B.1, I describe how the Eulerian and Lagrangian PDF of the flow are related to each other for compressible flows – Equation 7.62 only being valid in the incompressible limit. In Section B.2, I then derive the evolution equations for the means (mean density, mean velocity and means internal energy) and second-order moments (Reynolds stress tensor, variance of the internal energy and convective flux) of the turbulent flow, from first principles. Finally, in Section B.3, I present the core part of this Appendix, i.e. the adaptation of the Refined Langevin Model to compressible flows, in such a way that the equivalent mean equations coincide with the mean equations derived in Section B.2 from first principles.

B.1 Lagrangian vs Eulerian PDF for compressible flows

As I showed in Section 7.2, a Lagrangian stochastic model provides with a Fokker-Planck equation for the Lagrangian flow PDF f_L. By contrast, I am interested in Eulerian quantities, that can only be obtained through the Eulerian flow PDF f_E: it is therefore necessary to relate f_L to f_E. In Section 7.2.1, I gave the relation between the Eulerian and Lagrangian PDF of the flow f_E and f_L in the incompressible case, in the form of Equation 7.62. But in the compressible case, density must be added to the set of variables needed to describe the state of the flow, so that Equation 7.62 must be modified accordingly.

For the sake of simplicity, let me consider a 1D system where the only two variables one needs to describe the state of the flow are the velocity (as in the incompressible case) and the density. In an Eulerian frame of reference, the flow is described by means of the velocity and density at fixed location x, denoted as $u(x,t)$ and $\rho(x,t)$ respectively. Denoting their joint Eulerian PDF as $f_E((\rho,V);(x,t))$, any quantity $Q(\rho(x,t),u(x,t))$, defined as an arbitrary function of ρ and u, has an expectation given by

$$\overline{Q}(x,t) \equiv \int \mathrm{d}\rho' \int \mathrm{d}V'\; Q(\rho',V') f_E((\rho',V');(x,t)) \,, \tag{B.1}$$

which I recall defines the Reynolds average of the quantity Q. On the other hand, in a Lagrangian frame of reference, the flow is described by means of the position $X^+(x_0,t)$ and velocity $U^+(x_0,t)$ of the fluid particle located at x_0 at a fixed reference time t_0. Denoting their joint conditional Lagrangian flow PDF[1] as $f_L((x,V);t|x_0)$, then any arbitrary quantity $Q^+(X^+(x_0,t),U^+(x_0,t))$ pertaining to the fluid particle that was at the position x_0 at time t_0, has an expectation given by

$$E\left[Q^+(x_0,t)\right] = \int \mathrm{d}x' \int \mathrm{d}V'\ Q(x',V')\ f_L((x',V');t|x_0)\ . \tag{B.2}$$

Let me, furthermore, define the *fine-grained Lagrangian PDF*

$$f'_L((x,V);t|x_0) \equiv \delta\left(U^+(x_0,t)-V\right)\ \delta\left(X^+(x_0,t)-x\right)\ , \tag{B.3}$$

where δ is the Dirac distribution. The usefulness of the fine-grained Lagrangian PDF becomes apparent when one computes its expectation

$$\begin{aligned}\mathrm{E}\left[f'_L((x,V);t|x_0)\right] &= \int \mathrm{d}x' \int \mathrm{d}V'\ \delta(V'-V)\ \delta(x'-x)\ f_L((x',V');t|x_0)\\ &= f_L((x,V);t|x_0)\ ,\end{aligned} \tag{B.4}$$

where I have used Equation B.2 with $Q = f'_L$, and the properties of the Dirac distribution respectively.

In an incompressible flow, upon integrating f_L over x_0, one recovers f_E, as shown by Equation 7.62. In a compressible flow, however, things are not that simple, and it is much more practical to make the density appear in the integration, for reasons which will become clear in a moment. Let $\rho(x_0,t_0)$ be the density of the flow at point x_0 and time t_0. Since this quantity relates to the state of the flow at the initial time, it is not a random variable. One has

$$\begin{aligned}\int \mathrm{d}x_0\ \rho(x_0,t_0)\ f_L((x,V);t|x_0) &= \int \mathrm{d}x_0\ \rho(x_0,t_0)\ \mathrm{E}\left[f'_L((x,V);t|x_0)\right]\\ &= \mathrm{E}\left[\int \mathrm{d}x_0\ \rho(x_0,t_0)\ f'_L((x,V);t|x_0)\right]\\ &= \mathrm{E}\left[\int \mathrm{d}x_0\ \rho(x_0,t_0)\ \delta\left(U^+(x_0,t)-V\right)\ \delta\left(X^+(x_0,t)-x\right)\right]\ ,\end{aligned} \tag{B.5}$$

where I have used Equation B.4, the linearity of the expectation operator E, and Equation B.3, respectively. I then perform the change of variable $x_0 \mapsto x' \equiv X^+(x_0,t)$. This change of variable is possible because for any given realisation of the flow, there is a one-to-one mapping between the positions of the particles at time t_0 and their positions at time t – in other words, there can be no empty space in the flow, and two fluid particles cannot be at the same place at the same time. The Jacobian $J(x_0,t_0,x',t)$ of this change of variable, which is unity for an incompressible flow, is now equal to the ratio of density between the two space-time points considered

$$J(x_0,t_0,x',t) = \frac{\rho(x_0,t_0)}{\rho(x',t)}\ , \tag{B.6}$$

where $\rho(x',t)$, unlike $\rho_0(x_0,t_0)$, is a random variable. The introduction of the density in the beginning finds its usefulness here, because one has

$$\int \mathrm{d}x_0\ \rho(x_0,t_0)\ f_L((x,V);t|x_0) = \mathrm{E}\left[\int \mathrm{d}x'\ \rho(x',t)\ \delta(u'-V)\ \delta(x'-x)\right]\ , \tag{B.7}$$

where u' is defined as the velocity, at time t, of the particle which is at position x' at the same time t. But by definition of the Eulerian velocity, $u' = u(x',t)$, and one has

$$\begin{aligned}\int \mathrm{d}x_0\ \rho(x_0,t_0)\ f_L((x,V);t|x_0) &= \mathrm{E}\left[\int \mathrm{d}x'\ \rho(x',t)\ \delta(u(x',t)-V)\ \delta(x'-x)\right]\\ &= \mathrm{E}\left[\rho(x,t)\ \delta(u(x,t)-V)\right]\end{aligned} \tag{B.8}$$

[1] Note that, compared to the Lagrangian flow PDF defined in the main body of this thesis (see Section 7.2.1), I have integrated the PDF over all values of the initial velocity V_0, so that the condition now only involves the initial position x_0. Also note that, while ρ is included as a random variable in f_E, it does not appear in f_L: this is because in the Lagrangian frame of reference, the information on density is actually contained in the positions $X^+(x_0,t)$ of the fluid particles.

where we have used the properties of the Dirac distribution. Notice that the expectation now only contains the Eulerian quantities ρ and u (V, x and t being constant here), so that it coincides with the Reynolds average. As a result, we have

$$\begin{aligned}\int \mathrm{d}x_0\, \rho(x_0,t_0)\, f_L((x,V);t|x_0) &= \overline{\rho(x,t)\,\delta(u(x,t)-V)} \\ &= \int \mathrm{d}\rho' \int \mathrm{d}V'\, \rho'\, \delta(V'-V)\, f_E((\rho',V');(x,t)) \\ &= \int \mathrm{d}\rho'\, \rho'\, f_E((\rho',V);(x,t))\,, \end{aligned} \tag{B.9}$$

where I have used Equation B.1 and the properties of the Dirac distribution respectively.

Equation B.9 constitutes a relation between the Eulerian and Lagrangian flow PDF, which must replace Equation 7.62 for compressible flows. It will prove essential in Section B.3, upon relating Lagrangian stochastic models to their corresponding Reynolds-averaged equations. Note that Equation B.9 can be extended to flows for which more turbulent quantities are modelled. In that case, the variable V must be replaced with the vector of all random variables describing the flow – with the exception of the density ρ. Equation B.9 remains otherwise unchanged.

B.2 Mean equations

In Section B.3, I will modify the Refined Langevin Model in such a way that the corresponding Reynolds-averaged equations of the flow coincide, as best as possible, with those that can be derived from first principles. I had already started to derive the 'exact' Reynolds-averaged equations in Section 1.2.3, with the example of the Reynolds stress equation: in this section, I set out to complete the derivation. I start from the equations of hydrodynamics derived in Appendix A, and which I slightly rearrange thus

$$\frac{\partial \rho}{\partial t} + \frac{\partial \rho u_i}{\partial x_i} = 0\,, \tag{B.10}$$

$$\frac{\partial \rho u_i}{\partial t} + \frac{\partial \rho u_i u_j}{\partial x_j} = -\frac{\partial p}{\partial x_i} + \rho g_i + \frac{\partial \sigma_{ij}}{\partial x_j}\,, \tag{B.11}$$

$$\frac{\partial \rho e}{\partial t} + \frac{\partial \rho e u_i}{\partial x_i} = -p\frac{\partial u_i}{\partial x_i} + \sigma_{ij}\frac{\partial u_j}{\partial x_i} - \frac{\partial F_i^{\mathrm{rad}}}{\partial x_i}\,, \tag{B.12}$$

where all the notations correspond to those of Appendix A, and I decompose each variable into a mean and fluctuating part, where the mean is an ensemble average defined either as a Reynolds average or a Favre average

$$\begin{aligned} &\rho \equiv \overline{\rho} + \rho'\,, \qquad && u_i \equiv \widetilde{u_i} + u_i''\,, \qquad && p \equiv \overline{p} + p'\,, \\ &\sigma_{ij} \equiv \overline{\sigma_{ij}} + \sigma_{ij}'\,, \qquad && e \equiv \widetilde{e} + e''\,, \qquad && F_i^{\mathrm{rad}} \equiv \overline{F_i^{\mathrm{rad}}} + F_i'^{\mathrm{rad}}\,, \end{aligned} \tag{B.13}$$

where I recall that $\overline{.}$ denotes a Reynolds average, $'$ denotes fluctuations around a Reynolds average, $\widetilde{.}$ denotes a Favre average and $''$ denotes fluctuations around a Favre average.

I will consider that the flow exhibits a *plane-parallel geometry*, meaning that the mean flow is assumed to only depend on the radial coordinate, and to have no preferred horizontal direction. These assumptions are verified in the superficial layers of a star, both by the background turbulent part of the flow and by the oscillations, *even non-radial modes*. The reason is that, as I mentioned in Section 2.1.2, even non-radial modes exhibit quasi-vertical wavevectors close to the surface of the star. I will also consider that the gas is characterised by a polytropic relation between its various thermodynamic properties, which allows me to write (Canuto 1997)

$$\frac{p'}{\overline{p}} = \gamma\frac{\rho'}{\overline{\rho}} = \gamma m\frac{\rho e''}{\overline{\rho}\,\widetilde{e}}\,, \tag{B.14}$$

where γ is the polytropic index characterising the relation, and $m \equiv 1/(\gamma-1)$. Finally, I consider that the gas behaves like an ideal gas, so that

$$\overline{p} = (\Gamma_1 - 1)\overline{\rho}\,\widetilde{e}\,, \tag{B.15}$$

where Γ_1 is the first adiabatic exponent. Note that Γ_1 is a perfectly determined thermodynamic property of the fluid, whereas γ (or equivalently m) is a free parameter which controls how the fluid temperature reacts to heat transfers. In particular, in the adiabatic limit, we have $\gamma = \Gamma_1$.

B.2.1 Mean continuity equation

The Reynolds average of Equation B.10 yields

$$\frac{\partial \overline{\rho}}{\partial t} + \frac{\partial \overline{\rho}\widetilde{u_i}}{\partial x_i} = 0 \,. \tag{B.16}$$

As a consequence of the plane-parallel geometry, the only non-zero component of the Favre-averaged velocity is the vertical component, which I will simply denote as $\widetilde{u_v}$ in the following. Furthermore, every mean value – whether it be a Reynolds or Favre average – depends only on time t and the vertical coordinate x. The mean continuity equation therefore becomes

$$\frac{D\overline{\rho}}{Dt} + \overline{\rho}\frac{\partial \widetilde{u_v}}{\partial x} = 0 \,, \tag{B.17}$$

where the operator D/Dt, in the remainder of this Appendix, does not refer to the material time derivative defined by Equation A.4, but to the 'Favre-averaged particle time derivative' $D/Dt \equiv \partial_t + \widetilde{u_v}\,\partial_z$.

B.2.2 Moments of the velocity

Mean momentum equation

Taking the Reynolds average of the vertical component of Equation B.11, one finds

$$\frac{\partial \overline{\rho}\widetilde{u_v}}{\partial t} + \frac{\partial \overline{\rho}\widetilde{u_v u_i}}{\partial x_i} = -\frac{\partial \overline{p}}{\partial x_i} - \overline{\rho}g + \frac{\partial \overline{\sigma_{iv}}}{\partial x_i} \,, \tag{B.18}$$

where g is the norm of the gravitational acceleration, which I will consider not being perturbed by either the turbulence or the oscillations in the following. The second term on the left-hand side can be expanded thus

$$\widetilde{u_v u_i} = \widetilde{u_v}\widetilde{u_i} + \widetilde{u_v'' u_i''} = \left(\widetilde{u_v}^2 + \widetilde{u_v''^2}\right)\delta_{iv} \,, \tag{B.19}$$

where the second equality stems from the plane-parallel geometry. On the other hand, molecular forces only play a significant dissipative role for the small scale motions of the fluid, and can be disregarded in the large scale flow equation. Therefore

$$\frac{\partial \overline{\rho}\widetilde{u_v}}{\partial t} + \frac{\partial \overline{\rho}\widetilde{u_v}^2}{\partial x} + \frac{\partial \overline{\rho}\widetilde{u_v''^2}}{\partial x} = -\frac{\partial \overline{p}}{\partial x} - g\overline{\rho} \,. \tag{B.20}$$

Finally, I derive the following identity from the mean continuity equation and the definition of the operator D/Dt

$$\frac{\partial \overline{\rho}\overline{Q}}{\partial t} + \frac{\partial \overline{\rho}\overline{Q}\widetilde{u_v}}{\partial x} = \overline{\rho}\frac{D\overline{Q}}{Dt} \,, \tag{B.21}$$

where Q is an arbitrary physical quantity. Using this identity for $Q = \widetilde{u_v}$, the mean momentum equation finally reads

$$\overline{\rho}\frac{D\widetilde{u_v}}{Dt} + \frac{\partial \overline{\rho}\widetilde{u_v''^2}}{\partial x} = -\frac{\partial \overline{p}}{\partial x} - g\overline{\rho} \,. \tag{B.22}$$

Reynolds stress equation

It can be seen that the quantity $\widetilde{u_v''^2}$ appears in Equation B.22. This is one component of the Reynolds stress tensor $R_{ij} \equiv \widetilde{u_i'' u_j''}$, for which one needs an evolution equation as well. The plane-parallel geometry entails that only the diagonal components of this tensor are non-zero. Furthermore, the two horizontal components are equal. As a result, the entire Reynolds stress tensor is described by only two components, which are the vertical and horizontal diagonal stresses, denoted R_v and R_h in the following. In order to derive their evolution equations, let me write Equation B.11 in two different forms

$$\frac{\partial \rho u_i}{\partial t} + \frac{\partial \rho u_i u_k}{\partial x_k} = -\frac{\partial p}{\partial x_i} + g_i\rho + \frac{\partial \sigma_{ij}}{\partial x_j} \,, \tag{B.23}$$

$$\rho\frac{\partial u_j}{\partial t} + \rho u_k\frac{\partial u_j}{\partial x_k} = -\frac{\partial p}{\partial x_i} + g_i\rho + \frac{\partial \sigma_{ij}}{\partial x_j} \,, \tag{B.24}$$

where I used Equation B.10 to switch from one to the other. Multiplying Equation B.23 by u_j, Equation B.24 by u_i, and adding them together, one finds

$$\frac{\partial \rho u_i u_j}{\partial t} + \frac{\partial \rho u_i u_j u_k}{\partial x} = -\left(u_j \frac{\partial p}{\partial x_i} + u_i \frac{\partial p}{\partial x_j}\right) + \left(u_j g_i \rho + u_i g_j \rho\right) + \left(u_j \frac{\partial \sigma_{ij}}{\partial x_j} + u_i \frac{\partial \sigma_{ji}}{\partial x_i}\right) . \tag{B.25}$$

Taking the Reynolds average of this equation, and remarking that

$$\overline{\rho u_i u_j} = \overline{\rho}\widetilde{u_i}\widetilde{u_j} + \overline{\rho} R_{ij} , \tag{B.26}$$

$$\overline{\rho u_i u_j u_k} = \overline{\rho}\widetilde{u_i}\widetilde{u_j}\widetilde{u_k} + \overline{\rho}\widetilde{u_i} R_{jk} + \overline{\rho}\widetilde{u_j} R_{ik} + \overline{\rho}\widetilde{u_k} R_{ij} + \overline{\rho}\widetilde{u_i'' u_j'' u_k''} , \tag{B.27}$$

one finds

$$\begin{aligned} &\frac{\partial \overline{\rho}\widetilde{u_i}\widetilde{u_j}}{\partial t} + \frac{\partial \overline{\rho} R_{ij}}{\partial t} + \frac{\partial}{\partial x_k}\overline{\rho}\left(\widetilde{u_i}\widetilde{u_j}\widetilde{u_k} + \widetilde{u_i} R_{jk} + \widetilde{u_j} R_{ik} + \widetilde{u_k} R_{ij} + \widetilde{u_i'' u_j'' u_k''}\right) \\ &\quad = -\left(\widetilde{u_j}\frac{\partial \overline{p}}{\partial x_i} + \widetilde{u_i}\frac{\partial \overline{p}}{\partial x_j} + \overline{u_i''}\frac{\partial p'}{\partial x_j} + \overline{u_j''}\frac{\partial p'}{\partial x_i} + \overline{u_j''\frac{\partial p'}{\partial x_i}} + \overline{u_i''\frac{\partial p'}{\partial x_j}}\right) + \overline{\rho}(\widetilde{u_j} g_i + \widetilde{u_i} g_j) + \left(\overline{u_j''\frac{\partial \sigma_{ij}}{\partial x_j}} + \overline{u_i''\frac{\partial \sigma_{ji}}{\partial x_i}}\right) . \end{aligned} \tag{B.28}$$

Note that, as I did for the mean momentum equation, I neglected the term $\widetilde{u_i}\frac{\partial \overline{\sigma_{ij}}}{\partial x_j}$, which is negligible compared to the effect of the other large scale forces. However, the correlation of the molecular forces with the small scale velocity – represented by the last term in Equation B.28 – must be accounted for.

The first order terms – i.e. the terms only depending on mean values – can be rearranged by using Equation B.22. They are non-zero only if $i = j = v$, in which case one has

$$\frac{\partial \overline{\rho}\widetilde{u_v}^2}{\partial t} + \frac{\partial \overline{\rho}\widetilde{u_v}^3}{\partial x} = \overline{\rho}\frac{D\widetilde{u_v}^2}{Dt} = 2\overline{\rho}\widetilde{u_v}\frac{D\widetilde{u_v}}{Dt} , \tag{B.29}$$

where I used Equation B.21 with $Q = \widetilde{u_v}^2$ for the first equality. Replacing $D\widetilde{u_v}/Dt$ with Equation B.22, one finds

$$\frac{\partial \overline{\rho}\widetilde{u_v}^2}{\partial t} + \frac{\partial \overline{\rho}\widetilde{u_v}^3}{\partial x} = -2\widetilde{u_v}\frac{\partial \overline{\rho} R_v}{\partial x} - 2\widetilde{u_v}\frac{\partial \overline{p}}{\partial x} - 2\widetilde{u_v}\overline{\rho} g . \tag{B.30}$$

Replacing the first and third term in Equation B.28 by this expression, it can be seen that all the first-order terms on the right-hand side actually vanish, and one finds

$$\frac{\partial \overline{\rho} R_v}{\partial t} - 2\widetilde{u_v}\frac{\partial \overline{\rho} R_v}{\partial x} + 3\frac{\partial \overline{\rho}\widetilde{u_v} R_v}{\partial x} + \frac{\partial \overline{\rho}\widetilde{u_v''^3}}{\partial x} = -2\overline{u_v''}\frac{\partial \overline{p}}{\partial x} - 2\overline{u_v''\frac{\partial p'}{\partial x}} + 2\overline{u_v''\frac{\partial \sigma_{vj}}{\partial x_j}} , \tag{B.31}$$

$$\frac{\partial \overline{\rho} R_h}{\partial t} + \frac{\partial \overline{\rho}\widetilde{u_v} R_h}{\partial x} + \frac{\partial \overline{\rho}\widetilde{u_h''^2 u_v''}}{\partial x} = -2\overline{u_h''\frac{\partial p'}{\partial x_h}} + 2\overline{u_h''\frac{\partial \sigma_{hj}}{\partial x_j}} . \tag{B.32}$$

The indices h are not to be contracted over both horizontal directions; they simply refer to one arbitrary horizontal axis. Finally, using Equation B.21 for $Q = R_v$ and R_h respectively, one obtains

$$\frac{\partial \overline{\rho} R_v}{\partial t} - 2\widetilde{u_v}\frac{\partial \overline{\rho} R_v}{\partial x} + 3\frac{\partial \overline{\rho}\widetilde{u_v} R_v}{\partial x} = \frac{\partial \overline{\rho} R_v}{\partial t} + \frac{\partial \overline{\rho}\widetilde{u_v} R_v}{\partial x} + 2\overline{\rho} R_v\frac{\partial \widetilde{u_v}}{\partial x} = \overline{\rho}\frac{DR_v}{Dt} + 2\overline{\rho} R_v\frac{\partial \widetilde{u_v}}{\partial x} , \tag{B.33}$$

$$\frac{\partial \overline{\rho} R_h}{\partial t} + \frac{\partial \overline{\rho}\widetilde{u_v} R_h}{\partial x} = \overline{\rho}\frac{DR_h}{Dt} , \tag{B.34}$$

so that the Reynolds stress equations finally read

$$\overline{\rho}\frac{DR_v}{Dt} + \frac{\partial \overline{\rho}\widetilde{u_v''^3}}{\partial x} = -2\overline{\rho} R_v\frac{\partial \widetilde{u_v}}{\partial x} - 2\overline{u_v''}\frac{\partial \overline{p}}{\partial x} - 2\overline{u_v''\frac{\partial p'}{\partial x}} + 2\overline{u_v''\frac{\partial \sigma_{vj}}{\partial x_j}} , \tag{B.35}$$

$$\overline{\rho}\frac{DR_h}{Dt} + \frac{\partial \overline{\rho}\widetilde{u_h''^2 u_v''}}{\partial x} = -2\overline{u_h''\frac{\partial p'}{\partial x_h}} + 2\overline{u_h''\frac{\partial \sigma_{hj}}{\partial x_j}} . \tag{B.36}$$

B.2.3 Moments of the internal energy

Mean energy equation

Taking the Reynolds average of Equation B.12, one finds

$$\frac{\partial \widetilde{\rho e}}{\partial t} + \frac{\partial \overline{\rho} \widetilde{u_i} \widetilde{e}}{\partial x_i} + \frac{\partial \overline{\rho} \widetilde{u_i'' e''}}{\partial x_i} = -\overline{p \frac{\partial u_i}{\partial x_i}} + \overline{\sigma_{ij} \frac{\partial u_j}{\partial x_i}} - \frac{\partial \overline{F_i^{\mathrm{rad}}}}{\partial x_i} \,. \tag{B.37}$$

It can be seen that the mean energy equation features the second-order moment $F_e \equiv \widetilde{u_v'' e''}$, which corresponds to the vertical component of the *energy convective flux* (the other components vanish because of the plane-parallel geometry). Let me note that F_e does not correspond to the actual convective flux F^{conv} defined by Equation A.32, because the latter was defined as the *enthalpy* flux due to convection. However, if the plasma behaves as an ideal gas – which it does to a very good approximation in the stellar context –, the internal energy and enthalpy fluctuations are related through $h'' = \Gamma_1 e''$, so that $F^{\mathrm{conv}} = \Gamma_1 F_e$.

Using Equations 1.36 and 1.37, and neglecting the mean viscous stress tensor $\overline{\sigma_{ij}}$, the second-to-last term on the right-hand side of Equation B.37 can be rewritten in terms of the turbulent dissipation rate ϵ as

$$\overline{\sigma_{ij} \frac{\partial u_j}{\partial x_i}} = \overline{\rho} \epsilon \,. \tag{B.38}$$

Then, Equation B.37 becomes

$$\frac{\partial \widetilde{\rho e}}{\partial t} + \frac{\partial \overline{\rho e} \widetilde{u_v}}{\partial x} + \frac{\partial \overline{\rho} F_e}{\partial x} = -\overline{p} \frac{\partial \widetilde{u_v}}{\partial x} - \overline{p} \frac{\partial \overline{u_v''}}{\partial x} - \overline{p' \frac{\partial u_i''}{\partial x_i}} + \overline{\rho} \epsilon - \frac{\partial \overline{F_i^{\mathrm{rad}}}}{\partial x_i} \,, \tag{B.39}$$

where I have used the plane-parallel geometry several times to simplify the indices contractions. The first two terms on the left-hand side can be rearranged through Equation B.21 with $Q = \widetilde{e}$, and the mean energy equation finally reads

$$\overline{\rho} \frac{D \widetilde{e}}{D t} + \frac{\partial \overline{\rho} F_e}{\partial x} = -\overline{p} \frac{\partial \widetilde{u_v}}{\partial x} - \overline{p} \frac{\partial \overline{u_v''}}{\partial x} - \overline{p' \frac{\partial u_i''}{\partial x_i}} + \overline{\rho} \epsilon - \frac{\partial \overline{F^{\mathrm{rad}}}}{\partial x} \,, \tag{B.40}$$

where F^{rad} now refers to the vertical component of the radiative flux.

Energy variance equation

Let me write Equation B.12 in two different forms, using Equation B.10 to switch from one to the other

$$\frac{\partial \rho e}{\partial t} + \frac{\partial \rho e u_i}{\partial x_i} = -p \frac{\partial u_i}{\partial x_i} + \sigma_{ij} \frac{\partial u_j}{\partial x_i} - \frac{\partial F_i^{\mathrm{rad}}}{\partial x_i} \,, \tag{B.41}$$

$$\rho \frac{\partial e}{\partial t} + \rho u_i \frac{\partial e}{\partial x_i} = -p \frac{\partial u_i}{\partial x_i} + \sigma_{ij} \frac{\partial u_j}{\partial x_i} - \frac{\partial F_i^{\mathrm{rad}}}{\partial x_i} \,. \tag{B.42}$$

Multiplying both equations by e and adding them together, one finds

$$\frac{\partial \rho e^2}{\partial t} + \frac{\partial \rho e^2 u_i}{\partial x_i} = -2ep \frac{\partial u_i}{\partial x_i} + 2e\sigma_{ij} \frac{\partial u_j}{\partial x_i} - 2e \frac{\partial F_i^{\mathrm{rad}}}{\partial x_i} \,. \tag{B.43}$$

The Reynolds average of these various terms yields

$$\overline{\rho e^2} = \overline{\rho} \widetilde{e^2} + \overline{\rho} \widetilde{e''^2} \,, \tag{B.44}$$

$$\overline{\rho e^2 u_i} = \overline{\rho} \widetilde{e^2} \widetilde{u_i} + 2 \overline{\rho} \widetilde{e e''} \widetilde{u_i''} + \overline{\rho} \widetilde{u_i} \widetilde{e''^2} + \overline{\rho} \widetilde{e''^2 u_i''} \,, \tag{B.45}$$

$$\overline{ep \frac{\partial u_i}{\partial x_i}} = \widetilde{ep} \frac{\partial \widetilde{u_i}}{\partial x_i} + \overline{e''p} \frac{\partial \widetilde{u_i}}{\partial x_i} + \widetilde{ep} \frac{\partial \overline{u_i''}}{\partial x_i} + \overline{e''p'} \frac{\partial \widetilde{u_i}}{\partial x_i} + \overline{pe''} \overline{\frac{\partial u_i''}{\partial x_i}} + \widetilde{ep'} \overline{\frac{\partial u_i''}{\partial x_i}} + \overline{p'e''} \overline{\frac{\partial u_i''}{\partial x_i}} \,, \tag{B.46}$$

$$\overline{e \sigma_{ij} \frac{\partial u_i}{\partial x_j}} = \widetilde{e} \overline{\rho} \epsilon + \overline{e'' \sigma_{ij} \frac{\partial u_i}{\partial x_j}} \,, \tag{B.47}$$

$$\overline{e \frac{\partial F_i^{\mathrm{rad}}}{\partial x_i}} = \widetilde{e} \frac{\partial \overline{F_i^{\mathrm{rad}}}}{\partial x_i} + \overline{e'' \frac{\partial F_i^{\mathrm{rad}}}{\partial x_i}} \,. \tag{B.48}$$

For the moment, I only make two approximations regarding the energy variance equation, namely that 1) the last, third-order term in Equation B.46 is negligible in front of all others, especially the third-to-last term, which is only second-order, and 2) the fluctuating contribution of molecular forces (i.e. the second term on the right-hand side of Equation B.47) is negligible compared to its radiative counterpart (i.e. the last term in Equation B.48). Other than that, we retain all other terms, and, using the plane-parallel geometry to simplify several indices contractions, one finds

$$\begin{aligned}&\frac{\partial\overline{\rho}\widetilde{e^2}}{\partial t}+\frac{\partial\overline{\rho}\widetilde{e^{\prime\prime 2}}}{\partial t}+\frac{\partial}{\partial x}\overline{\rho}\left(\widetilde{e^2}\widetilde{u_v}+2\widetilde{e}F_e+\widetilde{u_v}\widetilde{e^{\prime\prime 2}}+\widetilde{e^{\prime\prime 2}u_v^{\prime\prime}}\right)\\&=-2\widetilde{e}\overline{p}\frac{\partial\widetilde{u_v}}{\partial x}-2\overline{e^{\prime\prime}p}\frac{\partial\widetilde{u_v}}{\partial x}-2\widetilde{e}\overline{p}\frac{\partial\overline{u_v^{\prime\prime}}}{\partial x}-2\overline{e^{\prime\prime}p^{\prime}}\frac{\partial\widetilde{u_v}}{\partial x}-2\overline{p}\overline{e^{\prime\prime}\frac{\partial u_i^{\prime\prime}}{\partial x_i}}-2\widetilde{e}\overline{p^{\prime}\frac{\partial u_i^{\prime\prime}}{\partial x_i}}+2\widetilde{e}\overline{\rho}\widetilde{\epsilon}-2\widetilde{e}\frac{\partial\overline{F^{\mathrm{rad}}}}{\partial x}-2\overline{e^{\prime\prime}\frac{\partial F_i^{\mathrm{rad}}}{\partial x_i}}\,.\end{aligned}\tag{B.49}$$

The first-order terms on the left-hand side can be expanded to reveal that they all vanish. Indeed, using Equation B.21 with $Q=\widetilde{e}^2$, one finds

$$\frac{\partial\overline{\rho}\widetilde{e}^2}{\partial t}+\frac{\partial\overline{\rho}\widetilde{e}^2\widetilde{u_v}}{\partial x}=\overline{\rho}\frac{D\widetilde{e}^2}{Dt}=2\overline{\rho}\widetilde{e}\frac{D\widetilde{e}}{Dt}\,.\tag{B.50}$$

Replacing $D\widetilde{e}/Dt$ by Equation B.12, the energy variance equation becomes

$$\frac{\partial\overline{\rho}\widetilde{e^{\prime\prime 2}}}{\partial t}+2\overline{\rho}F_e\frac{\partial\widetilde{e}}{\partial x}+\frac{\partial\overline{\rho}\widetilde{u_v}\widetilde{e^{\prime\prime 2}}}{\partial x}+\frac{\partial\overline{\rho}\widetilde{e^{\prime\prime 2}u_v^{\prime\prime}}}{\partial x}=-2\overline{e^{\prime\prime}p}\frac{\partial\widetilde{u_v}}{\partial x}-2\overline{e^{\prime\prime}p^{\prime}}\frac{\partial\widetilde{u_v}}{\partial x}-2\overline{p}\overline{e^{\prime\prime}\frac{\partial u_i^{\prime\prime}}{\partial x_i}}-2\overline{e^{\prime\prime}\frac{\partial F_i^{\mathrm{rad}}}{\partial x_i}}\,.\tag{B.51}$$

Finally, using Equation B.21 with $Q=\widetilde{e^{\prime\prime 2}}$, the first and third terms on the left-hand side of Equation B.51 yield $\overline{\rho}D\widetilde{e^{\prime\prime 2}}/Dt$. To shorten notations, and in analogy to the notations I used for the Reynolds stress tensor, I will denote the energy variance $\widetilde{e^{\prime\prime 2}}$ as R_e, in which case the energy variance equation finally reads

$$\overline{\rho}\frac{DR_e}{Dt}+\frac{\partial\overline{\rho}\widetilde{e^{\prime\prime 2}u_v^{\prime\prime}}}{\partial x}=-2\overline{\rho}F_e\frac{\partial\widetilde{e}}{\partial x}-2\overline{e^{\prime\prime}p}\frac{\partial\widetilde{u_v}}{\partial x}-2\overline{e^{\prime\prime}p^{\prime}}\frac{\partial\widetilde{u_v}}{\partial x}-2\overline{p}\overline{e^{\prime\prime}\frac{\partial u_i^{\prime\prime}}{\partial x_i}}-2\overline{e^{\prime\prime}\frac{\partial F_i^{\mathrm{rad}}}{\partial x_i}}\,.\tag{B.52}$$

B.2.4 Convective flux

Multiplying Equation B.11 by e and Equation B.12 by u_v, and adding them together, one finds

$$\frac{\partial\rho eu_v}{\partial t}+\frac{\partial\rho eu_vu_i}{\partial x_i}=-e\frac{\partial p}{\partial x}-pu_v\frac{\partial u_i}{\partial x_i}-\rho eg+e\frac{\partial\sigma_{vi}}{\partial x_i}+u_v\sigma_{ij}\frac{\partial u_j}{\partial x_i}-u_v\frac{\partial F_i^{\mathrm{rad}}}{\partial x_i}\,.\tag{B.53}$$

The Reynolds average of these various terms yields

$$\overline{\rho eu_v}=\overline{\rho}\widetilde{e}\widetilde{u_v}+\overline{\rho}F_e\,,\tag{B.54}$$

$$\overline{\rho eu_v^2}=\overline{\rho}\widetilde{e}\widetilde{u_v}^2+2\overline{\rho}\widetilde{u_v}F_e+\overline{\rho}\widetilde{e}R_v+\overline{\rho}\widetilde{e^{\prime\prime}u_v^{\prime\prime 2}}\,,\tag{B.55}$$

$$\overline{e\frac{\partial p}{\partial x}}=\widetilde{e}\frac{\partial\overline{p}}{\partial x}+\overline{e^{\prime\prime}}\frac{\partial\overline{p}}{\partial x}+\overline{e^{\prime\prime}\frac{\partial p^{\prime}}{\partial x}}\,,\tag{B.56}$$

$$\overline{pu_v\frac{\partial u_i}{\partial x_i}}=\overline{p}\widetilde{u_v}\frac{\partial\widetilde{u_v}}{\partial x}+\overline{p}\widetilde{u_v}\frac{\partial\overline{u_v^{\prime\prime}}}{\partial x}+\overline{pu_v^{\prime\prime}}\frac{\partial\widetilde{u_v}}{\partial x}+\overline{p^{\prime}u_v^{\prime\prime}}\frac{\partial\widetilde{u_v}}{\partial x}+\widetilde{u_v}\overline{p^{\prime}\frac{\partial u_i^{\prime\prime}}{\partial x_i}}+\overline{p}\overline{u_v^{\prime\prime}\frac{\partial u_i^{\prime\prime}}{\partial x_i}}+\overline{p^{\prime}u_v^{\prime\prime}\frac{\partial u_i^{\prime\prime}}{\partial x_i}}\,,\tag{B.57}$$

$$\overline{\rho eg}=\overline{\rho}\widetilde{e}g\,,\tag{B.58}$$

$$\overline{e\frac{\partial\sigma_{vi}}{\partial x_i}}=\widetilde{e}\frac{\partial\overline{\sigma_{vi}}}{\partial x_i}+\overline{e^{\prime\prime}\frac{\partial\sigma_{vi}}{\partial x_i}}\,,\tag{B.59}$$

$$\overline{u_v\sigma_{ij}\frac{\partial u_j}{\partial x_i}}=\overline{\rho}\widetilde{\epsilon}\widetilde{u_v}+\overline{u_v^{\prime\prime}\sigma_{ij}\frac{\partial u_j}{\partial x_i}}\,,\tag{B.60}$$

$$\overline{u_v\frac{\partial F_i^{\mathrm{rad}}}{\partial x_i}}=\widetilde{u_v}\frac{\partial\overline{F_i^{\mathrm{rad}}}}{\partial x_i}+\overline{u_v^{\prime\prime}\frac{\partial F_i^{\mathrm{rad}}}{\partial x_i}}\,.\tag{B.61}$$

Similarly to what I did with the energy variance equation, I only make two approximations for the moment: 1) I neglect the last term on the right-hand side of Equation B.56 compared to the second-to-last term, and 2) I neglect the correlation of molecular forces with fluctuating velocity and energy (i.e. the last terms on the right-hand sides of Equations B.59 and B.60) compared to their radiative counterpart (i.e. the last term on the right-hand side of Equation B.61). Furthermore, the first-order terms can be rearranged using Equations B.22 and B.40

$$\begin{aligned}\frac{\partial\overline{\rho}\widetilde{e}\widetilde{u_v}}{\partial t}+\frac{\partial\overline{\rho}\widetilde{e}\widetilde{u_v}^2}{\partial x}&=\overline{\rho}\frac{D\widetilde{e}\widetilde{u_v}}{Dt}=\overline{\rho e}\frac{D\widetilde{u_v}}{Dt}+\overline{\rho u_v}\frac{D\widetilde{e}}{Dt}\\&=\widetilde{e}\left(-\frac{\partial\overline{\rho}R_v}{\partial x}-\frac{\partial\overline{p}}{\partial x}-\overline{\rho}g+\frac{\partial\overline{\sigma_{vi}}}{\partial x_i}\right)+\widetilde{u_v}\left(-\frac{\partial\overline{\rho}F_e}{\partial x}-\overline{p}\frac{\partial\widetilde{u_v}}{\partial x}-\overline{p}\frac{\partial\overline{u_v'}}{\partial x}-\overline{p'\frac{\partial u_v''}{\partial x_i}}+\overline{\rho}\epsilon-\frac{\partial\overline{F_i^{\mathrm{rad}}}}{\partial x_i}\right).\end{aligned} \tag{B.62}$$

Replacing the first and third terms on the left-hand side of Equation B.53 by this expression, the equation simplifies considerably, and one finds

$$\begin{aligned}&\frac{\partial\overline{\rho}F_e}{\partial t}+\overline{\rho}R_v\frac{\partial\widetilde{e}}{\partial x}+\frac{\partial\overline{\rho}\widetilde{u_v}F_e}{\partial x}+\overline{\rho}F_e\frac{\partial\widetilde{u_v}}{\partial x}+\frac{\partial\overline{\rho}\widetilde{e''u_v''^2}}{\partial x}\\&\qquad=-\overline{e''}\frac{\partial\overline{p}}{\partial x}-\overline{e''\frac{\partial p'}{\partial x}}-\overline{u_v''}\overline{p}\frac{\partial\widetilde{u_v}}{\partial x}-\overline{p'u_v''}\frac{\partial\widetilde{u_v}}{\partial x}-\overline{\overline{p}u_v''\frac{\partial u_i''}{\partial x_i}}-\overline{u_v''\frac{\partial F_i^{\mathrm{rad}}}{\partial x_i}}.\end{aligned} \tag{B.63}$$

Finally, I use Equation B.21 with $Q=F_e$ to rearrange the first and third terms on the right-hand side, so that the convective flux equation finally reads

$$\overline{\rho}\frac{DF_e}{Dt}+\frac{\partial\overline{\rho}\widetilde{e''u_v''^2}}{\partial x}=-\overline{\rho}R_v\frac{\partial\widetilde{e}}{\partial x}-\overline{\rho}F_e\frac{\partial\widetilde{u_v}}{\partial x}-\overline{e''}\frac{\partial\overline{p}}{\partial x}-\overline{e''\frac{\partial p'}{\partial x}}-\overline{u_v''}\overline{p}\frac{\partial\widetilde{u_v}}{\partial x}-\overline{p'u_v''}\frac{\partial\widetilde{u_v}}{\partial x}-\overline{\overline{p}u_v''\frac{\partial u_i''}{\partial x_i}}-\overline{u_v''\frac{\partial F_i^{\mathrm{rad}}}{\partial x_i}}. \tag{B.64}$$

B.2.5 Dissipation equation

I follow the model of Canuto (1997) for the turbulent dissipation rate in compressible flows, based on an earlier incompressible model by the same author (Canuto 1992). The exact expression for the scalar dissipation ϵ is given by

$$\epsilon=\nu\left(\overline{\omega_i''\omega_i''}+\frac{4}{3}\overline{d^2}\right)+2\nu\frac{\partial}{\partial x_j}\left(\overline{\frac{\partial u_i''u_j''}{\partial x_i}}-2\overline{du_j''}\right), \tag{B.65}$$

where ν is the fluid kinematic viscosity, ω_i is the velocity anti-symmetric strain tensor contracted with the Levi-Civita symbol, and d is the divergence of u_i''. The last bracket is a diffusion term, and could be included in the formalism. But because the Reynolds number associated to stellar turbulent convection is so large, this term would be negligible compared to the other diffusion terms, so that there is not much point accounting for it in the first place. The two remaining terms – i.e. the first bracket on the right-hand side – are referred to as the solenoidal dissipation ϵ_s and the dilation dissipation ϵ_d. In the incompressible case, $\epsilon_d=0$ and $\epsilon=\epsilon_s$. In the compressible case, ϵ_d/ϵ_s typically scales as the Mach number squared. In the low Mach number limit, characteristic of the turbulent convection close to the surface of solar-like stars, it is therefore reasonable to consider $\epsilon_d\ll\epsilon_s$, and I will, in the following, consider that $\epsilon\sim\epsilon_s$. Following Canuto (1997), I adopt (see his Eq. 28d, reformulated with my notations)

$$\begin{aligned}\overline{\rho}\frac{D\epsilon}{Dt}+\frac{\partial\overline{\rho}\widetilde{\epsilon''u_v''}}{\partial x}&=C_{\epsilon1}\overline{\rho}\frac{\partial\widetilde{u_v}}{\partial x}\left(\frac{2}{3}-\left(\frac{1}{2}+\frac{R_h}{R_v}\right)^{-1}\right)\epsilon-C_{\epsilon2}\left(\frac{1}{2}R_v+R_h\right)^{-1}\overline{\rho}\epsilon^2\\&\quad-C_{\epsilon3}\overline{u_v''}\left(\frac{1}{2}R_v+R_h\right)^{-1}\frac{\partial\overline{p}}{\partial x}\epsilon-\frac{4}{3}\overline{\rho}\frac{\partial\widetilde{u_v}}{\partial x}\epsilon,\end{aligned} \tag{B.66}$$

where I deliberately left the second term on the left-hand side – i.e. the small-scale advection term – in its exact form. The phenomenological constants appearing in this equation are given by Sarkar et al. (1989): $C_{\epsilon1}=1.44$, $C_{\epsilon2}=4/3$, $C_{\epsilon3}=0.1$ and $C_{\epsilon4}=1.83$.

B.2.6 Closure relations

So far, the system of Reynolds-averaged equations, to which the Lagrangian stochastic model developed in Section B.3 should reduce, is comprised of Equations B.17, B.22, B.35, B.36, B.40, B.52, B.64 and B.66. But these equations still feature several second-order moments which require closing. I split them into three categories in the following.

Algebraic moments

Those are the second-order moments which do not include any gradient. They can be closed by using Equations B.14 and B.15, as well as the following identity, valid for any quantity Q decomposed according to its Favre average, and readily deduced from the fact that $\widetilde{Q''} = 0$

$$\overline{Q''} = -\frac{\overline{\rho' Q''}}{\overline{\rho}} \,. \tag{B.67}$$

One finds

$$\overline{u_v''} = -\frac{m}{\widetilde{e}} F_e \,, \tag{B.68}$$

$$\overline{p' u_v''} = \gamma m (\Gamma_1 - 1) \overline{\rho} F_e \,, \tag{B.69}$$

$$\overline{e''} = -\frac{m}{\widetilde{e}} R_e \,, \tag{B.70}$$

$$\overline{e'' p'} = \gamma m (\Gamma_1 - 1) \overline{\rho} R_e \,. \tag{B.71}$$

$$\tag{B.72}$$

Gradient moments

Those are the second-order moments featuring a fluctuating gradient, either of pressure or velocity. I already discussed one of them in Section 7.2.2 in the scope of incompressible flows, namely the *velocity-pressure-gradient* tensor Π_{ij}, which I recall is defined by

$$\Pi_{ij} \equiv \overline{u_i'' \frac{\partial p'}{\partial x_j}} + \overline{u_j'' \frac{\partial p'}{\partial x_i}} \,. \tag{B.73}$$

It is customary to decompose this tensor in the following way

$$\Pi_{ij} = \frac{\partial \overline{p' u_i''}}{\partial x_j} + \frac{\partial \overline{p' u_j''}}{\partial x_i} + \underbrace{\overline{p' \left(\frac{\partial u_j''}{\partial x_i} + \frac{\partial u_i''}{\partial x_j} \right)}}_{\equiv \mathcal{R}_{ij}} \,, \tag{B.74}$$

where $\mathcal{R}_{ij}$ is the *pressure-rate-of-strain* tensor (not to be confused with the Reynolds stress tensor R_{ij}). In Section 7.2.2, I discussed the various models for Π_{ij} with the assumption that $\frac{\partial \overline{p' u_i''}}{\partial x_j} + \frac{\partial \overline{p' u_j''}}{\partial x_i} = 0$, so that $\Pi_{ij} = \mathcal{R}_{ij}$. But here, the acoustic flux $\overline{p' u_i''}$ is already in closed form (see Equation B.69), so that the velocity-pressure-gradient and pressure-strain tensors are not equal: the closure models discussed in Section 7.2.2 then pertain to $\mathcal{R}_{ij}$, not Π_{ij}. I will consider the simplest model possible for this tensor, which is Rotta's return-to-isotropy model (see Section 7.2.2)

$$\mathcal{R}_{ij} = -2 C_R \overline{\rho} \epsilon b_{ij} \,, \tag{B.75}$$

where b_{ij} is the normalised anisotropy tensor

$$b_{ij} = \frac{R_{ij}}{R_{kk}} - \frac{1}{3} \delta_{ij} \,. \tag{B.76}$$

This model ensures that b_{ij} decays linearly in homogeneous incompressible turbulence. The decay rate depends on the phenomenological constant C_R, which must be greater than unity, lest the anisotropy tensor grows linearly instead of decaying. Regarding its value, I follow the specification of Pope (1994b), $C_R = 4.15$.

Next, let me consider the moment $\overline{e''\partial_i u_i''}$. Using Equations B.14 and B.15, one obtains

$$\begin{aligned}
\overline{e''\frac{\partial u_i''}{\partial x_i}} &= \overline{\gamma m \frac{\overline{\rho e}}{\overline{p}} \frac{p'}{\rho} \frac{\partial u_i''}{\partial x_i}} \\
&= \frac{\gamma m \widetilde{e}}{\overline{p}} \overline{\left(1 + \frac{\rho'}{\overline{\rho}}\right)^{-1} p' \frac{\partial u_i''}{\partial x_i}} \\
&\sim \frac{\gamma m \widetilde{e}}{\overline{p}} \overline{p' \frac{\partial u_i''}{\partial x_i}} \, .
\end{aligned} \tag{B.77}$$

Here, I neglected the third order moment $\overline{\rho' p' \partial_i u_i''}$, which is most likely not going to yield a dominant contribution to the energy variance equation. Using the definition of the pressure-rate-of-strain tensor, as well as Equation B.15, one finds

$$\overline{e''\frac{\partial u_i''}{\partial x_i}} = \frac{\gamma m}{(\Gamma_1 - 1)\overline{\rho}} \mathcal{R}_{ii} \, . \tag{B.78}$$

Considering Rotta's return-to-isotropy model, the pressure-rate-of-strain tensor is traceless, and this straightforwardly reduces to $\overline{e''\partial_i u_i''} = 0$.

Next, let me consider the moment $\overline{e''\partial_x p'}$

$$\begin{aligned}
\overline{e''\frac{\partial p'}{\partial x}} &= \overline{e'' \frac{\partial}{\partial x} \left(\frac{\gamma m \overline{p}}{\overline{\rho e}} \rho e'' \right)} \\
&= \frac{\gamma m \overline{p}}{\overline{\rho e}} \overline{e'' \frac{\partial \rho e''}{\partial x}} + \overline{\rho e''^2} \frac{\partial}{\partial x} \left(\frac{gammam \overline{p}}{\overline{\rho e}} \right) \\
&\sim \frac{\gamma m \overline{p}}{2\overline{\rho e}} \frac{\partial \overline{\rho e''^2}}{\partial x} + \overline{\rho e''^2} \frac{\partial}{\partial x} \left(\frac{gammam \overline{p}}{\overline{\rho e}} \right) ,
\end{aligned} \tag{B.79}$$

where I have simplified the first term by considering that the scales on which e'' varies is much smaller than the scales on which ρ varies, so that the ρ derivative can be disregarded compared to the e'' derivative. Using the definition of R_e and Equation B.15, one finds

$$\overline{e''\frac{\partial p'}{\partial x}} = \frac{\gamma m (\Gamma_1 - 1)}{2} \frac{\partial \overline{\rho} R_e}{\partial x} + \overline{\rho} R_e \frac{\partial gammam(\Gamma_1 - 1)}{\partial x} \, . \tag{B.80}$$

As for $\overline{u_v'' \partial_i u_i''}$, I will simply retain the most dominant term, so that

$$\overline{u_v''\frac{\partial u_i''}{\partial x_i}} \sim \frac{1}{2} \frac{\partial R_v}{\partial x} \, . \tag{B.81}$$

Radiative moments

Those are all the moments that involve the radiative flux F^{rad}, i.e. its Reynolds average $\overline{F^{\mathrm{rad}}}$, as well as the second-order moments $\overline{u_v'' \frac{\partial F_i^{\mathrm{rad}}}{\partial x_i}}$ and $\overline{e'' \frac{\partial F_i^{\mathrm{rad}}}{\partial x_i}}$. These second-order moments describe how the radiative transfer correlates with the turbulent motions, and should be accounted for appropriately in a more refined model. However, for the sake of simplicity, I will discard them from the equations on the variance of the energy R_e and the energy convective flux F_e respectively. As for the mean radiative flux, it can be expressed solely in terms of the mean quantities of the flow – for instance, in the diffusion approximation, it depends on the gradient of the mean temperature, i.e. the gradient of the mean internal energy $\widetilde{e}$. I will leave it in the form $\overline{F^{\mathrm{rad}}}$ in the following.

B.2.7 Final form of the mean equations

The system of evolution equations for all first- and second-order moments of the velocity and internal energy (mean density $\overline{\rho}$, mean vertical velocity $\widetilde{u_v}$ and mean internal energy $\widetilde{e}$ for the former; vertical Reynolds stress R_v, horizontal Reynolds stress R_h, internal energy variance R_e and energy convective flux F_e for the latter) as well as the turbulent dissipation rate ϵ, comprised of Equations B.17, B.22, B.35, B.36, B.40, B.52 and B.66, combined with the closure relations derived in Section B.2.6, yield the following system of Reynolds-averaged equations, to which I will consistently refer when developing the Lagrangian stochastic model in Section B.3

$$\frac{D\overline{\rho}}{Dt} + \overline{\rho}\frac{\partial \widetilde{u_v}}{\partial x} = 0 \,, \tag{B.82}$$

$$\overline{\rho}\frac{D\widetilde{u_v}}{Dt} + \frac{\partial \overline{\rho} R_v}{\partial x} = -\frac{\partial \overline{p}}{\partial x} - g\overline{\rho} \,, \tag{B.83}$$

$$\overline{\rho}\frac{DR_v}{Dt} + \frac{\partial \overline{\rho}\widetilde{u_v''^3}}{\partial x} = -2\overline{\rho}R_v\frac{\partial \widetilde{u_v}}{\partial x} + \frac{2mF_e}{\widetilde{e}}\frac{\partial \overline{p}}{\partial x} - 2\left(\frac{\partial \gamma m(\Gamma_1 - 1)\overline{\rho}F_e}{\partial x} + \frac{2C_R\overline{\rho}\epsilon(R_v - R_h)}{3(R_v + 2R_h)}\right) - \frac{2}{3}\overline{\rho}\epsilon \,, \tag{B.84}$$

$$\overline{\rho}\frac{DR_h}{Dt} + \frac{\partial \overline{\rho}\widetilde{u_h''^2 u_v''}}{\partial x} = -\frac{2C_R\overline{\rho}\epsilon(R_h - R_v)}{3(R_v + 2R_h)} - \frac{2}{3}\overline{\rho}\epsilon \,, \tag{B.85}$$

$$\overline{\rho}\frac{D\widetilde{e}}{Dt} + \frac{\partial \overline{\rho}F_e}{\partial x} = -\overline{p}\frac{\partial \widetilde{u_v}}{\partial x} + \overline{p}\frac{\partial mF_e/\widetilde{e}}{\partial x} + \overline{\rho}\epsilon - \frac{\partial \overline{F^{\mathrm{rad}}}}{\partial x} \,, \tag{B.86}$$

$$\overline{\rho}\frac{DR_e}{Dt} + \frac{\partial \overline{\rho}\widetilde{e''^2 u_v''}}{\partial x} = -2\overline{\rho}F_e\frac{\partial \widetilde{e}}{\partial x} + \frac{2mR_e}{\widetilde{e}}\overline{p}\frac{\partial \widetilde{u_v}}{\partial x} - 2\gamma m(\Gamma_1 - 1)\overline{\rho}R_e\frac{\partial \widetilde{u_v}}{\partial x} \,, \tag{B.87}$$

$$\begin{aligned}\overline{\rho}\frac{DF_e}{Dt} + \frac{\partial \overline{\rho}\widetilde{e'' u_v''^2}}{\partial x} = &-\overline{\rho}R_v\frac{\partial \widetilde{e}}{\partial x} - \overline{\rho}F_e\frac{\partial \widetilde{u_v}}{\partial x} + \frac{mR_e}{\widetilde{e}}\frac{\partial \overline{p}}{\partial x} - \frac{1}{2}\frac{\partial \gamma m(\Gamma_1 - 1)\overline{\rho}R_e}{\partial x} - \frac{1}{2}\overline{\rho}R_e\frac{\partial \gamma m(\Gamma_1 - 1)}{\partial x} \\ &+ \frac{mF_e}{\widetilde{e}}\overline{p}\frac{\partial \widetilde{u_v}}{\partial x} - \gamma m(\Gamma_1 - 1)\overline{\rho}F_e\frac{\partial \widetilde{u_v}}{\partial x} - \frac{1}{2}\overline{p}\frac{\partial R_v}{\partial x} \,,\end{aligned} \tag{B.88}$$

$$\begin{aligned}\overline{\rho}\frac{D\epsilon}{Dt} + \frac{\partial \overline{\rho}\widetilde{\epsilon'' u_v''}}{\partial x} = &C_{\epsilon 1}\overline{\rho}\frac{\partial \widetilde{u_v}}{\partial x}\left(\frac{2}{3} - \left(\frac{1}{2} + \frac{R_h}{R_v}\right)^{-1}\right)\epsilon - C_{\epsilon 2}\left(\frac{1}{2}R_v + R_h\right)^{-1}\overline{\rho}\epsilon^2 \\ &+ C_{\epsilon 3}\frac{mF_e}{\widetilde{e}}\left(\frac{1}{2}R_v + R_h\right)^{-1}\frac{\partial \overline{p}}{\partial x}\epsilon - \frac{4}{3}\overline{\rho}\frac{\partial \widetilde{u_v}}{\partial x}\epsilon \,.\end{aligned} \tag{B.89}$$

B.3 Lagrangian stochastic model for stellar turbulent convection

In Section 7.2.3, I presented the Refined Langevin Model as a Lagrangian stochastic model for incompressible flows where the turbulent frequency $\omega_t^\star$ associated to fluid particles is modelled alongside their velocity, according to the stochastic differential equations recalled here

$$\mathrm{d}x_i^\star = u_i^\star \, \mathrm{d}t \,, \tag{B.90}$$

$$\mathrm{d}u_i^\star = \left[-\frac{1}{\overline{\rho}}\frac{\partial \overline{p}}{\partial x_i} + g_i + L_{ij}\left(u_j^\star - \overline{u_j}\right)\right] \mathrm{d}t + \sqrt{C_0\omega_t^\star k} \, \mathrm{d}W_i \,, \tag{B.91}$$

$$\mathrm{d}\omega_t^\star = -\omega_t^\star\overline{\omega_t}\left[S_\omega + C_\chi\left(\ln\left(\frac{\omega_t^\star}{\overline{\omega_t}}\right) - \frac{1}{2}\sigma^2\right)\right] \mathrm{d}t + \omega_t^\star\sqrt{2C_\chi\overline{\omega_t}\sigma^2} \, \mathrm{d}W_\omega \,, \tag{B.92}$$

where

$$L_{ij} = G_{ij} - \frac{3}{4}\left[C_0\left(\omega_t^\star - \overline{\omega_t}\right) + \Delta C_0\overline{\omega_t}\right]A_{ij}^{-1} \tag{B.93}$$

is the modified drift tensor, compared to the original drift tensor G_{ij} used in the Generalised Langevin Model, $\Delta C_0 = 1.4$ is the difference between the values of the Kolmogorov constants calibrated for the GLM and RLM, and $A_{ij} \equiv \overline{u_i'' u_j''}/(2k/3)$. In the following section, I start from the RLM and modify it in order for the underlying, corresponding Reynolds-averaged equations to coincide with the mean equations derived in Section B.2. First, I adapt the velocity SDE – both vertical and horizontal – in Section B.3.1, and the turbulent frequency SDE in Section B.3.2. Furthermore, an additional thermodynamic variable is needed, in the form of the internal energy per unit mass $e^\star$ associated to each fluid particle individually, for which I derive a SDE, on the same template as the velocity SDE, in Section B.3.3.

B.3.1 Stochastic differential equations for velocity

Adapting Equation B.91

Let me compare the mean momentum and Reynolds stress equations obtained in the incompressible case from first principles (Equations 7.79 and 7.81 respectively), on the one hand, and their compressible counterparts Equations B.83 to B.85 on the other hand. There are several key differences between the two, each of which will lead me to modify the RLM accordingly

- the modelled quantities are now Favre-averages, not Reynolds-averages. As I will soon show, this is only a consequence of Equation B.9, and does not require any modification to the stochastic model;
- some of the mean fields present in the coefficients of the mean equations are also Favre averages. This only requires the Reynolds averages appearing in the RLM (for instance k in the diffusion coefficient) to be changed to Favre averages;
- the convective flux acts as an additional source of vertical Reynolds stress compared to the incompressible case. This term needs to be added to the drift coefficient in Equation B.91. Given the definition of the convective flux, it will be proportional to the internal energy fluctuations e''. The addition of this term in the velocity equation makes it necessary to add a stochastic differential equation for the particle internal energy $e^\star$, which is the subject of Section B.3.3.

Implementing these changes in Equation B.91 yields the following stochastic model for position and velocity

$$\mathrm{d}x^\star = u_v^\star \, dt \,, \tag{B.94}$$

$$\mathrm{d}u_v^\star = \left(-\frac{1}{\overline{\rho}}\frac{\partial \overline{p}}{\partial x} - g + G_{vv}\left(u_v^\star - \widetilde{u_v}\right) + G_{hv}u_h^\star - C_0\left(\frac{1}{4} + \frac{R_h}{2R_v}\right)\left(\omega_t^\star - \widetilde{\omega_t}\right)\left(u_v^\star - \widetilde{u_v}\right) + \frac{m}{\overline{\rho e}}\frac{\partial \overline{p}}{\partial x}\left(e^\star - \widetilde{e}\right)\right) \mathrm{d}t + \left(C_0\omega_t^\star\left(\frac{R_v}{2} + R_h\right)\right)^{1/2} \mathrm{d}W_v \,, \tag{B.95}$$

$$\mathrm{d}u_h^\star = \left(G_{vh}\left(u_v^\star - \widetilde{u_v}\right) + G_{hh}u_h^\star - C_0\left(\frac{R_v}{4R_h} + \frac{1}{2}\right)\left(\omega_t^\star - \widetilde{\omega_t}\right)u_h^\star \right) \mathrm{d}t + \left(C_0\omega_t^\star\left(\frac{R_v}{2} + R_h\right)\right)^{1/2} \mathrm{d}W_h \,, \tag{B.96}$$

where I have developed the index contraction between G_{ij} and $\left(u_j - \widetilde{u_j}\right)$ – the definition of G_{vv}, G_{vh}, G_{hv} and G_{hh} are quite straightforward in that context –, and I used the fact that, the Reynolds stress tensor being diagonal, one simply has $A_{ij}^{-1} = 1/A_{ij}$. I have also redefined k as a Favre average rather than a Reynolds average, so that

$$k \equiv \frac{1}{2}\left(\widetilde{u_x''u_x''} + \widetilde{u_y''u_y''} + \widetilde{u_z''u_z''}\right) = \frac{R_v}{2} + R_h \,. \tag{B.97}$$

Equivalent mean velocity and Reynolds stress equations

First, let me derive the Fokker-Planck equation governing the evolution of the *particle Lagrangian PDF* $f_L^\star((x^\star, u_v^\star, u_h^\star); t|x_0)$ from Equations B.94 to B.96, using the relation between an Ito SDE and its underlying Fokker-Planck equation introduced in Section 7.1.3

$$\begin{aligned}\frac{\partial f_L^\star}{\partial t} = &-\frac{\partial u_v^\star f_L^\star}{\partial x^\star} + \left(\frac{1}{\overline{\rho}}\frac{\partial \overline{p}}{\partial x} + g\right)\frac{\partial f_L^\star}{\partial u_v^\star} - G_{vv}\frac{\partial (u_v^\star - \widetilde{u_v})f_L^\star}{\partial u_v^\star} - G_{hv}\frac{\partial u_h^\star f_L^\star}{\partial u_v^\star} + C_0\left(\frac{1}{4} + \frac{R_h}{2R_v}\right)\frac{\partial (\omega_t^\star - \widetilde{\omega_t})(u_v^\star - \widetilde{u_v})f_L^\star}{\partial u_v^\star} \\ &- \frac{m}{2\overline{\rho e}}\frac{\partial \overline{p}}{\partial x}\frac{\partial (e^\star - \widetilde{e})f_L^\star}{\partial u_v^\star} - G_{vh}\frac{\partial (u_v^\star - \widetilde{u_v})f_L^\star}{\partial u_h^\star} - G_{hh}\frac{\partial u_h^\star f_L^\star}{\partial u_h^\star} + C_0\left(\frac{R_v}{4R_h} + \frac{1}{2}\right)\frac{\partial (\omega_t^\star - \widetilde{\omega_t})u_h^\star f_L^\star}{\partial u_h^\star} \\ &+ \frac{1}{2}C_0\left(\frac{R_v}{2} + R_h\right)\left(\frac{\partial^2 \omega_t^\star f_L^\star}{\partial u_v^{\star 2}} + \frac{\partial^2 \omega_t^\star f_L^\star}{\partial u_h^{\star 2}}\right) \,,\end{aligned} \tag{B.98}$$

where I have used the fact that the drift tensor G_{ij}, as well as the various mean quantities, do not depend on the stochastic variables themselves, and can therefore be pulled out of the derivatives with respect to $x^\star$, $u_v^\star$ and $u_h^\star$. Then, the fundamental assumption behind stochastic particle models is that for any x_0, one has

$$f_L^\star(x^\star, u_v^\star, u_h^\star, t|x_0) = f_L(x = x^\star, u_v = u_v^\star, u_h = u_h^\star, t|x_0) \,, \tag{B.99}$$

so that Equation B.98 also governs the evolution of the flow Lagrangian PDF f_L. From there, Equation B.9 allows me to derive the Eulerian PDF equation. Indeed, the initial density $\rho(x_0,t_0)$ depends on neither x, t, u_v nor u_h, so that multiplying Equation B.98 by $\rho(x_0,t_0)$, the latter can be included within all derivatives. I then integrate over x_0, and use Equation B.9 to obtain

$$\begin{aligned}
&\frac{\partial}{\partial t}\left(\int d\rho'\rho' f_E\right) = -\frac{\partial}{\partial x}\left(\int d\rho'\rho' u_v f_E\right) + \left(\frac{1}{\overline{\rho}}\frac{\partial \overline{p}}{\partial x} + g\right)\int d\rho' \frac{\partial \rho' f_E}{\partial u_v} - G_{vv}\int d\rho' \frac{\partial \rho'(u_v-\widetilde{u_v})f_E}{\partial u_v} \\
&- G_{hv}\int d\rho' \frac{\partial \rho' u_h f_E}{\partial u_v} + C_0\left(\frac{1}{4}+\frac{R_h}{2R_v}\right)\int d\rho' \frac{\partial \rho'(\omega_t-\widetilde{\omega_t})(u_v-\widetilde{u_v})f_E}{\partial u_v} - \frac{m}{\overline{\rho e}}\frac{\partial \overline{p}}{\partial x}\int d\rho' \frac{\partial \rho'(e-\widetilde{e})f_E}{\partial u_v} \\
&- G_{vh}\int d\rho' \frac{\partial \rho'(u_v-\widetilde{u_v})f_E}{\partial u_h} - G_{hh}\int d\rho' \frac{\partial \rho' u_h f_E}{\partial u_h} + C_0\left(\frac{R_v}{4R_h}+\frac{1}{2}\right)\int d\rho' \frac{\partial \rho'(\omega_t-\widetilde{\omega_t})u_h f_E}{\partial u_h} \\
&\qquad + \frac{1}{2}C_0\left(\frac{R_v}{2}+R_h\right)\int d\rho'\left(\frac{\partial^2 \rho'\omega_t f_E}{\partial u_v^2} + \frac{\partial^2 \rho'\omega_t f_E}{\partial u_h^2}\right), \qquad \text{(B.100)}
\end{aligned}$$

where I have used the fact that G_{ij}, C_0, as well as the mean fields, depend on x and t, but not u_v or u_h.

Then, multiplying Equation B.100 by any arbitrary quantity $Q(u_v,u_h,x,t)$ and integrating over both u_v and u_h, it can be seen that one obtains an evolution equation for the Favre average of $Q(x,t)$, not its Reynolds average. Applying this for $Q=1$, u_v, $(u_v-\widetilde{u_v})^2$ and u_h^2 respectively, one finds the following mean equations

$$\frac{\partial \overline{\rho}}{\partial t} = -\frac{\partial \overline{\rho u_v}}{\partial x}, \qquad \text{(B.101)}$$

$$\frac{\partial \overline{\rho u_v}}{\partial t} = -\frac{\partial \overline{\rho u_v^2}}{\partial x} - \left(\frac{1}{\overline{\rho}}\frac{\partial \overline{p}}{\partial x}+g\right)\overline{\rho} + G_{vv}\overline{\rho u_v''} + G_{hv}\overline{\rho u_h''} - C_0\left(\frac{1}{4}+\frac{R_h}{2R_v}\right)\overline{\rho\omega_t'' u_v''} + \frac{m}{\overline{\rho e}}\frac{\partial \overline{p}}{\partial x}\overline{\rho e''}, \qquad \text{(B.102)}$$

$$\begin{aligned}
\frac{\partial \overline{\rho u_v''^2}}{\partial t} &= -2\overline{\rho u_v''}\frac{\partial \widetilde{u_v}}{\partial t} - \frac{\partial \overline{\rho u_v''^2 u_v}}{\partial x} - 2\overline{\rho u_v'' u_v}\frac{\partial \widetilde{u_v}}{\partial x} - 2\left(\frac{1}{\overline{\rho}}\frac{\partial \overline{p}}{\partial x} - g\right)\overline{\rho u_v''} + 2G_{vv}\overline{\rho u_v''^2} + 2G_{hv}\overline{\rho u_v'' u_h''} \\
&\quad - 2C_0\left(\frac{1}{4}+\frac{R_h}{2R_v}\right)\overline{\rho\omega_t'' u_v''^2} + \frac{2m}{\overline{\rho e}}\frac{\partial \overline{p}}{\partial x}\overline{\rho u_v'' e''} + C_0\left(\frac{R_v}{2}+R_h\right)\overline{\rho\omega_t}, \qquad \text{(B.103)}
\end{aligned}$$

$$\frac{\partial \overline{\rho u_h''^2}}{\partial t} = -\frac{\partial \overline{\rho u_h''^2 u_v}}{\partial x} + 2G_{hh}\overline{\rho u_h''^2} + 2G_{vh}\overline{\rho u_v'' u_h''} - 2C_0\left(\frac{R_v}{4R_h}+\frac{1}{2}\right)\overline{\rho\omega_t'' u_h''^2} + C_0\left(\frac{R_v}{2}+R_h\right)\overline{\rho\omega_t}. \qquad \text{(B.104)}$$

The evaluation of the time and space derivatives in the PDF equation for $Q=(u_v-\widetilde{u_v})^2$ involves a tiny subtlety, because unlike the other quantities, it explicitly depends on x and t (through $\widetilde{u_v}$). As such, it does not commute with the partial derivatives with respect to t or x. The corresponding terms can however be computed thus

$$\begin{aligned}
&\int \mathrm{d}u_v \int \mathrm{d}u_h\, (u_v-\widetilde{u_v})^2 \frac{\partial}{\partial t}\left(\int \mathrm{d}\rho'\, \rho' f_E\right) \\
&= \int \mathrm{d}u_v \int \mathrm{d}u_h \int \mathrm{d}\rho'\, (u_v-\widetilde{u_v})^2 \frac{\partial \rho' f_E}{\partial t} \\
&= \int \mathrm{d}u_v \int \mathrm{d}u_h \int \mathrm{d}\rho'\, \frac{\partial \rho'(u_v-\widetilde{u_v})^2 f_E}{\partial t} - \int \mathrm{d}u_v \int \mathrm{d}u_h \int \mathrm{d}\rho'\, \rho' f_E \frac{\partial (u_v-\widetilde{u_v})^2}{\partial t} \\
&= \frac{\partial}{\partial t}\left(\int \mathrm{d}u_v \int \mathrm{d}u_h \int \mathrm{d}\rho'\, \rho'(u_v-\widetilde{u_v})^2 f_E\right) + \int \mathrm{d}u_v \int \mathrm{d}u_h \int \mathrm{d}\rho'\, \rho' f_E \times 2(u_v-\widetilde{u_v})\frac{\partial \widetilde{u_v}}{\partial t} \\
&= \frac{\partial \overline{\rho u_v''^2}}{\partial t} + 2\overline{\rho u_v''}\frac{\partial \widetilde{u_v}}{\partial t}, \qquad \text{(B.105)}
\end{aligned}$$

and similarly

$$\int \mathrm{d}u_v \int \mathrm{d}u_h (u_v-\widetilde{u_v})^2 \frac{\partial}{\partial x}\left(\int \mathrm{d}\rho'\, \rho' u_v f_E\right) = \frac{\partial \overline{\rho u_v''^2 u_v}}{\partial x} + 2\overline{\rho u_v'' u_v}\frac{\partial \widetilde{u_v}}{\partial x}. \qquad \text{(B.106)}$$

The last term of both equations lead to the first and third terms on the right-hand side of both Equations B.103 and B.104, which is why they have no equivalent in the other mean equations.

Using Equation B.101 to rearrange the left-hand side and the first term of the right-hand side on each of Equations B.102 to B.104, and using the definition of the Favre fluctuations to write $\overline{\rho Q''} = 0$ for any quantity Q, Equations B.101 to B.104 can be drastically reduced. It can be even more drastically reduced if one remembers that the RLM from which I started was derived *with the assumption that the random variables u_v and ω (or u_h and ω) are independent*. In that case, the terms proportional to $\overline{\rho u_v'' \omega''}$, $\overline{\rho \omega'' u_v''^2}$ and $\overline{\rho \omega'' u_h''^2}$ vanish. Finally, one obtains

$$\frac{D\overline{\rho}}{Dt} + \overline{\rho}\frac{\partial \widetilde{u_v}}{\partial x} = 0 \,, \tag{B.107}$$

$$\frac{D\widetilde{u_v}}{Dt} + \frac{1}{\overline{\rho}}\frac{\partial \overline{\rho} R_v}{\partial x} = -\frac{1}{\overline{\rho}}\frac{\partial \overline{p}}{\partial x} - g \,, \tag{B.108}$$

$$\frac{DR_v}{Dt} + \frac{1}{\overline{\rho}}\frac{\partial \widetilde{\overline{\rho} u_v''^3}}{\partial x} = -2R_v\frac{\partial \widetilde{u_v}}{\partial x} + 2G_{vv}R_v + \frac{2m}{\widetilde{\rho e}}\frac{\partial \overline{p}}{\partial x}F_e + C_0\left(\frac{R_v}{2} + R_h\right)\widetilde{\omega_t} \,, \tag{B.109}$$

$$\frac{DR_h}{Dt} + \frac{1}{\overline{\rho}}\frac{\partial \widetilde{\overline{\rho} u_h''^2 u_v''}}{\partial x} = 2G_{hh}R_h + C_0\left(\frac{R_v}{2} + R_h\right)\widetilde{\omega_t} \,. \tag{B.110}$$

Upon comparing Equations B.107 to B.110, on the one hand, to Equations B.82 to B.85 on the other hand, it is apparent that, exactly as in the RLM, the mean continuity and momentum equations are identical, while the only terms that are not modelled exactly in the Reynolds stress equations are the velocity-pressure-gradient and the dissipation. Identifying the two sets of equations with one another, one finds

$$\frac{1}{\overline{\rho}}\frac{\partial \gamma m(\Gamma_1 - 1)\overline{\rho}F_e}{\partial x} + \left(\frac{2C_R(R_v - R_h)}{3(R_v + 2R_h)} + \frac{1}{3}\right)\epsilon = -G_{vv}R_v - \frac{1}{2}C_0\left(\frac{R_v}{2} + R_h\right)\widetilde{\omega_t} \,, \tag{B.111}$$

$$\left(\frac{C_R(R_h - R_v)}{3(R_v + 2R_h)} + \frac{1}{3}\right)\epsilon = -G_{hh}R_h - \frac{1}{2}C_0\left(\frac{R_v}{2} + R_h\right)\widetilde{\omega_t} \,, \tag{B.112}$$

where I recall that $\epsilon = k\widetilde{\omega_t}$. I mentioned in Section 7.2.2 that the drift tensor G_{ij} is usually decomposed into

$$G_{vv} \equiv G_{vv}^a - \left(\frac{1}{2} + \frac{3}{4}C_0\right)\widetilde{\omega_t} \,, \tag{B.113}$$

$$G_{hh} \equiv G_{hh}^a - \left(\frac{1}{2} + \frac{3}{4}C_0\right)\widetilde{\omega_t} \,, \tag{B.114}$$

where G_{ij}^a constitutes the anisotropic part of the drift tensor and the other term is the isotropic drift tensor, to which G_{ij} reduces exactly in the incompressible homogeneous limit. Injecting Equations B.113 and B.114 in Equations B.111 and B.112, one finds the following expressions for the anisotropic drift tensor

$$G_{vv}^a = -\frac{1}{\overline{\rho}R_v}\frac{\partial \gamma m(\Gamma_1 - 1)\overline{\rho}F_e}{\partial x} + \widetilde{\omega_t}\left(\frac{R_h}{R_v} - 1\right)\left[\frac{1}{3}(C_R - 1) - \frac{1}{2}C_0\right] \,, \tag{B.115}$$

$$G_{hh}^a = \widetilde{\omega_t}\left(\frac{R_v}{R_h} - 1\right)\left[\frac{1}{6}(C_R - 1) - \frac{1}{4}C_0\right] \,. \tag{B.116}$$

It appears, in particular, that the two sources of drift anisotropy are the anisotropy of the Reynolds stress tensor itself, and the gradient of the vertical convective flux. With the drift tensor given by these specifications, the Kolmogorov constant given by $C_0 = 3.5$ in the scope of the RLM, and the Rotta constant given by $C_R = 1 + 3C_0/2 = 6.25$ (Pope 1994b), then Equations B.94 to B.96 forms a closed stochastic model for the position and velocity of the fluid particles representing the flow.

B.3.2 Stochastic differential equation for dissipation

I will retain the same SDE for turbulent frequency as in the RLM (see Equation B.92), with the only change being in the specific form taken by S_ω, which I recall represents the nondimensional decay rate of the mean turbulent frequency $\widetilde{\omega_t}$. The inclusion of Equation B.92 in the Lagrangian stochastic model leads to the addition

of the following contributions in the Fokker-Planck equation on the Eulerian flow PDF f_E

$$\frac{\partial}{\partial t}\left(\int d\rho' \rho' f_E\right) = [...] + \widetilde{\omega_t} S_\omega \int d\rho' \frac{\partial \rho' \omega_t f_E}{\partial \omega_t} + C_\chi \widetilde{\omega_t} \int d\rho' \frac{\partial}{\partial \omega_t}\left(\rho' \omega_t \left(\ln \frac{\omega_t}{\widetilde{\omega_t}} - \frac{1}{2}\sigma^2\right) f_E\right) + C_\chi \widetilde{\omega_t} \sigma^2 \int d\rho' \frac{\partial^2 \rho' \omega_t^2 f_E}{\partial \omega_t^2} , \quad \text{(B.117)}$$

where [...] refers to the right-hand side of Equation B.100.

In order to derive which form S_ω should take, let me derive the mean dissipation equation for ϵ stemming from Equation B.92, which I will then be able to compare to Equation B.89. Making use of Ito's formula (Equation 7.51) to perform the change of stochastic variables $\omega_t^\star \mapsto \epsilon^\star \equiv \omega_t^\star k(x^\star)$, one finds

$$\mathrm{d}\epsilon^\star = \left(u_v^\star \epsilon^\star \left.\frac{\partial \ln k}{\partial x}\right|_{x^\star} - \frac{1}{k}\epsilon^\star \widetilde{\epsilon}\left[S_\omega + C_\chi\left(\ln\left(\frac{\epsilon^\star}{\widetilde{\epsilon}}\right) - \frac{1}{2}\sigma^2\right)\right]\right) \mathrm{d}t + k^{-3/2}\epsilon^\star \sqrt{2C_\chi \widetilde{\epsilon}\sigma^2}\, \mathrm{d}W . \quad \text{(B.118)}$$

This yields the following evolution equation for $\widetilde{\epsilon}$

$$\overline{\rho}\frac{D\widetilde{\epsilon}}{Dt} + \frac{\partial \overline{\rho}\widetilde{\epsilon''u_v''}}{\partial x} = \overline{\rho}\widetilde{\epsilon u_v}\frac{\partial \ln \widetilde{k}}{\partial x} - \overline{\rho}\frac{\widetilde{\epsilon}^2}{\widetilde{k}} S_\omega . \quad \text{(B.119)}$$

Comparing this mean dissipation equation with Equation B.89, one finds

$$\overline{\rho}\widetilde{\epsilon u_v}\frac{\partial \ln k}{\partial x} - \overline{\rho}\frac{\widetilde{\epsilon}^2}{k} S_\omega = C_{\epsilon 1}\overline{\rho}\frac{\partial \widetilde{u_v}}{\partial x}\left[\frac{2}{3} - \left(\frac{1}{2} + \frac{R_v}{R_h}\right)^{-1}\right]\widetilde{\epsilon} - C_{\epsilon 2}\frac{\overline{\rho}\widetilde{\epsilon}^2}{k} + C_{\epsilon 3}\frac{mF_e}{\overline{\rho}\widetilde{\epsilon}k}\frac{\partial \overline{p}}{\partial x}\widetilde{\epsilon} - \frac{4}{3}\overline{\rho}\frac{\partial \widetilde{u_v}}{\partial x}\widetilde{\epsilon} . \quad \text{(B.120)}$$

Remarking that the model was derived with the assumption that dissipation and velocity are independent, so that $\widetilde{\epsilon u_v} = \widetilde{\epsilon}\widetilde{u_v}$, one can finally isolate S_ω to find

$$S_\omega = \frac{1}{\widetilde{\omega_t}}\left[\widetilde{u_v}\frac{\partial \ln k}{\partial x} + \left[\frac{4}{3} - C_{\epsilon 1}\left(\frac{2}{3} - \left(\frac{1}{2} + \frac{R_v}{R_h}\right)^{-1}\right)\right]\frac{\partial \widetilde{u_v}}{\partial x} - C_{\epsilon 3}\frac{mF_e}{\overline{\rho}\widetilde{\epsilon}k}\frac{\partial \overline{p}}{\partial x}\right] + C_{\epsilon 2} . \quad \text{(B.121)}$$

One can give a succinct physical interpretation of each term

- the first term is a consequence of the implicit assumption that it is $\widetilde{\epsilon}$, rather than $\widetilde{\omega_t}$, which is conserved when a particle moves through a region of inhomogeneous turbulent kinetic energy. Had I made the opposite assumption, this term would have disappeared from the definition of S_ω, but a similar term would have appeared instead in Equation B.89;

- the second term is a compressibility term, which vanishes in the incompressible limit. It is comprised of an isotropic contribution (the $4/3$ in the brackets) and an anisotropic contribution, which vanishes in isotropic turbulence (because then one would have $R_h = R_v$). This term tends to make $\widetilde{\omega_t}$ decay faster as the mean density locally decreases;

- the third term represents the fact that the convective flux acts as a source of turbulence: the stronger the convective flux, the faster $\widetilde{\omega_t}$ increases (or decreases, depending on whether the convective flux works along or against the mean pressure gradient);

- the last constant contribution corresponds to the nondimensional decay rate to which S_ω reduces in homogeneous turbulence in the standard dissipation model.

Together, Equation B.92, Equation B.121 and the specifications of the phenomenological constants σ^2, C_χ and $C_{\epsilon i}$ ($i = 1, 2, 3$) form a closed stochastic model for dissipation. I follow Pope and Chen (1990) and adopt the values $\sigma^2 = 1$, $C_\chi = 1.6$, $C_{\epsilon 1} = 1.44$, $C_{\epsilon 2} = 1.83$ and $C_{\epsilon 3} = 0.1$.

B.3.3 Stochastic differential equation for internal energy

Following the same template as Equation B.91 for the velocity SDE in the RLM, I write the SDE for internal energy as (see also Heinz 2013, Eq. 5.90c)

$$\mathrm{d}e^\star = \left(A + G_{ee}(e^\star - \widetilde{e}) + G_{ev}(u_v^\star - \widetilde{u_v}) + G_{eh}u_h^\star\right)\,\mathrm{d}t + \sqrt{\frac{3}{2}C_e\omega_t^\star R_e}\,\mathrm{d}W\,, \tag{B.122}$$

characterised by 1) a mean energy drift coefficient A, 2) the coefficients G_{ee}, G_{ev} and G_{eh}, which extend the velocity drift tensor G_{ij} to a joint velocity-energy drift tensor, and 3) the diffusion coefficient C_e, which plays for internal energy the role that the Kolmogorov constant plays for velocity. These coefficients may depend on the mean fields, but not on the stochastic variables themselves. Furthermore, they may be constrained by comparing the equivalent Reynolds-averaged equations for mean energy, energy variance and convective flux, to their first-principles respective counterparts given by Equations B.86 to B.88, which I set out to do in the following.

Equivalent mean energy and energy variance equations

The inclusion of Equation B.122 in the Lagrangian stochastic model leads to the addition of the following contributions in the Fokker-Planck equation on the Eulerian flow PDF f_E

$$\begin{aligned}\frac{\partial}{\partial t}\left(\int d\rho'\rho' f_E\right) = [...] - A\int d\rho'\frac{\partial \rho' f_E}{\partial e} - G_{ee}\int \mathrm{d}\rho'\,\frac{\partial \rho'(e-\widetilde{e})f_E}{\partial e} \\ - G_{ev}\int \mathrm{d}\rho'\,\frac{\partial \rho'(u_v-\widetilde{u_v})f_E}{\partial e} - G_{eh}\int \mathrm{d}\rho'\,\frac{\partial \rho' u_h f_E}{\partial e} + \frac{3}{4}C_eR_e\int \mathrm{d}\rho'\,\frac{\partial^2 \rho'\omega f_E}{\partial e^2}\,,\end{aligned} \tag{B.123}$$

where [...] refers to the sum of the right-hand sides of Equations B.100 and B.117. Multiplying Equation B.100 + Equation B.117 + Equation B.123 by e and $(e-\widetilde{e})^2$ alternatively, and integrating over the entire parameter space – i.e. over u_v, u_h, ω_t and e –, one finds the evolution equations for $\widetilde{e}$ and R_e

$$\frac{\partial \overline{\rho e}}{\partial t} = -\frac{\partial \overline{\rho u_v e}}{\partial x} + A\overline{\rho}\,, \tag{B.124}$$

$$\frac{\partial \overline{\rho e''^2}}{\partial t} = -\frac{\partial \overline{\rho e''^2 u_v}}{\partial x} - 2\overline{\rho e'' u_v}\frac{\partial \widetilde{e}}{\partial x} + 2G_{ee}\overline{\rho e''^2} + 2G_{ev}\overline{\rho e'' u_v''} + 2G_{eh}\overline{\rho e'' u_h''} + \frac{3}{2}C_eR_e\overline{\rho\omega_t}\,, \tag{B.125}$$

or, using the definition of the Favre average, the plane-parallel geometry of the flow, as well as Equation B.21

$$\overline{\rho}\frac{D\widetilde{e}}{Dt} + \frac{\partial \overline{\rho}F_e}{\partial x} = A\overline{\rho}\,, \tag{B.126}$$

$$\overline{\rho}\frac{DR_e}{Dt} + \frac{\partial \widetilde{\overline{\rho}e''^2 u_v''}}{\partial x} = -2\overline{\rho}F_e\frac{\partial \widetilde{e}}{\partial x} + 2\overline{\rho}G_{ee}R_e + 2G_{ev}\overline{\rho}F_e + \frac{3}{2}\overline{\rho}C_eR_e\widetilde{\omega}_t\,. \tag{B.127}$$

Comparing Equations B.126 and B.127 with Equations B.86 and B.87 respectively, it is apparent that the coefficient G_{ev} should vanish (because the mean $\widetilde{e}$ equation does not contain any term proportional to the convective flux), that the coefficient G_{eh} has no impact whatsoever, so that it can also be considered zero, and that the remaining coefficients A, G_{ee} and C_e are related to the "knowns" of the system through

$$A = \frac{\overline{p}}{\overline{\rho}}\frac{\partial}{\partial x}\left(\frac{mF_e}{\widetilde{e}} - \widetilde{u_v}\right) + \epsilon - \frac{1}{\overline{\rho}}\frac{\partial \overline{F^{\mathrm{rad}}}}{\partial x}\,, \tag{B.128}$$

$$G_{ee} + \frac{3}{4}C_e\widetilde{\omega}_t = \left(\frac{m\overline{p}}{\widetilde{\rho e}} - \gamma m(\Gamma_1 - 1)\right)\frac{\partial \widetilde{u_v}}{\partial x} = -(\Gamma_1 - 1)\frac{\partial \widetilde{u_v}}{\partial x}\,, \tag{B.129}$$

where I used the ideal gas law (Equation B.15), as well as the identity $m(\gamma-1) = 1$, to simplify the second equation. In analogy with Equations B.113 and B.114 for G_{ij}, I decompose the coefficient G_{ee} into

$$G_{ee} \equiv G_{ee}^a - \left(\frac{1}{2} + \frac{3}{4}C_e\right)\widetilde{\omega}_t\,, \tag{B.130}$$

so that the above constraints do not depend on the 'energy Kolmogorov constant' C_e anymore. Indeed, one obtains

$$A = \frac{\overline{p}}{\overline{\rho}}\frac{\partial}{\partial x}\left(\frac{mF_e}{\widetilde{e}} - \widetilde{u_v}\right) + \epsilon - \frac{1}{\overline{\rho}}\frac{\partial \overline{F^{\mathrm{rad}}}}{\partial x} \,, \tag{B.131}$$

$$G^a_{ee} = \frac{1}{2}\widetilde{\omega_t} - (\Gamma_1 - 1)\frac{\partial \widetilde{u_v}}{\partial x} \,, \tag{B.132}$$

$$G_{ev} = G_{eh} = 0 \,. \tag{B.133}$$

Together, Equations B.122 and B.130 to B.133 form a closed stochastic model for specific internal energy, so long as a value is specified for C_e. As a first approximation, I will consider that $C_e = C_0$.

Equivalent energy convective flux equation

Multiplying Equation B.100 + Equation B.117 + Equation B.123 by $(e - \widetilde{e})(u_v - \widetilde{u_v})$ and integrating over the entire parameter space – i.e. over all values of u_v, u_h, ω_t and e –, one obtains

$$\overline{\rho}\frac{DF_e}{Dt} + \overline{\rho}F_e\frac{\partial \widetilde{u_v}}{\partial x} + \overline{\rho}R_v\frac{\partial \widetilde{e}}{\partial x} + \frac{\partial \overline{\rho}\widetilde{u_v''^2 e''}}{\partial x} = \overline{\rho}G_{vv}F_e + \frac{m}{\widetilde{e}}\frac{\partial \overline{p}}{\partial x}R_e - \overline{\rho}(\Gamma_1 - 1)\frac{\partial \widetilde{u_v}}{\partial x}F_e - \frac{3}{4}C_e\widetilde{\omega_t}F_e \,, \tag{B.134}$$

where I replaced G_{ee} by its expression given by Equations B.130 and B.132, but I kept G_{vv} in this unspecified form for clarity. Comparing Equation B.134 to Equation B.88, it can be seen that several terms are already exactly modelled, without having to modify the stochastic model. On the right hand side of Equation B.88, the first two terms arise directly from the advective term in the Fokker-Planck equation; the third term stems from the buoyancy term in Equation B.95; the sixth and seventh terms, when put together using the ideal gas law (Equation B.15), are due to the return-to-local-mean contribution in Equation B.122. Of all the right-hand side terms, only the fourth, fifth and eighth terms are not modelled exactly. The identification with Equation B.134 yields

$$\left(\overline{\rho}G_{vv} - \frac{3}{4}\overline{\rho}C_e\widetilde{\omega_t}\right)F_e = -\overline{e''\frac{\partial p'}{\partial x}} - \overline{p u_v''\frac{\partial u_i''}{\partial x_i}} \,. \tag{B.135}$$

Note that there is no one-to-one correspondence between the two.

B.3.4 Final form of the Lagrangian stochastic model

Let me summarise in one place the Lagrangian stochastic model developed in this Appendix. The state of each fluid particle is entirely described by the position $x^\star$, the vertical component of the velocity $u_v^\star$, any horizontal component of the velocity $u_h^\star$, the turbulent frequency $\omega_t^\star$, and the internal energy $e^\star$. Each evolves according to an Ito stochastic differential equation, given by

$$\mathrm{d}x^\star = u_v^\star \, \mathrm{d}t \,, \tag{B.136}$$

$$\mathrm{d}u_v^\star = \left(-\frac{1}{\overline{\rho}}\frac{\partial \overline{p}}{\partial x} - g + G_{vv}\left(u_v^\star - \widetilde{u_v}\right) - \frac{1}{2}C_0\frac{k}{R_v}\left(\omega_t^\star - \widetilde{\omega_t}\right)\left(u_v^\star - \widetilde{u_v}\right) + \frac{m}{\overline{\rho}\widetilde{e}}\frac{\partial \overline{p}}{\partial x}\left(e^\star - \widetilde{e}\right)\right)\mathrm{d}t + \left(C_0\omega_t^\star k\right)^{1/2}\mathrm{d}W_v \,, \tag{B.137}$$

$$\mathrm{d}u_h^\star = \left(G_{hh}u_h^\star - \frac{1}{2}C_0\frac{k}{R_h}\left(\omega_t^\star - \widetilde{\omega_t}\right)u_h^\star\right)\mathrm{d}t + \left(C_0\omega_t^\star k\right)^{1/2}\mathrm{d}W_h \,, \tag{B.138}$$

$$\mathrm{d}\omega_t^\star = -\omega_t^\star\widetilde{\omega_t}\left(S_\omega + C_\chi\left[\ln\left(\frac{\omega_t^\star}{\widetilde{\omega_t}}\right) - \frac{1}{2}\sigma^2\right]\right)\mathrm{d}t + \omega_t^\star\left(2C_\chi\widetilde{\omega_t}\sigma^2\right)^{1/2}\mathrm{d}W_\omega \,, \tag{B.139}$$

$$\mathrm{d}e^\star = \left(\frac{\overline{p}}{\overline{\rho}}\frac{\partial}{\partial x}\left(\frac{mF_e}{\widetilde{e}} - \widetilde{u_v}\right) + k\widetilde{\omega_t} + G_{ee}(e^\star - \widetilde{e})\right)\mathrm{d}t + \left(\frac{3}{2}C_e\omega_t^\star R_e\right)^{1/2}\mathrm{d}W_e \,, \tag{B.140}$$

where $\mathrm{d}W_v$, $\mathrm{d}W_h$, $\mathrm{d}W_\omega$ and $\mathrm{d}W_e$ are four independent Wiener processes, one has

$$\overline{p} = (\Gamma_1 - 1)\widetilde{\rho e} \,, \tag{B.141}$$

$$k = \frac{1}{2} R_v + R_h \,, \tag{B.142}$$

$$G_{vv} = G^a_{vv} - \left(\frac{1}{2} + \frac{3}{4} C_0\right) \widetilde{\omega}_t \,, \tag{B.143}$$

$$G^a_{vv} = -\frac{1}{\overline{\rho} R_v} \frac{\partial \gamma m (\Gamma_1 - 1) \overline{\rho} F_e}{\partial x} + \widetilde{\omega}_t \left(\frac{R_h}{R_v} - 1\right) \left[\frac{C_R - 1}{3} - \frac{C_0}{2}\right] \,, \tag{B.144}$$

$$G_{hh} = G^a_{hh} - \left(\frac{1}{2} + \frac{3}{4} C_0\right) \widetilde{\omega}_t \,, \tag{B.145}$$

$$G^a_{hh} = \frac{1}{2} \widetilde{\omega}_t \left(\frac{R_h}{R_v} - 1\right) \left[\frac{C_R - 1}{3} - \frac{C_0}{2}\right] \,, \tag{B.146}$$

$$G_{ee} = G^a_{ee} - \left(\frac{1}{2} + \frac{3}{4} C_e\right) \,, \tag{B.147}$$

$$G^a_{ee} = \frac{1}{2} \widetilde{\omega}_t - (\Gamma_1 - 1) \frac{\partial \widetilde{u_v}}{\partial x} \,, \tag{B.148}$$

$$S_\omega = \frac{1}{\widetilde{\omega}_t} \left[\widetilde{u_v} \frac{\partial \ln k}{\partial x} + \left[\frac{4}{3} - C_{\epsilon 1} \left(\frac{2}{3} - \left(\frac{1}{2} + \frac{R_v}{R_h}\right)^{-1}\right)\right] \frac{\partial \widetilde{u_v}}{\partial x} - C_{\epsilon 3} \frac{m F_e}{\widetilde{\rho e} k} \frac{\partial \overline{p}}{\partial x}\right] + C_{\epsilon 2} \,, \tag{B.149}$$

and the various non-dimensional control parameters have the following values

$$C_0 = 3.5 \;\; ; \;\; C_{\epsilon 1} = 1.44 \;\; ; \;\; C_{\epsilon 2} = 1.83 \;\; ; \;\; C_{\epsilon 3} = 0.1 \;\; ; \;\; C_\chi = 1.6 \;\; ; \;\; \sigma^2 = 1.0 \;\; ; \;\; C_R = 4.15 \,. \tag{B.150}$$

All the mean fields appearing in the Lagrangian stochastic models – $\overline{\rho}$, $\widetilde{u_v}$, R_v, R_h, $\widetilde{\omega}_t$, $\widetilde{e}$, F_e and R_e – are already in closed form, as they can be extracted from the properties of the fluid particles themselves. I describe in Section 7.2.4 how this can be done in practice.

C Fokker-Planck amplitude equation for oscillations in the presence of stochastic noise

Contents

The goal of this Appendix is to detail the derivation of both the probability fluxes $\mathcal{G}$ and $\mathcal{H}$ and the components of the diffusion matrix $\mathcal{D}, \mathcal{E}$ and $\mathcal{F}$ appearing in the joint-amplitude-phase Fokker-Planck equation (Equation 8.30). In order to account for the finite memory time of $G(A,\Phi,t)$ and $H(A,\Phi,t)$ (defined as the right-hand sides of Equations 8.28 and 8.29 respectively), Stratonovich (1965) showed that one can define *effective* probability fluxes and diffusion coefficients thus

$$\mathcal{G} = \langle G \rangle + \left\{ \frac{\partial G}{\partial A} \; ; \; G^\tau \right\} + \left\{ \frac{\partial G}{\partial \Phi} \; ; \; H^\tau \right\} , \tag{C.1}$$

$$\mathcal{H} = \langle H \rangle + \left\{ \frac{\partial H}{\partial A} \; ; \; G^\tau \right\} + \left\{ \frac{\partial H}{\partial \Phi} \; ; \; H^\tau \right\} , \tag{C.2}$$

$$\mathcal{D} = 2 \left\{ G \; ; \; G^\tau \right\} , \tag{C.3}$$

$$\mathcal{E} = \left\{ G \; ; \; H^\tau \right\} + \left\{ H \; ; \; G^\tau \right\} , \tag{C.4}$$

$$\mathcal{F} = 2 \left\{ G \; ; \; G^\tau \right\} , \tag{C.5}$$

where $\langle . \rangle$ denotes an ensemble average, and the bilinear operator $\{.;.\}$ is defined by

$$\left\{ f_1 ; f_2^\tau \right\} \equiv \int_{-\infty}^{0} \mathrm{d}\tau \, \left[\left\langle f_1(t) f_2(t+\tau) \right\rangle - \left\langle f_1(t) \right\rangle \left\langle f_2(t+\tau) \right\rangle \right] . \tag{C.6}$$

Let me write each of the stochastic processes $c_i(t)$ $(i = 1, 2, 3)$ in polar form, so that

$$c_i(t) = C_i(t) \exp^{j\phi_i(t)} , \tag{C.7}$$

where $C_i(t)$ and $\phi_i(t)$ are both real. Then the functions $G(A,\Phi,t)$ and $H(A,\Phi,t)$ can be rewritten

$$G(A,\Phi,t) = \kappa A + C_1(t) \cos\left(\phi_1(t) - \phi(t)\right) + A C_2(t) \cos\left(\phi_2(t)\right) + A C_3(t) \cos\left(\phi_3(t) - 2\phi(t)\right) , \tag{C.8}$$

$$H(A,\Phi,t) = \frac{1}{A} C_1(t) \sin\left(\phi_1(t) - \phi(t)\right) + C_2(t) \sin\left(\phi_2(t)\right) + C_3(t) \sin\left(\phi_3(t) - 2\phi(t)\right) , \tag{C.9}$$

where I have introduced the *global phase* of the mode $\phi(t) \equiv \omega t + \Phi$.

C.1 Probability fluxes

Let me first derive the probability fluxes in parameter space $\mathcal{G}$ (in the A-direction) and $\mathcal{H}$ (in the Φ-direction). By construction, the stochastic processes $c_i(t)$ have zero mean, and as a result, the first term on the right-hand side of Equations C.1 and C.2 straightforwardly reduce to

$$\langle G \rangle = \kappa A , \tag{C.10}$$

$$\langle H \rangle = 0 . \tag{C.11}$$

As for the expansion of the bilinear operators $\{\ .\ ;\ .\ \}$, it can seem at first that a large number of terms must be computed. However, I am interested in the long-term variations of the mode amplitude, which occur on timescales much larger than ω^{-1}. As such, all terms oscillating at frequencies comparable to ω can be averaged out. As is customary in this type of situation, it appears that only contributions initially oscillating at the same frequency can 'interact' through the operator $\{\ .\ ;\ .\ \}$ to yield a non-oscillating contribution. As an illustrative example, let me compute the following contribution arising from the expansion of the very last term on the right-hand side of Equation C.1

$$\begin{aligned}
&\left\{C_1(t)\sin\left(\phi_1(t)-\phi(t)\right)\ ;\ C_3(t+\tau)\sin\left(\phi_3(t+\tau)-2\phi(t+\tau)\right)\right\}\\
&\quad=\int_{-\infty}^{0}\mathrm{d}\tau\ \left\langle C_1(t)C_3(t+\tau)\sin\left(\phi_1(t)-\omega t-\Phi\right)\sin\left(\phi_3(t+\tau)-2\omega(t+\tau)-2\Phi\right)\right\rangle\\
&\quad=\frac{1}{2}\int_{-\infty}^{0}\mathrm{d}\tau\ \left\langle C_1(t)C_3(t+\tau)\cos\left(\omega t+...\right)\right\rangle\mathrm{d}\tau+\frac{1}{2}\int_{-\infty}^{0}\left\langle C_1(t)C_3(t+\tau)\cos\left(3\omega t+...\right)\right\rangle\ .
\end{aligned}\tag{C.12}$$

This particular contribution therefore features a part oscillating at angular frequency ω, and another at 3ω. Under the hypothesis that the complex amplitude of the mode varies over timescales much longer than the period of the mode – a hypothesis that, as I already had the opportunity to show in the main body of this thesis, is valid for solar-like oscillations –, the impact of these two rapidly-oscillating contributions to the Fokker-Planck equation cancels out on average. This is fundamentally due to the fact that the two terms in the bilinear operator $\{\ .\ ;\ .\ \}$, in the contribution we considered in this example, oscillate in time with different angular frequencies (ω and 2ω respectively). It becomes apparent that only the contributions where the two terms are *synchronous* will effectively impact the Fokker-Planck equation. Keeping only these synchronous contributions into account in Equations C.1 and C.2, one finds

$$\begin{aligned}
\mathcal{G}=\kappa A&+\left\{\kappa\ ;\ \kappa A\right\}+\left\{C_2\cos\left(\phi_2\right)\ ;\ AC_2^\tau\cos\left(\phi_2^\tau\right)\right\}+\left\{C_3\cos\left(\phi_3-2\phi\right)\ ;\ AC_3^\tau\cos\left(\phi_3^\tau-2\phi^\tau\right)\right\}\\
&+\left\{C_1\sin\left(\phi_1-\phi\right)\ ;\ \frac{1}{A}C_1^\tau\sin\left(\phi_1^\tau-\phi^\tau\right)\right\}+\left\{2AC_3\sin\left(\phi_3-2\phi\right)\ ;\ C_3^\tau\sin\left(\phi_3^\tau-2\phi^\tau\right)\right\}\ ,
\end{aligned}\tag{C.13}$$

$$\begin{aligned}
\mathcal{H}=&\left\{-\frac{1}{A^2}C_1\sin\left(\phi_1-\phi\right)\ ;\ C_1^\tau\cos\left(\phi_1^\tau-\phi^\tau\right)\right\}+\left\{-\frac{1}{A}C_1\cos\left(\phi_1-\phi\right)\ ;\ \frac{1}{A}C_1^\tau\sin\left(\phi_1^\tau-\phi^\tau\right)\right\}\\
&+\left\{-2C_3\cos\left(\phi_3-2\phi\right)\ ;\ C_3^\tau\sin\left(\phi_3^\tau-2\phi^\tau\right)\right\}\ ,
\end{aligned}\tag{C.14}$$

where the time-dependent quantities are evaluated at time $t+\tau$ when the superscript τ is present, and at time t otherwise.

The second term on the right-hand side of Equation C.13 vanishes. Indeed, one has $\langle\kappa^2 A\rangle-\langle\kappa\rangle\langle\kappa A\rangle=0$, since all of these quantities are deterministic. As for all the other contributions, they can be computed in the fashion of

Equation C.12. I obtain, for the contributions of $\mathcal{G}$

$$\left\{C_2\cos\left(\phi_2\right)\ ;\ AC_2^\tau\cos\left(\phi_2^\tau\right)\right\} = A\int_{-\infty}^{0}\mathrm{d}\tau\ \langle \mathrm{Re}(c_2(t))\mathrm{Re}(c_2(t+\tau))\rangle\ , \tag{C.15}$$

$$\begin{aligned}&\left\{C_3\cos\left(\phi_3-2\omega t-2\Phi\right)\ ;\ AC_3^\tau\cos\left(\phi_3^\tau-2\omega(t+\tau)-2\Phi\right)\right\}\\ &\quad=\frac{1}{2}A\int_{-\infty}^{0}\mathrm{d}\tau\ \left\langle C_3C_3^\tau\cos\left(\phi_3-\phi_3^\tau+2\omega\tau\right)\right\rangle\ +\ \text{osc.} = \frac{1}{2}A\int_{-\infty}^{0}\mathrm{d}\tau\ \mathrm{Re}\left(\left\langle c_3(t)c_3^\star(t+\tau)\right\rangle\exp^{2j\omega\tau}\right)\ +\ \text{osc.}\,,\end{aligned} \tag{C.16}$$

$$\begin{aligned}&\left\{C_1\sin\left(\phi_1-\omega t-\Phi\right)\ ;\ \frac{1}{A}C_1^\tau\sin\left(\phi_1^\tau-\omega(t+\tau)-\Phi\right)\right\}\\ &\quad=\frac{1}{2A}\int_{-\infty}^{0}\mathrm{d}\tau\ \left\langle C_1C_1^\tau\cos\left(\phi_1-\phi_1^\tau+\omega\tau\right)\right\rangle\ +\ \text{osc.} = \frac{1}{2A}\int_{-\infty}^{0}\mathrm{d}\tau\ \mathrm{Re}\left(\left\langle c_1(t)c_1^\star(t+\tau)\right\rangle\exp^{j\omega\tau}\right)\ +\ \text{osc.}\,,\end{aligned} \tag{C.17}$$

$$\begin{aligned}&\left\{2AC_3\sin\left(\phi_3-2\omega t-2\Phi\right)\ ;\ C_3^\tau\sin\left(\phi_3^\tau-2\omega(t+\tau)-2\Phi\right)\right\}\\ &\quad=A\int_{-\infty}^{0}\mathrm{d}\tau\ \left\langle C_3C_3^\tau\cos\left(\phi_3-\phi_3^\tau+2\omega\tau\right)\right\rangle\ +\ \text{osc.} = A\int_{-\infty}^{0}\mathrm{d}\tau\ \mathrm{Re}\left(\left\langle c_3(t)c_3^\star(t+\tau)\right\rangle\exp^{2j\omega\tau}\right)\ +\ \text{osc.}\,,\end{aligned} \tag{C.18}$$

and for the contributions of $\mathcal{H}$

$$\begin{aligned}&\left\{-\frac{1}{A^2}C_1\sin\left(\phi_1-\omega t-\Phi\right)\ ;\ C_1^\tau\cos\left(\phi_1^\tau-\omega(t+\tau)-\Phi\right)\right\}\\ &\quad=-\frac{1}{2A^2}\int_{-\infty}^{0}\mathrm{d}\tau\ \left\langle C_1C_1^\tau\sin\left(\phi_1-\phi_1^\tau+\omega\tau\right)\right\rangle\ +\ \text{osc.} = -\frac{1}{2A^2}\int_{-\infty}^{0}\mathrm{d}\tau\ \mathrm{Im}\left(\left\langle c_1(t)c_1^\star(t+\tau)\right\rangle\exp^{j\omega\tau}\right)\ +\ \text{osc.}\,,\end{aligned} \tag{C.19}$$

$$\begin{aligned}&\left\{-\frac{1}{A}C_1\cos\left(\phi_1-\omega t-\Phi\right)\ ;\ \frac{1}{A}C_1^\tau\sin\left(\phi_1^\tau-\omega(t+\tau)-\Phi\right)\right\}\\ &\quad=-\frac{1}{2A^2}\int_{-\infty}^{0}\mathrm{d}\tau\ \left\langle C_1C_1^\tau\sin\left(-\phi_1+\phi_1^\tau-\omega\tau\right)\right\rangle\ +\ \text{osc.} = \frac{1}{2A^2}\int_{-\infty}^{0}\mathrm{d}\tau\ \mathrm{Im}\left(\left\langle c_1(t)c_1^\star(t+\tau)\right\rangle\exp^{j\omega\tau}\right)\ +\ \text{osc.}\,,\end{aligned} \tag{C.20}$$

$$\begin{aligned}&\left\{-2C_3\cos\left(\phi_3-2\omega t-2\Phi\right)\ ;\ C_3^\tau\sin\left(\phi_3^\tau-2\omega(t+\tau)-2\Phi\right)\right\}\\ &\quad=-\int_{-\infty}^{0}\mathrm{d}\tau\ \left\langle C_3C_3^\tau\sin\left(-\phi_3+\phi_3^\tau-2\omega\tau\right)\right\rangle\ +\ \text{osc.} = \int_{-\infty}^{0}\mathrm{d}\tau\ \mathrm{Im}\left(\left\langle c_3(t)c_3^\star(t+\tau)\right\rangle\exp^{2j\omega\tau}\right)\ +\ \text{osc.}\end{aligned} \tag{C.21}$$

In these expressions, the variables A and Φ are not explicit functions of time, but actual, independent variables on which the PDF w depends. This is the reason why I was able to pull A out of the time integrals, and also why Φ disappears entirely from the above expressions. Additionally, I have gathered all oscillatory components into the notation 'osc.', which will be filtered out in the following. Summing all these contributions together, one finds the expressions $\mathcal{G}(A,\Phi,t)$ and $\mathcal{H}(A,\Phi,t)$ given in the main body of this thesis (Equations 8.31 and 8.32).

C.2 Diffusion coefficients

The derivation of the diffusion coefficients is performed similarly. The only contributions that yield a non-oscillatory (and, therefore, non-vanishing) contribution to the Fokker-Planck equation are, for $\mathcal{D}$

$$2\left\{C_1\cos\left(\phi_1-\omega t-\Phi\right)\ ;\ C_1^\tau\cos\left(\phi_1^\tau-\omega(t+\tau)-\Phi\right)\right\}$$
$$=\int_{-\infty}^{0}\mathrm{d}\tau\ \left\langle C_1C_1^\tau\cos\left(\phi_1-\phi_1^\tau+\omega\tau\right)\right\rangle\ +\ \text{osc.}=\int_{-\infty}^{0}\mathrm{d}\tau\ \mathrm{Re}\left(\left\langle c_1(t)c_1^\star(t+\tau)\right\rangle\exp^{j\omega\tau}\right)\ +\ \text{osc.}\,, \tag{C.22}$$

$$2\left\{AC_2(t)\cos\left(\phi_2\right)\ ;\ AC_2^\tau\cos\left(\phi_2^\tau\right)\right\}=2A^2\int_{-\infty}^{0}\mathrm{d}\tau\ \langle\mathrm{Re}(c_2(t))\mathrm{Re}(c_2(t+\tau))\rangle\ , \tag{C.23}$$

$$2\left\{AC_3\cos\left(\phi_3-2\omega t-2\Phi\right)\ ;\ AC_3^\tau\cos\left(\phi_3^\tau-2\omega(t+\tau)-2\Phi\right)\right\}$$
$$=A^2\int_{-\infty}^{0}\mathrm{d}\tau\ \left\langle C_3C_3^\tau\cos\left(\phi_3-\phi_3^\tau+2\omega\tau\right)\right\rangle\ +\ \text{osc.}=A^2\int_{-\infty}^{0}\mathrm{d}\tau\ \mathrm{Re}\left(\left\langle c_3(t)c_3^\star(t+\tau)\right\rangle\exp^{2j\omega\tau}\right)\ +\ \text{osc.}\,, \tag{C.24}$$

and for $\mathcal{F}$

$$2\left\{\frac{1}{A}C_1\sin\left(\phi_1-\omega t-\Phi\right)\ ;\ \frac{1}{A}C_1^\tau\sin\left(\phi_1^\tau-\omega(t+\tau)-\Phi\right)\right\}$$
$$=\frac{1}{A^2}\int_{-\infty}^{0}\mathrm{d}\tau\ \left\langle C_1C_1^\tau\cos\left(\phi_1-\phi_1^\tau+\omega\tau\right)\right\rangle\ +\ \text{osc.}=\frac{1}{A^2}\int_{-\infty}^{0}\mathrm{d}\tau\ \mathrm{Re}\left(\left\langle c_1(t)c_1^\star(t+\tau)\right\rangle\exp^{j\omega\tau}\right)\ +\ \text{osc.}\,, \tag{C.25}$$

$$2\left\{C_2\sin\left(\phi_2\right)\ ;\ C_2^\tau\sin\left(\phi_2^\tau\right)\right\}=2\int_{-\infty}^{0}\mathrm{d}\tau\ \langle\mathrm{Im}(c_2(t))\mathrm{Im}(c_2(t+\tau))\rangle\ , \tag{C.26}$$

$$2\left\{C_3\sin\left(\phi_3-2\omega t-2\Phi\right)\ ;\ C_3^\tau\sin\left(\phi_3^\tau-2\omega(t+\tau)-2\Phi\right)\right\}$$
$$=\int_{-\infty}^{0}\mathrm{d}\tau\ \left\langle C_3C_3^\tau\cos\left(\phi_3-\phi_3^\tau+2\omega\tau\right)\right\rangle\ +\ \text{osc.}=\int_{-\infty}^{0}\mathrm{d}\tau\ \mathrm{Re}\left(\left\langle c_3(t)c_3^\star(t+\tau)\right\rangle\exp^{2j\omega\tau}\right)\ +\ \text{osc.}\,. \tag{C.27}$$

As for $\mathcal{E}$, it can be immediately seen that all the integrands appearing in $\{G;H^\tau\}$ are odd functions of τ. Therefore, since $\{H;G^\tau\}=\{G;H^{-\tau}\}$, one simply obtains

$$\mathcal{E}=\{G;H^\tau\}+\{G;H^{-\tau}\}=0\,. \tag{C.28}$$

Summing all these contributions together, one finds the expressions $\mathcal{D}(A,\Phi,t)$, $\mathcal{E}(A,\Phi,t)$ and $\mathcal{F}(A,\Phi,t)$ given in the main body of the thesis (Equations 8.33 to 8.35).

D Simplified amplitude formalism – Derivation of the autocorrelation spectra α_i

Contents

The evolution equations for the mean mode energy and phase, given by Equations 8.44 and 8.45, only depend on the constant, complex values of both coefficients α_1 and α_3. I recall here, for clarity, that those are defined as the complex autocorrelation spectra of the stochastic processes $c_1(t)$ and $c_3(t)$ evaluated at angular frequencies ω and 2ω respectively (see Equations 8.36 and 8.39)

$$\alpha_1 = \int_{-\infty}^{0} \mathrm{d}\tau \, \left\langle c_1(t) c_1^\star(t+\tau) \right\rangle \exp^{j\omega\tau} \, , \tag{D.1}$$

$$\alpha_3 = \int_{-\infty}^{0} \mathrm{d}\tau \, \left\langle c_3(t) c_3^\star(t+\tau) \right\rangle \exp^{2j\omega\tau} \, . \tag{D.2}$$

In turn, these stochastic processes are given by (see Equations 8.58 and 8.60)

$$c_1(t) = 2 \int \mathrm{d}^3\mathbf{x} \, \rho_0 \left[\Psi_{\xi,i} \xi_{t,j}(t) \partial_j u_{t,i}(t) + \Psi_{u,i} L_{0,i}(t) \right] \, , \tag{D.3}$$

$$c_3(t) = \int \mathrm{d}^3\mathbf{x} \, \rho_0 \left[\Psi_{\xi,i} \Psi_{\xi,j} \partial_j u_{t,i}(t) + \omega \Psi_{\xi,i} \xi_{t,j}(t) \partial_j \Psi_{u,i} + \Psi_{u,i} L^s_{1,i}(t) \right] \, , \tag{D.4}$$

where $\boldsymbol{\Psi}_\xi$ and $\boldsymbol{\Psi}_u$ are the normalised displacement and velocity eigenfunctions respectively, one has (see Equations 8.15 and 8.16)

$$L_{0,i} = -\frac{1}{\rho_0} \frac{\partial \left(\rho_0 u_{t,i} u_{t,j} - \rho_0 \overline{u_{t,i} u_{t,j}} \right)}{\partial x_j} \, , \tag{D.5}$$

$$\begin{aligned} L^s_{1,i} = &-\Psi_{u,j} \partial_j u_{t,i} - u_{t,j} \partial_j \Psi_{u,i} - \frac{G_{ij}}{\omega \rho_0} \int \mathrm{d}^3\mathbf{y} \, \rho_0(\mathbf{y}) \left(\Psi_{\xi,k} \partial_k \left(u_{t,j} K^{\mathbf{x}} \right) \right) \Big|_{\mathbf{y}} \\ &+ \left(\frac{\partial G_{ij}}{\partial \widetilde{u''_k u''_l}} \widetilde{u''_k u''_l}_1 + \frac{\partial G_{ij}}{\partial (\partial_k \widetilde{u}_l)} \partial_k \widetilde{u}_{l1} + \frac{\partial G_{ij}}{\partial \epsilon} \omega_t k_1 \right) u_{t,j} + \frac{1}{2} \sqrt{\frac{C_0 \omega_t}{k_0}} \eta_i k_1 \, , \end{aligned} \tag{D.6}$$

and the perturbation of the Reynolds stress tensor, mean shear tensor and turbulent kinetic energy are respectively

given by (see Eqs. C.15, C.11 and C.16 in the article reproduced in the end of Chapter 8)

$$\widetilde{u_i'' u_j''}_1 = -\frac{\widetilde{u_i'' u_j''}_0}{\omega\rho_0} \int \mathrm{d}^3\mathbf{y}\, \rho_0(\mathbf{y}) \left(\Psi_{\xi,k}\partial_k K^{\mathbf{x}}\right)\Big|_{\mathbf{y}} + \frac{1}{\omega\rho_0}\int \mathrm{d}^3\mathbf{y}\, \rho_0(\mathbf{y}) \left(\Psi_{\xi,k}\partial_k \left(u_{t,i}u_{t,j}K^{\mathbf{x}}\right)\right)\Big|_{\mathbf{y}} + \frac{1}{\rho_0}\int \mathrm{d}^3\mathbf{y}\, \rho_0(\mathbf{y}) \left(u_{t,i}\Psi_{u,j}K^{\mathbf{x}}\right)\Big|_{\mathbf{y}} + \frac{1}{\rho_0}\int \mathrm{d}^3\mathbf{y}\, \rho_0(\mathbf{y}) \left(u_{t,j}\Psi_{u,i}K^{\mathbf{x}}\right)\Big|_{\mathbf{y}} , \tag{D.7}$$

$$\partial_i \widetilde{u}_{j1} = -\frac{1}{\rho_0}\int \mathrm{d}^3\mathbf{y}\, \rho_0(\mathbf{y}) \left(\Psi_{u,j}\partial_i K^{\mathbf{x}}\right)\Big|_{\mathbf{y}} - \frac{1}{\omega\rho_0}\int \mathrm{d}^3\mathbf{y}\, \rho_0(\mathbf{y}) \left(\Psi_{\xi,k}\partial_k \left(u_{t,j}\partial_i K^{\mathbf{x}}\right)\right)\Big|_{\mathbf{y}} - \frac{1}{\rho_0^2}\frac{\partial\rho_0}{\partial x_i}\int \mathrm{d}^3\mathbf{y}\, \rho_0(\mathbf{y}) \left(\Psi_{u,j}K^{\mathbf{x}}\right)\Big|_{\mathbf{y}} - \frac{1}{\omega\rho_0^2}\frac{\partial\rho_0}{\partial x_i}\int \mathrm{d}^3\mathbf{y}\, \rho_0(\mathbf{y}) \left(\Psi_{\xi,k}\partial_k \left(u_{t,j}K^{\mathbf{x}}\right)\right)\Big|_{\mathbf{y}} , \tag{D.8}$$

$$k_1 = -\frac{k_0}{\omega\rho_0}\int \mathrm{d}^3\mathbf{y}\, \rho_0(\mathbf{y}) \left(\Psi_{\xi,k}\partial_k K^{\mathbf{x}}\right)\Big|_{\mathbf{y}} + \frac{1}{\omega\rho_0}\int \mathrm{d}^3\mathbf{y}\, \rho_0(\mathbf{y}) \left(\Psi_{\xi,k}\partial_k \left(\frac{1}{2}\mathbf{u}_t^2 K^{\mathbf{x}}\right)\right)\Big|_{\mathbf{y}} + \frac{1}{\rho_0}\int \mathrm{d}^3\mathbf{y}\, \rho_0(\mathbf{y}) \left(u_{t,i}\Psi_{u,i}K^{\mathbf{x}}\right)\Big|_{\mathbf{y}} . \tag{D.9}$$

The apparition of the factor ω^{-1} in front of every integral involving the displacement eigenfunction $\boldsymbol{\Psi}_\xi$ stems from the fact that the latter is defined in terms of $\omega\boldsymbol{\xi}_{\mathrm{osc}}$ rather than simply $\boldsymbol{\xi}_{\mathrm{osc}}$ (see Equation 8.51).

D.1 Contribution of the turbulent displacement field

In Section 8.1, I used a certain number of approximations to derive the present formalism. One of these approximations – which I labelled (H3) – consisted in adopting the anelastic approximation for turbulence, in the sense that I considered $\rho_t \ll \rho_0$, where ρ_t is the turbulent fluctuation of density, and ρ_0 is the equilibrium density. Using the continuity equation, this amounts to neglecting the quantity $\boldsymbol{\nabla}\cdot(\rho_0\boldsymbol{\xi}_t)$. As I will now show, this allows me to discard the first term on the right-hand side of Equation D.3 and the second term on the right-hand side of Equation D.4. Let me consider the former: performing an integration by part, I can put it in the following form

$$c_1(t) = [...] + 2\int_{\mathcal{S}} \mathrm{d}^2\mathbf{x}\, \rho_0\Psi_{\xi,i}u_{t,i}\, \boldsymbol{\xi}_t\cdot\mathbf{n} - 2\int \mathrm{d}^3\mathbf{x}\, u_{t,i}\boldsymbol{\nabla}\cdot\left(\rho_0\Psi_{\xi,i}\boldsymbol{\xi}_t\right) , \tag{D.10}$$

where the surface integral vanishes, on account of the product $\rho_0\boldsymbol{\Psi}_{\boldsymbol{\xi}}$ vanishing on the surface of the star. Furthermore, the typical length scale over which $\boldsymbol{\xi}_t$ varies is much smaller than the wavelength of the mode. This allows me to pull $\Psi_{\xi,i}$ out of the gradient in the last term, and one recognises $\boldsymbol{\nabla}\cdot(\rho_0\boldsymbol{\xi}_t)$, which I neglected on account of hypothesis (H3). The same procedure can be applied to the second term on the right-hand side of Equation D.4. As a result, in Equations D.3 and D.4, the only source of stochasticity comes from the turbulent velocity field $\mathbf{u}_t$ and the Wiener process $\boldsymbol{\eta}$, with no contribution from the turbulent displacement field $\boldsymbol{\xi}_t$.

D.2 Derivation of α_1

Plugging Equation D.5 into Equation D.3, one finds

$$\left\langle c_1(t)c_1^\star(t+\tau)\right\rangle = 4\left\langle \int \mathrm{d}^3\mathbf{x}\, \Psi_{u,i}^\star(\mathbf{x})\left[\,\partial_j\left(\rho_0 u_{t,j}u_{t,i}\right)\Big|_{\mathbf{x},t}\right]' \times \int \mathrm{d}^3\mathbf{x}'\, \Psi_{u,k}(\mathbf{x}')\left[\,\partial_l\left(\rho_0 u_{t,l}u_{t,k}\right)\Big|_{\mathbf{x}',t+\tau}\right]'\right\rangle$$
$$= \int \mathrm{d}^3\mathbf{x}\int \mathrm{d}^3\mathbf{x}'\, \Psi_{u,i}^\star(\mathbf{x})\Psi_{u,k}^\star(\mathbf{x}')\left\langle\left[\partial_j\left(\rho_0 u_{t,j}u_{t,i}\right)\Big|_{\mathbf{x},t}\right]'\left[\partial_l\left(\rho_0 u_{t,l}u_{t,k}\right)\Big|_{\mathbf{x}',t+\tau}\right]'\right\rangle . \tag{D.11}$$

It is only the *fluctuation* of the turbulent pressure gradient *around its equilibrium, time-independent state* that appears in this integral. Explicitly expanding this fluctuation into the difference between the total turbulent pressure gradient and the equilibrium turbulent pressure gradient leads to four different integrals. However, it is readily seen that only one of them – the one not involving the equilibrium turbulent pressure gradient at all – will have a non-zero ω-component in its Fourier transform in time, and therefore will contribute to α_1. As such, the fluctuating turbulent pressure gradient can be replaced with the total turbulent pressure gradient. After a double integration by

part, one obtains

$$\left\langle c_1(t)c_1^\star(t+\tau)\right\rangle = 4\int \mathrm{d}^3\mathbf{x}\int \mathrm{d}^3\mathbf{x}'\,\rho_0(\mathbf{x})\rho_0(\mathbf{x}')\left.\frac{\partial\Psi^\star_{u,i}}{\partial x_j}\right|_{\mathbf{x}}\left.\frac{\partial\Psi_{u,k}}{\partial x_l}\right|_{\mathbf{x}'}\left\langle u_{t,i}u_{t,j}(\mathbf{x},t)u_{t,k}u_{t,l}(\mathbf{x}',t+\tau)\right\rangle\,. \tag{D.12}$$

The surface contribution of the integration by part systematically vanishes, because the surface integral involves $\rho_0\boldsymbol{\Psi}_u$ at the outer boundary of the star, where the oscillation is evanescent.

In the scope of the JWKB approximation, the velocity eigenfunction can be *locally* approximated by the following expression

$$\Psi_{u,i}(\mathbf{x}) = \Psi_{u,i,0}(\mathbf{x})\exp^{j\mathbf{k}(\mathbf{x})\cdot\mathbf{x}}\,, \tag{D.13}$$

where $\boldsymbol{\Psi}_{u,0}(\mathbf{x})$ is the slowly-varying amplitude in space of the velocity eigenfunction, and $\mathbf{k}(\mathbf{x})$ is the space-dependent wavevector of the mode. Both $\boldsymbol{\Psi}_{u,0}$ and $\mathbf{k}$ are slowly varying functions of space (meaning that they vary on length scales much larger than $|\mathbf{k}|^{-1}$). As such, one has

$$\frac{\partial\Psi_{u,i}}{\partial x_j} \sim jk_j(\mathbf{x})\Psi_{u,i,0}(\mathbf{x})\exp^{j\mathbf{k}(\mathbf{x})\cdot\mathbf{x}}\,, \tag{D.14}$$

so that

$$\left\langle c_1(t)c_1^\star(t+\tau)\right\rangle = 4\int \mathrm{d}^3\mathbf{x}\int \mathrm{d}^3\mathbf{x}'\,\rho_0 k_j\Psi^\star_{u,i,0}(\mathbf{x})\rho_0 k_l\Psi_{u,k,0}(\mathbf{x}')\left\langle u_{t,i}u_{t,j}(\mathbf{x},t)u_{t,k}u_{t,l}(\mathbf{x}',t+\tau)\right\rangle\exp^{j(\mathbf{k}(\mathbf{x}')\cdot\mathbf{x}'-\mathbf{k}(\mathbf{x})\cdot\mathbf{x})}\,. \tag{D.15}$$

Then, I implement the following change of variables

$$\mathbf{X} \equiv \mathbf{x}\,, \tag{D.16}$$

$$\delta\mathbf{x} \equiv \mathbf{x}' - \mathbf{x}\,, \tag{D.17}$$

where $\mathbf{X}$ and $\delta\mathbf{x}$ represent the slow and fast space variables respectively. The implementation of this change of variables in Equation D.15 allows me to completely decouple the slowly-varying contributions of $\boldsymbol{\Psi}_{u,0}$ and $\mathbf{k}$ on the one hand, and the rapidly-varying contributions of $\exp(j\mathbf{k}\cdot\mathbf{x})$ and the turbulent velocity two-point correlations on the other hand. Indeed, one obtains[1]

$$\left\langle c_1(t)c_1^\star(t+\tau)\right\rangle = 4\int \mathrm{d}^3\mathbf{X}\int \mathrm{d}^3\delta\mathbf{x}\,\rho_0^2 k_j k_l\Psi^\star_{u,i,0}\Psi_{u,k,0}(\mathbf{X})\left\langle u_{t,i}u_{t,j}\left(\mathbf{X},t\right)u_{t,k}u_{t,l}\left(\mathbf{X}+\delta\mathbf{x},t+\tau\right)\right\rangle\exp^{j\mathbf{k}(\mathbf{X})\cdot\delta\mathbf{x})}\,. \tag{D.18}$$

Taking advantage of the scale decoupling, I can separate the integrals over $\mathbf{X}$ and $\delta\mathbf{x}$

$$\left\langle c_1(t)c_1^\star(t+\tau)\right\rangle = 4\int \mathrm{d}^3\mathbf{X}\,\rho_0^2 k_j k_l\Psi^\star_{u,i,0}\Psi_{u,k,0}(\mathbf{X})\int \mathrm{d}^3\delta\mathbf{x}\,\left\langle u_{t,i}u_{t,j}\left(\mathbf{X},t\right)u_{t,k}u_{t,l}\left(\mathbf{X}+\delta\mathbf{x},t+\tau\right)\right\rangle\exp^{j\mathbf{k}(\mathbf{X})\cdot\delta\mathbf{x}}\,. \tag{D.19}$$

Finally, using Equation D.1, the auto-correlation spectrum α_1 can be expressed thus

$$\alpha_1 = 4\int \mathrm{d}^3\mathbf{X}\,\rho_0^2 k_j k_l\Psi_{u,i,0}\Psi^\star_{u,k,0}\phi^{4b}_{ijkl}(\mathbf{k},\omega)\,, \tag{D.20}$$

where I have dropped all dependence on $\mathbf{X}$ for ease of notation (now that there is no longer any ambiguity), and ϕ^{4b}_{ijkl} is the *fourth-order correlation spectrum of the turbulent velocity* $\mathbf{u}_t$, defined as

$$\phi^4_{ijkl}(\mathbf{k},\omega) \equiv \int_{-\infty}^{0}\mathrm{d}\tau\int \mathrm{d}^3\delta\mathbf{x}\,\left\langle u_{t,i}u_{t,j}\left(\mathbf{X},t\right)u_{t,k}u_{t,l}\left(\mathbf{X}+\delta\mathbf{x},t+\tau\right)\right\rangle\exp^{j(\mathbf{k}\cdot\delta\mathbf{x}+\omega\tau)}\,. \tag{D.21}$$

Naturally, ϕ^{4b}_{ijkl} also depends on the slow variable $\mathbf{X}$ and time t, even though these dependence do not appear explicitly in Equation D.20.

[1] The Jacobian of the change of variable $(\mathbf{x},\mathbf{x}') \mapsto (\mathbf{X},\delta\mathbf{x})$ is straightforwardly estimated, and happens to equal unity.

D.3 Derivation of α_3

Plugging Equation D.6 into Equation D.4, one obtains

$$\begin{aligned} c_3(t) = &\int \mathrm{d}^3\mathbf{x}\, \rho_0(\mathbf{x})\Psi_{\xi,i}(\mathbf{x})\Psi_{\xi,j}(\mathbf{x})\partial_j u_{t,i}(\mathbf{x},t) - \int \mathrm{d}^3\mathbf{x}\, \rho_0(\mathbf{x})\Psi_{u,i}(\mathbf{x})\Psi_{u,j}(\mathbf{x})\partial_j u_{t,i}(\mathbf{x},t) \\ &- \int \mathrm{d}^3\mathbf{x}\, \rho_0(\mathbf{x})\Psi_{u,i}(\mathbf{x})u_{t,j}(\mathbf{x},t)\partial_j\Psi_{u,i} - \int \mathrm{d}^3\mathbf{x}\, \Psi_{u,i}(\mathbf{x})\frac{G_{ij,0}}{\omega}\int \mathrm{d}^3\mathbf{y}\, \rho_0(\mathbf{y})\Psi_{\xi,k}(\mathbf{y})\partial_k\left(u_{t,j}K^{\mathbf{x}}\right)\Big|_{\mathbf{y},t} \\ &+ \int \mathrm{d}^3\mathbf{x}\, \rho_0(\mathbf{x})\Psi_{u,i}(\mathbf{x})u_{t,j}(\mathbf{x},t)\frac{\partial G_{ij}}{\partial\widetilde{u_k''u_l''}}\widetilde{u_k''u_l''}_1(\mathbf{x}) + \int \mathrm{d}^3\mathbf{x}\, \rho_0(\mathbf{x})\Psi_{u,i}(\mathbf{x})u_{t,j}(\mathbf{x},t)\frac{\partial G_{ij}}{\partial(\partial_k\widetilde{u}_l)}\partial_k\widetilde{u}_{l1}(\mathbf{x}) \\ &+ \int \mathrm{d}^3\mathbf{x}\, \rho_0(\mathbf{x})\Psi_{u,i}(\mathbf{x})u_{t,j}(\mathbf{x},t)\frac{\partial G_{ij}}{\partial\epsilon}\omega_t k_1(\mathbf{x}) + \int \mathrm{d}^3\mathbf{x}\, \rho_0(\mathbf{x})\Psi_{u,i}(\mathbf{x})\frac{1}{2\omega}\sqrt{\frac{C_0\omega_t}{k_0(\mathbf{x})}}\eta_i(\mathbf{x},t)k_1(\mathbf{x})\,, \end{aligned} \tag{D.22}$$

where the perturbation of the Reynolds stress tensor, mean shear tensor and turbulent kinetic energy are given by Equations D.7 to D.9 respectively.

Let me consider the first four terms of Equation D.22, which I will denote as $c_{3a}(t)$ through $c_{3d}(t)$ in the following. They can be rearranged with integration by parts to yield

$$c_{3a}(t) = -\int \mathrm{d}^3\mathbf{x}\, u_{t,i}(\mathbf{x},t)\partial_j\left(\rho_0\Psi_{\xi,i}\Psi_{\xi,j}\right)\Big|_{\mathbf{x}}\,, \tag{D.23}$$

$$c_{3b}(t) = \int \mathrm{d}^3\mathbf{x}\, u_{t,i}(\mathbf{x},t)\partial_j\left(\rho_0\Psi_{u,i}\Psi_{u,j}\right)\Big|_{\mathbf{x}}\,, \tag{D.24}$$

$$c_{3c}(t) = \int \mathrm{d}^3\mathbf{x}\, \rho_0(\mathbf{x})u_{t,j}(\mathbf{x},t)\Psi_{u,i}(\mathbf{x})\,\partial_j\Psi_{u,i}\Big|_{\mathbf{x}}\,, \tag{D.25}$$

$$c_{3d}(t) = \int \mathrm{d}^3\mathbf{x}\, \Psi_{u,i}(\mathbf{x})\frac{G_{ij,0}}{\omega}\int \mathrm{d}^3\mathbf{y}\, u_{t,j}(\mathbf{y},t)K^{\mathbf{x}}(\mathbf{y})\,\partial_k\left(\rho_0\Psi_{\xi,k}\right)\Big|_{\mathbf{y}}\,. \tag{D.26}$$

$$\tag{D.27}$$

The last term can be further simplified by permuting the integrals over $\mathbf{x}$ and $\mathbf{y}$, which yields

$$c_{3d}(t) = \int \mathrm{d}^3\mathbf{y}\, u_{t,j}(\mathbf{y},t)\,\partial_k\left(\rho_0\Psi_{\xi,k}\right)\Big|_{\mathbf{y}}\int \mathrm{d}^3\mathbf{x}\, \Psi_{u,i}(\mathbf{x})\frac{G_{ij,0}}{\omega}K^{\mathbf{y}}(\mathbf{x})\,, \tag{D.28}$$

where I have used the isotropy[2] of the kernel function K to write $K^{\mathbf{x}}(\mathbf{y}) = K^{\mathbf{y}}(\mathbf{x})$. It can be seen that the integral over $\mathbf{x}$ corresponds to the kernel estimation at point $\mathbf{y}$ of the quantity $\Psi_{u,i}G_{ij,0}/(\omega\rho_0)$, which only involves quantities that are not stochastic. As such, this kernel estimation equals the actual value of this quantity at $\mathbf{y}$, and $c_{3d}(t)$ reduces to

$$c_{3d}(t) = \int \mathrm{d}^3\mathbf{y}\frac{G_{ij}}{\omega}u_{t,j}(\mathbf{y},t)\Psi_{u,i}(\mathbf{y})\,\partial_k\left(\rho_0\Psi_{\xi,k}\right)\Big|_{\mathbf{y}}\,. \tag{D.29}$$

As for the fifth, sixth and seventh terms on the right-hand side of Equation D.22, once they are expanded, they yield the following contributions: for the fifth term

$$c_{3e}(t) = \int \mathrm{d}^3\mathbf{x}\int \mathrm{d}^3\mathbf{y}\, u_{t,j}(\mathbf{x})\Psi_{u,i}(\mathbf{x})\left.\frac{\partial G_{ij}}{\partial\widetilde{u_k''u_l''}}\right|_{\mathbf{x}}\left.\frac{\widetilde{u_k''u_l''}_0}{\omega}\,\frac{\partial\rho_0\Psi_{\xi,m}}{\partial x_m}\right|_{\mathbf{y}}K^{\mathbf{x}}(\mathbf{y})\,, \tag{D.30}$$

$$c_{3f}(t) = 2\int \mathrm{d}^3\mathbf{x}\int \mathrm{d}^3\mathbf{y}\, u_{t,j}(\mathbf{x})u_{t,k}(\mathbf{y})\Psi_{u,i}(\mathbf{x})\left.\frac{\partial G_{ij}}{\partial\widetilde{u_k''u_l''}}\right|_{\mathbf{x}}\rho_0(\mathbf{y})\Psi_{u,l}(\mathbf{y})K^{\mathbf{x}}(\mathbf{y})\,, \tag{D.31}$$

$$c_{3g}(t) = -\int \mathrm{d}^3\mathbf{x}\int \mathrm{d}^3\mathbf{y}\, u_{t,j}(\mathbf{x})u_{t,k}(\mathbf{y})u_{t,l}(\mathbf{y})\frac{1}{\omega}\Psi_{u,i}(\mathbf{x})\left.\frac{\partial G_{ij}}{\partial\widetilde{u_k''u_l''}}\right|_{\mathbf{x}}\left.\frac{\partial\rho_0\Psi_{\xi,m}}{\partial x_m}\right|_{\mathbf{y}}K^{\mathbf{x}}(\mathbf{y})\,, \tag{D.32}$$

[2] I have not mentioned the isotropy property in Section 7.2.4, when I introduced the kernel function in the first place. In SPH, this property is required in order to yield unbiased mean gradients (see Section 9.1.2 for more details).

for the sixth term

$$c_{3h}(t) = \int \mathrm{d}^3\mathbf{x} \int \mathrm{d}^3\mathbf{y}\; u_{t,j}(\mathbf{x})\Psi_{u,i}(\mathbf{x}) \left.\frac{\partial G_{ij}}{\partial(\partial_k\widetilde{u_l})}\right|_{\mathbf{x}} \left.\frac{\partial\rho_0\Psi_{u,l}}{\partial x_k}\right|_{\mathbf{y}} K^{\mathbf{x}}(\mathbf{y})\,, \tag{D.33}$$

$$c_{3i}(t) = -\int \mathrm{d}^3\mathbf{x} \int \mathrm{d}^3\mathbf{y}\; u_{t,j}(\mathbf{x})\frac{\rho_0(\mathbf{y})}{\rho_0(\mathbf{x})}\Psi_{u,i}(\mathbf{x}) \left.\frac{\partial G_{ij}}{\partial(\partial_k\widetilde{u_l})}\right|_{\mathbf{x}} \left.\frac{\partial\rho_0}{\partial x_k}\right|_{\mathbf{x}} \Psi_{u,l}(\mathbf{y})K^{\mathbf{x}}(\mathbf{y})\,, \tag{D.34}$$

$$c_{3j}(t) = \int \mathrm{d}^3\mathbf{x} \int \mathrm{d}^3\mathbf{y}\; u_{t,j}(\mathbf{x})u_{t,k}(\mathbf{y})\frac{1}{\omega}\Psi_{u,i}(\mathbf{x}) \left.\frac{\partial G_{ij}}{\partial(\partial_l\widetilde{u_k})}\right|_{\mathbf{x}} \left.\frac{\partial\rho_0\Psi_{u,m}}{\partial x_m}\right|_{\mathbf{y}} \left.\frac{\partial K^{\mathbf{x}}}{\partial x_l}\right|_{\mathbf{y}}\,, \tag{D.35}$$

$$c_{3k}(t) = \int \mathrm{d}^3\mathbf{x} \int \mathrm{d}^3\mathbf{y}\; u_{t,j}(\mathbf{x})u_{t,k}(\mathbf{y})\frac{1}{\omega\rho_0(\mathbf{x})}\Psi_{u,i}(\mathbf{x}) \left.\frac{\partial G_{ij}}{\partial(\partial_l\widetilde{u_k})}\right|_{\mathbf{x}} \left.\frac{\partial\rho_0}{\partial x_l}\right|_{\mathbf{x}} \left.\frac{\partial\rho_0\Psi_{u,m}}{\partial x_m}\right|_{\mathbf{y}} K^{\mathbf{x}}(\mathbf{y})\,, \tag{D.36}$$

and for the seventh term

$$c_{3l}(t) = \int \mathrm{d}^3\mathbf{x} \int \mathrm{d}^3\mathbf{y}\; u_{t,j}(\mathbf{x})\Psi_{u,i}(\mathbf{x}) \left.\frac{\partial G_{ij}}{\partial\epsilon}\right|_{\mathbf{x}} \frac{\omega_t k_0(\mathbf{x})}{\omega} \left.\frac{\partial\rho_0\Psi_{\xi,m}}{\partial x_m}\right|_{\mathbf{y}} K^{\mathbf{x}}(\mathbf{y})\,, \tag{D.37}$$

$$c_{3m}(t) = \int \mathrm{d}^3\mathbf{x} \int \mathrm{d}^3\mathbf{y}\; u_{t,j}(\mathbf{x})u_{t,k}(\mathbf{y})\omega_t\Psi_{u,i}(\mathbf{x}) \left.\frac{\partial G_{ij}}{\partial\epsilon}\right|_{\mathbf{x}} \rho_0(\mathbf{y})\Psi_{u,k}(\mathbf{y})K^{\mathbf{x}}(\mathbf{y})\,, \tag{D.38}$$

$$c_{3n}(t) = -\int \mathrm{d}^3\mathbf{x} \int \mathrm{d}^3\mathbf{y}\; u_{t,j}(\mathbf{x})u_{t,k}(\mathbf{y})u_{t,l}(\mathbf{y})\frac{1}{2}\omega_t\Psi_{u,i}(\mathbf{x}) \left.\frac{\partial G_{ij}}{\partial\epsilon}\right|_{\mathbf{x}} \left.\frac{\partial\rho_0\Psi_{\xi,m}}{\partial x_m}\right|_{\mathbf{y}} \delta_{kl}K^{\mathbf{x}}(\mathbf{y})\,. \tag{D.39}$$

Finally, in the last term on the right-hand side of Equation D.22, the quantity under the integral is proportional to the stochastic process $\eta_i(\mathbf{x},t)$, which, by construction, is δ-correlated in both space and time. In particular, its correlation length scale is infinitesimally small compared to that of the turbulent velocity $\mathbf{u}_t(\mathbf{x},t)$. But as I showed in Section D.2, it is precisely the spatial coherence of the stochastic perturbations to the wave equation that explains its ability to impact the complex amplitude of the modes. As such, this part will not actually contribute to the final expression of α_3, or to the stochastic amplitude equations in any way, and I will discard it in the following.

Formally, $c_3(t)$ can be written as a sum of contributions that are either first-, second- or third-order in terms of the turbulent velocity $\mathbf{u}_t$

$$c_3(t) = \int \mathrm{d}^3\mathbf{x} \int \mathrm{d}^3\mathbf{y} \left(f_{1,i}(\mathbf{x},\mathbf{y})u_{t,i}(\mathbf{x},t) + f_{2,ij}(\mathbf{x},\mathbf{y})u_{t,i}(\mathbf{x},t)u_{t,j}(\mathbf{y},t) + f_{3,ijk}(\mathbf{x},\mathbf{y})u_{t,i}(\mathbf{x},t)u_{t,j}u_{t,k}(\mathbf{y},t)\right)\,, \tag{D.40}$$

where

$$\begin{aligned} f_{1,i}(\mathbf{x},\mathbf{y}) \equiv \Bigg[& -\partial_j\left(\rho_0\Psi_{\xi,i}\Psi_{\xi,j}\right) + \partial_j\left(\rho_0\Psi_{u,i}\Psi_{u,j}\right) + \rho_0\Psi_{u,j}\partial_i\Psi_{u,j} + \frac{G_{ji,0}}{\omega}\Psi_{u,j}\partial_k\left(\rho_0\Psi_{\xi,k}\right)\Bigg]\Bigg|_{\mathbf{x}} \delta(\mathbf{x}-\mathbf{y}) \\ & + \Bigg[\Psi_{u,j}(\mathbf{x}) \left.\frac{\partial G_{ji}}{\partial\widetilde{u_k''u_l''}}\right|_{\mathbf{x}} \frac{\widetilde{u_k''u_l''}_0}{\omega} \left.\frac{\partial\rho_0\Psi_{\xi,m}}{\partial x_m}\right|_{\mathbf{y}} + \Psi_{u,j}(\mathbf{x}) \left.\frac{\partial G_{ji}}{\partial(\partial_k\widetilde{u_l})}\right|_{\mathbf{x}} \left.\frac{\partial\rho_0\Psi_{u,l}}{\partial x_k}\right|_{\mathbf{y}} \\ & - \frac{\rho_0(\mathbf{y})}{\rho_0(\mathbf{x})}\Psi_{u,j}(\mathbf{x}) \left.\frac{\partial G_{ji}}{\partial(\partial_k\widetilde{u_l})}\right|_{\mathbf{x}} \left.\frac{\partial\rho_0}{\partial x_k}\right|_{\mathbf{x}} \Psi_{u,l}(\mathbf{y}) + \Psi_{u,j}(\mathbf{x}) \left.\frac{\partial G_{ji}}{\partial\epsilon}\right|_{\mathbf{x}} \frac{\omega_t k_0(\mathbf{x})}{\omega} \left.\frac{\partial\rho_0\Psi_{\xi,m}}{\partial x_m}\right|_{\mathbf{y}}\Bigg] K^{\mathbf{x}}(\mathbf{y})\,, \end{aligned} \tag{D.41}$$

$$\begin{aligned} f_{2,ij}(\mathbf{x},\mathbf{y}) \equiv \Bigg[& \Psi_{u,k}(\mathbf{x}) \left.\frac{\partial G_{ki}}{\partial\widetilde{u_j''u_l''}}\right|_{\mathbf{x}} \rho_0(\mathbf{y})\Psi_{u,l}(\mathbf{y}) + \Psi_{u,k}(\mathbf{x}) \left.\frac{\partial G_{ki}}{\partial\widetilde{u_l''u_j''}}\right|_{\mathbf{x}} \rho_0(\mathbf{y})\Psi_{u,l}(\mathbf{y}) \\ & + \frac{1}{\omega\rho_0(\mathbf{x})}\Psi_{u,k}(\mathbf{x}) \left.\frac{\partial G_{ki}}{\partial(\partial_l\widetilde{u_j})}\right|_{\mathbf{x}} \left.\frac{\partial\rho_0}{\partial x_l}\right|_{\mathbf{x}} \left.\frac{\partial\rho_0\Psi_{u,m}}{\partial x_m}\right|_{\mathbf{y}} + \omega_t\Psi_{u,k}(\mathbf{x}) \left.\frac{\partial G_{ki}}{\partial\epsilon}\right|_{\mathbf{x}} \rho_0(\mathbf{y})\Psi_{u,j}(\mathbf{y})\Bigg] K^{\mathbf{x}}(\mathbf{y}) \\ & + \frac{1}{\omega}\Psi_{u,k}(\mathbf{x}) \left.\frac{\partial G_{ki}}{\partial(\partial_l\widetilde{u_j})}\right|_{\mathbf{x}} \left.\frac{\partial\rho_0\Psi_{u,m}}{\partial x_m}\right|_{\mathbf{y}} \left.\frac{\partial K^{\mathbf{x}}}{\partial x_l}\right|_{\mathbf{y}}\,, \end{aligned} \tag{D.42}$$

$$f_{3,ijk}(\mathbf{x},\mathbf{y}) \equiv -\left[\frac{1}{\omega}\Psi_{u,l}(\mathbf{x}) \left.\frac{\partial G_{li}}{\partial\widetilde{u_j''u_k''}}\right|_{\mathbf{x}} \left.\frac{\partial\rho_0\Psi_{\xi,m}}{\partial x_m}\right|_{\mathbf{y}} + \frac{1}{2}\frac{\omega_t}{\omega}\Psi_{u,l}(\mathbf{x}) \left.\frac{\partial G_{li}}{\partial\epsilon}\right|_{\mathbf{x}} \left.\frac{\partial\rho_0\Psi_{\xi,m}}{\partial x_m}\right|_{\mathbf{y}} \delta_{jk}\right] K^{\mathbf{x}}(\mathbf{y})\,. \tag{D.43}$$

These expressions depend on the structure of the eigenmode both in terms of displacement $\boldsymbol{\Psi}_\xi$ and velocity $\boldsymbol{\Psi}_u$. However, I recall that these are simply related through

$$\boldsymbol{\Psi}_u(\mathbf{x}) = j\boldsymbol{\Psi}_\xi(\mathbf{x}) \,, \tag{D.44}$$

so that $f_{1,i}$, $f_{2,ij}$ and $f_{3,ijk}$ actually only depend on the normalised velocity eigenfunction $\boldsymbol{\Psi}_u$ and the equilibrium state of the star.

Forming the autocorrelation product of $c_3(t)$ from Equation D.40, it can be seen that the expansion involves correlation products of the turbulent velocity field $\mathbf{u}_t$ of various orders, ranging from 2 to 6. In the following, I will make the assumption, often used in the context of Gaussian turbulence, that 1) these moments can be cut at fourth order, and 2) the contribution of the third-order moment can be neglected compared to that of the second- or fourth-order. With this approximation in mind, I then proceed to adopt the JWKB approximation in the same form as in Section D.2 (see Equation D.13), which yields

$$\begin{aligned}
&\langle c_3(t) c_3^\star(t+\tau)\rangle = \\
&\int \mathrm{d}^3\mathbf{X}\,\mathrm{d}^3\delta\mathbf{x}\,\mathrm{d}^3\delta\mathbf{y_1}\,\mathrm{d}^3\delta\mathbf{y_2}\,\rho_0^2 F_i^{1a}(\mathbf{X}) F_j^{1a\star}(\mathbf{X}) \left\langle u_{t,i}(\mathbf{X}) u_{t,j}^\tau(\mathbf{X}+\delta\mathbf{x})\right\rangle \delta(\delta\mathbf{y_1})\delta(\delta\mathbf{y_2}) \exp^{j\mathbf{k}(\mathbf{X})\cdot(-2\delta\mathbf{x}+\delta\mathbf{y_1}-\delta\mathbf{y_2})} \\
&+ \int \mathrm{d}^3\mathbf{X}\,\mathrm{d}^3\delta\mathbf{x}\,\mathrm{d}^3\delta\mathbf{y_1}\,\mathrm{d}^3\delta\mathbf{y_2}\,\rho_0^2 F_i^{1a}(\mathbf{X}) F_j^{1b\star}(\mathbf{X}) \left\langle u_{t,i}(\mathbf{X}) u_{t,j}^\tau(\mathbf{X}+\delta\mathbf{x})\right\rangle \delta(\delta\mathbf{y_1}) K(\delta\mathbf{y_2}) \exp^{j\mathbf{k}(\mathbf{X})\cdot(-2\delta\mathbf{x}+\delta\mathbf{y_1}-\delta\mathbf{y_2})} \\
&+ \int \mathrm{d}^3\mathbf{X}\,\mathrm{d}^3\delta\mathbf{x}\,\mathrm{d}^3\delta\mathbf{y_1}\,\mathrm{d}^3\delta\mathbf{y_2}\,\rho_0^2 F_i^{1b}(\mathbf{X}) F_j^{1a\star}(\mathbf{X}) \left\langle u_{t,i}(\mathbf{X}) u_{t,j}^\tau(\mathbf{X}+\delta\mathbf{x})\right\rangle K(\delta\mathbf{y_1}) \delta(\delta\mathbf{y_2}) \exp^{j\mathbf{k}(\mathbf{X})\cdot(-2\delta\mathbf{x}+\delta\mathbf{y_1}-\delta\mathbf{y_2})} \\
&+ \int \mathrm{d}^3\mathbf{X}\,\mathrm{d}^3\delta\mathbf{x}\,\mathrm{d}^3\delta\mathbf{y_1}\,\mathrm{d}^3\delta\mathbf{y_2}\,\rho_0^2 F_i^{1b}(\mathbf{X}) F_j^{1b\star}(\mathbf{X}) \left\langle u_{t,i}(\mathbf{X}) u_{t,j}^\tau(\mathbf{X}+\delta\mathbf{x})\right\rangle K(\delta\mathbf{y_1}) K(\delta\mathbf{y_2}) \exp^{j\mathbf{k}(\mathbf{X})\cdot(-2\delta\mathbf{x}+\delta\mathbf{y_1}-\delta\mathbf{y_2})} \\
&+ \int \mathrm{d}^3\mathbf{X}\,\mathrm{d}^3\delta\mathbf{x}\,\mathrm{d}^3\delta\mathbf{y_1}\,\mathrm{d}^3\delta\mathbf{y_2}\,\rho_0^2 F_i^{1a}(\mathbf{X}) F_{jkl}^{3b\star}(\mathbf{X}) \left\langle u_{t,i}(\mathbf{X}) u_{t,j}^\tau(\mathbf{X}+\delta\mathbf{x}) u_{t,k}^\tau u_{t,l}^\tau(\mathbf{X}+\delta\mathbf{x}-\delta\mathbf{y_2})\right\rangle \\
&\qquad \delta(\delta\mathbf{y_1}) K(\delta\mathbf{y_2}) \exp^{j\mathbf{k}(\mathbf{X})\cdot(-2\delta\mathbf{x}+\delta\mathbf{y_1}-\delta\mathbf{y_2})} \\
&+ \int \mathrm{d}^3\mathbf{X}\,\mathrm{d}^3\delta\mathbf{x}\,\mathrm{d}^3\delta\mathbf{y_1}\,\mathrm{d}^3\delta\mathbf{y_2}\,\rho_0^2 F_i^{1b}(\mathbf{X}) F_{jkl}^{3b\star}(\mathbf{X}) \left\langle u_{t,i}(\mathbf{X}) u_{t,j}^\tau(\mathbf{X}+\delta\mathbf{x}) u_{t,k}^\tau u_{t,l}^\tau(\mathbf{X}+\delta\mathbf{x}-\delta\mathbf{y_2})\right\rangle \\
&\qquad K(\delta\mathbf{y_1}) K(\delta\mathbf{y_2}) \exp^{j\mathbf{k}(\mathbf{X})\cdot(-2\delta\mathbf{x}+\delta\mathbf{y_1}-\delta\mathbf{y_2})} \\
&+ \int \mathrm{d}^3\mathbf{X}\,\mathrm{d}^3\delta\mathbf{x}\,\mathrm{d}^3\delta\mathbf{y_1}\,\mathrm{d}^3\delta\mathbf{y_2}\,\rho_0^2 F_i^{1a\star}(\mathbf{X}) F_{jkl}^{3b}(\mathbf{X}) \left\langle u_{t,i}^\tau(\mathbf{X}+\delta\mathbf{x}) u_{t,j}(\mathbf{X}) u_{t,k} u_{t,l}(\mathbf{X}-\delta\mathbf{y_1})\right\rangle \\
&\qquad K(\delta\mathbf{y_1}) \delta(\delta\mathbf{y_2}) \exp^{j\mathbf{k}(\mathbf{X})\cdot(-2\delta\mathbf{x}+\delta\mathbf{y_1}-\delta\mathbf{y_2})} \\
&+ \int \mathrm{d}^3\mathbf{X}\,\mathrm{d}^3\delta\mathbf{x}\,\mathrm{d}^3\delta\mathbf{y_1}\,\mathrm{d}^3\delta\mathbf{y_2}\,\rho_0^2 F_i^{1b\star}(\mathbf{X}) F_{jkl}^{3b}(\mathbf{X}) \left\langle u_{t,i}^\tau(\mathbf{X}+\delta\mathbf{x}) u_{t,j}(\mathbf{X}) u_{t,k} u_{t,l}(\mathbf{X}-\delta\mathbf{y_1})\right\rangle \\
&\qquad K(\delta\mathbf{y_1}) K(\delta\mathbf{y_2}) \exp^{j\mathbf{k}(\mathbf{X})\cdot(-2\delta\mathbf{x}+\delta\mathbf{y_1}-\delta\mathbf{y_2})} \\
&+ \int \mathrm{d}^3\mathbf{X}\,\mathrm{d}^3\delta\mathbf{x}\,\mathrm{d}^3\delta\mathbf{y_1}\,\mathrm{d}^3\delta\mathbf{y_2}\,\rho_0^2 F_{ij}^{2}(\mathbf{X}) F_{kl}^{2\star}(\mathbf{X}) \left\langle u_{t,i}(\mathbf{X}) u_{t,j}(\mathbf{X}-\delta\mathbf{y_1}) u_{t,k}^\tau(\mathbf{X}+\delta\mathbf{x}) u_{t,l}^\tau(\mathbf{X}+\delta\mathbf{x}-\delta\mathbf{y_2})\right\rangle \\
&\qquad K(\delta\mathbf{y_1}) K(\delta\mathbf{y_2}) \exp^{j\mathbf{k}(\mathbf{X})\cdot(-2\delta\mathbf{x}+\delta\mathbf{y_1}-\delta\mathbf{y_2})} \\
&+ \int \mathrm{d}^3\mathbf{X}\,\mathrm{d}^3\delta\mathbf{x}\,\mathrm{d}^3\delta\mathbf{y_1}\,\mathrm{d}^3\delta\mathbf{y_2}\,\rho_0^2 F_{ijm}^{3a}(\mathbf{X}) F_{kl}^{2\star}(\mathbf{X}) \left\langle u_{t,i}(\mathbf{X}) u_{t,j}(\mathbf{X}-\delta\mathbf{y_1}) u_{t,k}^\tau(\mathbf{X}+\delta\mathbf{x}) u_{t,l}^\tau(\mathbf{X}+\delta\mathbf{x}-\delta\mathbf{y_2})\right\rangle \\
&\qquad \partial_m K(\delta\mathbf{y_1}) K(\delta\mathbf{y_2}) \exp^{j\mathbf{k}(\mathbf{X})\cdot(-2\delta\mathbf{x}+\delta\mathbf{y_1}-\delta\mathbf{y_2})} \\
&+ \int \mathrm{d}^3\mathbf{X}\,\mathrm{d}^3\delta\mathbf{x}\,\mathrm{d}^3\delta\mathbf{y_1}\,\mathrm{d}^3\delta\mathbf{y_2}\,\rho_0^2 F_{ij}^{2}(\mathbf{X}) F_{klm}^{3a\star}(\mathbf{X}) \left\langle u_{t,i}(\mathbf{X}) u_{t,j}(\mathbf{X}-\delta\mathbf{y_1}) u_{t,k}^\tau(\mathbf{X}+\delta\mathbf{x}) u_{t,l}^\tau(\mathbf{X}+\delta\mathbf{x}-\delta\mathbf{y_2})\right\rangle \\
&\qquad K(\delta\mathbf{y_1}) \partial_m K(\delta\mathbf{y_2}) \exp^{j\mathbf{k}(\mathbf{X})\cdot(-2\delta\mathbf{x}+\delta\mathbf{y_1}-\delta\mathbf{y_2})} \\
&+ \int \mathrm{d}^3\mathbf{X}\,\mathrm{d}^3\delta\mathbf{x}\,\mathrm{d}^3\delta\mathbf{y_1}\,\mathrm{d}^3\delta\mathbf{y_2}\,\rho_0^2 F_{ijm}^{3a}(\mathbf{X}) F_{kln}^{3a\star}(\mathbf{X}) \left\langle u_{t,i}(\mathbf{X}) u_{t,j}(\mathbf{X}-\delta\mathbf{y_1}) u_{t,k}^\tau(\mathbf{X}+\delta\mathbf{x}) u_{t,l}^\tau(\mathbf{X}+\delta\mathbf{x}-\delta\mathbf{y_2})\right\rangle \\
&\qquad \partial_m K(\delta\mathbf{y_1}) \partial_n K(\delta\mathbf{y_2}) \exp^{j\mathbf{k}(\mathbf{X})\cdot(-2\delta\mathbf{x}+\delta\mathbf{y_1}-\delta\mathbf{y_2})} \,,
\end{aligned} \tag{D.45}$$

where the subscript τ means that the turbulent velocity field is evaluated at time $t+\tau$, and I have introduced

$$F_i^{1a} = 4jk_j\Psi_{u,i,0}\Psi_{u,j,0} + jk_i\Psi_{u,j,0}\Psi_{u,j,0} + \frac{G_{ij,0}}{\omega}k_k\Psi_{u,j,0}\Psi_{u,k,0}\,, \tag{D.46}$$

$$F_i^{1b} = \frac{\partial G_{ij}}{\partial\widetilde{u_k''u_l''}}\frac{\widetilde{u_k''u_l''}_0}{\omega}k_m\Psi_{u,m,0}\Psi_{u,j,0} + \frac{\partial G_{ij}}{\partial(\partial_k\widetilde{u}_l)}jk_k\Psi_{u,j,0}\Psi_{u,l,0} + \frac{\partial G_{ij}}{\partial\epsilon}\frac{\omega_t k_0}{\omega}k_m\Psi_{u,j,0}\Psi_{u,m,0}\,, \tag{D.47}$$

$$F_{ij}^{2} = \left(\frac{\partial G_{ki}}{\partial\widetilde{u_j''u_l''}} + \frac{\partial G_{ki}}{\partial\widetilde{u_l''u_j''}}\right)\Psi_{u,l,0}\Psi_{u,k,0} + \frac{\partial G_{ki}}{\partial\epsilon}\omega_t\Psi_{u,j,0}\Psi_{u,k,0}\,, \tag{D.48}$$

$$F_{ijk}^{3a} = \frac{\partial G_{li}}{\partial(\partial_k\widetilde{u}_j)}\frac{1}{\omega}jk_m\Psi_{u,l,0}\Psi_{u,m,0}\,, \tag{D.49}$$

$$F_{ijk}^{3b} = -\frac{\partial G_{li}}{\partial\widetilde{u_j''u_k''}}\frac{1}{\omega}k_m\Psi_{u,l,0}\Psi_{u,m,0} - \frac{1}{2}\frac{\partial G_{li}}{\partial\epsilon}\frac{\omega_t}{\omega}k_m\Psi_{u,l,0}\Psi_{u,m,0}\delta_{jk}\,. \tag{D.50}$$

Equation D.45 can be drastically simplified by remarking that any integral involving the product of a function f with the kernel function K correspond, by construction, to the ensemble average of said function f (see Philidet et al. (2021) for more details). Similarly, if the integral is weighted by the gradient of the kernel function, then it corresponds to the ensemble average of the gradient of f (with a minus sign). But every quantity appearing in Equation D.45 is either already an ensemble average, or an equilibrium quantity, or else the normalised velocity eigenfunction $\mathbf{\Psi}_u$. Neither of these are stochastic quantities, which means they are equal to their own ensemble average. This allows me to perform the kind of simplification illustrated by Eq. (50) of Philidet et al. (2021), and I eventually find

$$\begin{aligned}
&\langle c_3(t)c_3(t+\tau)\rangle = \\
&\int \mathrm{d}^3\mathbf{X}\,\rho_0^2 F_i^1 F_j^{1\star}(\mathbf{X})\int \mathrm{d}^3\delta\mathbf{x}\,\left\langle u_{t,i}(\mathbf{X})u_{t,j}^{\tau}(\mathbf{X}+\delta\mathbf{x})\right\rangle \exp^{-2j\mathbf{k}(\mathbf{X})\cdot\delta\mathbf{x}} \\
&+\int \mathrm{d}^3\mathbf{X}\,\rho_0^2 F_i^1 F_{jkl}^{3b\star}(\mathbf{X})\int \mathrm{d}^3\delta\mathbf{x}\,\left\langle u_{t,i}(\mathbf{X})u_{t,j}^{\tau}u_{t,k}^{\tau}u_{t,l}^{\tau}(\mathbf{X}+\delta\mathbf{x})\right\rangle \exp^{-2j\mathbf{k}(\mathbf{X})\cdot\delta\mathbf{x}} \\
&+\int \mathrm{d}^3\mathbf{X}\,\rho_0^2 F_i^{1\star} F_{jkl}^{3b}(\mathbf{X})\int \mathrm{d}^3\delta\mathbf{x}\,\left\langle u_{t,i}^{\tau}(\mathbf{X})u_{t,j}u_{t,k}u_{t,l}(\mathbf{X}+\delta\mathbf{x})\right\rangle \exp^{-2j\mathbf{k}(\mathbf{X})\cdot\delta\mathbf{x}} \\
&+\int \mathrm{d}^3\mathbf{X}\,\rho_0^2 F_{ij}^2 F_{kl}^{2\star}(\mathbf{X})\int \mathrm{d}^3\delta\mathbf{x}\,\left\langle u_{t,i}u_{t,j}(\mathbf{X})u_{t,k}^{\tau}u_{t,l}^{\tau}(\mathbf{X}+\delta\mathbf{x})\right\rangle \exp^{-2j\mathbf{k}(\mathbf{X})\cdot\delta\mathbf{x}} \\
&+\int \mathrm{d}^3\mathbf{X}\,\rho_0^2 F_{ijm}^{3a} F_{kln}^{3a\star}(\mathbf{X})\int \mathrm{d}^3\delta\mathbf{x}\,\left\langle u_{t,i}\partial_m u_{t,j}(\mathbf{X}+\delta\mathbf{x})u_{t,k}^{\tau}\partial_n u_{t,l}^{\tau}(\mathbf{X}+\delta\mathbf{x})\right\rangle \exp^{-2j\mathbf{k}(\mathbf{X})\cdot\delta\mathbf{x}} \\
&+\int \mathrm{d}^3\mathbf{X}\,\rho_0^2 F_{ijm}^{3a} F_{kl}^{2\star}(\mathbf{X})\int \mathrm{d}^3\delta\mathbf{x}\,\left\langle u_{t,i}\partial_m u_{t,j}(\mathbf{X})u_{t,k}^{\tau}u_{t,l}^{\tau}(\mathbf{X}+\delta\mathbf{x})\right\rangle \exp^{-2j\mathbf{k}(\mathbf{X})\cdot\delta\mathbf{x}} \\
&+\int \mathrm{d}^3\mathbf{X}\,\rho_0^2 F_{ij}^2 F_{klm}^{3a\star}(\mathbf{X})\int \mathrm{d}^3\delta\mathbf{x}\,\left\langle u_{t,i}u_{t,j}(\mathbf{X})u_{t,k}^{\tau}\partial_m u_{t,l}^{\tau}(\mathbf{X}+\delta\mathbf{x})\right\rangle \exp^{-2j\mathbf{k}(\mathbf{X})\cdot\delta\mathbf{x}}\,,
\end{aligned} \tag{D.51}$$

where I defined $F^1 \equiv F^{1a} + F^{1b}$.

Finally, plugging this into Equation D.2, one finds the following expression

$$\begin{aligned}
\alpha_3 = \int \mathrm{d}^3\mathbf{X}\,\rho_0^2\Big(&F_i^1 F_j^{1\star}(\mathbf{X})\phi_{ij}^2(2\mathbf{k},2\omega) + 2\,\mathrm{Re}\left[F_i^1 F_{jkl}^{3b\star}(\mathbf{X})\phi_{ijkl}^{4a}(2\mathbf{k},2\omega)\right] + F_{ij}^2 F_{kl}^{2\star}(\mathbf{X})\phi_{ijkl}^{4b}(2\mathbf{k},2\omega) \\
&+ F_{ijm}^{3a} F_{kln}^{3a\star}(\mathbf{X})\phi_{ijkl}^{4c}(2\mathbf{k},2\omega) + 2\,\mathrm{Re}\left[F_{ijm}^{3a} F_{kl}^{2\star}(\mathbf{X})\phi_{ijkl}^{4d}(2\mathbf{k},2\omega)\right]\Big)\,,
\end{aligned} \tag{D.52}$$

where I have defined the following spectra on the same template as Equation D.21

$$\phi^{2}_{ij}(\mathbf{k},\omega) \equiv \int_{-\infty}^{0} \mathrm{d}\tau \int \mathrm{d}^3\delta\mathbf{x} \, \left\langle u_{t,i}\left(\mathbf{X}\right) u^{\tau}_{t,j}(\mathbf{X}+\mathbf{x})\right\rangle \exp^{j(\omega\tau-\mathbf{k}\cdot\delta\mathbf{x})} \, , \tag{D.53}$$

$$\phi^{4a}_{ijkl}(\mathbf{k},\omega) \equiv \int_{-\infty}^{0} \mathrm{d}\tau \int \mathrm{d}^3\delta\mathbf{x} \, \left\langle u_{t,i}\left(\mathbf{X}\right) u^{\tau}_{t,j} u^{\tau}_{t,k} u^{\tau}_{t,l}(\mathbf{X}+\mathbf{x})\right\rangle \exp^{j(\omega\tau-\mathbf{k}\cdot\delta\mathbf{x})} \, , \tag{D.54}$$

$$\phi^{4b}_{ijkl}(\mathbf{k},\omega) \equiv \int_{-\infty}^{0} \mathrm{d}\tau \int \mathrm{d}^3\delta\mathbf{x} \, \left\langle u_{t,i}u_{t,j}\left(\mathbf{X}\right) u^{\tau}_{t,k} u^{\tau}_{t,l}(\mathbf{X}+\mathbf{x})\right\rangle \exp^{j(\omega\tau-\mathbf{k}\cdot\delta\mathbf{x})} \, , \tag{D.55}$$

$$\phi^{4c}_{ijkl}(\mathbf{k},\omega) \equiv \int_{-\infty}^{0} \mathrm{d}\tau \int \mathrm{d}^3\delta\mathbf{x} \, \left\langle u_{t,i}\partial_m u_{t,j}\left(\mathbf{X}\right) u^{\tau}_{t,k} \partial_n u^{\tau}_{t,l}(\mathbf{X}+\mathbf{x})\right\rangle \exp^{j(\omega\tau-\mathbf{k}\cdot\delta\mathbf{x})} \, , \tag{D.56}$$

$$\phi^{4d}_{ijkl}(\mathbf{k},\omega) \equiv \int_{-\infty}^{0} \mathrm{d}\tau \int \mathrm{d}^3\delta\mathbf{x} \, \left\langle u_{t,i}\partial_m u_{t,j}\left(\mathbf{X}\right) u^{\tau}_{t,k} u^{\tau}_{t,l}(\mathbf{X}+\mathbf{x})\right\rangle \exp^{j(\omega\tau-\mathbf{k}\cdot\delta\mathbf{x})} \, . \tag{D.57}$$

Let me remark, as I did in Section D.2, that F^1, F^2, F^{3a} and F^{3b} are functions of $\mathbf{X}$, and that ϕ^{2}_{ij}, ϕ^{4a}_{ijkl}, ϕ^{4b}_{ijkl}, ϕ^{4c}_{ijkl} and ϕ^{4d}_{ijkl} also depend on both $\mathbf{X}$ and t, even though these dependence do not appear explicitly in Equation D.52.

D.4 Mode normalisation and final form of α_i

The last remaining modification to the explicit expressions of α_1 and α_3 concerns the normalisation condition on the mode $|\Psi\rangle$. Indeed, one needs to relate $\mathbf{\Psi}_{u,0}(\mathbf{x})$ to the actual velocity modal fluctuations $\mathbf{u}_{\mathrm{osc}}(\mathbf{x})$, as it can be obtained through an oscillation code for instance. By construction of the ket $|\Psi\rangle$, one has this very simple proportionality relation

$$\mathbf{\Psi}_u(\mathbf{x}) = \frac{\mathbf{u}_{\mathrm{osc}}(\mathbf{x})}{\sqrt{2\omega^2\mathcal{I}}} \, , \tag{D.58}$$

where the proportionality factor $1/\sqrt{2\omega^2\mathcal{I}}$ is given by the condition that $|\Psi\rangle$ must be normalised to unity, so that

$$\langle\Psi|\Psi\rangle = 1 \, . \tag{D.59}$$

Plugging Equations 8.51 and 8.56 into Equation D.59, this becomes

$$\int \mathrm{d}^3\mathbf{x} \, \rho_0(\mathbf{x}) \left(\left|\mathbf{\Psi}_\xi\right|^2 + |\mathbf{\Psi}_u|^2 \right) = 1 \, , \tag{D.60}$$

and since $\mathbf{\Psi}_u = j\mathbf{\Psi}_\xi$

$$2\int \mathrm{d}^3\mathbf{x} \, \rho_0(\mathbf{x}) \, |\mathbf{\Psi}_u(\mathbf{x})|^2 = 1 \, . \tag{D.61}$$

Finally, plugging Equation D.58, I find

$$\mathcal{I} = \int \mathrm{d}^3\mathbf{x} \, \rho_0(\mathbf{x}) \, |\boldsymbol{\xi}_{\mathrm{osc}}(\mathbf{x})|^2 \, , \tag{D.62}$$

which one recognises as the inertia of the mode (see Equation 2.97). One then finds the relation between $\mathbf{\Psi_{u,0}}$ and $\mathbf{u}_{\mathrm{osc}}$ by plugging Equation D.13 into Equation D.58. In turn, plugging Equation D.58 into Equations D.20 and D.52, one finds the final expressions for α_1 and α_3 reproduced in the main body of this thesis

$$\alpha_1 = \frac{2}{\omega^2\mathcal{I}} \int \mathrm{d}^3\mathbf{X} \, \rho_0^2 k_j k_l u_{\mathrm{osc,i}} u^{\star}_{\mathrm{osc,k}} \phi^{4b}_{ijkl}(\mathbf{k},\omega) \, , \tag{D.63}$$

$$\begin{aligned}\alpha_3 = \frac{1}{4\omega^4\mathcal{I}^2} \int \mathrm{d}^3\mathbf{X} \, \rho_0^2 \Big(& F^1_i F^{1\star}_j(\mathbf{X}) \phi^{2}_{ij}(2\mathbf{k},2\omega) + 2\,\mathrm{Re}\left[F^1_i F^{3b\star}_{jkl}(\mathbf{X})\phi^{4a}_{ijkl}(2\mathbf{k},2\omega)\right] + F^2_{ij}F^{2\star}_{kl}(\mathbf{X})\phi^{4b}_{ijkl}(2\mathbf{k},2\omega) \\ & + F^{3a}_{ijm}F^{3a\star}_{kln}(\mathbf{X})\phi^{4c}_{ijkl}(2\mathbf{k},2\omega) + 2\,\mathrm{Re}\left[F^{3a}_{ijm}F^{2\star}_{kl}(\mathbf{X})\phi^{4d}_{ijkl}(2\mathbf{k},2\omega)\right] \Big) \, ,\end{aligned} \tag{D.64}$$

and I recall, as a summary of the calculations detailed above, that

$$F_i^1 = 4jk_j u_{\mathrm{osc,i}} u_{\mathrm{osc,j}} + jk_i u_{\mathrm{osc,j}} u_{\mathrm{osc,j}} + \frac{G_{ij,0}}{\omega} k_k u_{\mathrm{osc,j}} u_{\mathrm{osc,k}} + \frac{\partial G_{ij}}{\partial \widetilde{u_k'' u_l''}} \frac{\widetilde{u_k'' u_l''}_0}{\omega} k_m u_{\mathrm{osc,m}} u_{\mathrm{osc,j}} + \frac{\partial G_{ij}}{\partial(\partial_k \widetilde{u_l})} jk_k u_{\mathrm{osc,j}} u_{\mathrm{osc,l}} + \frac{\partial G_{ij}}{\partial \epsilon} \frac{\omega_t k_0}{\omega} k_m u_{\mathrm{osc,j}} u_{\mathrm{osc,m}} \,, \tag{D.65}$$

$$F_{ij}^2 = \left(\frac{\partial G_{ki}}{\partial \widetilde{u_j'' u_l''}} + \frac{\partial G_{ki}}{\partial \widetilde{u_l'' u_j''}} \right) u_{\mathrm{osc,l}} u_{\mathrm{osc,k}} + \frac{\partial G_{ki}}{\partial \epsilon} \omega_t u_{\mathrm{osc,j}} u_{\mathrm{osc,k}} \,, \tag{D.66}$$

$$F_{ijk}^{3a} = \frac{\partial G_{li}}{\partial(\partial_k \widetilde{u_j})} \frac{1}{\omega} jk_m u_{\mathrm{osc,l}} u_{\mathrm{osc,m}} \,, \tag{D.67}$$

$$F_{ijk}^{3b} = -\frac{\partial G_{li}}{\partial \widetilde{u_j'' u_k''}} \frac{1}{\omega} k_m u_{\mathrm{osc,l}} u_{\mathrm{osc,m}} - \frac{1}{2} \frac{\partial G_{li}}{\partial \epsilon} \frac{\omega_t}{\omega} k_m u_{\mathrm{osc,l}} u_{\mathrm{osc,m}} \delta_{jk} \,, \tag{D.68}$$

and

$$\phi_{ij}^2(\mathbf{k}, \omega) \equiv \int_{-\infty}^{0} \mathrm{d}\tau \int \mathrm{d}^3\delta\mathbf{x} \, \left\langle u_{t,i}(\mathbf{X}) \, u_{t,j}^{\tau}(\mathbf{X} + \mathbf{x}) \right\rangle \exp^{j(\omega\tau - \mathbf{k}\cdot\delta\mathbf{x})} \,, \tag{D.69}$$

$$\phi_{ijkl}^{4a}(\mathbf{k}, \omega) \equiv \int_{-\infty}^{0} \mathrm{d}\tau \int \mathrm{d}^3\delta\mathbf{x} \, \left\langle u_{t,i}(\mathbf{X}) \, u_{t,j}^{\tau} u_{t,k}^{\tau} u_{t,l}^{\tau}(\mathbf{X} + \mathbf{x}) \right\rangle \exp^{j(\omega\tau - \mathbf{k}\cdot\delta\mathbf{x})} \,, \tag{D.70}$$

$$\phi_{ijkl}^{4b}(\mathbf{k}, \omega) \equiv \int_{-\infty}^{0} \mathrm{d}\tau \int \mathrm{d}^3\delta\mathbf{x} \, \left\langle u_{t,i} u_{t,j}(\mathbf{X}) \, u_{t,k}^{\tau} u_{t,l}^{\tau}(\mathbf{X} + \mathbf{x}) \right\rangle \exp^{j(\omega\tau - \mathbf{k}\cdot\delta\mathbf{x})} \,, \tag{D.71}$$

$$\phi_{ijkl}^{4c}(\mathbf{k}, \omega) \equiv \int_{-\infty}^{0} \mathrm{d}\tau \int \mathrm{d}^3\delta\mathbf{x} \, \left\langle u_{t,i} \partial_m u_{t,j}(\mathbf{X}) \, u_{t,k}^{\tau} \partial_n u_{t,l}^{\tau}(\mathbf{X} + \mathbf{x}) \right\rangle \exp^{j(\omega\tau - \mathbf{k}\cdot\delta\mathbf{x})} \,, \tag{D.72}$$

$$\phi_{ijkl}^{4d}(\mathbf{k}, \omega) \equiv \int_{-\infty}^{0} \mathrm{d}\tau \int \mathrm{d}^3\delta\mathbf{x} \, \left\langle u_{t,i} \partial_m u_{t,j}(\mathbf{X}) \, u_{t,k}^{\tau} u_{t,l}^{\tau}(\mathbf{X} + \mathbf{x}) \right\rangle \exp^{j(\omega\tau - \mathbf{k}\cdot\delta\mathbf{x})} \,. \tag{D.73}$$

Bibliography

Aarslev, M. J., Houdek, G., Handberg, R., and Christensen-Dalsgaard, J. (2018). Modelling linewidths of Kepler red giants in NGC 6819. *MNRAS*, 478(1):69–80.

Abrams, D. and Kumar, P. (1996). Asymmetries of Solar p-Mode Line Profiles. *ApJ*, 472:882.

Aerts, C., Christensen-Dalsgaard, J., and Kurtz, D. W. (2010). *Asteroseismology*.

Allen, M. P., Tildesley, D. J., and Banavar, J. R. (1989). Computer Simulation of Liquids. *Physics Today*, 42(3):105.

Allende Prieto, C., Lambert, D. L., and Asplund, M. (2001). The Forbidden Abundance of Oxygen in the Sun. *ApJ*, 556(1):L63–L66.

Allende Prieto, C., Lambert, D. L., and Asplund, M. (2002). A Reappraisal of the Solar Photospheric C/O Ratio. *ApJ*, 573(2):L137–L140.

Anand, M. S., Mongia, H. C., and Pope, S. B. (1989). *A PDF method for turbulent recirculating flows*, pages 672–693.

Ando, H. and Osaki, Y. (1975). Nonadiabatic nonradial oscillations: an application to the five-minute oscillation of the sun. *PASJ*, 27(4):581–603.

Andrews, D. G. and McIntyre, M. E. (1978). An exact theory of nonlinear waves on a Lagrangian-mean flow. *Journal of Fluid Mechanics*, 89:609–646.

Antia, H. M., Chitre, S. M., and Narasimha, D. (1982). Overstability of acoustic modes and the solar five-minute oscillations. *Sol. Phys.*, 77(1-2):303–327.

Appourchaux, T., Boumier, P., Leibacher, J. W., and Corbard, T. (2018). Searching for g modes. I. A new calibration of the GOLF instrument. *A&A*, 617:A108.

Asplund, M. (2000). Line formation in solar granulation. III. The photospheric Si and meteoritic Fe abundances. *A&A*, 359:755–758.

Asplund, M., Grevesse, N., Sauval, A. J., Allende Prieto, C., and Blomme, R. (2005a). Line formation in solar granulation. VI. [C I], C I, CH and C_2 lines and the photospheric C abundance. *A&A*, 431:693–705.

Asplund, M., Grevesse, N., Sauval, A. J., Allende Prieto, C., and Kiselman, D. (2004). Line formation in solar granulation. IV. [O I], O I and OH lines and the photospheric O abundance. *A&A*, 417:751–768.

Asplund, M., Grevesse, N., Sauval, A. J., Allende Prieto, C., and Kiselman, D. (2005b). Line formation in solar granulation. IV. [O I], O I and OH lines and the photospheric O abundance. *A&A*, 435(1):339–340.

Asplund, M., Nordlund, A., Trampedach, R., Allende Prieto, C., and Stein, R. F. (2000a). Line formation in solar granulation. I. Fe line shapes, shifts and asymmetries. *A&A*, 359:729–742.

Asplund, M., Nordlund, A., Trampedach, R., and Stein, R. F. (2000b). Line formation in solar granulation. II. The photospheric Fe abundance. *A&A*, 359:743–754.

Baglin, A., Auvergne, M., Boisnard, L., Lam-Trong, T., Barge, P., Catala, C., Deleuil, M., Michel, E., and Weiss, W. (2006). CoRoT: a high precision photometer for stellar ecolution and exoplanet finding. In *36th COSPAR Scientific Assembly*, volume 36, page 3749.

Bakosi, J. and Ristorcelli, J. R. (2011). Extending the Langevin model to variable-density pressure-gradient-driven turbulence. *Journal of Turbulence*, 12:19.

Ball, W. H., Beeck, B., Cameron, R. H., and Gizon, L. (2016). MESA meets MURaM. Surface effects in main-sequence solar-like oscillators computed using three-dimensional radiation hydrodynamics simulations. *A&A*, 592:A159.

Ball, W. H. and Gizon, L. (2014). A new correction of stellar oscillation frequencies for near-surface effects. *A&A*, 568:A123.

Ball, W. H. and Gizon, L. (2017). Surface-effect corrections for oscillation frequencies of evolved stars. *A&A*, 600:A128.

Balmforth, N. J. (1992a). Solar pulsational stability - I. Pulsation-mode thermodynamics. *MNRAS*, 255:603–649.

Balmforth, N. J. (1992b). Solar pulsational stability - II. Pulsation frequencies. *MNRAS*, 255:632.

Balmforth, N. J. (1992c). Solar pulsational stability - III. Acoustical excitation by turbulent convection. *MNRAS*, 255:639.

Balmforth, N. J. and Gough, D. O. (1990). Effluent Stellar Pulsation. *ApJ*, 362:256.

Barban, C., Hill, F., and Kras, S. (2004). Simultaneous Velocity-Intensity Spectral and Cross-Spectral Fitting of Helioseismic Data. *ApJ*, 602(1):516–527.

Basu, S. and Antia, H. M. (2000). Effect of Asymmetry in Peak Profiles on Solar Oscillation Frequencies. *ApJ*, 531(2):1088–1093.

Baudin, F., Samadi, R., Goupil, M. J., Appourchaux, T., Barban, C., Boumier, P., Chaplin, W. J., and Gouttebroze, P. (2005). Inferred acoustic rates of solar p modes from several helioseismic instruments. *A&A*, 433(1):349–356.

Beeck, B., Collet, R., Steffen, M., Asplund, M., Cameron, R. H., Freytag, B., Hayek, W., Ludwig, H. G., and Schüssler, M. (2012). Simulations of the solar near-surface layers with the CO5BOLD, MURaM, and Stagger codes. *A&A*, 539:A121.

Belkacem, K., Dupret, M. A., Baudin, F., Appourchaux, T., Marques, J. P., and Samadi, R. (2012). Damping rates of solar-like oscillations across the HR diagram. Theoretical calculations confronted to CoRoT and Kepler observations. *A&A*, 540:L7.

Belkacem, K., Kupka, F., Philidet, J., and Samadi, R. (2021). Surface effects and turbulent pressure. Assessing the Gas-Γ_1 and Reduced-Γ_1 empirical models. *A&A*, 646:L5.

Belkacem, K., Kupka, F., Samadi, R., and Grimm-Strele, H. (2019). Solar p-mode damping rates: Insight from a 3D hydrodynamical simulation. *A&A*, 625:A20.

Belkacem, K., Mathis, S., Goupil, M. J., and Samadi, R. (2009). Mode excitation by turbulent convection in rotating stars. I. Effect of uniform rotation. *A&A*, 508(1):345–353.

Belkacem, K., Samadi, R., Goupil, M. J., Baudin, F., Salabert, D., and Appourchaux, T. (2010). Turbulent eddy-time-correlation in the solar convective zone. *A&A*, 522:L2.

Belkacem, K., Samadi, R., Goupil, M. J., and Dupret, M. A. (2008). Stochastic excitation of non-radial modes. I. High-angular-degree p modes. *A&A*, 478(1):163–174.

Belkacem, K., Samadi, R., Goupil, M. J., Kupka, F., and Baudin, F. (2006). A closure model with plumes. II. Application to the stochastic excitation of solar p modes. *A&A*, 460(1):183–190.

Bellinger, E. P., Basu, S., Hekker, S., and Ball, W. H. (2017). Model-independent Measurement of Internal Stellar Structure in 16 Cygni A and B. *ApJ*, 851(2):80.

Benomar, O., Goupil, M., Belkacem, K., Appourchaux, T., Nielsen, M. B., Bazot, M., Gizon, L., Hanasoge, S., Sreenivasan, K. R., and Marchand, B. (2018). Asymmetry of Line Profiles of Stellar Oscillations Measured by Kepler for Ensembles of Solar-like Oscillators: Impact on Mode Frequencies and Dependence on Effective Temperature. *ApJ*, 857(2):119.

Bigot, L. and Dziembowski, W. A. (2002). On the Combined Effects of a Magnetic Field and Rotation on Acoustic Modes. In Aerts, C., Bedding, T. R., and Christensen-Dalsgaard, J., editors, *IAU Colloq. 185: Radial and Non-radial Pulsationsn as Probes of Stellar Physics*, volume 259 of *Astronomical Society of the Pacific Conference Series*, page 290.

Böhm-Vitense, E. (1958). Über die Wasserstoffkonvektionszone in Sternen verschiedener Effektivtemperaturen und Leuchtkräfte. Mit 5 Textabbildungen. *ZAp*, 46:108.

Böhm-Vitense, E. (1992). *Introduction to Stellar Astrophysics. Vol.3: Stellar structure and evolution*.

Borucki, W. J., Koch, D., Basri, G., Batalha, N., Brown, T., Caldwell, D., Caldwell, J., Christensen-Dalsgaard, J., Cochran, W. D., DeVore, E., Dunham, E. W., Dupree, A. K., Gautier, T. N., Geary, J. C., Gilliland, R., Gould, A., Howell, S. B., Jenkins, J. M., Kondo, Y., Latham, D. W., Marcy, G. W., Meibom, S., Kjeldsen, H., Lissauer, J. J., Monet, D. G., Morrison, D., Sasselov, D., Tarter, J., Boss, A., Brownlee, D., Owen, T., Buzasi, D., Charbonneau, D., Doyle, L., Fortney, J., Ford, E. B., Holman, M. J., Seager, S., Steffen, J. H., Welsh, W. F., Rowe, J., Anderson, H., Buchhave, L., Ciardi, D., Walkowicz, L., Sherry, W., Horch, E., Isaacson, H., Everett, M. E., Fischer, D., Torres, G., Johnson, J. A., Endl, M., MacQueen, P., Bryson, S. T., Dotson, J., Haas, M., Kolodziejczak, J., Van Cleve, J., Chandrasekaran, H., Twicken, J. D., Quintana, E. V., Clarke, B. D., Allen, C., Li, J., Wu, H., Tenenbaum, P., Verner, E., Bruhweiler, F., Barnes, J., and Prsa, A. (2010). Kepler Planet-Detection Mission: Introduction and First Results. *Science*, 327(5968):977.

Borue, V. and Orszag, S. A. (1995). Self-similar decay of three-dimensional homogeneous turbulence with hyperviscosity. *Phys. Rev. E*, 51(2):R856–R859.

Borue, V. and Orszag, S. A. (1996). Kolmogorov's refined similarity hypothesis for hyperviscous turbulence. *Phys. Rev. E*, 53(1):R21–R24.

Brandt, S. (1970). *Statistical and computational methods in data analysis*.

Broomhall, A. M., Chaplin, W. J., Elsworth, Y., Appourchaux, T., and New, R. (2010). A comparison of frequentist and Bayesian inference: searching for low-frequency p modes and g modes in Sun-as-a-star data. *MNRAS*, 406(2):767–781.

Buchler, J. R. and Goupil, M. J. (1984). Amplitude equations for nonadiabatic nonlinear stellar pulsators. I - The formalism. *ApJ*, 279:394–400.

Buchler, J. R., Goupil, M.-J., and Kovacs, G. (1993). Stellar pulsations with stochastic driving. *A&A*, 280(1):157–168.

Buldgen, G., Farnir, M., Pezzotti, C., Eggenberger, P., Salmon, S. J. A. J., Montalban, J., Ferguson, J. W., Khan, S., Bourrier, V., Rendle, B. M., Meynet, G., Miglio, A., and Noels, A. (2019). Revisiting Kepler-444. I. Seismic modeling and inversions of stellar structure. *A&A*, 630:A126.

Campbell, P. M. (1989). Some new algorithms for boundary value problems in smooth particle hydrodynamics. Technical Report.

Canuto, V. M. (1992). Turbulent Convection with Overshooting: Reynolds Stress Approach. *ApJ*, 392:218.

Canuto, V. M. (1993). Turbulent Convection with Overshooting: Reynolds Stress Approach. II. *ApJ*, 416:331.

Canuto, V. M. (1997). Compressible Turbulence. *ApJ*, 482(2):827–851.

Canuto, V. M. and Mazzitelli, I. (1991). Stellar Turbulent Convection: A New Model and Applications. *ApJ*, 370:295.

Chaplin, W. J. and Appourchaux, T. (1999). Depth of excitation and reversal of asymmetry of low-l solar P modes: a complementary analysis of BiSON* and VIRGO/SPM† data. *MNRAS*, 309(3):761–768.

Chaplin, W. J., Elsworth, Y., Isaak, G. R., Miller, B. A., and New, R. (1999). Skew-symmetric solar P modes in low-l BiSON ⁂ data. *MNRAS*, 308(2):424–430.

Chaplin, W. J., Elsworth, Y., and Toutain, T. (2008). A framework for describing correlated excitation of solar p-modes. *Astronomische Nachrichten*, 329(5):440.

Chaplin, W. J., Houdek, G., Elsworth, Y., Gough, D. O., Isaak, G. R., and New, R. (2005). On model predictions of the power spectral density of radial solar p modes. *MNRAS*, 360(3):859–868.

Chen, J. and Beraun, J. (2000). A generalized smoothed particle hydrodynamics method for nonlinear dynamic problems. *Computer Methods in Applied Mechanics and Engineering*, 190(1):225–239.

Chou, P. (1945). On velocity correlations and the solutions of the equations of turbulent fluctuation. *Quarterly of Applied Mathematics*, 3:38–54.

Christensen-Dalsgaard, J. (1981). The effect of non-adiabaticity on avoided crossings of non-radial stellar oscillations. *MNRAS*, 194:229–250.

Christensen-Dalsgaard, J. (1991). *Solar Oscillations and the Physics of the Solar Interior*, volume 388, page 11.

Christensen-Dalsgaard, J. (2004). Physics of solar-like oscillations. *Sol. Phys.*, 220(2):137–168.

Christensen-Dalsgaard, J. (2012). Stellar model fits and inversions. *Astronomische Nachrichten*, 333(10):914.

Christensen-Dalsgaard, J., Bedding, T. R., and Kjeldsen, H. (1995). Modeling Solar-like Oscillations in eta Bootis. *ApJ*, 443:L29.

Christensen-Dalsgaard, J., Dappen, W., Ajukov, S. V., Anderson, E. R., Antia, H. M., Basu, S., Baturin, V. A., Berthomieu, G., Chaboyer, B., Chitre, S. M., Cox, A. N., Demarque, P., Donatowicz, J., Dziembowski, W. A., Gabriel, M., Gough, D. O., Guenther, D. B., Guzik, J. A., Harvey, J. W., Hill, F., Houdek, G., Iglesias, C. A., Kosovichev, A. G., Leibacher, J. W., Morel, P., Proffitt, C. R., Provost, J., Reiter, J., Rhodes, E. J., J., Rogers, F. J., Roxburgh, I. W., Thompson, M. J., and Ulrich, R. K. (1996). The Current State of Solar Modeling. *Science*, 272(5266):1286–1292.

Christensen-Dalsgaard, J. and Gough, D. O. (1975). Nonadiabatic nonradial oscillations of a solar model. *Memoires of the Societe Royale des Sciences de Liege*, 8:309–316.

Christensen-Dalsgaard, J. and Gough, D. O. (1980). Is the Sun helium-deficient? *Nature*, 288(5791):544–547.

Christensen-Dalsgaard, J. and Thompson, M. J. (1997). On solar p-mode frequency shifts caused by near-surface model changes. *MNRAS*, 284(3):527–540.

Compton, D. L., Bedding, T. R., Ball, W. H., Stello, D., Huber, D., White, T. R., and Kjeldsen, H. (2018). Surface correction of main-sequence solar-like oscillators with the Kepler LEGACY sample. *MNRAS*, 479(4):4416–4431.

Cowling, T. G. (1941). The non-radial oscillations of polytropic stars. *MNRAS*, 101:367.

Cowling, T. G. and Newing, R. A. (1949). The Oscillations of a Rotating Star. *ApJ*, 109:149.

Cunningham, T., Tremblay, P.-E., Freytag, B., Ludwig, H.-G., and Koester, D. (2019). Convective overshoot and macroscopic diffusion in pure-hydrogen-atmosphere white dwarfs. *MNRAS*, 488(2):2503–2522.

Das, S. K. and Durbin, P. A. (2005). A Lagrangian stochastic model for dispersion in stratified turbulence. *Physics of Fluids*, 17(2):025109–025109–10.

Deal, M., Escobar, M. E., Vauclair, S., Vauclair, G., Hui-Bon-Hoa, A., and Richard, O. (2017). Asteroseismology of the exoplanet-host F-type star 94 Ceti: Impact of atomic diffusion on the stellar parameters. *A&A*, 601:A127.

Delarue, B. J. and Pope, S. B. (1997). Application of PDF methods to compressible turbulent flows. *Physics of Fluids*, 9(9):2704–2715.

Di Mauro, M. P. (2012). Helioseismology: A fantastic tool to probe the interior of the sun. *Lecture Notes in Physics*.

Di Mauro, M. P., Ventura, R., Corsaro, E., and Lustosa De Moura, B. (2018). The Rotational Shear Layer inside the Early Red-giant Star KIC 4448777. *ApJ*, 862(1):9.

Dintrans, B. and Rieutord, M. (2000). Oscillations of a rotating star: a non-perturbative theory. *A&A*, 354:86–98.

Dolginov, A. Z. and Muslimov, A. G. (1984). Nonradial Stellar Oscillations Excited by Turbulent Convection. *Ap&SS*, 98(1):15–36.

Duong-Hong, D., Phan-Thien, N., and Fan, X. (2004). An implementation of no-slip boundary conditions in DPD. *Computational Mechanics*, 35(1):24–29.

Dupret, M. A. (2001). Nonradial nonadiabatic stellar pulsations: A numerical method and its application to a beta Cephei model. *A&A*, 366:166–173.

Dupret, M. A., Belkacem, K., Samadi, R., Montalban, J., Moreira, O., Miglio, A., Godart, M., Ventura, P., Ludwig, H. G., Grigahcène, A., Goupil, M. J., Noels, A., and Caffau, E. (2009). Theoretical amplitudes and lifetimes of non-radial solar-like oscillations in red giants. *A&A*, 506(1):57–67.

Dupret, M. A., De Ridder, J., Neuforge, C., Aerts, C., and Scuflaire, R. (2002). Influence of non-adiabatic temperature variations on line profile variations of slowly rotating beta Cep stars and SPBs. I. Non-adiabatic eigenfunctions in the atmosphere of a pulsating star. *A&A*, 385:563–571.

Dupret, M. A., Grigahcène, A., Garrido, R., De Ridder, J., Scuflaire, R., and Gabriel, M. (2005a). Time-dependent convection seismic study of δ Sct stars. *MNRAS*, 361(2):476–486.

Dupret, M. A., Grigahcène, A., Garrido, R., De Ridder, J., Scuflaire, R., and Gabriel, M. (2005b). Time-dependent convection seismic study of five γ Doradus stars. *MNRAS*, 360(3):1143–1152.

Dupret, M. A., Grigahcène, A., Garrido, R., Gabriel, M., and Scuflaire, R. (2004). Theoretical instability strips for δ Scuti and γ Doradus stars. *A&A*, 414:L17–L20.

Dupret, M. A., Grigahcène, A., Garrido, R., Gabriel, M., and Scuflaire, R. (2005c). Convection-pulsation coupling. II. Excitation and stabilization mechanisms in δ Sct and γ Dor stars. *A&A*, 435(3):927–939.

Dupret, M. A., Samadi, R., Grigahcene, A., Goupil, M. J., and Gabriel, M. (2006). Non-local time-dependent treatments of convection in A-G type stars. *Communications in Asteroseismology*, 147:85–88.

Duvall, T. L., J., Jefferies, S. M., Harvey, J. W., Osaki, Y., and Pomerantz, M. A. (1993). Asymmetries of Solar Oscillation Line Profiles. *ApJ*, 410:829.

Dziembowski, W. (1977). Oscillating white dwarfs. *Acta Astron.*, 27(1):1–14.

Dziembowski, W. and Koester, D. (1981). Excitation of gravity modes in white dwarfs with chemically stratified envelopes. *A&A*, 97(1):16–26.

Dziembowski, W. A. and Goode, P. R. (1992). Effects of Differential Rotation on Stellar Oscillations: A Second-Order Theory. *ApJ*, 394:670.

Dziembowski, W. A. and Goupil, M. J. (1998). Effects of magnetic activity on solar-like oscillations. In Kjeldsen, H. and Bedding, T. R., editors, *The First MONS Workshop: Science with a Small Space Telescope*, page 69.

Fano, U. (1961). Quantum Theory of Interference Effects in the Mixing of Light from Phase-Independent Sources. *American Journal of Physics*, 29(8):539–545.

Farnir, M., Dupret, M. A., Salmon, S. J. A. J., Noels, A., and Buldgen, G. (2019). Comprehensive stellar seismic analysis. New method exploiting the glitches information in solar-like pulsators. *A&A*, 622:A98.

Favre, A. (1969). Statistical equations of turbulent gases(statistical equations for compressible gas, discussing turbulent quantities separated into fluctuating and macroscopic parts).

Fossat, E., Boumier, P., Corbard, T., Provost, J., Salabert, D., Schmider, F. X., Gabriel, A. H., Grec, G., Renaud, C., Robillot, J. M., Roca-Cortés, T., Turck-Chièze, S., Ulrich, R. K., and Lazrek, M. (2017). Asymptotic g modes: Evidence for a rapid rotation of the solar core. *A&A*, 604:A40.

Fossat, E. and Schmider, F. X. (2018). More about solar g modes. *A&A*, 612:L1.

Frenkel, D., Smit, B., and Ratner, M. A. (1997). Understanding Molecular Simulation: From Algorithms to Applications. *Physics Today*, 50(7):66.

Freytag, B., Ludwig, H. G., and Steffen, M. (1996). Hydrodynamical models of stellar convection. The role of overshoot in DA white dwarfs, A-type stars, and the Sun. *A&A*, 313:497–516.

Freytag, B., Steffen, M., Ludwig, H. G., Wedemeyer-Böhm, S., Schaffenberger, W., and Steiner, O. (2012). Simulations of stellar convection with CO5BOLD. *Journal of Computational Physics*, 231(3):919–959.

Gabriel, A. H., Connerade, J. P., Thiery, S., and Boumier, P. (2001). Application of Fano profiles to asymmetric resonances in helioseismology. *A&A*, 380:745–749.

Gabriel, M. (1992). On the solar p-mode spectrum excited by convection. *A&A*, 265(2):771–780.

Gabriel, M. (1993). The probability-density function of solar P modes and the location of the excitation mechanism. *A&A*, 274:931.

Gabriel, M. (1995). On the profile of the solar p-mode lines. *A&A*, 299:245.

Gabriel, M. (1996). Solar oscillations : theory. *Bulletin of the Astronomical Society of India*, 24:233.

García, R. A., Turck-Chièze, S., Jiménez-Reyes, S. J., Ballot, J., Pallé, P. L., Eff-Darwich, A., Mathur, S., and Provost, J. (2007). Tracking Solar Gravity Modes: The Dynamics of the Solar Core. *Science*, 316(5831):1591.

Gardiner, C. W. (1994). *Handbook of stochastic methods for physics, chemistry and the natural sciences*.

Gelly, B., Lazrek, M., Grec, G., Ayad, A., Schmider, F. X., Renaud, C., Salabert, D., and Fossat, E. (2002). Solar p-modes from 1979 days of the GOLF experiment. *A&A*, 394:285–297.

Georgobiani, D., Kosovichev, A. G., Nigam, R., Nordlund, A., and Stein, R. F. (2000). Numerical Simulations of Oscillation Modes of the Solar Convection Zone. *ApJ*, 530(2):L139–L142.

Georgobiani, D., Stein, R. F., and Nordlund, A. (2003). What Causes p-Mode Asymmetry Reversal? *ApJ*, 596(1):698–701.

Gizon, L. (2006). Line Profiles of Fundamental Modes of Solar Oscillation. *Central European Astrophysical Bulletin*, 30:1–9.

Glatzmaier, G. A. and Roberts, P. H. (1995). A three-dimensional convective dynamo solution with rotating and finitely conducting inner core and mantle. *Physics of the Earth and Planetary Interiors*, 91(1):63–75.

Goldreich, P. and Keeley, D. A. (1977a). Solar seismology. I. The stability of the solar p-modes. *ApJ*, 211:934–942.

Goldreich, P. and Keeley, D. A. (1977b). Solar seismology. II. The stochastic excitation of the solar p-modes by turbulent convection. *ApJ*, 212:243–251.

Goldreich, P. and Murray, N. (1994). The Effects of Scattering on Solar Oscillations. *ApJ*, 424:480.

Goldreich, P., Murray, N., and Kumar, P. (1994). Excitation of Solar p-Modes. *ApJ*, 424:466.

Goode, P. R., Strous, L. H., Rimmele, T. R., and Stebbins, R. T. (1998). On the Origin of Solar Oscillations. *ApJ*, 495(1):L27–L30.

Gough, D. (1977a). *The current state of stellar mixing-length theory*, volume 71, pages 15–56.

Gough, D. O. (1969). The Anelastic Approximation for Thermal Convection. *Journal of Atmospheric Sciences*, 26(3):448–456.

Gough, D. O. (1977b). Mixing-length theory for pulsating stars. *ApJ*, 214:196–213.

Goupil, M. J., Dziembowski, W. A., Goode, P. R., and Michel, E. (1996). Can we measure the rotation rate inside stars ? *A&A*, 305:487.

Graham, E. (1975). Numerical simulation of two-dimensional compressible convection. *Journal of Fluid Mechanics*, 70:689–703.

Grigahcène, A., Dupret, M. A., Gabriel, M., Garrido, R., and Scuflaire, R. (2005). Convection-pulsation coupling. I. A mixing-length perturbative theory. *A&A*, 434(3):1055–1062.

Grigahcène, A., Dupret, M. A., Sousa, S. G., Monteiro, M. J. P. F. G., Garrido, R., Scuflaire, R., and Gabriel, M. (2012). Towards an effective asteroseismology of solar-like stars: time-dependent convection effects on pulsation frequencies. *MNRAS*, 422(1):L43–L47.

Gruberbauer, M., Guenther, D. B., and Kallinger, T. (2012). Toward a New Kind of Asteroseismic Grid Fitting. *ApJ*, 749(2):109.

Gryanik, V. M., Borth, H., and Olbers, D. (2004). The theory of quasi-geostrophic von Kármán vortex streets in two-layer fluids on a beta-plane. *Journal of Fluid Mechanics*, 505:23–57.

Gryanik, V. M. and Hartmann, J. (2002). A Turbulence Closure for the Convective Boundary Layer Based on a Two-Scale Mass-Flux Approach. *Journal of Atmospheric Sciences*, 59(18):2729–2744.

Günther, D. B. (1994). Nonadiabatic Nonradial p-Mode Frequencies of the Standard Solar Model, with and without Helium Diffusion. *ApJ*, 422:400.

Guzik, J. A. and Cox, A. N. (1993). Using Solar p-Modes to Determine the Convection Zone Depth and Constrain Diffusion-produced Composition Gradients. *ApJ*, 411:394.

Guzik, J. A. and Swenson, F. J. (1997). Seismological Comparisons of Solar Models with Element Diffusion Using the MHD, Opal, and Sireff Equations of State. *ApJ*, 491(2):967–979.

Hansen, C. J., Cox, J. P., and van Horn, H. M. (1977). The effects of differential rotation on the splitting of nonradial modes of stellar oscillation. *ApJ*, 217:151–159.

Hartman, P. (2002). *Ordinary Differential Equations*. Society for Industrial and Applied Mathematics, second edition.

Haworth, D. C. and El Tahry, S. H. (1991). Probability density function approach for multidimensional turbulent flow calculations with application to in-cylinder flows in reciprocating engines. *AIAA Journal*, 29:208–218.

Haworth, D. C. and Pope, S. B. (1986). A generalized Langevin model for turbulent flows. *Physics of Fluids*, 29(2):387–405.

Haworth, D. C. and Pope, S. B. (1987). A pdf modeling study of self-similar turbulent free shear flows. *Physics of Fluids*, 30(4):1026–1044.

Heinz, S. (2013). *Statistical Mechanics of Turbulent Flows*. Springer Berlin Heidelberg.

Houdek, G. (1996). *Pulsation of Solar-type stars*. PhD thesis, -.

Houdek, G., Balmforth, N. J., Christensen-Dalsgaard, J., and Gough, D. O. (1999). Amplitudes of stochastically excited oscillations in main-sequence stars. *A&A*, 351:582–596.

Houdek, G. and Dupret, M.-A. (2015). Interaction Between Convection and Pulsation. *Living Reviews in Solar Physics*, 12(1):8.

Houdek, G., Rogl, J., Balmforth, N. J., and Christensen-Dalsgaard, J. (1995). Excitation of Solarlike Oscillations in Main-Sequence Stars. In Ulrich, R. K., Rhodes, E. J., J., and Dappen, W., editors, *GONG 1994. Helio- and Astro-Seismology from the Earth and Space*, volume 76 of *Astronomical Society of the Pacific Conference Series*, page 641.

Houdek, G., Trampedach, R., Aarslev, M. J., and Christensen-Dalsgaard, J. (2017). On the surface physics affecting solar oscillation frequencies. *MNRAS*, 464(1):L124–L128.

Howe, R., Broomhall, A. M., Chaplin, W. J., Elsworth, Y., and Jain, K. (2013). Low-degree multi-spectral p-mode fitting. In *Journal of Physics Conference Series*, volume 440 of *Journal of Physics Conference Series*, page 012011.

Howe, R., Davies, G. R., Chaplin, W. J., Elsworth, Y. P., and Hale, S. J. (2015). Validation of solar-cycle changes in low-degree helioseismic parameters from the Birmingham Solar-Oscillations Network. *MNRAS*, 454(4):4120–4141.

Hsu, A. T., Tsai, Y. L. P., and Raju, M. S. (1994). Probability density function approach for compressible turbulent reacting flows. *AIAA Journal*, 32(7):1407–1415.

Jacoutot, L., Kosovichev, A. G., Wray, A. A., and Mansour, N. N. (2008). Numerical Simulation of Excitation of Solar Oscillation Modes for Different Turbulent Models. *ApJ*, 682(2):1386–1391.

Jefferies, S. M., Severino, G., Moretti, P.-F., Oliviero, M., and Giebink, C. (2003). How Well Can We Infer the Properties of the Solar Acoustic Sources? *ApJ*, 596(1):L117–L120.

Jiménez-Reyes, S. J., Chaplin, W. J., Elsworth, Y., García, R. A., Howe, R., Socas-Navarro, H., and Toutain, T. (2007). On the Variation of the Peak Asymmetry of Low-l Solar p Modes. *ApJ*, 654(2):1135–1145.

Kiefer, R., Komm, R., Hill, F., Broomhall, A.-M., and Roth, M. (2018). GONG p-Mode Parameters Through Two Solar Cycles. *Sol. Phys.*, 293(11):151.

Kippenhahn, R. and Weigert, A. (1994). *Stellar Structure and Evolution*.

Kippenhahn, R., Weigert, A., and Hofmeister, E. (1967). Methods for Calculating Stellar Evolution. *Methods in Computational Physics*, 7:129–190.

Kitiashvili, I. N., Abramenko, V. I., Goode, P. R., Kosovichev, A. G., Lele, S. K., Mansour, N. N., Wray, A. A., and Yurchyshyn, V. B. (2013). Turbulent kinetic energy spectra of solar convection from New Solar Telescope observations and realistic magnetohydrodynamic simulations. *Physica Scripta Volume T*, 155:014025.

Kjeldsen, H., Bedding, T. R., and Christensen-Dalsgaard, J. (2008). Correcting Stellar Oscillation Frequencies for Near-Surface Effects. *ApJ*, 683(2):L175.

Kloeden, P. E. and Pletten, E. (1992). *Numerical solution of stochastic differential equations*. Springer-Verlag Berlin, New-York.

Kolmogorov, A. (1941). The Local Structure of Turbulence in Incompressible Viscous Fluid for Very Large Reynolds' Numbers. *Akademiia Nauk SSSR Doklady*, 30:301–305.

Kolmogorov, A. N. (1962). A refinement of previous hypotheses concerning the local structure of turbulence in a viscous incompressible fluid at high Reynolds number. *Journal of Fluid Mechanics*, 13:82–85.

Korzennik, S. G. (1998). Observational Analysis of Asymmetries in Velocity and Intensity Power Spectra. In Korzennik, S., editor, *Structure and Dynamics of the Interior of the Sun and Sun-like Stars*, volume 418 of *ESA Special Publication*, page 933.

Korzennik, S. G. (2005). A Mode-Fitting Methodology Optimized for Very Long Helioseismic Time Series. *ApJ*, 626(1):585–615.

Korzennik, S. G., Rabello-Soares, M. C., Schou, J., and Larson, T. P. (2013). Accurate Characterization of High-degree Modes Using MDI Observations. *ApJ*, 772(2):87.

Kumar, P. and Basu, S. (1999a). Line Asymmetry of Solar p-Modes: Properties of Acoustic Sources. *ApJ*, 519(1):396–399.

Kumar, P. and Basu, S. (1999b). Line Asymmetry of Solar p-Modes: Reversal of Asymmetry in Intensity Power Spectra. *ApJ*, 519(1):389–395.

Kumar, P. and Basu, S. (2000). Source Depth for Solar P-Modes. *ApJ*, 545(1):L65–L68.

Kupka, F. (2009). 3D stellar atmospheres for stellar structure models and asteroseismology. *Mem. Soc. Astron. Italiana*, 80:701.

Kupka, F. and Montgomery, M. H. (2002). A-star envelopes: a test of local and non-local models of convection. *MNRAS*, 330(1):L6–L10.

Kupka, F. and Muthsam, H. J. (2017). Modelling of stellar convection. *Living Reviews in Computational Astrophysics*, 3(1):1.

Kupka, F. and Robinson, F. J. (2007). On the effects of coherent structures on higher order moments in models of solar and stellar surface convection. *MNRAS*, 374(1):305–322.

Kupka, F., Zaussinger, F., and Montgomery, M. H. (2018). Mixing and overshooting in surface convection zones of DA white dwarfs: first results from ANTARES. *MNRAS*, 474(4):4660–4671.

Kurtz, D. W. (1982). Rapidly oscillating AP stars. *MNRAS*, 200:807–859.

Landau, L. D. and Lifshitz, E. M. (1976). *Mechanics, Third Edition: Volume 1 (Course of Theoretical Physics)*. Butterworth-Heinemann, 3 edition.

Latour, J., Spiegel, E. A., Toomre, J., and Zahn, J. P. (1976). Stellar convection theory. I. The anelastic modal equations. *ApJ*, 207:233–243.

Launder, B. E., Reece, G. J., and Rodi, W. (1975). Progress in the development of a Reynolds-stress turbulence closure. *Journal of Fluid Mechanics*, 68:537–566.

Lazrek, M., Baudin, F., Bertello, L., Boumier, P., Charra, J., Fierry-Fraillon, D., Fossat, E., Gabriel, A. H., García, R. A., Gelly, B., Gouiffes, C., Grec, G., Pallé, P. L., Pérez Hernández, F., Régulo, C., Renaud, C., Robillot, J. M., Roca Cortés, T., Turck-Chièze, S., and Ulrich, R. K. (1997). First Results on it P Modes from GOLF Experiment. *Sol. Phys.*, 175(2):227–246.

Lecoanet, D. and Quataert, E. (2013). Internal gravity wave excitation by turbulent convection. *MNRAS*, 430(3):2363–2376.

Leibacher, J. W. and Stein, R. F. (1971). A New Description of the Solar Five-Minute Oscillation. *Astrophys. Lett.*, 7:191–192.

Leighton, R. B., Noyes, R. W., and Simon, G. W. (1962). Velocity Fields in the Solar Atmosphere. I. Preliminary Report. *ApJ*, 135:474.

Lesieur, M. (2008). *Turbulence in Fluids*.

Li, L. H., Robinson, F. J., Demarque, P., Sofia, S., and Guenther, D. B. (2002). Inclusion of Turbulence in Solar Modeling. *ApJ*, 567(2):1192–1201.

Libbrecht, K. G. (1988). Solar p-Mode Phenomenology. *ApJ*, 334:510.

Libersky, L. D., Petschek, A. G., Carney, T. C., Hipp, J. R., and Allahdadi, F. A. (1993). High Strain Lagrangian Hydrodynamics. A Three-Dimensional SPH Code for Dynamic Material Response. *Journal of Computational Physics*, 109(1):67–75.

Lighthill, M. J. (1952). On Sound Generated Aerodynamically. I. General Theory. *Proceedings of the Royal Society of London Series A*, 211(1107):564–587.

Lignières, F., Rieutord, M., and Reese, D. (2006). Acoustic oscillations of rapidly rotating polytropic stars. I. Effects of the centrifugal distortion. *A&A*, 455(2):607–620.

Liu, M. B. and Liu, G. R. (2010). Smoothed Particle Hydrodynamics (SPH): an Overview and Recent Developments. *Arch Computat Methods Eng*, 17:25–76.

Ludwig, H.-G., Caffau, E., and Kučinskas, A. (2008). Radiation-hydrodynamics simulations of surface convection in low-mass stars: connections to stellar structure and asteroseismology. In Deng, L. and Chan, K. L., editors, *The Art of Modeling Stars in the 21st Century*, volume 252, pages 75–81.

Ludwig, H.-G., Freytag, B., and Steffen, M. (1999). A calibration of the mixing-length for solar-type stars based on hydrodynamical simulations. I. Methodical aspects and results for solar metallicity. *A&A*, 346:111–124.

Magic, Z., Collet, R., Asplund, M., Trampedach, R., Hayek, W., Chiavassa, A., Stein, R. F., and Nordlund, A. (2013). The Stagger-grid: A grid of 3D stellar atmosphere models. I. Methods and general properties. *A&A*, 557:A26.

Magic, Z. and Weiss, A. (2016). Surface-effect corrections for the solar model. *A&A*, 592:A24.

Magic, Z., Weiss, A., and Asplund, M. (2015). The Stagger-grid: A grid of 3D stellar atmosphere models. III. The relation to mixing length convection theory. *A&A*, 573:A89.

Manchon, L., Belkacem, K., Samadi, R., Sonoi, T., Marques, J. P. C., Ludwig, H. G., and Caffau, E. (2018). Influence of metallicity on the near-surface effect on oscillation frequencies. *A&A*, 620:A107.

Mathur, S., Metcalfe, T. S., Woitaszek, M., Bruntt, H., Verner, G. A., Christensen-Dalsgaard, J., Creevey, O. L., Doğan, G., Basu, S., Karoff, C., Stello, D., Appourchaux, T., Campante, T. L., Chaplin, W. J., García, R. A., Bedding, T. R., Benomar, O., Bonanno, A., Deheuvels, S., Elsworth, Y., Gaulme, P., Guzik, J. A., Handberg, R., Hekker, S., Herzberg, W., Monteiro, M. J. P. F. G., Piau, L., Quirion, P. O., Régulo, C., Roth, M., Salabert, D., Serenelli, A., Thompson, M. J., Trampedach, R., White, T. R., Ballot, J., Brandão, I. M., Molenda-Żakowicz, J., Kjeldsen, H., Twicken, J. D., Uddin, K., and Wohler, B. (2012). A Uniform Asteroseismic Analysis of 22 Solar-type Stars Observed by Kepler. *ApJ*, 749(2):152.

Metcalfe, T. S., Chaplin, W. J., Appourchaux, T., García, R. A., Basu, S., Brandão, I., Creevey, O. L., Deheuvels, S., Doğan, G., Eggenberger, P., Karoff, C., Miglio, A., Stello, D., Yildiz, M., Çelik, Z., Antia, H. M., Benomar, O., Howe, R., Régulo, C., Salabert, D., Stahn, T., Bedding, T. R., Davies, G. R., Elsworth, Y., Gizon, L., Hekker, S., Mathur, S., Mosser, B., Bryson, S. T., Still, M. D., Christensen-Dalsgaard, J., Gilliland, R. L., Kawaler, S. D., Kjeldsen, H., Ibrahim, K. A., Klaus, T. C., and Li, J. (2012). Asteroseismology of the Solar Analogs 16 Cyg A and B from Kepler Observations. *ApJ*, 748(1):L10.

Metcalfe, T. S., Creevey, O. L., Doğan, G., Mathur, S., Xu, H., Bedding, T. R., Chaplin, W. J., Christensen-Dalsgaard, J., Karoff, C., Trampedach, R., Benomar, O., Brown, B. P., Buzasi, D. L., Campante, T. L., Çelik, Z., Cunha, M. S., Davies, G. R., Deheuvels, S., Derekas, A., Di Mauro, M. P., García, R. A., Guzik, J. A., Howe, R., MacGregor, K. B., Mazumdar, A., Montalbán, J., Monteiro, M. J. P. F. G., Salabert, D., Serenelli, A., Stello, D., Ste&şacute, licki, M., Suran, M. D., Yildiz, M., Aksoy, C., Elsworth, Y., Gruberbauer, M., Guenther, D. B., Lebreton, Y., Molaverdikhani, K., Pricopi, D., Simoniello, R., and White, T. R. (2014). Properties of 42 Solar-type Kepler Targets from the Asteroseismic Modeling Portal. *ApJS*, 214(2):27.

Meyer, D. W. and Jenny, P. (2007). Consistent inflow and outflow boundary conditions for transported probability density function methods. *Journal of Computational Physics*, 226(2):1859–1873.

Miesch, M. S. (2005). Large-Scale Dynamics of the Convection Zone and Tachocline. *Living Reviews in Solar Physics*, 2(1):1.

Mihalas, D. and Mihalas, B. W. (1984). *Foundations of radiation hydrodynamics*.

Millionshchikov, M. (1941). On the theory of homogeneous isotropic turbulence. In *Dokl. Akad. Nauk SSSR*, volume 32, pages 611–614.

Monaghan, J. J. (1992). Smoothed particle hydrodynamics. *ARA&A*, 30:543–574.

Monaghan, J. J. (1994). Simulating Free Surface Flows with SPH. *Journal of Computational Physics*, 110(2):399–406.

Monin, A. S. and Yaglom, A. (1965). *Statistical fluid mechanics: mechanics of turbulence*. MIT, Cambridge.

Montgomery, M. H. and Kupka, F. (2004). White dwarf envelopes: further results of a non-local model of convection. *MNRAS*, 350(1):267–276.

Morris, J. P., Fox, P. J., and Zhu, Y. (1997). Modeling Low Reynolds Number Incompressible Flows Using SPH. *Journal of Computational Physics*, 136(1):214–226.

Muthsam, H. J., Kupka, F., Löw-Baselli, B., Obertscheider, C., Langer, M., and Lenz, P. (2010). ANTARES - A Numerical Tool for Astrophysical RESearch with applications to solar granulation. *New A*, 15(5):460–475.

Naot, D., Shavit, A., and Wolfshtein, M. (1973). Two-point correlation model and the redistribution of Reynolds stresses. *Physics of Fluids*, 16(6):738–743.

Nigam, R. and Kosovichev, A. G. (1998). Measuring the Sun's Eigenfrequencies from Velocity and Intensity Helioseismic Spectra: Asymmetrical Line Profile-fitting Formula. *ApJ*, 505(1):L51–L54.

Nigam, R. and Kosovichev, A. G. (1999). Phase and Amplitude Difference between Velocity and Intensity Helioseismic Spectra. *ApJ*, 510(2):L149–L152.

Nigam, R., Kosovichev, A. G., Scherrer, P. H., and Schou, J. (1998). Asymmetry in Velocity and Intensity Helioseismic Spectra: A Solution to a Long-standing Puzzle. *ApJ*, 495(2):L115–L118.

Nordlund, A., Stein, R. F., and Asplund, M. (2009). Solar Surface Convection. *Living Reviews in Solar Physics*, 6(1):2.

Oliviero, M., Moretti, P. F., Severino, G., Straus, T., Magrì, M., and Tripicchio, A. (2002). Preliminary Results on the Solar Photospheric Dynamics Observed with Vamos. *Sol. Phys.*, 209(1):21–35.

Otí Floranes, H., Christensen-Dalsgaard, J., and Thompson, M. J. (2005). The use of frequency-separation ratios for asteroseismology. *MNRAS*, 356(2):671–679.

Ouazzani, R. M., Roxburgh, I. W., and Dupret, M. A. (2015). Pulsations of rapidly rotating stars. II. Realistic modelling for intermediate-mass stars. *A&A*, 579:A116.

Pawula, R. F. (1967). Approximation of the Linear Boltzmann Equation by the Fokker-Planck Equation. *Physical Review*, 162(1):186–188.

Pesnell, W. D. (1990). Nonradial, Nonadiabatic Stellar Pulsations. *ApJ*, 363:227.

Philidet, J., Belkacem, K., Samadi, R., Barban, C., and Ludwig, H. G. (2020a). Modelling the asymmetries of the Sun's radial p-mode line profiles. *A&A*, 635:A81.

Philidet, J., Belkacem, K., Ludwig, H. G., Samadi, R., and Barban, C. (2020b). Velocity-intensity asymmetry reversal of solar radial p-modes. *A&A*, 644:A171.

Philidet, J., Belkacem, K., and Goupil, M. J. (2021). Coupling between Turbulence and Solar-like Oscillations: a combined Lagrangian PDF/SPH approach. I – The stochastic wave equation. *arXiv e-prints*, page arXiv:2109.05983.

Pinçon, C., Belkacem, K., and Goupil, M. J. (2016). Generation of internal gravity waves by penetrative convection. *A&A*, 588:A122.

Pope, S. B. (1981). Transport equation for the joint probability density function of velocity and scalars in turbulent flow. *Physics of Fluids*, 24(4):588–596.

Pope, S. B. (1983). A Lagrangian two-time probability density function equation for inhomogeneous turbulent flows. *Physics of Fluids*, 26(12):3448–3450.

Pope, S. B. (1985). PDF methods for turbulent reactive flows. *Progress in Energy and Combustion Science*, 11(2):119–192.

Pope, S. B. (1991). Application of the velocity-dissipation probability density function model to inhomogeneous turbulent flows. *Physics of Fluids A*, 3(8):1947–1957.

Pope, S. B. (1994a). Lagrangian pdf methods for turbulent flows. *Annual Review of Fluid Mechanics*, 26:23–63.

Pope, S. B. (1994b). On the relationship between stochastic Lagrangian models of turbulence and second-moment closures. *Physics of Fluids*, 6(2):973–985.

Pope, S. B. (2000). *Turbulent Flows*.

Pope, S. B. and Chen, Y. L. (1990). The velocity-dissipation probability density function model for turbulent flows. *Physics of Fluids A*, 2(8):1437–1449.

Prentice, A. J. R. and Dyt, C. P. (2003). A numerical simulation of supersonic turbulent convection relating to the formation of the Solar system. *MNRAS*, 341(2):644–656.

Press, W. H. (1981). Radiative and other effects from internal waves in solar and stellar interiors. *ApJ*, 245:286–303.

Rapaport, D. C. (2004). *The Art of Molecular Dynamics Simulation*.

Rast, M. P. (1999). The Thermal Starting Plume as an Acoustic Source. *ApJ*, 524(1):462–468.

Rast, M. P. and Bogdan, T. J. (1998). On the Asymmetry of Solar Acoustic Line Profiles. *ApJ*, 496(1):527–537.

Rast, M. P. and Toomre, J. (1993). Compressible Convection with Ionization. I. Stability, Flow Asymmetries, and Energy Transport. *ApJ*, 419:224.

Reese, D., Lignières, F., and Rieutord, M. (2006). Acoustic oscillations of rapidly rotating polytropic stars. II. Effects of the Coriolis and centrifugal accelerations. *A&A*, 455(2):621–637.

Reese, D. R., Dupret, M.-A., and Rieutord, M. (2017). Non-adiabatic pulsations in ESTER models. In *European Physical Journal Web of Conferences*, volume 160 of *European Physical Journal Web of Conferences*, page 02007.

Reese, D. R., MacGregor, K. B., Jackson, S., Skumanich, A., and Metcalfe, T. S. (2009). Pulsation modes in rapidly rotating stellar models based on the self-consistent field method. *A&A*, 506(1):189–201.

Revenga, M., Zúñiga, I., and Español, P. (1999). Boundary conditions in dissipative particle dynamics. *Computer Physics Communications*, 121-122:309–311.

Revenga, M., Zúñiga, I., Español, P., and Pagonabarraga, I. (1998). Boundary Models in DPD. *International Journal of Modern Physics C*, 9(8):1319–1328.

Richardson, L. F. (1922). *Weather prediction by numerical process*. Cambridge University Press.

Robinson, F. J., Demarque, P., Li, L. H., Sofia, S., Kim, Y. C., Chan, K. L., and Guenther, D. B. (2003). Three-dimensional convection simulations of the outer layers of the Sun using realistic physics. *MNRAS*, 340(3):923–936.

Rodean, H. C. (1996). Stochastic lagrangian models of turbulent diffusion. *Meteorological Monographs*, 26:1–84.

Roekaerts, D. (1991). Use of a Monte Carlo PDF method in a study of the influence of turbulent fluctuations on selectivity in a jet-stirred reactor. *Appl. Sci. Res.*, 48:271–300.

Rosenthal, C. S. (1998). Peaks and Troughs in Helioseismology: The Power Spectrum of Solar Oscillations. *ApJ*, 508(2):864–875.

Rosenthal, C. S., Christensen-Dalsgaard, J., Houdek, G., Monteiro, M. J. P. F. G., Nordlund, A., and Trampedach, R. (1995). Seismology of the Solar Surface Regions. In Hoeksema, J. T., Domingo, V., Fleck, B., and Battrick, B., editors, *Helioseismology*, volume 376 of *ESA Special Publication*, pages 459–464.

Rosenthal, C. S., Christensen-Dalsgaard, J., Nordlund, A., Stein, R. F., and Trampedach, R. (1999). Convective contributions to the frequencies of solar oscillations. *A&A*, 351:689–700.

Rotta, J. (1951). Statistische Theorie nichthomogener Turbulenz. *Zeitschrift fur Physik*, 129(6):547–572.

Roxburgh, I. W. (2005). The ratio of small to large separations of stellar p-modes. *A&A*, 434(2):665–669.

Roxburgh, I. W. and Vorontsov, S. V. (1995). An asymptotic description of solar acoustic oscillations with an elementary excitation source. *MNRAS*, 272(4):850–858.

Roxburgh, I. W. and Vorontsov, S. V. (1997). On the formation of spectral line profiles of solar P modes. *MNRAS*, 292(1):L33–L36.

Roxburgh, I. W. and Vorontsov, S. V. (2003). The ratio of small to large separations of acoustic oscillations as a diagnostic of the interior of solar-like stars. *A&A*, 411:215–220.

Saio, H. and Cox, J. P. (1980). Linear, nonadiabatic analysis of nonradial oscillations of massive near main sequence stars. *ApJ*, 236:549–559.

Samadi, R., Belkacem, K., and Sonoi, T. (2015). Stellar oscillations - II - The non-adiabatic case. In *EAS Publications Series*, volume 73-74 of *EAS Publications Series*, pages 111–191.

Samadi, R. and Goupil, M. J. (2001). Excitation of stellar p-modes by turbulent convection. I. Theoretical formulation. *A&A*, 370:136–146.

Samadi, R., Goupil, M. J., and Lebreton, Y. (2001). Excitation of stellar p-modes by turbulent convection. II. The Sun. *A&A*, 370:147–156.

Samadi, R., Nordlund, A., Stein, R. F., Goupil, M. J., and Roxburgh, I. (2003). Numerical constraints on the model of stochastic excitation of solar-type oscillations. *A&A*, 403:303–312.

Sánchez Cuberes, M., Vázquez, M., Bonet, J. A., and Sobotka, M. (2003). Centre-to-limb variation of solar granulation in the infrared. *A&A*, 397:1075–1081.

Sarkar, S., Erlebacher, G., Hussaini, M. Y., and Kreiss, H. O. (1989). The analysis and modeling of dilatational terms in compressible turbulence. Final Report Institute for Computer Applications in Science and Engineering.

Sato, Y. and Yamamoto, K. (1987). Lagrangian measurement of fluid-particle motion in an isotropic turbulent field. *Journal of Fluid Mechanics*, 175:183–199.

Sawford, B. L. and Borgas, M. S. (1994). On the continuity of stochastic models for the Lagrangian velocity in turbulence. *Physica D Nonlinear Phenomena*, 76(1-3):297–311.

Schlattl, H., Weiss, A., and Ludwig, H. G. (1997). A solar model with improved subatmospheric stratification. *A&A*, 322:646–652.

Schou, J. and Birch, A. C. (2020). Estimating the nonstructural component of the helioseismic surface term using hydrodynamic simulations. *A&A*, 638:A51.

Severino, G., Magrì, M., Oliviero, M., Straus, T., and Jefferies, S. M. (2001). The Solar Intensity-Velocity Cross Spectrum: A Powerful Diagnostic for Helioseismology. *ApJ*, 561(1):444–449.

Severino, G., Straus, T., and Steffen, M. (2008). Velocity and Intensity Power and Cross Spectra in Numerical Simulations of Solar Convection. *Sol. Phys.*, 251(1-2):549–562.

Shih, T. H. and Lumley, J. L. (1986). Second-order modeling of near-wall turbulence. *Physics of Fluids*, 29(4):971–975.

Skartlien, R. and Rast, M. P. (2000). p-Mode Intensity-Velocity Phase Differences and Convective Sources. *ApJ*, 535(1):464–472.

Smagorinsky, J. (1963). General Circulation Experiments with the Primitive Equations. *Monthly Weather Review*, 91(3):99.

Sonoi, T., Belkacem, K., Dupret, M. A., Samadi, R., Ludwig, H. G., Caffau, E., and Mosser, B. (2017). Computation of eigenfrequencies for equilibrium models including turbulent pressure. *A&A*, 600:A31.

Sonoi, T., Ludwig, H. G., Dupret, M. A., Montalbán, J., Samadi, R., Belkacem, K., Caffau, E., and Goupil, M. J. (2019). Calibration of mixing-length parameter α for MLT and FST models by matching with CO^{5}BOLD models. *A&A*, 621:A84.

Sonoi, T., Samadi, R., Belkacem, K., Ludwig, H. G., Caffau, E., and Mosser, B. (2015). Surface-effect corrections for solar-like oscillations using 3D hydrodynamical simulations. I. Adiabatic oscillations. *A&A*, 583:A112.

Soufi, F., Goupil, M. J., and Dziembowski, W. A. (1998). Effects of moderate rotation on stellar pulsation. I. Third order perturbation formalism. *A&A*, 334:911–924.

Soward, A. M. (1972). A Kinematic Theory of Large Magnetic Reynolds Number Dynamos. *Philosophical Transactions of the Royal Society of London Series A*, 272(1227):431–462.

Speziale, C. G., Sarkar, S., and Gatski, T. B. (1991). Modelling the pressure-strain correlation of turbulence - An invariant dynamical systems approach. *Journal of Fluid Mechanics*, 227:245–272.

Spiegel, E. A. (1963). A Generalization of the Mixing-Length Theory of Turbulent Convection. *ApJ*, 138:216.

Spiegel, E. A. and Veronis, G. (1960). On the Boussinesq Approximation for a Compressible Fluid. *ApJ*, 131:442.

Springel, V. (2010). Smoothed particle hydrodynamics in astrophysics. *Annual Review of Astronomy and Astrophysics*, 48(1):391–430.

Stein, R. F. (1967). Generation of Acoustic and Gravity Waves by Turbulence in an Isothermal Stratified Atmosphere. *Sol. Phys.*, 2(4):385–432.

Stein, R. F. and Nordlund, A. (1991). *Convection and Its Influence on Oscillations*, volume 388, page 195.

Stein, R. F. and Nordlund, A. (1998). Simulations of Solar Granulation. I. General Properties. *ApJ*, 499(2):914–933.

Stein, R. F. and Nordlund, A. (2001). Solar Oscillations and Convection. II. Excitation of Radial Oscillations. *ApJ*, 546(1):585–603.

Straka, C. W., Demarque, P., Guenther, D. B., Li, L., and Robinson, F. J. (2006). Space- and Ground-based Pulsation Data of η Bootis Explained with Stellar Models Including Turbulence. *ApJ*, 636(2):1078–1086.

Stratonovich, R. L. (1965). *Topics in the Theory of Random Noise*, volume I and II. New York: Gordon and Breach.

Thiery, S., Boumier, P., Gabriel, A. H., Bertello, L., Lazrek, M., García, R. A., Grec, G., Robillot, J. M., Roca Cortés, T., Turck-Chièze, S., and Ulrich, R. K. (2000). Analysis of asymmetric p-mode profiles in GOLF data. *A&A*, 355:743–750.

Thomson, D. J. (1987). Criteria for the selection of stochastic models of particle trajectories in turbulent flows. *Journal of Fluid Mechanics*, 180:529–556.

Toutain, T. and Appourchaux, T. (1994). Maximum likelihood estimators: an application to the estimation of the precision of helioseismic measurements. *A&A*, 289:649–658.

Toutain, T., Appourchaux, T., Fröhlich, C., Kosovichev, A. G., Nigam, R., and Scherrer, P. H. (1998). Asymmetry and Frequencies of Low-Degree p-Modes and the Structure of the Sun's Core. *ApJ*, 506(2):L147–L150.

Townsend, R. H. D. (2003). Asymptotic expressions for the angular dependence of low-frequency pulsation modes in rotating stars. *MNRAS*, 340(3):1020–1030.

Trampedach, R., Aarslev, M. J., Houdek, G., Collet, R., Christensen-Dalsgaard, J., Stein, R. F., and Asplund, M. (2017). The asteroseismic surface effect from a grid of 3D convection simulations - I. Frequency shifts from convective expansion of stellar atmospheres. *MNRAS*, 466(1):L43–L47.

Trampedach, R., Stein, R. F., Christensen-Dalsgaard, J., and Nordlund, A. (1999). Stellar Evolution with a Variable Mixing-Length Parameter. In Gimenez, A., Guinan, E. F., and Montesinos, B., editors, *Stellar Structure: Theory and Test of Connective Energy Transport*, volume 173 of *Astronomical Society of the Pacific Conference Series*, page 233.

Trampedach, R., Stein, R. F., Christensen-Dalsgaard, J., Nordlund, A., and Asplund, M. (2014). Improvements to stellar structure models, based on a grid of 3D convection simulations - II. Calibrating the mixing-length formulation. *MNRAS*, 445(4):4366–4384.

Tremblay, P. E., Ludwig, H. G., Freytag, B., Fontaine, G., Steffen, M., and Brassard, P. (2015). Calibration of the Mixing-length Theory for Convective White Dwarf Envelopes. *ApJ*, 799(2):142.

Tripathy, S. C., Antia, H. M., Jain, K., and Hill, F. (2009). Comparison of High-Degree Solar Acoustic Frequencies and Asymmetry Between Velocity and Intensity Data. *ApJ*, 691(1):365–371.

Tripathy, S. C., Jain, K., Hill, F., and Toner, C. G. (2003). On the p-mode Asymmetry between Velocity and Intensity from the GONG+ Data. *Bulletin of the Astronomical Society of India*, 31:321–323.

Uhlenbeck, G. E. and Ornstein, L. S. (1930). On the Theory of the Brownian Motion. *Physical Review*, 36(5):823–841.

Ulrich, R. K. (1970). The Five-Minute Oscillations on the Solar Surface. *ApJ*, 162:993.

Unno, W. (1967). Stellar Radial Pulsation Coupled with the Convection. *PASJ*, 19:140.

Unno, W. (1977). *Wave generation and pulsation in stars with convective zones*, volume 71, pages 315–324.

Unno, W. and Kato, S. (1962). On the Generation of Acoustic Noise from the Turbulent Atmosphere, I. *PASJ*, 14:417.

Unno, W., Osaki, Y., Ando, H., Saio, H., and Shibahashi, H. (1989). *Nonradial oscillations of stars*.

Vernazza, J. E., Avrett, E. H., and Loeser, R. (1981). Structure of the solar chromosphere. III. Models of the EUV brightness components of the quiet sun. *ApJS*, 45:635–725.

Viallet, M., Baraffe, I., and Walder, R. (2011). Towards a new generation of multi-dimensional stellar evolution models: development of an implicit hydrodynamic code. *A&A*, 531:A86.

Viallet, M., Goffrey, T., Baraffe, I., Folini, D., Geroux, C., Popov, M. V., Pratt, J., and Walder, R. (2016). A Jacobian-free Newton-Krylov method for time-implicit multidimensional hydrodynamics. Physics-based preconditioning for sound waves and thermal diffusion. *A&A*, 586:A153.

Vögler, A., Shelyag, S., Schüssler, M., Cattaneo, F., Emonet, T., and Linde, T. (2005). Simulations of magneto-convection in the solar photosphere. Equations, methods, and results of the MURaM code. *A&A*, 429:335–351.

Vorontsov, S. V. and Jefferies, S. M. (2013). Modeling Solar Oscillation Power Spectra. II. Parametric Model of Spectral Lines Observed in Doppler-velocity Measurements. *ApJ*, 778(1):75.

Wachter, R. and Kosovichev, A. G. (2005). Properties of the Solar Acoustic Source Inferred from Nonadiabatic Oscillation Spectra. *ApJ*, 627(1):550–561.

Wang, L., Ge, W., and Li, J. (2006). A new wall boundary condition in particle methods. *Computer Physics Communications*, 174(5):386–390.

Welton, W. C. (1998). Two-Dimensional PDF/SPH Simulations of Compressible Turbulent Flows. *Journal of Computational Physics*, 139(2):410–443.

Welton, W. C. and Pope, S. B. (1997). PDF Model Calculations of Compressible Turbulent Flows Using Smoothed Particle Hydrodynamics. *Journal of Computational Physics*, 134(1):150–168.

Willemsen, S. M., Hoefsloot, H. C. J., and Iedema, P. D. (2000). No-Slip Boundary Condition in Dissipative Particle Dynamics. *International Journal of Modern Physics C*, 11(5):881–890.

Wray, A. A., Bensassi, K., Kitiashvili, I. N., Mansour, N. N., and Kosovichev, A. G. (2015). Simulations of Stellar Magnetoconvection using the Radiative MHD Code 'StellarBox'. *arXiv e-prints*, page arXiv:1507.07999.

Xiong, D.-R. (1989). Radiation-hydrodynamic equations for stellar oscillations. *A&A*, 209:126–134.

Xiong, D. R., Cheng, Q. L., and Deng, L. (2000). Turbulent convection and pulsational stability of variable stars: non-adiabatic oscillations of the solar p-modes. *MNRAS*, 319(4):1079–1093.

Yeung, P. K. and Pope, S. B. (1989). Lagrangian statistics from direct numerical simulations of isotropic turbulence. *Journal of Fluid Mechanics*, 207:531–586.

Zahn, J. P. (1991). Convective penetration in stellar interiors. *A&A*, 252:179–188.

Zahn, J. P., Talon, S., and Matias, J. (1997). Angular momentum transport by internal waves in the solar interior. *A&A*, 322:320–328.

Zhou, Y., Asplund, M., and Collet, R. (2019). The Amplitude of Solar p-mode Oscillations from Three-dimensional Convection Simulations. *ApJ*, 880(1):13.

Zhou, Y., Asplund, M., Collet, R., and Joyce, M. (2020). Convective excitation and damping of solar-like oscillations. *MNRAS*, 495(4):4904–4923.

Øksendal Bernt Karsten (1992). *Stochastic differential equations : an introduction with applications / Bernt Øksendal*. Universitext. Springer-Verlag, Berlin New York Paris [etc, 3rd edition edition.

RÉSUMÉ

L'astérosismologie a révolutionné notre compréhension des intérieurs stellaires, grâce à l'observation des oscillations de la surface des étoiles. En ce qui concerne les oscillateurs de type solaire, qui possèdent une enveloppe convective, les mouvements turbulents dus à la convection ont un impact important sur les propriétés des modes acoustiques, tant du point de vue de leur fréquence que de leur amplitude. Ce couplage entre turbulence et oscillations offre une opportunité unique d'utiliser les propriétés observées des modes pour contraindre la convection stellaire – dont les propriétés restent encore relativement mal comprises à ce jour. Cependant, cette tâche nécessite une compréhension théorique solide du couplage en question.
La première partie de cette thèse se concentre sur l'asymétrie exhibée par les profils des modes dans le spectre des oscillateurs de type solaire, qui porte la signature de la localisation de leur source d'excitation proche de la surface de l'étoile. Je présente un formalisme conçu pour fournir des prédictions quantitatives concernant ces asymétries, mais également pour relier directement les asymétries observées aux propriétés sous-jacentes de la convection turbulente dans cette région. Ce formalisme me permet d'apporter un éclairage nouveau sur la question de l'origine physique de l'asymétrie, de son inversion entre les mesures en vitesse et en intensité, ainsi que du ratio entre les amplitudes des modes dans ces deux observables.
Dans une seconde partie, j'examine une nouvelle approche pour la modélisation du couplage entre turbulence et oscillations, fondée sur les modèles de turbulence Lagrangiens stochastiques. Je présente parallèlement des développements analytiques et une implémentation numérique basés sur cette classe de modèles, me permettant de simultanément relier le taux d'excitation des modes p de type solaire, leur taux d'amortissement, ainsi que la partie modale des effets de surface affectant leur fréquence, directement aux propriétés du champ de vitesse turbulent sous-jacent.

MOTS CLÉS

Turbulence, Sismologie, Physique stellaire, Convection

ABSTRACT

Asteroseismology has revolutionised our understanding of stellar interiors, through the observations of oscillations on the surface of stars. In solar-like oscillators, the turbulent motions caused by convection have a substantial impact on the properties of these oscillations, whether on their frequencies or their amplitude. This turbulence/oscillation coupling offers a unique way to constrain the little-understood properties of stellar convection using the observed acoustic mode properties, a task which requires a thorough theoretical understanding of this coupling.
The first part of this thesis focuses on the asymmetry displayed by the line profiles of solar-like oscillations, which carries the signature of the localisation of the driving source close to the surface of the star. I present a formalism designed to give quantitative predictions for solar-like mode asymmetry, and to directly relate the observed asymmetries to the underlying properties of turbulence in this region. This formalism gives us insight into the origin of asymmetry, its reversal between the velocity and intensity observables, as well as on the intensity/velocity amplitude ratios.
In a second part, I more generally investigate a new modelling approach for turbulence/oscillation coupling, based on Lagrangian stochastic models of turbulence. I jointly present analytical developments and a numerical implementation based on this class of models, which allow me to simultaneously relate the excitation rate of solar-like p-modes, their damping rate, as well as the modal surface effects affecting their frequency, directly to the statistical properties of the underlying turbulent velocity field, thus shedding a new light upon the physical processes at hand.

KEYWORDS

Turbulence, Seismology, Stellar physics, Convection